

Geological, fluid-chemical and petrochronological studies of the East Kemptville Sn(-Cu-Zn-Ag-In) deposit and its Devonian host batholith (Nova Scotia, Canada).

by

Luke Bickerton

A thesis submitted in partial fulfillment
of the requirements for the degree of
Doctor of Philosophy (PhD) in
Mineral Deposits and Precambrian Geology

The Faculty of Graduate Studies
Laurentian University
Sudbury, Ontario, Canada

© Luke Bickerton, 2021

Abstract

Primary tin ores form in magmatic-hydrothermal systems related to highly-evolved granites enriched in lithophile elements (e.g., Li, Cs, Rb, U). Causative magmas are sourced from melting (or contamination by) enriched crust, or from melting hydrothermally-altered mantle. These granites form in large, multi-phase complexes (batholiths) and concentrate tin through fractional crystallization. The latter increases volatiles (H₂O, F) in residual melts that are emplaced at shallow crustal depths, and thus the hydrothermal component to Sn-systems. Volatiles exsolve into aqueous fluids that contain soluble Sn²⁺. These fluids typically separate into highly-saline brines and vapours, and precipitate ore (SnO₂) via oxidation of the Sn²⁺. The fluids focus along fractures in the crust and their accumulation is dependent on fluid- versus lithostatic pressures.

The northern Appalachian evolution included incremental emplacement of numerous batholiths and tin occurrences. The largest of these is the South Mountain Batholith (SMB) in Nova Scotia, which was emplaced deep in the crust; although is host to multiple evolved granites, the SMB contains only one significant tin deposit at East Kemptville (EK). To establish the depositional setting of EK at a greater crustal depth, this thesis analyses its geology and fluid chemistry as well as stable (O) and radiogenic (Re-Os, U-Pb, Lu-Hf) isotopes for both EK mineralization and the zircon minerals that represent the SMB. The study addresses the absence of other significant tin deposits in the SMB by evaluating the source of metal endowment.

Due to its deep emplacement, the fluids at EK show no evidence of phase separation, yet abundant evidence of pressure-cycling. The latter allowed for replenishment of ore fluids during deposit formation; whereas initial tin formed via fluid-rock exchange, later ores formed from

mixing with foreign fluids. This segmented hydrothermal evolution at EK is reflected by a range of mineralization ages.

The zircon ages and chemistry indicate: 1) the SMB formed over 15-20 m.y. from altered mantle melts that underwent contamination by host rocks; and 2) the EK host is temporally and isotopically distinct from the SMB, and likely evolved from a lower crust-derived melt. The distinct source suggests other tin occurrences in the region share a similar origin.

Keywords

tin; granite; greisen; magmatic-hydrothermal; fluid inclusion; mineralization; zircon petrochronology; U-Pb geochronology; O isotope; Lu-Hf isotope; South Mountain Batholith; East Kemptville

Statement of co-authorship

This thesis consists of three separate manuscripts prepared for publication in peer-reviewed journals. Chapters two, three and four have been co-authored by the candidate and additional collaborators. Chapter two is intended for submission in *Economic Geology* or *Ore Geology Reviews* in Fall 2021. Chapter three is intended for submission to *Economic Geology* in Fall 2021. Chapter four is intended for submission *Canadian Journal of Earth Sciences* in Summer 2021.

The thesis was designed by Dr. Daniel Kontak, Dr. Iain Samson, Dr. Brendan Murphy and the candidate, as part of a Collaborative Research and Development (CRD) grant between the Natural Sciences and Engineering Research Council (NSERC) of Canada and Avalon Advanced Materials Inc. Financial and/or logistical support provided by strategic industry and government supporters (Chapter two – Avalon Advanced Materials Inc., NSERC; Chapter three – Avalon Advanced Materials Inc., NSERC; Chapter four – NSERC, Natural Resources Canada). All fieldwork, sample collection, sample preparation, petrography, and interpretation of analytical results were completed by the candidate with guidance by Drs. Daniel Kontak, Iain Samson, and Brendan Murphy. Dr. Daniel Kontak provided additional petrographic, geochemical, and microthermometric data he produced for the Nova Scotia Department of Natural Resources. Avalon Advanced Materials, Inc. provided access to drill core, the East Kemptville mine open-pit, drill logs, as well as geochemical and assay data. All chapters were edited by Drs. Kontak and Samson. Additional collaboration, technical support, expertise and constructive criticism was provided by co-authors listed herein.

Chapter two is co-authored by Daniel Kontak, Iain Samson, Brendan Murphy, Robert Creaser, Christopher Holm-Denoma. Fieldwork, sample selection and sample preparation were

completed by the candidate. The isotopic analytical work in this chapter was conducted by Drs. Creaser (Re-Os molybdenite) and Holm-Denoma (U-Pb cassiterite). Financial and logistical support for sample collection was coordinated by Bill Mercer and provided by Avalon Advanced Materials Inc. and NSERC.

Chapter three is co-authored by Daniel Kontak, Iain Samson, Zoltán Zajacz, Mitchell Kerr, and Mostafa Fayek. Fieldwork, sample selection and sample preparation were completed by the candidate. Fluid inclusion geochemical and laser Raman analytical work was performed by the candidate, with supervision by Drs. Zajacz, and Kerr, respectively. The O isotopic analytical work on quartz in this chapter was conducted by Dr. Fayek. Financial and logistical support for sample collection and analysis was coordinated by Bill Mercer and provided by Avalon Advanced Materials Inc. and NSERC.

Chapter four is co-authored by Daniel Kontak, Brendan Murphy, Dawn Kellett, Iain Samson, Jeffrey Marsh, Greg Dunning, and Richard Stern. Fieldwork, sample selection and sample preparation were completed by the candidate. The isotopic analytical work in this chapter was conducted by: the candidate for U-Pb zircon (SHRIMP-II), with supervision by Dr. Kellett, and U-Pb, Lu-Hf (including trace element) zircon, with supervision by Dr. Marsh; Dr. Dunning for U-Pb zircon (CA-ID-TIMS, including sample preparation); and Dr. Stern for O in zircon (SIMS, including sample preparation). Financial and logistical support for fieldwork, sample preparation, and analysis was provided by NSERC and National Resources Canada.

All manuscripts were edited by Drs. Daniel Kontak and Iain Samson (coauthors). Chapter four was also edited by Drs. Brendan Murphy and Dawn Kellett (coauthors).

Acknowledgments

I would like to thank my supervisors Daniel Kontak, Iain Samson, and Brendan Murphy for their mentorship, patience, and support throughout this project. Their thoughtful input and guidance have helped me develop into a well-rounded geoscientist. Their feedback and reviews of the project content have significantly improved the quality of the manuscripts in this thesis and have made me a better researcher. I would like to thank Dr. Alan Galley for acting as my internal examiner and Dr. Reimar Seltmann for acting as external examiner to provide thoughtful feedback and improve this thesis.

This project was funded through a Collaborative Research and Development grant between the Natural Sciences and Engineering Research Council (NSERC) of Canada and Avalon Advanced Materials Inc. I would like to recognize the support from Avalon Advanced Materials Inc. for getting me into the East Kemptville deposit to complete sample collection and field observations. Specifically, I would like to thank Bill Mercer for making this project possible.

Having completed my PhD partially based out of Saint Mary's University in Halifax, NS, I would like to warmly thank the SMU faculty and staff that have provided advice and technical support, including Jacob Hanley, Mitch Kerr, Fergus Tweedale, and Tara Inman.

Where I am today is largely a result of the encouragement and support of my family and close friends. I would like to thank my parents for their support throughout my academic career. I am grateful to both of you for everything.

Table of Contents

Abstract.....	iii
Statement of co-authorship	v
Acknowledgments.....	vii
Table of Contents.....	viii
List of Tables	xiii
List of Figures.....	xv
List of Electronic Appendices.....	xx
Chapter 1.....	1
Introduction to thesis.....	1
1.1 Background.....	1
1.2 Research Problems.....	5
1.3 Thesis objectives.....	8
1.4 Structure of thesis	10
1.5 Statement of original contributions.....	11
1.6 References.....	13
Chapter 2.....	20
Petrochronological constraints on the generation and assembly of the Late Devonian peraluminous South Mountain Batholith, Nova Scotia, Canada with implications for metallogenic inheritance.	20
2.1 Abstract.....	20
2.2 Introduction.....	21
2.3 Regional Geology	26
2.4 The South Mountain Batholith.....	29
2.4.1 Stage 1 Plutons.....	30

2.4.2 Stage 2 Plutons.....	32
2.5 Analytical Techniques.....	35
2.5.1 Mineral Separation and Sample Preparation.....	35
2.5.2 U-Pb Geochronology	37
2.5.3 Lu-Hf Isotopic Compositional Determination by LA-MC-ICP-MS	40
2.5.4 Oxygen Stable Isotope Determinations by SIMS	42
2.6 Results	44
2.6.1 Zircon Characterization	44
2.6.2 U-Pb Age Determinations: Preamble.....	45
2.6.3 U-Pb Age Determinations Results	47
2.6.4 Zircon Trace- and Rare Earth Element Compositions	51
2.6.5 Oxygen Stable Isotopic Composition of Zircon	58
2.6.6 Hf Isotopic Composition of Zircon.....	59
2.7 Discussion.....	63
2.7.1 Zircon chemistry and implications for magma evolution	63
2.7.2 Isotopic constraints on SMB magma source.....	69
2.7.3 Construction and evolution of the South Mountain Batholith.....	77
2.7.4 Implications for the tectonic setting of SMB emplacement.....	82
2.7.5 Metallogenic implications.....	87
2.8 Conclusions.....	89
2.9 Acknowledgements	92
2.10 References	92
Chapter 3.....	185
The East Kemptville Mesothermal Greisen-Hosted Sn-Zn-Cu-Ag-In Deposit, Nova Scotia, Canada: One ore body with two deposits	185

3.1 Abstract.....	185
3.2 Introduction.....	187
3.3 Geologic Setting and Related Mineralization	190
3.3.1 Regional geology	190
3.3.2 Geology of the Meguma terrane	190
3.3.3 Geology and mineralization of the SW Meguma terrane	193
3.3.4 The SW Nova Scotia Sn base-metal domain	195
3.4 The East Kemptville tin deposit.....	197
3.4.1 Discovery and previous studies	198
3.4.2 Host rocks	199
3.4.3 Alteration	203
3.4.4 Mineralization	207
3.4.5 Structure.....	213
3.5 Lithogeochemistry	216
3.5.1 Major element chemistry – Unmineralized rocks.....	217
3.5.2 Trace element chemistry	218
3.5.3 Rare-earth element (REE) chemistry	219
3.5.4 Major element chemistry – Mineralized rocks	220
3.6 Geochronology.....	221
3.6.1 Re-Os molybdenite dating	221
3.6.2 In situ U-Pb cassiterite dating	223
3.7 Discussion	225
3.7.1 Nature of the EKL and its role in deposit formation	225
3.7.2 Geological features and implications on ore zone formation	229
3.7.3 Structural evolution of the deposit.....	238

3.7.4 Implications of whole-rock lithochemistry for the EKL.....	241
3.7.5 Implications of geochronology for magmatic and hydrothermal events in the East Kemptville deposit area	248
3.7.6 An updated model for the East Kemptville Sn deposit.....	252
3.7.7 Source of Sn.....	256
3.8 Conclusions	258
3.9 Acknowledgments.....	261
3.10 References	261
Chapter 4.....	346
Geochemical constraints of ore-forming fluids in a mesothermal Sn-Zn-Cu-Ag-In deposit, East Kemptville, Nova Scotia (Canada).....	346
4.1 Abstract	346
4.2 Introduction	347
4.3 Geological Setting.....	352
4.3.1 Regional and Local Geological Setting	352
4.3.2 Davis Lake Pluton and East Kemptville Deposit.....	354
4.3.3 East Kemptville Mineralization and Paragenesis	356
4.4 Methods.....	357
4.4.1 Petrography	357
4.4.2 Microthermometry	357
4.4.3 Evaporate mound analysis	359
4.4.4 Confocal Laser Raman Microspectroscopy	359
4.4.5 LA-ICP-MS analysis.....	360
4.4.6 O isotopes.....	362
4.5 Results	363
4.5.1 Fluid inclusion petrography and types.....	363

4.5.2 Features of inclusions and microthermometric data	365
4.5.3 Evaporate mound analysis	368
4.5.4 LA-ICP-MS analysis.....	370
4.5.5 Confocal Laser Raman Microspectroscopy	371
4.5.6 O isotopes.....	372
4.6 Discussion	374
4.6.1 PT conditions during paragenetic evolution	375
4.6.2 Fluid chemistry	382
4.6.3 Implications of $\delta^{18}\text{O}$ data	389
4.6.4 Implications of anomalous salinity in East Kemptville Fluid Types	395
4.6.5 Cassiterite precipitation at the EKD	400
4.7 Conclusions	405
4.8 Acknowledgements	407
4.9 References.....	407
Chapter 5.....	490
5.1 Conclusions	490
5.2 Future Work	493

List of Tables

Table 2–1. South Mountain Batholith Historical Geochronology	178
Table 2–2. Summary of dated samples, zircon/monazite characteristics.....	179
Table 2–3. Compiled in situ zircon U-Pb Age determinations (antecrysts and autocrysts).....	181
Table 2–4. Coordinates and mean $^{206}\text{Pb}/^{238}\text{U}$ ages for CA-TIMS samples in this study.	182
Table 2–5. Summary of trace element data zircon domains in the SMB.....	183
Table 2–6. Summary of SIMS ^{18}O isotopes on zircon from the South Mountain Batholith	184
Table 3-1. Whole-rock major, minor, and rare-earth element abundances.....	342
Table 3-2. Re-Os Isotope Data for the East Kemptville molybdenite samples.....	343
Table 3-3. U-Pb Cassiterite Summary of East Kemptville and Duck Pond samples.....	344
Table 3-4. Historic geochronology of the DLP and EKL.	345
Table 4-1. Sn-W global deposit analogues for mineralizing fluids.....	484
Table 4-2. Summary of fluid inclusion types and properties in quartz and topaz.....	485
Table 4-3. Summary of results from LA-ICP-MS analyses of FIAs.	486
Table 4-4. Raman spectra for vapor phases of aqueous-carbonic inclusions.....	487
Table 4-5. $\delta^{18}\text{O}_{\text{V-SMOW}}$ results from SIMS analyses on quartz.	488

Table 4-6. $\delta^{18}\text{O}_{\text{V-SMOW}}$ results from TIMS analysis.....489

List of Figures

Figure 2-1. Regional tectonic affinity and magmatism in the northeast Appalachians.	136
Figure 2-2. Summary of tectono-stratigraphic relationships in the Canadian Appalachians.....	138
Figure 2-3. Representative bedrock geology and magmatic textures from the SMB.....	140
Figure 2-4. Representative images of zircon grains from the SMB.....	142
Figure 2-5. CL images of SMB zircons with interpreted domain types.	144
Figure 2-6. Summary of the inherited xenocrystic core age populations.	146
Figure 2-7. Compiled $^{206}\text{Pb}/^{238}\text{U}$ SHRIMP-II and CA-ID-TIMS ages of zircon from SMB.....	148
Figure 2-8. Concordia plots for SHRIMP-II zircon analyses.	150
Figure 2-9. Tera-Wasserburg concordia plots for LA-MC-ICP-MS zircon analyses.....	152
Figure 2-10. Concordia plots SMB zircons analyzed by CA-TIMS analysis.....	154
Figure 2-11. Trace element data for xenocrystic domains in SMB zircons.....	156
Figure 2-12. Trace element data for antecrystic and autocrystic domains in SMB zircons.	158
Figure 2-13. REE and Ti data for zircons from the SMB.....	160
Figure 2-14. Oxygen fugacity versus Ti-in-zircon temperatures for zircons from the SMB.....	162
Figure 2-15. Histograms of zircon $\delta^{18}\text{O}$ values for samples from plutons of the SMB.....	164

Figure 2-16. $\epsilon_{\text{Hf}}(t)$ versus $^{176}\text{Lu}/^{177}\text{Hf}$ for zircons from the SMB.	166
Figure 2-17. $\epsilon_{\text{Hf}}(t)$ vs. age plot for zircon from the SMB	168
Figure 2-18. $\delta^{18}\text{O}$ versus $\epsilon_{\text{Hf}}(t)$ for SMB zircon domains.....	170
Figure 2-19. Probability density plots of SMB xenocrystic zircon and regional wall-rocks.....	172
Figure 2-20. Schematic emplacement model for the South Mountain Batholith.....	174
Figure 2-21. Schematic geotectonic setting during SMB formation.	176
Figure 3-1. Tectonic terrane map of the northeastern Appalachians.	292
Figure 3-2. Regional geology of SW Nova Scotia.....	294
Figure 3-3. Plan view of EKL and the East Kemptville deposit.....	296
Figure 3-4. Grid mapping of the NE part of the East Kemptville mine (Main Zone).	298
Figure 3-5. Hand sample and outcrop photographs of East Kemptville host leucogranite.	300
Figure 3-6. Drill core and outcrop photographs of host granite and breccias from Baby Zone.	302
Figure 3-7. Schematic cross sections of both ore zones and example true section.....	305
Figure 3-8. Photograph and photomicrographs of deuterically altered host granite.....	307
Figure 3-9. Drill core, hand sample and outcrop photos of greisen development in the EKL. .	309
Figure 3-10. Plate of photomicrographs of greisens from the East Kemptville	311

Figure 3-11. Detailed paragenesis of the East Kemptville deposit	313
Figure 3-12. Photomicrographs of mineralized samples from the East Kemptville deposit.	315
Figure 3-13. Stitched SEM-EDS image of a zoned greisen in the East Kemptville deposit.	317
Figure 3-14. Example photographs of mineralized veins in the deposit.....	319
Figure 3-15. Example photographs of late-stage veins.....	321
Figure 3-16. Outcrop photographs with structural features of the East Kemptville deposit.	323
Figure 3-17. Whole rock lithogeochemistry of least-altered rocks in the deposit.	326
Figure 3-18. Alkali elements versus ore metals in all samples from the deposit.....	328
Figure 3-19. Tera-Wasserburg concordia diagrams for U-Pb cassiterite.....	330
Figure 3-20. Modified Pearce-element ratio diagrams for aluminosilicate mineral content.	332
Figure 3-21. Granite fertility discrimination diagram of Nb/Ta vs. Zr/Hf.	334
Figure 3-22. Compiled Re-Os molybdenite and U-Pb cassiterite mineralization ages.	336
Figure 3-23. Schematic formation model for the East Kemptville Sn-Cu-Zn-Ag-In deposit....	338
Figure 3-24. Multi-element plots for EKL and regional Meguma Metasedimentary rocks.	340
Figure 4-1. Regional geology of SW Nova Scotia and the East Kemptville deposit.	444
Figure 4-2. Outcrop photographs with structural features of the EKD.....	446

Figure 4-3. Summary paragenesis of the East Kemptville deposit	448
Figure 4-4. Hand sample photographs of mineralization at East Kempville.	450
Figure 4-5. Images of quartz thick-sections with a range of fluid inclusion content.....	452
Figure 4-6. H ₂ O-[Fe,Mn]Cl ₂ -NaCl phase diagram with FIA microthermometric data.	454
Figure 4-7. SEM images of induced decrepitate salt mounds.....	456
Figure 4-8. Example methodology for LA-ICP-MS analysis of fluid inclusions.....	458
Figure 4-9. Photomicrographs of fluid inclusions hosted by the deposit.....	460
Figure 4-10. Homogenization temperatures and salinities of East Kemptville FIAs.	462
Figure 4-11. Relative and absolute element concentrations of evaporate mounds.....	464
Figure 4-12. Trace element concentration of FIAs determined by LA-ICP-MS analysis.	466
Figure 4-13. Raman spectra (at 22°C) for aqueous carbonic fluid inclusions.	468
Figure 4-14. Comparative plots of $\delta^{18}\text{O}$ for quartz through the paragenesis.	470
Figure 4-15. Th(total) histograms, P–T plots and calculated isochores for each fluid type.	472
Figure 4-16. Th(halite) versus Th(liquid) for East Kemptville fluids and global analogues.....	474
Figure 4-17. Schematic evolution of fluid inclusion entrapment through paragenesis.	476
Figure 4-18. Ore metals relative to primary elements in the fluids through the paragenesis. ...	478

Figure 4-19. K/Rb versus various metals for fluid types through the paragenesis.480

Figure 4-20. Temperature versus $\delta^{18}\text{O}_{(\text{quartz})}$ through the deposit paragenesis. 482

List of Electronic Appendices

Chapter 2

Table EA 2-1: SHRIMP-II zircon data (U-Pb)

Table EA 2-2: CA-ID-TIMS zircon and monazite data (U-Pb)

Table EA 2-3: LA-MC-ICP-MS zircon data (U-Pb, trace elements)

Table EA 2-2: O isotope zircon SIMS data

Table EA 2-3: LA-MC-ICP-MS zircon data (Lu-Hf)

Chapter 3

Table EA 3-1: Compilation of geochronologic data from SW Nova Scotia

Table EA 3-2: Compiled whole rock litho geochemistry from the East Kemptville deposit

Table EA 3-3: U-Pb cassiterite geochronology LA-ICP-MS data

Chapter 4

Table EA 4-1: Microthermometric data on fluid inclusions

Table EA 4-2: Fluid inclusion evaporate mound SEM-EDS analytical results

Table EA 4-3: LA-ICP-MS analytical results from fluid inclusions

Chapter 1

Introduction to thesis

1.1 Background

Granitoid related ore deposits concentrate a range of elements that is more diverse than any other magmatic related deposits and occur in three broad categories (cf. Černý et al., 2005):

disseminated magmatic mineralization (Zr, Nb, REE, Y, U, Li, Sn, Cu, Au, W, and Ta); late magmatic-associated pegmatites (Li, REE, Rb, Cs, Be, Sn, and Ta); and magmatic-hydrothermal mineralization associated with veins, breccias, and greisens in and around intruding granites (Sn, W, Cu, and Mo). These latter deposits are additionally an important source of critical metals (e.g., Li, B, Be, In, Ge and Ga), which are defined as elements that are essential in industrial and high-technology applications and where global supply is limited or vulnerable. The increasing demand for refined Sn and critical metals (for use in solder, chemicals, tinplate, lead acid batteries, and copper alloys) necessitates further constraints on genetic factors controlling tin precipitation in various granitoid intrusive settings that will better the approach of exploration and extraction.

Three topics relevant to Sn mineralization are addressed in this thesis: (1) the lithochemical and structural controls over mineralization style in geologic settings that are atypical of known

tin districts globally; (2) the chemical evolution of hydrothermal fluids through pressure-temperature conditions that mineralization occurs; and (3) the character of the source and timing of emplacement for magmatism enriched in granophile elements that localize mineralized centres and define metallotects.

Cassiterite (SnO_2) is the predominant tin ore mineral and greisen deposits are the predominant style of tin deposit. Worldwide, cassiterite forms in greisens that typically evolve by interaction of orthomagmatic fluids and host rock under high temperatures (200-500°C; e.g., Naumov, 2011) and in high-level settings (i.e., <1 kbar). The host granites are typically highly fractionated, relatively K rich, metaluminous to peraluminous, part of the ilmenite series of granitoids (i.e., magmas with low oxygen fugacity values ($f\text{O}_2$); e.g., Ishihara, 1981; Blevin and Chappell, 1992; Linnen et al., 1996), and enriched in Sn, F, and other incompatible elements. The high degree of fractionation in the ore-forming melts is facilitated by volatiles that depolymerize the magma (e.g., F, Li, P, B; e.g., Pichavant et al., 1987; Černý, 1991; London, 1992; Raimbault et al., 1995) and the resultant orthomagmatic fluids are rich in ligands such as Cl, F, OH⁻, and H₂S.

Ore precipitation is initiated by significant changes in the physicochemical conditions of mineralizing fluids in greisenized host rocks. These changes cause destabilization of metal complexes in solution and the controlling variables include: temperature, pressure, pH (neutralization), and/or $f\text{O}_2$. The physicochemical variables are influenced by either a mixing process between hot metal-bearing fluids and cold, unmineralized external fluids (fluid-fluid

interaction, e.g., Mole Granite, Australia; Heinrich et al., 1999), or by either a redox or chemical reaction between a mineralizing fluid with host rocks (e.g., Fe and Ca in wall-rock reacting to W-bearing fluids forming wolframite and scheelite, Panasqueira, Portugal; Lecumberri-Sanchez et al., 2017).

To constrain the controls on ore deposition in primary tin deposits, studies that focus on the analysis of fluid inclusions are conducted. A compilation of determinations from tin greisens in these studies have generally found mineralizing fluids to be acidic and two-phase aqueous-carbonic with a highly variable gas content; with average compositions of volatile components to be, in decreasing abundance, CO₂, CH₄, N₂, and H₂S (e.g., Naumov, 2011; Bodnar et al., 2014). This range of volatiles is compatible with a metamorphic origin (i.e., metasedimentary), however, the typical salinity of mineralizing fluids in tin deposits suggests the presence of magmatic hypersaline brines (cf. Audétat et al., 2000). Likewise, stable isotopic signatures of mineralizing fluids in these deposits are variable, having recorded fluid equilibration with various rocks in their respective hydrothermal systems (e.g., Kelly and Rye, 1979; Sun and Eadington, 1987; Wilkinson et al., 1995; Vallance et al., 2001); reflective of heterogeneous fluid/rock interaction.

Mineralizing fluids that form greisens in Sn-W systems typically focus along permeable structures or within lithologic units that allow fluid migration (cf. Lehmann, 2020); thus, greisens essentially represent post-magmatic metasomatism of host rocks. They occur as lenses that are

subparallel to intrusive contacts along granitic cupulas or along fracture sets that act as fluid-pathways; ore concentrates at the intersects of these two, where maximum fluid-rock interaction is available (e.g., Pirajno, 2012; Lehmann, 2020). Host rock permeability, however, is a dynamic parameter that evolves over time and is influenced by geologic processes such as: deformation, fracturing, fluid overpressure, dissolution/precipitation, and/or hydrothermal alteration.

The global distribution of granitoid-related tin deposits suggests these systems mainly form in late-orogenic tectonic settings (cf. Jébrak and Marcoux, 2008). The spatio-temporal distribution of tin deposits that are exploited today is dominantly in late Paleozoic rocks of the Hercynian orogeny (e.g., the Iberian province, the English Cornwall, the Armorican, Central and Bohemian massifs; Štemprok, 1981; Romer and Kroner, 2016) and Mesozoic to Cenozoic rocks of the Cimmerian orogeny (e.g., the Southeast Asian Tin Belt; Schwartz et al., 1995; Hou and Zhang, 2014). In each setting, the granites that form these deposits typically have partial generation and/or contamination from aluminous crustal rocks (i.e., metapelite continental crust) that are thickened at the loci of melting during orogenic activity (Clark et al., 2011; Romer and Kroner, 2016). Additionally, the pre-concentration of metals in each region is both suggested to be a result of recycling lithophile element-enriched crustal rocks (e.g., Romer and Kroner, 2016), and/or a result of mantle input; via magma mixing or metasomatism by mantle-derived fluids (e.g., Walshe et al., 2011; Simons et al., 2016).

In the northern Appalachians, granitic magmatism is a key feature that is associated with a variety of base- and critical-metal mineralized centres (e.g., Cu, W-Mo, Sn, Sb, and Ta; c.f. van Staal, 2007) that span both time (ca. 410 to 360 Ma) and space (from Atlantic Canada to eastern Quebec). A number of these mineralized centres are past producers of global significance; e.g., Mt. Pleasant, New Brunswick (W-Mo); Lake George, New Brunswick (Sb); Gaspé Cu, Québec (Cu); and East Kemptville, Nova Scotia (Sn). Although these deposits collectively define a granophile element enriched metallogenic province, East Kemptville represents the only significant Sn mineralized centre that has been discovered in the region. The regional geology in southern Nova Scotia, where the East Kemptville Sn-Cu-Zn-Ag(-In) deposit is located, is similar to that found in the metallogenic provinces noted above; i.e., dominated by metasedimentary rocks and metaluminous to peraluminous granitoid intrusions emplaced syn- to post-tectonically (van Staal, 2007; Kellett et al., in press). Emplacement of peraluminous granites related to the East Kemptville deposit was accompanied by lesser dioritic, gabbroic, and lamprophyric magmatism, indicative of some co-spatial mantle input at this time (e.g., Clarke et al., 1997).

1.2 Research Problems

The characteristics of the East Kemptville deposit both overlap and depart from those of other analogous deposits. The local geology is dominated by the Meguma Supergroup and the South Mountain Batholith (SMB); in which the deposit is hosted by one of the most fractionated phases, the East Kemptville leucogranite (EKL). The EKL has a geochemical signature like

some fractionated granites, but a REE depletion (e.g., $L_{AN} < 5$) and an anomalous enrichment in F, Li, and Rb (e.g., Kontak, 1990). The EKL is related to a northeast-trending, sub-vertical brittle-ductile shear zone. Zoned and massive greisens are hosted along this shear zone and within a step-over feature along the same structural corridor (e.g., Halter et al., 1996). The deposit comprises two main ore zones along the corridor with contrasting character; thus, understanding the constraints on the structural evolution of the two ore zones is critical to better defining the extent and geometry of the deposit as well as the exploration for additional mineralized zones. Furthermore, the age of mineralization remains poorly constrained at East Kemptville, compared to other mineralized centres in the SMB; Re-Os molybdenite ages at ca. 371 ± 3 Ma, ca. 5 Ma younger than the batholith, have been reported in the central SMB (Selby and Creaser, 2004), but remain unexplained in a regional context. A single Re-Os age of 376 ± 3 Ma (Kontak et al., 2003) for a pegmatite (pre-greisen) sample in one of the ore zones at East Kemptville provides a maximum age for mineralization, although it is much older than a Pb-Pb isochron age of 366 ± 4 Ma obtained for the greisens in the deposit (Kontak and Chatterjee, 1992). Thus, the age of mineralization at East Kemptville needs refining based on both ore zones and interpretation compared to other mineralized centres in the SMB and rest of the metallotect.

The depth of deposit formation that is indicated by a majority of fluid inclusions through the paragenesis (ca. 3-4 kbars) is unusually high for such systems (e.g., Sinclair, 2007), in addition to contrasting with the low pressures that are indicated by hydrothermal collapse breccias that

dominate one of the ore zones at East Kemptville. Several fluid inclusion studies have provided a basis for understanding the pressure-temperature evolution of the hydrothermal system (i.e., Richardson, 1988; Richardson et al., 1989; Kontak, 1993), and these studies also used isotopic analysis (O, S, Sr) to understand the geochemical evolution of hydrothermal fluids in the deposit. These studies have suggested the East Kemptville hydrothermal evolution involved an orthomagmatic fluid, element exchange with the metasedimentary wall-rocks, and input from meteoric fluids. However, to adequately define the chemical composition of hydrothermal fluids in the deposit, the use of LA-ICP-MS analysis of well-defined individual fluid inclusion assemblages is required.

The sources of enrichment proposed for causative magmas associated with tin deposits include melting of heterogeneous mantle and either anatexis of, or contamination by, Sn-enriched supracrustal material. Typically, such magmas form incrementally as voluminous composite batholiths that host multiple deposits (described above). The SMB is a composite intrusion and, despite the considerable number of petrological studies that were conducted on it, there is a paucity of precise U-Pb geochronologic constraints on its emplacement. Thus, to interpret sources for the SMB and mineralized centres in the complex, defining the age range (i.e., duration of construction) by U-Pb zircon analysis and the chemical composition of the zircons from the various intrusive phases is required.

1.3 Thesis objectives

The primary objective of this thesis is to better understand tin deposit formation in a metasedimentary rock-hosted mesothermal intrusive setting, and to improve the understanding of geologic and metallogenic controls on mineralization in these settings. The following specific research questions will be addressed herein:

- 1) What are the geochemical and structural controls to the East Kemptville tin deposit, and why are there two ore zones of contrasting lithologic character?
 - a. Is the host leucogranite at East Kemptville the source for metals in the deposit or was metal enrichment brought by hydrothermal alteration and sourced elsewhere?
 - b. What is the influence of the East Kemptville shear zone on localization of mineralization and what are the implications on delineation of the ore resource?
 - c. Is there a genetic or timing difference in the mineralization between the two ore zones at East Kemptville?
- 2) What is the character and evolution of mineralizing fluids that formed the East Kemptville deposit, and what inferences can be made about their origin(s)?
 - a. What is the isotopic character of the entire mineral paragenesis in both ore zones at East Kemptville, and what does this imply about fluid source(s)?

- b. What is the temporal fractionation of metals across the fluid evolution, from early-stage cassiterite-greisens to later-stage base-metal sulfides, and what implications does this have on the infiltration of fluids with different chemistry than the original mineralizing fluid?
 - c. When in the paragenesis is C and other volatile species introduced to the ore system and what is the impact on ore deposition?
- 3) What is the genetic link between the SMB and Sn mineralization at East Kemptville as well as lithophile element enriched centres across the Canadian Appalachian metallotect?
- a. When did emplacement of granites with which the East Kemptville mineralization is spatially associated happen, and what was the duration of this magmatic event?
 - b. Is there a significant difference in age between the less-evolved phases of the SMB and the more-evolved, lithophile element enriched plutons of the SMB?
 - c. How do we differentiate the petrochemical nature of the relatively barren SW part of the SMB from its mineralized counterpart?
 - d. Can in situ zircon trace element chemistry and isotopic signature resolve the magmatic evolution of the SMB and where in this evolution does metal enrichment occur? What are the implications on metal enrichment in the metallotect as a whole?

1.4 Structure of thesis

This dissertation is presented as five chapters. Chapters two to four are written as standalone manuscripts intended for publication in peer-reviewed scientific journals. Therefore, there is some repetition in the introduction and geological background sections of these chapters.

Chapter two is written as a manuscript entitled “**Petrochronological constraints on the generation and assembly of the Late Devonian peraluminous South Mountain Batholith, Nova Scotia, Canada with implications for metallogenic inheritance.**” This manuscript has been written for submission to the Canadian Journal of Earth Sciences (anticipated submission in July, 2021). This manuscript describes the use of both zircon geochronology and in situ zircon petrochronology as tools to adequately constrain the emplacement history of peraluminous batholiths and to indicate the fertility or metallogenic potential for lithophile element enrichment in such intrusive complexes. This study focusses on the South Mountain Batholith, which hosts the East Kemptville Sn-Zn-Cu-Ag-In deposit.

Chapter three is a manuscript entitled “**The East Kemptville Mesothermal Greisen-Hosted Sn-Zn-Cu-Ag-In Deposit, Nova Scotia, Canada: One ore body with two deposits.**”. This manuscript is intended for submission to Economic Geology or Ore Geology Reviews (anticipated submission in September, 2021) and presents a detailed geologic setting of the East

Kemptville deposit and mineralization in southwest Nova Scotia by magmatic-hydrothermal fluids. Evidence for a structural control in the main ore zone of the deposit is provided through a detailed structural analysis and alteration mapping, whereas evidence for a change in mineralization style and timing elsewhere in the deposit is provided with both U-Pb cassiterite and Re-Os molybdenite geochronology as well as detailed petrographic analyses.

Chapter four is a manuscript entitled “**Geochemical constraints of ore-forming fluids in a mesothermal Sn-Zn-Cu-Ag-In deposit, East Kemptville, Nova Scotia (Canada).**”. This manuscript is intended for submission to *Economic Geology* (anticipated submission in September, 2021). This manuscript investigates the hydrothermal evolution of greisen-forming fluids in the East Kemptville deposit of southwest Nova Scotia, Canada. This study provides evidence for tin mineralization through a weakly efficient fluid reduction and pH change mechanism via interaction of moderately saline magmatic fluid with granitic host rock and later more efficient tin precipitation via solubility changes in a moderately saline magmatic fluid that results from instantaneous pressure changes along a host shear zone and interaction with reduced meteoric CO₂-bearing fluids.

1.5 Statement of original contributions

The following is a summary of original contributions presented by the candidate in this study:

1. A revised interpretation of distinct alteration stages at the East Kemptville Sn-Zn-Cu-Ag-In deposit, in association with periodic activation along the host shear zone and induced permeability in the host EKL by hydrothermal circulation.
2. A detailed characterization of the contrasting geologic characteristics from the two ore zones (Baby and Main) that comprise the East Kemptville deposit, and a resultant interpretation of the deposit petrogenesis.
3. A new interpretation of mineralization age at East Kemptville, both of cassiterite (U-Pb) and of molybdenite at various stages through the paragenesis (Re-Os), and the significance in a regional context.
4. Detailed, integrated fluid inclusion investigation through the paragenesis at East Kemptville; a follow-up to previous works by Dr. Daniel Kontak. This includes a description of evaporate mound analyses and chemical composition, as well as carbonic volatile content identification in fluids interpreted to be syn- to post-mineralization.
5. The first description of in situ O isotopic character of quartz at various stages through the East Kemptville paragenesis to complement bulk O isotopic work done previously.
6. A comprehensive interpretation of U-Pb crystallization ages for the various zircon types that occur in the multiple intrusive phases which make up the South Mountain Batholith (SMB).

7. A description of trace element and isotopic (O, Lu-Hf) signature for the various zircon types and ages from each major SMB plutonic phase.
8. A new interpretation of source(s) of Sn enrichment in the Canadian Appalachian Sn-W metallogeny.

1.6 References

- Audétat, A., Gunther, D., and Heinrich, C.A., 2000. Causes for large scale metal zonation around mineralized plutons: fluid inclusion LA-ICP-MS evidence from the Mole Granite, Australia. *Economic Geology*, 95: 1563–1581.
- Blevin, P. L., and Chappell, B. W., 1992. The role of magma sources, oxidation states and fractionation in determining the granite metallogeny of eastern Australia. *Transactions of the Royal Society of Edinburgh: Earth Sciences*, 83(1-2): 305–316.
- Bodnar, R.J., Lecumberri-Sanchez, P., Moncada, D., and Steele-MacInnis, M., 2014. Fluid Inclusions in Hydrothermal Ore Deposits. In: *Treatise on Geochemistry, Second Edition*, H. D. Holland and K. K. Turekian (eds.), 13: 119–142.
- Černý, P., Blevin, P.L., Cuney, M., London, D., 2005. Granite related ore deposits. *Economic Geology 100th Anniversary Volume*: 337–370.

- Clark, C., Fitzsimmons, I.C.W., and Healy, D., 2011. How does the continental crust get really hot? *Elements*, 7: 235–240.
- Clarke, D.B., MacDonald, M.A., and Tate, M.C., 1997. Late Devonian mafic-felsic magmatism in the Meguma Zone, Nova Scotia. In: *The nature of magmatism in the Appalachian Orogen*, A.K. Sinha, J.B. Whalen, J.P. Hogan (eds.), Geological Society America Memoir 191: 107–127.
- Halter, W.E., Williams-Jones, A.E., and Kontak, D.J., 1996. The role of greisenization in cassiterite precipitation at the East Kemptville tin deposit, Nova Scotia. *Economic Geology*, 91: 368–385.
- Heinrich, C.A., Gunther, D., Audétat, A., Ulrich, T., and Frischknecht, R., 1999. Metal fractionation between magmatic brine and vapor, determined by microanalysis of fluid inclusions. *Geology*, 27(8): 755–758.
- Hou, Z., and Zhang, H., 2015. Geodynamics and metallogeny of the eastern Tethyan metallogenic domain. *Ore Geology Reviews*, 70: 346–384.
- Ishihara, S., 1981. The granitoid series and mineralization. *Economic Geology 75th Anniversary Volume*, 458–484.
- Jébrak M., and Marcoux E., 2008. *Geology of Mineral Resources*. Géologie Québec. 685p.
- Kellett, D.A., Piette-Lauzière, N., Mohammadi, N., Bickerton, L, Kontak, D., Rogers, .N and Larson, K., in press, Spatio-temporal distribution of Devonian post-accretionary

- granitoids in the Canadian Appalachians: implications for tectonic controls on intrusion-related mineralization; in Targeted Geoscience Initiative 5: Contributions to the understanding and exploration of porphyry deposits, (ed.) A. Plouffe and E. Schetselaar: Geological Survey of Canada, Bulletin 616, p. xxx-xxx.
- Kelly, W. C. and Rye, R. O., 1979. Geologic, fluid inclusion and stable isotope studies of the tin-tungsten deposits of Panasqueira, Portugal. *Economic Geology*, 74: 1721–1822.
- Kontak, D.J., 1990. The East Kemptville topaz-muscovite leucogranite, Nova Scotia. Geological setting and whole rock geochemistry. *Canadian Mineralogist*, 28: 787–825.
- Kontak, D.J., 1993. Geological, geochemical, and isotopic studies of the East Kemptville Sn-(Zn-Cu-Ag) deposit, Yarmouth County, Nova Scotia, Canada: 8th Quadrennial IAGOD Symposium, Ottawa, Canada, Proceedings: 383–409.
- Kontak, D.J. and Chatterjee, A.K., 1992. The East Kemptville tin deposit, Yarmouth County, Nova Scotia. A Pb isotope study of the leucogranite and mineralized greisens: Evidence for a 366 Ma metallogenic event. *Canadian Journal of Earth Sciences*, 29: 1180–1196.
- Kontak, D.J., Dunning, G., and Creaser, R., 2003. U/Pb and Re/Os dating of the South Mountain and Musquodobit batholiths, Nova Scotia: evidence for protracted magmatic-hydrothermal events. Joint Meeting Northeastern Section Geological Society of America-Atlantic Geoscience Society, Program with Abstracts.

- Lecumberri-Sanchez, P., Vieira, R., Heinrich, C.A., Pinto, F., Wälle, M., 2017. Fluid-rock interaction is decisive for the formation of tungsten deposits. *Geology*, 45: 579–582.
- Lehmann, B., 2020. Formation of tin ore deposits: A reassessment. *Lithos*, 14pp.
- Linnen, R.L., Pichavant, M., Holtz, F., 1996. The combined effects of fO_2 and melt composition on SnO_2 solubility and tin diffusivity in haplogranitic melts. *Geochim. Cosmochim. Acta*, 60: 4965–4976.
- London, D., 1992. Phosphorus in S-type magmas: the P_2O_5 content of feldspars from peraluminous granites, pegmatites, and rhyolites. *American Mineralogist*, 77(1-2): 126–145.
- Naumov, V.B., Dorofeev, V.A., Mironova, O.F., 2011. Physicochemical parameters of the formation of hydrothermal deposits: a fluid inclusion study. I. Tin and tungsten deposits. *Geochemistry International*, 49: 1002–1021.
- Pichavant, M., Boher, M., Stenger, J.-F., Aissa, M., and Charoy, B., 1987. Relations de phase des granites de Beauvoir à 1 et 3 kbar en conditions de saturation en H_2O : *Géologie de la France*, no. 2–3: 77–86.
- Pirajno, F., 2012. *Hydrothermal mineral deposits: principles and fundamental concepts for the exploration geologist*. Springer Science & Business Media.

- Raimbault, L., Cuney, M., Azencott, C., Duthou, J.L., and Joron, J.L., 1995. Geochemical evidence for a multistage magmatic genesis of Ta-Sn-Li mineralization in the granite at Beauvoir, French Massif Central. *Economic Geology*, 90(3): 548–576.
- Richardson, J.M., 1988. Field and alteration relationships of alteration and greisen-hosted mineralization at the East Kemptville tin deposit, Davis Lake monzogranite, southwest Nova Scotia, Canada. In: *Granite related mineral deposits*, R.P. Taylor, and D.F. Strong, D.F. (eds). Canadian Institute of Mining and Metallurgy, Special volume 39: 265–279.
- Richardson J.M., Blenkinsopp, J., and Bell, K., 1989. Extreme enrichment in strontium initial ratios in ore-related fluids. *Contributions Mineralogy and Petrology*, 104: 516–529.
- Romer, R.L., and Kroner, U., 2016. Phanerozoic tin and tungsten mineralization—Tectonic controls on the distribution of enriched protoliths and heat sources for crustal melting. *Gondwana Research*, 31: 60–95.
- Selby, D., and Creaser, R.A., 2004. Macroscale NTIMS and microscale LA-MC-ICP-MS Re-Os isotopic analysis of molybdenite: Testing spatial restrictions for reliable Re-Os age determinations, and implications for the decoupling of Re and Os within molybdenite. *Geochimica Cosmochimica Acta*, 68: 3897–3908.
- Schwartz, M.O., Rajah, S.S., Askury, A.K., Putthapiban, P., and Djaswadi, S., 1995. The Southeast Asian tin belt. *Earth-Science Reviews*, 38: 95–293.

- Simons, B., Shail, R.K., and Andersen, J.C., 2016. The petrogenesis of the Early Permian Variscan granites of the Cornubian Batholith: lower plate post-collisional peraluminous magmatism in the Rhenohercynian Zone of SW England. *Lithos*, 260: 76–94.
- Sinclair, D., 2007. Porphyry Deposits. In: *Mineral Deposits of Canada*, W.D. Goodfellow (ed), Geological Association of Canada, Special Publication 5: 223–244.
- Štemprok, M., 1981. Tin and tungsten deposits of the west-central European Variscides. *Proceedings of the fifth quadrennial IAGOD Symposium*.
- Sun, S. S. and Eadington, P.J., 1987. Oxygen isotope evidence for the mixing of magmatic and meteoric waters during tin mineralization in the Mole Granite, New South Wales, Australia. *Economic Geology*, 82(1): 43–52.
- Vallance, J., Cathelineau, M., Marignac, C., Boiron, M. C., Fourcade, S., Martineau, F., and Fabre, C., 2001. Microfracturing and fluid mixing in granites: W–(Sn) ore deposition at Vaulry (NW French Massif Central). *Tectonophysics*, 336(1-4): 43–61.
- van Staal, C.R., 2007. Pre-Carboniferous tectonic evolution and metallogeny of the Canadian Appalachians. In: *Mineral Deposits of Canada*, W.D. Goodfellow (ed), Geological Association of Canada, Special Publication 5: 793–818.
- Walshe, J.L., Solomon, M., Whitford, D.J., Sun, S.S., and Foden, J.D., 2011. The role of the mantle in the genesis of tin deposits and tin provinces of Eastern Australia. *Economic Geology*, 106(2): 297–305.

Wilkinson, J.J., Jenkin, G.R.T., Fallick, A.E., and Foster, R.P., 1995. Oxygen and hydrogen isotopic evolution of Variscan crustal fluids, south Cornwall, UK. *Chemical Geology*, 123(1-4): 239–254.

Chapter 2

Petrochronological constraints on the generation and assembly of the Late Devonian peraluminous South Mountain Batholith, Nova Scotia, Canada with implications for metallogenic inheritance.

2.1 Abstract

Magmas associated with Sn-W deposits include those sourced from melts of metasomatized mantle and either anatexis of, or contamination by, enriched supracrustal sequences. The South Mountain Batholith (SMB; Nova Scotia, Canada) is the largest intrusive complex in the Appalachians and hosts one significant Sn deposit at East Kemptville (EK) within the Davis Lake Pluton (DLP). Here we present isotopes and petrochronology of SMB zircon to constrain the magma and metal sources. CA-ID-TIMS zircon dates from the SMB indicate a temporal transition from granodiorite (378.7 ± 1.2 to 375.4 ± 0.8 Ma) to leucogranite (375.4 to 371.8 ± 0.8 Ma). Furthermore, in situ SHRIMP, LA-MC-ICP-MS, and SIMS analyses of distinct zircon domains reveal: 1) autocryst $\delta^{18}\text{O}$ values between +7.3 and +9.1‰ (V-SMOW); 2) antecryst crystallization ages ca. 3–15 Ma older than SMB emplacement; 3) isotopes, REE signatures, and derived $f\text{O}_2$ values are similar in antecrysts and autocrysts; 4) abundant xenocrysts (~420 Ma to 2.2 Ga); and 5) the ϵ_{Hf} signature in autocrysts from the 371.8 ± 0.8 Ma DLP is higher (+1.74 to +4.38) than those from the rest of the SMB (-2.99 to +1.68). Collectively the data suggest that the construction of the SMB occurred from 390-370 Ma with abundant contamination of the

primary magma which $\delta^{18}\text{O}$ and ϵ_{Hf} zircon values suggest was sourced in the mantle source, and the DLP represents a temporally and petrogenetically distinct magmatic phase. Thus the EK deposit and similar polymetallic occurrences in the region likely sourced their Sn from lower crustal melts distinct from the mantle-derived melts that influenced the rest of the SMB.

2.2 Introduction

The processes responsible for the construction of large granitoid batholiths are of first order importance to understanding the formation and evolution of the continental crust and related mineral deposits. Granophile-type Sn-W deposits and associated polymetallic base-metal (e.g. Cu, Zn, Sb, In) mineralization are commonly hosted in peraluminous, relatively reduced intrusions (e.g., Ishihara, 1981; Blevin and Chappell, 1992; Linnen et al., 1996; Černý et al., 2005) enriched in fluxing components that lower solidus temperatures thereby facilitating extensive fractionation (e.g., B, P, F, Li; Pichavant et al., 1987; Černý, 1991; London, 1992; Raimbault et al., 1995; Černý et al., 2005). A vast amount of field, geochronological, geophysical, and geochemical evidence (e.g., Brown, 1994; Petford et al., 2000; Vigneresse, 2004) suggests the composite granitoid batholiths that host such deposits are the end products of crustal-scale magmatic plumbing systems in which plutons are assembled by incremental emplacement of relatively small magma batches (e.g., Petford et al., 1993; Paterson and Vernon, 1995; Cruden, 1998; Brown and McClelland, 2000). Comprehensive geochronological, geochemical and isotopic studies can determine the processes responsible for both compositional

diversity and metallogenic inheritance of these granitoid batholiths by documenting the longevity of magmatism, as well as source and contaminating influences on magma composition.

Zircon and monazite are robust and ubiquitous minerals in granitoid rocks which preserve their U-Pb isotopic composition over a wide range of temperatures (e.g., Cherniak and Watson, 2003). Application of U-Pb geochronology to these minerals in a variety of granitoid batholiths suggest the duration of batholith construction typically ranges from $\sim 10^4$ to 10^6 years (e.g., Brown and Fletcher, 1999; Coleman et al., 2004; Schaltegger et al., 2009; Memeti et al., 2010; Schoene et al., 2012; Broderick et al., 2015; Samperton et al., 2015; Miles and Woodcock, 2018). However, integration of U-Pb zircon geochronology with intra-grain textural observations, as provided via cathodoluminescence (CL), is required to fully constrain the timescales involved in batholith construction. Detailed CL studies of growth patterns in zircon (e.g., Corfu et al., 2003; Harley et al., 2007; Erdmann et al., 2013) document discrete domains that commonly record the dynamic and temporal evolution of a magma plumbing system (e.g., Barboni et al., 2015; Miles and Woodcock, 2018). These domains include (cf. Miller et al., 2007): 1) inherited xenocrystic, representing host rock contamination or source rock; 2) inherited antecrystic, reflecting early magma gestation prior to batholith construction; 3) autocrystic, i.e., formed within a crystallizing melt during emplacement; or 4) formed by partial replacement involving post-magma emplacement metamorphic (e.g., Hoskin and Black, 2000) and/or hydrothermal zircon growth (cf. Schaltegger, 2007).

Complex growth zoning patterns in zircon potentially record the dynamic and temporal evolution of a magma plumbing system (e.g., Barboni et al., 2015; Miles and Woodcock, 2018) and necessitate a multi-method approach to dating zircon growth. Chemical abrasion isotope dilution thermal ionization mass spectrometry (CA-ID-TIMS) is the most precise method available for dating zircon, but importantly, analytical methods that utilize chemical abrasion but do not account for complex growth zones or inherited components could yield erroneous ages (i.e., not reflecting times of crystallization) as the HF-leaching procedure does not simply dissolve the outermost zircon layers but rather burrows into grains in unpredictable, asymmetric ways (Mattinson, 2011). Zircon textural or geochemical information obtained prior to chemical abrasion may not be connected to the age that is eventually measured (cf. Schoene and Baxter, 2017).

To document the origin, evolution and emplacement of magmas that construct a batholith, it is paramount that the ages of different domains in zircon (and relevant monazite) be determined, and this requires an integrated approach to achieve both high spatial- and age-precision data. Chemical abrasion isotope dilution thermal ionization mass spectrometry (CA-ID-TIMS) is the most precise method available for dating zircon (e.g., Mattinson, 2005; Crowley et al., 2007). However, such studies rarely consider complex domains or the presence of robust inherited components which could yield erroneous ages (i.e., not reflective of crystallization age) due to the unpredictable, asymmetric dissolution of damaged parts of the zircon during the HF leaching procedure (Mattinson, 2011). The use of an ion beam sputtering sensitive high-

resolution ion microprobe (SHRIMP) can provide analyses in an essentially non-destructive manner, albeit with difficulty in measuring Pb/U measurements with less than 1% accuracy, and can identify zircon grains with a prolonged or episodic magmatic history by targeting discrete domains identified by CL images.

Previous studies characterizing the construction of the composite South Mountain Batholith (SMB) of southern Nova Scotia, Canada, the largest intrusion in the Appalachian orogen, have concentrated on its petrologic evolution by examining field, geochemical, and geophysical evidence (e.g., Benn et al., 1999; Culshaw and Bhatnagar, 2001; MacDonald, 2001; Clarke et al., 2004, 2009). However, a comprehensive study using robust geochronology to constrain the absolute time and duration of emplacement (i.e., longevity) has not been done, thereby inhibiting our understanding of processes such as melt generation and subsequent batholith emplacement, construction, and its related metallogeny. Previously published U-Pb geochronological data constrained the crystallization of its less evolved phases to ca. 385 Ma and more evolved phases to ca. 370 Ma (Keppie et al., 1993), which implies a ~15 m.y. emplacement window; this is at least an order of magnitude longer than the range in ages typical of batholith emplacement (e.g., Petford et al., 2000; Coleman et al., 2004; Glazner et al., 2004). This study presents new in-situ SHRIMP U-Pb dates that distinguish and constrain the ages of antecrystic and xenocrystic domains (e.g., Samperton et al., 2015; Schaltegger and Davies, 2017; Smith et al., 2019), and CA-ID-TIMS dates from autocrysts which yield the precise time of crystallization of the most pristine magmatic zircon and monazite autocrysts (e.g., Parrish and Noble, 2003; Mattinson,

2005). In addition to the above methods, U-Pb dating by laser-ablation multi-collector inductively coupled plasma mass spectrometry (LA-MC-ICP-MS) was completed to correlate chemical measurements to each domain type.

To understand the processes of melt generation, magmatic evolution, and related metallogeny of the South Mountain Batholith (SMB) in southern Nova Scotia, Canada, we adopt the aforementioned approach to constrain the U-Pb crystallization ages of zircon for each of the main intrusive phases of this composite batholith. The results constrain, for the first time, the age and duration of SMB emplacement, which has implications for the larger-scale regional tectono-magmatic evolution as well as the spatial and temporal relationships between magmatism and granophile mineralization (e.g., Sn, W, and U). Furthermore, the integration of precise CA-ID-TIMS dating with in situ dating using SHRIMP and LA-MC-ICP-MS provides the bases to distinguish ages of xenocrystic, antecrystic, autocrystic, and post-emplacement (i.e., sub-solidus) zircon growth. To address the petrogenesis of the SMB and its metallogenic implications, the zircon dating was complemented with in situ isotopic (Lu-Hf and $\delta^{18}\text{O}$) and geochemical (trace and rare earth elements [REE]) analyses using LA-ICP-MS and secondary ion-mass spectrometry (SIMS). Collectively, these data allow for a detailed temporal reconstruction of the SMB, and constrain the sources of the magma and its contamination, as well as the tectonic setting and metallogenic potential for the SMB.

2.3 Regional Geology

The SMB lies within the Meguma terrane of southern mainland Nova Scotia (Fig. 2–1), which is predominantly underlain by Ediacaran–Early Ordovician metasedimentary rocks of the Meguma Supergroup and abundant peraluminous granitoid intrusive rocks, including the SMB and smaller satellite plutons (White, 2010). The Meguma Supergroup is subdivided into the Goldenville and Halifax groups, which collectively consist of interbedded metasandstone, metasilstone, and slate that are unconformably overlain by metasedimentary and metavolcanic rocks of the Silurian–Devonian Rockville Notch Group, including ca. 440 Ma volcanic rocks of the White Rock Formation (White, 2010).

The Meguma terrane is the most outboard of several Gondwana-derived terranes that accreted to the eastern Laurentian margin during the Paleozoic (i.e., Ganderia, Avalonia and Meguma, Fig. 2–1A; Bird and Dewey, 1970; Murphy and Nance, 1989; van Staal, 1994; Waldron et al., 1998, 2015). Lithostratigraphic and detrital zircon data suggest the Meguma Supergroup was predominantly derived from the West African craton along the northern margin of Gondwana (White et al., 2006; 2018; Waldron et al., 2009; White and Barr, 2010). The Meguma terrane underwent prolonged deformation from the late Early Devonian (410–395 Ma), as recorded by $^{40}\text{Ar}/^{39}\text{Ar}$ muscovite and Re-Os in vein-hosted arsenopyrite throughout the terrane (e.g., Muecke et al., 1988; Kontak et al., 1998; Hicks et al., 1999; Morelli et al., 2005), through to the Early Carboniferous (375–350 Ma), as recorded by U-Pb zircon crystallization ages of deformed

granite and $^{40}\text{Ar}/^{39}\text{Ar}$ muscovite along discrete shear zones in the terrane (e.g., Keppie and Dallmeyer, 1987; Archibald et al., 2018). The latter deformation is localized to major structures in the Meguma terrane and is synchronous with metamorphism recorded central New England, attributed to a “Neo-Acadian” orogeny (Robinson et al., 1998). Early Devonian-Early Carboniferous tectonothermal events in the Meguma terrane are widely attributed to the Neocadian orogeny (van Staal, 2007; van Staal et al., 2009, in press; Waldron et al., 2009; White et al., 2007, 2018) and reflect dextral transpression of the Meguma terrane along the eastern composite Laurentian margin (e.g., Keppie et al., 1991; Murphy and Keppie, 2005; Murphy et al., 2011; Fig. 2–2). The Avalon terrane, which had accreted to Laurentia during the earlier Acadian orogeny (~421–417 Ma), is thought to have underthrust the converging Meguma terrane during this time interval (e.g., van Staal et al., 2009; Fig. 2–2).

A variety of geochronological studies, summarized in Table 2–1, have broadly constrained the age of the SMB and the spatially affiliated intrusions to the Late Devonian (~385–370 Ma), and occurrences of younger granitic plutons in the southwest part of the Meguma terrane to ca. 360 Ma (e.g., Wedgeport and Clayton Hill granites). The former include numerous relatively small mafic intrusive rocks that range in composition from tonalite and diorite (e.g., the Bog Island Lake, BG in Fig. 2–1A; Giles and Chatterjee, 1987) to lamprophyre (e.g., the Pope’s Harbour dykes, PH in Fig. 2–1A; Owen et al., 1988). Intermediate to felsic plutons of similar age to the SMB are also exposed along the periphery of the SMB (e.g., Kinsar, Shelburne, Port Mouton, Barrington Passage, and Wedgeport plutons; Fig. 2–1A); the intermediate phases are interpreted

to have formed through hybridization of mafic-intermediate and felsic magmas (e.g., Tate and Clarke, 1997; Tate et al., 1997).

The younger ca. 360 Ma granitic magmatism in the southwest part of the Meguma terrane is pene-contemporaneous with Neocadian deformation (e.g., Culshaw and Reynolds, 1997; Culshaw and Lee, 2006) and as well as basin-fill molasse deposits of the late Famennian Horton Group (Martel et al., 1993). The Horton Group is the oldest stratigraphic unit to be deposited on the Avalon-Meguma terrane boundary. It unconformably overlies the Meguma Supergroup along the northern margin of the Meguma terrane where it also onlaps the SMB; and has a clast inventory that indicates provenance from the Meguma Supergroup, the Rockville Notch Group, and the SMB (Murphy, 2000). Thus, at least the northern part of the SMB was exhumed by ca. 355 Ma.

The SMB is the largest of granitoid plutons and published data suggest it is ~5 to 10 Ma older than the less voluminous, basic- to intermediate intrusions and dike rocks (e.g., Weekend dikes; Owen et al., 1988; Kempster et al., 1989) that occur around its periphery and the periphery of other similar-aged intrusions, such as the Musquodoboit Batholith (e.g., MacDonald et al., 1992; Clarke et al., 1993; Kontak and Reynolds, 1994; Keppie and Krogh, 1999; MacLean et al., 2003; Fig. 2-1 and Table 2-1). Field observations combined with gravity, seismic and aeromagnetic studies have indicated that basement faults controlled the emplacement of these intrusions and

were important conduits for the later focusing of hydrothermal fluids (e.g., Keen et al., 1991; Horne et al., 1992; Kontak, 1994; Benn et al., 1997; MacDonald, 2001).

2.4 The South Mountain Batholith

The SMB of southwest Nova Scotia is a composite intrusive complex dominated by granodiorite to monzogranite (Clarke et al., 1988, 1993, 1997; MacDonald et al., 1992; McDonald, 2001) and with a surface exposure of over 7300 km² it is the largest batholith in the Appalachian orogen.

The SMB has a bulk composition that is peraluminous, as indicated by the presence of corundum in the normative mineralogy, and is high in P₂O₅ and MgO (e.g., McKenzie and Clarke, 1975;

Clarke et al., 2005). A number of studies along its northeastern and southeastern margins

constrain emplacement pressure to ca. 3.5 kbar (e.g., Halter and Williams-Jones, 1999; Carruzzo et al., 2000; Kontak et al., 2002a; Hilchie and Jamieson, 2008, 2014; Kontak and Keyser, 2011).

The conventional interpretation is that the SMB was generated via partial melting of unexposed basement rocks beneath the Meguma Supergroup to produce its general peraluminous nature

(Clarke et al., 1988); the SMB was subsequently modified due to combined assimilation

fractional crystallization processes (AFC; Clarke et al., 2004), the former involving Meguma

metasedimentary rocks (e.g., MacDonald et al., 1992; Clarke et al., 1997; Clarke and Carruzzo, 2007; Shellnutt and Dostal, 2012; MacDonald and Clarke, 2017).

Detailed mapping of the SMB, done for the first time in the mid-late 1980s and summarized in MacDonald (2001), defined its composite nature, which was interpreted to reflect two distinct magmatic stages: an early granodiorite that forms a border phase to the batholith and is referred to as stage 1, and later more evolved phases of monzogranitic composition, consisting of at least five plutons and referred to as stage 2 (Fig. 2–1B). From west to east, these latter intrusions include the Davis Lake (DLP), West Dalhousie (WDP), East Dalhousie (EDP), New Ross (NRP) and Halifax (HP). The multi-phase SMB hosts numerous polymetallic (Sn, W, Mo, Cu, Zn, U, Ta, Nb) occurrences hosted in the more-evolved plutons (MacDonald, 2001); however, the only significant economic deposit to date is the East Kemptville greisen-type Sn-(Zn-Cu-Ag-In) deposit, which is hosted in an evolved muscovite-topaz leucogranite phase of the DLP (Richardson, 1988; Kontak, 1990; Halter et al., 1996; Kontak et al., 2002a; Bickerton et al., submitted).

In this study, the SMB was sampled for U-Pb geochronology at spatially representative locations in the outer granodiorite as well as in each of the evolved plutons, to complement and refine previous geochronology of both the SMB and its peripheral plutons (compiled in Table 2–1). Sample locations are shown in Fig. 2–1B, with precise coordinates in Table 2–2.

2.4.1 Stage 1 Plutons

The majority of the SMB is a biotite-muscovite granodiorite that locally transitions to leucocratic phases and melanocratic segregations. These rocks typically contain fabrics, such as aligned

megacrysts and preferred orientations of schlieren and xenoliths, which reflect magmatic flow (e.g., Fig. 2–3A, B, C). Along its margins, the granodiorite typically contains abundant, variably-sized and corroded xenoliths of the immediate wall-rock unit (i.e., lithologies of the host Meguma terrane; e.g., Fig. 2–3C).

In many stage 1 plutons, primary cordierite (e.g., Fig. 2–3D), andalusite, topaz, almandine-rich garnet, and tourmaline occur locally (e.g., Clarke et al., 2005; Erdmann et al., 2009; Clarke, 2010; Lackey et al., 2011). The cordierite and garnet, both high in aluminum content, are thought to represent peritectic phases that crystallized during partial melting of pelitic xenoliths under fluid-absent conditions (cf. MacDonald and Clarke, 2017) and preservation of such partially melted xenoliths is common (e.g., Fig. 2–3E, F).

Five samples were collected from different locations in these early-stage intrusive phases (Fig. 2–1B, Table 2–2) for detailed U-Pb geochronology analysis. Of these, two samples were dated using CA-ID-TIMS (16BIC-073 and 15SMB-ORIG), three were dated via SHRIMP (16BIC-074, 16BIC-080, and 16BIC-075), and three duplicate samples were dated via LA-MC-ICP-MS (16BIC-073, 16BIC-074B, and 16BIC-075). Sample 15SMB-ORIG was collected from a 1.5 km deep drill hole made by the Nova Scotia Department of Natural Resources as part of a study on compositional variability with depth in the SMB (Chatterjee and Dostal, 2003).

2.4.2 Stage 2 Plutons

The poorly exposed WDP, the smallest of the more evolved plutons, is located along the west-northwestern margin of the SMB where a number of small leucomonzogranite to leucogranite bodies are mapped (Fig. 2–1B). Two samples of muscovite-biotite monzogranite were collected from this phase: 16BIC-083 is from the community of West Springhill near the western periphery of the SMB; here the unit is a leucocratic phase that is exposed outside of its previously mapped contact and is located adjacent to an inferred along-strike projection of the Chebogue Point shear zone (CPSZ, White and Barr 2010; Fig. 2–1B); 19BIC-086 comes from near the community of West Dalhousie in the central part of a muscovite-biotite monzogranite intrusion. 16BIC-083 and 16BIC-083B, from the same outcrop, were used for SHRIMP and LA-MC-ICP-MS analysis, respectively, whereas 19BIC-086 underwent CA-ID-TIMS analysis (Table 2–2).

The EDP is a poorly exposed leucomonzogranite along the NE-trending East Kemptville–East Dalhousie shear zone (EKEDSZ, Fig. 2–1B). It is similar to the WDP and NRP (see below) in terms of the range of textures and compositions. Two samples were collected from this unit (Fig. 2–1B), one for SHRIMP analysis (16BIC-084) and the other for CA-ID-TIMS analysis (16BIC-076; Table 2–2). Duplicates of each were analyzed by LA-MC-ICP-MS.

The NRP leucogranite, which occurs in the New Ross area, is the third largest pluton of the SMB in terms of area and thus it is not surprising that it defines the most pronounced negative

Bouger gravity anomaly in the SMB; this anomaly has been modeled to suggest a deep root zone extending to a depth of 10-20 km (Garland, 1953; Clarke and Chatterjee, 1988). The geochemical signature of this pluton indicates it is one of the most fractionated phases in the SMB (MacDonald, 2001) and it is characterized by a variety of polymetallic mineralization (i.e., Sn, W, U, Mo, Cu, Mn) that relates to areas of pegmatite-, greisen- and quartz veining (O'Reilly et al., 1982; Carruzzo et al., 2000).

Four samples collected from the NRP were used for SHRIMP (16BIC-081 and 16BIC-082) and CA-ID-TIMS analysis (16BIC-077 and 19BIC-087; Table 2–2). Duplicates of 16BIC-077, 16BIC-081, and 16-BIC-082 were also analyzed by LA-MC-ICP-MS. Sample 16BIC-081 is a monzogranite representative of the central part of the NRP, whereas 16BIC-082 and 19BIC-087 are leucomonzogranites from outside of the mapped pluton (off its southeastern tip on the Aspotogan Peninsula), although interpreted here to represent a late phase of the NRP (Fig. 2–1B). Sample 19BIC-087 was collected to follow up the anomalously young age determined from SHRIMP analysis on sample 16BIC-082 in the same area (see results below). Sample 16BIC-077 is a leucomonzogranite from a section along the inferred NE projection of the Rossignol shear zone (RSZ; Fig. 2–1B) located to the southwest.

The HP, a complexly zoned intrusion of granodiorite to leucomonzogranite, is the most easterly pluton of the SMB and considered to be one of its more-evolved phases (MacDonald and Horne, 1988). It is well exposed along an extensive coastal section.

Three samples were collected from the HP: two for SHRIMP (16BIC-079 and 16-BIC-085) and one for CA-ID-TIMS (16BIC-078; Table 2–2) analysis. Each of the three sample locations were used to collect additional samples for LA-MC-ICP-MS analysis. Sample 16BIC-079 is a muscovite-biotite monzogranite from the periphery of the pluton, 16BIC-085, from its southwestern margin, and 16BIC-078, from its interior (Fig. 2–1B) are both leucomonzogranite.

The DLP, at the most southwestern extent of the SMB, is one of its most evolved phases. It is poorly exposed, but abundant subcrops may occur northeast of the community of East Kemptville. Representative drilling across the pluton indicates the DLP as zoned from an early biotite granodiorite to a highly fractionated muscovite leucogranite with the latter enriched in Li, U, F, Ta, and Sn (Dostal and Chatterjee, 1995).

Two leucogranite samples from the DLP (16BIC-072 and 16BIC-071; Fig. 2–1B) were collected northeast of East Kemptville for SHRIMP and CA-ID-TIMS analysis, respectively, whereas duplicates of each were used for LA-MC-ICP-MS analysis (Table 2–2). Sample 16BIC-072 is from subcrop in the interior of the DLP, proximal to the inferred southwestern projection of the Tobeatic shear zone (TSZ; Giles, 1985), whereas sample 16BIC-071 is from an outcrop at the southwestern edge of the pluton proximal the southwestern projection of the EKEDSZ (Horne et al., 1988; 2006; Fig. 2–1B).

2.5 Analytical Techniques

2.5.1 Mineral Separation and Sample Preparation

Zircon were separated from samples for either U-Pb dating, $\delta^{18}\text{O}$ analysis or combined trace element and Hf isotopic analysis. Specific sample preparation protocols are specific to each of the procedures and laboratories used.

2.5.1.1 Sensitive High-Resolution Ion Microprobe (SHRIMP) Analysis

The zircon grains from ten ~10 kg rock samples were separated using conventional methods of crushing followed by gravity and electric-pulse disaggregation at Overburden Drilling Management in Ottawa, Ontario (Averill and Huneault, 2006; Cabri et al., 2008). Zircon grains in the concentrates, which range from greater than 10,000 grains in the less-evolved granodiorite samples to approximately 5000 grains in the more-evolved leucocratic samples, were hand-picked and mounted in epoxy resin together with the zircon reference materials Temora-2 (primary; Black et al., 2004), z6266 (Stern and Amelin, 2003), and z9910 (unpublished internal laboratory standard). The accepted $^{206}\text{Pb}/^{238}\text{U}$ age of z9910 is 441.2 ± 0.4 Ma, based on 5 ID-TIMS fractions (B. Davis and V. McNicoll, unpublished data with reported TIMS long-term average age of 440.7 ± 7 Ma). The grain mount was subsequently polished to reveal approximate zircon midsections. The internal features of zircon grains (i.e., zoning, internal domains, and alteration) were characterized via cathodoluminescence (CL) and backscattered electron (BSE) imaging

utilizing a Cambridge Instruments scanning electron microscope (SEM) at the Geological Survey of Canada, Ottawa; representative BSE and CL images are available in the Electronic Appendix Table EA 2-1. All reported errors are at 2 sigma and include the external long-term reproducibility of the 9910 reference zircon (constant external error of 0.59%, 95% conf.).

2.5.1.2 Chemical Abrasion Isotope Dilution Thermal Ionization Mass Spectrometry (CA-ID-TIMS) Analysis

Samples were processed using standard techniques of crushing and concentration of a heavy mineral separate by density and magnetic techniques followed by hand-picking to select zircon and monazite fractions from each sample. Some monazite and zircon grains are physically abraded to remove visible alteration (cf. Krogh, 1982), as indicated by ‘*Abr*’ in Table EA 2-2 (Electronic Appendix), whereas euhedral gem-quality zircon and monazite are not abraded. The morphology and internal texture of zircon were examined prior to U–Pb age determination. The overall morphology of zircon was characterized by transmitted light using a standard petrographic microscope and the internal textures were observed using a (FEI Quanta 400) SEM and a CL detector at Memorial University (e.g., Fig. 2–4A, B, C).

2.5.1.3 Secondary Ion-Mass Spectrometry (SIMS) Oxygen Stable Isotopes Analysis and Laser Ablation Multi Collector-Inductively Coupled Plasma-Mass Spectrometry (LA-MC-ICP-MS)

Approximately 20 to 30 zircon grains were separated from each of the fifteen igneous rock samples that were also used for U-Pb geochronology and O and Hf analysis, in addition to further in situ analysis for U-Pb dating trace-element chemistry. Mount preparation was carried out at the Canadian Centre for Isotopic Microanalysis (CCIM), University of Alberta where zircon grains were epoxy-embedded and polished to their mid-sections using diamond grits. The prepared 25 mm SIMS mount (M1560B) was coated with 25 nm of high-purity Au prior to imaging on an SEM utilizing a Zeiss EVO MA15 instrument equipped with a high-sensitivity, broadband CL and BSE detectors. Beam conditions in this study were 15 kV and 3–5 nA sample current. Another 100 nm of Au was subsequently deposited on the mount prior to SIMS analysis.

2.5.2 U-Pb Geochronology

2.5.2.1 SHRIMP U-Pb Analysis

In situ U-Pb isotopic analyses of zircon were carried out using the SHRIMP in the J.C. Roddick Ion Microprobe Laboratory at the Geological Survey of Canada in Ottawa. Abundances of U and Pb isotopes are measured in situ in individual zircons by SHRIMP, generating an approximately

17 x 20 μm elliptical spot, 1 to 5 μm deep, on the target. Precise locations of analyses in this study were selected after evaluating the internal structure of the grains revealed in the BSE and CL imagery (e.g., Fig. 2–4D to F). Standard operating techniques for the SHRIMP employed in this study are described in Stern (1997). All reported errors are at 2 sigma and include the external long-term reproducibility of secondary standard 9910 reference zircon (constant external error of 0.59%, 95% confidence). The TIMS age for standard z9910 is 441 Ma during our analytical session, z9910 calibrated against primary standard 10493 Temora yielded 440.70 ± 0.70 Ma ($n = 42$, MSWD = 1.4).

In SHRIMP analysis, spot selection is based on growth zones within the zircon (see Table EA 2-1, Electronic Appendix). Results from spots placed on domains interpreted as antecrystic or metamict/overgrowth are shown in Table EA 2-1; these analyses typically yield dates that overlap or are slightly older than the dominant autocrystic zircon age population. Xenocrystic cores have CL and BSE responses distinct from zircon rims and the mantles to cores. In addition to the contrasts in CL and BSE responses, xenocrystic cores typically yield ages significantly older than the rest of the zircon U-Pb SHRIMP analyses.

2.5.2.2 CA-ID-TIMS U-Pb Analysis

Analytical work was carried out in the radiogenic isotope facility at Memorial University of Newfoundland. In CA-ID-TIMS analysis, zircon and monazite grains are selected for analysis according to criteria of morphology and clarity. The analytical methods for these analyses were

carried out as reported by Sánchez-García et al. (2008). High-quality zircon and monazite grains with no visible inherited core are removed from epoxy mounts and chemically abraded (cf. Mattinson, 2005) to minimize or eliminate Pb-loss. All zircons are washed in dilute nitric acid, then distilled water prior to dissolution. The ion exchange chemistry followed a miniaturized version of that described by Krogh (1973). Lead and U isotopic ratios are measured by thermal ionization mass spectrometry, and results are calculated using ISOPLOT (Ludwig, 2003) for weighted average $^{206}\text{Pb}/^{238}\text{U}$ ages, or Davis (1982) for linear regressions (Table EA 2-2, Electronic Appendix). Uncertainties on all ages are reported at the 95% confidence interval.

2.5.2.3 LA-MC-ICP-MS U-Pb and Trace Element Analysis

Trace-element and U-Pb data on zircon were collected simultaneously by using a Photon Machines Analyte G2 193-nm excimer laser ablation system ($\lambda = 193$ nm) coupled to a Thermo Neptune Plus with Jet Interface ICP-mass spectrometer at the Mineral Exploration Research Centre Isotope Geochemistry Lab (MERC-IGL), Laurentian University. In situ analytical techniques were employed following McFarlane (2016). In this study, a laser spot diameter of 40 μm , a low energy density of 2 J/cm^2 and 7 Hz pulse frequency ensured conditions that minimize isotopic fractionation. Each analysis included a background acquisition of approximately 30 s and a signal acquisition of 10 s. The instrument mass bias was controlled through 40 measurements of the 91500 reference zircon (CA-ID-TIMS $^{207}\text{Pb}/^{206}\text{Pb}$ age of 1065 ± 1 Ma; Wiedenbeck et al., 1995) during the course of the analyses, which yielded a mean $^{207}\text{Pb}/^{206}\text{Pb}$ age

of 1063.5 ± 6.6 Ma (MSWD = 1.5; Table EA 2-3b, Electronic Appendix). Secondary reference zircon crystals were repeatedly analyzed to assess the accuracy of the mass bias correction: 10 analyses of Plesovice (337.1 ± 0.37 Ma; Sláma et al., 2008) yielded an average $^{206}\text{Pb}/^{238}\text{U}$ age of 338.1 ± 3.0 Ma (MSWD = 4.4; Electronic Appendix Fig. EA 2-3b) and 10 analyses of reference material Temora2 (416.8 ± 1.3 Ma; Black et al., 2004) yielded a mean $^{206}\text{Pb}/^{238}\text{U}$ age of 418.5 ± 3.2 Ma (MSWD = 2.4; Electronic Appendix Fig. EA 2-3e). No common Pb correction was applied to results. Trace-element concentrations are quantified by normalizing to SRM610 glass reference material and using stoichiometric Si as an internal standard. Titanium concentrations are normalized to zircon reference materials 91500, GJ1, AUSZ7-5, and AUSZ7-1 (Szymanowski et al., 2018) and, in this study, resulted in an average correction factor of 1.2 ($2s = 0.06$; Table EA 2-3, Electronic Appendix). Downhole U-Pb fractionation and instrumental mass bias were corrected by matrix-matched normalization using the GJ-1 reference zircon. Data reduction was performed using the VizualAge data reduction package (Petrus and Kamber, 2012) in Iolite v. 3.32 (Paton et al., 2011). All sample and reference material data are provided in Table EA 2-3 (Electronic Appendix). A summary of in situ zircon U-Pb isotope data is shown in Table 2–3 and a summary of trace-element data in Table 2–5.

2.5.3 Lu-Hf Isotopic Compositional Determination by LA-MC-ICP-MS

The Lu-Hf isotopes in zircon were acquired by employing LA-MC-ICP-MS at the MERC-IGL in Sudbury, Ontario, Canada. The spot selection for $^{176}\text{Hf}/^{177}\text{Hf}$ isotope ratio analysis was based on

domains that yielded U–Pb, trace element, and (wherever possible) O-isotope results. The Lu-Hf analyses are performed using a Photon Machines Analyte G2 193-nm laser ablation system coupled to a Thermo Neptune Plus with Jet Interface ICP-mass spectrometer. For one Hf isotope analysis, a zircon is ablated for 60 seconds using a spot diameter of 40 μm , an energy density of 6 J/cm^2 and a repetition rate of 7 Hz. The first 30 s of each analysis is used to determine instrumental background count, and is followed by 60 s of laser ablation sampling. The Thermo Neptune Plus MC-ICP-MS has a fixed detector array of 9 Faraday cups that simultaneously analysed masses ^{171}Yb , ^{173}Yb , ^{174}Yb , ^{175}Lu , ^{176}Hf , ^{176}Yb , ^{176}Lu , ^{177}Hf , ^{178}Hf , and ^{179}Hf . Hafnium isotope data baselines are automatically subtracted from the sample data by the Neptune software and the data are further corrected for mass bias and isobaric interferences of ^{176}Yb and ^{176}Lu on ^{176}Hf ; $^{176}\text{Yb}/^{173}\text{Yb} = 1.35272$, $^{176}\text{Lu}/^{175}\text{Lu} = 0.02655$, and $^{179}\text{Hf}/^{177}\text{Hf} = 0.7325$ ratios are used, assuming exponential mass fractionation law of Russell et al. (1978).

For this study, a primary reference material of Plesovice standard zircon ($^{176}\text{Hf}/^{177}\text{Hf} = 0.282482$; Sláma et al., 2008) was analysed to check the accuracy and external reproducibility of the method, which yielded $^{176}\text{Hf}/^{177}\text{Hf}$ of 0.282482 ($n = 43$). Secondary reference materials of standard zircon included 91500 ($^{176}\text{Hf}/^{177}\text{Hf} = 0.282306$; Wiedenbeck et al., 1995), R33 ($^{176}\text{Hf}/^{177}\text{Hf} = 0.282755$; Kemp et al. 2017), Temora2 ($^{176}\text{Hf}/^{177}\text{Hf} = 0.282680$; Woodhead and Hergt, 2005), and MUN1/3 ($^{176}\text{Hf}/^{177}\text{Hf} = 0.282140$; Fisher et al., 2011); these were also analysed to check the accuracy and external reproducibility of the method and yielded average $^{176}\text{Hf}/^{177}\text{Hf}$ values of 0.282303 ($n = 10$), 0.282749 ($n = 10$), 0.282658 ($n = 10$), and 0.282129 (n

= 10), respectively. The reference material results agree with the LA-MC-ICP-MS long-term average of reference zircons at the MERC-IGL. Initial ratios are calculated via a ^{176}Lu decay constant value of $\sim 1.86 \times 10^{-11} \text{ year}^{-1}$ (Scherer et al., 2001), as well as chondritic uniform reservoir (CHUR) ratios of 0.282785 for $(^{176}\text{Hf}/^{177}\text{Hf})_{\text{CHUR}}$ and 0.0336 for $(^{176}\text{Lu}/^{177}\text{Hf})_{\text{CHUR}}$ (Bouvier et al., 2008). All Hf isotope analytical results are provided in the Electronic Appendix Table EA 2-5. The results quoted in the text are given with their corresponding 2σ errors, unless stated otherwise.

2.5.4 Oxygen Stable Isotope Determinations by SIMS

Oxygen isotopes (^{18}O , ^{16}O) in zircon are analyzed using a Cameca IMS 1280 multicollector ion microprobe. In this study, a $^{133}\text{Cs}^+$ primary beam was operated with impact energy of 20 keV and beam current of $\sim 2.0 \text{ nA}$. The $\sim 10 \mu\text{m}$ diameter probe was rastered ($20 \times 20 \mu\text{m}$) for 30 s prior to acquisition, and then $3 \times 3 \mu\text{m}$ during analysis. A normal incidence electron gun is utilized for charge compensation. Negative secondary ions are extracted through 10 kV into the secondary (Transfer) column. Transfer conditions for this study included a $122 \mu\text{m}$ entrance slit, a $5 \times 5 \text{ mm}$ pre-ESA (field) aperture, and 100x (MA80) sample magnification at the field aperture, transmitting all regions of the sputtered area; no energy filtering was employed. The mass/charge separated oxygen ions are detected simultaneously in Faraday cups L'2 ($^{16}\text{O}^-$) and H'2 ($^{18}\text{O}^-$) at mass resolutions ($m/\Delta m$ at 10 %) of 1950 and 2250, respectively. Secondary ion count rates for $^{16}\text{O}^-$ and $^{18}\text{O}^-$ are typically $\sim 2 \times 10^9$ and 4×10^6 counts/s utilizing $10^{10} \Omega$ and $10^{11} \Omega$ amplifier

circuits, respectively. Faraday cup baselines are measured at the start of each analytical session. For this study, a single analysis took 240 s, including pre-analysis rastering, automated secondary ion tuning, and 75 s of continuous peak counting.

Instrumental mass fractionation (IMF) was monitored in this study by repeated analysis of the zircon primary reference material S0081 ($\delta^{18}\text{O}_{\text{VSMOW}} = +4.87\text{‰}$; R. Stern, unpublished laser fluorination data, University of Oregon), once after every four unknowns. A secondary zircon reference material, TEM2 ($\delta^{18}\text{O}_{\text{VSMOW}} = +8.2\text{‰}$; Black et al., 2004) was also analysed after every 12 unknowns. The $^{18}\text{O}/^{16}\text{O}$ data set for S0081 was processed collectively for single analytical sessions, yielding a standard deviation of 0.09‰ (this followed correction for systematic within-session drift of 0.15‰). The individual spot uncertainties in $\delta^{18}\text{O}_{\text{VSMOW}}$ for the unknowns had a median of $\pm 0.21\text{‰}$ at 95% confidence, which included errors relating to within-spot counting statistics, between-spot (geometric) effects, and correction for instrumental mass fractionation. Results for multiple spots on multiple grains of the secondary reference material (TEM2) yielded a weighted mean $\delta^{18}\text{O}_{\text{VSMOW}} = +8.22\text{‰}$ (MSWD = 0.78; $n = 34$, $\sigma = 0.09\text{‰}$), consistent with the reference value. All sample and reference material data are provided in Table EA 2-4 (Electronic Appendix) and a summary of zircon O isotope data is shown in Table 2–6.

2.6 Results

2.6.1 Zircon Characterization

The zircons used for this study are considered representative of the entire population found in the SMB since they were extracted from a wide range of SMB lithologies. In general, they range from 25 to 500 μm in length and have external morphologies that include irregular stubby and partially resorbed, regular elongate prismatic, and the most dominant which is equant prismatic. The zircons analyzed herein contain four types of internal domains identified by texture, zoning, CL response, and chemistry (i.e., trace elements and crystallization age). These domain types include: xenocrysts (inherited), antecrysts (inherited), autocrysts, and post-emplacement or metamict growth domains, as summarized in Figure 2–5. Xenocrystic zircon form cores that are mantled by well-zoned magmatic zircon; the former domains are typically rounded or irregular in shape with zonation patterns that range from convoluted to unzoned (e.g., Fig. 5A). If the growth zones are narrow, mineral dissolution (i.e., CA-ID-TIMS) or in situ analysis (i.e., LA-ICP-MS or SHRIMP) could necessarily or inadvertently sample multiple growth zones resulting in a mixed age with little geological significance (cf. Mundil et al., 2001; Miller et al., 2007). To avoid these latter problems, zircon selection for CA-ID-TIMS analysis targeted the least damaged and most homogenous crystals, whereas homogeneous portions of grains from both interior (cores or mantles to cores) and exterior (rims) were selected for in situ analysis.

The CL response of zircon reflect U, Hf and Y concentrations (e.g., Poller et al., 2001), thus the contrast between domains indicates the potential for different crystallization ages (e.g., Figs. 2–4D, E, F and 2–5). Zircon domains interpreted as antecrystic are typically characterized by oscillatory- to sector-zoning, and by irregularly to partially resorbed margins rimmed by autocrystic overgrowths. The autocrystic zones are recognized by their continuous oscillatory zoning and bright CL response, relative to other zircon domains and typically form rims around inherited domains (e.g., Fig. 2–5A, B, C). Where metamict and overgrowth domains are present, both typically have chaotic- to weakly convoluted zoning which is indicative of a metamorphic or metasomatic origin (Corfu et al., 2003); these domains commonly truncate the earlier zones of the crystal. The widespread occurrence of metamict and overgrowth domains suggests that zircon dissolution, resorption, and/or recrystallization occurred in the SMB, as is typical of zircon in intermediate peraluminous granites (cf. de la Rosa et al., 2002; Hoskin and Schaltegger, 2003).

2.6.2 U-Pb Age Determinations: Preamble

U-Pb crystallization ages of zircon and monazite from the six intrusive phases that comprise the SMB and represent its compositional diversity were calculated from a total of 18 samples employing three different U-Pb dating methods (Table 2–2). Post-analysis, assessment of the final spot placements were used to remove erroneous analyses from final crystallization age determinations. This was done by omitting data obtained from spot analyses placed either on

significantly damaged parts of the crystal or clearly overlapping different growth domains. The geological significance of weighted mean $^{206}\text{Pb}/^{238}\text{U}$ ages, concordia ages, and individual crystallization ages are discussed in the context of the internal crystal structure (i.e., zonation, morphology, domain classification), zircon geochemical and isotopic characteristics, as well as field relationships among phases of the SMB and regional structures. The resultant full data sets are presented in Electronic Appendices Tables EA 2-1 (SHRIMP zircon analyses, including erroneous analyses), EA 2-2 (CA-ID-TIMS zircon and monazite analyses), and EA 2-3 (LA-MC-ICP-MS zircon analyses).

The spots analysed by LA-MC-ICPMS were wider and deeper than the SHRIMP spots, and thus results are typically relatively discordant. For concordant data, the age interpretations are based on the weighted mean average $^{206}\text{Pb}/^{238}\text{U}$ ages; these data are presented in the text, with corresponding 2σ error, unless stated otherwise. For data that were determined to be discordant, the age interpretations were calculated from concordia intercepts of simple Pb-loss lines or common Pb-mixing lines, where possible. The full data tables U-Pb zircon and monazite geochronology results from samples collected from each major phase of the SMB are provided in the Electronic Appendices.

2.6.3 U-Pb Age Determinations Results

2.6.3.1 SHRIMP and LA-ICP-MS data

Zircon crystallization, its subsequent resorption and/or recrystallization, and alteration can each play a role in the final ages yielded by a single grain. The SHRIMP and LA-MC-ICP-MS spot analysis on zircon thus targeted distinct autocrystic, antecrystic, xenocrystic, and late replacement domains (cf. Miller et al., 2007), as initially characterized texturally. Post-analysis, assessment of the final spot placements was used to remove erroneous data from final crystallization age determinations. Data omitted include spot analyses placed either on significantly damaged crystal domains or those overlapping different growth domains. Analytical spots placed on xenocrystic cores are further subdivided by their respective zircon crystallization age groupings. The in-situ zircon U-Pb results are herein presented in the context of domain types characterized above. In keeping with the sequential development of the zircon domains, the data are presented from oldest to youngest, thus xenocryst, antecryst, autocryst and metasomatic overgrowth/recrystallized.

The spots analysed by LA-MC-ICP-MS yielded crystallization ages (not corrected to common Pb) that are consistent with, though less concordant than, the ^{204}Pb -corrected $^{206}\text{Pb}/^{238}\text{U}$ ages from equivalent SHRIMP spots (see below). Thus, the interpretation of LA-MC-ICP-MS data relies on the trace element and Lu-Hf results. For data with error ellipses that overlap concordia,

age interpretations are based on the weighted mean average $^{206}\text{Pb}/^{238}\text{U}$ ages; these data are presented below with the corresponding 2σ error.

The xenocrystic zircon domains collectively yield age populations that can be divided into three sub-groups based on distinct peaks in probability density space (Fig. 2–6): 1) ~400 to 470 Ma; 2) ~480 to 670 Ma; and 3) >700 Ma. Low density clusters also occur at ~700 to 850 Ma, ca. 1.5 Ga, and ~1.9 to 2.2 Ga. The $^{207}\text{Pb}/^{206}\text{Pb}$ chronometer is applied to data that yielded ages >850 Ma, thus included in the comparison, for a more robust measure of concordance in older zircon population, shifted from the typical 1.5 Ga cut-off (Spencer et al., 2016) to accommodate zircon with the ~1.5 Ga age spectra. The xenocrystic zircon ages are similar to the detrital zircon populations documented in the upper part of Meguma Supergroup stratigraphy and overlying Silurian-Devonian rocks (i.e., Halifax Group, upper Goldenville Group, White Rock and Torbrook formations; summary in Waldron et al., 2009). The ~540 to 770 Ma zircon population is also shared by clastic sedimentary units of the adjacent Avalon terrane (cf. Barr et al., 2012; Henderson et al., 2016). A small anomalous xenocryst population also occurs at ~1.5 Ga (6 analyses across 4 samples; Fig. 2–6).

A majority of antecryst domains form mantles around xenocrysts and are characterized by abrupt changes in zonation or morphology based on CL and backscattered electron images (e.g., Fig. 2–5A, B). These data typically record crystallization ages ~3 to 15 m.y. older than their respective autocrystic domains (Table 2–3; Figs. 2–7, 2–8 and 2–9). Furthermore, the antecryst zircon

domains collectively yield ^{204}Pb -corrected weighted mean $^{206}\text{Pb}/^{238}\text{U}$ (SHRIMP) ages from 391.0 ± 3.1 to 385.9 ± 3.8 Ma in the less evolved phases (16BIC-080 and 16BIC-075, respectively; Fig. 2–8A, C), and from 388.3 ± 3.9 to 377.8 ± 3.6 Ma in the more evolved phases (16BIC-079 and 16BIC-082, respectively; e.g., Fig. 2–8I, J).

The autocryst domains typically occur as oscillatory zoned rims to older cores and yield ^{204}Pb -corrected $^{206}\text{Pb}/^{238}\text{U}$ ages ranging from ~ 381 to 369 Ma. These ages (Table 2–3) may be subdivided spatially and temporally into two groups: 1) autocrysts from less evolved granodiorite and WDP monzogranite range from 381.1 ± 3.8 to 375.9 ± 4.1 Ma (16BIC-075 and 16BIC-074, respectively); and 2) autocrysts from the more evolved EDP, NRP, HP, and DLP intrusive units that range from 376.8 ± 3.8 to 370.2 ± 3.7 Ma (16BIC-084 and 16BIC-079, respectively) that includes a younger outlier at 368.5 ± 3.7 Ma (16BIC-082) (Table 2–3, Fig. 2–7A).

The Stage II WDP monzogranite sample (16BIC-083) has lithological characteristics and a SHRIMP crystallization age similar to the less evolved Stage I granodiorite (378.1 ± 3.8 Ma, Table 2–3; Figs. 2–7A, 2–8D). This age is complemented by a CA-ID-TIMS sample from the mapped WDP (below, Fig. 2–7A) and thus, for the purpose of this study, we have categorized this pluton as part of the early-stage suite in the SMB (i.e., Stage I; purple fields in Fig. 2–7).

A number of zircon grains analysed in situ for U-Pb have unzoned overgrowth or replacement domains that yield concordant dates which are 10–15 Ma younger than the autocryst ages in their respective samples (i.e., analyses with blue error bars/ellipses in Figs. 2–7, 2–8 and 2–9).

Although these analyses yield ages of ca. 360 Ma (± 10 Ma; Figs. 2–7, 2–8D), they are considered suspect as discordance in a majority of the overgrowth/replacement analyses is likely a result of surface-related Pb-loss and/or significant underestimation of common Pb in these domains (cf. Heaman and Parrish, 1991).

2.6.3.2 CA-ID-TIMS data

Zircon and monazite CA-ID-TIMS data provide high-resolution ages that address the timing and duration of SMB emplacement and related temporal overlap of the relatively primitive (granodiorite) and more evolved (monzogranite to leucogranite) plutonic phases (Table 2–4, Figs. 2–7A, B). Monzogranite sample 19BIC-087, collected from within the proposed NRP (i.e., stage 2 Panuke Lake; MacDonald et al., 1992), yielded an interpreted crystallization age of 377.5 ± 1.1 Ma, and is ~ 5 Ma older than crystallization ages of the other NRP samples dated in this study (Fig. 2–7A). Therefore, we suggest sample 19BIC-087 represents a monzogranitic phase from the early-stage crystallization of the SMB, rather than being representative of the NRP. Given this proposed reclassification, the $^{206}\text{Pb}/^{238}\text{U}$ ages for stage 1 granodiorite and WDP samples fall between 378.8 ± 1.1 Ma (19BIC-086) and 375.2 ± 1.1 Ma (16BIC-073; weighted means in Figs. 2–7A, 2–10A–C, and concordia intercept in Fig. 2–10D), whereas samples from the stage 2 plutons fall between 375.4 ± 0.8 and 371.8 ± 0.8 Ma (Table 2–4, Figs. 2–7A and indistinguishable concordia ages in Figs. 2–10D to H). Together these data indicate the two

stages slightly overlap temporally and that final crystallization of the entire batholith was prolonged for ~8 m.y.

Notably, the muscovite leucogranite sample from the DLP (16BIC-071), which is an important phase of the SMB given that it hosts the East Kemptville Sn deposit, has zircon and monazite that yielded a discordia upper intercept age of $374 \pm 17/-12$ Ma. To resolve the latter in regard to the large associated error, the same sample was analyzed by LA-MC-ICP-MS which yielded a weighted mean $^{206}\text{Pb}/^{238}\text{U}$ age of 373.3 ± 2.2 Ma (Table 2–3, Fig. 2–7B and a similar Discordia intercept age in Fig. 2–9O), which is considered its time of crystallization. The DLP, therefore, is likely representative of the more evolved SMB phases defined by the other CA-ID-TIMS results.

2.6.4 Zircon Trace- and Rare Earth Element Compositions

The trace-element concentrations in the different zircon domains representative of each of the main plutons in the SMB are summarized in Table 2–5 and Figures 2–11 to 2–13 with the complete dataset available in Table EA 2-3 (Electronic Appendix). For the autocrystic and antecrystic domains, the element concentrations or ratios either vary from linear or curvilinear discrimination pathways and show a variance in age, or show no apparent trend; notably, the number of outliers significantly increases in the most discordant fifth of the data (final discordance >67%). Zircon domains with U-Pb ages partially reset by post-emplacement processes are nonetheless interpreted to have consistent trace-element composition up to a 67% final discordance cut-off, and the petrochemical data herein is presented in this context.

For the xenocrysts, the Hf contents are again uniform and in fact similar to that in the SMB magmatic zircon phases, whereas Th/U shows systematically low values in the ~470 – 400 Ma age population (i.e., <0.3; Fig. 2–11A) and higher and more variable values in the rest of the xenocrysts with no discernable age trend (Fig. 2–11B, C). Zircon domains for a majority of the antecrysts and autocrysts have a consistent range of Hf concentration regardless of their U-Pb age (Fig. 2–12), whereas the Th/U values, which typically increase with fractionation (cf. Kirkland et al., 2015), are highest in the autocrysts (Fig. 2–12).

SMB zircon display typical chondrite-normalized REE patterns for zircon with the heavy REE (HREE) being more enriched (i.e., >3 or 4 orders of magnitude) relative to the light REE (LREE; Table 2–5). The enrichment of HREE relative to middle REE (MREE; i.e., $[\text{Yb/Gd}]_N$) also generally decreases with higher Th/U (Fig. 2–13A). Figure 2–13B presents the Ce-in zircon anomalies (Ce/Ce^*) in magmatic zircon domains against their respective $(\text{Yb/Gd})_N$ values, for which there is no apparent trend. The range of negative Eu anomalies (Eu/Eu^*) for all zircon domains from each phase of the SMB overlap, although the range narrows to slightly lower values with younger ages (Fig. 2–13C; Table 2–5).

For in situ zircon analysis, crystallization temperatures for each spot were determined using the Ti-in-zircon geothermometer of Ferry and Watson (2007) at fixed external activities of SiO_2 and TiO_2 . For the purpose of this study, the activity of SiO_2 and TiO_2 were assumed to be 1 and 0.5,

respectively, based on Si saturation as well as the absence of magmatic rutile throughout the SMB (cf. Clarke and Carruzzo, 2007).

The magmatic oxygen fugacity (fO_2) values were estimated using an internally-consistent model for zircon-melt partitioning of Ce and a redox equilibrium which is calibrated for silicate melts (Smythe and Brenan, 2015; 2016). This model applies Ti-in-zircon temperatures, Ce-in-zircon anomalies (each noted above), the REE and high field strength element (HFSE) concentration of both the measured zircon and the representative whole rock, as well as a presumed concentration of dissolved H₂O in the melt at the time of crystallization, estimated to be ~2 wt. % (Clarke et al., 2004). The estimated water content is based on LOI values (~0.5-1 wt. %) from previous whole-rock geochemical studies (i.e., Clarke et al., 1993; MacDonald, 2001; Chatterjee and Dostal, 2003) throughout the SMB that, when pressure-corrected to the emplacement depth of the batholith, as noted above, equate to a magma with a minimum of ~2 wt. % H₂O (e.g., Clemens, 1984; Johnson et al., 1994). The fO_2 values of xenocrysts were determined using empirical relationships in Trail et al. (2012) with assumed peraluminous melt compositions and thus should be considered as less reliable values but useful for comparison with the magmatic zircon domains.

2.6.4.1 Xenocrystic cores

The trace and REE data from spot analyses on xenocrystic cores (n = 89) are summarized in three dominant age populations as well as their respective Hf vs. U-Pb age, Hf vs. Th/U, and

chondrite-normalized REE patterns are (Fig. 2–11). Consistent with the antecryst and autocryst domains throughout the SMB, all xenocrystic zircon cores have elemental concentrations of Hf with both decreasing age and decreasing Th/U values (Fig. 2–11). All the xenocrystic zircon cores exhibit characteristic REE trends for zircon with enrichment of HREE relative to LREE. The Σ REEs and Σ LREEs in these populations typically have ranges similar to their respective autocryst and antecryst domains (Table EA 2-3, Electronic Appendix), with a wider range of enriched Σ LREEs in the younger ca. 470–400 Ma domains (Fig. 2–11). The xenocrystic cores have variably positive Ce anomalies, and negative Eu anomalies that are typically less pronounced than those of the antecryst and autocryst zircon domains throughout the SMB (Fig. 2–11). The youngest group of xenocrystic zircon cores (470 to 400 Ma) have moderate to very high U concentrations (59–5380 ppm) and variably low Th/U ratios (0.01–0.47; Fig. 2–11). The next youngest group of xenocrystic zircon cores (670 to 480 Ma) has low to moderate U concentrations (10–1196 ppm, outlier at 9800 ppm) and low to moderate Th/U ratios (0.02–2.40; Fig. 2–11). The oldest group of xenocrystic zircon cores (> 700 Ma) have low U concentrations (20–594 ppm, outlier at 1061 ppm) and low Th/U ratios (0.07–1.01; Fig. 2–11).

2.6.4.2 Antecrystic domains

The spot analysis on antecrystic domains in zircon (n = 34) yielded a wide range for U (161 to 2204 ppm) with concentrations typically lower in antecrysts from the early phases (200–867 ppm; Table 2–5). Furthermore, these domains typically contain moderate to low Th contents

(20–183 ppm) in the majority of the lithologies with the exception of higher concentrations in zircons from the more evolved DLP (81–403 ppm; Table 2–5). The antecrysts have remarkably consistent ranges for both Σ REE and Σ LREE with values that are similar to those for autocryst domains (Table 2–5). The chondrite-normalized REE profiles are dominantly similar throughout all lithologies, but a slight increase in LREE is noted for the later units (i.e., EDP and DLP; Fig. 2–12). However, these domains from all phases typically have lower, on average, Ce/Ce* values compared to the other zircon domains, though their range (1.1 to 39.1, with an outlier at 67; Table 2–5) overlaps with that of the autocrysts (Fig. 2–13A). The Eu/Eu* values are typically indistinguishable from their respective autocryst zones (Table 2–5), but are generally lower in the more evolved plutons (Fig. 2–13A). The Ti-in-zircon values indicate lower crystallization temperatures compared to the younger domains; the temperatures range from 742 to 981°C in the DLP and from 671 to 829°C in all other plutons (Table 2–5). These domains have fO_2 values that are low, relative to FMQ (Fig. 2–14A), with Δ FMQ ranging from -1.3 to -7.2.

2.6.4.3 Autocrystic domains: SMB granodiorite and WDP

The spot analysis for autocrystic domains in zircon from the granodiorites and the WDP (n=26) have a consistent range in U (from 70 to 863 ppm) and Th (17-217 ppm), similar values to their respective antecrysts (Table 2–5). The derived Th/U ratios, which is a monitor of fractionation, are notably lower in the younger plutons (Fig. 2–12). The Σ REE and Σ LREE population are similar to their respective antecrystic domains in all units (Table 2–5) and the REE profiles for

these domains are normal for zircon. The Ce/Ce* values are moderately positive (2.1–53.6; Table 2–5) and the Eu/Eu* values are low to overlapping those of the autocrystic domains in the more evolved units (Fig. 2–13A). The Ti-in-zircon values for the early units indicate a wide range of crystallization temperatures (669 to 874°C) which overlap those of autocrysts from the rest of the batholith but are somewhat higher than for some of their respective antecrystic domains (Fig. 2–13D). These domains in the early phases have fO_2 values that are similar to those of their respective antecrysts, with ΔFMQ ranging from -1.6 to -6.8 (Fig. 2–14B), and are consistent with the values in autocrysts from later phases (Table 2–5).

2.6.4.4 Autocrystic domains: SMB evolved phases (EDP, NRP, HP, DLP)

The spot analysis on autocrystic domains in zircon from more evolved phases (i.e., the EDP, NRP, HP, and DLP; $n = 50$) have a wide range in U concentrations (119 to 2617 ppm) that is, in general, similar to the values in their respective antecrystic domains and to those of autocryst populations from each of the more evolved phases. Notably, however, autocrysts in the EDP have a narrow range of U values (163–452 ppm; Table 2–5). These domains in the more evolved phases, apart from the DLP, contain moderate to low Th contents (18–268 ppm), whereas in the DLP they have a wider range of higher Th values (66–442 ppm; Table 2–5) that are similar to their respective antecrystic populations. The Th/U ratios for these domains in the more evolved phases are lower in the younger phases (Fig. 2–12). The ΣREE , including $\Sigma LREE$, in these populations have ranges similar to their respective antecryst domains as well as the autocrysts

from the earlier phases (Table 2–5). The REE profile for these domains is normal for zircon with weakly to moderately positive Ce/Ce* values (1.5–50; Table 2–5) that are higher than their respective antecrysts and are similar to autocrysts in the early phases. The range of weakly positive Eu/Eu* values for samples from more evolved phases (0.00–0.11; Table 2–5) are similar to similar domains in less evolved parts of the batholith, as well as their respective antecrysts (Fig. 2–12A). The Ti-in-zircon data for domains in the more evolved phases indicate a wide range of crystallization temperatures that vary between 663 and 894°C in the EDP, NRP, and HP, and between 742 and 981°C in the DLP (Table 2–5). These temperatures are higher on average, but generally overlap with values from their respective antecryst domains and with those of autocrysts from the early phases (Fig. 2–13B). The calculated fO_2 values for these domains in the more evolved are similar to those of their respective antecryst population and to autocrysts in earlier phases, with ΔFMQ from -0.1 to -6.4 (Fig. 2–13B). For the DLP, these domains have a narrow range of less reduced ΔFMQ from -0.8 to -4.5 (Table 2–5).

2.6.4.5 Late overgrowth/recrystallized domains

The recrystallized and late overgrowth domains in zircon from all phases of the SMB ($n = 45$) have widely variable U (83 to 1693 ppm), Hf (8430 and 13050 ppm), and Th concentrations (17 to 304 ppm) that generally overlap with the ranges of values in autocrystic and antecrystic domains for each respective zircon (Table 2–5). Although more variable in detail, the $\Sigma REEs$ as well as $\Sigma LREEs$ in these metamict or recrystallized domains have ranges similar to those in

their respective autocryst and antecryst domains in zircon from each SMB phase in this study (Table 2–5). The Ce/Ce* values in domains that are metamict/recrystallized are highly variable and typically more positive than respective autocryst and antecryst domains (1.4 to 49.4 with anomalous values at 78.0 and 79.8; Table 2–5). The Ti-in-zircon thermometer and Ce-in-zircon oxygen barometer were not applied to these data as the methods of calculation used assume the zircons measured grew in a magmatic setting. The metamict and recrystallized zircon domains have typically suffered Pb loss or have modified compositions, making them unsuitable for the zircon-based thermometer/barometers utilized above (e.g., Siégel et al., 2018).

2.6.5 Oxygen Stable Isotopic Composition of Zircon

The locations for the in situ $\delta^{18}\text{O}$ analysis was adjacent to the later in situ LA-MC-ICP-MS spots to allow direct correlation of $\delta^{18}\text{O}$ and U-Pb age and trace element data. The spots were selected based on the CL images to target the various domains in zircon grains, thus inherited domains (i.e., xenocrystic or antecrystic cores versus mantles) and autocrystic rims. The resultant $\delta^{18}\text{O}$ data are summarized in Table 2–6 and Figure 2–15.

The ranges of $\delta^{18}\text{O}$ values for the non-xenocrystic domains of zircons are all as follows: 1) antecrysts for the early stage granodiorite (ca. 390–385 Ma) are 7.10 ± 0.24 to $8.76 \pm 0.18\text{‰}$ ($n = 9$, Fig. 2–15A); 2) antecrysts for the more evolved plutons (ca. 385–378 Ma) are 7.28 ± 0.19 to $9.16 \pm 0.21\text{‰}$ ($n = 29$, Fig. 2–15B); 3) autocrysts for the less evolved phases (i.e., early granodiorite and monzogranite of the WDP) are 7.81 ± 0.20 to $9.19 \pm 0.21\text{‰}$ ($n = 26$, Fig. 2–15C).

and Table 2–6) and overlap with the higher values in their respective ca. 390–385 Ma antecryst populations; 4) autocrysts from the more evolved phases, excluding the DLP (i.e., EDP, NRP, and HP) are between 8.26 ± 0.23 and $9.13 \pm 0.23\%$ and are similar to that in the less evolved autocrysts ($n = 36$; Table 2–6 and Fig. 2–15D); 5) autocrysts in the DLP display two sub-populations (Fig. 2–15E), lower values that range between 7.31 ± 0.28 and $7.95 \pm 0.26\%$ ($n = 7$) and are less than equivalent to zircon domains in the rest of the SMB, and a higher range of values between 8.10 ± 0.25 and $8.88 \pm 0.15\%$ ($n = 12$; Table 2–6) that are indistinguishable from the autocrysts throughout the SMB; 6) metamict and recrystallized domains from across the SMB have values from 7.68 ± 0.23 to $9.18 \pm 0.24\%$ and thus are somewhat similar to the different magmatic domains ($n = 26$; Fig. 2–15F).

The xenocrystic cores for zircon grains from throughout the SMB record the most variability in $\delta^{18}\text{O}$ values (Fig. 2–15G). The $\delta^{18}\text{O}$ values also weakly correlate with age as follows: 1) for ages from ~400 to 470 Ma, they vary from 7.71 ± 0.16 to $9.44 \pm 0.20\%$ with an average $8.68 \pm 0.21\%$ ($n = 12$); 2) for ages from ~480 to 670 Ma, they vary from 4.31 ± 0.27 to $11.38 \pm 0.24\%$ ($n = 38$); and 3) for ages >700 Ma, they vary from 3.45 ± 0.18 to $9.92 \pm 0.18\%$ ($n = 12$; Table 2–6).

2.6.6 Hf Isotopic Composition of Zircon

Hafnium isotope analyses were obtained on zircon domains previously dated and analyzed for trace elements with the same instrument, as noted previously. A total of 377 analyses on 321

domains were obtained for all phases of the SMB as follows: 1) 92 for xenocrysts; 2) 71 for antecrysts; 3) 105 for autocrysts; and 4) 49 on metamict/recrystallized domains; an additional 60 analyses were discounted due to domain overlap or inclusion of xenocrystic minerals. The data are presented in Table EA 2-5 (Electronic Appendix) and Figure 2–16 where, due to the variation in crystallization ages from different domains, the data are presented based on domain classification.

2.6.6.1 Antecrystic domains

The antecrystic domains analysed include those in the less evolved early-stage granodiorite and WDP (396.9 ± 6.8 to 382.5 ± 4.7 Ma) and those in the more evolved phases (391.2 ± 4.8 to 375.7 ± 3.1 Ma; Table 2–3). There is a wide range of overlapping $^{176}\text{Lu}/^{177}\text{Hf}$ values (0.000057–0.003365) and with two dominant populations of resultant $\epsilon_{\text{Hf}}(t)$ values based on the host pluton: 1) -3.7 ± 0.5 and $+2.0 \pm 0.6$ in both the less evolved SMB and WDP, as well as the EDP, NRP, and HP; and 2) $+1.8 \pm 0.5$ and $+4.6 \pm 0.8$ for antecrysts hosted in the DLP (Fig. 2–16A). These values are very similar to those from the respective autocrystic domains in the zircons analyzed.

2.6.6.2 Autocrystic domains for granodiorite and WDP

The oscillatory zoned autocrystic domains in three samples from the early-stage granodiorite (16BIC-073, 16BIC-074B, 16BIC-080) and a monzogranite sample from the WDP (16BIC-083) were analyzed, which range in age from 381.5 ± 3.8 to 375.7 ± 3.9 Ma (Table 2–3). These

domains have a wide range of overlapping $^{176}\text{Lu}/^{177}\text{Hf}$ values (0.000514–0.003190; $n = 28$, excluding an outlier value at 0.00517) and similar resultant $\epsilon_{\text{Hf}}(t)$ values of -3.1 ± 0.6 to $+1.9 \pm 1.7$ (Fig. 2–16B). The $\epsilon_{\text{Hf}}(t)$ values are similar to those determined from their respective antecrysts.

2.6.6.3 Autocryst domains for evolved phases (EDP, NRP, HP, DLP)

The oscillatory zoned autocrystic domains in samples collected from the evolved phases of the SMB included two samples from the EDP (16BIC-076 and 16BIC-084), three from the NRP (16BIC-077, 16BIC-081 and 16BIC-082), three from the HP (16BIC-078, 16BIC-079 and 16BIC-085), and two from the DLP leucogranite (16BIC-071 and 16BIC-072). These domains, which range from 377.3 ± 3.8 to 368.2 ± 3.5 Ma (Table 2–3) and yielded the following data: 1) early-stage granodiorite and monzogranite have overlapping $^{176}\text{Lu}/^{177}\text{Hf}$ values (0.000368–0.003403) with two dominant populations of resultant $\epsilon_{\text{Hf}}(t)$ values based on the host pluton: 1) -3.1 ± 0.6 and $+1.4 \pm 0.7$ in autocrysts from the EDP, NRP, and HP ($n = 51$ and an outlier at -4.6 ± 0.7); and 2) $+0.9 \pm 0.6$ and $+4.4 \pm 0.7$ in autocrysts from the DLP ($n = 22$; Fig. 2–16B). The $\epsilon_{\text{Hf}}(t)$ subpopulations are similar to those characterized in the respective antecrystic domains from each pluton.

2.6.6.4 *Metamict/recrystallized domains*

The interpreted metamict and recrystallized domains throughout the SMB that were analyzed (n = 43) are interpreted to represent post-emplacement growth zones for which their ages range from 371.5 ± 3.2 to 334.3 ± 4.2 Ma (Table EA 2-5, Electronic Appendix). These domains have $^{176}\text{Lu}/^{177}\text{Hf}$ in the range 0.000269–0.002710 and resultant $\epsilon_{\text{Hf}}(t)$ values between -6.0 and 4.0 (n = 42, excluding an outlier at -17.7; Fig. 2–16C).

2.6.6.5 *Xenocrystic cores*

Analysis of xenocrystic cores, presumably inherited from wall-rock lithologies, throughout the SMB have $^{176}\text{Lu}/^{177}\text{Hf}$ ratios that vary with respect to their ages (Fig. 2–16D). A total of 19 spots of ~400 to 470 Ma have $^{176}\text{Lu}/^{177}\text{Hf}$ in the range 0.000381–0.002954 (median = 0.001470) and $\epsilon_{\text{Hf}}(t)$ between -5.5 and 5.6 (median = 0.17, n = 18; excluding an outlier value at -9.8). A total of 46 spots on cores between ~480 to 670 Ma have $^{176}\text{Lu}/^{177}\text{Hf}$ in the range 0.000308–0.003126 (median = 0.001088) and $\epsilon_{\text{Hf}}(t)$ between -19.0 and +9.4 (median = -0.16, n = 45; excluding an outlier value at -35.9). A total of 16 spots on cores older than 700 Ma have a smaller range of $^{176}\text{Lu}/^{177}\text{Hf}$ from 0.000286–0.002840 (average mean = 0.00092 ± 0.00063) and a wide range of $\epsilon_{\text{Hf}}(t)$ between -22.8 and 10.9 (median = 0.30, n = 14; excluding two outlier data at 34.7 and 37.9).

2.7 Discussion

The U-Pb zircon and monazite geochronological data presented herein constrain the absolute age and duration of SMB emplacement. In addition, the trace-element chemistry and complementary Lu-Hf and oxygen-isotopic analyses for various zircon domain types (i.e., autocrystic, antecrystic, xenocrystic) provide insights into the source reservoirs, temperatures and redox conditions of the magma. These data, when combined with field relationships and petrographic observations, lead to models for the construction and evolution of the SMB, its metallogenic affiliation, and for the tectonic setting into which it was emplaced.

2.7.1 Zircon chemistry and implications for magma evolution

Trace-element and REE data from temporally-constrained magmatic zircon domains document intra-grain and inter-pluton variability that provide insights into magma evolution in the crustal-scale SMB plumbing system. The trace-element geochemistry can also distinguish zircon crystallized during progressive magma fractionation in crustal melts and/or in melts that were influenced by mixing or contamination (e.g., Claiborne et al., 2010; Wotzlaw et al., 2013; Marsh and Stockli, 2015; Buret et al., 2016). In the SMB, magmatic zircon geochemistry shows evidence of both magma fractionation, as exemplified by the increasing $(Yb/Gd)_N$ with decreasing Th/U (e.g., Claiborne et al., 2010; Buret et al., 2016), and contamination/mixing of

different rock types, as exemplified by wide ranges in Th/U, Ce/Ce*, and Eu/Eu* (e.g., Belousova et al., 2002; Fig. 2–13) throughout the evolution of the SMB.

The chemical signature of the SMB xenocrysts has two dominant populations, distinguished by age. The younger population (i.e., 470–400 Ma) typically has lower Th/U values, negative Eu/Eu*, HREE enrichment, lacks a significant positive Ce anomaly (and calculated lower fO_2 values), and exhibits a wide range of LREE enrichment relative to chondrite (Fig. 2–12A). Collectively, these data suggest a metamorphic origin for these domains (e.g., Rubatto, 2002) that do not overlap with detrital ages from the Meguma Supergroup. The youngest of these xenocrysts (i.e., at ca. 400 Ma) do, however, overlap in age and Th/U signature to a population of zircon from granulite xenoliths in the Pope's Harbour dike (Fig. 2–1A), which are thought to be metamorphic and representative of Avalonian lower crust that had underthrust Meguma rocks by ca. 380 Ma (Shellnutt et al., 2019); the latter time constraint being prior to construction of the SMB. In contrast to a metamorphic signature of the younger population, the older population of SMB xenocrysts (i.e., >470 Ma) have a wide range of trace-element features that include a moderate Th/U values, HREE enrichment, moderately negative Eu/Eu* values, and strongly positive Ce/Ce* values (and calculated higher fO_2 values; Fig. 2–12B, C). The latter data suggest crystallization from felsic magmas (e.g., Hinton and Upton, 1991; Hoskin and Ireland, 2000) and collectively likely represent a detrital provenance.

In situ analysis of magmatic zircon domains shows no systematic trend of either Hf concentration or relative REE content with age and, with the exception of the DLP, only a weak decrease in Th/U with decreasing age (Fig. 2–12). Although Th/U values have been used to monitor fractionation in granites (cf. Kirkland et al., 2015), the relatively flat profiles for SMB zircons suggest that this ratio may not be as effective in composite magmatic complexes with extensive contamination. However, this ratio can be used to generally identify discrete magma pulses in the SMB. In addition to similar Th/U in the SMB magmatic zircon domains, relatively homogeneous Hf and REE compositions suggest that: 1) melts that crystallized both domain types (autocrystic and antecrystic) were sourced from a similarly equilibrated chemical reservoir; and/or 2) progressive crystallization within the SMB magmas did not cause systematic compositional changes in the zircon crystallized from them.

The SMB samples with anomalously young zircon domains (i.e., ca. 360 Ma “late overgrowth/recrystallization” domains in samples 16BIC-071, -072, -076, -080, -083 and -084; Figs. 2–7A, –B, 2–8, and 2–9) are located either within or along the strike-trace of regional shear zones through the SMB (Fig. 2–1B). Relative to their respective autocryst domains and the rest of the SMB, the trace element signature of these zircons typically includes a range of overlapping but, on average, higher LREE values and larger positive Ce anomalies (Ce/Ce^* ; Table 2–5). The latter part of this signature is a typical response to greater oxygen partial pressure in the magmatic-hydrothermal setting post-SMB emplacement, and has been ascribed to

hydrothermal zircon in magmatic-hydrothermal transitional settings for Sn-hosting granites elsewhere (i.e., Mole Granite, Australia, Pettke et al., 2005; Schaltegger, 2007).

Titanium-in-zircon thermometry provides reliable estimates of silicic melt temperatures at the time of zircon crystallization (Ferry and Watson, 2007). Application of this technique on data from a majority of SMB zircon domains suggests crystallization occurred in low- to moderate-temperature magmas; between ~675 and 825°C for the antecrysts (Figs. 2–14A and Table 2–5) and between ~700 and 900°C for the autocrysts (Fig. 2–14B and Table 2–5), hence they broadly overlap. Abundant xenocrysts and partially resorbed antecrystic zircons in granites are typical of low-temperature peraluminous melts (e.g., Miller et al., 2003) and the combination of these textural observations and Ti-in-zircon measurements from the peraluminous SMB support this characterization. The antecryst and autocryst crystallization temperatures of most of the SMB intrusive phases are similar; however, the DLP at the SW end of the SMB exhibits a wider range for zircon crystallization temperatures of ~750 to 1000°C. The latter data indicate a high temperature for some of the zircon and is in conflict with the general idea that highly evolved magmas typically crystallize at lower temperatures than their less evolved equivalents (cf. F-bearing melts in Černý et al., 2005). The higher crystallization temperatures for zircon from the more evolved DLP suggest different processes may have influenced the melt temperature, such as melting of a dehydrated crustal melt source or a source melt reservoir that was thermally reheated by mafic intrusions (Huber et al., 2009).

The derived oxygen fugacity (fO_2) values, as determined using the Ce-in-zircon method (Trail et al., 2012 for the xenocrysts; Smythe and Brenan, 2015, 2016, for the antecrysts and autocrysts), were used to constrain the redox conditions for zircon domains throughout the SMB. The values, which dominantly overlap for the two magmatic zircon domain types, range from 0.1 to 7 log units below the FMQ buffer (Fig. 2–14A, B) and indicate that each magma batch that constructed the SMB was strongly reduced. The younger xenocryst population (i.e., ~470–400 Ma) also overlaps with these values, however a majority of the older xenocrysts (i.e., >470 Ma) have a wider range of fO_2 values (-9.5 to +12.4 Δ FMQ); a majority of which are markedly less reduced than the magmatic zircon domains (Fig. 2–14C). The strongly reduced signature of SMB magmas is similar to abyssal spinel peridotites, such as those recorded in xenoliths from the lherzolite massifs in northern Morocco and southern Spain (maroon field in Fig. 2–14A); these xenoliths are thought to represent the variably metasomatized lithospheric mantle beneath this region (Woodland et al., 1992, 2006; Frets et al., 2014).

The reduced nature of melts that constructed the SMB is ascribed, at least in part, to interaction with the carbonaceous host Meguma Supergroup (e.g., White, 2010); which has been shown to be a contaminant in the SMB magmas from both field (Clarke and Chatterjee, 1988; MacDonald and Horne, 1988; MacDonald, 2001) and petrographic observations (Erdmann et al., 2007; Clarke and Carruzzo, 2007; Clarke et al., 2009), as a well as by modelling of its whole-rock chemistry (Clarke et al., 2004) and isotopic features (Clarke and Halliday, 1980; Longstaffe et al., 1980; Poulson et al., 1991). These features are common in many other peraluminous

granitoid suites (e.g., Sierra Nevada batholith in southwest USA, Lackey et al., 2006; the Lachlan Fold Belt in southeast Australia, Clemens, 2003; Sierra Norte-Ambargasta batholith in western Argentina, Iannizzotto et al., 2013; the French Massif Central, France et al., 2016; the Nanling Range in southeast China, Zhang et al., 2017), many of which are host to Sn-W deposits (e.g., Taylor, 1979; Černý et al., 2005; Lehmann, 2020). The variation in redox conditions recorded by xenocrysts in the SMB (Fig. 2–14C), however, suggests the contaminant which sourced these younger xenocrysts was the primary factor in reducing the SMB melts.

Antecrysts and autocrysts hosted by the less evolved granodiorite and the WDP have average fO_2 values that are, on average, lower but dominantly overlap with equivalent zircon domain types in the more evolved NRP, HP, EDP, and DLP (Fig. 2–14A, B; Table 2–5). The autocryst fO_2 values for zircon in the more evolved SMB plutons are similar to those determined by Chavez (2019), who used the same Ce-in-zircon calibration, and determined ΔFMQ values of 1.05 to -5.23 for the HP and NRP (calculated assuming ~5 wt. % H_2O in the melt). The autocrysts in the DLP, however, have fO_2 values and Ti-in-zircon crystallization temperatures that are generally higher than those in the rest of the SMB implying the melt which formed the DLP was less reduced and hotter compared to melts that formed the rest of the SMB. The higher ΔFMQ values in the DLP autocrysts relative to the rest of the SMB suggest that during the evolution of the magmatic plumbing system involved interaction with a less reduced magma at depth and/or the melt which formed the DLP had less interaction with reducing contaminants, which is further addressed below.

The typical oxidized I-type magmas in the northern Appalachians are represented by the blue field in Figure 2–14B (Magaguadavic Granite suite of southern New Brunswick) have fO_2 values 2 to 7 log units higher than those recorded by zircon in a majority of the SMB, although values from fractionated I-type granites (i.e., Mount Pleasant, New Brunswick) do overlap with much of the SMB data (Yang and Lentz, 2005). Examples of strongly contaminated and reduced I-type intrusions (grey field in Fig. 2–14B; Ague and Brimhall, 1988) also have similar values to the zircon in the more evolved parts of the SMB; this field also partially overlaps with zircon from the DLP. The DLP, however, has zircon values consistent with a less contaminated magma compared to the rest of the SMB data.

2.7.2 Isotopic constraints on SMB magma source

2.7.2.1 Implications of the $\delta^{18}O$ zircon data

The $\delta^{18}O$ values of zircon constrain sources of contamination in a crystallizing melt, with the following assumptions (cf. Roberts et al., 2013): 1) for mantle-derived melts, zircon has a $\delta^{18}O$ value of $+5.3 \pm 0.3\text{‰}$ (Valley et al., 1998); 2) values $>6.5\text{‰}$ are attributed to melting or assimilation of sedimentary and/or altered volcanic rocks; and 3) values $<5\text{‰}$ are attributed to melting of hydrothermally altered material (Valley et al., 2005). There is evidence, however, of $\delta^{18}O$ heterogeneity in the mantle reservoir such that mantle-derived melts may become enriched in ^{18}O by up to $+2\text{‰}$ compared to typical mantle values due to metasomatism by ^{18}O -enriched

fluids, likely derived from dehydration of subducted sediments (e.g., Eiler et al., 2005; Auer et al., 2009; Johnson et al., 2009; Roberts et al., 2013). The SMB $\delta^{18}\text{O}_{\text{zircon}}$ data (Fig. 2–15) generally indicate the following with respect to contamination and melt source signature: 1) a slight increase for average values from antecrystic to autocrystic domains of about 1‰ that reflects partial contamination of the melt (cf. Taylor and Sheppard, 1986); 2) the values for magmatic domains exceed by several units per mil those of primitive mantle-derived melts (see above); and 3) the overgrowth/recrystallized domains of ca. 360 Ma have higher values due to interaction with fluids of variable signatures (i.e., equilibrated with wall rocks or surficial fluids), as has been proposed by previous studies (e.g., Carruzzo et al., 2004; Kontak and Kyser, 2011).

The $\delta^{18}\text{O}$ signatures for both autocrystic and antecrystic zircon in a majority of the SMB (i.e., excluding the DLP) range between +7.8 and +9.2‰ (outliers at +7.1 and +7.3‰; Fig. 2–15D, E), whereas the late overgrowth/recrystallized domains extend to higher values. The narrow range of $\delta^{18}\text{O}$ zircon values ($\pm \leq 1.4\text{‰}$) indicates the SMB magma was isotopically homogeneous, thus either derived from a similar source (with a relatively uniform $\delta^{18}\text{O}$) or shared a common source with similar degrees of contamination across the batholith. Importantly, when the $\delta^{18}\text{O}_{\text{zircon}}$ data are corrected for approximately +1‰ fractionation of ^{18}O between zircon and melt ($\Delta_{\text{WR-zircon}}$; Valley et al., 1994), the derived melt values range between ~8.8 and 10.2‰, and therefore overlap with the range of whole-rock data for the batholith (9 to 13‰, compiled in Kontak et al., 2002b). The higher values in zircon are a well-known phenomenon in cooling intrusive bodies (e.g., Taylor and Sheppard, 1986), and are attributed in the SMB to the role of late-stage

interaction of crystallized igneous rocks with cooling orthomagmatic fluids and/or fluids equilibrated with the Meguma metasedimentary rocks (as summarized in Carruzzo et al., (2004) and Kontak and Kyser (2011)). The lower melt $\delta^{18}\text{O}$ values are thus likely representative of the primary $\delta^{18}\text{O}$ signature for the SMB.

To assess contamination in the SMB by Meguma metasedimentary rocks, as suggested by Clarke et al. (2004), the $\delta^{18}\text{O}_{\text{zircon}}$ data are compared to whole-rock values in the latter, which range from +10.1 to +13.3‰ (Fig. 2–15; Longstaffe et al., 1980). Using a mean value of 11‰ for the hypothesized contaminant, mass balance indicates that for initial melt $\delta^{18}\text{O}$ values of 7, 8 and 9‰ (i.e., zircon values of 6, 7, and 8‰, respectively), approximately 50, 30 and 0% contamination (respectively) is required. For comparison, Clarke et al. (2004) suggested, based on major element and Sr and Nd isotopic data, that up to 30% contamination by Meguma metasedimentary rocks may have occurred, with a possible role of Avalonian-equivalent rocks (note, however, that Shellnut and Dostal (2012) suggest <20% contamination). The $\delta^{18}\text{O}_{\text{zircon}}$ values are consistent with this interpretation, however the uniform signature across the SMB and its lithologies indicate the source contamination must have occurred early in the magmatic evolution. The latter is therefore in conflict with the model of Clarke et al. (2004), which attributes some of the observed chemical variation in the SMB to late heterogeneous contamination.

The $\delta^{18}\text{O}$ values from both antecrystic and autocrystic zircon of the DLP are significantly lower than those found in the rest of the SMB and are also characterized by a large range (from +7.3 to +8.9‰, Table 2–6). In addition, two subpopulations are prominent for the autocryst values of +7.3 to +7.7‰ and +8.1 to +8.9‰ (Fig. 2–15E). Given the data are from a single sample and the range is greater than that expected from analytical variability (i.e., ± 0.21 ‰) and $\delta^{18}\text{O}$ values in zircon are not affected by magma fractionation (cf. Bindeman and Valley, 2002), it is likely that these values reflect the influence of a contaminant, such as the Meguma host rocks.

2.7.2.2 *Lu-Hf and ϵ_{Hf} data*

In addition to the O isotopic data, the Lu-Hf isotopic signature and derived ϵ_{Hf} values for zircon domains can be used to determine the influence of different isotopic melt reservoirs on magmas. For example, a wide variation in ϵ_{Hf} in a given zircon domain is typically attributed to source heterogeneity and/or open system processes (e.g., crustal assimilation) during magma evolution (e.g., Kemp et al., 2007; Appleby et al., 2010; Gagnevin et al., 2011; Wang et al., 2013; Ge et al., 2015). Furthermore, an evolving magmatic complex may source melts from an isotopically heterogeneous reservoir; thus isolated magma batches may contain a juvenile ϵ_{Hf} signature with respect to the rest of the complex, such as documented for zircon from the DLP compared to the rest of the SMB. However, as the ϵ_{Hf} signatures of both antecrysts and autocrysts match the majority of the xenocryst data, open system processes are likely restricted to the early stages of

magma evolution. Below we explore the implications of these data for the different zircon domains.

The ϵ_{Hf} values of the xenocrystic zircon domains provide insight to source rocks or wall-rocks that may have been entrained into the SMB melts. Some ϵ_{Hf} values yield model ages that preserve an earlier evolutionary history of Mesoproterozoic to Archean magmatic events (Fig. 2–17A). Collectively, the ϵ_{Hf} versus age distribution pattern for the xenocrysts are similar to that of detrital zircon populations from the Meguma Supergroup, as well as Ordovician sedimentary rocks in the Anti-Atlas of Morocco (Fig. 2–17A), (i.e., the West African Craton, Linnemann et al., 2004; Gärtner et al., 2015; 2016). These data support many other studies suggesting the Ediacaran-Early Ordovician Meguma Supergroup metasedimentary rocks were derived from the West African craton along the northern margin of Gondwana (e.g., White et al., 2006; Waldron et al 2009; White and Barr, 2010; Henderson et al., 2016). The presence of these xenocrysts in the SMB reflects either partial melting or assimilation of a sedimentary package at depth with affinities to the Meguma Supergroup metasedimentary rocks.

Magmatic zircon domains in the SMB have overlapping $^{176}\text{Lu}/^{177}\text{Hf}$ and calculated ϵ_{Hf} values with an overall variation (+3 to +6) that exceeds the analytical reproducibility of the standard zircons (i.e., $\pm 0.39 \epsilon_{\text{Hf}}$, 2σ). The ϵ_{Hf} values in both the antecrysts and autocrysts are, on average, markedly more juvenile in the less evolved SMB granodiorite (-3.7 to +2.0) compared to the

more evolved NRP, HP, and EDP (combined range of -2.8 to +0.5); this trend is particularly pronounced in the DLP for which ϵ_{Hf} is +1.8 to +4.6 (Fig. 2–16). These juvenile values are significantly higher than those expected from melting evolved Mesoproterozoic crust, but they are ~10–15 epsilon units lower than values expected from depleted mantle-derived melts (Fig. 2–17B); suggesting the SMB magma evolution likely included a juvenile melt that partially assimilated evolved crustal material. This scenario is supported by the $\delta^{18}\text{O}$ data discussed above and is consistent with the wall-rock assimilation model of Clarke et al. (2004).

The mixing/assimilation of source melts for the SMB magmas and the Meguma metasedimentary wall-rock create systematic variations in $\delta^{18}\text{O}$ and ϵ_{Hf} values for both autocrystic and antecrystic domains throughout the batholith (Fig. 2–18). The spread of data within $\delta^{18}\text{O} - \epsilon_{\text{Hf}}$ space can thus be used to determine influence from the different isotopic reservoirs. The overall shape of mixing/assimilation curves between reservoirs of metasedimentary rock and the mantle within $\delta^{18}\text{O} - \epsilon_{\text{Hf}}$ space can be predicted based on ratios of elemental O and Hf concentrations between each component; as the oxygen concentration in metasedimentary rock and the mantle are broadly similar, the shapes of mixing/assimilation curves are largely controlled by the relative Hf concentrations in the samples and their respective source reservoirs (or reservoir proxies; e.g., Appleby et al., 2010; Roberts et al., 2013; Ge et al., 2015). The mixing/assimilation of Hf and O from each end-member unit imparts representative $\delta^{18}\text{O}$ and ϵ_{Hf} signatures to the end products. The potential end-member components of the SMB include: 1) metasedimentary rocks from the

lower Meguma terrane (i.e., the Goldenville Group, $Hf_{ms} = 8.5$ ppm; White and Goodwin, 2011); 2) typical depleted mantle; and/or 3) a metasomatized mantle with a relatively enriched $\delta^{18}O$ signature (Fig. 2–18). The more juvenile source materials (i.e., 2 and 3) are assumed to have a geochemical composition similar to mafic intrusions that are broadly coeval with, and proximal to, the SMB. Thus, in this model, we input Hf compositions of 3.1 ppm from the ca. 377 Ma Bog Island gabbro (Hf_{bg} ; Clarke et al., 1993; Tate et al., 1997) and 5.3 ppm from the ca. 373 Ma Shelburne Pluton diorite (Hf_{dio} , southwest of the DLP; Currie et al., 1998, see locations in Fig. 2–1A). The estimated ~30% assimilation of metasedimentary wall-rock by the SMB (Clarke et al., 2004) suggests a majority of zircon data should plot on mixing lines between the potential end-member source reservoirs. The hyperbolae displayed in Figure 2–18 show mixing lines calculated for potential source rocks noted above (from Langmuir et al., 1978): the Meguma metasedimentary rocks, juvenile depleted mantle and metasomatized mantle (as represented by the Bog Island gabbro and the Shelburne Pluton, respectively). The ϵ_{Hf} values are calculated at $t = \sim 370$ Ma, and mixing lines are constructed using the ratios of average Hf content in the assimilant (Hf_{ms}) compared to proposed source reservoirs (Hf_{bg} and Hf_{dio} , Fig. 2–18). The limitations on characterizing the source reservoirs are: 1) a lack of published Lu-Hf isotopic data for Meguma metasedimentary rocks (note wide range in ϵ_{Hf} , Fig. 2–18) compared to the SMB zircon data; and 2) the unknown $\delta^{18}O$ signature of sources for juvenile melts that contribute to the SMB plumbing system. Based on the best fit mixing curve (Fig. 2–18), the source reservoir is likely at least +1‰ enriched in $\delta^{18}O$ relative to a typical depleted mantle composition (i.e., +5.0

to 5.5‰; Valley et al., 1998). This enrichment in $\delta^{18}\text{O}$ may reflect metasomatized mantle, which is typically up to +2‰ heavier due to alteration by fluids released by subducted sediments (e.g., Eiler et al., 2005; Auer et al., 2009; Johnson et al., 2009; Roberts et al., 2013).

A majority of the zircon Hf–O isotopic data in our model of mixing/assimilation to form SMB magmas (Fig. 2–18) requires the juvenile source to have higher $\delta^{18}\text{O}$ and a lower ϵ_{Hf} than expected for typical depleted mantle for a reasonable amount of contamination that is consistent with the ~30% estimated for the SMB by Clarke et al. (2004). The $\text{Hf}_{\text{bg}}/\text{Hf}_{\text{ms}}$ mixing curves calculated between a metasomatized mantle source and metasedimentary wall-rock fits the majority of the data and suggests the metasomatized mantle had an average ϵ_{Hf} value of ca. +7.5 (Fig. 2–18); i.e., at least 4 epsilon units lower than a typical depleted (asthenospheric) mantle source. This ϵ_{Hf} average value, however, does fall into the range of expected ϵ_{Hf} values of mantle-derived crustal sources with model ages between ~1.1 Ga and 550 Ma (blue field in Fig. 2–17A, B). These model ages are typical of an arc crust derived from metasomatized lithospheric mantle, as represented by mafic to felsic volcanic rocks, gabbro, granitoids, and gneisses in the Avalon terrane; which have been suggested to underlie Avalonian basement (Nance and Murphy, 1996; Murphy et al., 2000, 2008, 2018). Avalonian arc crust is also thought either to represent a basement to Meguma terrane rocks (e.g., Keppie et al., 1991; Keppie and Krogh, 2000) or to have underthrust the Meguma terrane during the Acadian orogeny, prior to SMB magmatism (e.g., Keen et al., 1991; Greenough et al., 1999; Shellnutt et al., 2019).

2.7.3 Construction and evolution of the South Mountain Batholith

The new U-Pb zircon and monazite data presented herein constrain the intrusive history of the main plutonic phases that comprise the composite SMB; together these data imply a protracted magmatic evolution prior to its final emplacement. The CA-ID-TIMS analysis of high-quality oscillatory-zoned zircon crystals document the final emplacement of the SMB: 378.7 ± 0.6 to 375.6 ± 0.5 Ma for the less evolved plutons versus 375.4 ± 0.8 to 371.8 ± 0.8 Ma for the more evolved plutons (Figs. 2–7A and 2–10). This range in crystallization ages, together with similar age determinations via in situ methods (i.e., SHRIMP and LA-MC-ICP-MS), collectively outline approximately 8 m.y. of continuous magmatism. The emplacement time-frame of the SMB is typical of mid- to upper-crustal batholiths constructed by incremental injection of magma batches over a relatively short duration (e.g., Brown and McClelland, 2000; Coleman et al., 2004; Broderick et al., 2015; Samperton et al., 2015; Schaltegger et al., 2019).

The age population distribution and isotopic characteristics of xenocrystic zircon in the SMB suggest a magmatic plumbing system that likely assimilated a variety of sources (Figs. 2–19A and 2–20, insets). The age distribution of the xenocrysts is similar to that of detrital zircons in the Silurian-Devonian Rockville Notch Group (cf. White et al., 2018) as well as the lower Paleozoic Goldenville Group (cf. Waldron et al., 2009), which underlie much of the Meguma terrane (Fig. 2–19B and C, respectively). The youngest concordant dates in xenocrystic zircon cores (24 analyses) are between ~400 and 500 Ma, with the highest density at ca. 433 Ma (Fig. 2–19A).

This population closely matches the Upper Ordovician–Lower Silurian felsic volcanic rocks of the White Rock Formation (e.g., MacDonald et al., 2002) and their intrusive equivalent (e.g., the 439 \pm 4/–3 Ma Brenton Pluton; Keppie et al., 2018), and zircon in granulite xenoliths from the ca. 370 Ma Pope’s Harbour dyke located to the northeast of the SMB (Owen et al., 1988; Shellnutt et al., 2019; Figs. 2–1A and 2–19D). The Brenton Pluton and lamprophyre dykes on the shores of the eastern Meguma terrane, which includes Pope’s Harbour, carry xenocrysts and granulite xenoliths, respectively, that are interpreted to represent lower crustal material (Owen et al., 1988; Eberz et al., 1991; Greenough et al., 1999; Keppie et al., 2018; Shellnutt et al., 2019; Fig. 2–20). The granulite xenoliths carry detrital zircon that have ages (i.e., ~420 Ma, ~660 Ma, and minor groups at ~1100 and ~2200 Ma) indicative of an Avalonia provenance with protolith depositional ages interpreted as ~420 Ma (cf. Shellnutt et al. 2019). This interpretation is consistent with the distribution of $\delta^{18}\text{O}$, ϵ_{Hf} , and $^{176}\text{Lu}/^{177}\text{Hf}$ values in xenocrysts from the SMB (Figs. 2–15G and 2–16D, respectively), which also suggest derivation from a variety of sources – from the lithospheric mantle to evolved Mesoproterozoic and Archean-aged crust.

The age and chemistry of antecrystic and autocrystic zircon domains typically record incremental stages of a magma generation and evolution, including the role of magma-mixing and host-rock assimilation (e.g., Hoskin and Schaltegger, 2003). The local preservation of antecrystic zircon domains suggest the SMB formed from multiple injections into a crystal mush that did not undergo complete crystal-resorption of the earlier zircon phases (cf. Miller et al., 2007; Miles and Woodcock, 2018). Our study identifies antecrysts that are, on average, between ~3 to 15

m.y. older than those of autocryst populations from the same samples. The resorption textures observed in the antecrysts suggest their crystallization in an early crystal mush that oscillated between zircon-saturation and undersaturation as it was repeatedly injected by new melt, as has been suggested for other magmatic settings (e.g., de la Rosa et al., 2002; Zeck and Williams, 2002; Bachmann and Bergantz, 2006).

The antecrysts have trace element chemical characteristics that are apparently indistinguishable from younger autocryst domains (i.e., wide range of Hf, Ce/Ce*, and Eu/Eu*, bivariate spread of Th/U and Yb/Gd values). The Ti-in-zircon geothermometer indicates crystallization temperatures for antecrysts are between 670–830°C in most of the SMB plutons, which compares to 740–980°C for the DLP (Table 2–5). These temperatures are, on average, lower than those calculated for their respective autocryst domains, although the ranges overlap (660–895°C in most of the SMB and 727 and 1008°C in the DLP; Table 2–5). The antecrysts are interpreted, therefore, to represent early magmas that likely crystallized in melt-rich roots in the lower crust ~3 to 15 m.y. before the construction of the SMB (Fig. 2–20). The trace-element similarities between antecrysts and autocrysts suggest the magmas that the antecrysts crystallized from may have been early, but they are part of the SMB plumbing system.

In contrast with zircon from the rest of the SMB, zircons in the DLP typically have higher ϵ_{Hf} values (Fig. 2–16B) and a subpopulation of lower $\delta^{18}\text{O}$ values. Both of these differences suggest an additional contribution from a more juvenile source compared to the rest of the SMB. The Hf-

O isotopic data for the zircons in the DLP are consistent with an assimilation-fractionation mixing model suggesting melts were derived from a metasomatized mantle-like source that subsequently underwent contamination by Meguma metasedimentary rock (Fig. 2–18). In contrast with the assimilation-fractionation mixing models from most of the SMB, mixing models that fit the DLP data used a melt reservoir proxy with a Hf concentration similar to the Shelburne Pluton diorite located ~20 km southwest of the DLP (Fig. 2–1A). Transitional from the diorite mass, the ca. 373 Ma Shelburne Pluton contains felsic phases that are compositionally similar to the SMB (Currie et al., 1998); the interpreted hybridization and mingling of peraluminous granitoid and metaluminous gabbroic to dioritic phases indicates mantle-derived magma played a significant role in the origin and emplacement of the Shelburne Pluton. We suggest, therefore, that the DLP shares isotopic characteristics with this and possibly other younger plutons with a juvenile source component in southwest Nova Scotia (e.g., Port Mouton Pluton, Fallon et al., 2001; Wedgeport Pluton, MacLean et al., 2003; Clayton Hill Pluton, Kontak et al., 2013), and formed from melts that were derived from a metasomatized mantle-like source and thus distinct from the sources for the rest of the SMB (Fig. 2–18).

Within ~10 Ma of the SMB emplacement, rapid differential uplift and unroofing is recorded in the Meguma terrane relative to the Avalon terrane by ca. 360 Ma (Fig. 2–2; e.g., Keppie, 1979; Keppie and Dallmeyer, 1995; Murphy, 2000) and indicates exhumation and ultimately exposure of the northern SMB from initial depths of ~10-12 km (e.g., Hilchie and Jamieson, 2008; Kontak and Kyser, 2011). Dextral transpressional movement along the Meguma-Avalonia terrane

boundary and related shear zones through the Meguma terrane (e.g., Fig. 2–1B, 2–20B) is recorded by dynamically recrystallized muscovite and biotite with $^{40}\text{Ar}/^{39}\text{Ar}$ plateau ages between 360 and 370 Ma (Keppie and Dallmeyer, 1987). These crustal faults (Fig. 2–1B) were thus active as transtensional pathways during and after SMB emplacement, and likely controlled incremental melt addition during SMB emplacement (i.e., repetition of Fig. 2–20A to B), prior to accommodating differential uplift and exhumation of the batholith. A Cenozoic analogue may be the Red River shear zone in SE Asia, where exhumation of high-grade metamorphic rocks and syn-kinematic granitoids occurred by transpression along ductile shear zones (Leloup et al., 2001).

The youngest U-Pb zircon ages recorded are metamict/recrystallized and unzoned overgrowth domains which yield dates around 360 Ma. This age is correlative with: 1) exhumation of the SMB, as constrained by the deposition of the late Famennian-Early Tournaisian Horton Group which locally onlaps the SMB and other ca. 375 Ma granites (e.g., Kelly pluton in eastern Meguma terrane; Archibald et al., 2018); 2) widespread fluid flux, as recorded by dating of new mineral growth and partial resetting of others (e.g., Ravenhurst et al., 1987; Culshaw and Reynolds, 1997; Hicks et al., 1999; Keppie et al., 2002; Reynolds et al., 2004; Keppie and Dallmeyer, 2005; Archibald et al., 2018); and 3) localized magmatism in the southwest Meguma terrane, such as the Wedgeport and Clayton Hill plutons (MacLean et al., 2003; Kontak et al., 2013). Thus, these young zircon domains may be a local expression of regional magmatic-hydrothermal activity that has generated and mobilized fluids that have penetrated the SMB. The

geochemistry, O and Lu-Hf isotopic signatures of these domains indicate that the fluid composition reflects a juvenile source that partially equilibrated with the SMB host-rock as well as Meguma metasedimentary wall-rock (Table 2–5; Figs. 2–15F and 2–16C).

Taken together, the U-Pb ages and Hf-O isotopic compositions of zircon suggest the SMB formed in four main stages: 1) melts were derived from a depleted mantle source beginning at ca. 390-385 Ma (Fig. 2–20A), as recorded by zircon antecrysts, and continued until ca. 375 Ma, as recorded by autocrysts in the less evolved parts of the SMB (Fig. 2–7A, –B); 2) these melts assimilated up to ~30% Meguma metasedimentary material; 3) between ca. 375 and 371 Ma, magma production continued (Fig. 2–20B) with related extensive fractionation that coincided with emplacement of the more evolved plutons within the SMB (i.e., HP, NRP, EDP); and 4) at ca. 371 Ma final emplacement of the SMB occurred with a change in the locus of magmatism to its southwestern part with the formation of the DLP. The latter was generated from a metasomatized mantle-like source similar in isotopic composition to that of typical Avalonian crust (Fig. 2–18).

2.7.4 Implications for the tectonic setting of SMB emplacement

The new geochronological data presented here indicate the SMB magmas were generated over a protracted interval that spans the duration of regional deformation and metamorphism associated with the Acadian and Neoacadian orogenic events. These events are commonly interpreted to reflect the accretion of the Avalon and Meguma terranes (respectively) to the eastern Laurentian

margin, between ca. 420 and 365 Ma (e.g. van Staal 2007; van Staal et al., 2009, 2021; Fig. 2–21). Subsequent (late Devonian) rapid uplift of the Meguma terrane relative to Avalonia and other inboard terranes (i.e., Ganderia), resulted in exposure of the SMB by ca. 360 Ma (Fig. 2–2; Keppie and Dallmeyer, 1995; Murphy, 2000; Archibald et al., 2018).

Our data provide the following additional constraints related to the SMB magmatism in the Meguma terrane: 1) overlapping crystallization ages for the antecrysts and autocrysts indicate melt generation and magmatic conditions were more prolonged (~10–15 m.y.) than previously realized; 2) the onset of magmatism at ca. 395 Ma occurred during ductile deformation of the host rock, as documented by $^{40}\text{Ar}/^{39}\text{Ar}$ data from both the Meguma Supergroup and White Rock Formation (e.g., Muecke et al., 1988; Kontak et al., 1998; Hicks et al., 1999; Reynolds et al., 2012); 3) $\delta^{18}\text{O}$ and ϵ_{HF} values in zircon from less evolved parts of the SMB (i.e., ~379 to 376 Ma) are consistent with melts that were both sourced from a metasomatized mantle, consistent with regional models of subduction beneath the Meguma terrane (e.g., van Staal et al., 2021), and significantly (~30%) contaminated by Meguma metasedimentary rocks; and 4) zircons in the DLP (i.e., at 373.4 ± 3.7 Ma) have chemical and isotopic signatures implying this stage in the SMB evolution produced higher (ca. 727 to 1008°C) temperature melts derived from lower Avalonian crust.

Our data indicate that the onset of magmatism at ca. 395 Ma was coeval with late stages of regional deformation in the Meguma terrane (i.e., ~415–390 Ma) associated with dextral

transpression between the Avalon and Meguma terranes. The early melts that crystallized a majority of the antecrysts in the SMB have isotopic signatures consistent with a sub-lithospheric mantle source beneath either the Meguma or Avalonia terranes (e.g., Fig. 2–21B). Between 385 and 375 Ma, antecryst zircon crystallization ages record an interval of sustained magmatism coeval with regional deformation and metamorphism which are interpreted to reflect continued dextral transpression during Neocadian orogenic events (cf. van Staal and Barr, 2012; Fig. 2–21C).

Sustained magmatic temperatures as recorded by zircon has been attributed elsewhere to internal (radioactive) heat production of overthickened crust (e.g., Lucazeau and Vasseur, 1989; Cuney et al., 1990; Jamieson et al., 1998). Although the Meguma crust was overthickened and the lower crust was likely dehydrated, as indicated by P-T conditions derived for granulite-facies rocks preserved as xenoliths in the Pope's Harbour dike (Owen et al., 1988; Eberz et al., 1991), heating from thermal relaxation (e.g. England and Thompson, 1984; Gaudemer et al., 1988) of such a crust is typically expected to produce ~5 weight per cent melt over 40 m.y. after thickening (e.g., Thompson and Connolly, 1995). Modelling of water-fluxed lower crust melting processes (~8 kbar), however, show that addition of ~4.5 wt. % water into a mafic dioritic crust at 900°C can generate ~40% melt, and at 750 °C will produce ~30% tonalitic to trondhjemitic melts (Collins et al., 2020). Thus, the addition of water is important for generation of large volumes of melt in an anhydrous lower crust (Castro, 2020). For a majority of the SMB magmas, melt derivation from a metasomatized mantle indicates direct infiltration of water from oblique

subduction processes (down-going Rheic oceanic slab) along the Laurentian margin at the onset of SMB magmatism (i.e., ca. 395 Ma; Fig. 2–21B). Although no direct evidence of subduction during this time interval is preserved in the current level of exposure, the widespread regional magmatism of this age in the northern Appalachians is interpreted to represent subduction processes followed by slab-breakoff and mantle upwelling (e.g., van Staal et al., 2009, 2021; Wilson et al., 2017; Kellett et al., in press).

The terminal stages of SMB emplacement occurred between ~375 and 370 Ma, and crystallized the most evolved plutons (i.e., Stage II of MacDonald, 2001), including the DLP which hosts the most isotopically juvenile zircons in the batholith. The DLP zircons have combined Lu-Hf and O isotopic signatures suggesting the DLP parental melts were sourced from an intermediate crustal component that likely formed from water-bearing, metasomatized mantle-derived magmas (i.e., a pre-existing fractionated mafic underplate, Castro 2020, and references therein). A candidate for the intermediate crustal component is that of the Avalonian lower crust, which would have underthrust the Meguma terrane during convergence between these terranes (~380-375 Ma; Fig. 2–21C).

Accretion of the Avalonia-Meguma terranes along the Laurentian margin is interpreted here to have resulted in break-off of a subducted slab of Rheic oceanic lithosphere by ca. 371 Ma (Fig. 2–21C). The sinking of this orphaned slab would initially subject the underthrust Avalonian sub-continental lithospheric mantle to melting from an upwelling asthenosphere (Fig. 2–21D).

This process is consistent with the juvenile isotopic signature and higher average crystallization temperatures in DLP zircon compared to zircons in older SMB plutons. Additionally, asthenospheric upwelling would result in thinning of the lithosphere beneath the Avalonia/Meguma terrane boundaries and thus re-activation of deep crustal faults, allowing for significant differential uplift between these terranes along the Laurentian margin (Fig. 2–21D).

The data presented here suggest the emplacement of most of the SMB occurred between 378–372 Ma, i.e. ca. 15–20 Ma after magmatism commenced, suggesting the delayed onset of favourable conditions for melt ascent into the upper crust. We suggest that the progressive downward development of fault conduits, as a result of terrane convergence between Meguma and Avalonia (i.e., during the Neoacadian), penetrated to the zone of magma generation and prompted the magma ascent. The evidence for such deep-seated structures that controlled magma ascent has been suggested in field observations (i.e., outline of the SMB external contacts, internal faults/shear zones and jointing) that mirror those in the Meguma Supergroup, and studies on the gravity, seismic and aeromagnetic signature of the SMB that indicate the SMB roots follow penetrative structures traced as deep as the Moho (e.g., Keen et al., 1991; Horne et al., 1992; Benn et al., 1997; MacDonald, 2001). Therefore, the evolution of the SMB magmatic plumbing system likely involved a change from a ductile lower crustal infrastructure, where early melts were generated and gestated, to a brittle upper crustal regime. This change coincided with the accretion of the Meguma terrane to Avalonia and the Laurentian margin. The latter

structural reactivation in a brittle regime not only facilitated magma ascent but also the preferential emplacement of granitoid magmas into releasing bends along the structures.

2.7.5 Metallogenic implications

A variety of Cu, W-Mo, Sn, Sb and Ta mineralized centres associated with Devonian-Carboniferous granitic magmatism occur in different tectonic terranes in the northern Appalachians (van Staal, 2007; Kellett et al., in press; Fig. 2–1A). Mineralization associated with the SMB varies in character and includes polymetallic (Sn, W, Mo, Cu, Ta, Nb, Zn) occurrences, typically in the more-evolved plutons; however, the only significant Sn deposit that contains economic concentrations of metals is the Sn-Zn-Cu-Ag-In East Kemptville deposit near the southwest contact of the ca. 370 Ma DLP (Fig. 2–1A). Between ~370 and 355 Ma mafic- to intermediate magmatism is associated with numerous sites of Sn-polymetallic occurrences along shear zones through the southwest margin of the DLP (e.g., Clarke et al., 1997). These mineral occurrence have collectively been referred to as a Sn-Ag domain (Chatterjee and Strong, 1985; Kontak, 1990; MacDonald, 2001).

Typically, Sn ore-forming magmas have low oxygen fugacities with Sn in its reduced state (i.e., Sn²⁺), thereby inhibiting substitution into ferromagnesian minerals resulting in Sn enrichment in fractionated magmas (Ishihara, 1981; Blevin and Chappell, 1992; Linnen et al., 1996); globally, these magmas have typically been emplaced into or adjacent to graphite-bearing as well as Sn- and/or W-enriched pelitic rocks (cf. Romer and Kroner, 2015). The contamination of the SMB

by graphite-bearing metasedimentary rocks in the southwestern part of the batholith, as documented above, would have resulted in reduced magmas and therefore allowed for Sn enrichment during fractionation. Although the SMB magmas were strongly reduced, the presence of this signature in antecrysts, autocrysts (Fig. 2–14A, B), and the youngest xenocrysts (representative of crustal material beneath the Meguma Supergroup) suggests the source melts were reduced, implying the potential for protracted Sn enrichment during fractionation. The contrasting oxidized fO_2 signatures from xenocrysts typical of the Meguma Supergroup detrital population (Fig. 2–14C) indicate the melts became less reduced as they assimilated wall-rock material. Other parts of the SMB are equally as contaminated as the DLP, yet do not contain significant Sn mineralization. Additionally, metasedimentary rocks in the southwest part of the Meguma terrane are depleted in B, Sn, and Ta with respect to the rest of the terrane (Chapter 3); indicating localized contamination would not result in enriched Sn for this part of the SMB.

Whereas the bulk of the SMB is intermediate to felsic and does not contain significant concentration of Sn-polymetallic occurrences, intrusions in the Sn-Ag domain southwest of the DLP either: 1) overlap in age with the SMB but show evidence of a more juvenile source melt; or 2) are ca. 10 m.y. younger than the SMB but mafic to intermediate with A-type characteristics (see Kontak et al., 2013, for a summary). Therefore, the data suggest that metal occurrences in the southwestern part of the terrane does not reflect contamination in the SMB by locally Sn-enriched crustal wall-rock (e.g., Romer and Kroner, 2015); rather, magmatism in the area (i.e.,

DLP and later intrusives of the Sn-Ag domain) were likely derived from a metal-enriched melt source (i.e., metasomatized mantle), different from that which sourced of earlier SMB magmas.

Regionally, in addition to the East Kemptville deposit, the northern Appalachians host the Mount Pleasant W-Mo deposit (associated with the ca. 368 Ma Mount Douglas Granite; e.g., Mohammadi et al., 2020) and the Ackley Sn-W-Mo deposit (hosted by the ca. 372 Ma Ackley Granite; e.g., Kontak et al., 1988; Kellett et al., 2014); both hosted by intrusive complexes interpreted to straddle the Avalonia-Ganderia boundary.

The induced melting of a sub-Avalonian metasomatized mantle by ca. 370 Ma (Fig. 2–21D) by asthenospheric upwelling as discussed above likely occurred beneath both the Avalonian-Meguma and Avalonian-Ganderia terrane boundaries. This interpretation suggests that across the Canadian Appalachians, Sn-W deposits associated with ~370-360 Ma magmatic-hydrothermal activity (Fig. 2–1A) originated by melting a common Sn-enriched source that is represented by sub-continental lithospheric mantle or lower crust to the Avalon terrane (Fig. 2–21D).

2.8 Conclusions

Comprehensive U-Pb zircon dating from representative samples of the 7300 km² composite peraluminous SMB has yielded a range in ages from various CL-defined zircon domain types. The CA-TIMS autocryst zircon dates from the SMB indicate the batholith was constructed in a magmatic system that was long-lived, but crystallized in two main intrusive events: 1) early

phases of granodiorite to monzogranite that crystallized between 378.7 ± 0.6 Ma and 375.6 ± 0.5 Ma, which includes a more evolved leucomonzogranite pluton (i.e., WDP) that previously was considered to be part of a later stage event; and 2) the less voluminous but highly fractionated DLP, EDP, NRP, and HP that crystallized between 375.4 ± 0.8 Ma and 371.8 ± 0.8 Ma.

Together, these intrusive phases record approximately 8 m.y. of overlapping magmatic activity.

SHRIMP and LA-MC-ICP-MS dating of abundant xenocrystic zircon cores document a varied age population (~400 Ma to 2.2 Ga) that is very similar to that of the detrital zircon population in Meguma terrane metasedimentary rocks, including a younger group of dates (i.e., ~470-400 Ma) not present in the upper crust, but characteristic of granulite xenoliths in lamprophyre dykes, interpreted to represent the current basement underlying the Meguma terrane of interpreted Avalon affinity.

The 8 m.y. emplacement window is defined by autocrysts, although in situ SHRIMP and LA-MC-ICP-MS analyses of antecrysts record multiple crystallization events that are ca. 3–15 Ma older than the autocryst ages (dominantly between ~390 and 380 Ma). The antecryst ages represent crystallization from early melts in the lower crust that were subsequently resorbed and/or entrained into the SMB magmatic plumbing system. In situ SIMS and LA-MC-ICP-MS analyses for both antecrystic and autocrystic zircon domains in most plutons, with the exception of the DLP, document similar $\delta^{18}\text{O}$, REE and ϵ_{HF} signatures, as well as derived $f\text{O}_2$ values that

make up the SMB. These similarities are a record of the extensive contamination in the SMB by metasedimentary rocks of the Meguma terrane.

The DLP has an ε_{Hf} signature in zircon autocrysts (+1.74 to +4.38) that is higher than those in the rest of the SMB (-2.99 to +1.68). Relative to the rest of the SMB, these zircon also have, on average, higher calculated Ti-in-zircon crystallization temperatures, a population of lower $\delta^{18}\text{O}$ values, and overlapping $f\text{O}_2$ values. Combined, these data suggest the DLP underwent less contamination by upper crustal rocks and/or was derived from a melt source more juvenile than that of the SMB, with characteristics of a metasomatized mantle. The latter feature is important in assessing metallic (Sn, W, Mo, Cu, Ta, Nb, Zn) fertility in the northern Appalachians as the DLP and surrounding post SMB-emplacement granitoids are associated with such mineral occurrences, unlike the rest of the SMB. Throughout the accretionary Appalachian orogen, similar aged sub-economic deposits occur associated with mantle-derived fractionated magmatism; suggesting metal endowment is related to the melt generation stage of these intrusions.

The tectonic setting during the SMB formation initially (i.e., ~395 Ma) was coeval with dextral transpressional accretion of the Meguma terrane to Avalonia, as evidenced by regional deformation in the upper crust through the Meguma terrane at ~415–390 Ma (e.g., Murphy et al., 2011). Subsequent evolution of the setting is documented by contamination of the SMB, whereby early antecrysts and rare xenocrysts that reflect a source component consistent with a

sub-lithospheric mantle consistent with the root zone to Avalonia, that suggests westward overthrusting of Meguma terrane between 385 and 375 Ma. The sustained magmatic conditions recorded in zircon from the SMB is attributed to regional deformation and metamorphism in the Meguma terrane during the Neocadian orogenic event.

2.9 Acknowledgements

This project was partially funded from NSERC CRD grants to DJK and IMS as well as Natural Resources Canada as part of the Targeted Geoscience Initiative program of the Geological Survey of Canada (DAK). The authors acknowledge Dr. Isabelle Coutand for assistance with sample preparation and would like to thank Dr. James Brennan, Fergus Tweedale, and the late Dr. Trevor McHattie for thoughtful discussions that aided geological interpretation. We would like to thank Nicole Rayner for assistance with SHRIMP analysis.

2.10 References

Ague, J.J., and Brimhall, G.H., 1988, Magmatic arc asymmetry and distribution of anomalous plutonic belts in the batholiths of California: Effects of assimilation, crustal thickness, and depth of crystallization: Geological Society of America Bulletin, v. 100, no. 6, p. 912-927.

- Annen, C., Blundy, J.D., Leuthold, J., Sparks, R.S.J., 2015, Construction and evolution of igneous bodies: towards an integrated perspective of crustal magmatism: *Lithos*, v. 230, p. 206–221.
- Archibald, D.B., and Murphy, J.B., 2021, A slab failure origin for the Donegal composite batholith, Ireland as indicated by trace-element geochemistry: Geological Society, London, Special Publications, v. 503, no. 1, p. 347-370.
- Archibald, D.B., Murphy, J.B., Reddy, S.M., Jourdan, F., Gillespie, J., and Glorie, S., 2018, Post-accretionary exhumation of the Meguma terrane relative to the Avalon terrane in the Canadian Appalachians: *Tectonophysics*, v. 747, p.343-356.
- Auer, S., Bindeman, I., Wallace, P., Ponomareva, V. and Portnyagin, M., 2009, The origin of hydrous, high- $\delta^{18}\text{O}$ voluminous volcanism: diverse oxygen isotope values and high magmatic water contents within the volcanic record of Klyuchevskoy volcano, Kamchatka, Russia. *Contributions to Mineralogy and Petrology*, v. 157, no. 2, p. 209.
- Averill, S.A., and Huneault, R., 2006, Overburden Drilling Management Ltd: Exploring heavy minerals: *EXPLORE*, Newsletter of the Association of Applied Geochemists, v. 133, p. 1-5.
- Bachmann, O., and Bergantz, G.W., 2006, Gas percolation in upper-crustal silicic crystal mushes as a mechanism for upward heat advection and rejuvenation of near-solidus magma bodies: *Journal of Volcanology and Geothermal research*, v. 149, p. 85-102.

- Barboni, M., Annen, C., and Schoene, B., 2015, Evaluating the construction and evolution of upper crustal magma reservoirs with coupled U/Pb zircon geochronology and thermal modeling: A case study from the Mt. Capanne pluton (Elba, Italy): *Earth and Planetary Science Letters*, v. 432, p. 436–448.
- Barr, S.M., Hamilton, M.A., Samson, S.D., Satkoski, A.M., White, C.E., 2012, Provenance variations in northern Appalachian Avalonia based on detrital zircon age patterns in Ediacaran and Cambrian sedimentary rocks, New Brunswick and Nova Scotia, Canada: *Canadian Journal of Earth Sciences*, v. 49, p. 533–546.
- Beckman, V., Möller, C., Söderlund, U. and Andersson, J., 2017, Zircon growth during progressive recrystallization of gabbro to garnet amphibolite, Eastern Segment, Sveconorwegian orogen: *Journal of Petrology*, v. 58, p. 167-187.
- Benn, K., Horne, R.J., Kontak, D.J., Pignotta, G.S., and Evans, N.G., 1997, Syn-Acadian emplacement model for the South Mountain Batholith, Meguma Terrane, Nova Scotia: Magnetic fabric and structural analyses: *Geological Society of America Bulletin*, v. 109, p. 1279-1293.
- Benn, K., Roest, W.R., Rochette, P., Evans, N.G., and Pignotta, G.S., 1999, Geophysical and structural signatures of syntectonic batholith construction: the South Mountain Batholith, Meguma Terrane, Nova Scotia: *Geophysical Journal International*, v. 136, p.144-158.

- Bird, J.M., and Dewey, J.F., 1970, Lithosphere platecontinental margin tectonics and the evolution of the Appalachian Orogen: Geological Society of America Bulletin, v. 81, p. 1031–1060.
- Black, L. P., Kamo, S. L., Allen, C. M., Davis, D., Aleinikoff, J. N., Valley, J. W., Mundil, R., Campbell, I. H., Korsch, R. J., Williams, I. S., and Foudoulis, C., 2004. Improved $^{206}\text{Pb}/^{238}\text{U}$ microprobe geochronology by the monitoring of a trace-element-related matrix effect; SHRIMP, ID-TIMS, ELA-ICP-MS and oxygen isotope documentation for a series of zircon standards: Chemical Geology, v. 205, p. 115-140.
- Blevin, P.L. and Chappell, B.W., 1992, The role of magma sources, oxidation states and fractionation in determining the granite metallogeny of eastern Australia: Transactions of the Royal Society of Edinburgh: Earth Sciences, v. 83, p.305-316.
- Bouvier, A., Vervoort, J.D. and Patchett, P.J., 2008, The Lu–Hf and Sm–Nd isotopic composition of CHUR: constraints from unequilibrated chondrites and implications for the bulk composition of terrestrial planets: Earth and Planetary Science Letters, v. 273, p.48-57.
- Broderick, C., Wotzlaw, J., Frick, D., Gerndez, A., Ulianov, A., Gunther, D., Schaltegger, U., 2015, Linking the thermal evolution and emplacement history of an upper crustal pluton to its lower-crustal roots using zircon geochronology and geochemistry (southern

- Adamello batholith, N. Italy): *Contributions to Mineralogy and Petrology*, v. 170, p. 1–17.
- Brown, E.H., and McClelland, W.C., 2000, Pluton emplacement by sheeting and vertical ballooning in part of the southeast Coast Plutonic Complex, British Columbia: *Geological Society of America Bulletin*, v. 112, p. 708-719.
- Brown, M., 1994, The generation, segregation, ascent and emplacement of granite magma: the migmatite-to-crustally-derived granite connection in thickened orogens: *Earth-Science Reviews*, v. 36, p. 83-130.
- Brown, S.J.A., Fletcher, I.R., 1999, SHRIMP U-Pb dating of the preeruption growth history of zircons from the 340 ka Whakamaru Ignimbrite, New Zealand; evidence for N250 k.y. magma residence times: *Geology*, v. 27, p. 1035–1038.
- Buret, Y., Von Quadt, A., Heinrich, C., Selby, D., Wälle, M., and Peytcheva, I., 2016, From a long-lived upper-crustal magma chamber to rapid porphyry copper emplacement: Reading the geochemistry of zircon crystals at Bajo de la Alumbrera (NW Argentina): *Earth and Planetary Science Letters*, v. 450, p. 120-131.
- Cabri, L.J., Rudashevsky, N.S., Rudashevsky, V.N. and Oberthür, T., 2008, Electric-Pulse Disaggregation (EPD), Hydroseparation (HS) and their use in combination for mineral processing and advanced characterization of ores. in *Canadian Mineral Processors 40th Annual Meeting, Proceedings*, v. 14, p. 211-235.

- Carruzzo, S., Kontak, D.J., and Clarke, D.B., 2000, Granite-hosted mineral deposits of the New Ross area, South Mountain Batholith, Nova Scotia, Canada: P, T and X constraints of fluids using fluid inclusion thermometry and decrepitate analysis: Transactions of the Royal Society of Edinburgh: Earth Sciences, v. 91, p. 303–319.
- Černý, P., 1991, Rare-element granitic pegmatites. Part II: Regional to global environments and petrogenesis: Geoscience Canada.
- Černý, P., Blevin, P. L., Cuney, M., and London, D., 2005, Granite related ore deposits: Economic Geology 100th Anniversary Volume, p. 337–370.
- Chatterjee, A.K., Strong, D.F., 1985, Geochemical characteristics of the polymetallic tin domain, southwestern Nova Scotia, Canada. in Taylor, R.P., and Strong, D.F., eds., Granite-Related Mineral Deposits: Geology, Petrogenesis and Tectonic Setting: Canadian Institute of Mining and Metallurgy, Extended Abstract, p. 41-52.
- Chatterjee A.K., Cormier, R.F., 1991, A Rb-Sr geochronological study of the Davis Lake pluton, South Mountain batholith, southern Nova Scotia: evidence for a 374Ma time of emplacement. Mines and Minerals Branch Report of activities, part A. Nova Scotia Department of Natural Resources Report.
- Chatterjee, A., and Dostal, J., 2003, Deep drill hole in the Devonian South Mountain batholith, Nova Scotia: a potential for hidden mineral deposits within the batholith: Atlantic Geology, v. 38, p.1-10.

- Chavez, J., 2019, Redox state of the South Mountain Batholith: A reconnaissance study using zircon geochemistry: unpublished B.Sc. Thesis, Dalhousie University, Halifax, Canada, 53 pp.
- Cherniak, D.J. and Watson, E.B., 2003, Diffusion in zircon: Reviews in mineralogy and geochemistry, v. 53, p.113-143.
- Claiborne, L.L., Miller, C.F. and Wooden, J.L., 2010, Trace element composition of igneous zircon: a thermal and compositional record of the accumulation and evolution of a large silicic batholith, Spirit Mountain, Nevada: Contributions to Mineralogy and Petrology, v. 160, p.511-531.
- Clarke, D.B., 2010, The Meguma Lithotectonic Terrane. in Clarke, D.B., ed., Eurogranites 2010 Field Excursion Guidebook, Nova Scotia: Atlantic Geoscience Society, Special Publication, v. 37, p. 5-31.
- Clarke, D.B., and Carruzzo, S, 2007, Assimilation of country-rock ilmenite and rutile in the South Mountain Batholith, Nova Scotia, Canada: Canadian Mineralogist, v. 45, p. 31-42.
- Clarke, D.B., and Chatterjee, A.K., 1988, Physical and chemical processes in the South Mountain Batholith. in Taylor, R.P., and Strong, D.F., eds., Recent advances in the geology of granite-related mineral deposits: Special Volume - Canadian Institute of Mining and Metallurgy, v. 39, p. 223-233.

- Clarke, D.B., and Halliday, A.N., 1980, Strontium isotope geology of the South Mountain batholith, Nova Scotia: *Geochimica et Cosmochimica Acta*, v. 44, p. 1045–1058.
- Clarke, D.B., Halliday, A.N. and Hamilton, P.J., 1988, Neodymium and strontium isotopic constraints on the origin of the peraluminous granitoids of the South Mountain Batholith, Nova Scotia, Canada: *Chemical Geology: Isotope Geoscience section*, v. 73, p.15-24.
- Clarke, D.B., MacDonald, M.A., Reynolds, P.H., Longstaffe, F.J., 1993, Leucogranites from the Eastern Part of the South Mountain Batholith, Nova Scotia: *Journal of Petrology*, v. 34, p. 653–679.
- Clarke, D.B., MacDonald, M.A., and Tate, M.C., 1997, Late Devonian mafic-felsic magmatism in the Meguma Zone, Nova Scotia. in Sinha, A.K., Whalen, J.B., Hogan, J.P., eds., *The nature of magmatism in the Appalachian Orogen: Geological Society America Memoir*, v. 191, p. 107–127.
- Clarke, D. B., Fallon, R., and Heaman, L.M., 2000, Interaction among upper crustal, lower crustal, and mantle materials in the Port Mouton pluton, Meguma Lithotectonic Zone, southwest Nova Scotia: *Canadian Journal of Earth Sciences*, v. 37, p. 579-600.
- Clarke, D.B., MacDonald, M.A., and Erdmann, S., 2004, Chemical variation in Al_2O_3 -CaO- Na_2O - K_2O space: controls on the peraluminosity of the South Mountain Batholith: *Canadian Journal of Earth Sciences*, v. 41, p. 785-798.

- Clarke, D.B., Dorais, M., Barbarin, B., Barker, D., Cesare, B., Clarke, G., El Baghdadi, M., Erdmann, S., Förster, H.J., Gaeta, M. and Gottesmann, B., 2005, Occurrence and origin of andalusite in peraluminous felsic igneous rocks: *Journal of Petrology*, v. 46, p.441-472.
- Clarke, D.B., Erdmann, S., Samson, H. and Jamieson, R.A., 2009, Contamination of the South Mountain Batholith by sulfides from the country rocks: *The Canadian Mineralogist*, v. 47, p.1159-1176.
- Clemens, J.D., 1984, Water contents of silicic to intermediate magmas: *Lithos*, v. 17, p. 273-287.
- Clemens, J., 2003, S-type granitic magmas—petrogenetic issues, models and evidence: *Earth-Science Reviews*, v. 61, p. 1–18.
- Coleman, D.S., Gray, W., Glazner, A.F., 2004, Rethinking the emplacement and evolution of zoned plutons: Geochronologic evidence for incremental assembly of the Tuolumne Intrusive Suite, California: *Geology*, v. 32, p. 433–436.
- Corfu, F., Hanchar, J., Hoskin, P.W.O., and Kinny, P., 2003, Atlas of zircon textures: *Reviews in Mineralogy and Geochemistry*, v. 53.
- Courtney-Davies, L., Ciobanu, C.L., Verdugo-Ihl, M.R., Slattery, A., Cook, N.J., Dmitrijeva, M., Keyser, W., Wade, B.P., Domnick, U.I., Ehrig, K. and Xu, J., 2019, Zircon at the Nanoscale Records Metasomatic Processes Leading to Large Magmatic–Hydrothermal Ore Systems: *Minerals*, v. 9, p. 364.

- Culshaw, N., and Reynolds, P., 1997, $^{40}\text{Ar}/^{39}\text{Ar}$ age of shear zones in the southwest Meguma Zone between Yarmouth and Meteghan, Nova Scotia: *Canadian Journal of Earth Sciences*, v. 34, p. 848-853.
- Culshaw, N. and Lee, S.K., 2006, The Acadian fold belt in the Meguma Terrane, Nova Scotia: Cross sections, fold mechanisms, and tectonic implications: *Tectonics*, v. 25, 16p.
- Culshaw, N., and Bhatnagar, P., 2001, The interplay of regional structure and emplacement mechanisms at the contact of the South Mountain Batholith, Nova Scotia: floor-down or wall-up?: *Canadian Journal of Earth Sciences*, v. 38, p.1285-1299.
- Cuney, M., 1990, Structural and magmatic control of late-Hercynian uranium concentrations; the la Crouzille district (Haute-Vienne Department, France). *Controles magmatiques et structuraux de la metallogenese uranifere tardi-hercynienne; exemple du district de la Crouzille (Haute-Vienne): Chronique de la Recherche Miniere (France)*, v. 58, p. 499.
- Currie, K.L., Whalen, J.B., Davis, W.J., Longstaffe, F.J., and Cousens, B.L., 1998, Geochemical evolution of peraluminous plutons in southern Nova Scotia, Canada—a pegmatite-poor suite: *Lithos*, v. 44, p. 117-140.
- Cruden, A.R., 1998, On the emplacement of tabular granites: *Journal of the Geological Society of London*, v. 155, p. 853-862.
- Davis, D.W., 1982, Optimum linear regression and error estimation applied to U-Pb data: *Canadian Journal of Earth Sciences*, v. 19, p. 2141-2149.

- de la Rosa, J.D., Jenner, G.A. and Castro, A., 2002, A study of inherited zircons in granitoid rocks from the South Portuguese and Ossa-Morena Zones, Iberian Massif: support for the exotic origin of the South Portuguese Zone: *Tectonophysics*, v. 352, p. 245-256.
- Dostal, J., and Chatterjee, A.K., 1995, Origin of topaz-bearing and related peraluminous granites of the Late Devonian Davis Lake pluton, Nova Scotia, Canada: crystal versus fluid fractionation: *Chemical Geology*, v. 123, p.67-88.
- Eberz, G.W., Clarke, D.B., Chatterjee, A.K., and Giles, P.S., 1991, Chemical and isotopic composition of the lower crust beneath the Meguma lithotectonic zone, Nova Scotia: evidence from granulite facies xenoliths: *Contributions to Mineralogy and Petrology*, v. 109, p. 69–88.
- Eiler, J.M., Carr, M.J., Reagan, M. and Stolper, E., 2005, Oxygen isotope constraints on the sources of Central American arc lavas: *Geochemistry, Geophysics, Geosystems*, v. 6.
- England, P.C. and Thompson, A.B., 1984, Pressure—temperature—time paths of regional metamorphism I. Heat transfer during the evolution of regions of thickened continental crust: *Journal of Petrology*, v. 25, p.894-928.
- Erdmann, S., London, D., Morgan, G.G.B., and Clarke, D.B., 2007, The contamination of granitic magma by sedimentary country-rock material: an experimental study: *Canadian Mineralogist*, v. 45, p. 43-61.

- Erdmann, S., Jamieson, R.A., and MacDonald, M.A., 2009, Evaluating the Origin of Garnet, Cordierite, and Biotite in Granitic Rocks: a Case Study from the South Mountain Batholith, Nova Scotia: *Journal of Petrology*, v. 50, p. 1477–1503.
- Erdmann, S., Wodicka, N., Jackson, S.E., and Corrigan, D., 2013, Zircon textures and composition: refractory recorders of magmatic volatile evolution?: *Contributions to Mineralogy and Petrology*, v. 165, p.45-71.
- Fallon, R. P., Reynolds, P. H., and Clarke, D.B., 2001, A comparative $^{40}\text{Ar}/^{39}\text{Ar}$ conventional and laserprobe study of muscovite from the Port Mouton pluton, southwest Nova Scotia: *Canadian Journal of Earth Sciences*, v. 38, p. 347-357.
- Farina, F., Stevens, G., Villaros, A., 2012. Multi-batch, incremental assembly of a dynamic magma chamber: the case of the Peninsula pluton granite (Cape Granite Suite, South Africa): *Contributions to Mineralogy and Petrology*, v. 106, p.193–216.
- Ferry, J.M., and Watson, E.B., 2007, New thermodynamic models and revised calibrations for the Ti-in-zircon and Zr-in-rutile thermometers: *Contributions to Mineralogy and Petrology*, v. 154, p. 429–437.
- Fisher, C.M., Hanchar, J.M., Samson, S.D., Dhuime, B., Blichert-Toft, J., Vervoort, J.D. and Lam, R., 2011, Synthetic zircon doped with hafnium and rare earth elements: A reference material for in situ hafnium isotope analysis: *Chemical Geology*, v. 286, p. 32-47.

- France, L., Demacon, M., Gurenko, A.A. and Briot, D., 2016, Oxygen isotopes reveal crustal contamination and a large, still partially molten magma chamber in Chaîne des Puys (French Massif Central): *Lithos*, v. 260, p. 328-338.
- Frets, E.C., Tommasi, A., Garrido, C.J., Vauchez, A., Mainprice, D., Targuisti, K. and Amri, I., 2014, The Beni Bousera peridotite (Rif Belt, Morocco): an oblique-slip low-angle shear zone thinning the subcontinental mantle lithosphere: *Journal of Petrology*, v. 55, p. 283-313.
- Gaudemer, Y., Jaupart, C. and Tapponnier, P., 1988, Thermal control on post-orogenic extension in collision belts: *Earth and Planetary Science Letters*, v. 89, p.48-62.
- Garland, G.D., 1953, Gravity measurements in the Maritime Provinces. Ottawa, Publ. Dom. Obs., v. 16, p. 185-275.
- Gärtner, A., Villeneuve, M., Linnemann, U., Gerdes, A., Youbi, N., Guillou, O. and Rjimati, E.C., 2016, History of the west African Neoproterozoic ocean: key to the geotectonic history of circum-Atlantic peri-Gondwana (Adrar Souttoug massif, Moroccan Sahara): *Gondwana Research*, v. 29, p. 220-233.
- Geisler, T., Schaltegger, U. and Tomaschek, F., 2007, Re-equilibration of zircon in aqueous fluids and melts: *Elements*, v. 3, p. 43-50.
- Giles, P.S., 1985, A major post-Visean sinistral shear zone – new perspectives on Devonian and Carboniferous rocks of southern Nova Scotia. in Chatterjee, A.K. and Clarke, D.B., eds.,

- Guide to the granites and mineral deposits of southwestern Nova Scotia: Nova Scotia Department of Mines and Energy, v. 85, p. 233-248.
- Giles, P.S. and Chatterjee, A.K., 1987, Evolution of the Liscomb Complex and its relevance to metallogeny in the Eastern Meguma Terrane: Nova Scotia Department of Mines, Report, v. 87, p.1.
- Glazner, A.F., Bartley, J.M., Coleman, D.S., Gray, W., and Taylor, R.Z., 2004, Are plutons assembled over millions of years by amalgamation from small magma chambers?: GSA Today, v. 14, p. 4.
- Greenough, J.D., Krogh, T.E., Kamo, S.L., Owen, J.V. and Ruffman, A., 1999, Precise U-Pb dating of Meguma basement xenoliths: new evidence for Avalonian underthrusting: Canadian Journal of Earth Sciences, v. 36, p. 15-22.
- Griffin, W.L., Pearson, N.J., Belousova, E., Jackson, S.V., Van Acherbergh, E., O'Reilly, S.Y., and Shee, S.R., 2000, The Hf isotope composition of cratonic mantle: LAM-MC-ICPMS analysis of zircon megacrysts in kimberlites: Geochimica et cosmochimica acta, v. 64, p. 133-147.
- Griffin, W.L., Wang, X., Jackson, S.E., Pearson, N.J., O'Reilly, S.Y., Xu, X. and Zhou, X., 2002, Zircon chemistry and magma mixing, SE China: in-situ analysis of Hf isotopes, Tonglu and Pingtan igneous complexes: Lithos, v. 61, p. 237-269.

- Haggerty, S.E., 1978,. The redox state of planetary basalts: *Geophysical Research Letters*, v. 5, p. 443-446.
- Halter W.E., and Williams-Jones, A.E., 1999, Application of topaz muscovite F-OH exchange as a geothermometer: *Economic Geology*, v. 94, p. 1249–1258.
- Halter, W.E., Williams-Jones, A.E. and Kontak, D.J., 1996, The role of greisenization in cassiterite precipitation at the East Kemptville tin deposit, Nova Scotia: *Economic Geology*, v. 91, p. 368-385.
- Harley, S.L., Kelly, N.M. and Möller, A., 2007, Zircon behaviour and the thermal histories of mountain chains: *Elements*, v. 3, p. 25-30.
- Harper, C.L., 1988, On the nature of time in the cosmological perspective. Unpublished Ph.D. Thesis, Oxford University, 508 pp.
- Heaman, L., and Parrish, R., 1991, U-Pb Geochronology of accessory minerals, in Heaman, L., and Ludden, J. N., eds., *Applications of Radiogenic Isotope Systems to Problems to Geology: Short Course Handbook: Mineralogical Association of Canada*, p. 59–100.
- Hibbard, J.P., van Staal, C.R., Rankin, D., and Williams, H., 2006, *Geology, Lithotectonic Map of the Appalachian Orogen, Canada–United States of America: Geological Survey of Canada, Map 2096A, scale 1:1 500 000.*

- Hicks, R.J., Jamieson, R.A. and Reynolds, P.H., 1999, Detrital and metamorphic $^{40}\text{Ar}/^{39}\text{Ar}$ ages from muscovite and whole-rock samples, Meguma Supergroup, southern Nova Scotia: Canadian Journal of Earth Sciences, v. 36, p. 23-32.
- Hilchie L, Jamieson, R.A., 2008, Graphite thermometry in the Halifax contact aureole: Atlantic Geology, v. 44, p. 16–17.
- Hilchie, L.J., and Jamieson, R.A., 2014. Graphite thermometry in a low-pressure contact aureole, Halifax, Nova Scotia: Lithos, v. 208, p. 21-33.
- Hinton, R.W. and Upton, B.G.J., 1991, The chemistry of zircon: variations within and between large crystals from syenite and alkali basalt xenoliths: Geochimica et Cosmochimica Acta, v. 55, p. 3287-3302.
- Horne, R.J., MacDonald, M.A., Corey, M.C., and Ham, L.J., 1992, Structure and emplacement of the South Mountain Batholith, southwestern Nova Scotia: Atlantic Geology, v. 28, p. 29-50.
- Horne, R.J., Corey, M.C., Ham, L.J. and MacDonald, M.A., 1988, Primary and secondary structural features in the eastern portion of the South Mountain Batholith, southwestern Nova Scotia: Implications for regional stress orientations during intrusion: Maritime Sediments and Atlantic Geology, v. 24, p. 71-82.
- Horne, R.J., King, M.S. Kontak, D.J., O'Reilly, G.A., and Black, D., 2006, The Kemptville shear zone: Regional shear related to emplacement and mineralization. in MacDonald, D.R.,

- ed., Mines and Minerals Branch Report of Activities 2005: Nova Scotia Department of Natural Resources, Report 2006-1, p. 19-37.
- Hoskin, P.W.O. and Black, L.P., 2000, Metamorphic zircon formation by solid-state recrystallization of protolith igneous zircon: *Journal of metamorphic Geology*, v. 18, p. 423-439.
- Hoskin, P.W. and Ireland, T.R., 2000, Rare earth element chemistry of zircon and its use as a provenance indicator: *Geology*, v. 28, p. 627-630.
- Hoskin, P.W. and Schaltegger, U., 2003, The composition of zircon and igneous and metamorphic petrogenesis: *Reviews in mineralogy and geochemistry*, v. 53, p. 27-62.
- Huber, C., Bachmann, O. and Manga, M., 2009, Homogenization processes in silicic magma chambers by stirring and mushification (latent heat buffering): *Earth and Planetary Science Letters*, v. 283, p. 38-47.
- Iannizzotto, N.F., Rapela, C.W., Baldo, E.G.A., Galindo, C., Fanning, C.M., Pankhurst, R.J., 2013, The Sierra Norte-Ambargasta batholith: late Ediacaran-early Cambrian magmatism associated with Pampean transpressional tectonics: *Journal of South American Earth Science*, v. 42, p. 127-143.
- Ishihara, S., 1981, The granitoid series and mineralization. in Skinner, B.J., ed., *Economic Geology*, 75th anniversary volume: New Haven, Connecticut: Economic Geology Publishing Co., p. 458-484.

- Jamieson, R.A., Beaumont, C., Fullsack, P., and Lee, B., 1998, Barrovian regional metamorphism: Where's the heat?: Geological Society, London, Special Publications, v. 138, p. 23-51.
- Johnson, M.C., Anderson Jr., A. T., Rutherford, M.J., 1994, Pre-eruptive volatile contents of magmas, in Carroll, Michael R., and John R. Holloway, eds., Volatiles in magmas: Reviews in Mineralogy, v. 30, p. 281–330.
- Johnson, E.R., Wallace, P.J., Delgado Granados, H., Manea, V.C., Kent, A.J., Bindeman, I.N. and Donegan, C.S., 2009. Subduction-related volatile recycling and magma generation beneath Central Mexico: insights from melt inclusions, oxygen isotopes and geodynamic models. *Journal of Petrology*, v. 50, p. 1729-1764.
- Keen, C.E., Kay, W.A., Keppie, D., Marillier, F., Pe-Piper, G., and Waldron, J.W.F., 1991, Deep seismic reflection data from the Bay of Fundy and Gulf of Maine: tectonic implications for the northern Appalachians: *Canadian Journal of Earth Sciences*, v. 28, p. 1096-1111.
- Kellett, D.A., Rogers, N., McNicoll, V., Kerr, A. and van Staal, C., 2014, New age data refine extent and duration of Paleozoic and Neoproterozoic plutonism at Ganderia–Avalonia boundary, Newfoundland: *Canadian Journal of Earth Sciences*, v. 51, p. 943-972.
- Kellett, D.A., Piette-Lauzière, N., Mohammadi, N., Bickerton, L, Kontak, D., Rogers, .N and Larson, K., in press, Spatio-temporal distribution of Devonian post-accretionary granitoids in the Canadian Appalachians: implications for tectonic controls on intrusion-

- related mineralization; in Targeted Geoscience Initiative 5: Contributions to the understanding and exploration of porphyry deposits, (ed.) A. Plouffe and E. Schetselaar: Geological Survey of Canada, Bulletin 616, p. xxx-xxx.
- Kellett, D. A., Rogers, N., McNicoll, V., Kerr, A., and van Staal, C., 2014, New age data refine extent and duration of Paleozoic and Neoproterozoic plutonism at Ganderia–Avalonia boundary, Newfoundland: *Canadian Journal of Earth Sciences*, v. 51, p. 943–972.
- Kemp, A.I., Vervoort, J.D., Bjorkman, K.E. and Iaccheri, L.M., 2017, Hafnium Isotope Characteristics of Palaeoarchaeon Zircon OG 1/OGC from the Owens Gully Diorite, Pilbara Craton, Western Australia: *Geostandards and Geoanalytical Research*, v. 41, p. 659-673.
- Kempster, R.M.F., Clarke, D.B., Reynolds, P.H., and Chatterjee, A.K., 1989, Late Devonian lamprophyric dykes in the Meguma Zone of Nova Scotia: *Canadian Journal of Earth Sciences*, v. 26, p. 611-613.
- Keppie, J.D., 1979, Geological map of the province of Nova Scotia geophysical edition: Nova Scotia Department of Mines and Energy, Halifax, N.S., scale 1 : 500 000.
- Keppie, J.D., and Dallmeyer, R.D., 1987, Dating transcurrent terrane accretion: an example from the Meguma and Avalon composite terranes in the northern Appalachians: *Tectonics*, v. 6, p. 831-847.

- Keppie, J.D., and Dallmeyer, R.D., 1995, Late Paleozoic collision, delamination, short-lived magmatism, and rapid denudation in the Meguma Terrane (Nova Scotia, Canada): constraints from $^{40}\text{Ar}/^{39}\text{Ar}$ isotopic data: *Canadian Journal of Earth Sciences*, v. 32, p. 644-659.
- Keppie, J.D., and Krogh, T.E., 1999, U-Pb geochronology of Devonian granites in the Meguma terrane of Nova Scotia, Canada: evidence for hotspot melting of a Neoproterozoic source. *Journal of Geology*, v. 107, p. 555–568.
- Keppie, J.D. and Krogh, T.E., 2000, 440 Ma igneous activity in the Meguma Terrane, Nova Scotia, Canada; part of the Appalachian overstep sequence?: *American Journal of Science*, v. 300, p. 528-538.
- Keppie, J. D., Currie, K. L., Murphy, J. B., Pickerill, R. K., Fyffe, L.R., and St. Julien, P., 1985, Appalachian geotraverse (Canadian Mainland): Geological Association of Canada Excursion 1.
- Keppie, J. D., Nance, R. D., Murphy, J. B., and Dostal, J., 1991, Northern Appalachians: Avalon and Meguma terranes. in *The West African orogens and circum-Atlantic correlatives*, p. 315-333.
- Keppie, J.D., Dallmeyer, R.D., Krogh, T.E., and Aftalion, M., 1993, Dating mineralization using several isotopic methods: an example from the South Mountain Batholith, Nova Scotia, Canada: *Chemical Geology*, v. 103, p. 251–270.

- Keppie, D.F., Keppie, J.D. and Murphy, J.B., 2002, Saddle reef auriferous veins in a conical fold termination (Oldham anticline, Meguma terrane, Nova Scotia, Canada): reconciliation of structural and age data: *Canadian Journal of Earth Sciences*, v. 39, p. 53-63.
- Keppie, J.D., Shellnutt, J.G., Dostal, J. and Keppie, D.F., 2018, An autochthonous Avalonian basement source for the latest Ordovician Brenton Pluton in the Meguma terrane of Nova Scotia: U–Pb–Hf isotopic constraints and paleogeographic implications: *International Journal of Earth Sciences*, v. 107, p. 955-969.
- Kerr, A., and McNicoll, V., 2012, New U–Pb geochronological constraints from mineralized granites in southern Newfoundland, in *Current Research: Newfoundland Department of Natural Resources, Geological Survey, Report 12-1*, p. 21–38.
- Kirkland, C.L., Smithies, R.H., Taylor, R.J.M., Evans, N., and McDonald, B., 2015, Zircon Th/U ratios in magmatic environs: *Lithos*, v. 212, p. 397-414.
- Kontak, D.J., 1990. The East Kemptville topaz-muscovite leucogranite, Nova Scotia. I. Geological setting and whole rock geochemistry: *Canadian Mineralogist*, v. 28, p. 787–825.
- Kontak, D.J., 1994, Geological and geochemical studies of alteration processes in a fluorine-rich environment: the East Kemptville Sn-(Zn-Cu-Ag) deposit, Yarmouth County, Nova Scotia, Canada. In Lentz, D.R., ed., *Alteration and Alteration Processes associated with*

Ore-forming Systems: Geological Association of Canada, Short Course Notes, v. 11, p. 261-314.

Kontak, D.J., and Chatterjee, A.K., 1992, The East Kemptville tin deposit, Yarmouth County, Nova Scotia. A Pb isotope study of the leucogranite and mineralized greisens: Evidence for a 366 Ma metallogenic event: Canadian Journal of Earth Sciences, v. 29, p. 1180-1196.

Kontak, D.J. and Cormier, R.F., 1991, Geochronological evidence for multiple tectono-thermal overprinting events in the East Kemptville muscovite-topaz leucogranite, Yarmouth County, Nova Scotia, Canada: Canadian Journal of Earth Science, v. 28, p. 209-224.

Kontak, D.J. and Kyser, T.K., 2011, Fingerprinting multiple fluid reservoirs in a 380 Ma Intrusion-Related Gold (IRG) setting, Nova Scotia, Canada: Implications for the nature and origin of IRG deposits: Mineralium Deposita, v. 46, p. 337-363.

Kontak, D.J. and Reynolds, P.H., 1994, $^{40}\text{Ar}/^{39}\text{Ar}$ dating of metamorphic and igneous rocks of the Liscomb Complex, Meguma Terrane, southern Nova Scotia, Canada: Canadian Journal of Earth Sciences, v. 31, p. 1643-1653.

Kontak, D.J., Tuach, J., Strong, D.F., Archibald, D.A., and Farrar, E., 1988, Plutonic and hydrothermal events in the Ackley Granite, southeast Newfoundland, as indicated by total-fusion $^{40}\text{Ar}/^{39}\text{Ar}$ geochronology: Canadian Journal of Earth Sciences, v. 25, p. 1151-1160.

- Kontak, D.J., Horne, R.J., Sandeman, H., Archibald, D., and Lee, J. K., 1998, $^{40}\text{Ar}/^{39}\text{Ar}$ dating of ribbon-textured veins and wall-rock material from Meguma lode gold deposits, Nova Scotia: implications for timing and duration of vein formation in slate-belt hosted vein gold deposits: *Canadian Journal of Earth Sciences*, v. 35, p. 746-761.
- Kontak, D.J., Horne, R.J., Ansdell, K., and Archibald, D.A., 1999, Carboniferous barite-fluorite mineralization in the Late Devonian Kinsac Pluton, southern Nova Scotia: *Atlantic Geology*, v. 35.
- Kontak, D.J., Dostal, J., Ansdell, K., Halter, W., Martin, R.F, and Williams-Jones, A.E., 2002a, The nature and origin of pegmatite in a fluorine-rich leucogranite, East Kemptville, Nova Scotia: *Transactions of the Royal Society of Edinburgh: Earth Sciences*, v. 92, p. 173-200.
- Kontak, D.J., Dostal, J., Kyser, K. and Archibald, D.A., 2002b, A petrological, geochemical, isotopic and fluid inclusion study of 370 Ma pegmatite-aplite sheets, Peggy's Cove, Nova Scotia, Canada: *Canadian Mineralogist*, v. 40, p. 1249-1286.
- Kontak D.J., Ham L.J., Dunning G., 2004, U-Pb dating of the Musquodoboit Batholith, southern Nova Scotia: evidence for a protracted magmatic-hydrothermal event: *Atlantic Geology*, v. 40, p. 207–216.
- Kontak, D.J., Horne, R.J., Creaser, R.A., Petrus, J.A., and Archibald, D. 2013. A petrological and geochronological study of a 360 Ma metallogenic event in Maritime Canada with

- implications for lithophile-metal mineralization in the Canadian Appalachians: *Canadian Journal of Earth Sciences*, v. 50, p. 1147–1163.
- Krogh, T.E., 1973, A low-contamination method for hydrothermal decomposition of zircon and extraction of U and Pb for isotopic age determinations: *Geochim. Cosmochim. Acta*, v. 37, p. 485-494.
- Krogh, T.E., 1982, Improved accuracy of U-Pb zircon ages by the creation of more concordant systems using an air abrasion technique: *Geochim. Cosmochim. Acta*, v. 46, p. 637 -649.
- Krogh, T.E. and Keppie, J.D., 1990, Age of detrital zircon and titanite in the Meguma Group, southern Nova Scotia, Canada: clues to the origin of the Meguma Terrane: *Tectonophysics*, v. 177, p. 307-323.
- Lackey, J.S., Valley, J.W., and Hinke, H.J., 2006, Deciphering the source and contamination history of peraluminous magmas using $\delta^{18}\text{O}$ of accessory-minerals: examples from garnet-bearing plutons of the Sierra Nevada batholith: *Contributions to Mineralogy and Petrology*, v. 151, p. 20-44.
- Lackey, J., Erdmann, S., Hark, J., Nowak, R., Murray, K., Clarke, D, and Valley, J., 2011, Tracing garnet origins in granitoid rocks by oxygen isotope analysis: examples from the South Mountain Batholith, Nova Scotia: *The Canadian Mineralogist*, v. 49, p. 417-439.

- Langmuir, C.H., Vocke Jr, R.D., Hanson, G.N. and Hart, S.R., 1978, A general mixing equation with applications to Icelandic basalts: *Earth and Planetary Science Letters*, v. 37, p. 380-392.
- Lehmann, B., 2020, Formation of tin ore deposits: A reassessment: *Lithos*.
- Linnen, R.L., Pichavant, M. and Holtz, F., 1996, The combined effects of fO₂ and melt composition on SnO₂ solubility and tin diffusivity in haplogranitic melts: *Geochimica et Cosmochimica Acta*, v. 60, p. 4965-4976.
- London, D., 1992, Phosphorus in S-type magmas: the P₂O₅ content of feldspars from peraluminous granites, pegmatites, and rhyolites: *American Mineralogist*, v. 77, p. 126-145.
- Longstaffe, F.J., Smith, T.E., and Muehlenbachs, K., 1980, Oxygen isotope evidence for the genesis of Upper Paleozoic granitoids from southwestern Nova Scotia: *Canadian Journal of Earth Sciences*, v. 17, p. 132-141.
- Lucazeau, F., and Vasseur, G., 1989, Heat flow density data from France and surrounding margins: *Tectonophysics*, v. 164, p. 251-258.
- Ludwig, K.R., 2003, User's Manual for Isoplot 3.00; Berkeley Geochronology Center, Special Publication 4.

- MacDonald, L.A., Barr, S.M., White, C.E. and Ketchum, J.W., 2002, Petrology, age, and tectonic setting of the White Rock Formation, Meguma terrane, Nova Scotia: evidence for Silurian continental rifting: *Canadian Journal of Earth Sciences*, v. 39, p. 259-277.
- MacDonald, M.A., 2001, Geology of the South Mountain Batholith, southwestern Nova Scotia: Nova Scotia Department of Natural Resources Open File Report ME2001-2.
- MacDonald, M.A. and Clarke, D.B., 2017, Occurrence, origin, and significance of melagranites in the South Mountain Batholith, Nova Scotia: *Canadian Journal of Earth Sciences*, v. 54, p. 693-713.
- MacDonald, M.A. and Horne, R. J., 1988. Petrology of the zoned, peraluminous Halifax pluton, south-central Nova Scotia: *Maritime Sediments and Atlantic Geology*, v. 24, p. 33-46
- MacDonald, M.A., Horne, R.J., Corey, M.C., and Ham, L.J., 1992, An overview of recent bedrock mapping and follow-up petrological studies of the South Mountain Batholith, southwestern Nova Scotia, Canada: *Atlantic Geology*, v. 28, p. 7-28.
- MacLean, N.J., Barr, S.M., White, C.E. and Ketchum, J.W., 2003, New U-Pb (zircon) age and geochemistry of the Wedgeport Pluton, Meguma terrane, Nova Scotia.
- Martel, A.T., McGregor, D.C. and Utting, J., 1993. Stratigraphic significance of Upper Devonian and Lower Carboniferous miospores from the type area of the Horton Group, Nova Scotia. *Canadian Journal of Earth Sciences*, v. 30, p. 1091-1098.

- MacHattie, T.G., White, C.E., Beresford V.P., and Reid, M.G., 2013, The Eastern Cobequid Highlands: Redefined Geology and Related Economic Potential: Part 2. Open File Illustration 2013-017.
- Marsh, J.H. and Stockli, D.F., 2015, Zircon U–Pb and trace element zoning characteristics in an anatectic granulite domain: Insights from LASS-ICP-MS depth profiling: *Lithos*, v. 239, p. 170-185.
- Mattinson, J.M., 2005, Zircon U–Pb chemical abrasion (“CA-TIMS”) method: Combined annealing and multi-step partial dissolution analysis for improved precision and accuracy of zircon ages: *Chemical Geology*, v. 220, p. 47–66.
- Mattinson, J.M., 2011, Extending the Krogh legacy: development of the CATIMS method for zircon U–Pb geochronology: *Canadian Journal of Earth Sciences*, v. 48, p. 95–105.
- McDonough, W.F. and Sun, S.S., 1995, The composition of the Earth. *Chemical geology*, 120, p. 223-253.
- McFarlane, C.R.M., 2016, Allanite U-Pb geochronology by 193 nm LA ICPMS using NIST610 glass for external calibration: *Chemical Geology*, v. 438, p. 91–102.
- McKenzie, C.B., and Clarke, D.B., 1975, Petrology of the South Mountain Batholith, Nova Scotia: *Canadian Journal of Earth Sciences*, v. 12, p. 1209-1218.
- McLeod, M.J., Johnson, S.C., Krogh, T.E., 2003, Archived U–Pb (zircon) dates from southern New Brunswick: *Atlantic Geology*, v. 39, p. 209–225.

- McNicoll, V.J., Squires, G.C., Wardle, R.J., Dunning, G.R. and O'Brien, B.H., 2006, U–Pb geochronological evidence for Devonian deformation and gold mineralization in the eastern Dunnage Zone, Newfoundland, in *Current Research: Government of Newfoundland and Labrador, Department of Natural Resources, Geological Survey, Report 06-1*, p. 45–60.
- Memeti, V., Paterson, S., Matzel, J., Mundil, R., Okaya, D., 2010, Magmatic lobes as “snapshots” of magma chamber growth and evolution in large, composite batholiths: an example from the Tuolumne intrusion, Sierra Nevada, California: *Geological Society of America Bulletin*, v. 122, p. 1912–1931.
- Miles, A.J., Woodcock, N.H., 2018, A combined geochronological approach to investigating long lived granite magmatism, the Shap granite, UK: *Lithos*, v. 304–307, p. 245-257.
- Miller, C.F., McDowell, S.M. and Mapes, R.W., 2003, Hot and cold granites? Implications of zircon saturation temperatures and preservation of inheritance: *Geology*, v. 31: p. 529-532.
- Miller, J.S., Matzel, J.E.P., Miller, C.F., Burgess, S.D., and Miller, R.B., 2007, Zircon growth and recycling during the assembly of large, composite arc plutons: *Journal of Volcanology and Geothermal Research*, v. 167, p. 282–299.

- Mohammadi, N., McFarlane, C.R., Lentz, D.R., and Thorne, K.G., 2020, Timing of magmatic crystallization and Sn–W–Mo greisen vein formation within the Mount Douglas Granite, New Brunswick, Canada: *Canadian Journal of Earth Sciences*, v. 57, p. 814–839.
- Morelli, R.M., Creaser, R.A., Selby, D., Kontak, D.J., and Horne, R.J., 2005, Rhenium-osmium geochronology of arsenopyrite in Meguma Group gold deposits, Meguma terrane, Nova Scotia, Canada: Evidence for multiple gold-mineralizing events: *Economic Geology*, v. 100, p. 1229-1242.
- Muecke, G.K., Elias, P., and Reynolds, P.H., 1988, Hercynian/Alleghanian overprinting of an Acadian terrane: $^{40}\text{Ar}/^{39}\text{Ar}$ studies in the Meguma zone, Nova Scotia, Canada. *Chemical Geology: Isotope Geoscience section*, v. 73, p. 153-167.
- Murphy, J.B., 2000, Tectonic influence on sedimentation along the southern flank of the late Paleozoic Magdalen basin in the Canadian Appalachians: Geochemical and isotopic constraints on the Horton Group in the St. Marys basin, Nova Scotia: *Geological Society of America Bulletin*, v. 112, p. 997-1011.
- Murphy, J.B., and Nance, R.D., 1989, Model for the evolution of the Avalonian-Cadomian belt: *Geology*, v. 17, p. 735-738.
- Murphy, J.B. and Keppie, J.D., 2005, The Acadian orogeny in the northern Appalachians: *International Geology Review*, v. 47, p. 663-687.

- Murphy, J.B. and Hamilton, M.A., 2000, Orogenesis and basin development: U-Pb detrital zircon age constraints on evolution of the Late Paleozoic St. Marys Basin, central mainland Nova Scotia: *The Journal of Geology*, v. 108, p. 53-71.
- Murphy, J.B., Dostal, J. and Keppie, J.D., 2008, Neoproterozoic–Early Devonian magmatism in the Antigonish Highlands, Avalon terrane, Nova Scotia: tracking the evolution of the mantle and crustal sources during the evolution of the Rheic Ocean: *Tectonophysics*, v. 461, p. 181-201.
- Murphy, J.B., Waldron, J.W., Kontak, D.J., Pe-Piper, G. and Piper, D.J., 2011, Minas Fault Zone: Late Paleozoic history of an intra-continental orogenic transform fault in the Canadian Appalachians: *Journal of Structural Geology*, v. 33, p. 312-328.
- Murphy, J.B., Shellnutt, J.G. and Collins, W.J., 2018, Late Neoproterozoic to Carboniferous genesis of A-type magmas in Avalonia of northern Nova Scotia: repeated partial melting of anhydrous lower crust in contrasting tectonic environments: *International Journal of Earth Sciences*, v. 107, p. 587-599.
- Mundil, R., Metcalfe, I., Ludwig, K.R., Renne, P.R., Oberli, F. and Nicoll, R.S., 2001, Timing of the Permian–Triassic biotic crisis: implications from new zircon U/Pb age data (and their limitations): *Earth and Planetary Science Letters*, v. 187, p. 131-145.
- Nance, R.D., and Murphy, J.B., 1996, Basement isotopic signatures and Neoproterozoic paleogeography of Avalonian –Cadmian and related terranes in the circum-North

- Atlantic, in Nance, R.D., Thompson, M.D., eds., *Avalonian and Related Peri-Gondwanan Terranes of the Circum-North Atlantic: Geological Society of America Special Paper*, v. 304, p. 333–346.
- O'Reilly, G.A., Farley, E.J., and Charest, M.H., 1982, *Metasomatic–hydrothermal mineral deposits of the New Ross– Mahone Bay area, Nova Scotia: Nova Scotia Department of Mines and Energy, Paper 82-2.*
- Owen, J.V., Greenough, J.D., Hy, C., Ruffman, A., 1988, Xenoliths in a mafic dyke at Popes Harbour, Nova Scotia: implications for the basement to the Meguma Group: *Canadian Journal of Earth Sciences*, v. 25, p. 1464–1471.
- Parrish, R.R., Noble, S.R., 2003, Zircon U-Th-Pb Geochronology by Isotope Dilution -- Thermal Ionization Mass Spectrometry (ID-TIMS): *Reviews in Mineralogy and Geochemistry*, v. 53, p. 183–213.
- Paterson, S.R., and Vernon, R.H., 1995, Bursting the bubble of ballooning plutons: a return to nested diapirs emplaced by multiple processes: *Geological Society of America Bulletin*, v. 107, p. 1356-1380.
- Paton, C., Hellstrom, J., Paul, B., Woodhead, J. and Hergt, J., 2011, Iolite: Freeware for the visualisation and processing of mass spectrometric data: *Journal of Analytical Atomic Spectrometry*, v. 26, p. 2508-2518.

- Petford, N., Kerr, R.C. and Lister, J.R., 1993, Dike transport of granitoid magmas: *Geology*, v. 21, p. 845-848.
- Petford, N., Cruden, A.R., McCaffrey, K.J.W., and Vigneresse, J.-L., 2000, Granite magma formation, transport and emplacement in the Earth's crust: *Nature*, v. 408, p. 669–673.
- Petrus, J.A. and Kamber, B.S., 2012, VizualAge: A novel approach to laser ablation ICP-MS U-Pb geochronology data reduction: *Geostandards and Geoanalytical Research*, v. 36, p. 247-270.
- Pettke, T., Audétat, A., Schaltegger, U., and Heinrich, C.A., 2005, Magmatic-to-hydrothermal crystallization in the W–Sn mineralized Mole Granite (NSW, Australia): Part II: Evolving zircon and thorite trace element chemistry: *Chemical Geology*, v. 220, p. 191-213.
- Pichavant, M., 1987, The Macusani glasses, SE Peru: evidence of chemical fractionation in peraluminous magmas. *Magmatic Process: Physicochemical Principles: Geochem. Soc. Spec. Publ.*, 1, p. 359-373.
- Pietranik, A.B., Hawkesworth, C.J., Storey, C.D., Kemp, A.I.S., Sircombe, K.N., Whitehouse, M.J., and Bleeker, W., 2008, Episodic, mafic crust formation from 4.5 to 2.8 Ga: New evidence from detrital zircons, Slave craton, Canada: *Geology*, v. 36, p. 875-878.

- Poller, U., Huth, J., Hoppe, P. and Williams, I.S., 2001, REE, U, Th, and Hf distribution in zircon from western Carpathian Variscan granitoids: a combined cathodoluminescence and ion microprobe study: *American Journal of Science*, v. 301, p. 858-867.
- Poulson, S.R., Kubilius, W.P., and Ohmoto, H., 1991, Geochemical behavior of sulfur in granitoids during intrusion of the South Mountain Batholith, Nova Scotia, Canada: *Geochimica et Cosmochimica Acta*, v. 55, p. 3809-3830.
- Raimbault, L., Cuney, M., Azencott, C., Duthou, J.L. and Joron, J.L., 1995, Geochemical evidence for a multistage magmatic genesis of Ta-Sn-Li mineralization in the granite at Beauvoir, French Massif Central: *Economic Geology*, v. 90, p. 548-576.
- Reynolds, P.H., Zentilli, M. and Muecke, G.K., 1981, K–Ar and $^{40}\text{Ar}/^{39}\text{Ar}$ geochronology of granitoid rocks from southern Nova Scotia: its bearing on the geological evolution of the Meguma Zone of the Appalachians: *Canadian Journal of Earth Sciences*, v. 18, p. 386-394.
- Richards, J.P., 2003, Tectono-magmatic precursors for porphyry Cu-(Mo-Au) deposit formation: *Economic geology*, v. 98, p. 1515-1533.
- Richardson, J.M., 1988, Field and alteration relationships of alteration and greisen-hosted mineralization at the East Kemptville tin deposit, Davis Lake monzogranite, southwest Nova Scotia, Canada, in Taylor, R.P., and Strong, D.F., eds., *Granite related mineral deposits: Canadian Institute of Mining and Metallurgy, Special*, v. 39, p. 265-279.

- Richardson J.M., Bell, K., Blenkinsopp, J., and Watkinson, D., 1989. Rb-Sr age and geochemical distinctions between the Carboniferous tin-bearing Davis Lake complex and the Devonian South Mountain batholith, Meguma Terrane, Nova Scotia: *Canadian Journal of Earth Sciences*, v. 26, p. 2044-2061.
- Roberts, N.M., Slagstad, T., Parrish, R.R., Norry, M.J., Marker, M. and Horstwood, M.S., 2013, Sedimentary recycling in arc magmas: geochemical and U–Pb–Hf–O constraints on the Mesoproterozoic Suldal Arc, SW Norway: *Contributions to Mineralogy and Petrology*, v. 165, p. 507-523.
- Robinson, P., Tucker, R.D., Bradley, D., Berry, H.N., and Osberg, P.H., 1998, Paleozoic orogens in New England, USA: *Geologiska Foreningens Stockholm Forhandlingar*, v. 120, p. 119-148.
- Romer, R.L. and Kroner, U., 2015, Sediment and weathering control on the distribution of Paleozoic magmatic tin–tungsten mineralization. *Mineralium Deposita*, v. 50, p. 327-338.
- Rubatto, D., 2002, Zircon trace element geochemistry: partitioning with garnet and the link between U–Pb ages and metamorphism: *Chemical geology*, v. 184, p. 123-138.
- Rubatto, D. and Hermann, J., 2007. Zircon behaviour in deeply subducted rocks. *Elements*, 3(1), pp.31-35.

- Russell, W.A., Papanastassiou, D.A., and Tombrello, T.A., 1978, Ca isotope fractionation on the Earth and other solar system materials: *Geochimica et Cosmochimica Acta*, v. 42, p. 1075-1090.
- Samperton, K.M., Schoene, B., Cottle, J.M., Keller, C.B., Crowley, J.L., Schmitz, M.D., 2015. Magma emplacement, differentiation and cooling in the middle crust: integrated zircon geochronological-geochemical constraints from the Bergell Intrusion, Central Alps: *Chemical Geology*, v. 417, p. 322–340.
- Sánchez-García, T., Quesada, C., Bellido, F., Dunning, G.R., G.R., and González del Tánago, J., 2008, Two-step magma flooding of the upper crust during rifting: the early Paleozoic of the Ossa Morena Zone (SW Iberia): *Tectonophysics*, v. 461, p. 72–90.
- Schaltegger, U., 2007, Hydrothermal zircon: *Elements*, v. 3, p. 51-79.
- Schaltegger, U. and Davies, J.H., 2017, Petrochronology of zircon and baddeleyite in igneous rocks: Reconstructing magmatic processes at high temporal resolution: *Reviews in Mineralogy and Geochemistry*, v. 83, p. 297-328.
- Schaltegger, U., Brack, P., Ovtcharova, M., Peytcheva, I., Schoene, B., Stracke, A., Marocchi, M., Bargossi, G.M., 2009, Zircon and titanite recording 1.5million years of magma accretion, crystallisation and initial cooling in a composite pluton (southern Adamello batholith, northern Italy): *Earth and Planetary Science Letters*, v. 286, p. 208–218.

- Schaltegger, U., Nowak, A., Ulianov, A., Fisher, C. M., Gerdes, A., Spikings, R., Whitehouse, M. J., Bindeman, I., Hanchar, J. M., Duff, J., Vervoort, J. D., Sheldrake, T., Caricchi, L., Brack, P. Müntener, O., 2019, Zircon Petrochronology and $^{40}\text{Ar}/^{39}\text{Ar}$ Thermochronology of the Adamello Intrusive Suite, N. Italy: Monitoring the Growth and Decay of an Incrementally Assembled Magmatic System: *Journal of Petrology*, v. 60, p. 701–722.
- Scherer, E., Münker, C. and Mezger, K., 2001, Calibration of the lutetium-hafnium clock: *Science*, v. 293, p. 683-687.
- Schoene, B., and Baxter, E.F., 2017, Petrochronology and TIMS: *Reviews in Mineralogy and Geochemistry*, v. 83, p. 231-260.
- Schoene, B., Schaltegger, U., Brack, P., Latkoczy, C., Stracke, A., Gunther, D., 2012, Rates of magma differentiation and emplacement in a ballooning pluton recorded by U-Pb TIMS-TEA, Adamello batholith, Italy: *Earth and Planetary Science Letters*, v. 355, p. 162–173.
- Selby, D., and Creaser, R., 2004, Macro-scale NTIMS and micro-scale LA-MCICP-MS Re-Os isotopic analysis of molybdenite: Testing spatial restrictions for reliable Re-Os age determinations, and implications for the decoupling of Re and Os within molybdenite: *Geochimica et Cosmochimica Acta*, v. 68, p. 3897–3912.

- Shellnutt, J.G., and Dostal, J., 2012, An evaluation of crustal assimilation within the Late Devonian South Mountain Batholith, SW Nova Scotia: *Geological Magazine*, v. 149, p. 353-365.
- Shellnutt, J.G., Owen, J.V., Yeh, M.W., Dostal, J., and Nguyen, D.T., 2019, Long-lived association between Avalonia and the Meguma terrane deduced from zircon geochronology of metasedimentary granulites: *Scientific reports*, v. 9, p. 1-11.
- Siegél, C., Bryan, S.E., Allen, C.M. and Gust, D.A., 2018, Use and abuse of zircon-based thermometers: a critical review and a recommended approach to identify antecrystic zircons: *Earth-Science Reviews*, v. 176, p. 87-116.
- Sláma, J., Košler, J., Condon, D.J., Crowley, J.L., Gerdes, A., Hanchar, J.M., Horstwood, M.S., Morris, G.A., Nasdala, L., Norberg, N. and Schaltegger, U., 2008, Plešovice zircon—a new natural reference material for U–Pb and Hf isotopic microanalysis: *Chemical Geology*, v. 249, p. 1-35.
- Smith, W.D., Darling, J.R., Bullen, D.S., Lasalle, S., Pereira, I., Moreira, H., Allen, C.J. and Tapster, S., 2019, Zircon perspectives on the age and origin of evolved S-type granites from the Cornubian Batholith, Southwest England: *Lithos*, v. 336, p. 14-26.
- Smythe, D.J. and Brenan, J.M., 2015, Cerium oxidation state in silicate melts: Combined fO_2 , temperature and compositional effects: *Geochimica et Cosmochimica Acta*, v. 170, p. 173-187.

- Smythe, D.J. and Brenan, J.M., 2016, Magmatic oxygen fugacity estimated using zircon-melt partitioning of cerium: *Earth and Planetary Science Letters*, v. 453, p. 260-266.
- Stern, R.A., 1997, A SHRIMP II Ion Microprobe at the Geological Survey of Canada: *Geoscience Canada*, v. 23, p. 73–76.
- Stern, R.A., and Amelin, Y., 2003, Assessment of errors in SIMS zircon U–Pb geochronology using a natural zircon standard and NIST SRM 610 glass: *Chemical Geology*, v. 197, p. 111-142.
- Szymanowski, D., Fehr, M.A., Guillong, M., Coble, M.A., Wotzlaw, J.F., Nasdala, L., Ellis, B.S., Bachmann, O. and Schönbacher, M., 2018, Isotope-dilution anchoring of zircon reference materials for accurate Ti-in-zircon thermometry: *Chemical Geology*, v. 481, p. 146-154.
- Tate, M.C. and Clarke, D.B., 1997, Compositional diversity among Late Devonian peraluminous granitoid intrusions in the Meguma Zone of Nova Scotia, Canada: *Lithos*, v. 39, p. 179 – 194.
- Tate, M.C., Clarke, D.B. and Heaman, L.M., 1997, Progressive hybridisation between Late Devonian mafic-intermediate and felsic magmas in the Meguma Zone of Nova Scotia, Canada: *Contributions to Mineralogy and Petrology*, v. 126, p. 401-415.
- Taylor, R.G., 1979, *Geology of Tin Deposits*. Elsevier, Amsterdam: 543pp.

- Thompson, A.B. and Connolly, J.A., 1995, Melting of the continental crust: some thermal and petrological constraints on anatexis in continental collision zones and other tectonic settings: *Journal of Geophysical Research: Solid Earth*, v. 100, p. 15565-15579.
- Trail, D., Watson, E.B. and Tailby, N.D., 2012, Ce and Eu anomalies in zircon as proxies for the oxidation state of magmas: *Geochimica et Cosmochimica Acta*, v. 97, p. 70-87.
- Valley, J.W., 2003, Oxygen isotopes in zircon. *Reviews in mineralogy and geochemistry*, v. 53, p. 343-385.
- Valley, J.W., Chiarenzelli, J.R., and McLelland, J.M., 1994, Oxygen isotope geochemistry of zircon: *Earth and Planetary Science Letters*, v. 126, p. 187 – 206.
- Valley, J.W., Kinny, P.D., Schulze, D.J. and Spicuzza, M.J., 1998, Zircon megacrysts from kimberlite: oxygen isotope variability among mantle melts: *Contributions to mineralogy and petrology*, v. 133, p. 1-11.
- Valley, J.W., Lackey, J.S., Cavosie, A.J., Clechenko, C.C., Spicuzza, M.J., Basei, M.A.S., Bindeman, I.N., Ferreira, V.P., Sial, A.N., King, E.M. and Peck, W.H., 2005, 4.4 billion years of crustal maturation: oxygen isotope ratios of magmatic zircon. *Contributions to Mineralogy and Petrology*, v. 150, p. 561-580.
- van Staal, C.R., 1994, The Brunswick subduction complex in the Canadian Appalachians: record of the Late Ordovician to Late Silurian collision between Laurentia and the Gander margin of Avalon: *Tectonics*, v. 13, p. 946-962.

- van Staal, C.R., 2007, Pre-Carboniferous tectonic evolution and metallogeny of the Canadian Appalachians, in Mineral Deposits of Canada, Goodfellow, W.D., ed.: Geological Association of Canada, Special Publication 5, p. 793–818.
- van Staal, C.R., and Barr, S.M., 2012, Lithospheric architecture and tectonic evolution of the Canadian Appalachians and associated Atlantic margin: Geological Association of Canada, Special Paper, v. 49, p. 41-95.
- van Staal, C. R., Whalen, J. B., Valverde-Vaquero, P., Zagorevski, A., and Rogers, N, 2009, Pre-Carboniferous, episodic accretion-related, orogenesis along the Laurentian margin of the northern Appalachians. Geological Society, London, Special Publications, v. 327, p. 271-316.
- van Staal, C.R., Barr, S.M., Waldron, J.W.F., Schofield, D.I., Zagorevski, A., and White, C.E., 2021, Provenance and Paleozoic tectonic evolution of Ganderia and its relationships with Avalonia and Megumia in the Appalachian-Caledonide orogen: Gondwana Research (in press).
- Vigneresse, J. L., 2004, A new paradigm for granite generation. Transactions of the Royal Society of Edinburgh: Earth Sciences, v. 95, p. 11-22.
- Vigneresse, J.L., and Tikoff, B., 1999, Strain partitioning during partial melting and crystallizing felsic magmas: Tectonophysics, v. 312, p. 117–132.

- Waldron, J.W.F., Anderson, S., Cawood, P., Goodwin, L.B., Hall, J., Jamieson, R.A., Palmer, S. E., Stockmal, G.S., and Williams, P.F., 1998, Evolution of the Appalachian Laurentian margin: Lithoprobe results in western Newfoundland: *Canadian Journal of Earth Sciences*, v. 35, p. 1271–1287.
- Waldron, J.W., White, C.E., Barr, S.M., Simonetti, A. and Heaman, L.M., 2009, Provenance of the Meguma terrane, Nova Scotia: rifted margin of early Paleozoic Gondwana: *Canadian Journal of Earth Sciences*, v. 46, p. 1-8.
- Waldron, J.W.F., Barr, S.M., Park, A.F., White, C.E., and Hibbard, J., 2015, Late Paleozoic strike-slip faults in Maritime Canada and their role in the reconfiguration of the northern Appalachian orogen: *Tectonics*, v. 34, p. 1661–1684.
- Wiedenbeck, M.A.P.C., Alle, P., Corfu, F., Griffin, W.L., Meier, M., Oberli, F.V., Quadt, A.V., Roddick, J.C. and Spiegel, W., 1995, Three natural zircon standards for U-Th-Pb, Lu-Hf, trace element and REE analyses: *Geostandards newsletter*, v. 19, p. 1-23.
- White, C.E., 2010, Stratigraphy of the Lower Paleozoic Goldenville and Halifax groups in southwestern Nova Scotia: *Atlantic Geology*, v. 46, p. 136-154.
- White, C.E., and Barr, S.M., 2010, Lithochemistry of the Lower Paleozoic Goldenville and Halifax groups, southwestern Nova Scotia, Canada: Implications for stratigraphy, provenance, and tectonic setting of the Meguma terrane, in Tollo, R.P., Bartholomew, M.J., Hibbard, J.P., and Karabinos, P.M., eds., *From Rodinia to Pangea: The*

- Lithotectonic Record of the Appalachian Region: Geological Society of America Memoir 206, p. 347–366.
- White, C.E., Barr, S.M. and Toole, R.M., 2006, New insights on the origin of the Meguma Group in southwestern Nova Scotia, Canada: Nova Scotia Department of Natural Resources, Mineral Resource Branch, Open File Illustration, ME, 2.
- White, C.E., Barr, S.M., Horne, R.J., and Hamilton, M.A., 2007, The Neocadian orogeny in the Meguma terrane, Nova Scotia, Canada, in 42st Annual Meeting Geological Society of America, Northeastern Section, March 12-14, 2007, Abstracts with Programs 2007, v. 39, p. 69.
- White, C. E., Barr, S. M., and Linnemann, U., 2018, U–Pb (zircon) ages and provenance of the White Rock Formation of the Rockville Notch Group, Meguma terrane, Nova Scotia, Canada: evidence for the “Sardian gap” and West African origin: Canadian Journal of Earth Sciences, v. 55, p. 589-603.
- Woodhead, J.D. and Hergt, J.M., 2005, A preliminary appraisal of seven natural zircon reference materials for in situ Hf isotope determination: Geostandards and Geoanalytical Research, v. 29, p. 183-195.
- Woodland, A.B., Kornprobst, J., and Wood, B.J., 1992. Oxygen thermobarometry of orogenic lherzolite massifs: Journal of Petrology, v. 33, p. 203-230.

- Woodland, A.B., Kornprobst, J., and Tabit, A., 2006, Ferric iron in orogenic lherzolite massifs and controls of oxygen fugacity in the upper mantle: *Lithos*, v. 89, p. 222-241.
- Wotzlaw, J.F., Schaltegger, U., Frick, D.A., Dungan, M.A., Gerdes, A. and Günther, D., 2013, Tracking the evolution of large-volume silicic magma reservoirs from assembly to supereruption, *Geology*, v. 41, p. 867-870.
- Yang, X.M. and Lentz, D.R., 2005, Chemical composition of rock-forming minerals in gold-related granitoid intrusions, southwestern New Brunswick, Canada: implications for crystallization conditions, volatile exsolution, and fluorine-chlorine activity: *Contributions to Mineralogy and Petrology*, v. 150, p. 287-305.
- Zeck, H.P. and Williams, I.S., 2002, Inherited and Magmatic Zircon from Neogene Hoyazo Cordierite Dacite, SE Spain—Anatectic Source Rock Provenance and Magmatic Evolution, in *Memoriam Professor Chris Powell*, † 2001.07. 21: *Journal of Petrology*, v. 43, p. 1089-1104.
- Zhang, W., 2015, Petrological and Metallogenic Studies of the Nashwaak Granite and Felsic Dykes Associated with the Sisson Brook W-Mo-(Cu) Deposit, West-Central New Brunswick, Canada: Ph.D. Thesis, University of New Brunswick, Fredericton, NB, Canada.

Zhang, Y., Yang, J.H., Chen, J.Y., Wang, H. and Xiang, Y.X., 2017, Petrogenesis of Jurassic tungsten-bearing granites in the Nanling Range, South China: Evidence from whole-rock geochemistry and zircon U–Pb and Hf–O isotopes: *Lithos*, v. 278, p. 166-180.

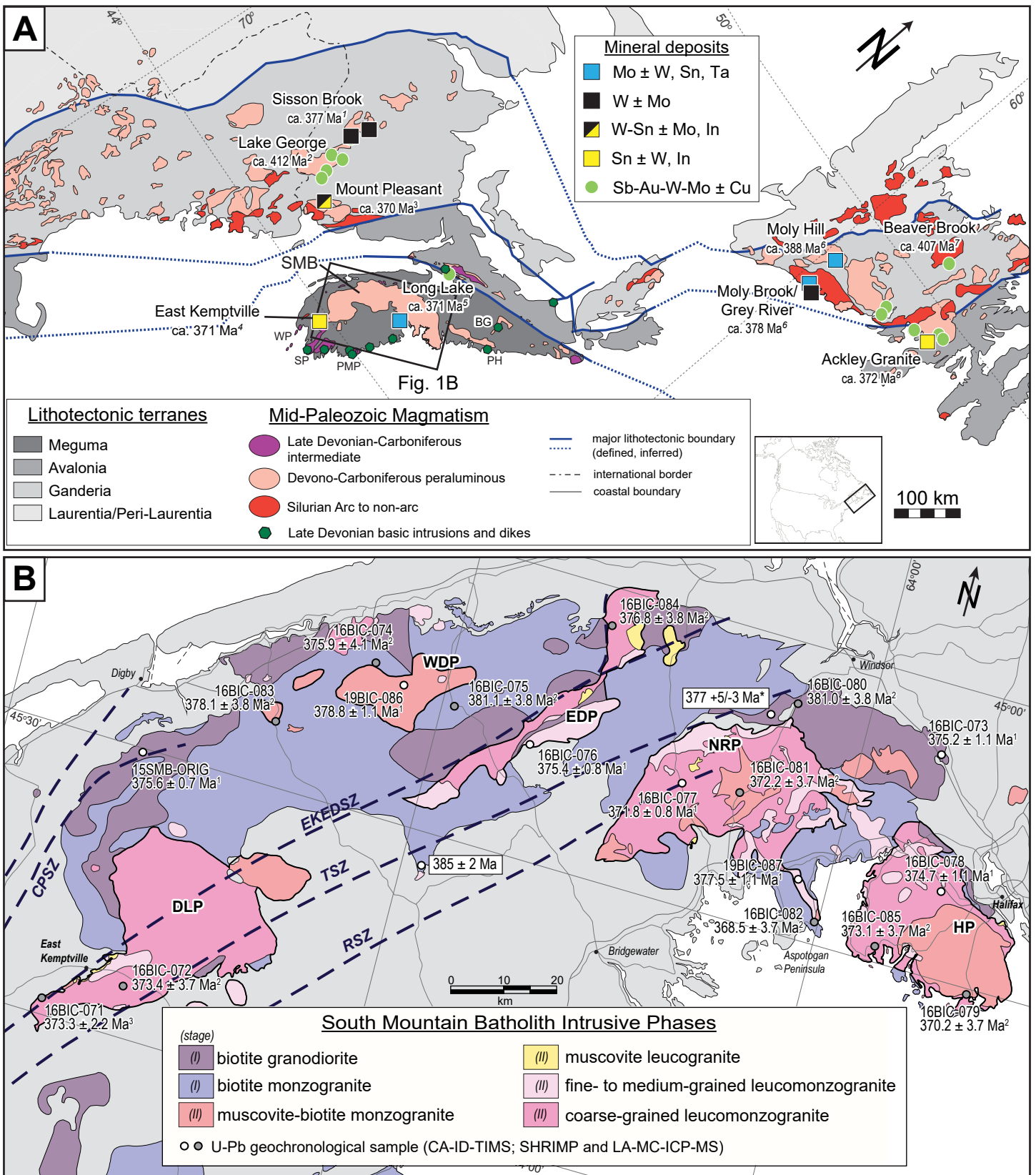


Figure 2-1

Figure 2–1. (A) Geological terrane map of the northeast Appalachians emphasizing locations of Paleozoic magmatism, including the South Mountain Batholith (SMB) in southwestern Nova Scotia. Isolated occurrences of basic- and intermediate intrusions peripheral to the SMB are noted by dark green-filled hexagons. BG – Bog Island Gabbro, PH – Pope’s Harbour dyke, PMP – Port Mouton pluton, SP – Shelburne Pluton, WP – Wedgeport pluton. Modified after Hibbard et al. (2006) and van Staal (2007). *1 – Zhang (2015); 2 – McLeod et al. (2003), 3 – Mohammadi et al. (2020); 4 – this study; 5 – Selby and Creaser (2004); 6 – Kerr and McNicoll (2012); 7 – McNicoll et al. (2006); 8 – Kellett et al. (2014). **(B)** Bedrock geology of the SMB showing its various plutonic phases; note that darker is less evolved and lighter more evolved. The Stage II plutons of MacDonald et al. (1992; DLP – Davis Lake Pluton, WDP – West Dalhousie Pluton, EDP – East Dalhousie Pluton, NRP – New Ross Pluton, HP – Halifax Pluton) are outlined with thicker black lines. The method of U-Pb analysis used in this study is indicated for each reported age, selected based on probability of concordance and MSWD: 1 – CA-TIMS, 2 – SHRIMP-II, 3 – LA-ICP-MS. Regional shear zones are outlined by dashed lines: CPSZ – Chebogue Point shear zone (White and Barr, 2010), EKEDSZ – East Kemptville-East Dalhousie shear zone (Horne et al., 1988, 2006), TSZ – Tobeatic shear zone (Giles, 1985), RSZ – Rossignol shear zone (Keppie et al., 1985). The U-Pb zircon geochronology sample locations from this study (white symbols, CA-TIMS; dark grey symbols, SHRIMP-II and LA-MC-ICP-MS) and the two previous U-Pb zircon (TIMS) (Keppie et al., 1993) noted with white boxes on map are shown.

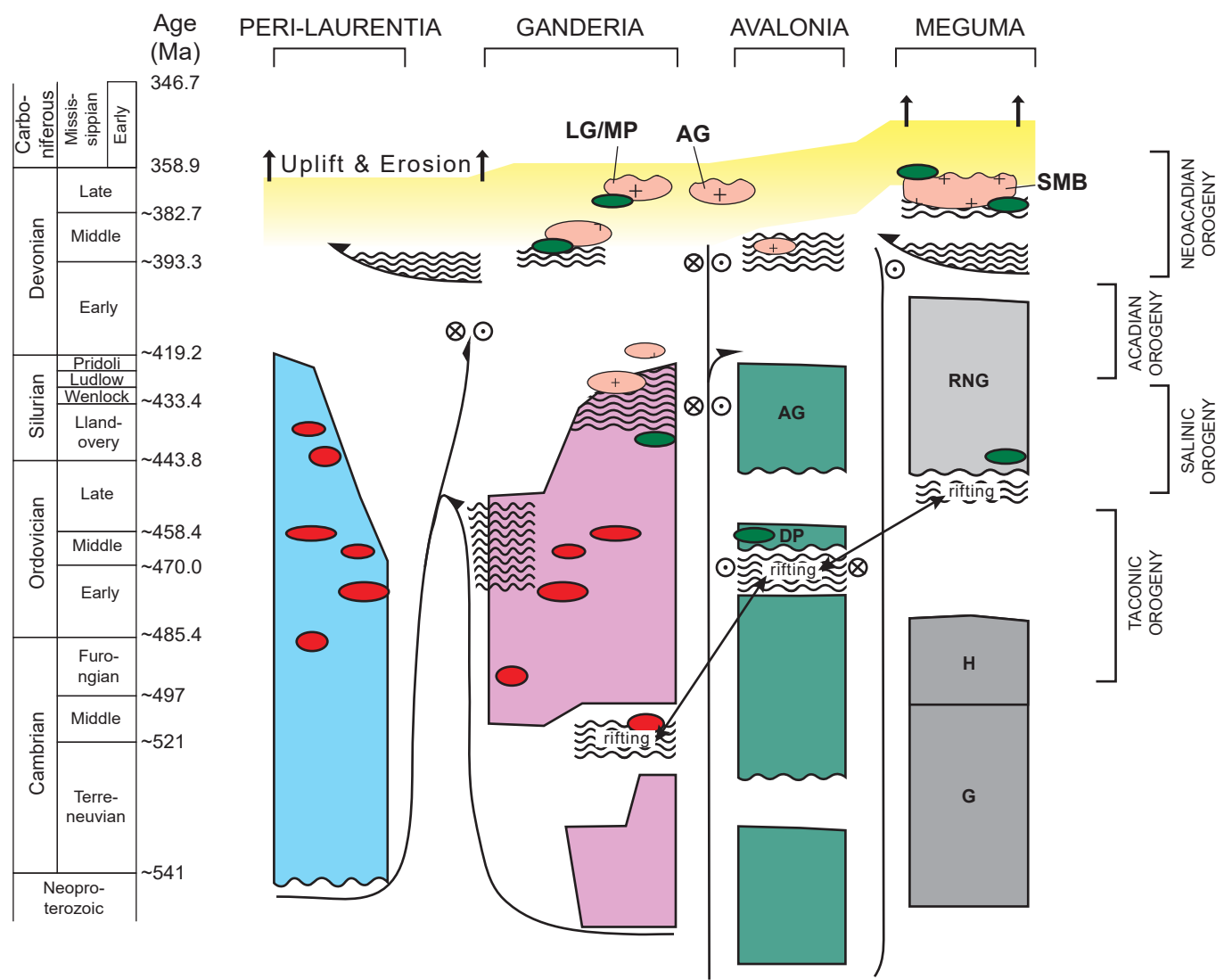
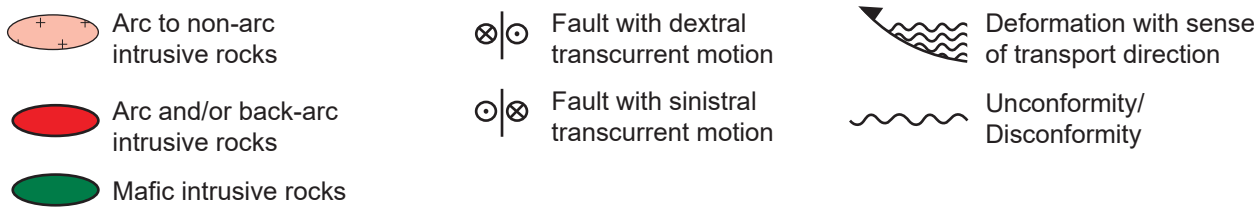


Figure 2-2

Figure 2–2. Simplified summary of tectono-stratigraphic relationships of various tectonic elements in the Canadian Appalachians (modified after van Staal, 2007). Note that rifting and separation from Gondwana becomes progressively younger from Ganderia to Meguma. AG - Arisaig Group; DP - Dunn Point volcanic rocks; G - Goldenville Group; H - Halifax Group; LG/MP - Lake George/Mount Pleasant (Mohammadi et al., 2020); AG - Ackley Granite (Kellett et al., 2014); RNG - Rockville Notch Group (White et al., 2018); SMB - South Mountain batholith.



Figure 2-3

Figure 2–3. Representative examples of bedrock geology and magmatic textures from the South Mountain Batholith (SMB). (A) Halifax Pluton (Sambro area) showing a massive medium-grained K-feldspar megacrystic monzogranite with partial alignment of feldspars. (B) Halifax Pluton (Prospect area) showing massive medium-grained, K-feldspar megacrystic biotite leucomonzogranite with alignment of feldspar megacrysts and hosting a melanocratic (biotite-rich) enclave. Note presence of K-feldspar megacrysts in both phases. (C) Outcrop of stage 1 medium- to coarse-grained biotite granodiorite containing multiple xenoliths of Meguma metasedimentary rock with variable size and shape/resorption. From the eastern SMB in the Mt. Uniacke area (photo courtesy of F. Tweedale). (D) Halifax Pluton (Duncan’s Cove area) coarse-grained cordierite (arrows) muscovite-leucomonzogranite. (E) Halifax Pluton (Prospect area) showing melanocratic enclave in massive medium-grained biotite monzogranite. (F) Melanocratic enclave with growth of K-feldspar megacryst in a medium-grained biotite-granodiorite from the western SMB (Milford area).

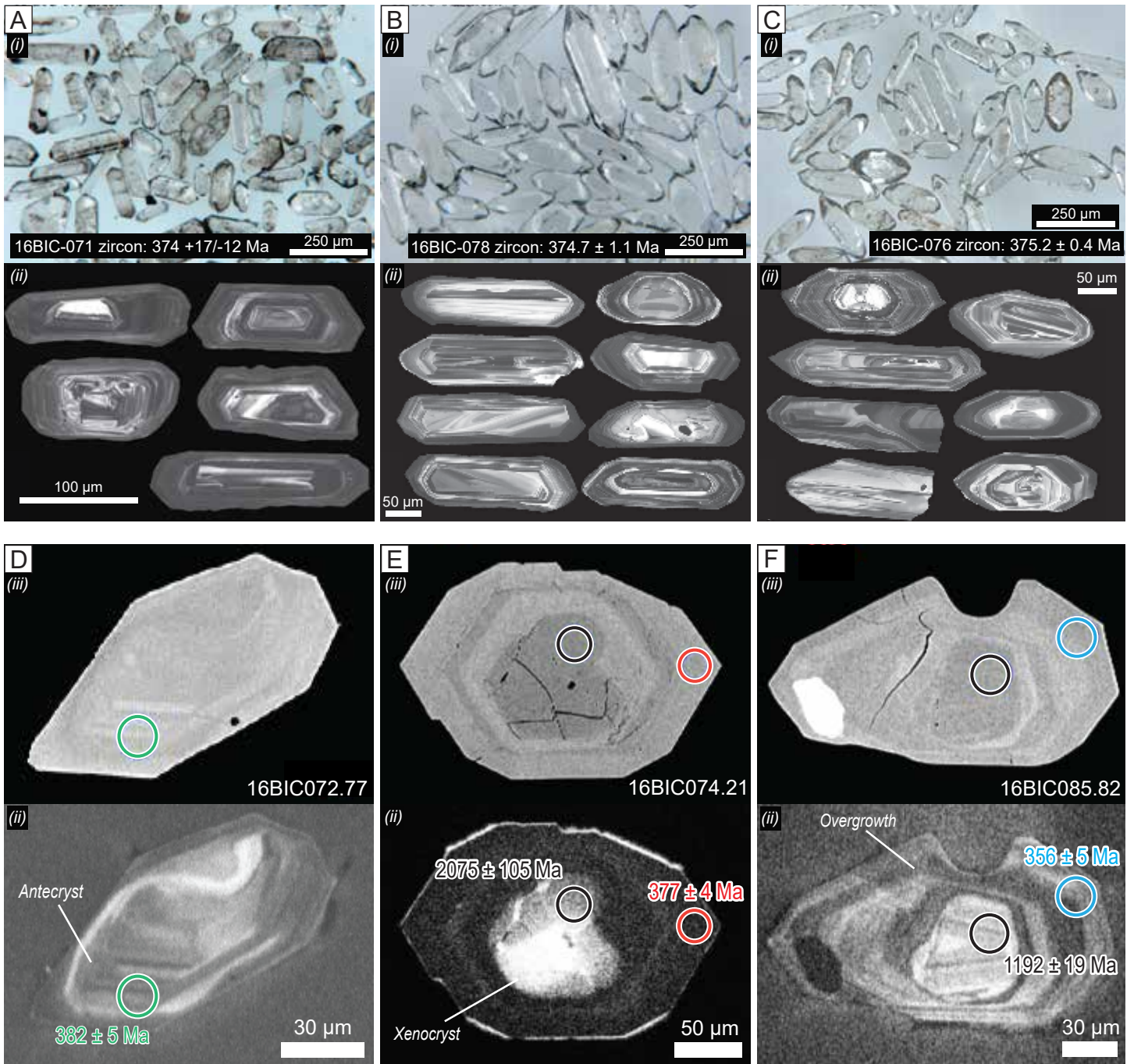


Figure 2-4

Figure 2–4. Representative images of zircon grains from the South Mountain Batholith dated by CA-TIMS and SHRIMP-II as seen using transmitted light (i; A-C), cathodoluminescence (ii; CL; D-F), and backscatter electrons (iii; BSE; E-G). Analytical spot locations are indicated and CA-TIMS ages labelled, where applicable in the BSE images (see text for discussion). Labels beside the circles show the U-Pb age determinations (note that $^{206}\text{Pb}/^{238}\text{U}$ ages are reported for ages < ca. 800 Ma and $^{207}\text{Pb}/^{206}\text{Pb}$ ages are reported for ages >ca. 800 Ma). The different age domains for the in situ SHRIMP ages are indicated as follows: 1) black circle xenocryst; 2) green circle antecryst; 3) red circle autocryst; and 4) blue circle younger overgrowth. Sample numbers are noted in the upper portion of each pair of images.

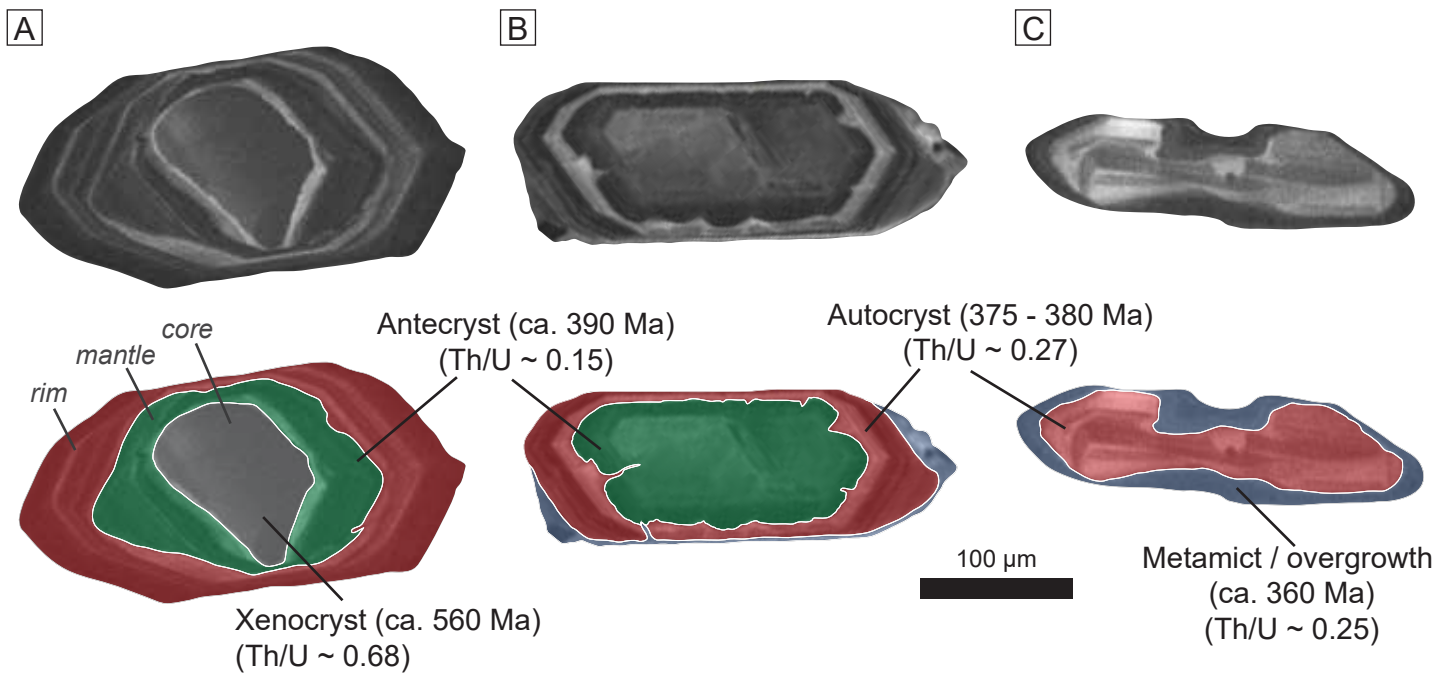


Figure 2-5

Figure 2-5. Cathodoluminescence images and interpreted domains for zircons from the South Mountain Batholith showing textural complexities and isotopic differences in each grain. The criteria of morphology, zoning, and resorption with respect to the structure of a grain (i.e., rim, mantle, and core) were used to identify domains of inherited xenocrystic cores (e.g., grey domain in A), antecrystic mantles to cores and inner grains (e.g., green domains in A and B), autocrystic crystallization (red domains in A-C), and anomalously young zircon metamict zone replacement/overgrowth domains (e.g., blue domains in B and C). The domain classification was complemented using the respective U-Pb ages and Th/U ratios from analysis.

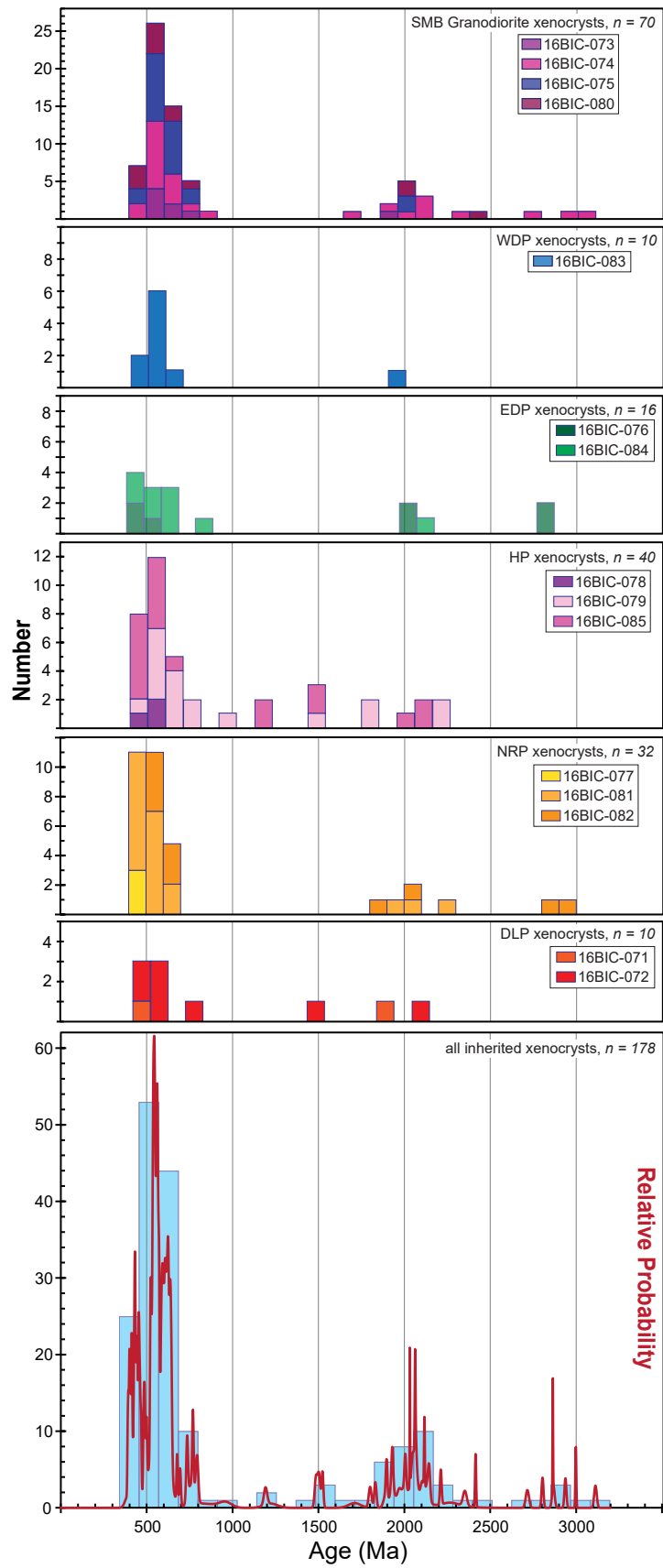
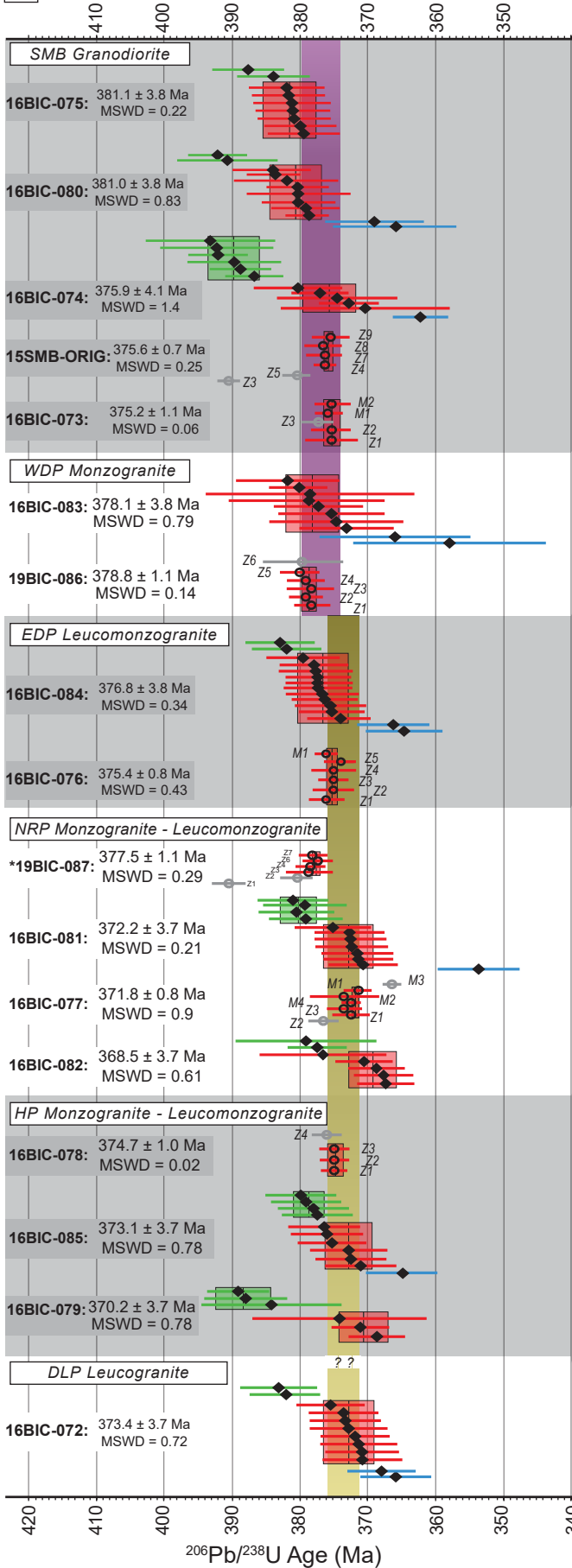


Figure 2-6

Figure 2–6. Histograms summarizing the inherited xenocrystic core age populations for zircons from each plutonic phase in the South Mountain Batholith. The legend in each plot identifies the sample in the plutonic phases and number of cores analysed (n value). The bottom plot is the compiled inherited xenocrystic cores from all the phases dated with the relative probability shown by the red line. Bin width is approximately 100 Ma.

A U-Pb Age Results: SHRIMP-II and CA-TIMS



B U-Pb Age Results: LA-MC-ICP-MS

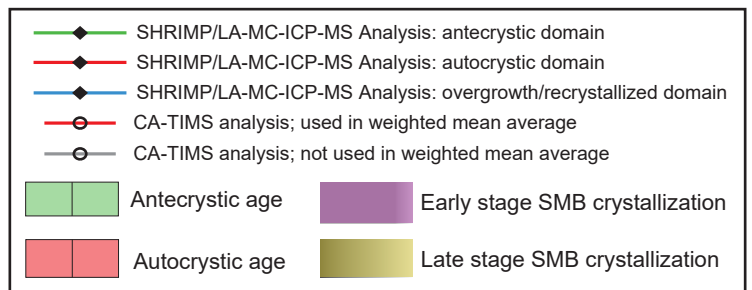
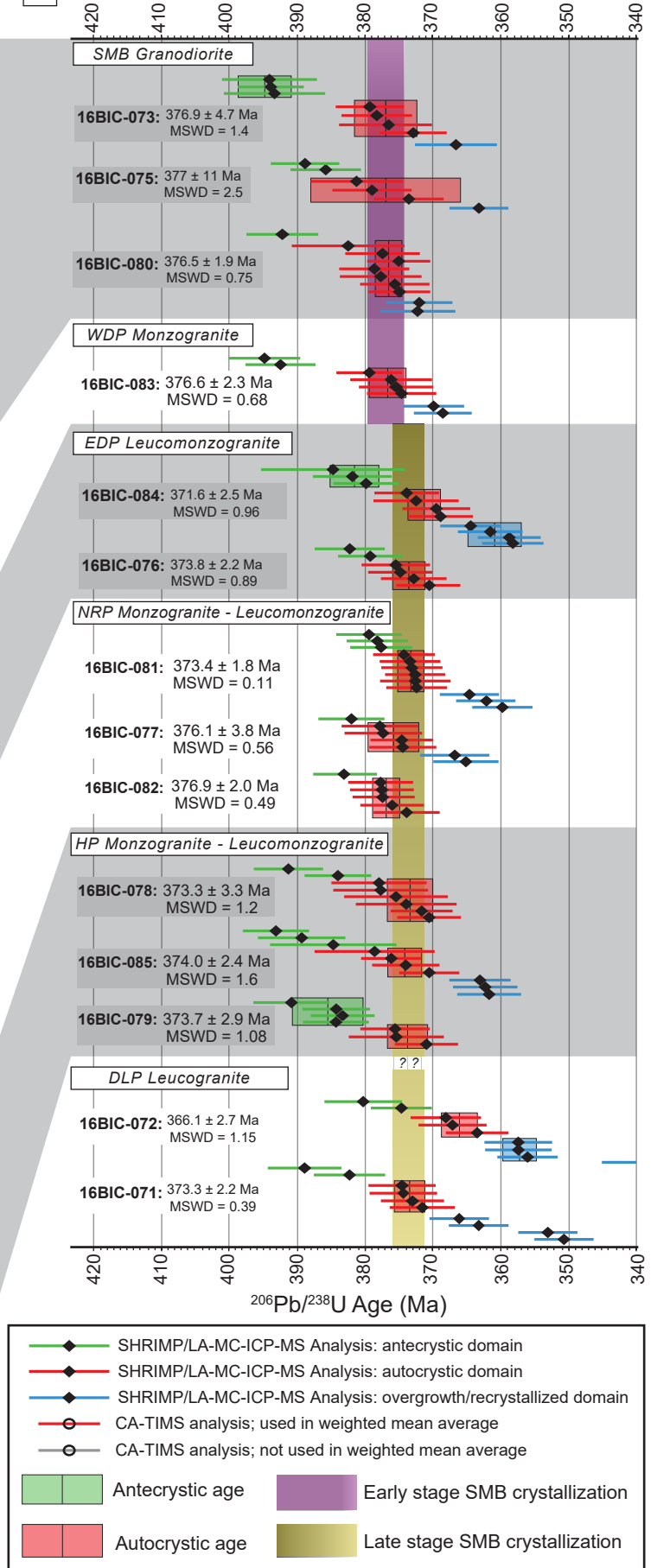


Figure 2-7

Figure 2–7. A) Compilation of $^{206}\text{Pb}/^{238}\text{U}$ age determinations of zircon from all units of the South Mountain Batholith (SMB) by SHRIMP-II and CA-ID-TIMS techniques. B) Compilation of $^{206}\text{Pb}/^{238}\text{U}$ age determinations of zircon from all units of the SMB by LA-MC-ICP-MS technique. The weighted mean average $^{206}\text{Pb}/^{238}\text{U}$ ages of each sample is highlighted in background of each spot/grain analysis. Grain analyses coloured grey were not included in the weighted mean due to discordance and spot analyses that are discordant or overlapping zircon domains are omitted from this figure. Zircon domain affinity is interpreted from zircon morphology, zonation, and isotopic signature in all U-Pb chronometers. The crystallization age ranges of early and late-stage granitoids are interpreted from CA-TIMS analyses; these fields are duplicated onto the field of LA-MC-ICP-MS analyses. Note the late stage crystallization field is projected to the DLP results, despite there being no concordant CA-TIMS analysis from this pluton, and overlaps with the autocrystic SHRIMP-II age; the late stage crystallization field, however, is older than the interpreted LA-MC-ICP-MS interpreted age from the same sample.

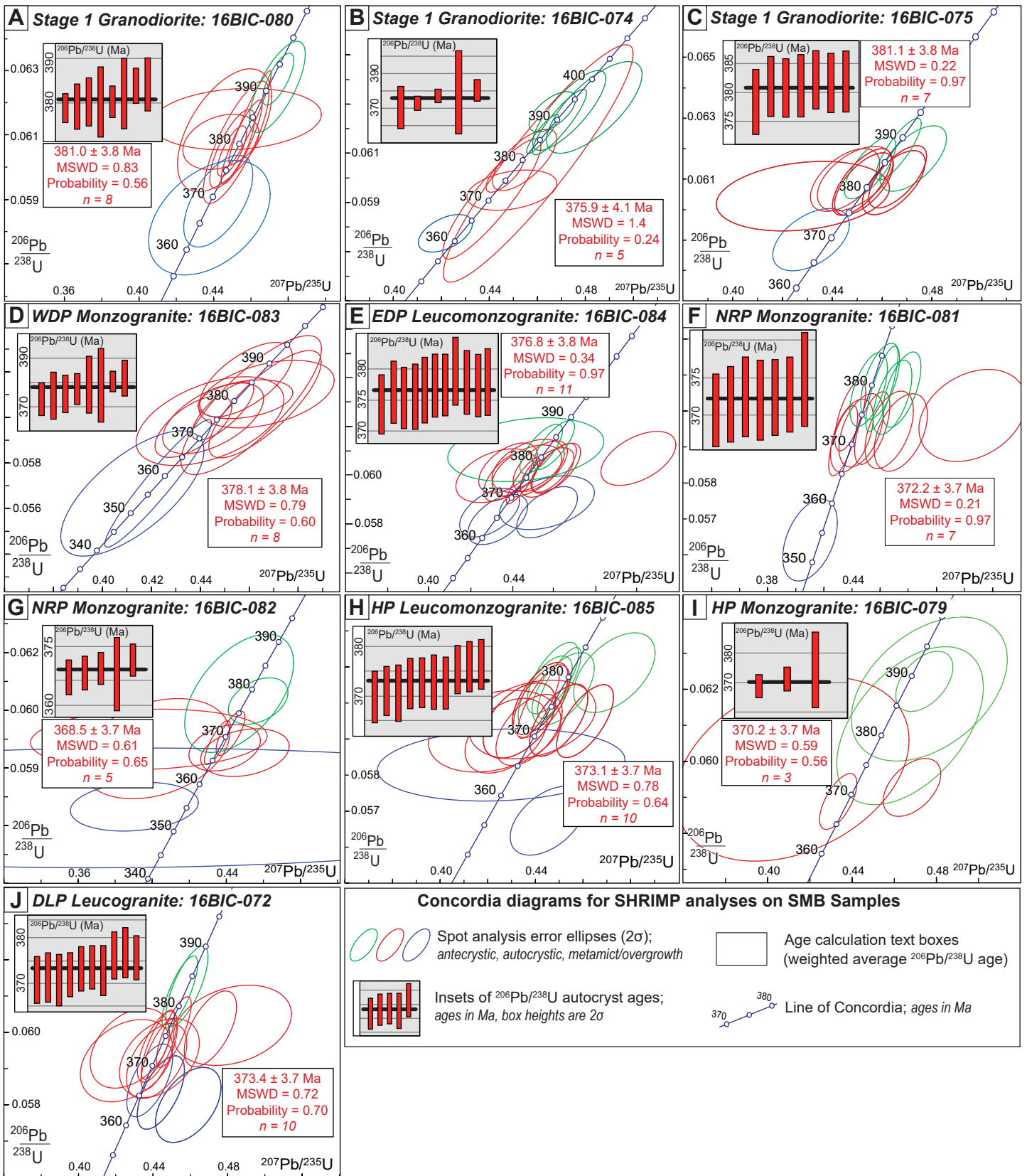


Figure 2–8

Figure 2–8. Concordia plots for select zircon grains from plutons in the South Mountain Batholith analyzed by SHRIMP-II. Coloured lead-loss lines are through age data from Table EA 2-1 (Electronic Appendix), with colour representing respective interpretation, described in the legend. The intercept age of Pb-loss lines to the concordia are noted in sharp cornered boxes and concordia ages are noted in rounded corner boxes; note that ages were calculated from equations in Isoplot 3 (Ludwig 2003). Decay constant errors included are 2σ and errors of autocrystic ages are adjusted to minimum 1% of final age. The MSWD and probability of concordance are also noted in each box.

LA-MC-ICP-MS Analyses Tera-Wasserburg Concordia Diagrams for SMB Samples

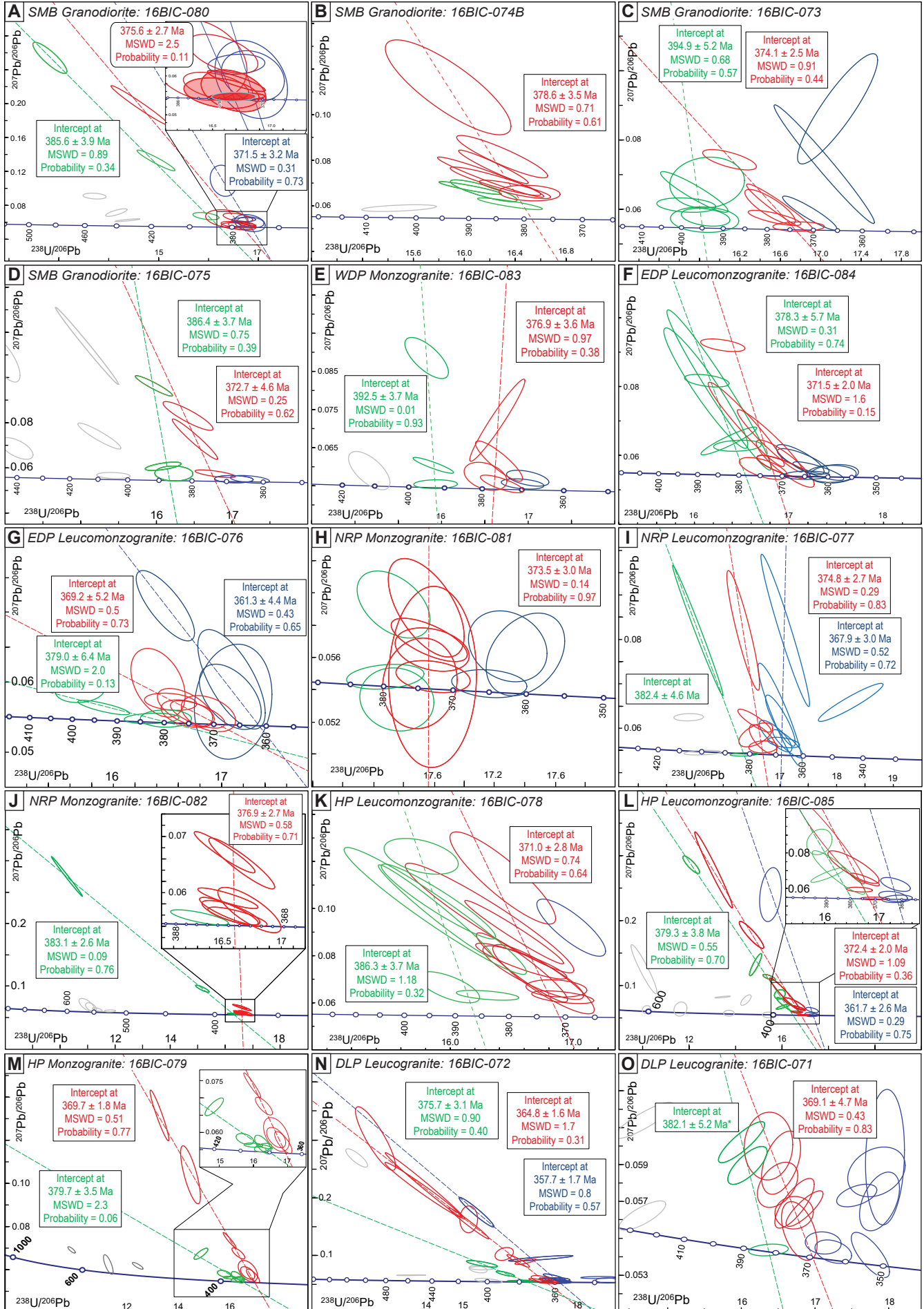


Figure 2-9

Figure 2–9. Tera-Wasserburg concordia plots for select zircon grains from plutons in the South Mountain Batholith analyzed by LA-MC-ICP-MS. Coloured Pb-loss lines are through age data from Table EA 2-3 (Electronic Appendix) with colours representing respective interpretation; note the same legend as in Figure 2–8. Ages were calculated from equations in Isoplot 3 (Ludwig 2003).

CA-TIMS Analyses Concordia Diagrams for SMB Samples

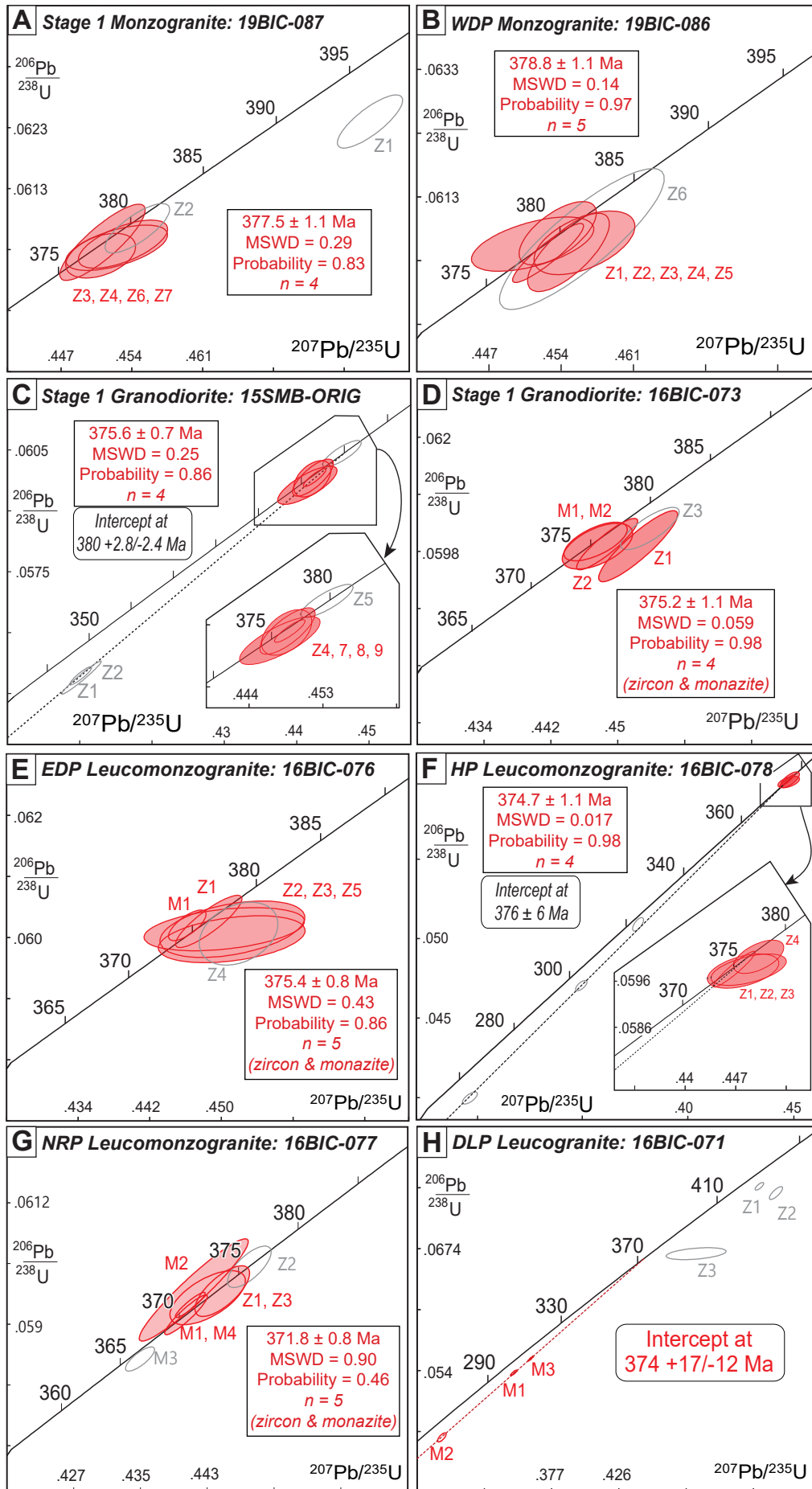


Figure 2-10

Figure 2–10. Concordia plots for select zircon grains from plutons in the South Mountain Batholith analyzed by CA-TIMS analysis. Error ellipses highlighted in red are those used in the weighted mean $^{206}\text{Pb}/^{238}\text{U}$ crystallization ages (Table EA 2-2, Electronic Appendix) and those in grey are not used in the age calculations. Concordia and intercept ages are noted in each plot, legend the same as in Figure 2–8. Ages were calculated from equations in Isoplot 3 (Ludwig 2003).

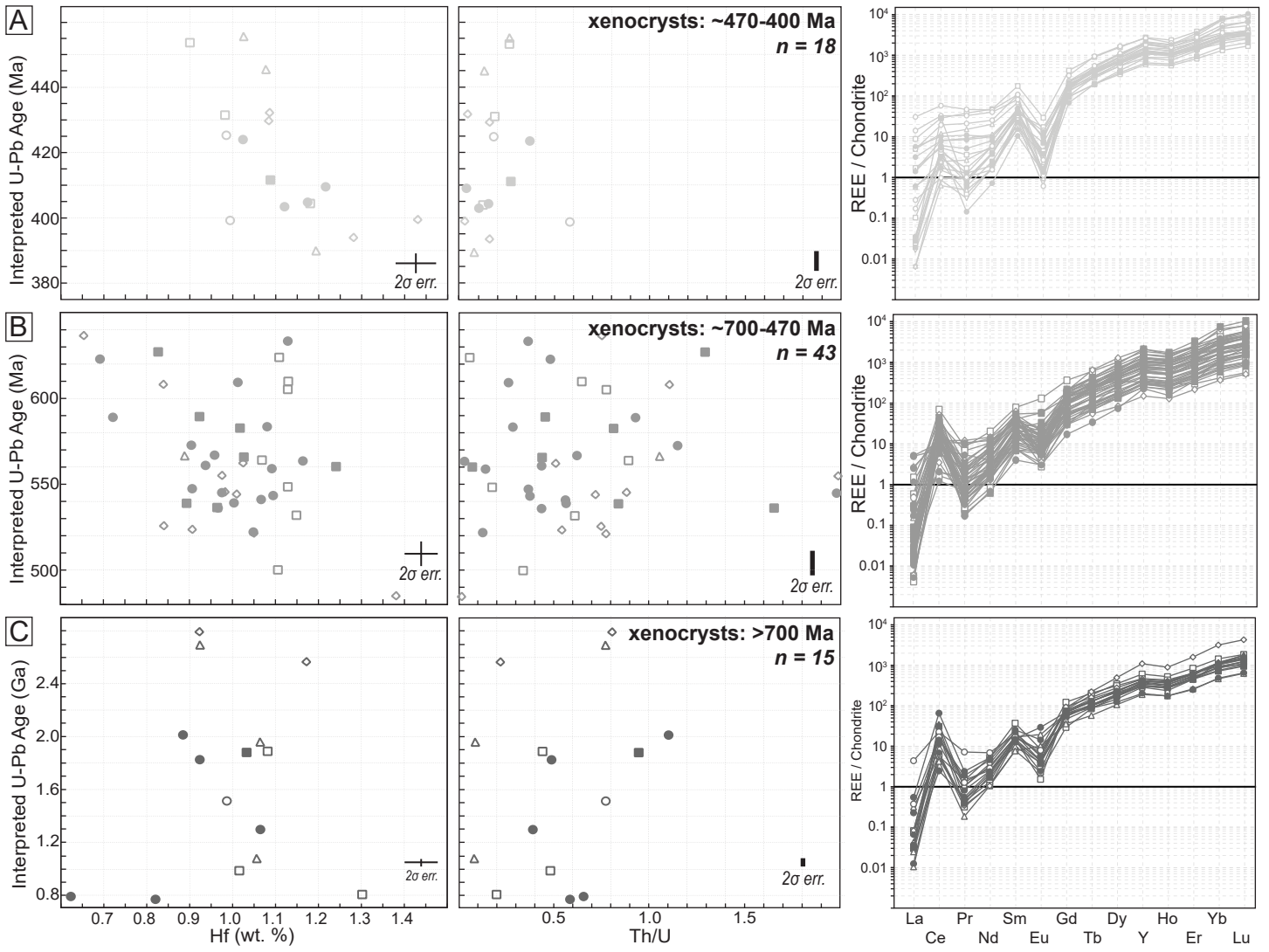


Figure 2-11

Figure 2–11. Trace element data for xenocrystic domains in zircons from all phases of the South Mountain Batholith subdivided based on U-Pb ages. On the left are plots of Hf concentration (left) and Th/U ratio (right) versus zircon U-Pb age, whereas on the right are chondrite-normalized rare-earth element plots (normalizing values after McDonough and Sun, 1995). Note the data shown only include those with <67% discordance in the U-Pb analysis. The age subdivisions, as determined from LA-MC-ICP-MS and SHRIMP-II analyses (Tables EA 2-1 and EA 2-3), and number of spots presented are denoted in top middle of each diagram.

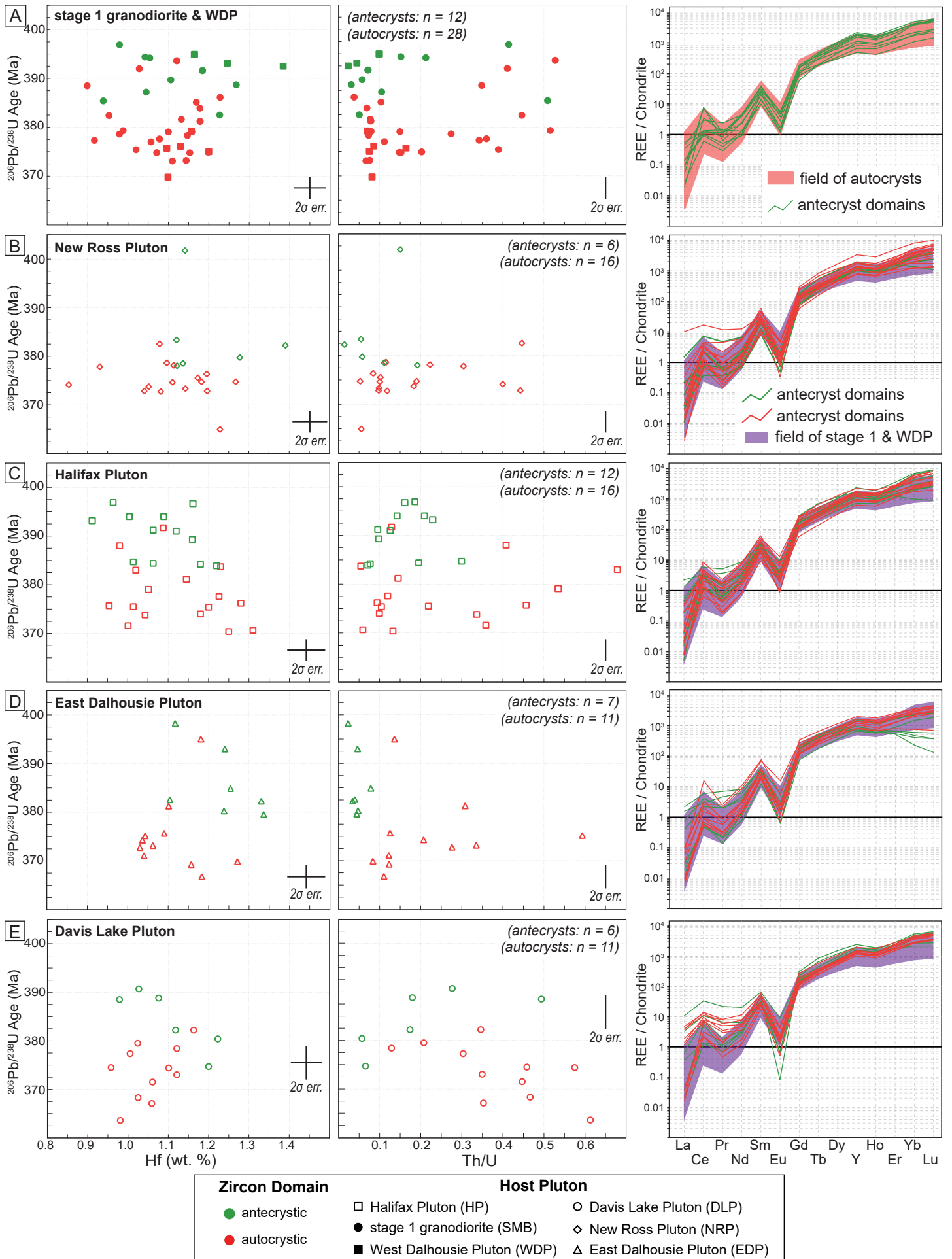


Figure 2-12

Figure 2–12. Trace element data for antecrystic and autocrystic domains in zircons from early and late-stage phases of the South Mountain Batholith. On the left are plots of Hf concentration (left) and Th/U ratio (right) versus zircon U-Pb age, whereas on the right are chondrite-normalized rare-earth element plots (normalizing values after McDonough and Sun, 1995). The plutonic affiliation and number of spot analyses presented are denoted in top left corner of each diagram. Note the data shown only include those with <67% discordance in the U-Pb analysis. Data displayed are for: 1) the less evolved plutons that includes the granodiorites and also the West Dalhousie pluton (WDP); and 2) the more evolved phases that includes the New Ross Pluton (NRP), the Halifax Pluton (HP), the East Dalhousie pluton (EDP), and the Davis Lake Pluton (DLP).

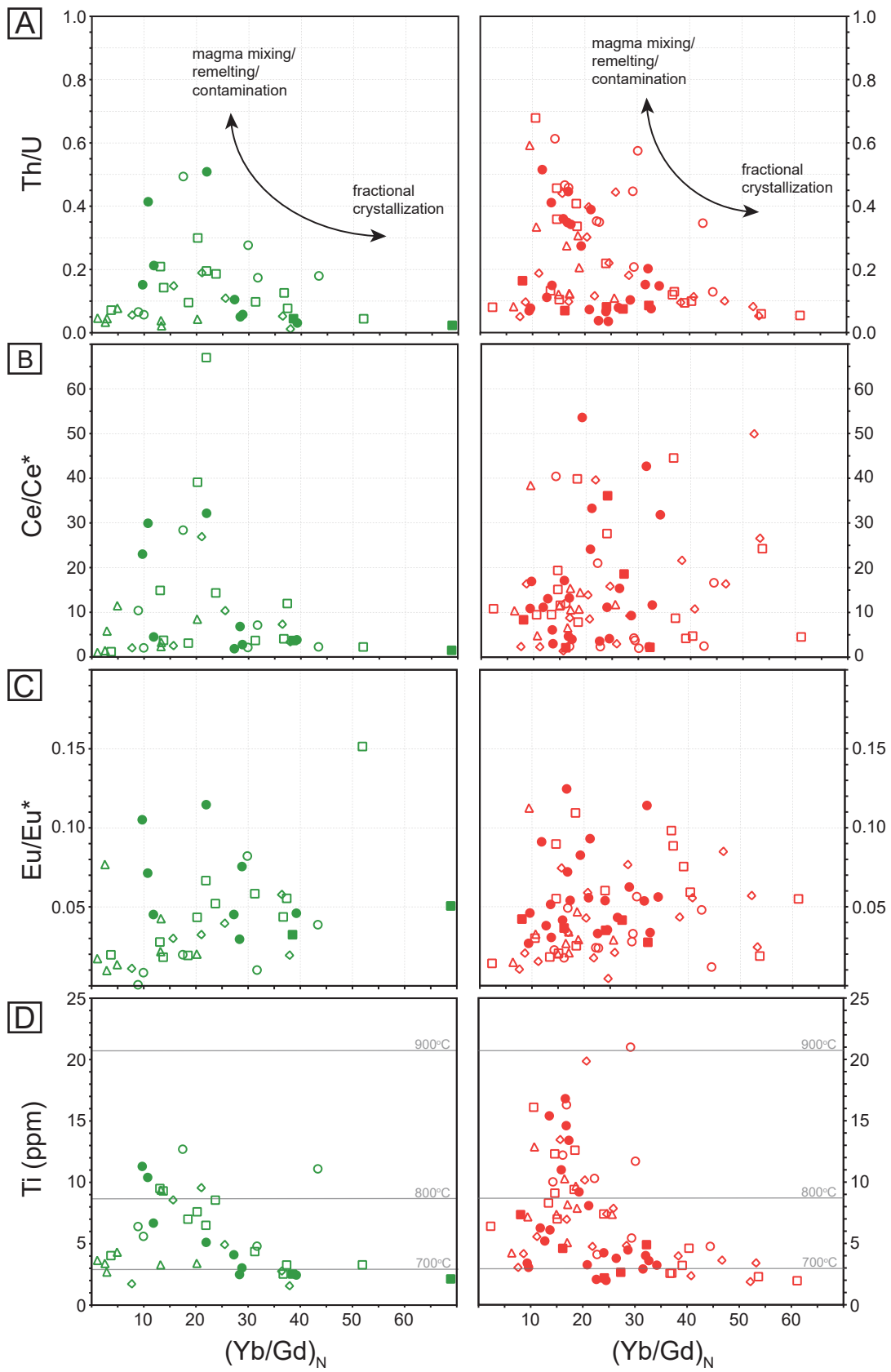


Figure 2-13

Figure 2–13. Rare-earth element and Ti data for antecrystic (left) and autocrystic (right) domains in zircons from across the South Mountain Batholith. Plots show the Yb/Gd ratio normalized to chondrite ($[Yb/Gd]_N$) versus: **A**) Th/U (including indicated fractionation and mixing/contamination pathways based on trace-element chemistry; e.g., Claiborne et al., 2010; Buret et al., 2016); **B**) Ce anomalies (Ce/Ce^*); **C**) Eu anomalies ($Eu/Eu^* = 2Eu_N/(Sm_N + Gd_N)$, $Ce/Ce^* = 2Ce_N/(La_N + Pr_N)$); and **D**) Ti concentration (note the average 2σ error for all data = 1.7 ppm) as well as the Ti-in-zircon temperatures (from Ferry and Watson, 2007). Legend for all data is same as Figure 2–12. Note the data displayed are those with <67% discordance from U-Pb analysis.

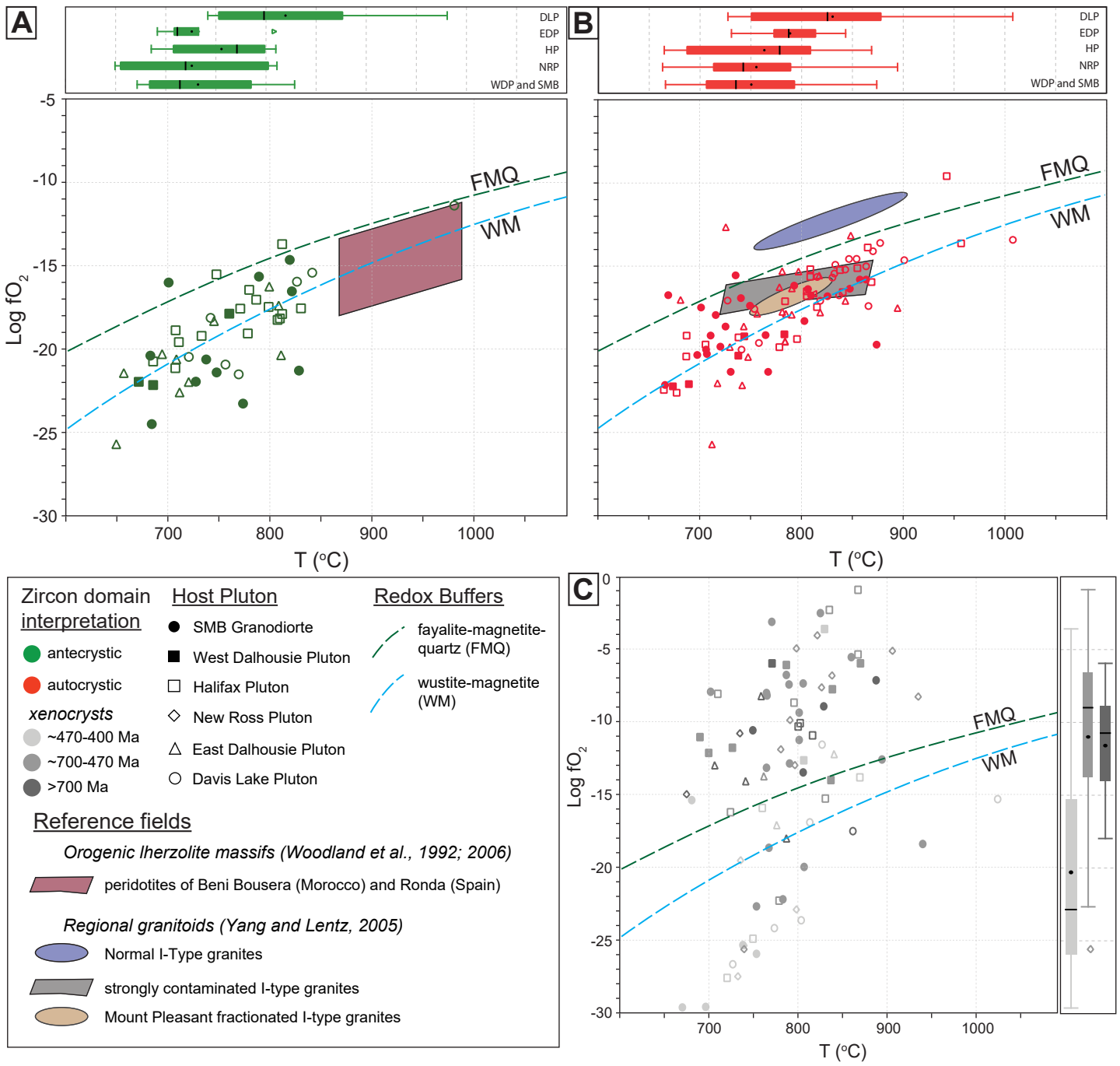


Figure 2-14

Figure 2–14. Plots of oxygen fugacity (fO_2) versus Ti-in-zircon temperatures (Ferry and Watson, 2007) for spot analysis on antecrystic (A), autocrystic (B), and xenocrystic (C) domains in zircons from the South Mountain Batholith. The dashed green and blue curves correspond to the variation in fO_2 with T along the fayalite-magnetite-quartz (FMQ) and the wüstite-magnetite (WM) buffers, respectively (Haggerty, 1978). The maroon field in A represents bulk rock values from spinel peridotite xenoliths in the orogenic Iherzolite Beni Bousera and Ronda massifs in Morocco and Spain, respectively; these xenoliths are interpreted to represent the sub-continental lithospheric mantle that is variably metasomatized (Woodland et al., 1992; 2006). The reference fields in B include those that denote fO_2 (bulk) and T (zircon) values from various granite types in New Brunswick, adjacent to the SMB; blue – oxidized I-type magmas of the Magaguadavic suite, orange – fractionated I-type magmas of the Mount Pleasant and Mount Douglas suite (Yang and Lentz, 2005). The grey field in B represents strongly contaminated and reduced I-type intrusions (bulk from batholiths of California; Ague and Brimhall, 1988).

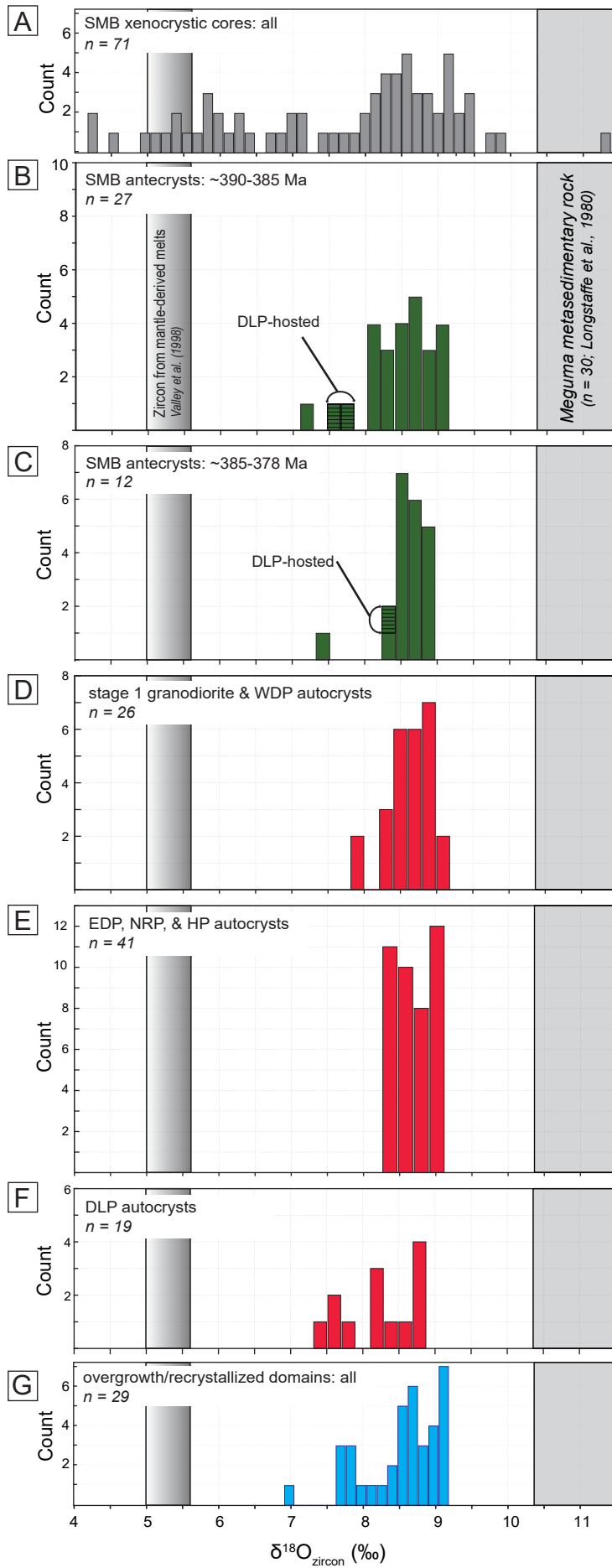


Figure 2-15

Figure 2–15. Histograms of zircon $\delta^{18}\text{O}$ values for samples from plutons of the South Mountain Batholith. Note that the colours represent different zircon domain types, as noted in the text and previous figures. Fields of mantle zircon ($5.3 \pm 0.3\text{‰}$; Valley et al., 1998) and Meguma metasedimentary rock (10.1 to 12.9‰; Longstaffe et al., 1980) are shown. Note that the fractionation of $\delta^{18}\text{O}(\text{whole rock})$ versus $\delta^{18}\text{O}(\text{zircon})$, i.e., $\Delta(\text{WR-Zrc})$ for samples with an SiO_2 % like that of the South Mountain Batholith average $\sim 1\text{‰}$ (Valley et al., 1994). Values are in per mil (‰; VSMOW); bin widths approximately 0.2 to 0.14‰.

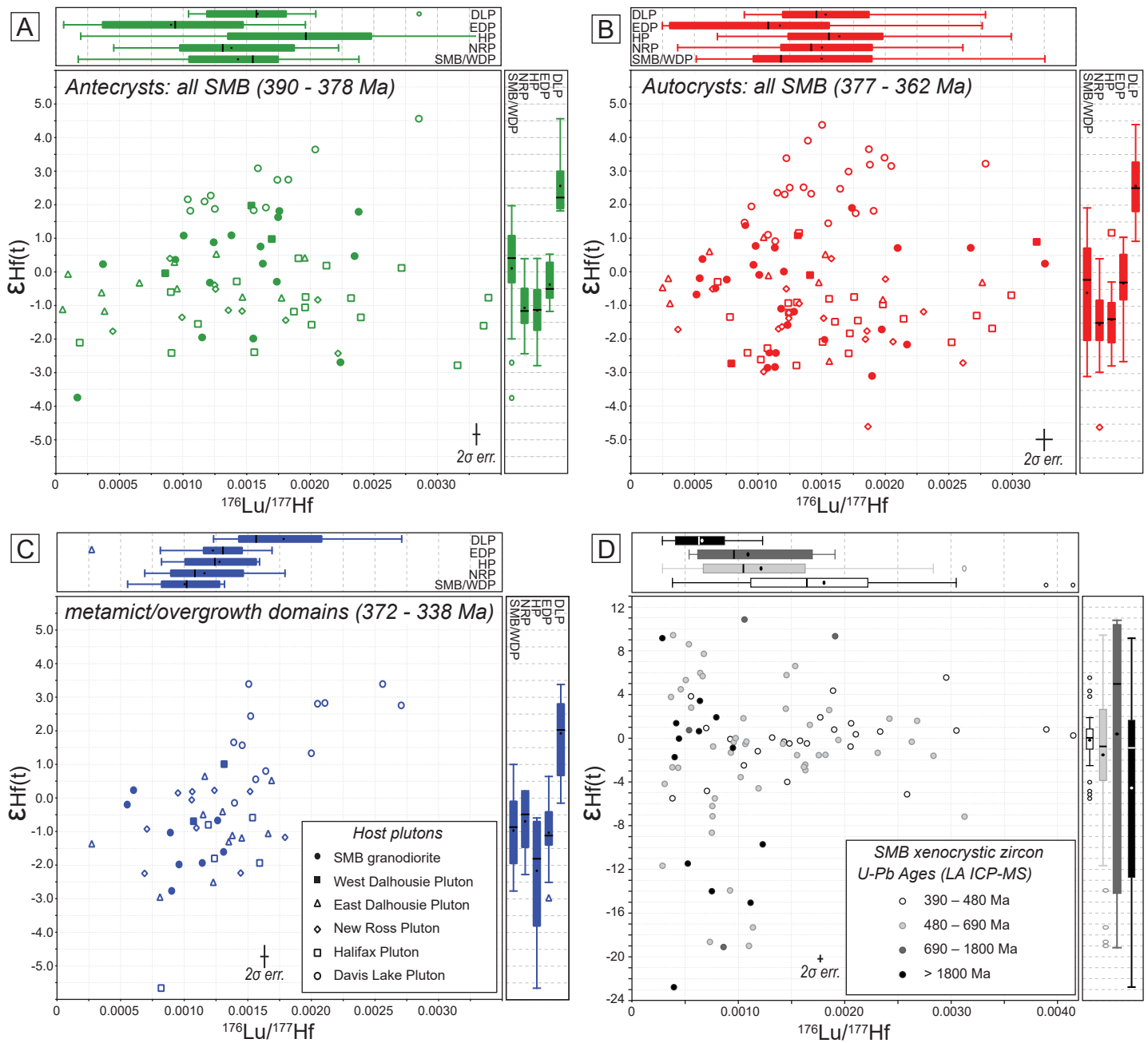


Figure 2–16

Figure 2–16. Plots of $\varepsilon_{\text{Hf}}(t)$ (calculated at the time of crystallisation) versus $^{176}\text{Lu}/^{177}\text{Hf}$ for zircons from different phases of the South Mountain Batholith (2σ error bars are indicated). Data displays distribution of spots placed on: **A**) antecrystic domains; **B**) autocrystic domains; **C**) metamict and replacement domains; and **D**) xenocrystic domains of various ages from throughout the batholith. Symbols for A, B, and C depicted in inset for (C), whereas the legend for D is shown in the inset. Complete dataset found in Table EA 2-5 (Electronic Appendix).

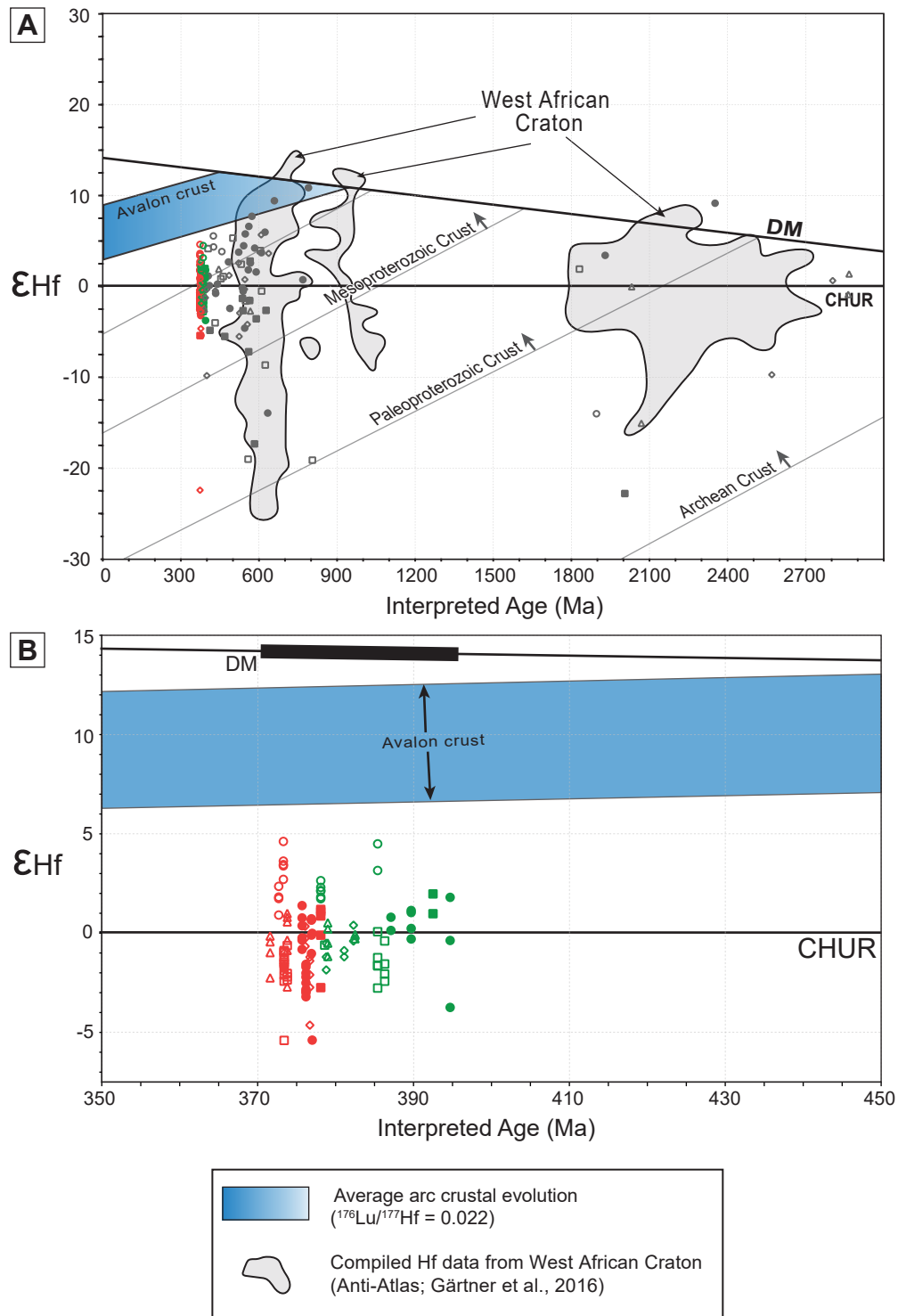


Figure 2–17

Figure 2–17. A) $\epsilon_{\text{Hf}(t)}$ vs. age plot for autocrystic and antecrystic zircon domains as well as analyses of inherited xenocrystic cores from the SMB. For reference, the evolutionary arrays for Archaean, Paleoproterozoic, and Mesoproterozoic crust with average upper crustal $^{176}\text{Lu}/^{177}\text{Hf}$ values of 0.015 (Griffin et al., 2002) are shown as well as the evolutionary array for a more mafic crust ($^{176}\text{Lu}/^{177}\text{Hf} = 0.022$; Pietranik et al., 2008) representative of the Avalon terrane (T_{DM} constraints derived from ϵ_{Nd} values and growth lines in Nance and Murphy, 1996). Grey fields represent $\epsilon_{\text{Hf}(t)}$ data for detrital zircon from the West African craton (Gärtner et al., 2016). Note the most radiogenic Hf isotopic compositions of the ca. 375 Ma granitoids plot above the 1.6–2.5 Ga and older crustal evolution arrays that contain xenocrystic data, indicating potential mixing between melted Meguma crust and more juvenile material. The $\epsilon_{\text{Hf}(t)}$ data were calculated using the decay constant of $1.867 \times 10^{-11} \text{ year}^{-1}$ (Scherer et al., 2001), and the CHUR parameters of Bouvier et al. (2008). **B)** Closer view of $\epsilon_{\text{Hf}(t)}$ ratios versus concordant U–Pb zircon age for autocrystic and antecrystic zircon domain analyses in this study. Note the higher $\epsilon_{\text{Hf}(t)}$ values in the zircon from the DLP. DM—depleted mantle; depleted mantle curve from Griffin et al. (2000).

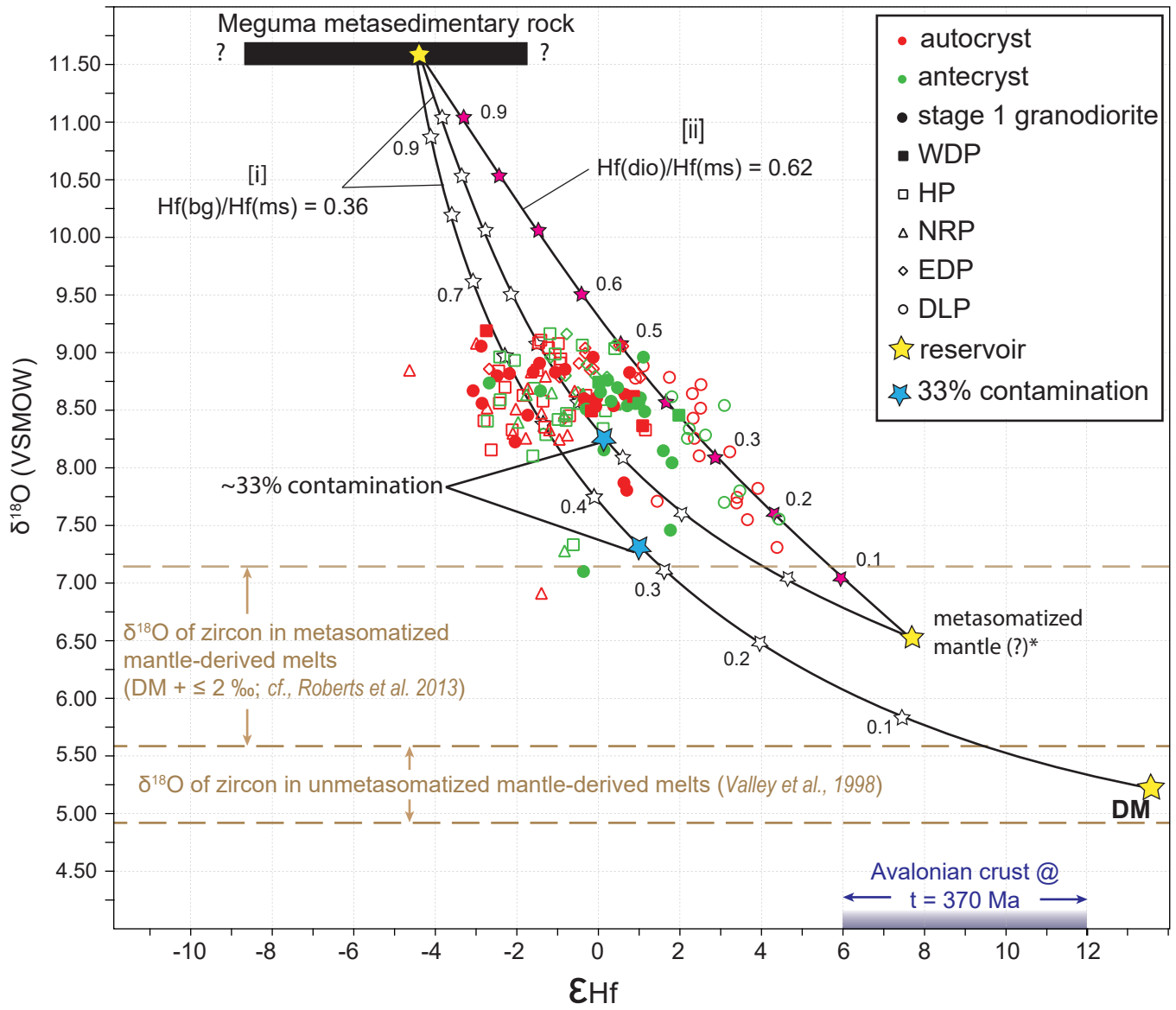


Figure 2–18

Figure 2–18. Plot of $\delta^{18}\text{O}$ versus $\epsilon_{\text{Hf}(t)}$ for the autocrystic and antecrystic domains in zircons of the South Mountain Batholith from this study. Also shown is the range of zircon $\epsilon_{\text{Hf}(t)}$ and $\delta^{18}\text{O}$ values for the Meguma metasedimentary rocks ($\epsilon_{\text{Hf}(t)}$ = unknown, $\delta^{18}\text{O}$ = $+11.6 \pm 1.6\text{‰}$; shaded black) and the $\epsilon_{\text{Hf}(t)}$ range expected for typical arc crust the same age as Avalonia at $t = 370$ Ma (shaded purple). Three mixing lines were constructed (after Langmuir et al., 1978) between metasedimentary rocks and various juvenile materials derived from depleted ($\delta^{18}\text{O} = 5.3 \pm 0.3\text{‰}$, $\epsilon_{\text{Hf}(t)} = +13.5$), or relatively metasomatized ($\delta^{18}\text{O} = 6.3 \pm 0.3\text{‰}$, $\epsilon_{\text{Hf}(t)} = +9.25 \pm 2.25\text{‰}$) mantle reservoirs. The $\delta^{18}\text{O}$ value of zircon in mantle-derived melts ($5.3 \pm 0.3\text{‰}$, 1σ) is from Valley (2003). The $\text{Hf}_{(\text{bg})}/\text{Hf}_{(\text{ms})}$ and $\text{Hf}_{(\text{dio})}/\text{Hf}_{(\text{ms})}$ are the ratios of Hf concentrations for more juvenile material (bg = Bog Island Gabbro, dio = diorite of the Shelburne Pluton, Fig. 2–1A) and the Meguma metasedimentary rocks of the Goldenville Group (ms). The $\epsilon_{\text{Hf}(t)}$ values of Meguma metasedimentary rock were estimated based on best fit between the mixing lines, juvenile end members, and data from this study. The antecrystic domains are also plotted as they are interpreted to preserve primary magmatic Hf-O isotopic composition from early melts.

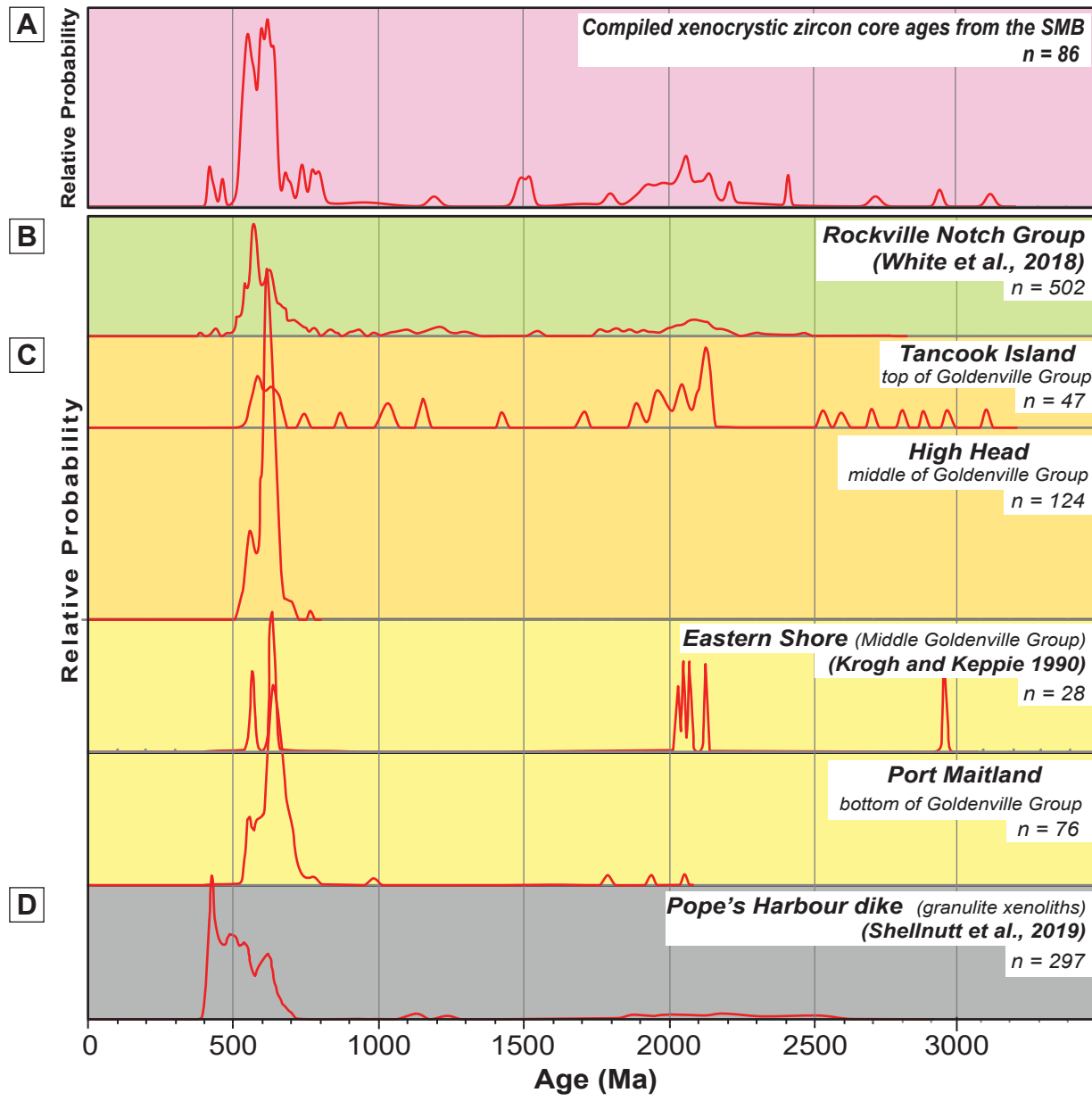


Figure 2–19

Figure 2–19. Relative probability density plots of: (A) compiled xenocrystic zircons in the SMB from this study, (B) metavolcanic zircon in the Silurian Rockville Notch Group, (C) detrital zircon studies from various formations that comprise the Goldenville Group in the Meguma terrane, and (D) xenolith detrital and metamorphic zircon in granulite xenoliths from the Pope’s Harbour dike (Fig. 2–1A).

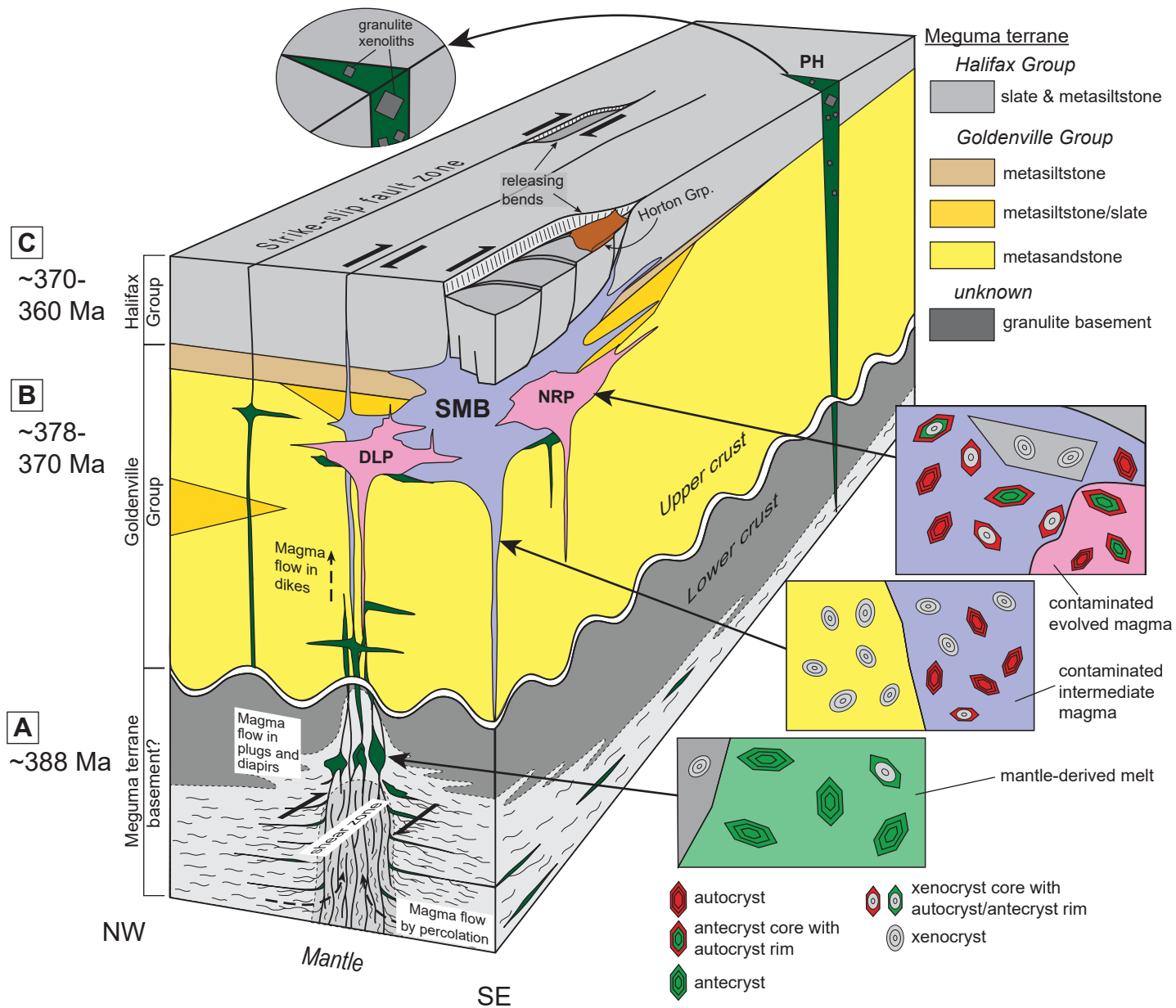


Figure 2-20

Figure 2–20. Schematic diagram that depicts the emplacement model for the South Mountain batholith based on the translithospheric shear zone model of Richards (2003), inspired by Brown (1994) and Vigneresse and Tikoff (1999). **(A)** After the onset of recorded deformation in the Meguma terrane and during early antecryst crystallization (ca. 388 Ma); formation of a lower crustal magmatic zone, where melt flows by percolation to low pressure areas (i.e., extensional shear bands along major faults), into which magma is drawn and begins to rise as buoyant plugs or diapirs, coalescing and becoming contaminated by the lower crust. **(B)** By ~378-370 Ma, the upward flow of SMB magmas forms continuous dikes along shear zones that resupply the mid-crustal magma chamber for ca. 10-15 Ma; the shear zones are expressed at surface by brittle strike-slip faults with step-overs and transtensional zones. Superimposed on the diagram by colour is a simplified stratigraphy of the Meguma terrane (modified after White, 2010; White et al., 2018). PH – Pope’s Harbour dike. The inset diagrams show schematic depictions of zircon domain character and inheritance by the different melt stages through the evolution of the SMB (modified after Miles and Woodcock, 2018; Archibald et al., 2021), see main text for detailed explanation.

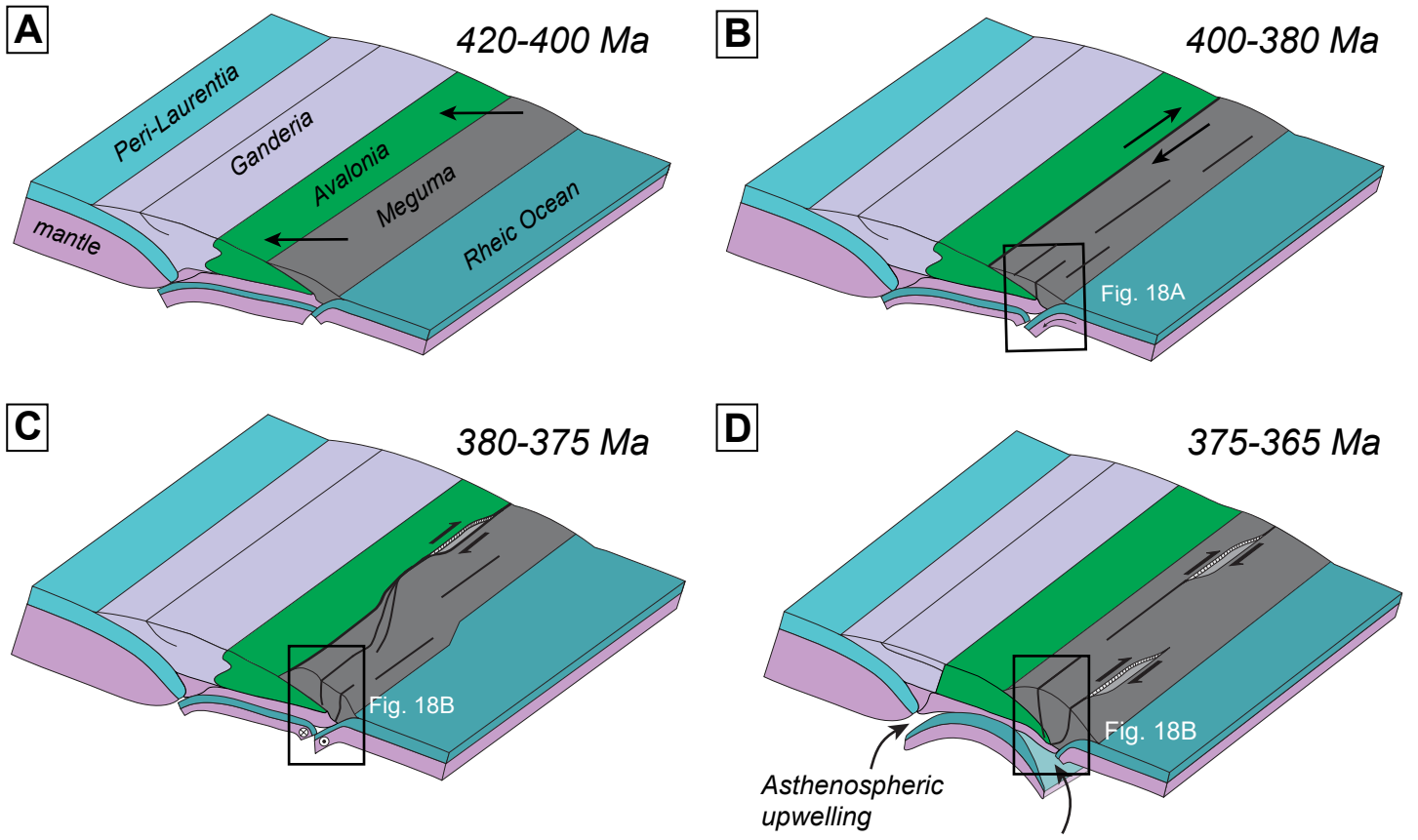


Figure 2-21

Figure 2–21. Schematic simplified geotectonic setting outboard of the Laurentian margin depicting the juxtaposed Ganderia-Avalonia-Meguma terranes prior to and during the emplacement window of the South Mountain Batholith and associated magmatism, modified after van Staal et al. (2021): **A**) ~420–400 Ma; **B**) ~400–380 Ma; **C**) ~380–375 Ma; and **D**) 375–365 Ma.

Table 2–1. South Mountain Batholith Historical Geochronology

Intrusion	Mineral	Chronometer (Method)	Age (Ma)	Error (Ma)	Reference
<u>SMB</u>					
Westfield - leucogranite	zircon	U-Pb (ID-TIMS)	385	± 2	Keppie et al. (1993)
Millet Brook - leucomonzogranite	monazite	²⁰⁷ Pb/ ²⁰⁶ Pb (ID-TIMS)	384	± 4	Keppie et al. (1993)
Millet Brook - granodiorite	zircon	U-Pb (ID-TIMS)	377	± 4	Keppie et al. (1993)
DLP	whole-rock	Rb/Sr (isochron)	<i>375</i>	± 3	Chatterjee & Cormier (1991)
DLP - leucomonzogranite	biotite	⁴⁰ Ar/ ³⁹ Ar (step-heating)	<i>372</i>		Reynolds et al. (1981)
South Mountain - bio granodiorite	whole-rock	Rb-Sr (isochron)	<i>371.8</i>	± 2.2	Clarke & Halliday (1980)
South Mountain - monzogranite	muscovite	K/Ar (step-heating)	<i>371</i>	± 5	Harper (1988)
DLP - biotite-monzogranite	biotite	⁴⁰ Ar/ ³⁹ Ar (step-heating)	<i>370</i>		Reynolds et al. (1981)
Westfield - leucogranite	muscovite	⁴⁰ Ar/ ³⁹ Ar (step-heating)	<i>368.2</i>	± 6	Keppie et al. (1993)
EKLG - leucogranite	whole-rock	U-Pb (isochron)	367	± 10	Kontak & Chatterjee (1992)
DLP	muscovite	⁴⁰ Ar/ ³⁹ Ar (step-heating)	<i>366</i>		Reynolds et al. (1981)
EKLG - leucogranite	whole-rock	Pb-Pb (isochron)	366	± 4	Kontak & Chatterjee (1992)
South Mountain - monzogranite	whole-rock	Rb-Sr (isochron)	<i>364.3</i>	± 1.3	Clarke & Halliday (1980)
EKLG - leucogranite	whole-rock	Rb/Sr (isochron)	<i>344</i>	± 5	Kontak & Cormier (1991)
DLP	whole-rock	Rb/Sr (isochron)	<i>330</i>	± 7	Richardson et al. (1989)
<u>SMB Periphery</u>					
Halfway Cove - granite	zircon	U-Pb (ID-TIMS)	379	± 2	Keppie & Krough (1999)
Port Mouton - tonalite	monazite	U-Pb (ID-TIMS)	378	± 3	Currie et al. (1998)
Musquodobit - monzogranite	zircon	U-Pb (ID-TIMS)	378	± 1	Kontak et al. (2004)
Shelburne - diorite	zircon	U-Pb (ID-TIMS)	377	± 4	Clarke et al. (1997)
Shelburne - diorite	titanite	U-Pb (ID-TIMS)	<i>377</i>	± 4	Currie et al. (1998)
Shelburne - diorite-tonalite	zircon	U-Pb (ID-TIMS)	376	± 2	Tate et al. (1997)
Polson Mountain - AF granite	zircon	U-Pb (LAM-ICP-MS)	374.9	± 3.0	MacHattie et al. (2013)
Barrington Passage - granite	zircon	U-Pb (ID-TIMS)	373	± 2	Keppie & Krough (1999)
Shelburne - granodiorite	monazite	U-Pb (ID-TIMS)	373	± 1	Currie et al. (1998)
Port Mouton - tonalite	monazite	U-Pb (ID-TIMS)	373	± 1	Clarke et al. (2000)
Kinsac - monzogranite	biotite	⁴⁰ Ar/ ³⁹ Ar (step-heating)	<i>373</i>		Reynolds et al. (1981)
Shelburne - granite	zircon	U-Pb (ID-TIMS)	372	± 3	Keppie & Krough (1999)
Barrington Passage - granite	monazite	U-Pb (ID-TIMS)	372	± 2	Keppie & Krough (1999)
East Jeddore - lamprophyre	hornblende	⁴⁰ Ar/ ³⁹ Ar (step-heating)	<i>370</i>	± 2	Kempster et al. (1989)
Larry's River - granite	monazite	U-Pb (ID-TIMS)	371	± 2	Keppie & Krough (1999)
Shelburne - granodiorite	zircon	U-Pb (ID-TIMS)	371	± 2	Keppie & Dallmeyer (1995)
Port Mouton - granodiorite	monazite	U-Pb (ID-TIMS)	368	± 1	Currie et al. (1998)
Polson Mountain - AF granite	zircon	U-Pb (LAM-ICP-MS)	367.6	± 4.4	MacHattie et al. (2013)
Sober Island - lamprophyre	hornblende	⁴⁰ Ar/ ³⁹ Ar (step-heating)	<i>367</i>	± 2	Kempster et al. (1989)
Kinsac - monzogranite	muscovite	⁴⁰ Ar/ ³⁹ Ar (step-heating)	<i>363</i>		Reynolds et al. (1981)
Musquodobit - monzogranite	biotite	⁴⁰ Ar/ ³⁹ Ar (step-heating)	<i>363</i>		Reynolds et al. (1981)
Barrington Passage - tonalite	titanite	U-Pb (ID-TIMS)	<i>361</i>		Currie et al. (1998)
Shelburne - granodiorite	muscovite	⁴⁰ Ar/ ³⁹ Ar (step-heating)	<i>342</i>	± 18	Keppie & Dallmeyer (1995)
Kinsac - monzogranite	K-Feldspar	⁴⁰ Ar/ ³⁹ Ar (step-heating)	<i>354</i>		Kontak et al. (1999)
Port Mouton - granodiorite	muscovite	⁴⁰ Ar/ ³⁹ Ar (step-heating)	<i>339</i>	± 14	Keppie & Dallmeyer (1995)
Shelburne - granodiorite	biotite	⁴⁰ Ar/ ³⁹ Ar (step-heating)	<i>330</i>	± 21	Keppie & Dallmeyer (1995)
Port Mouton - granodiorite	biotite	⁴⁰ Ar/ ³⁹ Ar (step-heating)	<i>320</i>	± 20	Keppie & Dallmeyer (1995)

Note: Bold ages represent crystallization ages and italics represent post-crystallization cooling ages. DLP = Davis Lake Pluton, EKLG = East Kemptville Leucogranite, ID-TIMS = Isotope dilution-thermal ionization mass spectrometry, LAM-ICP-MS = Laser ablation microprobe-inductively coupled-mass spectrometry, AF = alkali-feldspar.

Table 2–2. Summary of dated samples, their zircon/monazite characteristics, and methods applied.

Pluton/ Sample	Location coordinates (UTM Zone 20)		Zircon Appearance		Internal Zircon Domain Character				Analyses Conducted (<i>Lab</i>)					
	Easting	Northing	Length (μm)	Morphology	Core	Mantle (inner)	Rim	Comments	SHRIMP (<i>GSC</i>)	<i>n</i>	LA-MC- -ICP-MS (<i>MERC-IGL</i>)	<i>n</i>	CA-TIMS (<i>MUN</i>)	<i>n</i>
<i>SMB Granodiorite</i>														
16BIC-080	404224	4970953	30-250	<i>stubby, semi-prismatic</i>	abundant; typically rounded, unzoned	oscillatory to sector zonation	oscillatory zonation	common unzoned rims and altered zones yield anomalously young ages	×	32	×	19		
16BIC-074/B*	323125	4957515	100-800	<i>equant to prismatic</i>	abundant; unzoned to chaotic zonation	oscillatory to complex zonation	oscillatory zonation	-	×	34	×	23		
16BIC-073	435103	4967603	150-500	<i>equant prismatic to partially resorbed</i>	abundant; rounded, chaotic zonation	oscillatory to complex zonation	oscillatory zonation	rare unzoned replacement domains yield anomalously young ages			×	27	×	5
16BIC-075	340550	4953911	50-500	<i>stubby resorbed to elongate prismatic</i>	abundant; metamict and chaotic zonation	oscillatory to complex zonation	oscillatory zonation	one altered zircon core yielded an anomalously young age	×	33	×	27		
15SMB-ORIG	283542	4929425	150-500	<i>elongate to equant prismatic</i>	-	-	-	clear zircon					×	9
<i>WDP</i>														
16BIC-083	307486	4941565	50-250	<i>elongate to stubby prismatic</i>	common		thin oscillatory zonation	rare unzoned rims yield anomalously young ages	×	14	×	22		
19BIC-086	329747	4954969	150-500	<i>prismatic</i>	-	-	-	high quality, clear zircon					×	6
<i>EDP</i>														
16BIC-084	365126	4976534	25-400	<i>equant prismatic</i>	rare; rounded, metamict	oscillatory to complex zoning	oscillatory to massive zoned	common unzoned rim domains yield anomalously young ages	×	32	×	27		
16BIC-076	357086	4951239	100-300	<i>elongate to equant prismatic</i>	rare; rounded, metamict	oscillatory zonation	oscillatory zonation	common unzoned rim domains yield anomalously young ages			×	24	×	6

Table 2–2 (cont'd.)

Pluton/ Sample	Coordinates		Zircon Appearance		Internal Zircon Domain Character				Analyses Conducted (<i>Lab</i>)					
	Easting	Northing	Length (μm)	Morphology	Core	Mantle (inner)	Rim	Comments	SHRIMP (<i>GSC</i>)	<i>n</i>	LA-MC- -ICP-MS (<i>MERC-IGL</i>)	<i>n</i>	CA-TIMS (<i>MUN</i>)	<i>n</i>
<i>NRP</i>														
16BIC-081	398505	4951936	25-250	<i>short prismatic, typically partially resorbed</i>	common; metamict and chaotic zonation	oscillatory zonation	oscillatory zonation	rare unzoned, low-U replacement zones yield anomalously young ages	×	34	×	27		
16BIC-077	386598	4950683	100-400	<i>equant to elongate prismatic</i>	rare; partially resorped metamict	oscillatory to sector zonation	thin oscillatory zonation	abundant high quality, clear zircon			×	20	×	7
16BIC-082	418635	4930449	100-250	<i>equant prismatic, rarely stubby</i>	common; massive zonation	oscillatory zonation	oscillatory zonation	rare unzoned rims yield anomalously young ages	×	18	×	20		
19BIC-087	413351	4938150	100-400	<i>sharp prismatic</i>	-	-	-	high quality, clear					×	7
<i>HP</i>														
16BIC-078	441162	4943598	150-500	<i>clear, prismatic</i>	common; massive to chaotic zonation	oscillatory zonation	oscillatory zonation	clear zircon			×	24	×	7
16BIC-085	431611	4930022	50-400	<i>stubby to equant prismatic</i>	common; rounded, massive zonation	fine to massive oscillatory zonation	fine to massive oscillatory zonation	rare unzoned rims yield anomalously young ages	×	34	×	34		
16BIC-079	451579	4925522	50-300	<i>stubby to equant prismatic, rarely resorbed</i>	common; metamict, massive zonation	oscillatory zonation	oscillatory zonation	-	×	26	×	20		
<i>DLP</i>														
16BIC-072	291843	4885311	25-500	<i>stubby prismatic</i>	rare; rounded, massive to complex zonation	oscillatory zonation	oscillatory zonation	rare unzoned rims and replacment zones yield anomalously young ages	×	31	×	39		
16BIC-071	277008	4879125	50-300	<i>equant to elongate prismatic</i>	rare; rounded, massive to complex zonation	oscillatory zonation	oscillatory zonation	majority of grains metamict and discoloured			×	24	×	6

*16BIC-074B (collected for LA-MC-ICP-MS) was sampled separately from 16BIC-074 (collected for SHRIMP) but at same outcrop. *n* = number of analyses by a given method on the respective sample zircon population. A summary of the U-Pb geochronology results for each sample is found in Tables 3 and 4 and Figures 7, 8, 9 and 10.

Table 2–3. Compiled in situ zircon U-Pb Age determinations (antecrysts and autocrysts)

Pluton/ Sample	Method	Antecrystic zircon				Autocrystic zircon			
		Age 2 σ (Ma)	n	MSWD	prob.	Age 2 σ (Ma)	n	MSWD	prob.
SMB Granodiorite									
16BIC-074	SHRIMP	389.7 \pm 3.9	7	0.94	0.46	375.7 \pm 3.9	6	1.40	0.24
16BIC-074B	LA-ICP-MS	386.4 \pm 9.3	3	2.40	0.09	378.6 \pm 3.5	7	0.71	0.61
16BIC-075	SHRIMP	385.9 \pm 3.8	3	0.55	0.58	381.5 \pm 3.8	9	0.46	0.89
	LA-ICP-MS	386.4 \pm 3.8	3	0.75	0.39	372.7 \pm 5.6	3	0.25	0.62
16BIC-080	SHRIMP	391.0 \pm 3.1	3	0.18	0.67	380.2 \pm 3.8	7	0.48	0.83
	LA-ICP-MS	385.6 \pm 3.9	3	0.89	0.34	376.5 \pm 1.9	7	0.75	0.61
16BIC-073	LA-ICP-MS	394.9 \pm 3.3	3	0.23	0.80	376.2 \pm 2.0	6	0.46	0.81
WDP									
16BIC-083	SHRIMP	-	-	-	-	378.0 \pm 3.8	7	0.08	0.78
	LA-ICP-MS	392.5 \pm 3.7	3	0.01	0.93	376.6 \pm 2.3	4	0.68	0.57
EDP									
16BIC-084	SHRIMP	382.5 \pm 3.8	3	0.05	0.95	377.4 \pm 3.8	6	0.55	0.48
	LA-ICP-MS	381.5 \pm 3.3	3	0.41	0.66	371.6 \pm 2.5	4	0.96	0.41
16BIC-076	LA-ICP-MS	379.0 \pm 6.4	4	2.00	0.13	373.8 \pm 2.2	4	0.89	0.45
NRP									
16BIC-077	LA-ICP-MS	382.4 \pm 4.6	2*	-	-	368.2 \pm 3.5	6	0.65	0.58
16BIC-081	SHRIMP	380.2 \pm 3.8	4	0.13	0.94	372.4 \pm 3.7	5	0.43	0.79
	LA-ICP-MS	378.8 \pm 2.6	3	0.15	0.86	373.4 \pm 1.8	6	0.11	0.99
16BIC-082	SHRIMP	377.8 \pm 3.6	2	0.09	0.77	369.1 \pm 3.7	5	1.20	0.30
	LA-ICP-MS	383.1 \pm 2.6	3	0.09	0.76	376.9 \pm 2.0	5	0.49	0.75
HP									
16BIC-079	SHRIMP	388.3 \pm 3.9	3	0.43	0.65	371.1 \pm 3.7	4	0.87	0.46
	LA-ICP-MS	385.4 \pm 5.2	4	1.9	0.12	369.7 \pm 1.8	7	0.51	0.77
16BIC-085	SHRIMP	378.6 \pm 3.8	4	0.18	0.91	374.1 \pm 3.7	6	0.74	0.59
	LA-ICP-MS	379.3 \pm 3.8	6	0.55	0.70	372.4 \pm 2.0	7	1.09	0.36
16BIC-078	LA-ICP-MS	386.3 \pm 3.7	6	1.18	0.32	373.3 \pm 3.3	6	1.20	0.30
DLP									
16BIC-072	SHRIMP	382.8 \pm 3.6	2	0.07	0.80	372.7 \pm 3.7	8	0.44	0.88
	LA-ICP-MS	375.7 \pm 3.1	6	0.90	0.40	366.1 \pm 2.7	3	1.15	0.32
16BIC-071	LA-ICP-MS	382.1 \pm 5.2	3*	-	-	373.3 \pm 2.2	4	0.39	0.76

Italics indicate a discordia age whereas all other ages are $^{206}\text{Pb}/^{238}\text{U}$ ages.

Note: the number of grains/spots are those selected for the weighted mean average based on grain/spot quality and paragenetic association.

Probability indicates the probability of fit or discordance (discordia, weighted mean $^{206}\text{Pb}/^{238}\text{U}$ ages). n = number of spot analyses

*indicates isochron is suspect in nature due to the spread and number of data.

Table 2–4. Compilation of geographic coordinates and weighted-mean $^{206}\text{Pb}/^{238}\text{U}$ ages for CA-TIMS samples in this study.

Pluton	Sample	Location coordinates		Mineral	Number of Grains	Mean $^{206}\text{Pb}/^{238}\text{U}$		MSWD	Probability
		UTM (Zone 20)				Age (Ma)	2 σ (Ma)		
		Easting	Northing						
SMB (early phase)									
	16BIC-073	435103	4967603	zircon	4	375.2	± 1.1	0.059	0.98
	15SMB-ORIG	283542	4929425	zircon	4	375.6	± 0.7	0.25	0.86
West Dalhousie Pluton (WDP)									
	19BIC-086	329747	4954969	zircon	5	378.8	± 1.1	0.14	0.97
East Dalhousie Pluton (EDP)									
	16BIC-076	357086	4951239	zircon/ monazite	5	375.4	± 0.8	0.43	0.86
Halifax Pluton (HP)									
	16BIC-078	441162	4943598	zircon	4	374.7	± 1.1	0.017	0.98
Davis Lake Pluton (DLP)									
	16BIC-071*	277008	4879125	monazite	3	374*	+17/-12		
New Ross Pluton (NRP)									
	16BIC-077	386598	4950683	zircon/ monazite	5	371.8	± 0.8	0.90	0.46
	19BIC-087	413351	4938150	zircon	4	377.5	± 1.1	0.29	0.83

*Ages from monazite and zircon in this sample were discordant, monazite ages fall on a simple lead–loss line (20% probability of fit) that has an upper intercept of 374 +17/-12 Ma.

Note: number of grains/spots are those selected for the weighted mean average based on grain/spot quality and paragenetic association.

Table 2–5. Summary of trace element data from different zircon domains in each pluton of the SMB.

Domain Type	<i>n</i>	Hf (ppm)	Th (ppm)	U (ppm)	ΣREE (ppm)	ΣLREE (ppm)	Ce/Ce*	Eu/Eu*	T (°C) ±	<i>f</i> O ₂ (ΔFMQ)
<i>Granodiorite & WDP</i>										
antecrystic	9	10540 (9390 - 13840)	43 (20 - 152)	406 (200 - 867)	1362 (491 - 2007)	34.8 (15.5 - 47.6)	4.5 (1.5 - 32.2)	0.05 (0.03 - 0.11)	671 - 829 34	-4.6 (-5.9 to -1.0)
autocrystic	26	11050 (8990 - 12280)	45 (17 - 217)	360 (70 - 863)	1202 (383 - 1714)	32.3 (18.9 - 69.2)	11.4 (2.1 - 53.6)	0.05 (0.03 - 0.12)	669 - 874 34	-4.2 (-6.8 to -1.6)
replacement/metamict	8	10340 (9280 - 12660)	42 (24 - 129)	254 (83 - 422)	814 (491 - 1820)	34.6 (26.6 - 82.6)	15.0 (1.4 - 79.8)	0.06 (0.03 - 0.26)	- -	-
<i>Halifax Pluton</i>										
antecrystic	11	10890 (9640 - 12200)	56 (25 - 183)	350 (161 - 1452)	1163 (785 - 2487)	40.9 (26.1 - 67.2)	4.1 (1.2 - 67.0)	0.04 (0.02 - 0.15)	686 - 810 36	-3.7 (-4.8 to -2.6)
autocrystic	14	11340 (9540 - 13100)	50 (18 - 123)	290 (123 - 920)	1671 (762 - 2034)	33.8 (14.8 - 91.5)	10.6 (4.2 - 44.5)	0.06 (0.02 - 0.11)	665 - 869 36	-3.4 (-5.5 to -2.0)
replacement/metamict	4	11015 (10800 - 12200)	57 (28 - 82)	259 (203 - 303)	1170 (493 - 1400)	37.0 (34.1 - 50.8)	25.4 (3.5 - 78.0)	0.07 (0.02 - 0.08)	- -	-
<i>East Dalhousie Pluton</i>										
antecrystic	4	11785 (11040 - 13360)	47 (25 - 58)	1282 (570 - 1876)	895 (497 - 1190)	43.2 (18.6 - 48.9)	4.6 (2.4 - 8.5)	0.02 (0.01 - 0.04)	692 - 809 34	-5.3 (-6.5 to -4.2)
autocrystic	9	10620 (10300 - 11830)	60 (20 - 268)	289 (163 - 452)	1287 (913 - 1789)	45.2 (28.3 - 92.0)	11.6 (4.9 - 38.5)	0.03 (0.02 - 0.11)	748 - 843 34	-4.4 (-5.7 to -0.5)
replacement/metamict	9	11360 (8540 - 13050)	31 (23 - 148)	274 (119 - 430)	852 (454 - 2598)	38.5 (26.6 - 136.0)	15.2 (4.3 - 44.7)	0.03 (0.01 - 0.20)	- -	-
<i>New Ross Pluton</i>										
antecrystic	4	11285 (11200 - 11410)	64 (29 - 94)	556 (338 - 629)	1111 (889 - 1291)	33.4 (20 - 39.8)	8.9 (2.6 - 27)	0.04 (0.03 - 0.06)	694 - 811 33	-3.9 (-5.2 to -2.3)
autocrystic	16	11115 (8530 - 12670)	72 (25 - 136)	452 (119 - 2617)	1322 (634 - 1999)	36.1 (14.8 - 62.7)	12.4 (1.5 - 50)	0.04 (0.00 - 0.09)	663 - 894 34	-3.8 (-6.4 - -0.1)
replacement/metamict	9	11000 (10620 - 12430)	100 (25 - 229)	293 (217 - 1320)	1185 (772 - 2025)	38.2 (23.8 - 63.8)	17.6 (1.8 - 49.4)	0.03 (0.01 - 0.04)	- -	-
<i>Davis Lake Pluton</i>										
antecrystic	6	10970 (9790 - 12230)	195 (81 - 403)	1443 (250 - 2204)	1646 (1153 - 2055)	42.5 (39.1 - 82.4)	4.7 (2.0 - 28.4)	0.01 (0.00 - 0.08)	742 - 981 37	-2.7 (-6.2 to -1.9)
autocrystic	11	10590 (9400 - 11630)	218 (66 - 442)	682 (186 - 1133)	1377 (1058 - 2260)	42 (26.7 - 136.5)	4.3 (2.0 - 40.4)	0.03 (0.01 - 0.06)	727 - 1008 39	-2.4 (-4.5 to -0.8)
replacement/metamict	15	10790 (8430 - 11940)	194 (62 - 304)	439 (171 - 1693)	1460 (1150 - 2284)	52.1 (19.3 - 79.3)	14.7 (1.8 - 37.9)	0.02 (0.01 - 0.12)	- -	-

Summarized data from select analyses with < 67 % discordance. See Table S3 for complete dataset. Median values are marked in bold font and data range is indicated within the parentheses. T (°C) = Ti-in-zircon temperatures (Ferry and Watson, 2007), aSiO₂ = 1 and aTiO₂ = 0.5, are shown as ranges, with average error adjacent. T (°C) and *f*O₂ values for replacement/metamict domains not calculated as these are not interpreted as magmatic. *n* = number of analyses included in summary statistics. WDP - West Dalhousie Pluton

Table 2–6. Summary of SIMS ^{18}O isotopes on zircon from the South Mountain Batholith

Domain Type	<i>n</i>	Interpreted U-Pb Age Range (ca., Ma)	Typical Spot Location	Range of $\delta^{18}\text{O}$ (VSMOW, ‰)	Average Error (2 σ ; ‰)
<i>SMB Granodiorite & WDP (less evolved)</i>					
antecrystic	21	387 - 395	core/mantle	6.19 - 8.16	0.21
autocrystic	35	372 - 380	rim	7.81 - 9.06	0.21
replacement/metamict	10	362 - 371	rim	7.90 - 9.19	0.21
xenocrystic	29	411 - 2352	core	4.31 - 11.38	0.20
<i>Halifax Pluton (HP)</i>					
antecrystic	17	378 - 388	core/mantle	7.33 - 9.16	0.20
autocrystic	21	371 - 373	rim	8.16 - 9.11	0.21
replacement/metamict	5	362 - 369	rim	8.84 - 9.16	0.21
xenocrystic	13	400 - 1831	core	4.56 - 9.44	0.23
<i>East Dalhousie Pluton (EDP)</i>					
antecrystic	9	379 - 390	core/mantle	8.65 - 9.16	0.22
autocrystic	14	374 - 377	rim	8.43 - 9.06	0.20
replacement/metamict	6	359 - 361	inner rim	7.97 - 9.13	0.22
xenocrystic	7	438 - 2867	core	5.89 - 9.92	0.21
<i>New Ross Pluton (NRP)</i>					
antecrystic	8	380 - 383	core/mantle	7.28 - 8.65	0.22
autocrystic	23	373 - 377	rim	8.25 - 9.08	0.20
replacement/metamict	9	344 - 368	rim/inner rim	6.91 - 8.76	0.21
xenocrystic	16	400 - 2804	core	3.45 - 8.97	0.19
<i>Davis Lake Pluton (DLP)</i>					
antecrystic	8	380 - 396	core/mantle	7.56 - 8.62	0.22
autocrystic	19	367 - 372	rim	7.31 - 8.88	0.22
replacement/metamict	7	354 - 362	rim	7.68 - 8.66	0.19
xenocrystic	3	425 - 1896	core	4.20 - 8.56	0.19

Note: range of $\delta^{18}\text{O}$ for autocrysts are in bold.

Chapter 3

The East Kemptville Mesothermal Greisen-Hosted Sn-Zn-Cu-Ag-In Deposit, Nova Scotia, Canada: One ore body with two deposits

3.1 Abstract

The East Kemptville Sn(-Cu-Zn-Ag-In) deposit (Nova Scotia, Canada), with two greisen-style ore zones with contrasting geologic character, comprises the most significant Sn deposit in the northern Appalachian Sn–W metallogenic belt. Its mesothermal setting (~3.5 kbars) is unusual for greisen-style deposits in general, and is one of numerous regional Sn-polymetallic occurrences in the area which also includes the proximal Duck Pond skarn-style deposit. The host East Kemptville Leucogranite (EKL) is part of the Davis Lake Pluton, and at the southwestern end of a ca. 375-380 Ma composite peraluminous South Mountain Batholith (SMB).

In the deposit area, zoned and massive greisens overprint the deuteric altered, topaz-rich EKL. The latter is characterized locally by layered pegmatites, stockscheiders, miaroles, and USTs which rarely contain magmatic cassiterite; these features attest to the volatile- and Sn-rich nature of the EKL when emplaced. The two ore zones, the Baby and Main, are localized in fractured EKL related to a long-lived, NE-trending regional fault zone. However, whereas the Baby Zone is characterized by massive greisens and magmatic-hydrothermal breccias, the Main Zone has abundant zoned greisens proximal the fault zone.

Geochemically, the EKL is strongly peraluminous ($ASI = 1.40$) and enriched in P, Li, Rb, Cs, Sn, W, and U relative to the SMB along with differing Nb/Ta and Zr/Hf values. Notable differences between the ore zones include higher P_2O_5 concentrations, U/Th ratios, and tetrad effect (TE_{1,3} of 1.39 versus 1.15) in the Main Zone, and higher Y and REE in the Baby Zone. The geochemical differences suggest accessory-mineral fractionation between the two zones, but differing progenitor magmas cannot be excluded.

Mineralization ages (U-Pb cassiterite, Re-Os molybdenite) define three general ages: 1) Main Zone cassiterite ranges from 376 to 365.4 Ma (369.4 ± 4.5 Ma) and vein molybdenite is 370.2 ± 1.6 Ma; 2) two Main Zone vein molybdenites record ages of 359.4 ± 1.8 Ma and 354.9 ± 2.0 Ma; and 3) Baby Zone molybdenite at 343.7 ± 1.7 Ma is associated with a magmatic breccia and is similar in age to cassiterite from the nearby Duck Pond deposit of 347 ± 12 Ma. These ages are consistent with other mineralization in the region indicating that two distinct magmatic-hydrothermal systems existed.

These data confirm a magmatic-hydrothermal origin for the East Kemptville deposit which we relate to a deeper, more evolved equivalent to the host rock EKL. The nature of the ore zones reflects the high confining pressure and overall structural controls of the setting. The latter features also account for the telescoped nature of mineralization and lack of a distinct vertical zoning to the Sn(-Cu-Zn-Ag-In) mineralization.

3.2 Introduction

Magmatic-hydrothermal deposits with primary enrichment in Sn and W \pm polymetallic base-metals (e.g., Cu, Zn, In) occur in a variety of styles (i.e., greisens, veins, skarns, porphyry, pegmatites). These deposits have long been noted to be hosted in, or proximal to highly fractionated, peraluminous felsic intrusions (e.g., Taylor, 1979; Heinrich, 1990; Černý et al., 2005; Lehmann, 2020). Globally they define metallogenic districts (e.g., Schuiling, 1967; Kelly and Turneure, 1970; Schwartz et al., 1995) wherein mineralization typically occurs with magmatism regionally hosted in Sn- and/or W-enriched graphitic metasilstones and slates, as suggested for the Appalachian Sn-W metallogenic district (Romer and Kroner, 2015, 2016). Such sedimentary rocks are the wall-rocks to the Sn mineralized leucogranite at East Kemptville, Nova Scotia (e.g., Kontak and Dostal, 1992; White, 2010a; White and Barr, 2010). The Sn-W endowment in these global metallogenic districts has been attributed to two divergent processes: 1) the mantle, which is the source of the melts that subsequently fractionate ore elements into economic concentrations (e.g., Schuiling, 1967; Sillitoe, 1975); and 2) enriched clastic sedimentary sequences (e.g., metaturbidities) that either contribute Sn and W via crust-derived partial melts that may be the progenitors to these deposits (Sato, 2012; Romer and Kroner, 2015, 2016), or by extensive crustal contamination to mantle-derived melts and subsequent fractionation (e.g., Blevin and Chappell, 1992, 1995).

The northern Appalachian region hosts a variety of base- and rare-metal mineralized centres that include Cu, Sn, W-Mo, Sb and Ta that are associated with widespread granitic magmatism (e.g., van Staal, 2007; Sinclair et al., 2011; Fig. 3–1). These deposits range in age from ca. 410 to 360 Ma and have a spatial distribution which spans across a large area of eastern Canada (Fig. 3–1). The style of mineralization ranges from shallow porphyry and epithermal-hosted systems with association greisen-, vein-, and breccia-hosted mineralization (e.g., Ackley greisen Sn deposit; Mt. Pleasant greisen, vein and breccia W-Sn deposit; Lake George vein-hosted Sb deposit; Gaspé porphyry Cu-Mo). In contrast to these granite-associated deposits is the mesothermal Sn greisen and base-metal vein system of East Kemptville (Nova Scotia; Richardson et al., 1982; Kontak, 1990a; Halter et al., 1995a), which records a depth of formation (i.e., ca. 3.5 kbars) that is deeper than most Sn settings (Taylor 1979; Černý et al., 2005). Another anomalous feature for this area compared to other Sn districts is that there has only been a single primary Sn producer of Sn, this being the East Kemptville Sn-Cu-Zn-Ag-In deposit. Mined from 1985 to 1992, and the most significant primary Sn deposit in North America, the deposit had historical reserves of 56 Mt at 0.17% Sn (Richardson et al., 1982) with an in-ground measured and indicated resource of 22.97 Mt at 0.15% Sn (using a 0.1% Sn cut-off grade; Gowans et al., 2018).

Previous studies at East Kemptville (Richardson, 1988; Kontak, 1990a, b, 1991, 1994; Halter et al., 1996, 1998; Kontak et al. 2001) noted a number of characteristics that differentiate it from typical greisen-style Sn deposits: 1) it formed under greater than typical pressures (i.e., ca. 3.5

kbars as opposed to <1 kbar; Halter et al., 1996; Kontak et al., 2001); 2) the host batholith is not uniformly enriched in Sn with typical contents <5–10 ppm (MacDonald, 2001; cf. Lehmann, 1990); and 3) other sites of significant Sn mineralization are apparently absent in the host South Mountain Batholith (SMB) intrusive complex (Fig. 3–1).

The aim of the present contribution, which forms part of a broader fluid-chemical study of the greisen and vein mineralization and a petrochronology study of the host SMB, is to provide an update on the geology and petrology of this important Sn deposit setting which has not been reexamined for nearly three decades. The work presented here has also benefited from 2014–2015 drilling of the deposit area which has provided information for part of the deposit that was not previously available. Herein we assess and discuss the nature of alteration and related mineralization, structural features of the ore zones, litho-geochemistry of the intrusive host rocks, and the absolute age of the mineralization through Re-Os and in situ U-Pb dating of molybdenite and cassiterite, respectively. Previous studies have shown that the East Kemptville deposit is hosted by two discrete ore zones, characterized by: 1) high-tonnage, low-grade Sn in discontinuous fracture-controlled greisens (Main Zone); and 2) low-tonnage, higher-grade massive greisens that transition upwards to a pipe-shaped igneous-hydrothermal breccia body (Baby Zone). The results of the current study provide the basis to better define the ore zones and for reconstructing the deposit and thus to compare it with more typical greisen-style Sn systems and identify local controls on mineralization.

3.3 Geologic Setting and Related Mineralization

3.3.1 Regional geology

The northern Appalachians of Atlantic Canada are underlain by several tectonic terranes (peri-Laurentia, Ganderia, Avalonia, and Meguma; Fig. 3–1) that accreted to the evolving continental margin during consecutive Paleozoic orogenic events: the Taconic, Salinic, Acadian, and Neoacadian (van Staal et al., 2009, and references therein). The youngest of these orogenic events, the Neoacadian, is attributed to the accretion of the Meguma terrane which forms the most outboard of the terranes. This later deformation was, importantly, accompanied by widespread and abundant ca. 385-360 Ma meta- to peraluminous magmatism and associated mineralization across the accreted terranes (Fig. 3–1; e.g., van Staal, 2007). These accretionary events were followed by a later, more intense and restricted regional deformation at ca. 300 Ma (Muecke et al., 1988; Culshaw and Reynolds, 1997) associated with the terminal continent-continent collision (Alleghanian orogeny) between Gondwana and Laurentia (e.g., Keppie, 1993; Hibbard et al., 2010). In the context of this study, this later deformation is significant as it overprints the mineralized East Kemptville area.

3.3.2 Geology of the Meguma terrane

The Meguma terrane is dominated by a thick (>12 km) sequence of Ediacaran to Lower Ordovician clastic metaturbiditic rocks (the Meguma Supergroup) that formed along the rifted

western margin of Gondwana (White, 2010b; White and Barr, 2010; White et al., 2012) into which was emplaced voluminous felsic magmas. The Meguma sedimentary rocks are subdivided into two major packages - the metasandstone-dominated Goldenville Group and the overlying metasilstone/slate-dominated Halifax Group (e.g., White, 2010b). The transition between these two groups is historically referred to as the Goldenville-Halifax Transition zone (GHTZ), which is characterized by alternating facies of sandy and slaty metaturbidites through a thickness of ~1 km in the SW part of the terrane (Waldron, 1992). Notably, the GHTZ contains elevated concentrations of Mn, C, Ba and trace metals (Pb, Zn, Cu, Mo, W, Au) relative to the rest of the Meguma metasedimentary rocks (Zentilli et al., 1986; Sangster, 1990) and rarely localizes Sn-W and base-metal (Zn-Pb) mineralization (Sangster, 1990). Along the northwestern margin of the Meguma terrane, the Halifax Group is disconformably overlain by Silurian-Devonian bimodal metavolcanic to metasedimentary rocks of the Rockville Notch Group (White, 2010a; White and Barr, 2017).

All of the above stratigraphy was regionally deformed and variably metamorphosed (greenschist, but locally amphibolite facies) during the Early- to Late Devonian Neocadian orogenic event (ca. 405–365 Ma; Dallmeyer and Keppie, 1987; Hicks et al., 1999; Culshaw and Lee, 2006), and intruded by syntectonic meta- to peraluminous felsic bodies; the largest of these bodies is the voluminous (7300 km²) SMB (Benn et al., 1997, 1999; Clarke et al., 1997, 2004). The composite SMB has been divided into two intrusive suites which, based on textural and mineralogical

characteristics, are referred to as stage I and II (Fig. 3–1) that correspond to early granodiorite to monzogranite and later monzogranite to leucogranite, respectively (MacDonald, 2001). The emplacement ages of these suites overlap at ~383 to 375 Ma for stage I and ~379 to 370 Ma for stage II (Bickerton et al., 2018). The SMB is therefore similar in age to the nearby Musquodoboit Batholith of 377.5 ± 0.6 Ma (Kontak et al., 2004), as well as mafic- to hybridized intermediate satellite intrusions to the SMB (Figs. 3–1 and 3–2). The pressures of emplacement of the SMB and Musquodoboit batholith are estimated at ~3 to 3.5 kbars based on muscovite thermobarometry and graphite thermometry (Massonne et al., 2010; Hilchie and Jamieson, 2014).

The Neocadian deformation is related at least in part to the dextral transpressive motion of the Meguma terrane against Avalonia along a terrane-bounding fault system (Fig. 3–1; Murphy et al. 2011). The younger limit for the Neocadian deformation and associated granitic magmatism in the terrane is provided by the unconformably overlying late Famennian Horton Group which is located along the northern margin of the Meguma terrane. This unit contains clasts of granitic material and onlaps the northern part of the SMB with a depositional age of ~355 Ma, providing a minimum exhumation age for the SMB in this area (Martel et al., 1993; Murphy, 2000). Fault systems active during the Neocadian that occur within the Meguma terrane and are manifested as wide, brittle-ductile fault zones (e.g., the East Kemptville-East Dalhousie, EKEDSZ, and the Tobeatic Shear Zone) that record Ar–Ar tectonothermal ages between 370 and 300 Ma (e.g.,

Kontak et al., 1995, and references therein; Fig. 3–2). Full details on historic geochronology in the SW part of the Meguma terrane are provided in Table EA 3-1 (Electronic Appendix).. The prolonged activity along these fault zones accommodates the rapid exhumation of the SMB, as well as subsequent Carboniferous deformation related to the docking of Gondwana (Africa) outboard of the Meguma terrane (Moran et al. 2007; Waldron et al. 2015). These regional NE-trending fault zones are also interpreted to have been active during granite intrusion and thus strongly influenced localization of the SMB, as well as its genetically hosted Sn-W-Cu-Mo and U-Mn mineralization (e.g., Horne et al., 1992; Benn et al., 1997).

Mineralization associated with the SMB varies in character and includes polymetallic (Sn, W, Mo, Mn, Cu, Ta, Nb, Zn) occurrences in the more-evolved plutons, the styles of which include greisens (e.g., East Kemptville deposit), veins (e.g., New Ross Mn Mines; Millet Brook U deposit), granite-pegmatite (e.g., Long Lake Mo in the New Ross Pluton; Carruzzo et al., 2000), and peribatholithic (e.g., Duck Pond Sn deposit; Pitre and Richardson, 1989). However, the only significant deposit of economic note is the greisen-style East Kemptville (Sn-Zn-Cu-Ag-In) at the SW margin of the SMB (Figs. 3–1 and 3–2).

3.3.3 Geology and mineralization of the SW Meguma terrane

Key aspects of the geology of the SW part of the Meguma terrane are the the SMB, plutonic rocks peripheral to the SMB, and the metasedimentary rocks of the Meguma Supergroup, as well as mixed volcanic and sedimentary rocks of the Silurian-Devonian White Rock Formation. All of

these units are folded and faulted along NE-trending fold axes and faults. Here, the basal Goldenville Group, which dominates the area, consists of metasandstone and metasilstone, the latter of which transitions through the calcareous and sulfidic GHTZ into the overlying shale-rich Halifax Group (e.g., White, 2010b). Notably, the GHTZ occurs locally along the EKEDSZ and hosts several Sn(-Cu-Zn-Ag) sites of mineralization WSW of East Kemptville, which are further described below.

The SMB in this area is dominated by an evolved stage II intrusion, the Davis Lake Pluton (DLP; Dostal et al., 2004; Fig. 3–2). The zoned DLP is dominated by coarse-grained biotite-muscovite monzogranite and leucomonzogranite with a minor, but important elongate body of topaz-muscovite leucogranite at its SW margin, the East Kemptville leucogranite (EKL), which hosts the East Kemptville deposit (Figs. 3–2 and 3–3A). The northern, less-evolved part of the DLP is monzogranite that contains orthoclase, zoned oligoclase (An₅₋₃₅), biotite, and minor muscovite in contrast to the SW part that is dominated by highly differentiated leucomonzogranite with abundant muscovite, albite (An₀₋₅), topaz (5-8 modal %), and minor biotite (Kontak, 1990a; Dostal and Chatterjee, 1995). Geochemical zoning of the DLP is defined by incompatible trace elements (e.g., Rb, Li, U, Ta, Sn) and variation in both elemental (e.g., K/Rb, Nb/Ta, La/Sm) and isotopic (i.e., ²⁰⁶Pb/²⁰⁴Pb, ⁸⁷Sr/⁸⁶Sr) ratios which is interpreted to reflect fluid-mediated fractionation (Dostal et al., 2004, and references therein). Other ca. 360 Ma intrusions that are present south and west of the DLP host minor Sn-W-Mo-Cu-Zn mineralization and are small

with more evolved A-type geochemical characteristics (Fig. 3–2; see Kontak et al., 2013, for a summary).

The elongate EKL is localized along the major NE-trending EKEDSZ (Figs. 3–2 and 3–3) which, as noted above, is one of several regional structures that controlled the emplacement of the SMB (Kontak et al., 1990; Horne et al., 1992). This series of NE-trending faults is characterized by brittle deformation in the central part of the SMB (e.g., Benn et al., 1997) and typically ductile deformation at their SW ends of the faults (e.g., Culshaw and Liesa, 1997). The range of $^{40}\text{Ar}/^{39}\text{Ar}$ and Rb/Sr dates obtained from syn-faulting mineral growth (Fig. 3–2) suggest a protracted history of movement along the EKEDSZ and similar fault zones, from ~350 to 300 Ma (Dallmeyer and Keppie, 1987; Kontak et al., 1995). Evidence for sense of movement along these faults is rarely observed, although local preservation of vertical slickensides and the absence of significant lateral offsets indicate it is mostly vertical; thus consistent with uplift and erosion of the SMB (Horne et al., 1992). Some dextral horizontal displacement, however, has been interpreted from C-S fabrics in the EKEDSZ (Kontak et al., 1986), consistent with the regional, subparallel terrane boundary sense of movement during the Upper Paleozoic (e.g., Murphy et al., 2011).

3.3.4 The SW Nova Scotia Sn base-metal domain

The area at the western termination of the SMB and further westwards hosts numerous mineralized occurrences of Sn-polymetallic mineralization (Fig. 3–2) and has been referred to as

the SW Nova Scotia Sn-Ag domain (Chatterjee et al., 1983; Chatterjee and Strong, 1985; Kontak et al., 1990). The most significant of these is the East Kemptville deposit, with a defined resource of 56 Mt at 0.17% Sn which is described in detail below, and the nearby Duck Pond deposit with inferred reserves of 5.1 Mt at 0.13% Sn (Moyle, 1985; Pitre and Richardson, 1989). As seen in Figure 3–2, the latter deposit and other mineralized occurrences SW of East Kemptville are hosted in Meguma Supergroup rocks, in particular in or near the GHTZ (e.g., Pearl Lake, Kempt Snare, Gardners Meadow, Dominique; see Kontak et al., 1990, for details). This mineralization is variably manifested as quartz-vein hosted, muscovite greisens, chlorite lodes, and garnetiferous skarns. Rarely, a granitic affinity has also been confirmed based on drilling (e.g., Kempt Snare deposit; Soehl et al., 1989). The ages of lithophile-element mineral occurrences in this region are poorly constrained, but previous studies suggest at least two periods of mineralization. For example, there is a Re-Os molybdenite age of ca. 355 Ma for the skarn-type Gardners Meadow occurrence (Kontak et al., 2014), whereas Sn-Cu-Zn mineralized chlorite lodes in the Dominique deposit are plausibly related to the proximal 360 Ma Plymouth granite (Kontak et al., 1990). Greisen, vein, and skarn Sn-W-Cu-Au mineralization is also present ~25 km NW of East Kemptville, associated with the ca. 360 Ma Clayton Hill Pluton (Kontak et al., 2013).

Although not part of this study, the Duck Pond prospect is noted due its proximity to East Kemptville (~2 km west; Fig. 3–2) and because results for in situ U-Pb cassiterite dating are

provided below. This setting is a vein- and strata-bound Sn prospect hosted by interbedded meta-wacke and meta-argillite of the GHTZ (Pitre and Richardson, 1989; Kontak et al., 1990).

3.4 The East Kemptville tin deposit

In contrast to the other Sn base-metal occurrences in SW Nova Scotia, the East Kemptville greisen-type Sn-Zn-Cu-Ag-In deposit is wholly contained within the evolved EKL (Fig. 3–3A; Richardson et al., 1982; Richardson, 1988; Kontak, 1990a, 1991), an elongate body that intrudes the Goldenville Group along the EKEDSZ (Fig. 3–3B). The deposit has a surface expression of <1 km² and the host leucogranite displays variable alteration from least altered to intensely greisenized with veined zones that generally align parallel to a NE trending penetrative fabric (Fig. 3–3C, D, and inset). Rare pegmatitic dikes associated with the EKL also occur in the adjacent wall-rocks and typically align parallel to the prominent NE fabric. The two main ore zones, the Baby and Main, both contain ore-grade greisens that are preferentially concentrated along the main NE-trending, sub-vertical fault zone which has a poorly documented kinematic evolution.

Collectively, the deposit and host EKL record a protracted history of magmatic, hydrothermal, and tectonic events that are here described using both previous work (lithogeochemistry; Rb-Sr, Ar-Ar, and Pb-Pb geochronology) and new data collected from recent diamond drilling, surface grid mapping (Fig. 3–3C), petrography, microanalysis (scanning-electron microprobe back-

scattered electron imaging, SEM-BSE; energy dispersive X-ray spectroscopy, SEM-EDS; cathodoluminescence, CL), and geochronology (Re-Os molybdenite, in situ U-Pb cassiterite).

3.4.1 Discovery and previous studies

The East Kemptville deposit was discovered in 1978 through the use of geochemical and drift prospecting by Shell Canada Resources (McAuslan et al., 1980). Subsequent drilling delineated the deposit and its two ore zones with initial estimated reserves of 56 Mt at 0.17% Sn (Richardson et al., 1982; Moyle, 1985), thus making East Kemptville one of the lower-grade but higher tonnage greisen-hosted deposits globally (cf. Mlynarczyk et al., 2003). Open-pit ore production began in 1985 and continued until 1992 when mine operations ceased due to a decline in global Sn prices.

Several deposit-scale studies constrained deposit formation (Richardson, 1998; Kontak, 1990a, b, 1994; Kontak and Chatterjee, 1992; Kontak et al., 2001; Halter et al., 1995a, 1996, 1998), as well as the setting of the regional host pluton to the EKL (i.e., the DLP; Dostal and Chatterjee, 1995; Dostal et al., 2004). Previous studies recognized the presence of two Sn and base-metal ore zones - the high-tonnage, low-grade Main Zone in the NE and low-tonnage, higher-grade Baby Zone to the SW (Fig. 3–3B). Although the Main Zone was extensively studied, the Baby Zone was not due to its lack of exposure and limited historical drilling; importantly, one of its features is the presence of magmatic-hydrothermal breccias, which are absent in the Main Zone and have not been previously described in detail.

3.4.2 Host rocks

The deposit area is underlain by two lithologies, the EKL and metasandstones (Fig. 3–3B). The character of the host EKL in both the Baby and Main ore zones varies from a muscovite (\pm rare biotite) leucogranite to a topaz-muscovite leucogranite. Where least altered, the EKL is dominantly a medium-grained, seriate- to equigranular-textured leucomonzogranite, but rarely aphanite facies of unknown extent are present (Fig. 3–5Ai and Aii, respectively) along with later fine-grained felsic dike rocks that manifest thin (<5 mm) silica borders (i.e., pressure quench features; Fig. 3–5B). The country rock is dominantly fine-grained, grey to black metapsammities and metapelites that show variable amounts of alteration, veining and localized Sn- and Cu-Zn mineralization (Kontak and Dostal, 1992). Proximal to the intrusive contacts (≤ 50 m), the wall-rock is hornfelsed and characterized by poikilitic cordierite and rarely by garnet (1–5 mm), whereas within the EKL there is grain size reduction and local stockscheiders (Fig. 3–5C), banded aplite-pegmatites (<1 m) with UST features (i.e., well-developed quartz layers in aplite, Fig. 3–5D, E; cf. Kirwin, 2005), and thin cassiterite-bearing micro-pegmatites and miaroles (Fig. 3–5F and G, respectively) occur. In addition to the UST features, minor occurrences of interconnected granitic-veins are seen throughout the Main Zone (e.g., Fig. 3–5H) that resemble the fluid-saturation textures described by Candela and Blevin (1995). The least-altered EKL has a primary mineralogy and approximate modes (after Kontak, 1990a) of quartz (37%), albite (30%), K-feldspar (19%), muscovite (8%), and topaz (5%). Trace amounts (<0.5 modal %) of secondary dark mica (variable amounts of Mg- and Fe-rich lepidolite as well as Li-rich biotite;

e.g., Kendall, 2017) also occur, accompanied by accessory apatite, triplite, uraninite, cassiterite, and pyrrhotite, sphalerite, pyrite, chalcopyrite. The quartz, albite, muscovite and topaz mostly have subhedral habits with sutured grain-boundaries, whereas K-feldspar, now microcline (Kontak, 1990a), occurs as coarse euhedral to subhedral grains with film, flame and bleb perthite and is variably replaced by albite. Lastly, traces of dark Fe-Li mica in the EKL occur as fine-grained subhedral inclusions within quartz and feldspar.

The Baby Zone is hosted by a greisenized equivalent to the EKL, but it is texturally distinct. Where least altered, it typically has a seriate texture with coarse- to megacrystic, often reddish, perthitic K-feldspar and zoned blue quartz phenocrysts set in a medium-grained quartz-plagioclase-K-feldspar-muscovite-topaz groundmass with trace dark mica (Fig. 3–6A, B). In this zone, a pipe-shaped breccia body surrounded by greisenized EKL consists of two domains that are referred to magmatic (IBX) and hydrothermal (HBX) with the former more abundant and beneath the hydrothermal one. The magmatic breccia (e.g., Fig. 3–6C, D) is both matrix and fragment supported and consists of a matrix of fine-grained to very fine-grained and quartz-phyric leucogranite. The core of the breccia is matrix-supported and chaotic (Fig. 3–6C), with partially resorbed to angular wall-rock fragments (10–30 cm) dominated by country-rock greywacke and argillite which typically have thin reaction rims; infrequently, fragments are completely hornfelsed or composed entirely of quartz vein material (Fig. 3–6D). Towards its margins (i.e., ≤ 5 m from the contact), the magmatic breccia changes character to a fragment-

supported (angular, 5–15 cm sized) mosaic-type breccia that displays spalled and shingled fragments and rarely small (0.5–3 cm) rounded fragments of quartz (cf. terminology of Sibson, 1986; Jébrak, 1997; and Woodcock and Mort, 2008).

The fragment-supported hydrothermal breccia typically overlies and transitions into the magmatic breccia (Fig. 3–6E). The cement of this breccia is dominated by quartz that varies between pervasive fine grained (Fig. 3–6F) to granular, with lesser fluorite, Li-Fe mica, and trace albite; it also contains variable (minor to trace) cassiterite (Fig. 3–6G), chalcopyrite (Fig. 3–6H), pyrite, and molybdenite. The typical nature of the brecciation in the HBX includes fluid-assisted crackle style with granular quartz-dominant cement (Fig. 3–6G, H, I, J).

The transition between the hydrothermal and magmatic breccias in the Baby Zone forms a discrete boundary between a porphyritic matrix-supported IBX to a fragment-supported HBX locally containing chlorite-altered fragments from the HBX (Fig. 3–6J). At the upper boundaries of the IBX, fine-grained to porphyritic leucogranite matrix typically transitions to a quenched felsic phase that appears as silicification (e.g., Fig. 3–6K, L), not unlike parts of the HBX. The matrix to typical IBX intervals comprises microcrystalline felsic groundmass and subhedral to euhedral phenocrysts of quartz and feldspar (0.1–0.6 cm) with rare muscovite; the phenocrysts are variably crowded, but typically make up ~30 to 40% of the matrix (Fig. 3–6M, N) and less commonly up to 70% (Fig. 3–6L, left). The shape of coarse quartz phenocrysts in the IBX matrix (e.g., Fig. 3–6J) is of a low-temperature polymorph (i.e., α -quartz; Martel et al., 2021).

Importantly to timing of events, the IBX post-dates mineralization as it has traces of mineralized fragments, both of veined and greisenized wall-rock and fragments of quartz \pm sulfide material (Fig. 3–6D, E, M, N) as well as, very rarely, fragments of fine-grained EKL (Fig. 3–6M, O). The upper part of the IBX contains evidence of fluid exsolution features seen as the thin intergrowth of Fe-Li mica and quartz, in sequence, from the edges of wall-rock fragments into the IBX matrix (e.g., Fig. 3–6O). Additionally, thin (<3 cm) fine-grained dikes extend from the IBX matrix and contain rare molybdenite (Fig. 3–6P).

The Baby and Main zones both contain the same suite of ore elements (Sn, Zn, Cu, Ag, In) and each is centered along discrete fault domains that are part of the regional EKEDSZ (Figs. 3–2 and 3–3). The host lithologies and their relationships to the individual ore zones differ, despite their close proximity (Figs. 3–4, 3–7A, B). The greisens in the Main Zone are subvertical, 25–30 m wide zones hosted in or proximal the EKEDSZ (Fig. 3–7A), and are locally found beneath shallowly-dipping intrusive contacts between the EKL and the country-rocks. Greisen development and Sn-grade in the Baby Zone is also related to vertical structures as well as more pervasive patches in the EKL beneath and adjacent to the IBX, or less commonly within the HBX (Fig. 3–7B). Notably, greisens are not typically associated with the magmatic breccia through the center of the Baby Zone but the hydrothermal breccias do contain tin mineralization.

3.4.3 Alteration

The textures and mineralogy of the EKL reflect pervasive metasomatism. The degree of alteration in parts of the EKL distal to the ore-bearing greisens is weaker than the metasomatism typically documented in granitoids hosting ore in other Sn-provinces; e.g., microclinization in the Erzgebirge (Štemprok, 1987) or albitization in the Australian tin fields (Witt, 1988; Charoy and Pollard, 1989). The alteration described below includes the background or deuteritic type in the EKL most distal from greisens followed by the more proximal massive- and zoned-style greisens.

3.4.3.1 Background (deuteritic) alteration

The least-altered EKL is a light buff to pinkish leucogranite (Fig. 3–5A) with sub- to euhedral primary phases of K-feldspar, plagioclase, quartz, muscovite, and topaz. In both of the ore zones, a pervasive background alteration is characterized by development of a grey-to green discolouration that distorts primary textures (Fig. 3–8A). This stage of alteration, identified petrographically and with SEM-EDS analysis, relates to sericitization of the K-feldspar, albitization of Ca-plagioclase, and replacement of primary muscovite by a secondary muscovite. Changes to the major silicate phases include: 1) formation of variably perthitic K-feldspar along with its partial sericitization (Fig. 3–8B) along with inversion to microcline, the latter of which relates to fluid-rock interaction and/or subsequent deformation processes (Kontak, 1990a; Kontak et al., 1996). Importantly, the following features are observed: 1) cassiterite forming with

sericite where fractures traverse K-feldspar; 2) secondary muscovite that replaces and is texturally and chemically distinct (less Fe-rich) from earlier primary type along its grain boundaries and cleavage with rare sulfide inclusions, based BSE imagery (Fig. 3–8C, D); 3) a chemically distinct type of biotite comprising a clear variety with relatively low FeO (~1-4 wt. %) that is replaced by a dark-brown pitted variety with higher FeO content (~8-12 wt. %; Kontak, 1994); and 4) albite characterized by disseminated, small euhedral fluorapatite crystals readily seen in CL images (Fig. 3–8E, F). This alteration general preserves the overall texture of the EKL, as seen in the CL images, but in detail there is, particularly in the feldspars, development of pitted textures via coupled dissolution precipitation (CDP; Putnis, 2002, 2009). The pitted domains are characterized by the formation of fine-grained secondary phases, including oxides (Nb, Ta, Sn), sulfides (Fe, Cu, Pb, Zn), phosphates, and silicates (Fig. 3–8C).

3.4.3.2 Zoned and massive greisens

The types of greisens and their development have been described extensively in the past (Kontak et al., 1986; Richardson, 1988; Kontak, 1990a, b, 1994; Halter et al., 1995a, 1996, 1998). The greisen zones have a strong NE-SW striking, steeply-dipping preferred orientation, as noted by others and confirmed here (Figs. 3–3 and 3–4), and are interpreted to be a product of fluid-rock interaction with a progression of overprinting mineralogical stages due to sequential mineral reactions that progressed via CDP. The spatial transition between deuteric alteration and greisenization of precursor EKL is recognizable as discrete boundaries between a light buff

colored and a darker grey-green (or rust colour in oxidized outcrops), respectively (Fig. 3–9A, B, C). The type of greisens observed relates to whether a complete zoned greisen has formed (Fig. 3–9C, D), if only a part of such a greisen is observed, or if only the more distal zones (i.e., incipient stages) of the zoned greisen are developed. Whereas the latter reflects a lower fluid:rock ratio process, the cores to zoned greisens (i.e., topaz-rich; Fig. 3–9E, left) represent much higher fluid:rock ratios (Halter et al., 1995a, 1996).

The zoned greisens vary in thickness (cm to ≤ 1 m) from their mineralized cores to least altered EKL (Fig. 3–9C). They typically have, from the rim to core, dominant mineral assemblages (in order of abundance) of: 1) quartz, albite (after K-feldspar and Ca-rich plagioclase), muscovite, and minor magmatic topaz with trace cassiterite, pyrite; 2) quartz, mica (sericite, Fe-Li mica), and minor magmatic topaz with weak cassiterite, pyrite, chalcopyrite; 3) quartz, hydrothermal topaz, mica (sericite, Fe-Li mica) greisen with interstitial sulfides and disseminated cassiterite; 4) hydrothermal topaz and quartz; and 5) a core of coarse cassiterite and interstitial sulfides with trace Fe-Li mica (Fig. 3–9C, D, E). Locally, individual zones can be thicker (>30 cm) and thus appear massive/homogeneous (e.g., rare dominant topaz(-quartz) greisens, Fig. 3–9F).

Importantly, cassiterite in these latter zones is texturally late, as compared to that in distal zones it tends to be coarser and more euhedral and lines pores created during alteration (e.g., Kontak, 1994; Halter et al., 1996). The noted sequence represents the progressive alteration of the host

EKL with the following sequential transformations: K-feldspar to albite (1), albite to sericite (2), and sericite to hydrothermal topaz (3, 4; Halter et al., 1996).

Unlike the zoned greisens, the massive greisens are fine- to medium-grained, typically texturally homogeneous, and range in colour from green-grey to dark grey or black (e.g., Fig. 3–9G, H). The C content in dark greisens, which can be up to 0.15 wt. % (Kontak, 1994), in part causes variation of grey scale (i.e., light to dark) in massive greisens, whereas C in zoned greisens concentrates along greisen cores. The massive greisens are steeply dipping and vary in size (i.e., <1–20 m) with the widest likely representative of coalesced zones of more narrowly altered EKL. In the Baby Zone, massive greisens are wider and have generally steeply dipping geometries, and are found proximal to fault planes crossing the deposit and intrusive contacts (Fig. 3–7B). Individually, the mineral assemblages of the massive greisens can vary such that, for example, quartz-muscovite-(Fe-Li)mica, quartz-topaz-(Fe-Li)mica (Fig. 3–9G), quartz-(Fe-Li)mica (Fig. 3–9H). An excellent example of massive greisen formation at a broad scale is seen in upper 100 m of a deep drill hole (EK-90-1), studied in detail by Halter et al. (1995), where intervals of quartz-topaz greisen graded into mixed quartz-topaz and quartz-topaz-sericite greisen.

In detail, greisens with massive character are homogeneous and fine-grained with respect to typical EKL, and have irregular sutured crystal grain-boundaries as well as abundant interconnected dissolution cavities infilled by late mineralization and overprinting networks of

irregular quartz- and base-metal bearing veinlets (Fig. 3–10A). The pocket-infill includes lining of mineralization that is typically coarser than the host matrix and includes euhedral quartz, topaz, cassiterite, apatite, fluorite, chalcopyrite, pyrite, and sphalerite (Fig. 3–10B, C).

3.4.4 Mineralization

A general paragenesis of the mineralized greisens and veins at the East Kemptville deposit was first presented by Richardson (1988), where the mineralization was subdivided into the following stages: 1) massive greisen development; 2) greisen-bordered microfractures (i.e., zoned greisens); 3) white quartz-sulfide-phosphate veins; 3) ribbed veins (i.e., extensional veins); 4) quartz-carbonate-fluorite veins; 5) barren quartz veins; 6) clay-fluorite infill; and 7) crusts and crystals (i.e., zeolite-carbonate late fracture fill). Additional textural, petrographic, and microtextural observations of alteration and mineralization at the deposit done as part of this study allows for modification of the paragenesis to the following stages (Fig. 3–11): 1) crystallization of EKL; 2) deuteric alteration of the EKL; 3) the main mineralization stage, which may be subdivided into initial greisenization and infill of oxides ($\text{Sn} \pm \text{W}$) which partially overlaps with the base-metal sulfides and subsequent quartz-sulfide veins ($\text{Zn}, \text{Cu} \pm \text{Ag}, \text{In}$); 4) phosphate \pm albite-bearing veins; 5) barren quartz-carbonate-fluorite veins that crosscut the base-metal bearing veins, and 6) complex assemblages of late quartz-carbonate-clay-zeolite veinlets that overprint all of the previous stages. Each mineralization stage is described in detail below.

3.4.4.1 Zoned greisen mineralization

Zoned greisens are typically along, or parallel to, sub-vertical fault zones, now shear planes in many cases. They are typically <1 m and locally carry significant grade (e.g., estimated volumetric 25% cassiterite over the zoned interval). Their vertical extent varies, but drilling has shown that they extend deep into the deposit along the EKEDSZ. The oxide and base-metal mineralization includes cassiterite (the principal Sn ore) with chalcopyrite and lesser pyrite, sphalerite, pyrrhotite, and stannite. The cores of these zones are composed of coarse euhedral quartz-topaz-cassiterite (Fig. 3–9D, E) that is bordered by finer-grained greisen. The core material fills porosity generated due to dissolution via alteration and includes euhedral cassiterite proximal zoned greisen cores and pyrite distal to the greisen cores (e.g., Fig. 3–12A); these assemblages are crosscut by base-metal sulfide bearing veins (i.e., pyrite, pyrrhotite, chalcopyrite, sphalerite; Fig. 3–12A, B, C). The greisens also may contain, atypically, arsenopyrite and wolframite as a part of the infill mineralization (e.g., Fig. 3–12D).

A representative section through a zoned greisen was constructed using a mosaic of BSE images color-coded by element (i.e., Al, Si, K) with its mineralogy schematically represented (Fig. 3–13A, B). The image shows pockets of infill mineralization lining pores in the greisen generated by CDP processes (i.e., dissolution) of the EKL. The resultant fine-grained greisen typically contains ore minerals (i.e., cassiterite, wolframite, pyrrhotite, arsenopyrite, pyrite), although less voluminous than in the greisen core or overprinting veins (e.g., Fig. 3–13C). Examples of

textures relevant to the paragenesis include: 1) proximal the core, euhedral topaz, cassiterite, and quartz filling porosity are overprinted by later chalcopyrite with stannite at the interface of cassiterite and chalcopyrite (Fig. 3–13D, E); 2) distal to the core, secondary alteration assemblages partially replace K-feldspar (e.g., Fe-rich mica, pyrite, fluorite, chalcopyrite; Fig. 3–13F); and 3) also distal to the core, early fine-grained cassiterite is frequently replaced by stannite and chalcopyrite (Fig. 3–13G).

3.4.4.2 Massive greisen mineralization

The nature of the massive greisen may vary, but their typically homogeneous grades (~0.4 wt. % Sn) and ease of processing make them economically important. They typically contain disseminated- to patchy, fine- to medium-grained cassiterite of variable habit, as part of the infill paragenetic stage. The thickest massive greisen known to date is in the Baby zone, where it occurs adjacent to and beneath the magmatic breccia (Fig. 3–7B), is a semi-consistent 100 m intercept of dark grey-green quartz-topaz-mica (\pm cassiterite-sulfide) greisen with moderate grade (mean value of 0.43 wt. % Sn over 119 m) that was intercepted by a vertical drill hole (EK-90-1; Kontak, 1994; Halter et al., 1995a). This greisen was also intersected by later angled drilling that indicated an approximate width of 100-120 m. These greisens contain interconnected fractures with mineralization representative of a zoned greisen core, described above (e.g., Fig. 3–9G, H, 3–10A). In the Baby Zone, field relationships indicate a relationship of the greisens with brittle deformation and brecciation. These features suggest fluids accessed

areas of tightly-spaced fracture networks that enhanced fluid:rock interaction in contrast to the more focused fluid flux in zoned greisens.

3.4.4.3 Base-metal veins

Mineralization in both ore zones dominantly comprises oxides hosted by greisens, but a significant part of the ore reserve is associated with base-metal sulfides (i.e., Cu-Zn-Ag were also produced from the deposit). These sulfides occur as either irregular infill of the greisen pores or as part of planar to locally sigmoidal quartz veins of cm-scale thickness (1-3, but rarely to 10-20 cm) that lack any associated alteration (e.g., Fig. 3–14). In terms of abundance, the former provided the bulk of the base-metal production. The veins are predominantly aligned NE-SW, with lesser amount orthogonal to this (Kontak et al., 1986), and sub-parallel to the EKEDSZ. They are proximal (<150 m) the upper contact of the EKL with the overlying metasedimentary rocks, but also locally extended into the latter, but only for a few meters.

The vein-type base-metal mineralization dominantly comprises chalcopyrite, sphalerite (In-enriched; Willson, 2019), and pyrite, with lesser pyrrhotite, arsenopyrite, wolframite and rare molybdenite, bismuthinite, and galena. Early, fine-grained arsenopyrite, pyrrhotite, and pyrite are disseminated through the greisenized EKL and occur locally as coarser crystals in veins that have diffuse boundaries (Fig. 3–14A). Elsewhere in the deposit, these veins are more discrete, typically with clear to milky quartz, pyrrhotite, and pyrite (Fig. 3–14B), with rare wolframite. The most abundant vein type that carries base-metal sulfides contains an assemblage comprising

quartz-pyrite-pyrrhotite-chalcopyrite-sphalerite \pm molybdenite, siderite that is pervasive through the deposit (Fig. 3–14C–F). This dominant vein assemblage typically has variable proportions of sphalerite and chalcopyrite, with chalcopyrite being more abundant where veins crosscut metasedimentary host rock (Fig. 3–14C) and some heavily greisenized EKL (Fig. 3–14D); sphalerite was more abundant where veins crosscut less altered EKL (Fig. 3–14E). The veins crosscut zoned greisens at any angle (e.g., Fig. 3–14F). Molybdenite rarely occurs, either in mineralized pegmatites or as accessory-minerals in mineralized veins through the paragenesis that include: 1) coarse grains in veins with no apparent affinity to greisenization and ore mineralization (Fig. 3–14G); 2) coarse grains intergrown with euhedral wolframite hosted in a Main Zone granular quartz vein (Fig. 3–14H); and 3) fine grains in late quartz-dominant veins overprinting ore mineralization in the Main Zone (Fig. 3–14I).

3.4.4.4 Phosphate-bearing veins

A generation of quartz-dominant and phosphate \pm albite-bearing veins crosscut, and hence post-date, the greisen and base-metal stages. They typically occur as discontinuous, ladder to en-echelon, 1 cm-wide extensional veins with syntaxial, locally fibrous, infill growth (e.g., Fig. 3–15A). This vein generation contains bands of clear quartz and sub- to euhedral albite with phosphate minerals in some examples (Fig. 3–15A, B). The phosphate minerals include fluoroapatite, hydroxylapatite, triplite and less commonly vivianite (e.g., Fig. 3–15C, D) as well as rare childrenite, phosphophyllite, and mcauslanite (cf. ribbed veins of Richardson, 1988).

3.4.4.5 Quartz-carbonate veins

Post-mineralization activity along the EKEDSZ gave rise to a series of low-temperature alteration, vein, and infill assemblages that crosscut each of the above hydrothermal products. The earliest of these assemblages include a series of barren veins that contain quartz with lesser carbonate and trace fluorite (Fig. 3–15E). These veins are 0.2–5 cm wide, subvertical, and appear to form en-echelon sets that strike near-perpendicular and narrowly oblique to the EKEDSZ (described with structure below).

3.4.4.6 Late veins

The last generation of veins includes a low-temperature complex assemblage of carbonate, phosphate, and zeolite minerals that are typically found along late shear planes and pockets or open-space joint surfaces (e.g., Fig. 3–15F, G). This generation of veins typically occurs as open-space filling of white-yellow clays (dickite, montmorillonite) and deep-purple zoned fluorite. Less typically, the late veins occur as crusts of euhedral, fine-grained (0.2 to 0.3 cm) crystals of stilbite intergrown with lesser siderite, dolomite, and variably colored (pink to brown, purple, yellow) anhedral fluorite; typically, this assemblage is coated by fine-grained pyrite (e.g., Fig. 3–15H).

3.4.5 Structure

The deposit area is characterized by a NE-trending, sub-vertical penetrative fabric (Fig. 3–16H) related to deformation associated with the EKEDSZ and is heterogeneously developed as micro-shear planes throughout the deposit area (Kontak et al., 1986; Kontak and Cormier, 1991; Kontak, 1994). The latter structure is characterized by multiple, semi-ductile faults having similar strike (ca. 045°) and dip (sub-vertical) orientations that penetrates the EKL and the meta-wacke country rocks. The above foliation is subparallel to the EKL intrusive contact at approximately $045/75^{\circ}$ (Fig. 3–3A). Discrete shear planes (0.1–2 m), identified in drill core through the deposit and recorded in drill logs, were confirmed from surface observations and categorized for interpolation in 3-D space. Two examples of major faults through the deposit include: 1) a well-defined ~40 m-wide shear zone that crosscuts the Main Zone and the SE part of the Baby Zone, and which truncates breccia in the latter; and 2) a ~20 m-wide shear zone approximately 120 m SE of the aforementioned fault that is characterized by a strong penetrative foliation along multiple thin shear planes through the Main Zone (e.g., Fig. 3–3B, C).

The delineation of brittle and ductile structural domains in both the Baby and Main zones was completed by compiling historic descriptions of structure in drill logs. These results defined contrasting structural domains between the ore zones such that the terminology used in drill logs from the Baby Zone dominantly refers to brittle deformation whereas those from the Main Zone suggest ductile deformation. This distinction was confirmed with outcrop observations in the

northern part of the deposit (Figs. 3–3 and 3–16C, D, I) and is also consistent with observations of earlier workers noted above.

At surface, a vertical normal offset is visible in the Main Zone along the contact between the EKL and its country rock which created an inlier of metasedimentary rocks referred to historically as the keel zone (e.g., Richardson et al., 1982; Fig. 3–16A, B). The NW contact of this feature is demarcated by a 15 cm-wide mylonitized zone that overprints an original brittle fault, oriented at $046^{\circ}/84^{\circ}\text{W}$ (Richardson et al., 1990a; Fig. 16C), whereas in the SE there is an intrusive contact between the sedimentary rocks and chilled EKL. The original brittle structural feature is parallel to most zoned greisens in the Main Zone (e.g., Fig. 3–16E, F, G). The latter feature also contains quartz-albite-sphalerite fibre veins (Fig. 3–16D) that indicate late ore fluid infiltration synchronous to vertical slip, with a NW side-up sense of movement. This is significant as this structure has also regionally been noted to host well-developed greisen and Sn mineralization (see Fig. 3–2; Richardson et al., 1982; Halter et al., 1995a).

The zoned greisens are dominantly recognized as NE-trending, steep brittle features locally overprinted by shear planes. The brittle features were the preferred conduits for greisenizing fluids, based on numerous structural measurements across the Main Zone (Richardson et al., 1982; Kontak et al., 1986; Kontak 1994; Figs. 3–3C inset, 3–4, and 3–16G). The time of their formation is best seen in areas of least deformed rocks where vertically-oriented greisens are noted to cut conjugate cooling joints in the EKL (Fig. 3–16E). The greisens and unmineralized

EKL are further deformed by a penetrative sub-vertical foliation (Fig. 3–16H) that is aligned parallel to the greisen development. The above mentioned features are also cut by later brittle features that include a variably spaced (2–15 cm) shallow SE-dipping cleavage (Fig. 3–16F, I) and the fracturing of quartz-topaz rich greisen cores and infilled by fluorite and pyrite (e.g., Figs. 3–9E, 3–13A).

In contrast to the brittle features, post-greisen ductile deformation through the deposit is predominantly recorded by normal to dextral shear-sense manifested as kinematic indicators, for example: 1) stretched quartz grains that form sigmoid-shaped porphyroclasts and strong alignment of muscovite, with localized C-C' fabric (Fig. 3–16J); 2) post-mineralization deformation and segmentation of both greisen and vein mineralogy (i.e., cassiterite-topaz and quartz-sulfides, Fig. 3–16K); 3) syn-kinematic quartz vein development along fault planes with slickenslide development indicative of normal movement (Fig. 3–16L); 4) thin shear planes that offset greisens and aplitic dikes (e.g., Fig. 3–16M); 5) en-echelon shear vein sets containing barren quartz±carbonate (noted above, Fig. 3–16N); 6) minor extensional quartz-phosphate-albite-fluorite veins with syntaxial fiber-textures (e.g., Fig. 3–16O); and 7) late shear planes that are locally filled with assemblages of chlorite and graphite (e.g., Fig. 3–16P). Petrographically, the EKL proximal shear planes through the deposit (<20 m) contain brittle-ductile fabrics, such as quartz with undulose extinction and irregular subgrains, feldspar with bent twinned lamellae,

and kinking of micas. However, the degree of stain in the EKL varies considerably with a continuum from relatively undeformed to discrete zones with intense shearing (Kontak, 1990a).

3.5 Lithochemistry

To determine the compositional evolution of the EKL with respect to the DLP and document the petrogenetic relationship between the host rocks to the two ore zones, whole-rock lithochemical data from previous studies (Kontak, 1990a; Richardson et al., 1990a; MacDonald, 2001) are combined with newer analyses of drill core (courtesy of Avalon Advanced Materials Inc. drill programs in 2014 and 2015; Table EA 3-2, Electronic Appendix) and outcrop samples from this study (Table 3–1). For archived samples, analytical details are provided in the cited papers, whereas analyses for the latter two sample suites were done by ALS Laboratory Group Ltd. (Canada) using the lithium borate fusion inductively coupled plasma-atomic emission spectroscopy (ICP-AES; method ME-ICP06) for major elements, solution inductively coupled plasma-mass spectrometry (ICP-MS; method ME-MS81) for trace elements, and four-acid digestion (method ME-4ACD81) for volatile trace elements.

Out of the final dataset, the least-altered samples from the EKL and DLP were selected for use by filtering the compiled dataset in the order of: 1) excluding any samples that were logged as greisens (i.e., altered) or to have moderate vein density; 2) excluding samples with a high aluminum saturation index (ASI, apatite-corrected; Zen, 1986) that would suggest alteration (i.e.,

values >1.55); and 3) only including samples in the lowest quartile of Sn concentrations (<200 ppm). Samples deemed to record the effects of greisenization were returned to the dataset and used to assess the nature of metasomatism in the context of mineralization.

These data are shown for selected elements and ratios in Figure 3–17 and 3–18, where they are compared also to other petrologically relevant data: the average S-type granite of the Lachland Fold Belt, Australia (Chappell and White, 1992) and the volatile- and metal-rich Macusani glass of Peru (Pichavant et al., 1987).

3.5.1 Major element chemistry – Unmineralized rocks

The geochemical database for the least altered, relatively unmineralized intrusive rocks (i.e., Sn < 200 ppm) is filtered spatially and lithologically to compare the petrogenetic signatures. Major element concentrations (Fig. 3–17A) are similar for all EKL samples, but with subtle differences compared to the DLP (data from Dostal and Chatterjee, 1995). Similarities between the two intrusive suites include SiO₂ (71–79 wt. % in EKL versus 68.5–77 wt. % in the DLP), Al₂O₃ (12–20 wt. % in both), and \sum Fe (1.0–2.8 wt. % FeO* in EKL and 1.1–4.2 wt. % in DLP). In contrast, differences between EKL and the DLP include relative depletion of TiO₂ (0.01–0.1 wt. % versus 0.03–0.75 wt. %) and MgO (0.01–0.23 versus 0.7–1.9 wt. %). The ASI values for the DLP in the filtered dataset average 1.01 ± 0.24 , which compares to the EKL (both Main and Baby zones overlap) average of 1.40 ± 0.07 . Although the major element contents for the EKL from the two ore zones are similar, some differences are noted: the less mineralized host granite

in the Baby Zone is enriched in SiO_2 and shows a wider range in wt. % Al_2O_3 , whereas similar rocks in the Main Zone have a higher values and a wider range for wt. % P_2O_5 , from 0.09 to 1.18 wt. % (average = 0.46 ± 0.08) versus 0.11 to 0.21 wt. % (average = 0.16 ± 0.03) in the Baby Zone.

3.5.2 Trace element chemistry

The trace element data for least altered, relatively unmineralized EKL samples proximal to both ore zones compare to the specialized granites of Tischendorf (1978) with: enrichment in Sn, W, Cs, P, Ta, Rb, and U; similar Th, K, and Nb; and depletion in Sr, Ti, and Zr (e.g., Fig. 3–17B). These relative concentrations are also much more enriched in the lithophile elements (i.e., Li, Cs, Rb) compared to the typical S-type intrusive rocks (e.g., Rb shown here; Chappell and White, 1992). These latter relative elemental concentrations are, however, similar to that of the Macusani glass with comparably complementary depletions in Ba and Sr relative to specialized granites of Tischendorf (1978).

Selected trace elements for the EKL and DLP suites are plotted versus SiO_2 in Figure 3–17A and the overall ranges and average values for trace- and rare-earth (REE) elements relative to primitive mantle (McDonough and Sun, 1995) are summarized in spidergram plots in Figure 3–17B. Relative to the DLP, the data for the EKL show enrichment in (range in ppm) Li (330–1230), Rb (325–1230), U (9–36), Ga (22–76), Nb (8–185), and Cs (9–48), in addition to the ore elements (range, median in ppm): Sn (5–197, 96), Cu (1–10000, 72), W (0.4–152, 14), and Zn

(29–5030, 320). Although the EKL is highly evolved relative to the DLP, there is variable depletion of (range, median in ppm; Fig. 3–17B) Sr (9–196, 36), Ba (2–233, 9), and Zr (22–51, 31). Trace-element abundances are similar for the EKL in the two ore zones with the exception of Th and Nd, which are lower in the Main Zone samples. In EKL for both ore zones and the DLP, trace element ratios display subtle differences in terms of fractionation trends. With increasing SiO₂, the DLP shows an increase in U/Th and a decrease in Zr/Y with Baby Zone samples overlapping with the most evolved parts of the DLP (Fig. 3–17A). In contrast, the Main Zone samples have distinctly higher U/Th and Zr/Y (Fig. 3–17A). Such chemical differences for the EKL between the Main and Baby zones was also noted by Halter et al. (1995).

3.5.3 Rare-earth element (REE) chemistry

The REE concentrations for EKL and DLP samples normalized to chondritic values (McDonough and Sun, 1995) are shown in Figure 3–17C. The EKL samples generally have lower Σ REE than the DLP, whereas those from the Baby Zone (average Σ REE = 30 ppm) have higher overall abundances than the Main Zone (average Σ REE = 12 ppm); this same observation was also noted by Halter et al. (1995). For the EKL suites, each is slightly enriched in LREE relative to HREE, with the Baby Zone having flatter profiles than the Main Zone. The average (Lu/La)_N values are 0.51 for the DLP, 0.47 for the Main Zone, and 0.89 for the Baby Zone (Fig. 3–17C). The EKL samples also exhibit a subtle depletion from LREE to MREE ([La/Sm]_N = 1.21–1.26), have significant negative Eu anomalies (i.e., Eu/Eu* < 1), but with a narrower range

for the Baby Zone (0.02–0.53) than the Main Zone (0.02–0.91), and variable positive Ce anomalies ($Ce/Ce^* = 0.39\text{--}4.30$). On average, the EKL from the two ore zones have contrasting HREE profiles, with a slight depletion from MREE to HREE in the Main Zone ($[Gd/Lu]_N = 1.31$) and a slight enrichment in the Baby Zone ($[Gd/Lu]_N = 0.81$; Fig. 3–17C). This is reflected by the overall higher and much greater spread in REEs of the Baby Zone relative to the Main Zone, including a range of values noted in the felsic matrix to magmatic breccias of the Baby Zone (Fig. 3–17D).

The EKL samples from both ore zones show a lanthanide tetrad effect that is typical of highly fractionated, peraluminous F-rich melts (cf. Masuda and Akagi, 1990). The degree of the tetrad effect ($TE_{1,3}$) may be calculated using the first and third tetrad, and Irber (1999) has proposed that a well-developed tetrad effect in REE bulk-rock data (i.e., $TE_{1,3} > 1.10$) is exclusively related to highly evolved and altered granites containing late-stage minerals such as albite, Li-mica, tourmaline, topaz, and/or fluorite. The calculated values of the tetrad effect in the EKL ore zones average 1.39 in the Main Zone and 1.15 in the Baby Zone.

3.5.4 Major element chemistry – Mineralized rocks

The variation of major element chemistry in mineralized rocks from both suites of granites (i.e., the DLP and both ore zones in the EKL) is compared to total ore metal content in Figure 3–18 (with Sn-only in the inset of Fig. 3–18A). For comparison, these data are also plotted with the average S-type granite from the Lachlan fold Belt (Chappell and White, 1992), as well as the

bulk average ore sample (with a cut-off at 0.05 wt. % Sn) from the deposit, calculated from Table EA 3-2 to have $\sum[\text{Sn} + \text{Zn} + \text{Cu}] = 6200$ ppm (Fig. 3–18A). It should be noted that for the drill-core samples, core lengths were generally 1 m and were in many cases mixture of EKL and variably greisenized EKL with, in rare cases, zoned greisens with high-grade Sn.

Overall, the data show little change in the total alkalis with increasing metal concentrations until a slight decrease at ca. 1000 ppm (Fig 3–18A), which is also reflected by the fact that the alkali ratio remains close to unity (Fig. 3–18B, C). Further increase in metal content is seen to be reflected first with an increase in Na_2O (Fig. 3–18B) and the K_2O , which relates to formation of albite followed by sericite in greisens (Halter et al., 1995a, 1996). For the low-grade and less mineralized samples, there are similar alkali contents to the DLP suite (Fig. 3–18A). The erratic correlation of metal content with Al_2O_3 likely is a reflection of well poorly sericite alteration zones and well mineralized quartz-topaz zones, both of which have enriched Al_2O_3 (Fig. 3–18D). Lastly, for the highest grade samples, there is marked enrichment in SiO_2 which relates to the formation of quartz \pm topaz greisen zones (Fig. 3–18E).

3.6 Geochronology

3.6.1 Re-Os molybdenite dating

Four molybdenite-bearing samples were used to obtain Re-Os dates to constrain the age of mineralization and to compare with a previous Re-Os molybdenite age (see below) for

molybdenite hosted in a pegmatite from the Baby Zone (initially reported by Kontak et al., 2003). Samples used include three from the Main Zone and one from the Baby Zone: 1) a fine-grained molybdenite from the edge of a micro-dike from the Baby Zone (EKAV-15-15; Fig. 3–6P); 2) coarse molybdenite in a granular quartz vein (EKDJK-18-01; Fig. 3–14G) from the Main zone; 3) coarse molybdenite intergrown with coarse, euhedral wolframite in a granular quartz vein (EKDJK-18-02; Fig. 3–14H) from the Main Zone; and 4) coarse molybdenite in a quartz vein from the Main Zone (EKAV-15-17; Fig. 3–14I).

Samples were prepared and analyzed at the University of Alberta Radiogenic Isotope Facility. They were first coarsely crushed and milled, and all the molybdenite removed using magnetic and gravity concentration methods. The molybdenite was then crushed and homogenized to a 100-300 mg aliquot used for isotopic analysis. As the material used was not overly coarse, only one aliquot was analyzed for each sample since decoupling of Re and Os was not considered an issue for these samples (cf. Selby and Creaser, 2004). The isotopic abundances of Re and Os were determined using isotope dilution mass spectrometry using Carius tube, solvent extraction, and chromatographic techniques. Complete analytical procedures and error calculations are given in Selby et al. (2007).

Details of the samples, results of Re-Os analysis, and calculated model ages for all molybdenite samples, including the pegmatite sample first presented by Kontak et al. (2003), are summarized in Table 3–2 and later in Figure 3–22. The data for the latter sample (EK-95-11-3) yielded an age

of 376.2 ± 3.3 Ma and is provided here, as it has not been formerly published. For the other four samples, the Re-Os ages are: 370.2 ± 1.6 (EKDJK-18-01); 359.4 ± 1.8 (EKDJK-18-02); 354.9 ± 2.0 Ma (EKAV-15-17); and 343.7 ± 1.7 Ma (EK-AV-15-15; Fig. 3–22).

3.6.2 In situ U-Pb cassiterite dating

Representative samples of cassiterite were used for in situ U-Pb geochronology via LA-ICP-MS at the U.S. Geological Survey, Southwest Isotope Research Laboratory, Denver, CO. Details of the samples and analytical results are given in Table EA 3-3 (Electronic Appendix). A summary of the U-Pb data and Terra-Wasserberg plots with calculated ages for the samples are given in Table 3–3 and Figure 3–19.

The samples used comprised six samples from the East Kemptville deposit and one from the Duck Pond deposit (Fig. 3–2). For those from East Kemptville, four samples were of coarse-grained cassiterite from the cores of zoned greisens in the Main zone (e.g., Fig. 3–9D; samples EKDJK-87-2, 8, 10, EKDJK-89-11), a coarse-grained cassiterite lining a miarole in microgranite in the Main Zone (Fig. 3–5F, G; EKDJK-2016), and a sample of disseminated cassiterite in massive topaz greisen from the top of the Baby Zone (e.g., Fig. 3–9G; EKDJK-90-1). The Duck Pond prospect sample contained coarse cassiterite grains hosted in a lens of manganiferous metapelite within the GHTZ (Fig. 3–19F inset; DP-20-224.9).

The cassiterite, either in polished thin section or grains mounted in epoxy, was first imaged using cathodoluminescence (CL) and backscatter electron (BSE) techniques to assess zonation and irregularities (e.g., inclusions) within grains. Details of the analytical methods employed follow those in Neymark et al. (2018) whereby a Teledyne Photon Machines Excite-Analyte™ 193 nm excimer laser coupled to a Nu Instruments Attom™ high-resolution sector field ICPMS were used to acquire U-Th-Pb data. Similar to the Neymark et al. (2018) study, the following conditions were used: 1) system was optimized using NIST 610 glass prior to analysis; 2) ablation was in the raster mode to achieve maximum signal intensity; and 3) optimal peak shapes at masses 208 and 238 were used with low inter-element fractionation monitored by Th/U (typically ~0.9–1.0). The laser ablation spot sizes used on cassiterite varied between 85 μm , 115 μm and 135 μm , depending on crystal size and/or signal intensity of the unknown (i.e., larger spot sizes used for cassiterite with lower U concentration), and pits are shallow (~10 μm) after 40 s of ablation at 5 Hz repetition rate. As with Neymark et al. (2018), the data are normalized to cassiterite internal standards to correct for matrix effects related to using the NIST 610 standard.

For Main zone samples, the results follow: 1) the miarolitic hosted cassiterite (EKDJK-2016) yielded an age of 370.6 ± 7.8 (n = 30, MSWD of 1.70); and 2) for the zoned greisen samples, ages are 367 ± 12 (EKDJK-87-2, n = 30, MSWD = 2.8), 368.6 ± 8.9 (EKDJK-87-8, n = 60, MSWD = 8.1), 365.4 ± 4.3 Ma (EKDJK-87-10, n = 30, MSWD = 2.5), and 367.5 ± 9.4 (EKDJK-89-11, n = 60, MSWD = 8.8). The single sample from the Baby zone remains to be analyzed and

results will be reported at a later date. Lastly, the Duck Pond prospect samples yielded an age of 347 ± 12 Ma (DP-20-224.9, $n = 60$, MSWD = 2.3).

3.7 Discussion

The up-to-date geological, petrological, and geochronological (Re-Os molybdenite, U-Pb cassiterite) information on the East Kemptville deposit allows us to fully assess the two ore zones and the relationship among alteration, mineralization, and structure, in addition to the geochemical signatures of the igneous and hydrothermal stages, and the absolute time(s) of mineralization. Below we discuss: 1) the nature of the EKL and its role in deposit formation; 2) the geologic character and differences between the two ore zones and the implications for reconstructing the evolution of the deposit; 3) the structural aspects of the deposit; 4) implications of the whole-rock lithochemistry; 5) dating (U-Pb cassiterite, Re-Os molybdenite) of magmatic and hydrothermal events in each ore zone and its implications for deposit formation and exploration; 6) an updated model for the formation of the deposit; and 7) aspects of potential Sn endowment.

3.7.1 Nature of the EKL and its role in deposit formation

Field, petrographic, and petrologic evidence presented indicate the EKL crystallized from a highly-differentiated volatile-rich (i.e., F, H₂O) melt with trace element concentrations comparable to the specialized granites of Tischendorf (1978). The EKL has enrichment in

lithophile elements and select metals (Sn, Zn) that is similar to F-rich melts, such as those represented by the Peruvian Macusani glass (Fig. 3–17A; Pichavant et al., 1987) or Beauvoir Granite (cf. Cuney et al., 1992). Although situated at the SW edge of the DLP and similar in age (discussed below), the EKL lacks both field-relationships and clear geochemical trends that suggest derivation from the DLP. This contrast has been suggested by Kontak (1990a) to represent a discontinuity in the fractionation that is resolved by a common melt source residing at depth, rather than locally. The transport of fractionated magmas away from their source has also been proposed for the Cornubian plutons, where exposed differentiated intrusions are distal (i.e., above) to the source batholith (cf. Chappell and Hine, 2006).

Features such as stockscheider pegmatites proximal to the EKL intrusive contacts that transition to layered aplite-pegmatite with USTs, as well as cassiterite-bearing miaroles and micro-pegmatites are evidence for metal and volatile enrichment of late-stage melts and commensurate volatile saturation in the terminal fractionation stages of the EKL. These late fluids caused the abundant and pervasive deuteric alteration in the EKL (Kontak, 1990a, 1991) that is characterized by: 1) widespread pitting of feldspars, due to CDP (Putnis, 2002; Parsons et al., 2005); 2) formation of variably perthitic K-feldspar; 3) replacement of primary muscovite by a Fe-poor type (Fig. 3–8D), and abundant secondary phases (i.e., triplite, cassiterite, Nb-Ta oxides, ferberite; Kontak, 1991); and 4) pervasive formation of secondary disseminated apatite in albitized plagioclase (Fig. 3–8E). Also relevant in this regard is the association of low-grade Sn

and base-metal mineralization with sericitized feldspar (Fig. 3–13A, F, G). The latter feature, along with the presence of magmatic cassiterite in the EKL miaroles and pegmatites (e.g., Fig. 3–5F, G), suggests that the earliest fluid event recorded in the deposit setting was stanniferous. Thus, the anomalous Sn-enrichment documented in the least altered rocks that pre-date greisen formation and characterize the EKL (Fig. 3–17A) is to be expected and has been independently demonstrated by others (cf. Fig. 45A of Stanley, 2020).

Greisens in the deposit are interpreted to overprint deuteritic alteration and follow brittle fractures parallel to the EKEDSZ that are observed to truncate cooling joints in the EKL (e.g., Fig. 3–16E). Importantly, therefore, greisens developed after the cooling of the host leucogranite and indicates that the cassiterite seen in pegmatites and miaroles are distinct from that hosted in the greisens. This complements earlier interpretation of an evolving melt source at depth (Kontak, 1990a; Halter et al., 1995a; Kontak et al., 2001) and thereby implicating a potential petrogenetic connection between the EKL and DLP.

The presence of magmatically-derived cassiterite, as locally observed in pegmatites, indicates the EKL fractionated to an extent that it saturated in cassiterite; typical Sn concentrations of the least altered EKL are ~0.06 wt. % (Fig. 3–3D). However, for the EKL to source all the Sn localized in the deposit, one would expect abundant cassiterite to have formed in pegmatites and the granite itself through the deposit prior to greisen formation, which is not observed. A limitation to the formation of such widespread stanniferous pegmatites, similar for example to the Nong Sua tin

pegmatites of Thailand described by Linnen et al (1992), is the depth of emplacement estimated at 3.5 kbars (Halter et al., 1996; Kontak et al., 2001). Granite-derived abyssal pegmatites that form under such pressures are typically sparse, poorly mineralized, and rarely economic (cf. Černý and Ecrin, 2005).

The alteration distal to ore-bearing greisens is generally weaker in the EKL than the well-documented occurrence of microclinization and albitization in host granitoids from other Sn-provinces of similar character (e.g., Taylor, 1979; Pollard, 1983; Černý et al., 2005). Whereas the primary mineralogy of least altered EKL away from zoned greisens is uniform and granitic, as previously noted (Kontak, 1990a), we do note however the rare and localized occurrence of albitites: 1) as part of the regional DLP ca. 5 km SE of the deposit area where albite-quartz-biotite-magnetite breccia hosts cassiterite mineralization (Richardson et al., 1990b); and 2) at 510 m depth of the deep hole (EK-90-1) in the Baby Zone where 5 m of albitite was intersected (Halter et al., 1995a, 1995b). Thus, the generally uniform nature of the EKL contrasts with typical assemblages of Li-F granites in the Erzgebirge Mountains that include massive pervasive albitization which precedes Li-rich Sn-W greisenization (e.g., Krásno, Cínovec; cf. Štemprok, 2005); proximal greisen development in the Krásno area (from Jarchofský, 2006) that includes quartz (20-30%), albite (30-50%), zinnwaldite (10-15%), and topaz (3-8%), and those in the Podlesí granite (Breiter, 2002) that includes less albite content (17-19%) and higher K-feldspar (35-40%), both twinned (microcline) and perthitic varieties. The formation of these assemblages

in apical parts of granites in the Erzgebirge are interpreted to precede greisen formation and relate to subsolidus alteration (e.g., Dolejš, and Štemprok, 2001), thus similar in their paragenesis to the generally weaker deuteritic alteration in the EKL. Thus, the absence of significant massive, pervasive albitization and microclinization through much of the EKL proximal greisens is interpreted as evidence for a differentiated melt at depth to have sourced the fluid budget necessary for significant greisenization in the deposit, rather than the late stage EKL-sourced fluids. Notably, however, the presence of deuteritic alteration and noted Sn mineralization in miaroles and pegmatites does not exclude the EKL from contributing a relatively minor component of Sn to the deposit.

The occurrences of topaz-bearing leucogranites in the SMB is not restricted to the EKL. Although these similar leucogranites contain far less topaz (trace to 0.7% versus up to 8% in the EKL; Kontak, 1990a), they are found in the New Ross and East Dalhousie plutons (MacDonald et al., 1992; Clarke et al., 1993). Despite the petrogenetic similarities to the EKL, these leucogranites do not contain significant tin mineralization, but instead host greisen-style prospects with other metal associations (e.g., Long Lake Mo-W, Fig. 3-1; MacDonald, 2001).

3.7.2 Geological features and implications on ore zone formation

The geological features and textural differences between the Baby and Main ore zones provide evidence of geologic setting and timing of mineralization in each zone. Of note is these differences may in part reflect sampling bias since a deep diamond drill hole (EK-90-1 drilled to

about 1 km; Kontak, 1994; Halter et al., 1995a) accessed the very least altered parts of the Baby Zone, whereas sampling of the Main Zone was at or the near-surface. Thus, least- altered Main Zone samples may not be as representative as the equivalent from the Baby Zone.

The primary lithological difference between both ore zones is the presence of magmatic and hydrothermal breccias in the Baby Zone. The fragment inventory of these breccias is dominated by Meguma metasedimentary wall-rocks. Whereas these wall-rock sourced fragments in the HBX are relatively uniform in their composition and texture, those in the IBX are variably altered and locally hornfelsed which suggests incorporation after an earlier magmatic (\pm hydrothermal) event. Additionally, the IBX very rarely contains sub-angular fragments of fine-grained altered leucogranite similar to the EKL, and fragments of hydrothermally brecciated material; together these observations suggest the magmatic brecciation occurred after emplacement of the host EKL and HBX. The imbalance in these breccia fragment types (i.e., wall-rock versus host rock (i.e., EKL)) indicates the brecciation was dominantly implosive (i.e., collapsing) in nature and due to the confining pressures at the depth of emplacement (i.e., 3.5 kbars; Halter et al., 1996; Kontak et al., 2001). Alternatively, the morphology of the EKL roof zone prior to brecciation may have included a down-faulted fenster of wall-rocks in the EKL, similar to the keel zone noted by Richardson et al. (1982) in the northeastern part of the Main Zone, that was dominantly affected by localized brecciation.

The matrix to the IBX unit is a very fine-grained to microcrystalline felsic (quartz-feldspar) material that is typically quartz \pm feldspar-phyric (Fig. 3–6J, K, L, M, N). The variable character of the matrix is locally due to magmatic flow differentiation and crystal filtration (i.e., crystal-rich magma was too coarse to fill breccia openings, Fig. 3–6L), and likely due to pressure quenching in the more porphyritic examples (Fig. 3–6K, N; cf. explosive breccias in Dilles, 1987). The presence of quartz seams with UST features bordering the fine-grained matrix of the IBX (Fig. 3–6O) is further evidence of pressure quenching (cf. Kirwin, 2005). Additionally, that the shape of coarse quartz phenocrysts in the IBX matrix (e.g., Fig. 3–6J) is of a low-temperature polymorph (i.e., α -quartz), indicates it crystallized at temperatures $<800^{\circ}\text{C}$ and at ~ 3.5 kbar (cf. Martel et al., 2021).

The upper breccia contacts in the IBX show a gradual transition outwards from fine grained to porphyritic matrix to microcrystalline felsic matrix and silicified wall-rock (Fig. 3–6K, L); the contact between IBX and HBX, however, is locally observed to be a discrete boundary (Fig. 3–6J). Whereas the latter feature suggests a temporal gap between the breccias, the former may represent a minor hydrothermal phase of the IBX that is not associated with typical HBX documented higher in the system (Fig. 3–7B).

The dominantly Sn- and base-metal rich greisen-style mineralization in the Baby Zone that is hosted beneath and adjacent to IBX intervals as well as in localized coarse segregations in chlorite-bearing HBX pockets (Fig. 3–6G) contrasts with the dominantly unmineralized IBX;

mineralization in the IBX is restricted to crosscutting sulfide-bearing veins and molybdenite localized to the edges of magmatic breccia zones (Fig. 3–6P). Fluid exsolution and USTs in the IBX show no evidence of cassiterite which is in contrast to the minor cassiterite contained in pegmatites of the northern Main Zone (Fig. 3–7A).

The magmatic fluid exsolution textures and pressure quenched dike rocks in both ore zones suggest cycling of fluid pressure in a volatile saturated magma (e.g., Kirkham and Sinclair, 1988; Lowenstern and Sinclair, 1996) occurred in both settings, likely at different times (i.e., formation of the EKL and during mineralization events). Similar features are common in rare-metal evolved and mineralized felsic intrusions (e.g., Podlesí stock, Czech Republic; Breiter et al., 1997, 2005). Furthermore, the characteristic magmatic to hydrothermal breccias of the Baby Zone also suggest cycling of fluid pressure from an evolved magmatic body, not unlike what is recorded by porphyry systems (e.g., Seedorff et al., 2005; Sillitoe, 2010). Evidence for movement along the EKEDSZ synchronous with ore formation indicates this structure played a role in forming these features as the deposit evolved, which is discussed below.

3.7.2.1 Implications of mineral paragenesis for deposit formation

The derived mineral paragenesis (Fig. 3–11) for the deposit includes an early primary magmatic assemblage overprinted by a variety of later hydrothermal stages: alteration assemblages, greisen formation, and a variety of crosscutting veins. Mineralization occurred after the deuteritic

alteration of EKL, as noted by the presence of early magmatic cassiterite in pegmatites and miaroles and weakly disseminated in the altered EKL; economic grades were reached by the additional infill and base-metal vein mineralization stages. The latest stages of mineralization, although precipitated from F- and P-bearing fluids, are likely a result of a fault-controlled overprint of the deposit. Thus an early volatile-rich magma related to extreme fractionation of the EKL locally formed primary cassiterite in pegmatites which was synchronous with, or succeeded by, an early weakly mineralized deuteritic alteration stage that preceded the the structurally-controlled greisen event localized to sub-vertical faults that parallel the EKEDSZ. The early deuteritic alteration features are typical of deuteritic alteration in granites, both barren and mineralized, due to decomposition of mica and feldspar into a diversity of secondary phases (e.g., Lee et al., 1995; Eliasson and Petersson, 1996; Ishihara et al., 2008; Petersson et al., 2014). Early alteration of feldspars by CDP processes (e.g., Lee et al., 1995; Putnis, 2002; Parsons et al., 2005), in particular, results in irregular, porous textures relative to primary feldspars and a change in composition to a mosaic of sub-grains; these features are weakly pervasive through the deposit (e.g., Fig. 3–8), but are not as extensive as those documented in host granitoids from other Sn-provinces, as noted above. The former is attributed to lower fluid:rock ratios whereas the latter reflects much higher ratios due to a protracted and sustained fluid flux.

Mineralogical changes associated with the main ore stage is restricted to zones of greisenization where variable degrees of CDP modified the EKL. This process is best recorded in zoned

greisens where coarse topaz-cassiterite (e.g., Fig. 3–9C, D) was deposited in greisen cores as a result of CDP with higher fluid:rock ratios relative to alteration distal from the cores. In the areas distal to greisen cores, relict cassiterite formed from earlier magmatic crystallization or deuteric alteration is partially to wholly replaced by stannite and chalcopyrite (Fig. 3–13G). The latter replacement of cassiterite (i.e., distal to greisen cores) suggests greisenizing fluids that have been buffered by host rock composition distal to greisen cores dissolved the cassiterite and precipitated sulfides. Alternatively, the texture represents an advancing alteration front whereby earlier precipitated early cassiterite (Halter et al., 1998) was overprinted by later fluxing of base-metal-bearing fluids.

Five main generations of veins are noted in the deposit – these crosscut the greisens and generally each has a different infill mineralogy with earlier stages containing base-metal sulfides (see above and Fig 11). The base-metal sulfides crosscut and rim early cassiterite, and thus post-date Sn mineralization. Samples in the deposit with greater base-metal bearing vein density are represented by the relative increase in SiO₂ with higher grades (Fig. 3–18E), reflecting additional quartz content. The veins, regardless of their type or relative age, notably lack alteration haloes, indicating mineralizing fluids at this stage of the paragenesis had equilibrated with their EKL host. This is further supported by the apparent correlation between host rock lithochemistry and vein mineralogy; for example, later veins that crosscut greisens precipitate fluorite-albite whereas the same interpreted vein generation typically includes phosphate infill where

crosscutting deuterically altered EKL (Willson, 2019). Thus, the system was partially rock buffered during deposition of base-metal sulfide veins and also the later vein types.

The evolution of mineralogical changes in the EKL, from deuteritic alteration to greisenization, is recognized in molar geochemical ratios with increasing metal grade. The Pearce-element ratio mass-transfer approach to igneous fractionation may also be applied to metasomatism. Thus, changes in element ratios commensurate with Sn grade are summarized in Figure 3–20 which show a net alkali loss or gain with changes to mineralogical assemblages (e.g., Stanley and Madeisky, 1994; Stanley, 2020). Relative to rocks of the DLP, the unmineralized EKL from both ore zones (Fig. 3–20A) shows slight depletion of K and weak enrichment of Na; this trend is due to sericitization and albitization of feldspars during deuteritic alteration, respectively. The trend is analogous to that of the fractionated peraluminous granites that host the Sn-W deposits of the Erzgebirge (central Europe), which show a similar evolution caused by microclinization in the least altered parts of the deposits (Fig. 3–20A; Štemprok, 1987; Breiter, 2012). With an increase in Sn content (<750 ppm; Fig. 3–20B) the molar plots show loss of Na but with uniform K/Al values. This reflects development of the sericite greisens in both ore zones as feldspar is replaced commensurate with further CDP reactions as fluid:rock ratio increases. The highest grades (>750 ppm Sn; Fig. 3–20C) show complete loss of the alkalis with formation of the quartz-topaz greisens.

Between the ore zones, the relative molar geochemistry is similar with some differences: 1) although both ore zones record a net alkali-loss (i.e., hydrolysis of feldspar with minor early albitization) with early alteration, those from the Main Zone maintain, on average, a similar mineralogy to the DLP and least-altered EKL relative to the Baby Zone samples; 2) the subsequent addition of K \pm (Fe, Li)-bearing micas is apparently pervasive in the Main Zone, whereas the albitization stage of greisen formation is more apparent in the Baby Zone (Fig. 3–20A, B); and 3) in higher grade rocks (>750 ppm Sn) greisenization further depletes both ore zones in alkalis with the addition of topaz, a feature that is more prominent in the Baby Zone data (Fig. 3–20C). The latter is likely a result of the massive nature of the greisen zones in the Baby Zone. As noted before, the database is built from drill core samples that have minimum lengths of 1 to 1.5 meters, thus the thinner zoned greisens (relative to massive), which are more abundant in the Main Zone, are diluted by the chemistry of less altered EKL in each sample.

Overall, the mineralogical differences between ore zones suggest the Baby Zone has more extensive bulk greisenization (i.e., less diluted by weakly altered rocks), with a higher number of samples experiencing high to complete net-loss of alkalis in the EKL host. The mineralizing fluid:rock interaction in the Baby Zone is therefore either: 1) longer lived, allowing for more advanced greisenization and penetration of the advancing fluid front; and/or 2) more pervasive with increased access to host rock for mineralizing fluids. The latter would allow for homogeneous greisen textures and grade in this ore zone.

3.7.2.2 *Ore metal distribution and lack of zoning*

On a deposit scale, the typical metal zonation observed in granophile-element deposits (i.e., Sn-W-As upwards or outwards to U-Ni-Co, Cu, and subsequently Pb-Zn-Ag; e.g., Taylor, 1979; Heinrich 1995; Cerny et al., 2005) is not present at East Kemptville. Thus, despite a clear paragenesis noted (Fig. 3–11), there is little evidence for either a vertical or horizontal mineral and metal zonation with respect to Sn (cassiterite) and the base-metals (polymetallic veins); instead there is both a spatial and temporal overlap of the distinct ore stages. This contrasts markedly with genetic models for typical Sn-deposits that are based on congruency of base-metal veins located peripheral to Sn-W rich cores (e.g., Taylor, 1979; Taylor and Pollard, 1988), a zonation that has been observed both laterally (e.g., Cornwall, UK, and Erzgebirge, central Europe: Štemprok, 1995) and vertically (e.g., San Rafael, Peru: Kontak and Clark, 2002; Bolivian deposits: Kelly and Turneure, 1970).

The apparent lack of metal and mineral zoning in the deposit may be reconciled in two ways: 1) the main base-metal stage that typically occurs at higher levels than the Sn-greisens were exhumed and subsequently eroded; or 2) telescoping of the system resulted in overprinting of metal stages due to the inability of mineralizing fluids to ascend vertically, as noted in other magmatic-hydrothermal settings (e.g., Minas Pirquitas Sn-Ag-Zn deposit, Argentina: Slater et al., 2021; porphyry systems in general; Sillitoe, 2010). For the latter scenario, eventually fluids precipitated sulfides either by cooling or interaction with wall-rock, host rock, or external fluids.

This possibility is supported by the absence of significant mineralized veins and alteration in the metasedimentary wall-rocks surrounding the deposit (Kontak and Dostal, 1992); thus indicating outward infiltration of ore-bearing fluids was minimal and the wall-rocks were not reactive to mineralizing fluids during deposit formation. Additionally, the structural component of the greisens throughout the deposit provided fluid-pathways for overprinting mineralization and telescoping zonation. These structures could have also acted as an escape mechanism for mineralizing fluids as well, although this is not evidenced at East Kemptville. Similar deep-seated structurally-hosted deposits in the Mesozoic granite belts of SE Asia (Myanmar to Malaysia) have no significant mineral zonation (e.g., Taylor, 1979; Cobbing et al., 1986; Schwartz et al., 1995), and thus this may be characteristic of the deposit setting.

3.7.3 Structural evolution of the deposit

The overall shape of the EKL intrusion (Fig. 3–3A) is elongated NE-SW, similar to the DLP at its SW termination, as well as the trend of fold axes and regional shear zones in the Meguma terrane (Fig. 3–2). These observations reflect the regional fabric and stresses during emplacement of the SMB (Horne et al., 1992; Benn et al., 1997), along which the more evolved plutons were generally emplaced. The regional shear zones have also been interpreted to extend into and to have influenced the emplacement of the highly-differentiated, and locally elongated, New Ross and East Dalhousie plutons (e.g., Horne et al., 1992; MacDonald, 2001).

Primary features in the EKL that formed during its terminal stage of evolution, that is from the most fractionated and volatile enriched melts, include pegmatites and pegmatite-aplite dikes that typically occur near its roof zone (i.e., stockscheiders) and generally aligned parallel to its intrusive contact. The latter distribution reflects fluid saturation at the latest stages of melt crystallization (i.e., 2nd boiling; Burnham, 1979). Additionally, rare micro-pegmatite dikes in the adjacent wall-rocks typically align parallel to the prominent NE fabric through the EKL (Fig. 3–3, inset). Kontak et al. (2001) also noted the similar alignment of the coarse pyramidal-shaped quartz in such pegmatites in the deposit. Thus the EKEDSZ and the dominant strain regime that localized this fault/shear structure likely existed prior to emplacement of the EKL. The latter was responsible for the formation of the keel feature in the Main Zone whereby metasedimentary wall-rocks were juxtaposed against the EKL. Lastly, the stockscheider pegmatites noted in the roof zone proximal these faults become more elongated and rotated parallel to the fault contacts (Fig. 3–5C) suggesting their possible re-orientation during the latest stage of EKL formation.

The NE-trends and steep dips of structures associated with the EKEDSZ is recorded in the deposit area by fracture planes that define zoned greisens (Fig. 3–16G) and sub-parallel mineralized veins. The NE-orientation of mineralization is further evidenced by alignment of higher Sn grades in the historic blast hole database (Fig. 3D) and the general trend of heavier alteration in the deposit area (Fig. 3–4). This is also the preferred orientation of shear planes and a penetrative foliation proximal the main faults (e.g., Fig. 3–16C, H, J); notably, the ductile

deformation is observed to locally overprint greisen development (Fig. 3–16K) and influence vein development (e.g., fibrous quartz-albite veins, Fig. 3–16O). Thus, the deposit setting was one dominated by NE-trending fractures and brittle features during the main mineralization stages and subsequently experienced ductile deformation, localized to shear planes through the deposit that record similar orientations.

The compilation of deformation textures recorded in historic drill logs and relogging in this study is combined with outcrop observations to define the brittle and ductile features in the Baby and Main zones. The Main Zone contains abundant ductile deformation features, such as shears, which are likely reactivated fractures with strain partitioned into alteration zones closely related to Sn grade. In contrast, the Baby Zone dominantly displays brittle deformation, as seen in breccias, and higher grades occur along irregular and densely spaced fracture networks. This apparent contrast in deformation style between the ore zones suggests variable strain partitioning in rocks between the ore zones. This may be explained by mineralogy with the Baby Zone having more quartz and topaz and the Main Zone more sericite (e.g., Fig. 3–20), thereby behaving in a more brittle fashion to movement along the EKEDSZ.

Both ore zones required the formation of brittle features (fractures) for the fluxing of fluids to generate and localize greisen formation. Such fluid-rock interaction is enhanced and continually renewed in settings with protracted movement along such features (i.e., long-lived deformation). The brittle fractures that accommodate greisen formation at East Kemptville were subject to

reactivation and an increase in metamorphic grade as evidenced by ductile deformation in greisenized rocks along the EKEDSZ (Fig. 3–16K). The latter (ductile) conditions may focus additional fluid flow along shear planes during creep (cf. Micklethwaite et al., 2010), however the former (brittle) would have produced damage zones in step-overs along the EKEDSZ, best exemplified by abundant fracture networks in the Baby Zone (cf. Kim et al., 2004). This mechanism for brittle feature development also accommodates offset in flanking strike-slip faults, and may be subject to co-seismic negative fluid pressures as well as implosive brecciation (Sibson, 1986). Such conditions have been proposed for brittle features and the incursion of meteoric fluids into deeper settings of altered rock subject to ductile conditions, for example: the Martha Hill lode Au-Ag vein system (North Island, New Zealand; Spörli and Cargill, 2011); and the Tuolumne Intrusive Complex (Sierra Nevada, USA; Hartman et al., 2018). Therefore, protracted deformation along the EKEDSZ in the deposit setting created the contrast in character of the ore due to a step-over near the Baby Zone. Importantly, this mechanism also accounts for introduction of mineralizing fluids from outside the system.

3.7.4 Implications of whole-rock lithochemistry for the EKL

Chemical similarities of the EKL to the specialized granites of Tischendorf (1978) and Taylor (1979) includes enrichment in ‘granophile elements’ (Sn, W, As, U, Na, P, Li, and F; i.e., in part the BELIP suite of Strong, 1981) and negative anomalies in Ba, Sr, Nb, and Ti (Fig. 3–17B). Relative to typical peraluminous S-type granites from the Lachlan Fold Belt (Chappell and

White, 1992; Fig. 3–17A), the DLP and EKL (to a greater extent) have enrichment and depletion in the elements noted above, in addition to their overall higher SiO₂ contents. The latter feature likely reflects the volatile content in the EKL melt (i.e., F, B, H₂O), which depressed the solidus temperature of felsic melts and extended fractional crystallization (e.g., Manning and Pichavant, 1988; London, 1997). This process appears to be more prevalent in samples from the Baby Zone based on element enrichments (Fig. 3–17A, C, D). Additionally, the volatile content allows for Na and Al enrichment in the residual melt and crystallization of more albitic plagioclase due to a shifting of the cotectic (Manning, 1981; London et al., 1989).

The Zr/Hf ratio has been used as a geochemical indicator for fractionation as Hf is more incompatible relative to Zr (e.g., Zraisky et al., 2009). In a similar fashion, Nb/Ta may be used as an indicator of fractionation or magmatic-hydrothermal processes; i.e., the solubility of Nb and Ta, with minor fractionation of Nb over Ta, is greatly enhanced in reduced, F-rich fluids such as suggested for the DLP (Dostal and Chatterjee, 2000). Thus, the low Nb/Ta ratio that exists in the EKL is likely due to interaction with sub-solidus fluids which may be sourced externally rather than fractionation of the host, a process recorded elsewhere in highly-fractionated and mineralized peraluminous granites (Zraisky et al., 2010). The Nb/Ta versus Zr/Hf plot (Fig. 3–20) shows the degree of fractionation for peraluminous granitoids and the mineralization affinity (modified from Ballouard et al., 2016). The least-altered EKL samples have low Nb/Ta and Zr/Hf, and cluster in the field of rare metal-mineralized granites; alongside

the Li-mica granites and greisens from the Erzgebirge area. This suggests these samples are either highly fractionated with respect to granites hosting other Sn-deposits, or have undergone pervasive interaction with F-rich magmatic-hydrothermal fluids. As the EKL is no more fractionated than other Sn-bearing granites, metasomatic processes are more likely for the low Nb/Ta and Zr/Hf in the EKL due to its F-saturated nature (based on the presence of primary topaz; Kontak, 1990a) and evidence of late-stage volatile saturation (i.e., presence of pegmatites, stockscheiders, and miaroles noted above). The zoning observed in the DLP, from coarse-grained biotite-muscovite monzogranite to fine-grained leucomonzogranite, has been interpreted to reflect magmatic differentiation late in its evolution (Dostal and Chatterjee, 1995; Dostal et al., 2004). However, the Nb/Ta and Zr/Hf ratios in the DLP represent a spread of data between barren granites and Sn-W-(U) granites, with no apparent fractionation vector to the EKL samples from this study. This is in contrast with the spatial fractionation vector interpreted by Dostal and Chatterjee (2000) based on various elemental enrichments and depletions relative to decreased Nb/Ta values proximal the EKL. The latter may reflect alteration brought about by fluids transported along the EKEDSZ, as even the least altered EKL samples do have significant depletion in Nb/Ta values. The Zr/Hf values, however, are distinct from the rest of the DLP samples. Thus, either the EKL evolved separately or differently from the DLP fractionation process, or was sourced from a more highly-differentiated phase which may or may not be related to the DLP and is not exposed at surface.

The concentrations of the majority of major and trace elements in the least-altered EKL from both ore zones are similar with few exceptions. The latter includes markedly higher P_2O_5 and U/Th ratios in the Main Zone, with lower Y and HREE concentrations relative to the Baby Zone (Fig. 3–17A). These differences represent a contrast between the host granites in each ore zone that is similar to that recorded between mineralized granites in the Erzgebirge district of central Europe. The latter comprise: 1) a strongly peraluminous ca. 330–320 Ma granites enriched in P, F, Rb, Li, U, Sn, W, Nb, Ta, and depleted in HREEs; and 2) a weakly peraluminous 325–295 Ma granite with depletion in P and increased F, Li, Be, Sn, W, Nb, Ta, Th, Y, and HREEs (Breiter, 2012). Notably, a significant convex tetrad effect is present in the EKL from both ore zones, the magnitude of which varies between an average $TE_{1,3}$ of 1.39 in the Main Zone and 1.15 in the Baby Zone (Iber, 1999; Fig. 3–17C). The tetrad effect itself is indicative of the extreme fractionation in the EKL-forming melts, and has been proposed as evidence for elemental mobility during late stage magmatic-hydrothermal interaction and deuteric alteration (e.g., Bau, 1996; Jahn et al., 2001; Dostal et al., 2015; Zoheir et al., 2020). However, the tetrad effect has also been proposed as a result of fractionation of monazite and xenotime in F-rich melts which have reduced viscosities and therefore facilitate the settling or escape of late crystal phases (Duc-Tin and Keppler, 2015). Thus the contrast of tetrad effects between the ore zones may reflect fractionation of these accessory phases in the Main Zone relative to the Baby Zone.

In addition to influencing the tetrad effect, crystallization of each of apatite ($\text{Ca}_5[\text{PO}_4]_3[\text{F},\text{Cl},\text{OH}]$), monazite ($[\text{Ce}, \text{LREE}]\text{PO}_4$) and xenotime ($[\text{Y}, \text{HREE}]\text{PO}_4$) would sequester much of the P and REEs in the EKL. Furthermore, relative to each other, monazite and xenotime crystallize in sequence and typically concentrate Th and U + Y, respectively (e.g., Voncken, 2016). The spatial heterogeneity in these elements between ore zones (Fig. 3–17D) suggests that EKL rocks in the Baby Zone contain, overall, a greater amount of accessory-minerals, in agreement with the documented difference in tetrad effect magnitude. The Main Zone samples that do contain higher REEs are also typically characterized by monazite (\pm apatite) relative to the xenotime, suggesting this part of the deposit crystallized prior to the related melt in the Baby Zone that carries more xenotime. Although the geochemical differences between ore zones can apparently be resolved by relative abundances of accessory phases, this interpretation cannot be fully assessed without thorough petrography, which should also account for the abundant apatite inclusions in the deuterically altered EKL samples from both ore zones (e.g., Fig. 3–8E, F).

The differences between EKL samples in both ore zones also cannot be classified as separate intrusive events by field observations, as at present no discrete contacts between granites in each ore zone are recognized. The geochemical differences are, however, not inconsistent with other features identified distal to potential contacts; namely field setting and textures (i.e., equigranular medium-grained muscovite-topaz-leucogranite in the Main Zone versus seriate textured biotite-

muscovite leucogranite with coarse, zoned blueish quartz in the Baby Zone; Figs. 3–5A and 3–6B, respectively). From a mineralization standpoint, both the Baby and Main zones contain typical ore elements (i.e., Sn, Cu, Zn, Ag, In, Bi, W) that are coupled with FeO concentration and are restricted to greisenized host rock. However, as discussed above and despite the geochemical and spatial differences, mineralization in the two ore zones is interpreted to be structurally controlled (i.e., hosted by fractures formed by the EKEDSZ). Therefore, although the leucogranites of the Main and Baby zones may represent different magma pulses with slightly different chemical attributes, as suggested by others (e.g., Halter et al., 1995a; Stanley, 2020), this evolution may not have significant influence on mineralization in the deposit.

3.7.4.1 Geochemical evolution of greisens and related mineralization

The relationship between greisen development and Sn and base-metal grades is assessed using the lithogeochemical data for variably mineralized rocks in the deposit (Figs. 3–18 and 3–20). To be noted, the trends in these plots are partially influenced by the fact that the analyzed material was 1 m core lengths which had mixed proportions of variably altered EKL and greisens. We note, however, that similar plots presented in earlier studies (Kontak, 1994; Kontak et al., 2001) using smaller selected material for EKL and greisens produced similar trends noted in Figure 3–18A.

As seen in Figure 3–18A, there is a general trend of decreasing Na₂O and K₂O as ore grade increases (i.e., $\sum[\text{Sn} + \text{Zn} + \text{Cu}]$ as well as $\sum\text{Sn}$; Fig. 3–18A). As discussed above, deuteric

alteration resulted in early albitization of plagioclase and sericitization of K-feldspar, and greisenization further sericitized the EKL (Fig. 3–20A, B). These processes are reflected in the subtle addition of Na^{2+} and remobilization (but conservation) of K^+ with increasing grades as high as ~0.05 wt. % Sn and ~4000 ppm $\sum[\text{Sn} + \text{Zn} + \text{Cu}]$; i.e., similar to the bulk average ore sample from the deposit (e.g., Fig. 3–18B, C). The metal enrichment associated with roughly constant $\sum(\text{Na}_2\text{O} + \text{K}_2\text{O})$ in the EKL is thus tied to the presence of cassiterite formation related to several plausible processes: 1) magmatic, as seen in micro-pegmatites and miaroles (Fig. 3–5F, G); 2) deuteric, as seen associated with altered feldspars (Fig. 3–13G); and/or 3) incipient development of greisens (e.g., Heinrich, 1990). The treatment of the same dataset by Stanley (2020) also showed the presence of elevated Sn in least altered EKL (see his Fig. 45A) and thus evidence for an early Sn event.

The relatively constant alkali content versus metal values for increasing grade to the bulk ore sample from the deposit (Fig. 3–18A) suggests the original resource of 56 Mt at 0.17% Sn (Richardson et al., 1982; Moyle, 1985) had similar major element concentrations to the least altered DLP and EKL, in stark contrast with rocks with only remotely higher grades. This indicates that the deposit resource represents significant dilution of altered, yet barren to low-grade EKL material and is a factor to be considered for mineral processing in the deposit.

A decrease in alkali element concentrations (Fig. 3–18A) is recorded in rocks with grades similar to higher than that of the bulk average ore sample, as noted above. This inflection represents the

addition of SiO_2 and Al_2O_3 with greisens and significant veins (Figs. 3–18A, D, E; 3–20B, C). Samples with coarser cassiterite and dominant quartz-topaz assemblages were subject to high fluid:rock interaction during deposit formation. This stage thus involved CDP of the EKL with commensurate generation of voids and infill by (i.e., addition of) coarse-grained ore mineralogy. Notably, the decrease in alkalis is more apparent in data from the Baby Zone relative to the Main Zone (Fig. 3–18A, inset); this likely reflects the massive versus zoned greisen style and length of sample intervals, as noted above. In addition to greisen cores, earlier cassiterite (i.e., magmatic and/or deuteric) is overprinted by later mineralizing fluids, as evidenced from the rimming of early cassiterite by stannite and chalcopyrite (e.g., Fig. 3–13A, F, G). The later mineralizing event is evident in higher grade samples that exhibit relatively static K_2O and Al_2O_3 content with higher metal content relative to the least altered samples (Fig. 3–18D). Samples that show complete loss of alkalis and extreme enrichment in SiO_2 (i.e., up to ~88 wt. %; Fig. 3–18E) represent samples of bulk to high-density veining, or hydrothermal brecciation in the Baby Zone, that dominantly contain base-metal ore elements.

3.7.5 Implications of geochronology for magmatic and hydrothermal events in the East Kemptville deposit area

Together with the numerous previous attempts to date the host rock and ore events in the deposit setting (Table 3–4), the present study provides further constraints on the ore-stage event via dating of molybdenite and cassiterite, methods that were not available to earlier workers and

both of which are not easily reset. The timing of the earliest magmatic stage of the ore system, that is the crystallization of the DLP, is constrained by (Fig. 3–22): 1) a 372.8 ± 3.0 Ma U-Pb zircon age (Bickerton et al., 2018); 2) a 375 ± 3 Ma Rb-Sr whole rock isochron (Chatterjee and Cormier, 1991); 3) a 378 ± 3.6 Ma Pb-Pb isochron age for K-feldspars (Dostal and Chatterjee, 1995), although this has a large MSWD value of 6.4 incorporated into the error; and 4) a ca. 375 Ma Ar-Ar biotite age (corrected for updated decay constant; Reynolds et al., 1981). For the EKL, the best estimate of its formation is provided by a Pb-Pb isochron plot for whole rock and minerals (muscovite, K-feldspar) of 367 ± 13 Ma that incorporate an MSWD = 15.8 (Kontak and Chatterjee, 1992). The latter study also provided the best previous age constraint on greisen formation based on a Pb-Pb age of 366 ± 4.5 Ma.

The new ages for magmatic activity at the deposit, based on Re-Os molybdenite and U-Pb cassiterite ages, are represented by a Re-Os molybdenite age of 376 ± 3 Ma for a pegmatite from the Baby Zone and U-Pb cassiterite age of 370.6 ± 7.6 Ma from the Main Zone. These ages overlap with earlier data for the DLP and EKL and thus, importantly, the new data indicate the earliest onset of mineralization in the system was synchronous with magmatic events recorded in the DLP and EKL.

The Re-Os molybdenite and U-Pb cassiterite ages for the mineralized greisens and veins indicate a large range for hydrothermal activity, albeit of three general ages (Fig. 3–22). The older results for hydrothermal events overlap with the aforementioned U-Pb age for magmatic cassiterite and

the Pb-Pb age for the greisen noted above. In contrast to the cassiterite ages, however, the Re-Os molybdenite ages for vein material may indicate three distinct hydrothermal events that overlap with both the early cassiterite ages and the Duck Pond cassiterite age, and potentially outline a hydrothermal event between these two. Thus, these results can be interpreted in at least three different ways: 1) a protracted magmatic-hydrothermal event spanning some 30 Ma; 2) several distinct episodic magmatic-hydrothermal systems; and/or 3) variably resetting of the samples. Each of these is considered below.

Evidence for a protracted magmatic-hydrothermal event is not without precedent, as the Cornish Sn-polymetallic system is documented to span ca. 30 Ma based on multiple studies (Darbyshire and Shepherd, 1985; Chen et al., 1993; Smith et al., 2019; Moscati and Neymark, 2020). In comparison, although the longevity of magmatism for the SMB is extensive, i.e., constrained by U-Pb zircon ages to ca. 15 Ma (see summary in Bickerton et al., 2018), the dating of similar hydrothermal events in the SMB by Re-Os molybdenite and Ar-Ar micas in the New Ross area give restricted ages at ca. 371 Ma (Carruzzo et al., 2000; Selby and Creaser, 2004). Thus, this scenario is discarded. As for episodic events, we note a younger magmatic-hydrothermal event at ca. 360 Ma is well documented in the SW Nova Scotia Sn domain (Fig. 3–2, Table EA 3-1), as noted above. In this scenario, the Duck Pond deposit and the younger ca. 359-355 Ma Re-Os molybdenite ages may indicate a younger event. However, the extent of this event in the East Kemptville deposit setting remains relatively untested in this regard, but do note the pending U-

Pb dating of cassiterite in the Baby Zone where the youngest Re-O age of 343.7 Ma was obtained (see Fig. 3–22). A relevant aspect of the Baby Zone is the presence of the late breccia bodies which are barren. Thus, it might also be considered that this event has acted to mobilize earlier molybdenite and thus overprint the system.

Lastly, the presence of widespread deformation related to the ca. 300 Ma Alleghanian orogenesis in this part of the Meguma terrane (e.g., Muecke et al., 1988; Culshaw and Liesa, 1997; Culshaw and Reynolds, 1997) wholly or partially reset Rb-Sr and Ar-Ar chronometers in the deposit area (see Kontak and Cormier, 1991; Kontak et al., 1995). Although the Re-Os system is generally considered to be robust based on dating overprinted mineralized settings (e.g., Stein et al., 2001; Selby et al., 2007), fine-grained molybdenite is known to sometimes give aberrant results as reflected by younger apparent ages (our unpublished data). Thus, given the highly anomalous age of 343.7 Ma for the Baby Zone sample and its fine grained texture (Fig. 3–6P) relative to the coarse molybdenite used from each of the other samples dated, this possibility cannot be ruled out.

The implications of the geochronology summarized above combined with earlier studies clearly indicate the presence of at least two distinct magmatic-hydrothermal events in the study area; informally referred to as the East Kemptville and Duck Pond events. Whereas the former appears to be constrained to the SW termination of the SMB, the latter event represents the contiguous

development of Sn mineralization in the area which is relevant in the context of both metallogeny and future exploration for additional economic Sn deposits.

3.7.6 An updated model for the East Kemptville Sn deposit

The evidence presented herein indicates the East Kemptville deposit setting evolved from the initial emplacement of the EKL which was followed by the greisen stage that hosts Sn mineralization through several overprinting vein types, both mineralized and barren. Absolute age dating indicates magmatism commenced at ca. 375 Ma and that hydrothermal activity continued for perhaps 10 Ma, or longer if maximum errors are considered. New work relevant to deposit formation is absolute age dating, integration of structural data, recognition of breccias in the Baby Zone and an extensive modern lithogeochemical database. These data and observations provide the basis for a modified model for deposit formation (cf. Halter et al., 1995).

The F-rich melt which gave rise to the EKL was sourced from a highly evolved magma, likely petrogenetically related at source to the zoned DLP, although some geochemical data indicate aspects of this need to be further assessed (e.g., Hf/Zr versus Nb/Ta). Field observations reveal mineralogical and textural features (e.g., stockschieders, layered aplite/pegmatite, USTs, miaroles; Fig. 3–5) that the magma was volatile-saturated upon emplacement. Fluid release that resulted from magma solidification caused the pervasive deuteric alteration of the host (Kontak, 1990a). Also of importance is evidence for the stanniferous nature of this magma, based on the presence of magmatic cassiterite (i.e., in pegmatites and miaroles; Fig. 3–5F, G). Thus, the EKL

likely represents the cupola of a larger progenitor Sn-and base-metal-rich magma that gave rise to the deposit due to its continued fractionation at deeper levels and exploitation of the EKEDSZ (Fig. 3–23A) which facilitated fluid transport to the ore environment, as suggested earlier (Halter et al., 1995).

An important part of the deposit formation is the preferred alignment of the EKL with the EKEDSZ (Figs. 3–2 inset and 3–3A), a feature that is part of a larger structural control to all phases of the SMB, but in particular the later evolved intrusions (Horne et al., 1992). Along with the early greisen development, pegmatites are also aligned with the structural grain, as is the orientation of contained coarse quartz crystals; thus indicates a strong structural control to the ore system from its inception.

A protracted history of activation along the EKEDSZ faults includes movement subsequent to emplacement of the EKL. This included a normal component which juxtaposed Meguma metasedimentary rocks and the EKL (i.e., the keel zone in Richardson et al., 1982; Fig. 3–16A, B). Movement along this structure is inferred to have developed NE-striking and steeply dipping fractures through the deposit area. These latter features localized negative fluid pressure and were exploited as flow conduits by upward migrating greisenizing fluids likely sourced from the same reservoir as for the EKL (see Fig. 3–23A). The importance of this structure for Sn mineralization is evidenced from the contoured Sn grades in the rock proximal the EKEDSZ (Figs. 3–3D, 3–4).

There is no evidence that the East Kemptville greisenizing fluids escaped the system, as an extensive vein system in the wall-rocks is lacking (Kontak and Dostal, 1992) which suggests such fluids were likely entrapped due to sufficient confining pressures outside the ore zones. This prevented metal- and mineral zonation in the deposit area to form, as is common in these deposit settings globally. However, in the latter case, as noted above, the deposits formed at shallower crustal levels where confining pressures and related deviatoric stresses were much different.

Whereas greisen development is dominantly restricted to fault-parallel fractures in the Main Zone, the character of greisens in the Baby Zone indicate there was a more interconnected and extensive fracture networks; similar to the brittle features expected from a step-over zone along a regional shear zone (i.e., the EKEDSZ; cf. Kim et al., 2004). The current spatial distribution of the two ore zones supports the latter setting, as the dominant shear planes recognized in the Baby Zone are offset from the expected NE-SW projection from their documented location in the Main Zone (Figs. 3-3, 3-23A). If the Baby Zone cassiterite is younger (i.e., similar in age to the Duck Pond at ca. 345 Ma), such a change in stress conditions is expected over time.

Cassiterite precipitation in the zoned greisens is attributed to orthomagmatic fluids that underwent a decrease in fO_2 , coupled with an increase in pH during alteration of the EKL (Halter et al., 1996). The multiple-pass fluid flow model of Halter et al. (1998), modeled after that of Heinrich (1990), involved prolonged fluid-rock interaction that led to zoned greisen formation

along fracture planes. This model also explains formation of the massive greisens whereby fluids accessed areas with greater density of fractures, hence a pervasive greisenization could occur. Additionally, the hydrothermal breccias (HBX) that are locally mineralized in the Baby Zone suggest mineralizing fluid were less restricted to the EKL than in the Main Zone, and infiltrated the down-dropped block of metasedimentary rocks through brecciating fluid pathways (e.g., Fig. 3–23B).

Although no cassiterite from the Baby Zone was dated, if the HBX unit formed synchronously with mineralization in the Main Zone, the U-Pb cassiterite and Re-Os molybdenite from this stage of the paragenesis indicate an age between ca. 370 and 360 Ma (Fig. 3–22). The high-grade, but low-tonnage of the Baby zone, therefore, reflects a localized zone of greater permeability for mineralizing fluids that brecciated the wall-rock sometime between EKL emplacement at ca. 370 Ma and the precipitation of mineralized veins in the Main Zone at ca. 360 Ma.

Subsequent to the main mineralizing event, the Baby Zone step-over is further exploited by a magmatic breccia (IBX) that follows the EKEDSZ, overprints the main greisen event and HBX formation, and is dominantly barren of Sn and base-metals (Fig. 3–23C). The timing of this event is weakly constrained by Re-Os molybdenite to ca. 345 Ma (Fig. 3–22); thus of similar age to the Duck Pond event. Ductile deformation along the EKEDSZ is subsequently recorded by each of the above stages, particularly along fractures parallel to the EKEDSZ in the Main Zone,

indicating the regional structure was re-activated with significant strain at this time. This is further evidenced by the widespread resetting of Rb-Sr and Ar-Ar chronometers in the southwestern Meguma terrane, including in the EKL (Kontak and Cormier, 1991; Kontak et al., 1995), which is attributed to tectonothermal activity rarely reported in the eastern part of the terrane. The latter is likely due to the rapid differential uplift recorded by the Horton Group which onlaps the exhumed northern part of the SMB by ~355 Ma (Martel et al., 1993; Murphy, 2000; Archibald et al., 2018). Thus the southwestern end of the SMB likely remained at depth and was subject to a series of tectonothermal events between 370 and 310 Ma (e.g., Kontak et al., 1995, and references therein) along major shear zones such as the EKEDSZ which in part relate to the Alleghanian orogeny (Culshaw and Liesa, 1997; Culshaw and Reynolds, 1997).

3.7.7 Source of Sn

The source of metals (e.g., Sn, W) in progenitor magmas hosting or related to rare-metal mineralization has long been debated (e.g., Schuiling, 1967; Schneider and Lehmann, 1977; Romer and Kroner, 2015, 2016; Jiang et al., 2018; Neymark et al., 2021). The genesis of Sn-W deposits in the northern Appalachians has recently been suggested to represent magma contamination by metal-enriched protolith(s), whereby the melts eventually fractionate to form LCT-type pegmatites and evolved felsic magmas with associated Sn \pm W magmatic-hydrothermal fluids (e.g., Romer and Kroner, 2015, 2016); this model is similar to the proposed origin for Sn-enrichment in the Erzgebirge Mountains. The SMB hosts the East Kemptville

deposit in the most fractionated part of one of its stage 2 intrusions, the DLP (Kontak, 1990a; Dostal and Chatterjee, 1995; Dostal et al., 2004). The SMB, based on its $^{87}\text{Sr}/^{86}\text{Sr}$ and $^{143}\text{Nd}/^{144}\text{Nd}$ isotopic signatures and a major element chemistry, has been interpreted to have assimilated up to ~30% Meguma metasedimentary country-rock (Clarke et al., 2004), although more recent work suggests a maximum of 10–20% (Shellnutt and Dostal, 2012). Thus, we assess the chemistry of the metasedimentary country rocks as a potential source of metals for the SMB by comparing their whole-rock lithochemical signature in the SW part of the Meguma terrane against that of the DLP and the EKL in both the Main and Baby zones.

The trace-element contents of the relevant sedimentary and igneous rocks are shown normalized to the upper continental crust in Figure 3–24. In Figure 3–24A, the data for the Meguma metasedimentary rocks proximal and distal to the deposit area (labelled as “Proximal DLP” and “Distal to DLP”, respectively), whereas Figure 3–24B shows values for the least-altered EKL from both ore zones as well as the DLP. The Meguma metasedimentary rocks proximal to the deposit have a signature that is similar to that of the upper-continental crust, with enrichment of Mo and W. Although the EKL in both ore zones and the DLP are enriched in Sn and Ta relative to upper continental crust (Fig. 3–24B), the surrounding wall-rocks regionally show anomalous depletions in these elements. Metasedimentary rocks distal to the deposit are also enriched in Mo and W, however, they have an enrichment in Sn relative to the deposit proximal samples (Fig. 3–24A). Thus, given the wall-rock chemistry and the absence of Sn mineralization through the rest

of the SMB, local metal endowment by contamination of Sn-enriched metasedimentary rocks is not reasonable for the DLP. In addition and also relevant to the contamination model, we note that the EKL is not anomalous in its $\delta^{18}\text{O}$ values compared to the SMB (Kontak, 1990a; Kontak et al., 2001), as the contaminant model would imply with assimilation of Meguma sedimentary rocks with much higher $\delta^{18}\text{O}$ signatures (e.g., Longstaffe et al., 1980).

3.8 Conclusions

Alteration at the East Kemptville deposit occurred in distinct mineralogical stages after emplacement of the EKL with a spatial and temporal overlap: 1) deuteric alteration through the deposit area represented by weak pervasive partial replacement of calcic plagioclase and K-feldspar by albite, sericite, and apatite precipitation, the latter of which occurs in the pore space created by albitization; 2) strong to intense sericitization and muscovite \pm Fe-Li mica formation that is localized to zones proximal brittle fractures through the deposit and represent the early stages of greisen formation, as proposed by Halter et al. (1996); and 3) complete replacement of the host EKL by quartz and topaz with lesser muscovite and ore mineralization that represent well developed greisens (e.g., zoned greisen cores). Chemically, the evolution of each alteration stage above is recognized by distribution of Pearce element ratios for alkali elements and Al in the deposit; they reflect a subtle increase in Na during deuteric event (1), a relative increase in Al and K during initial greisen formation (2), and a steep drop in alkali element content with relative increases in Al in the final stages of greisen formation (3).

The two dominant character types of greisens in the deposit (i.e., massive and zoned) likely reflect the variation in fluid:rock interaction through the deposit: 1) the wide intervals of massive greisens have uniform texture and grade due to pervasive greisen formation in zones with a high density of brittle fractures, allowing for interconnected fluid flow during CDP processes; and 2) zoned greisens which display typical cores of coarse quartz-topaz-cassiterite that transition to outer zones of sericitized EKL represent multiple pass fluid flow along NE-trending vertical brittle fractures, these fractures are parallel to the regional EKEDSZ and acted as critical transport conduits for the mineralizing fluids in the deposit area. Notably, the higher density brittle fracture patterns (and thus massive greisens) are interpreted to favor the Baby Zone due to its localization in a step-over transtensional zone along the EKEDSZ, whereas the Main Zone represents dominantly transpressional fracture development.

The absence of metal zonation typical to granophile-element deposits at East Kemptville (i.e., no vertical or horizontal mineral and metal zonation) is reconciled by telescoping of a system where mineralizing fluids were unable to escape the host EKL due to significant lithostatic pressures that allowed for wall-rocks to act as an impermeable cap during deposit formation. Although no metal or mineral zonation is observed, there is a parity between ore zones in the typical grades, historically, due to the dominant character type of greisens: high-grade samples in the Main Zone are restricted to the cores of zoned greisens, and thus are diluted in bulk sampling by a gangue mineralogy with alkali content similar to weakly altered EKL; and 2) high-grade samples

in the Baby Zone, however, are typically part of more homogeneous massive greisens with fine-grained cassiterite and quartz-topaz gangue mineralogy through the rock that is sampled.

The age of early greisen-related mineralization at the East Kemptville deposit is associated with U-Pb cassiterite at 370 ± 4 Ma and Re-Os molybdenite at 371 ± 2.0 Ma. This age is ca. 5–10 Ma younger than the interpreted crystallization of the host EKL, determined from molybdenite in a pegmatite at the East Kemptville deposit to be 376.2 ± 3.3 Ma, and ≥ 10 Ma older than younger mineralization associated with veins that crosscut the deposit as part of reactivation along the EKEDSZ corridor; i.e., Re-Os molybdenite in veinlets at 354.9 ± 2.0 Ma and 343.7 ± 1.7 Ma.

In a regional context, the East Kemptville deposit is similar in age to other Sn-deposits in the northern Appalachians. These mineralized centers are associated with intrusions of similar composition to that of the EKL, however, East Kemptville differs in that it is formed in a mesothermal setting and is hosted by country rocks of the Meguma terrane; at the most outboard lithotectonic entity in the northern Appalachians. The latter has been proposed as a source of Sn via contamination in melts that formed the SMB, and thus led to enrichment in the East Kemptville deposit (Romer and Kroner, 2015, 2016). However, the distinct host terranes to other Sn deposits in the region with various host lithologies, in addition a relative depletion of Sn in metasedimentary rock proximal the mineralized EKL with respect to similar host rocks for the unmineralized parts of the SMB, is evidence to the contrary. To resolve a potential Sn-source and mode of ore deposition at East Kemptville, further investigation into the petrogenesis of the

host Davis Lake Pluton and SMB, as well as of the hydrothermal evolution of the deposit is warranted to place East Kemptville history relative to the rest of the metallogenic belt.

3.9 Acknowledgments

Funding for this project was provided by Avalon Advanced Materials, Inc. and by the National Science and Engineering Research Council of Canada (NSERC) as part of a collaborative research and development (CRD) grant to I.M. Samson, D.J. Kontak, and J.B. Murphy. Thanks to Cliff Stanley and Jason Willson for a valuable discussion, the latter of whom also provided assistance in the field. Many thanks to the staff at Laurentian University and Saint Mary's University for support during this study. We thank Bill Mercer (Avalon Advanced Materials, Inc.) for providing unpublished geochemical data from the East Kemptville deposit area. We also like to thank Chris White for assistance in compiling litho-geochemical data from the region.

3.10 References

Archibald, D.B., Murphy, J.B., Reddy, S.M., Jourdan, F., Gillespie, J., and Glorie, S., 2018, Post-accretionary exhumation of the Meguma terrane relative to the Avalon terrane in the Canadian Appalachians: *Tectonophysics*, v. 747, p. 343–356.

- Ballouard, C., Poujol, M., Boulvais, P., Branquet, Y., Tartèse, R. and Vigneresse, J.L., 2016, Nb-Ta fractionation in peraluminous granites: A marker of the magmatic-hydrothermal transition: *Geology*, v. 44, p. 231–234.
- Bau, M., 1996, Controls on the fractionation of isovalent trace elements in magmatic and aqueous systems: evidence from Y/Ho, Zr/Hf, and lanthanide tetrad effect: *Contributions to Mineralogy and Petrology*, v. 123, p. 323–333.
- Benn, K., Horne, R.J., Kontak, D.J., Pignotta, G.S., and Evans, N.G., 1997, Syn-Acadian emplacement model for the South Mountain Batholith, Meguma Terrane, Nova Scotia: Magnetic fabric and structural analyses: *Geological Society of America Bulletin*, v. 109, p. 1279–1293.
- Benn, K., Roest, W.R., Rochette, P., Evans, N.G., and Pignotta, G.S., 1999, Geophysical and structural signatures of syntectonic batholith construction: the South Mountain Batholith, Meguma Terrane, Nova Scotia: *Geophysics Journal International*, v. 136, p. 144–158.
- Bickerton, L., Kontak, D.J., Samson, I.M., Murphy, J.B., and Kellett, D.A., 2018, U-Pb geochronology of the South Mountain Batholith, Nova Scotia, in Rogers, N., ed., *Targeted Geoscience Initiative: 2017 report of activities, volume 1: Geological Survey of Canada, Open File 8358*, p. 51–55.

- Blevin, P.L. and Chappell, B.W., 1992, The role of magma sources, oxidation states and fractionation in determining the granite metallogeny of eastern Australia: *Transactions of the Royal Society of Edinburgh: Earth Sciences*, v. 83, p. 305–316.
- Blevin, P.L. and Chappell, B.W., 1995, Chemistry, origin, and evolution of mineralized granites in the Lachlan fold belt, Australia; the metallogeny of I- and S-type granites: *Economic Geology*, v. 90, p. 1604–1619.
- Burnham, C.W., 1979, Magmas and hydrothermal fluids, in Barnes, H.L., ed., *Geochemistry of hydrothermal ore deposits*: John Wiley and Sons, New York, p. 71–136.
- Breiter, K., 2002, From explosive breccia to unidirectional solidification textures: magmatic evolution of a phosphorus- and fluorine-rich granite system (Podlesí, Krušné hory Mts., Czech Republic): *Bulletin Czech Geological Survey*, v. 77, p. 67–92.
- Breiter, K., Frýda, J., Seltmann, R., and Thomas, R., 1997, Mineralogical evidence for two magmatic stages in the evolution of an extremely fractionated P-rich rare-metal granite: the Podlesí stock, Krušné hory, Czech Republic: *Journal of Petrology*, v. 38, p. 1723–1739.
- Breiter, K., Müller, A., Leichmann, J. and Gabašová, A., 2005, Textural and chemical evolution of a fractionated granitic system: the Podlesí stock, Czech Republic: *Lithos*, v. 80, p. 323–345.

- Breiter, K., 2012, Nearly contemporaneous evolution of the A- and S-type fractionated granites in the Krušné hory/Erzgebirge Mts., Central Europe: *Lithos*, v. 151, p. 105–121.
- Candela, P.A., and Blevin, P.L., 1995, Do some miarolitic granites preserve evidence of magmatic volatile phase permeability?: *Economic Geology*, v. 90, p. 2310–2316.
- Carruzzo S., Kontak D.J., and Clarke D. B., 2000, Granite-hosted mineral deposits of the New Ross area, South Mountain, Nova Scotia, Canada: P, T and X constraints of fluids using fluid inclusion thermometry and decrepitate analysis: *Transactions of the Royal Society Edinburgh Earth Science*, v. 91, p. 303–319.
- Černý, P., and Ercit, T.S., 2005, The classification of granitic pegmatites revisited: *The Canadian Mineralogist*, v. 43, p. 2005–2026.
- Černý, P., Blevin, P.L., Cuney, M., London, D., 2005, Granite related ore deposits: *Economic Geology 100th Anniversary Volume*, p. 337–370.
- Chappell, B.W. and White, A.J.R., 1992, I- and S-type granites in the Lachlan Fold Belt. *Transactions of the Royal Society of Edinburgh: Earth Sciences*, v. 83, p. 1–26.
- Chappell, B.W., and Hine, R., 2006, The Cornubian Batholith: an example of magmatic fractionation on a crustal scale: *Resource Geology*, v. 56, p. 203–244.
- Charoy, B., and Pollard, P.J., 1989, Albite-Rich, Silica-Depleted Metasomatic Rocks at Emuford, Northeast Queensland: *Mineralogical, Geochemical, and Fluid Inclusion*

- Constraints on Hydrothermal Evolution and Tin Mineralization: *Economic Geology*, v. 84, p. 1850–1874.
- Chatterjee, A.K., and Cormier, R.F., 1991, A Rb-Sr geochronological study of the Davis Lake pluton, South Mountain batholith, southern Nova Scotia: evidence of a 374 Ma time of emplacement, in MacDonald, D.R., ed., *Nova Scotia Department of Mines and Energy: Report 91-A*, 19p.
- Chatterjee, A.K., and Strong, D.F., 1985, Geochemical characteristics of the polymetallic tin domain, southwestern Nova Scotia, Canada [ext. abs.]: in Taylor, R.P. and Strong, D.F., eds., *Granite-Related Mineral Deposits: Geology, Petrogenesis and Tectonic Setting: Canadian Institute of Mining and Metallurgy, Extended Abstracts*, p. 41–52.
- Chatterjee, A.K., Strong, D.F., and Muecke, G.K., 1983, A multivariate approach to geochemical distinction between tin-specialized and uranium-specialized granites of southern Nova Scotia: *Canadian Journal of Earth Sciences*, v. 20, p. 420–430.
- Chen, Y., Clark, A.H., Farrar, E., Wasteneys, H., Hodgson, M.J. and Bromley, A.V., 1993, Diachronous and independent histories of plutonism and mineralization in the Cornubian Batholith, southwest England: *Journal of the Geological Society*, v. 150, p. 1183–1191.
- Clarke, D.B., MacDonald, M.A., Reynolds, P.H., and Longstaffe, F.J., 1993, Leucogranites from the eastern part of the South Mountain Batholith, Nova Scotia: *Journal of Petrology*, v. 34, p. 653–679.

- Clarke, D.B., MacDonald, M.A., and Tate, M.C., 1997, Late Devonian mafic-felsic magmatism in the Meguma Zone, Nova Scotia, in Sinha, A.K., Whalen, J.B., Hogan, J.P., eds., The nature of magmatism in the Appalachian Orogen: Geological Society America Memoir, v. 191, p. 107–127.
- Clarke, D.B., MacDonald, M.A., and Erdmann, S., 2004, Chemical variation in Al_2O_3 – CaO – Na_2O – K_2O space: controls on the peraluminosity of the South Mountain Batholith: Canadian Journal of Earth Sciences, v. 41, p. 785–798.
- Cobbing, E.J., Mallick, D.I.J., Pitfield, P.E.J., and Teoh, L.H., 1986, The granites of the Southeast Asian tin belt: Journal of the Geological Society of London, v. 143, p. 537–550.
- Culshaw, N., and Liesa, M., 1997, Alleghanian reactivation of the Acadian fold belt, Meguma Zone, southwest Nova Scotia: Canadian Journal of Earth Sciences, v. 34, p. 833–847.
- Culshaw, N., and Reynolds, P., 1997, $^{40}\text{Ar}/^{39}\text{Ar}$ age of shear zones in the southwest Meguma Zone between Yarmouth and Meteghan, Nova Scotia: Canadian Journal of Earth Sciences, v. 34, p. 848–853.
- Culshaw, N., and Lee, S.K., 2006, The Acadian fold belt in the Meguma Terrane, Nova Scotia: Cross sections, fold mechanisms, and tectonic implications: Tectonics, v. 25, 16p.

- Cuney, M., Marignac, C., and Weisbrod, A., 1992, The Beauvoir Topaz-Lepidolite Albite Granite (Massif Central, France): The Disseminated Magmatic Sn-Li-Ta-Nb-Be Mineralization. *Economic Geology*, v. 87, p. 1766–1794.
- Dallmeyer, R.D., and Keppie, J. D., 1987, Polyphase Late Paleozoic tectonothermal evolution of the southwestern Meguma Terrane, Nova Scotia: evidence from $^{40}\text{Ar}/^{39}\text{Ar}$ mineral ages: *Canadian Journal of Earth Sciences*, v. 24, p. 1242–1254.
- Darbyshire, D.P.F., and Shepherd, T.J., 1985, Chronology of granite magmatism and associated mineralization, SW England: *Journal of the Geological Society*, v. 142, p. 1159–1177.
- Dilles, J.H., 1987, Petrology of the Yerington Batholith, Nevada; evidence for evolution of porphyry copper ore fluids: *Economic Geology*, v. 82, p. 1750–1789.
- Dolejš, D., and Štemprok, M., 2001, Magmatic and hydrothermal evolution of Li-F granites: Cínovec and Krásno intrusions, Krušné hory batholith, Czech Republic: *Bulletin Czech Geological Survey*, v. 76, p. 77–99.
- Dostal, J., and Chatterjee, A. K., 1995, Origin of topaz-bearing and related peraluminous granites of late Devonian Davis Lake pluton, Nova Scotia, Canada: *Chemical Geology*, v. 123, p. 67–88.
- Dostal, J., and Chatterjee, A.K., 2000, Contrasting behaviour of Nb/Ta and Zr/Hf ratios in a peraluminous granitic pluton (Nova Scotia, Canada): *Chemical Geology*, v. 163, p. 207–218.

- Dostal, J., Chatterjee, A.K., and Kontak, D.J., 2004, Chemical and isotopic (Pb, Sr) zonation in a peraluminous granite pluton: role of fluid fractionation: *Contributions to Mineralogy and Petrology*, v. 147, p. 74–90.
- Dostal, J., Kontak, D.J., Gerel, O., Shellnut, J.G., Fayek, M., 2015, Cretaceous ongonites (topaz-bearing albite-rich microleucogranites) from Ongon Khairkhan, Central Mongolia: Products of extreme magmatic fractionation and pervasive metasomatic fluid:rock interaction: *Lithos*, v. 236–237, p. 173–189.
- Duc-Tin, Q., and Keppler, H., 2015, Monazite and xenotime solubility in granitic melts and the origin of the lanthanide tetrad effect: *Contributions to Mineralogy and Petrology*, v. 169, p. 1–26.
- Eliasson, T., and Petersson, J., 1996, Deuteric accessory phases in the Bohus granite, SW Sweden. *GFF*, v. 118, p. 12–13.
- Halter, W.E., Williams-Jones, A.E., and Kontak, D.J., 1995a, Origin and Evolution of the Greisenizing Fluid at the East Kemptville Tin Deposit, Nova Scotia, Canada: *Economic Geology*, v. 93, p. 1026–1051.
- Halter, W.E., Williams-Jones, A.E., and Kontak, D.J., 1995b, REE mobility during albitite formation at the East Kemptville tin deposit, Nova Scotia, in MacDonald, D.R., ed., *Mines and Minerals Branch Report of Activities 1994: Nova Scotia Department of Natural Resources*, Report 95-1, p. 91-97.

- Halter, W.E., Williams-Jones, A.E., and Kontak, D.J., 1996, The role of greisenization in cassiterite precipitation at the East Kemptville tin deposit, Nova Scotia: *Economic Geology*, v. 91, p. 368–385.
- Halter W.E., Williams-Jones A.E., and Kontak D.J., 1998, Origin and evolution of the greisenizing fluid at the East Kemptville tin deposit, Nova Scotia, Canada: *Economic Geology*, 93, 1026–1051.
- Hartman, S.M., Paterson, S.R., Holk, G.J. and Kirkpatrick, J.D., 2018, Structural and hydrothermal evolution of a strike-slip shear zone during a ductile-brittle transition, Sierra Nevada, CA: *Journal of Structural Geology*, v. 113, p. 134–154.
- Heinrich, C.A., 1990, The chemistry of hydrothermal tin (-tungsten) ore deposition: *Economic Geology*, v. 85, p. 457–481.
- Heinrich C.A., 1995, Geochemical evolution and hydrothermal mineral deposition in Sn (-W-base-metalbase-metal) and other granite-related ore systems: Some conclusions from Australian examples: *Short Course Handbook*, Mineralogical Association of Canada, v. 23, p. 203–220.
- Hibbard, J.P., van Staal, C.R., and Rankin, D.W., 2010, Comparative analysis of the geological evolution of the northern and southern Appalachian orogen: Late Ordovician–Permian, in Tollo, R.P., Bartholomew, M.J., Hibbard, J.P., and Karabinos, P.M., eds., *From Rodinia*

- to Pangea: The Lithotectonic Record of the Appalachian Region: Geological Society of America Memoir, v. 206, p. 51–69.
- Hicks, R.J., Jamieson, R.A. and Reynolds, P.H., 1999, Detrital and metamorphic $^{40}\text{Ar}/^{39}\text{Ar}$ ages from muscovite and whole-rock samples, Meguma Supergroup, southern Nova Scotia: Canadian Journal of Earth Sciences, v. 36, p. 23–32.
- Hilchie, L.J., and Jamieson, R.A., 2014, Graphite thermometry in a low-pressure contact aureole, Halifax, Nova Scotia: Lithos, v. 208, p. 21–33.
- Horne, R.J., MacDonald, M.A., Corey, M.C., and Ham, L.J., 1992, Structure and emplacement of the South Mountain Batholith, southwestern Nova Scotia: Atlantic Geology, v. 28, p. 29–50.
- Irber, W., 1999, The lanthanide tetrad effect and its correlation with K/Rb, Eu/Eu*, Sr/Eu, Y/Ho, and Zr/Hf of evolving peraluminous granite suites. *Geochimica Cosmochimica Acta*, v. 63, p. 489–508.
- Ishihara, S., Hua, R., Hoshino, M., and Murakami, H., 2008, REE abundance and REE minerals in granitic rocks in the Nanling Range, Jianxi Province, Southern China, and generation of REE-rich weathered crust deposits: *Resource Geology*, v. 58, p. 355–372.
- Jahn, B.M., Wu, F., Capdevila, R., Martineau, F., Zhao, Z. and Wang, Y., 2001, Highly evolved juvenile granites with tetrad REE patterns: the Woduhe and Baerzhe granites from the Great Xing'an Mountains in NE China: *Lithos*, v. 59, p. 171–198.

- Jarchovský, T., 2006, The nature and genesis of greisen stocks at Krásno, Slavkovský les area—Western Bohemia, Czech Republic: *Journal of the Czech Geological Society*, v. 51, p. 201–216.
- Jébrak, M., 1997, Hydrothermal breccias in vein-type ore deposits: A review of mechanisms, morphology and size distribution: *Ore Geology Reviews*, v. 12, p. 111–134.
- Jiang, W., Li, H., Evans, N.J., Wu, J. and Cao, J., 2018, Metal Sources of World-Class Polymetallic W–Sn Skarns in the Nanling Range, South China: Granites versus Sedimentary Rocks?: *Minerals*, v. 8, p. 265.
- Kelly, W.C., and Turneure, F.S., 1970, Mineralogy, paragenesis and geothermometry of the tin and tungsten deposits of the Eastern Andes, Bolivia: *Economic Geology*, v. 65, p. 609–680.
- Kendall, T.G., 2017, An investigation of infrared spectral features related to the presence of lithium in micas, East Kemptville tin deposit, Nova Scotia: BSc thesis, Saint Mary's University: 53p.
- Keppie, J.D., 1993, Synthesis of Palaeozoic deformational events and terrane accretion in the Canadian Appalachians: *Geologische Rundschau*, v. 82, p. 381–431.
- Kerr, A., and McNicoll, V., 2012, New U–Pb geochronological constraints from mineralized granites in southern Newfoundland, in *Current Research: Newfoundland Department of Natural Resources, Geological Survey, Report 12-1*, p. 21–38.

- Kim, Y.-S., Peacock, D.C.P., and Sanderson, D.J., 2004, Fault damage zones: *Journal of Structural Geology*, v. 26, p. 503–517.
- Kirkham, R.V., and Sinclair, W.D., 1988, Comb quartz layers in felsic intrusions and their relationship to porphyry deposits, in Taylor, R.P. and Strong, D.F., eds., *Recent advances in the geology of granite-related mineral deposits: Canadian Institute of Mining and Metallurgy Special Volume 39*, p. 50–71.
- Kirwin, D.J., 2005, Unidirectional solidification textures associated with intrusion-related Mongolian mineral deposits, in Seltmann, R., Gerel, O., and Kirwin, D.J., eds., *Geodynamics and Metallogeny of Mongolia with a Special Emphasis on Copper and Gold Deposits: International Association on the Genesis of Ore Deposits, Guidebook Series 11*, CERCAMS/NHM London, p. 63–84.
- Kontak, D.J., 1990a, The East Kemptville topaz-muscovite leucogranite, Nova Scotia. I. Geological setting and whole rock geochemistry: *Canadian Mineralogist*, v. 28, p. 787–825.
- Kontak, D.J., 1990b, A sulfur isotopic study of main-stage tin and base-metal-base-metal mineralization at the East Kemptville tin deposit, Yarmouth County, Nova Scotia, Canada: evidence for magmatic origin of metals and sulfur: *Economic Geology*, v. 85, p. 399–407.

- Kontak, D.J., 1991, The East Kemptville topaz-muscovite leucogranite, Nova Scotia: U. Mineral chemistry: *Canadian Mineralogist*, v. 29, p. 37–60.
- Kontak, D.J., 1994, Geological and geochemical studies of alteration processes in a fluorine-rich environment: the East Kemptville Sn-(Zn-Cu-Ag) deposit, Yarmouth County, Nova Scotia, Canada, in Lentz, D.R., ed., *Alteration and Alteration Processes associated with Ore-forming Systems: Geological Association of Canada, Short Course Notes*, v. 11, p. 261–314.
- Kontak, D.J., and Chatterjee, A.K., 1992, The East Kemptville tin deposit, Yarmouth County, Nova Scotia: a Pb-isotope study of the leucogranite and mineralized greisens- evidence for a 366 Ma metallogenic event, *Canadian Journal of Earth Science*, v. 29, p. 1180–1196.
- Kontak, D.J., and Clark, A.H., 2002, Genesis of the giant, bonanza San Rafael lode tin deposit, Peru: origin and significance of pervasive alteration: *Economic Geology*, v. 97, p. 1741–1777.
- Kontak, D.J., and Cormier, R.F., 1991, Geochronological evidence for multiple tectono-thermal overprinting events in the East Kemptville muscovite-topaz leucogranite, Yarmouth County, Nova Scotia, Canada: *Canadian Journal of Earth Science*, v. 28, p. 209–224.

- Kontak, D.J., and Dostal, J., 1992, The East Kemptville tin deposit, Yarmouth County, southwestern Nova Scotia: a lithogeochemical study of the wallrock metasedimentary rocks: *Atlantic Geology*, v. 28, p. 63–83.
- Kontak, D.J., Mulja, T., and Hingston, R., 1986, The East Kemptville Sn deposit: preliminary results from recent mapping, in Bates, J.L., and MacDonald, D.R., eds., Tenth annual open house and review of activities: Nova Scotia Department of Mines and Energy, Information Series 12, p. 97–103.
- Kontak, D.J., Tuach, J., Strong, D.F., Archibald, D.A., and Farrar, E., 1988, Plutonic and hydrothermal events in the Ackley Granite, southeast Newfoundland, as indicated by total-fusion $^{40}\text{Ar}/^{39}\text{Ar}$ geochronology: *Canadian Journal of Earth Sciences*, v. 25, p. 1151-1160.
- Kontak, D.J., O'Reilly, G.A., and Chatterjee, A.K., 1990, The southwest Nova Scotia tin domain, Yarmouth County, Nova Scotia: implications for tin metallogeny in the Meguma Terrane, Nova Scotia, in MacDonald, D.R., ed., Mines and Minerals Branch Report of Activities for 1989, Part B: Nova Scotia Department of Mines and Energy, Report 90-1, p. 13–32.
- Kontak, D.J., Farrar, E., McBride, S.M., and Martin, R.F., 1995, Mineral chemistry and $^{40}\text{Ar}/^{39}\text{Ar}$ dating of muscovite from the East Kemptville leucogranite, southern Nova Scotia: evidence for localised resetting of $^{40}\text{Ar}/^{39}\text{Ar}$ systematics in a shear zone: *Canadian Mineralogist*, v. 33, p. 1237–1253.

- Kontak, D.J., Martin, R.F. and Richard, L., 1996, Patterns of phosphorus enrichment in alkali feldspar, South Mountain batholith, Nova Scotia, Canada: *European Journal of Mineralogy*, v. 8, p. 805-824.
- Kontak, D.J., Dostal, J., Ansdell, K., Halter, W., Martin, R.F. and Williams-Jones, A.E., 2001, The nature and origin of pegmatite in a fluorine-rich leucogranite, East Kemptville, Nova Scotia: *Transactions of the Royal Society of Edinburgh: Earth Sciences*, v. 92, p. 173–200.
- Kontak, D.J., Dunning, G., and Creaser, R., 2003, U/Pb and Re/Os dating of the South Mountain and Musquodoboit batholiths, Nova Scotia: evidence for protracted magmatic-hydrothermal events: *Joint Meeting Northeastern Section Geological Society of America-Atlantic Geoscience Society, Program with Abstracts*.
- Kontak, D.J., Ham, L.J. and Dunning, G., 2004, U-Pb dating of the Musquodoboit Batholith, southern Nova Scotia: evidence for a protracted magmatic-hydrothermal event in a Devonian intrusion: *Atlantic Geology*, v. 40, p. 207–216.
- Kontak, D.J., Horne, R.J., Bertrand, A., and Creaser, R., 2012, Post 380 Ma granophile mineralization in southwest Nova Scotia, Canada: Evidence from the Clayton Hill and Gardners Meadow mineralized centres: *Atlantic Geology*, v. 48, p. 34–35.
- Kontak, D.J., Horne, R.J., Creaser, R.A., Petrus, J.A., and Archibald, D., 2013, A petrological and geochronological study of a 360 Ma metallogenic event in Maritime Canada with

- implications for lithophile-metal mineralization in the Canadian Appalachians: *Canadian Journal of Earth Sciences*, v. 50, p. 1147–1163.
- Kontak, D.J., Alimohammadi, M., and Watts, K., 2014, The Gardners Meadow Sn-Zn-Cu showing of southwest Nova Scotia: A small but not insignificant ca. 360 Ma metallogenic event: *Atlantic Geoscience Society Abstracts: 40th Annual Colloquium & Annual General Meeting 2014*.
- Lee, M.R., Waldron, K.A., and Parsons, I., 1995, Exsolution and alteration microtextures in alkali feldspar phenocrysts from the Shap granite. *Mineralogical Magazine*, v. 59, p. 63–78.
- Lehmann, B., 2020, Formation of tin ore deposits: A reassessment: *Lithos*, 105756.
- Linnen, R.L., Williams-Jones, A.E., and Martin, R.F., 1992, Evidence of magmatic cassiterite mineralisation at the Nong Sua aplite pegmatite complex, Thailand: *Canadian Mineralogist*, v. 30, p. 739-61.
- London, D., 1997, Estimating abundances of volatile and other mobile components in evolved silicic melts through mineral–melt equilibria: *Journal of Petrology*, v. 38, p. 1691–1706.
- London, D., Morgan, C.B., Hervig, R.I., 1989, Vapour-undersaturated experiments with Macusani glass+ H₂O at 200 MPa, and their internal differentiation of granitic pegmatites: *Contributions to Mineralogy and Petrology*, v. 102, p. 1–17.

- Longstaffe, F.J., Smith, T.E. and Muehlenbachs, K., 1980, Oxygen isotope evidence for the genesis of Upper Paleozoic granitoids from southwestern Nova Scotia: *Canadian Journal of Earth Sciences*, v. 17, p. 132–141.
- Lowenstern, J.B., and Sinclair, W.D., 1996, Exsolved magmatic fluid and its role in the formation of comb-layered quartz at the Cretaceous Logtung W- Mo deposit, Yukon Territory, Canada: *Transactions of the Royal Society of Edinburgh: Earth Sciences*, v. 87, p. 291–303.
- MacDonald, M.A., Horne, R.J., Corey, M.C., and Ham, L.J., 1992, An overview of recent bedrock mapping and follow-up petrological studies of the South Mountain batholith, southwestern Nova Scotia, Canada: *Atlantic Geology*, v. 28, p. 7–28.
- MacDonald, M.A., 2001, *Geology of the South Mountain Batholith, southwestern Nova Scotia*: Nova Scotia Department of Natural Resources Open File Report ME2001-2.
- Manning, D.A.C., 1981, The effect of fluorine on liquidus phase relationships in the system Qz–Ab–Or with excess water at 1 kbar: *Contributions to Mineralogy and Petrology*, v. 76, p. 206–215.
- Manning, D.A.C., Pichavant, M., 1988, Volatiles and their bearing on the behavior of metals in granitic systems, in Taylor, R.P., and Strong, D.F., eds., *Recent Advances in the Geology of Granite-Related Mineral Deposits*: Canadian Institute of Mining and Metallurgy, Special Volume 39, p. 13–24.

- Mark, G., 1998, Albitite formation by selective pervasive sodic alteration of tonalite plutons in the Cloncurry district, Queensland: *Australian Journal of Earth Sciences*, v. 45, p. 765–774.
- Martel, A.T., McGregor, D.C. and Utting, J., 1993, Stratigraphic significance of Upper Devonian and Lower Carboniferous miospores from the type area of the Horton Group, Nova Scotia: *Canadian Journal of Earth Sciences*, v. 30, p. 1091–1098.
- Martel, C., Pichavant, M., Di Carlo, I., Champallier, R., Wille, G., Castro, J.M., Devineau, K., Davydova, V.O. and Kushnir, A.R., 2021, Experimental Constraints on the Crystallization of Silica Phases in Silicic Magmas: *Journal of Petrology*, v. 62, p. 1–18.
- Massonne, H.J., Clarke, D.B., and MacDonald, M.A., 2010, Intrusion level of the Musquodoboit Batholith in Nova Scotia, Canada—a case study: *Zeitschrift für Geologische Wissenschaften*, v. 38, p. 181–194.
- Masuda, A., and Akagi, T., 1990, Lanthanide tetrad effect observed in leucogranites from China: *Geochemical Journal*, v. 23, p. 245–253.
- McAuslan, D.A., Dickie, G.B., Sarkar, P., Sinclair, P.E., and Wilson, B.H., 1980, The history of discovery and the description of the East Kemptville tin deposit southwest Nova Scotia: *Canadian Institute of Mining and Metallurgy*, v. 73, p. 78–79.
- McDonough, W.F., and Sun, S.S., 1995, The composition of the Earth: *Chemical geology*, v. 120, p. 223–253.

- McNicoll, V.J., Squires, G.C., Wardle, R.J., Dunning, G.R. and O'Brien, B.H., 2006, U–Pb geochronological evidence for Devonian deformation and gold mineralization in the eastern Dunnage Zone, Newfoundland, in *Current Research: Government of Newfoundland and Labrador, Department of Natural Resources, Geological Survey, Report 06-1*, p. 45–60.
- Micklethwaite, S., Sheldon, H.A., and Baker, T., 2010, Active fault and shear processes and their implications for mineral deposit formation and discovery: *Journal of Structural Geology*, v. 32, p. 151–165.
- Moran, P.C., Barr, S.M., White, C.E., and Hamilton, M.A., 2007, Petrology, age, and tectonic setting of the Seal Island pluton, offshore southwestern Nova Scotia: *Canadian Journal of Earth Sciences*, v. 44, p. 1467–1478.
- Morrissy, C.J., and Ruitenberg, A.A., 1980, Geology of the Lake George antimony deposit, southern New Brunswick: *Canadian Institute of Mining and Metallurgy Bulletin*, v. 73.
- Moscatti, R.J. and Neymark, L.A., 2020, U–Pb geochronology of tin deposits associated with the Cornubian Batholith of southwest England: Direct dating of cassiterite by in situ LA-ICPMS: *Mineralium Deposita*, v. 55, p. 1–20.
- Moyle, J.E., 1985, East Kemptville tin project, in Chatterjee, A.K., and Clarke, D.B., eds., *Guide to the Granites and Mineral Deposits of Southwestern Nova Scotia: Nova Scotia Department of Mines and Energy*, v. 85, p. 199–200.

- Muecke, G.K., Elias, P., and Reynolds, P.H., 1988, Hercynian/Alleghanian overprinting of an Acadian terrane: $^{40}\text{Ar}/^{39}\text{Ar}$ studies in the Meguma zone, Nova Scotia, Canada: *Chemical Geology: Isotope Geoscience section*, v. 73, p. 153–167.
- Murphy, J.B., 2000, Tectonic influence on sedimentation along the southern flank of the late Paleozoic Magdalen basin in the Canadian Appalachians: Geochemical and isotopic constraints on the Horton Group in the St. Mary's basin, Nova Scotia: *Geological Society of America Bulletin*, v. 112, p. 997–1011.
- Murphy, J.B., Waldron, J.W., Kontak, D.J., Pe-Piper, G. and Piper, D.J., 2011, Minas Fault Zone: Late Paleozoic history of an intra-continental orogenic transform fault in the Canadian Appalachians: *Journal of Structural Geology*, v. 33, p. 312-328.
- Neymark, L.A., Holm-Denoma, C.S., Moscati, R.J., 2018, In situ LA-ICPMS U–Pb dating of cassiterite without a known-age matrix-matched reference material: Examples from worldwide tin deposits spanning the Proterozoic to the Tertiary: *Chemical Geology*, v. 483, p. 410–425.
- Neymark, L.A., Holm-Denoma, C.S., Larin, A.M., Moscati, R.J. and Plotkina, Y.V., 2021, LA-ICPMS U-Pb dating reveals cassiterite inheritance in the Yazov granite, Eastern Siberia: Implications for tin mineralization: *Mineralium Deposita*, p. 1–18.
- O'Reilly, G.A., Demont, G.J., Poole, J.C., and Fisher, B.E., compilers, 2016, DP ME 2, Version 11: Nova Scotia Mineral Occurrence Database. Digital product accessed March 2018.

- Parsons, I., Thompson, P., Lee, M.R., and Cayzer, N., 2005, Alkali feldspar microtextures as provenance indicators in siliciclastic rocks and their role in feldspar dissolution during transport and diagenesis: *Journal of Sedimentary Research*, v. 75, p. 921–942.
- Petersson, J., Fallick, A.E., Broman, C., and Eliasson, T., 2014, Imprints of multiple fluid regimes on episyenites in the Bohus granite, Sweden: *Lithos*, v. 196, p. 99–114.
- Pichavant, M., Boher, M., Stenger, J.-F., Aissa, M., and Charoy, B., 1987, Relations de phase des granites de Beauvoir à 1 et 3 kbar en conditions de saturation en H₂O: *Géologie de la France*, no. 2–3: p. 77–86.
- Pitre, C.V., and Richardson, J.M., 1989, Paragenesis of veins of the Duck Pond tin prospect, Meguma Group, East Kemptville, Nova Scotia: *Canadian Journal of Earth Sciences*, v. 26, p. 2032–2043.
- Pollard, P.J., 1983, Magmatic and post-magmatic processes in the formation of rocks associated with rare-element deposits: *Transactions Institute Mining and Metallurgy*, v. 2B, p. 1-9.
- Putnis, A., 2002, Mineral replacement reactions: from macroscopic observations to microscopic mechanisms: *Mineralogical Magazine*, v. 66, p. 689–708.
- Putnis, A., 2009, Mineral replacement reactions: *Reviews in mineralogy and geochemistry*, v. 70, p. 87–124.
- Reynolds, P.H., Zentilli, M., and Muecke, G.K., 1981, K-Ar and ⁴⁰Ar/³⁹Ar geochronology of granitoid rocks from southern Nova Scotia: its bearing on the geological evolution of the

- Meguma Zone of the Appalachians: *Canadian Journal of Earth Sciences*, v. 18, p. 386–394.
- Richardson, J.M., 1988, Field and alteration relationships of alteration and greisen-hosted mineralization at the East Kemptville tin deposit, Davis Lake monzogranite, southwest Nova Scotia, Canada, in Taylor, R.P., and Strong, D.F., eds., *Granite related mineral deposits: Canadian Institute of Mining and Metallurgy, Special*, v. 39, 265–279.
- Richardson, J.M.G., Spooner, E.T.C., and McAuslan, D.A., 1982, The East Kemptville tin deposit, Nova Scotia: an example of a large tonnage, low grade, greisen-hosted deposit in the endocontact zone of a granite batholith: *Geological Survey of Canada Current Research*, p. 27-32.
- Richardson, J.M., Bell, K., Blenkinsopp, J., and Watkinson, D., 1989, Rb-Sr age and geochemical distinctions between the Carboniferous tin-bearing Davis Lake complex and the Devonian South Mountain batholith, Meguma Terrane, Nova Scotia: *Canadian Journal of Earth Sciences*, v. 26: p. 2044–2061.
- Richardson, J. M., Bell, K., Watkinson, D. H., and Blenkinsop, J., 1990a, Genesis and fluid evolution of the East Kemptville greisen-hosted tin mine, southwestern Nova Scotia, Canada, in Stein, H. J., and Hannah, J. L., eds., *Ore-bearing granite systems; Pedogenesis and mineralizing processes: Geological Society of America Special Paper 246*.

- Richardson, J.M., Kontak, D.J., Chatterjee, A.K., Boyle, D.R., Cormier, R.F., and Pitre, C.V., 1990b, The East Kemptville polymetallic tin domain, in Boyle, D.R., Mineral Deposits of New Brunswick and Nova Scotia (Field Trip 2): 8th IAGOD Symposium, Geological Survey of Canada Open File 2157, p. 88–132.
- Romer, R.L., Kroner, U., 2015, Sediment and weathering control on the distribution of Paleozoic magmatic tin–tungsten mineralization: *Mineralium Deposita*, v. 50, p. 327–338.
- Romer, R.L., Kroner, U., 2016, Phanerozoic tin and tungsten mineralization—Tectonic controls on the distribution of enriched protoliths and heat sources for crustal melting: *Gondwana Research*, v. 31, p. 60–95.
- Rudnick R.L., and Gao S., 2003, Composition of the Continental Crust, in Rudnick, R.L., ed., *Treatise on Geochemistry* vol 3. Elsevier, Amsterdam, p. 1–64.
- Sandeman, H.A.I., Peddle, C., and Newman, R., 2018, Beaver Brook Antimony Mine revisited: An update on operations and new structural and geological observations, *Current Research*, Government of Newfoundland and Labrador: Department of Natural Resources, Geological Survey, Report, v. 18, p. 123–152.
- Sangster, A.L., ed., 1990. *Mineral Deposit Studies in Nova Scotia* (No. 8). Energy, Mines and Resources Canada.

- Sato, K., 2012, Sedimentary Crust and Metallogeny of Granitoid Affinity: Implications from the Geotectonic Histories of the Circum-Japan Sea Region, Central Andes and Southeastern Australia: *Resource Geology*, v. 62, p. 329–351.
- Schneider, H.J., and Lehmann, B., 1977, Contribution to a new genetical concept on the Bolivian tin province, in, *Time-and strata-bound ore deposits*, Springer, Berlin, Heidelberg, p. 153–168.
- Schuiling, R.D., 1967, Tin belts on the continents around the Atlantic ocean: *Economic Geology*, v. 62, p. 540–550.
- Schwartz, M.O., Rajah, S.S., Askury, A.K., Putthapiban, P., and Djaswadi, S., 1995, The Southeast Asian tin belt: *Earth-Science Reviews*, v. 38, p. 95–293.
- Seedorff, E., Dilles, J.H., Proffett, J.M., Jr., Einaudi, M.T., Zurcher, L., Stavast, W.J.A., Johnson, D.A., and Barton, M.D., 2005, Porphyry deposits: Characteristics and origin of hypogene features: *Economic Geology 100th Anniversary Volume*, p. 251–298.
- Selby, D., and Creaser, R.A. 2004, Macroscale NTIMS and microscale LA-MC-ICP-MS Re-Os isotopic analysis of molybdenite: Testing spatial restrictions for reliable Re-Os age determinations, and implications for the decoupling of Re and Os within molybdenite: *Geochimica Cosmochimica Acta*, v. 68, p. 3897–3908.
- Selby, D., Creaser, R.A., Stein, H.J., Markey, R.J. and Hannah, J.L., 2007, Assessment of the ¹⁸⁷Re decay constant by cross calibration of Re–Os molybdenite and U–Pb zircon

- chronometers in magmatic ore systems: *Geochimica et Cosmochimica Acta*, v. 71, p. 1999–2013.
- Shellnutt, J.G., and Dostal, J., 2012, An evaluation of crustal assimilation within the late Devonian South Mountain Batholith, SW Nova Scotia: *Geological Magazine*, v. 149, p. 353–365.
- Sibson, R.H., 1986, Brecciation processes in fault zones: Inferences from Earthquake rupturing: *Pure and Applied Geophysics*, v. 124, p. 159–175.
- Sillitoe, R.H., 2010, Porphyry copper systems: *Economic Geology*, v. 105, p. 3–41.
- Sillitoe, R.H., Halls, C. and Grant, J.N., 1975, Porphyry tin deposits in Bolivia: *Economic Geology*, v. 70, p. 913–927.
- Sinclair, W.D., Gonevchuk, G.A., Korostelev, P.G., Semenyak, B.I., Rodionov, S., Seltmann, R., Štemprok, M., 2011, World Distribution of Tin and Tungsten Deposits: Geological Survey of Canada, Open File 5482, scale 1: 35 000 000.
- Slater, E., Kontak, D.J., and McDonald, A., 2021, Origin of a Miocene multi-stage epithermal Ag-Zn-Pb-Sn deposit: The Cortaderas breccia body, Pirquitas Mine, NW Argentina: *Mineralium Deposita*, v. 56, p. 381–406.
- Smith, W.D., Darling, J.R., Bullen, D.S., Lasalle, S., Pereira, I., Moreira, H., Allen, C.J. and Tapster, S., 2019, Zircon perspectives on the age and origin of evolved S-type granites from the Cornubian Batholith, Southwest England: *Lithos*, v. 336, p. 14–26.

- Smoliar, M.I., Walker, R.J., and Morgan, J.W., 1996, Re-Os ages of group IIA, IIIA, IVA, and IVB iron meteorites: *Science*, v. 271, p. 1099–1102.
- Soehl, T.P., O'Reilly, G.A., Clarke, D.B., and Reynolds, P.H., 1989, The Graphite-Bearing Kempt Snare Lake Greisenised Leucogranite Cupola, Yarmouth County Nova Scotia: Nova Scotia Department of Mines and Energy, Report of Activities 89-1 Part B, p. 51-69.
- Spörli, K.B. and Cargill, H., 2011, Structural evolution of a world-class epithermal orebody: The Martha Hill deposit, Waihi, New Zealand: *Economic Geology*, v. 106, p. 975–998.
- Stanley, C.R., 2020, Molar element ratio analysis of lithogeochemical data: a toolbox for use in mineral exploration and mining: *Geochemistry: Exploration, Environment, Analysis*, v. 20, p. 233–256.
- Stanley, C.R., and Madeisky, H.E., 1994, Lithogeochemical exploration for hydrothermal ore deposits using Pearce element ratio analysis, in Lentz, D.R., ed., *Alteration and Alteration Processes associated with Ore-forming Systems: Geological Association of Canada, Short Course Notes*, v. 11, p. 193–211.
- Stein, H.J., Markey, R.J., Morgan, J.W., Hannah, J.L., and Scherstén, A., 2001, The remarkable Re–Os chronometer in molybdenite: how and why it works: *Terra Nova*, v. 13, p. 479–486.
- Štemprok, M., 1987, Greisenization (a review): *Geologische Rundschau*, v. 76, p. 169–175.

- Štemprok, M., 1995, A comparison of the Krušné Hory-Erzgebirge (Czech Republic–Germany) and Cornish (UK) granites and their related mineralizations, in *Proc Ussher Soc*, v. 8, p. 347–356.
- Štemprok, M., Pivec, E. and Langrová, A., 2005, The petrogenesis of a wolframite-bearing greisen in the Vykmanov granite stock, Western Krušné hory pluton (Czech Republic): *Bulletin of Geosciences*, v. 80, p. 163–184.
- Strong, D.F., 1981, Ore deposit models-5. A model for granophile mineral deposits: *Geoscience Canada*, v. 8, p. 155–161.
- Taylor, R.G., 1979, *Geology of Tin Deposits*: Elsevier, Amsterdam.
- Taylor, R.G., and Pollard, P., 1988, Pervasive hydrothermal alteration in tin-bearing granites and implications for the evolution of ore-bearing magmatic fluids, in Taylor, R.P. and Strong, D.F., eds., *Recent Advances in the Geology of Granite-Related Mineral Deposits*: Canadian Institute of Mining and Metallurgy, Special Volume 39, p. 86–95.
- Taylor, S.R. and McLennan, S.M., 1981, The composition and evolution of the continental crust: rare earth element evidence from sedimentary rocks: *Philosophical Transactions of the Royal Society of London. Series A, Mathematical and Physical Sciences*, v. 301, p. 381–399.
- Thorne, K.G., Fyffe, L.R., and Creaser, R.A., 2013, Re-Os geochronological constraints on the W–Mo mineralizing event in the Mount Pleasant Caldera Complex: implications for the

- timing of subvolcanic magmatism and caldera development: *Atlantic Geology*, v. 49, p. 131–150.
- Tischendorf, G., 1978, Geochemical and petrographic characteristics of silicic magmatic rocks associated with rare element mineralization, in Štemprok, M., Burnol, L., and Tischendorf, G., *Metallization associated with acid magmatism*, v. 2: Geological Survey of Czechoslovakia, Prague, p. 41–96.
- van Staal, C.R., 2007. Pre-Carboniferous tectonic evolution and metallogeny of the Canadian Appalachians, in Goodfellow, W.D., ed., *Mineral Deposits of Canada: Geological Association of Canada, Special Publication*, v. 5, p. 793–818.
- van Staal, C.R., Whalen, J.B., Valverde-Vaquero, P., Zagorevski, A., and Rogers, N., 2009, Pre-Carboniferous, episodic accretion-related, orogenesis along the Laurentian margin of the northern Appalachians: *Geological Society, London, Special Publications*, v. 327, p. 271–316.
- Voncken, J.H.L., 2016, *The rare earth elements: an introduction*. Delft University of Technology, Delft. Springer International Publishing: Imprint: Springer, 127p.
- Waldron, J.W., 1992, The Goldenville–Halifax transition, Mahone Bay, Nova Scotia: relative sea-level rise in the Meguma source terrane: *Canadian Journal of Earth Sciences*, v. 29, p. 1091–1105.

- Waldron, J.W.F., Barr, S.M., Park, A.F., White, C.E., and Hibbard, J., 2015, Late Paleozoic strike-slip faults in Maritime Canada and their role in the reconfiguration of the northern Appalachian orogen: *Tectonics*, v. 34, p. 1661–1684.
- White, C.E., 2010a, Compilation of geochemical and petrographic data from the western and southern parts of the Goldenville and Halifax Groups, Nova Scotia: Halifax, Nova Scotia Department of Natural Resources: Mineral Resources Branch Open-File Report ME 2010-1, 9 p.
- White, C.E., 2010b, Stratigraphy of the Lower Paleozoic Goldenville and Halifax groups in southwestern Nova Scotia, *Atlantic Geology*, v. 46, p. 136–154.
- White, C.E., and Barr, S.M., 2010, Lithochemistry of the Lower Paleozoic Goldenville and Halifax groups, southwestern Nova Scotia, Canada: Implications for stratigraphy, provenance, and tectonic setting of the Meguma terrane, in Tollo, R.P., Bartholomew, M.J., Hibbard, J.P., and Karabinos, P.M., eds., *From Rodinia to Pangea: The Lithotectonic Record of the Appalachian Region*: Geological Society of America Memoir, v. 206, p. 347–366.
- White, C.E., and Barr, S.M., 2017, Stratigraphy and depositional setting of the Silurian–Devonian Rockville Notch Group, Meguma terrane, Nova Scotia, Canada: *Atlantic Geology*, v. 53, p. 337–365.

- White, C.E., Palacios, T., Jensen, S., and Barr, S.M., 2012, Cambrian–Ordovician acritarchs in the Meguma terrane, Nova Scotia, Canada: resolution of Early Paleozoic stratigraphy and implications for paleogeography: *Geological Society of America Bulletin*, v. 124, p. 1773–1792.
- Willson, J., 2019, Character and genesis of Indium mineralization, East Kemptville, Nova Scotia: MSc Thesis, University of Windsor, Windsor, Ontario, Canada, 111p.
- Witt, W.K., 1988, Evolution of High-Temperature Hydrothermal Fluids Associated with Greisenization and Feldspathic Alteration of a Tin-Mineralized Granite, Northeast Queensland: *Economic Geology*, v. 83, p. 310–334.
- Woodcock, N.H., and Mort, K., 2008, Classification of fault breccias and related fault rocks: *Geological Magazine*, v. 145, p. 435–440.
- Zaraisky, G.P., Aksyuk, A.M., Devyatova, V.N., Udoratina, O.V., and Chevychelov, V.Y., 2009, The Zr/Hf ratio as a fractionation indicator of rare-metal granites: *Petrology*, v. 17, p. 25–45.
- Zaraisky, G.P., Korzhinskaya, V., and Kotova, N., 2010, Experimental studies of Ta₂O₅ and columbite–tantalite solubility in fluoride solutions from 300 to 550°C and 50 to 100 MPa: *Mineralogy and Petrology*, v. 99, p. 287–300.
- Zen, E.A., 1986, Aluminum enrichment in silicate melts by fractional crystallization: some mineralogic and petrographic constraints: *Journal of Petrology*, v. 27, p. 1095–1117.

- Zentilli, M., and Reynolds, P.H., 1985, $^{40}\text{Ar}/^{39}\text{Ar}$ dating of micas from the East Kemptville tin deposit, Yarmouth County, Nova Scotia: *Canadian Journal of Earth Sciences*, v. 22, p. 1546–1548.
- Zentilli, M., Graves, M. C., Mulja, T., and MacInnis, I., 1986, Geochemical characterization of the Goldenville-Halifax transition of the Meguma Group of Nova Scotia: preliminary report, in *Current research, part A*. Geological Survey of Canada, Paper 86-1A, p. 423–428.
- Zhang, W., 2015, Petrological and Metallogenic Studies of the Nashwaak Granite and Felsic Dykes Associated with the Sisson Book W-Mo-(Cu) Deposit, West-Central New Brunswick, Canada: Ph.D. Thesis, University of New Brunswick, Fredericton, NB, Canada.
- Zoheir, B., Lehmann, B., Emam, A., Radwan, A., Zhang, R., Bain, W.M., Steele-MacInnis, M. and Nolte, N., 2020, Extreme fractionation and magmatic–hydrothermal transition in the formation of the Abu Dabbab rare-metal granite, Eastern Desert, Egypt: *Lithos*, v. 352, 105329.

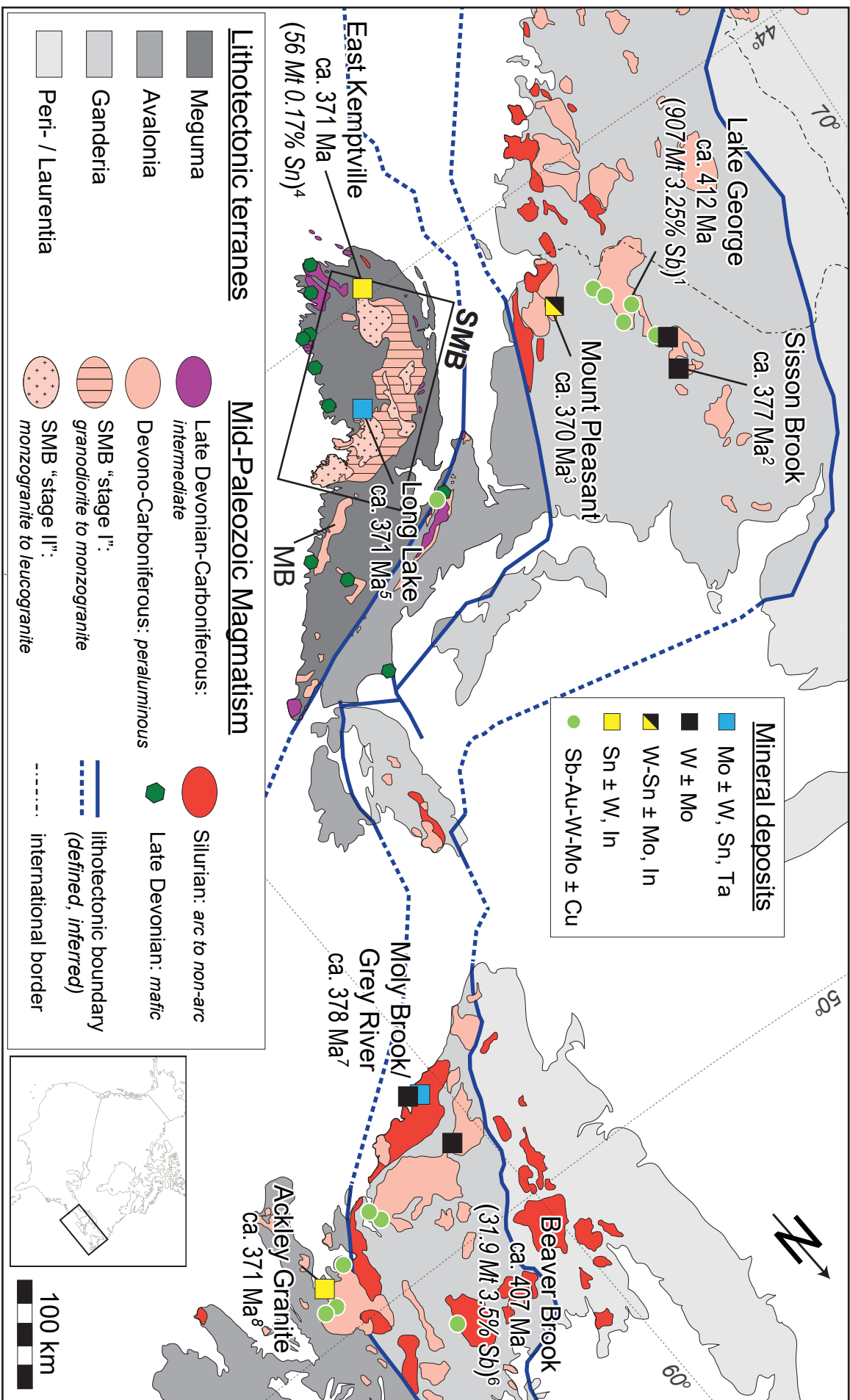


Figure 3-1

Figure 3–1. Tectonic terrane map of the northeastern Appalachians with major terranes shaded in grey (after Hibbard et al., 2006). Major lithotectonic-bounding faults (outlined in blue), Devonian-Carboniferous granitic magmatism (including the South Mountain Batholith, SMB, and the Musquodoboit batholith, MB), and polymetallic lithophile element-enriched mineral deposits associated with the Paleozoic magmatism are pictured (after van Staal, 2007). 1 - Morrissy and Ruitenberg (1980); 2 - Zhang (2015); 3 - Thorne et al. (2013); 4 - Richardson et al. (1982); 5 - Selby and Creaser (2004); 6 - McNicoll et al. (2006), Sandeman et al. (2018); 7 - Kerr and McNicoll (2012); 8 – Kontak et al. (1988).

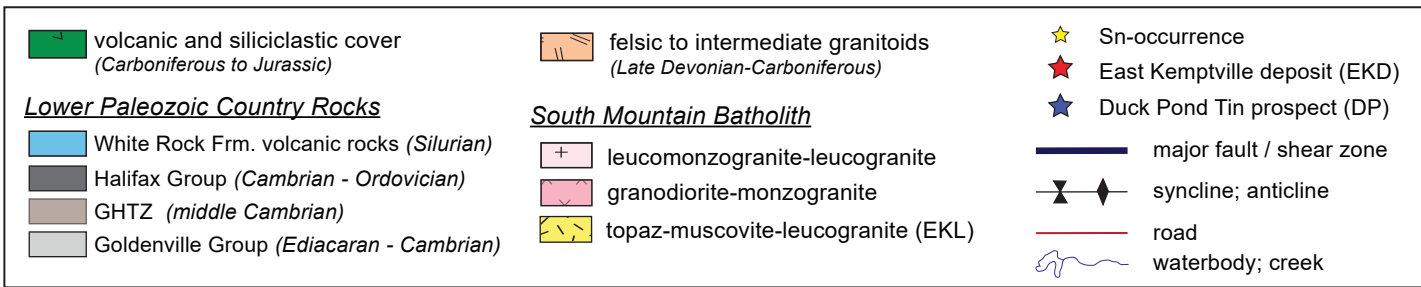
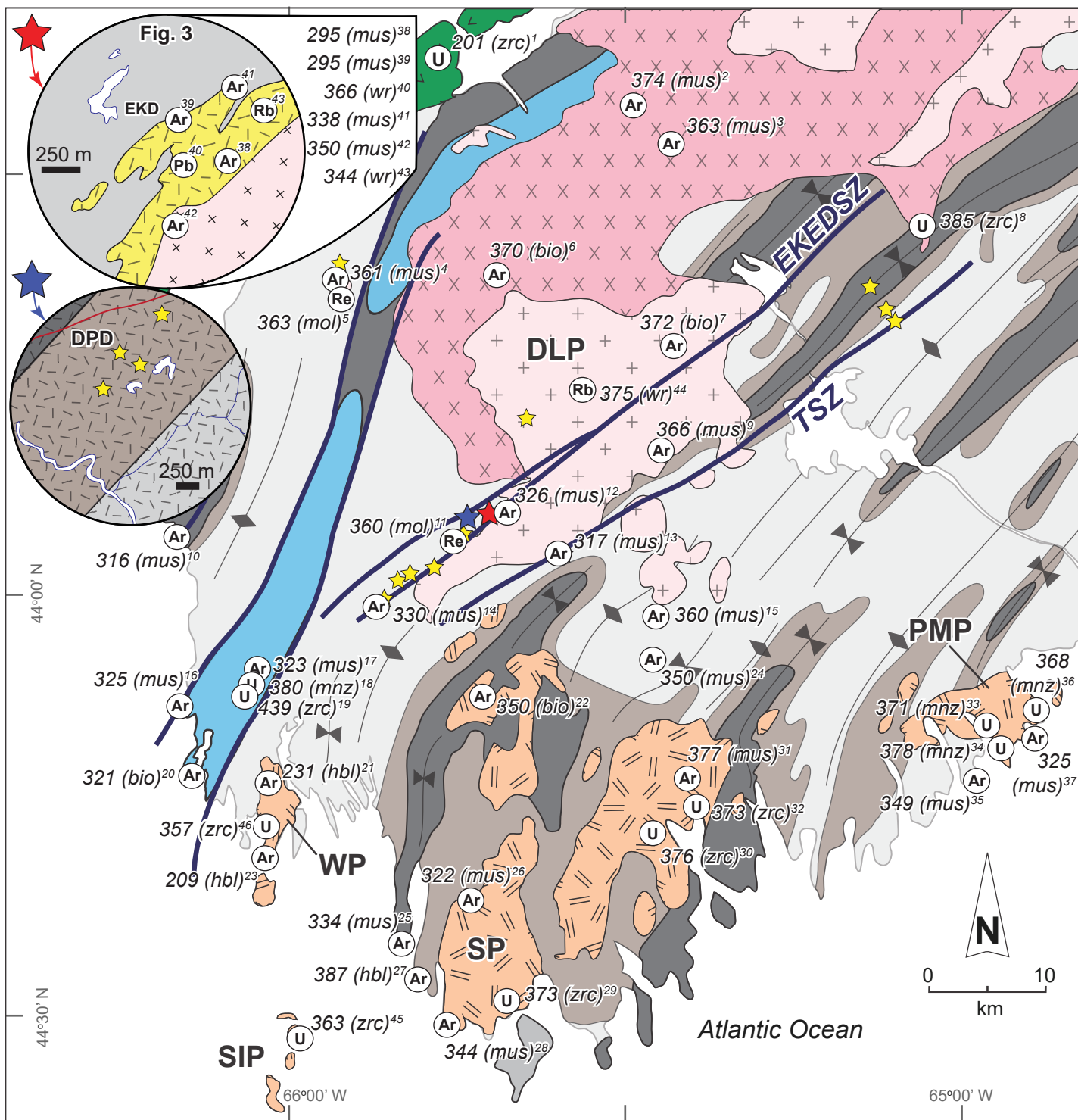


Figure 3-2

Figure 3–2. Regional geology of SW Nova Scotia, Canada (modified after White, 2010a), displaying the Davis Lake pluton (DLP), the distribution of SMB satellite intermediate plutons, metasedimentary rocks of the Meguma terrane, and historic geochronological data in the area. References and details for plotted geochronological data are listed in Table EA 3-1 (Electronic Appendix). Insets: overviews of the East Kemptville deposit (EKD; located at the SW edge of the Davis Lake Pluton) and the Duck Pond prospect (DP; located ~2 km WSW of the EKD). Hybridized intermediate granitoid intrusions coeval with the SMB (WP – Wedgeport Pluton, SP – Sandwich Point Pluton, SIP – Seal Island Pluton, PMP – Point Mouton Pluton), regional fold axes, and Sn mineral occurrences (O’Reilly et al., 2016) in this part of the province are also shown. Major shear zones: TSZ – Tobeatic Shear Zone, and EKEDSZ – East Kemptville East Dalhousie Shear Zone. Note the variability in Ar-Ar ages, the relatively constrained U-Pb ages in the SMB (ca. 385 Ma) and the spatially associated felsic to intermediate granitoids (ca. 375 Ma in the SP, 370 Ma in the PMP, and 360 Ma in the WP).

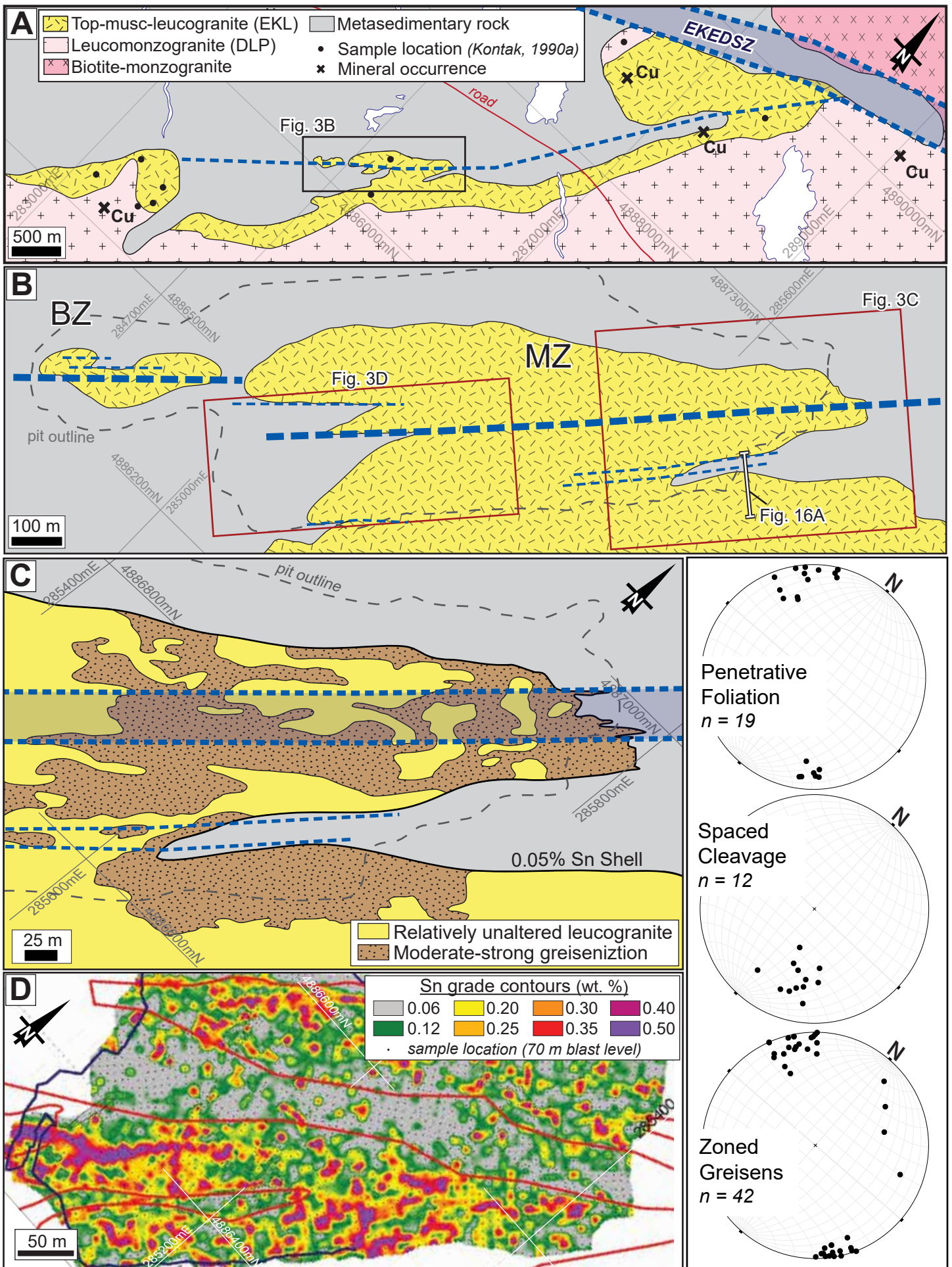


Figure 3-3

Figure 3–3. (A) Plan view of East Kemptville leucogranite (EKL) and the associated East Kemptville-East Dalhousie shear zone (EKEDSZ), a splay of which transects the East Kemptville deposit (area inset in Fig. 3–2). Note the EKL intrudes along the SW contact of the Davis Lake pluton (DLP) and Goldenville Group metasedimentary rocks. Black dots represent hand samples for whole-rock lithogeochemistry from Kontak (1990a). (B) Plan view bedrock geology map of the East Kemptville deposit (outlined in Fig. 3–3A) with ore zones labelled (BZ – Baby zone, MZ – Main zone) as well as current pit outline (dashed grey) and surficial traces of the sub-vertical faults (dashed blue; interpreted from surface mapping and drill core logging). Field photo of pit wall with fault offset (Fig. 3–15A) outlined. (C) Plan view alteration map of the northeastern part of the deposit (outlined in Fig. 3–3B; constructed through surficial grid mapping at a 5 x 5 m resolution). The boundary of 0.05% Sn roughly outlines the EKL and greisenization is aligned somewhat to the shear zone (shaded blue) and the EKL-metasedimentary host rock contact. (D) Plan view contoured Sn grade map determined from blast hole powder data at the 70 m level of the southern part of the Main Zone (outlined in Fig. 3–3B), the blue line represents an outline of the 070m pit level and red line the ore zones defined in a block model for the deposit (B. Hudgins pers comm. with D. Kontak, 2009). Bottom right inset shows stereonet plots that plot orientation measurements of main deformation fabrics (i.e., penetrative foliation and spaced cleavage) and zoned greisens, determined from surface mapping. Note the alignment of zoned greisens are parallel with the penetrative foliation, fault planes through the deposit (B, C), and dominant trend of higher grades in the open pit (D).

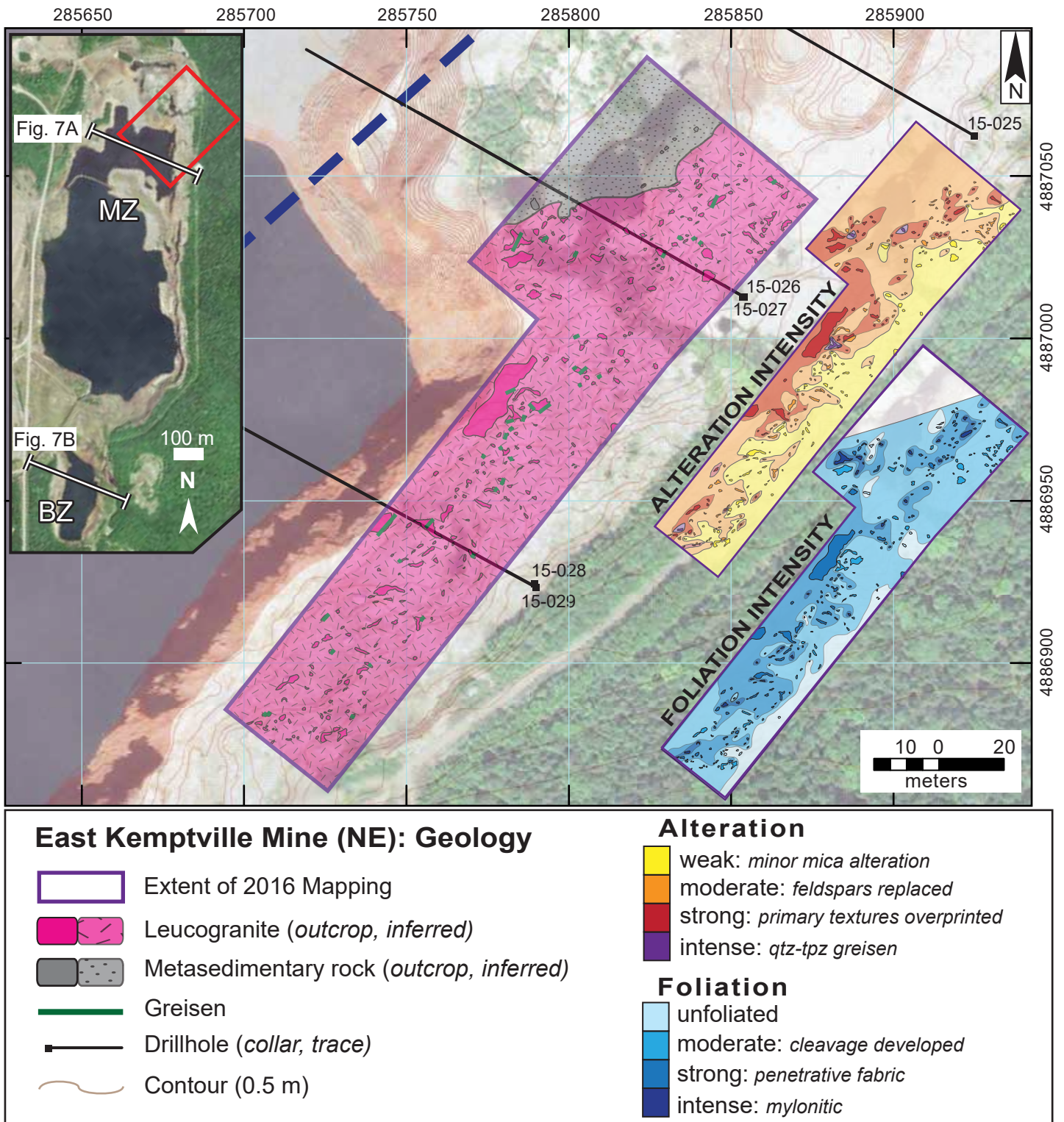


Figure 3-4

Figure 3–4. Outcrop mapping in the NE part of the East Kemptville mine; data measurements were taken on a 3 x 3 m grid basis, and intensity of alteration and foliation were measured to create contours for increased greisenization and deformation (bottom-right insets; criteria for intensity shown in legend). Compilation of structural measurements shown in stereonet inset of Figure 3–3. Inset to top left shows aerial photograph (taken June 15, 2018; courtesy of Avalon Advanced Materials Inc.) of East Kemptville mine with: ore zones labelled (flooded open-pits); surficial expression of interpreted cross-sections shown in Figure 3–7A, B; and the area of bedrock mapping (red box).

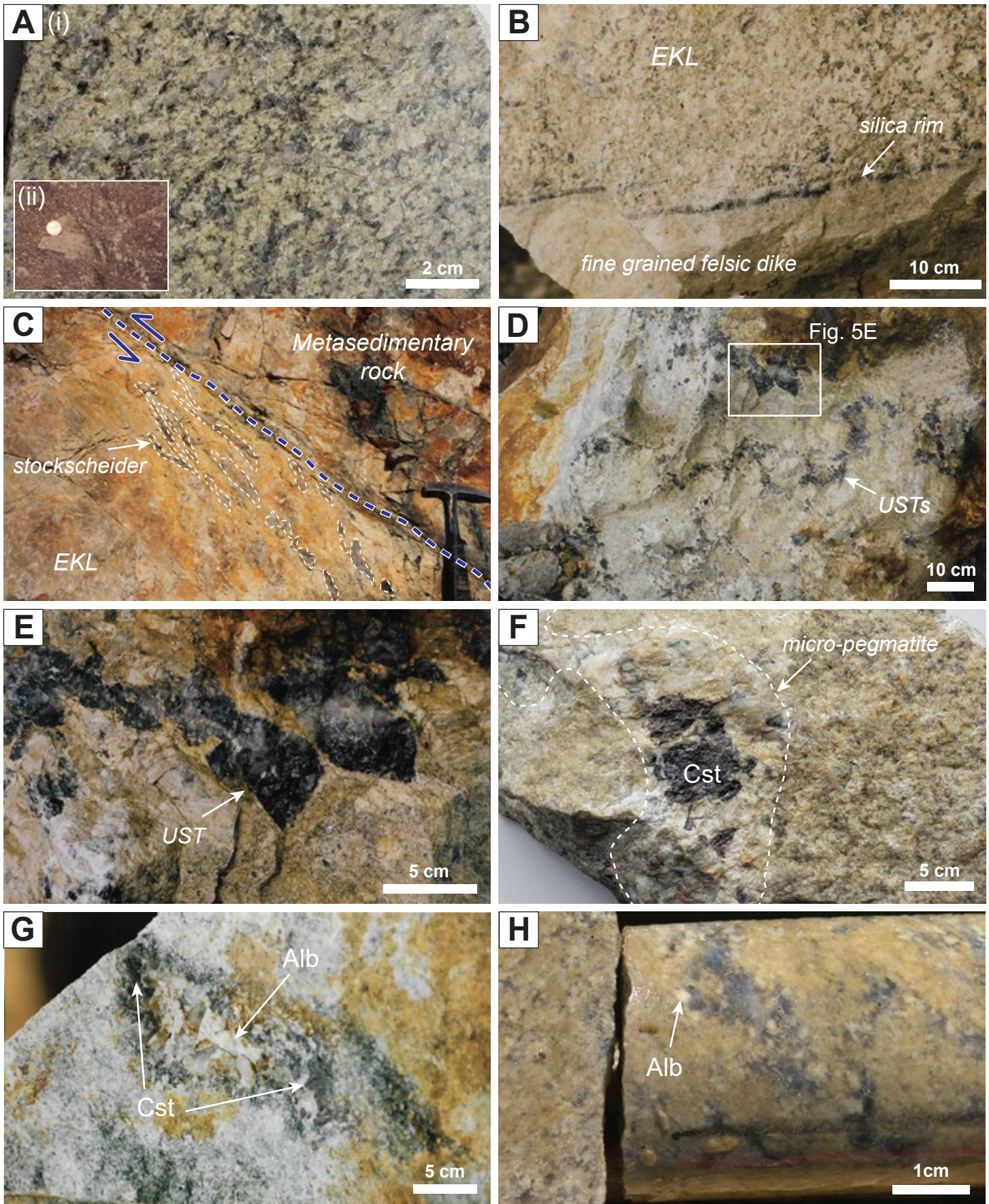


Figure 3–5

Figure 3–5. (A) Hand sample of light buff medium-grained (i), and an inset of fine-grained (ii), equigranular East Kemptville muscovite-topaz-leucogranite (EKL). (B) Fine grained quenched felsic dike in EKL with a thin layer of fine grained silica that is the result of fluid exsolution by depressurization. (C) Outcrop photo of sheared contact (dashed blue) between host metasedimentary rock and EKL, note the presence of coarse stockscheider quartz-pegmatites (outlined) that become less amorphous and more elongated parallel to fault towards the contact. (D-E) Outcrop example of unidirectional solidification textures (USTs) of elongated quartz (arrow in E) indicating localized fluid saturation in the EKL. (F) Thin pegmatite in the EKL (outlined, arrow) with coarse cassiterite (Cst). (G) Hand sample with miarole rimmed by coarse albite (Alb) and containing primary cassiterite. (H) Hand sample of granitic rock with interconnected granitic-veins. Granitic-veins rimmed by albite and filled with quartz ± muscovite.

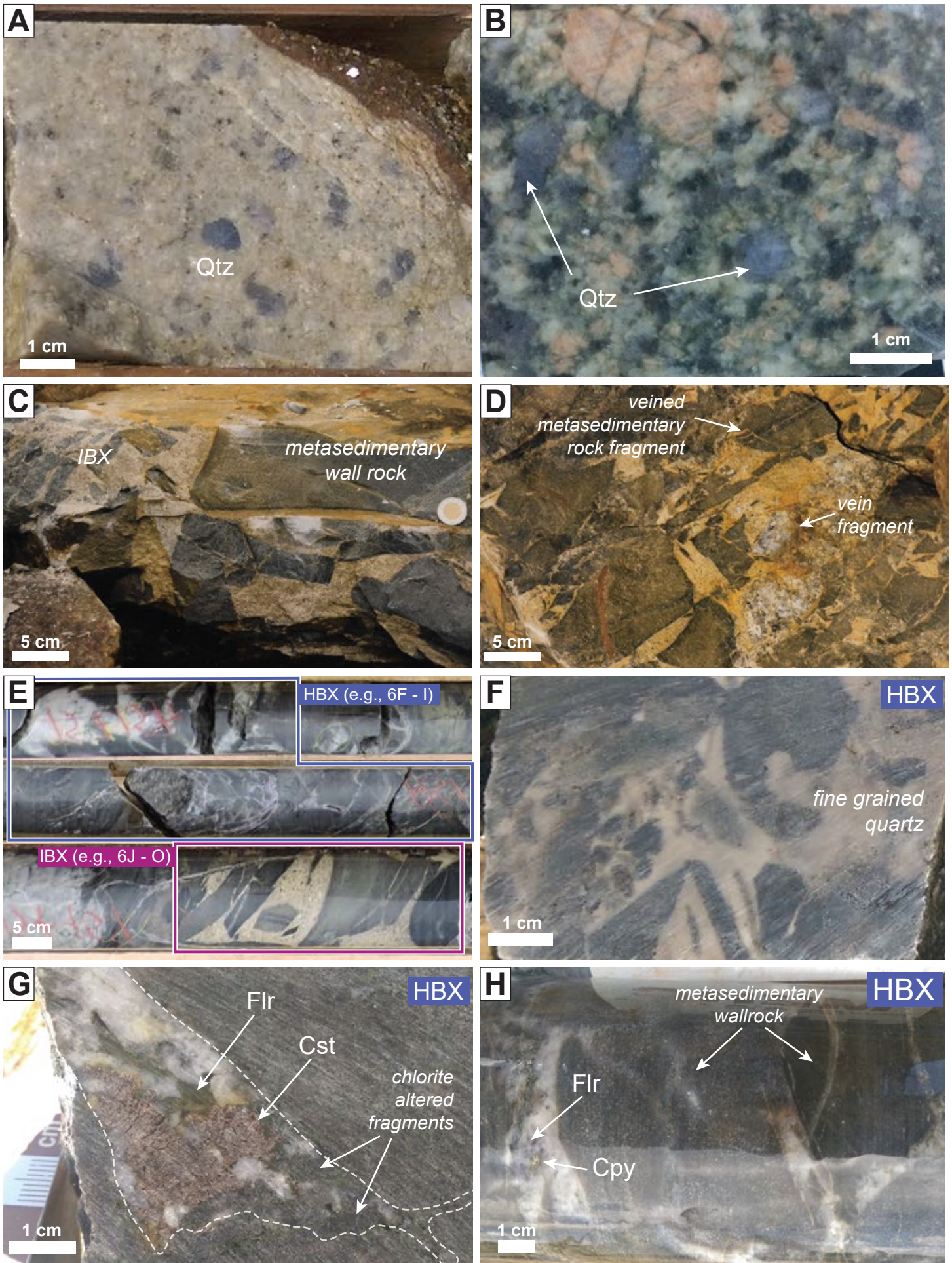


Figure 3-6

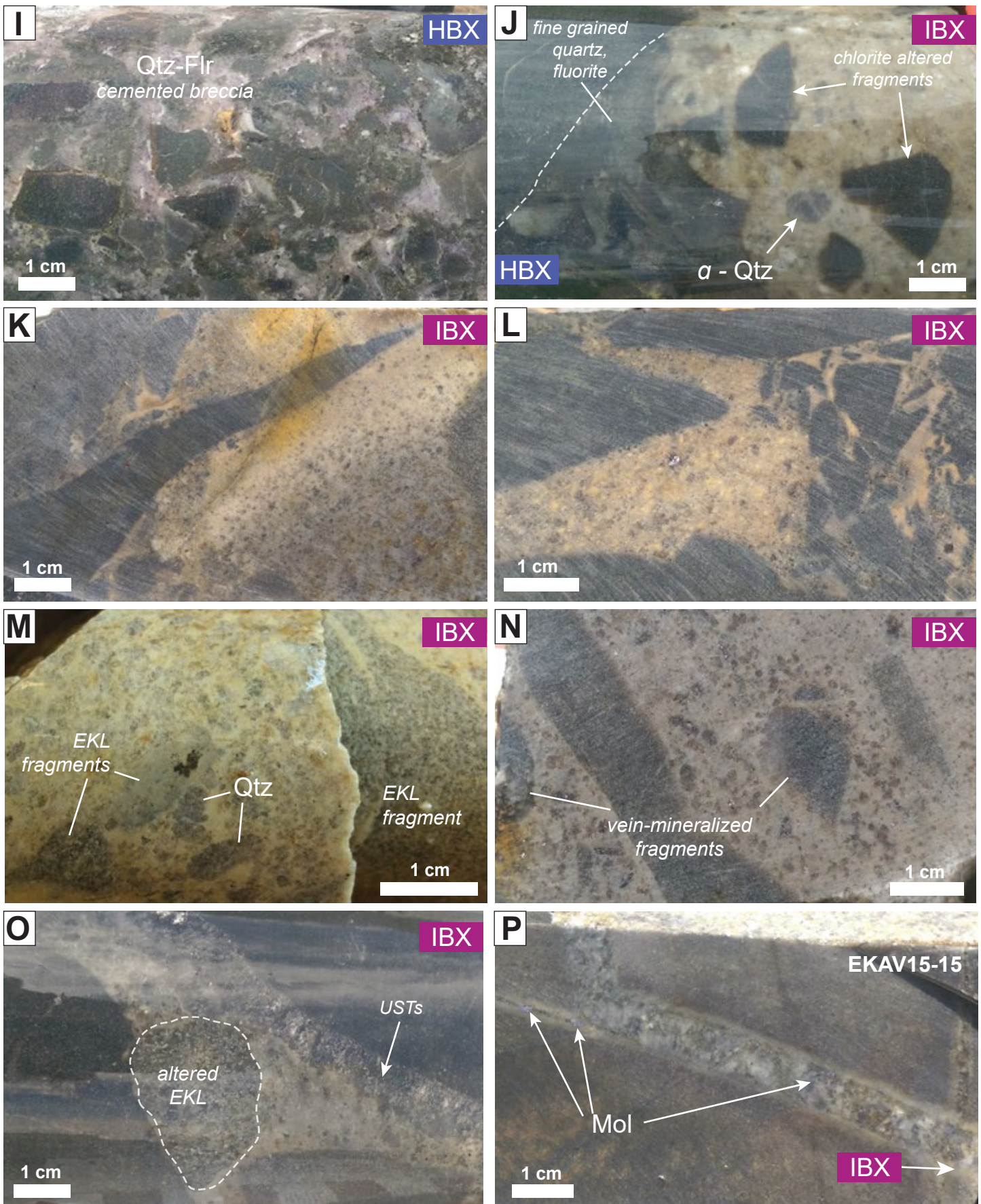


Figure 3-6, continued

Figure 3–6. (A) Example drill core from depth (162 m) in Baby zone of light buff seriate textured, to quartz-phyric (Qtz), weakly sericite-altered East Kemptville leucogranite (EKL). (B) Hand sample of seriate textured fine- to medium-grained biotite-muscovite leucogranite with coarse zoned blueish quartz (Qtz, arrows), white subhedral plagioclase (medium- to coarse-grained), and megacrystic perthitic K-feldspar (from drill core through bottom of Baby zone). (C–D) Outcrop photos of magmatic breccia from the Baby Zone, typical fragment size, angularity, and lithologic proportions are shown in C, example of mineralized fragments shown in D (note veined wall-rock fragment as well as whole fragment of quartz-sulfide vein). (E) Example of transition between hydrothermal breccia (HBX, higher depth) and magmatic breccia (IBX, lower depth) as seen in drill core; note outlines show typical intervals of each respective unit that are exemplified in F–L. (F–I) Examples of variable character in HBX in drill core: (F) HBX proximal IBX with pervasive fine grained silicification; (G) mineralized HBX with quartz-fluorite (Flr) and mica (Fe-Li) cement with coarse cassiterite (Cst) and chlorite-altered fragments in silicified wall-rock; (H) HBX with variably altered wall-rock and a cement of quartz-fluorite-chalcopyrite (Cpy); (I) HBX with variable fragment composition and cement dominantly of quartz, lesser fluorite, trace molybdenite; (J) discrete contact between typical IBX, with quartz-feldspar-phyric matrix, and quartz-chlorite-fluorite cemented HBX, note the spalled chlorite-altered fragments from the HBX in the IBX matrix and the alpha-type quartz phenocrysts (α -Qtz). (K–O) Examples of IBX with fine grained quartz-feldspar-phyric matrix in the Baby Zone, including: (K, L) examples of filter pressing of felsic melt by breccia fragments and space restriction, followed by quenching, resulting in variation of phenocryst size; (M, N, O) IBX with fragments of quartz \pm mineralized vein and rare altered EKL; evidence of fluid exsolution along fragment boundaries with coarse mica and quartz growth into the crystallizing IBX matrix (O). (P) Example of felsic micro-dike that extends from IBX matrix near border of unit; note molybdenite (Mol) mineralization along edges of dike (EKAV-15-15; Table 3–2).

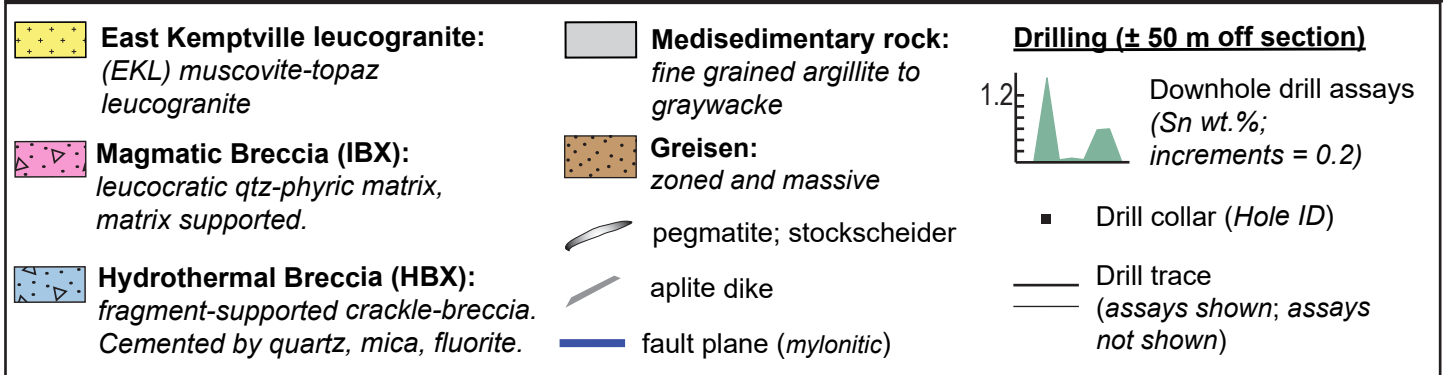
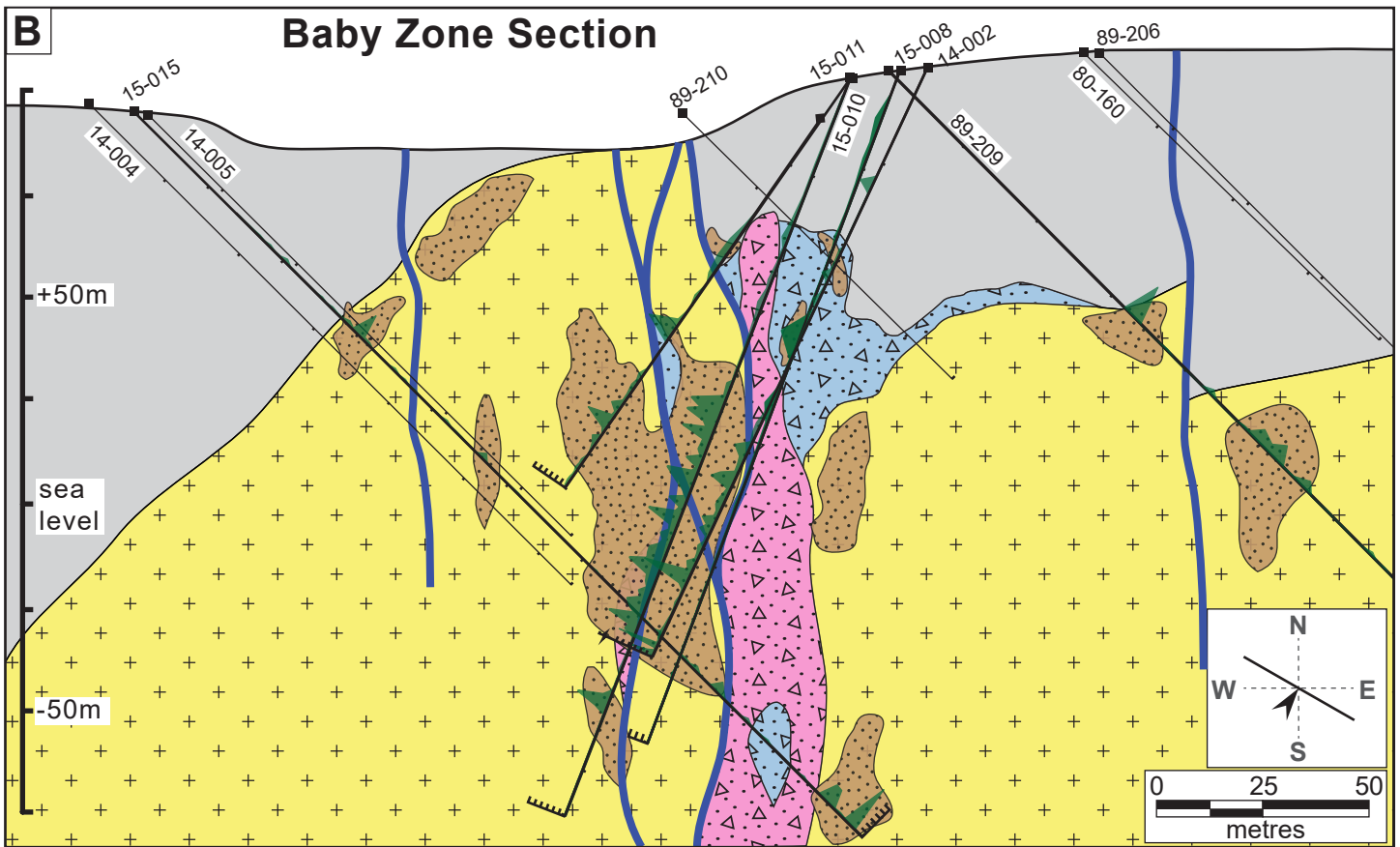
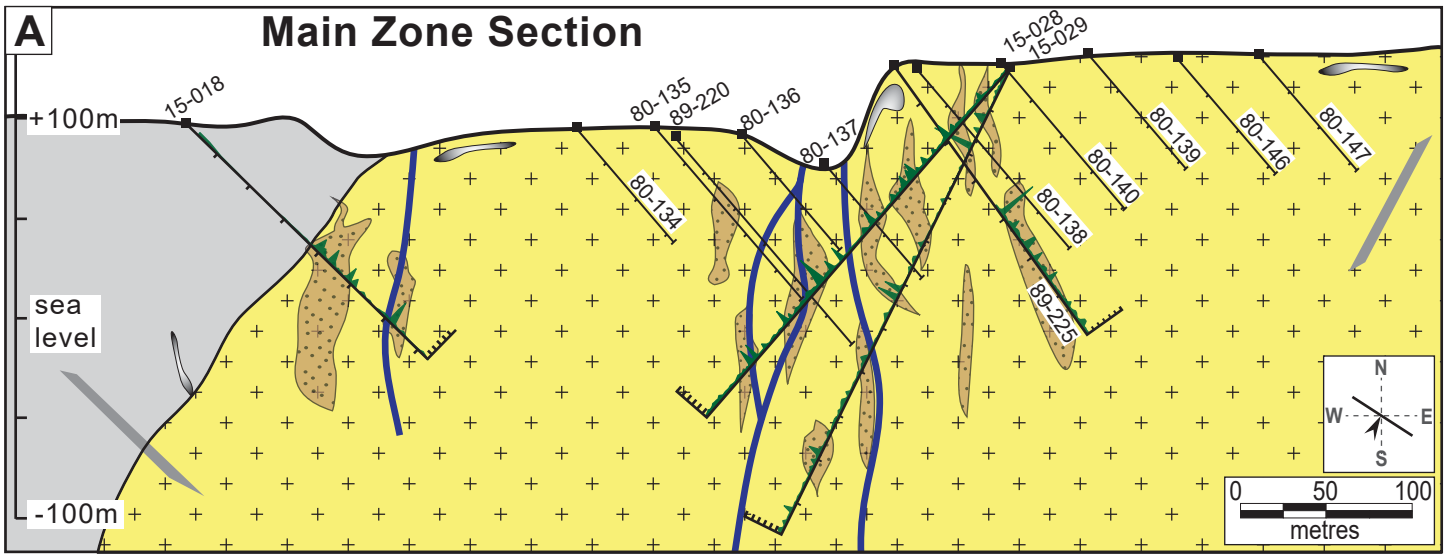


Figure 3-7

Figure 3–7. Scaled interpreted cross-sectional views of the Main (**A**) and Baby (**B**) ore zones; constructed from historic and recent drilling from holes that plot ± 50 m off section (shown as traces). Down-hole Sn grade (wt. %) for recent drilling on section is shown along drill traces. (**A**) Cross-sectional view of the Main Zone with interpreted faulting and greisenization. Note inferred presence of minor pegmatites and aplite dikes that were observed at surface, the alignment of which were either parallel to the main foliation or intrusive contacts. (**B**) Cross sectional view of the Baby Zone with interpreted extent of hydrothermal and igneous breccias and thicker/continuous greisens (massive), relative to the Main Zone. Note these sections were used to construct the schematic formational model in Figure 3–23.

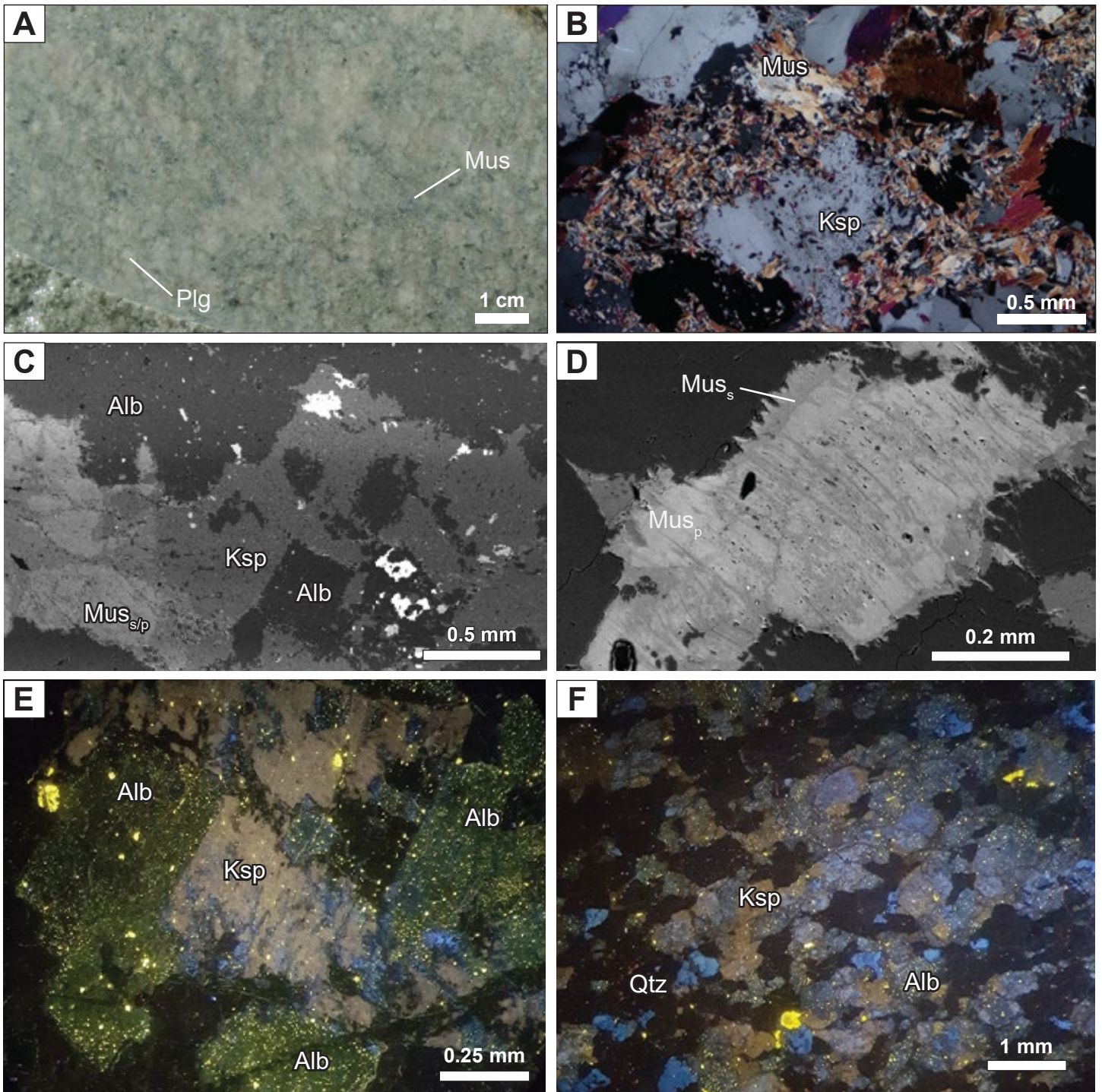


Figure 3-8

Figure 3–8. (A) Hand sample of moderately sericitized East Kemptville leucogranite (EKL). Primary texture somewhat preserved, rock is dominantly quartz, muscovite (Mus; after K-feldspar), partially albitized calcic plagioclase (Plg). (B) Photomicrograph in cross-polarized light of partial K-feldspar (Ksp) and muscovite replacement by sericite from deuterically altered EKL (e.g., 8A). (C) BSE image of weakly altered primary mineralogy of the EKL with albitized plagioclase (Alb) and partially replaced K-feldspar; both have a pitted texture and contain trace chalcopyrite, sphalerite, and cassiterite. (D) BSE image of irregular intergrowth between primary muscovite (Mus_p; lighter shade; 3-4 wt. % F) and secondary muscovite (Mus_s; darker shade and at grain boundaries; 6-8 wt. % F). (E–F) CL images of deuterically altered EKL with fine-grained disseminated apatite visible in bright yellow; note predominance of apatite in the albitized plagioclase crystals with a pitted texture. Qtz – quartz.

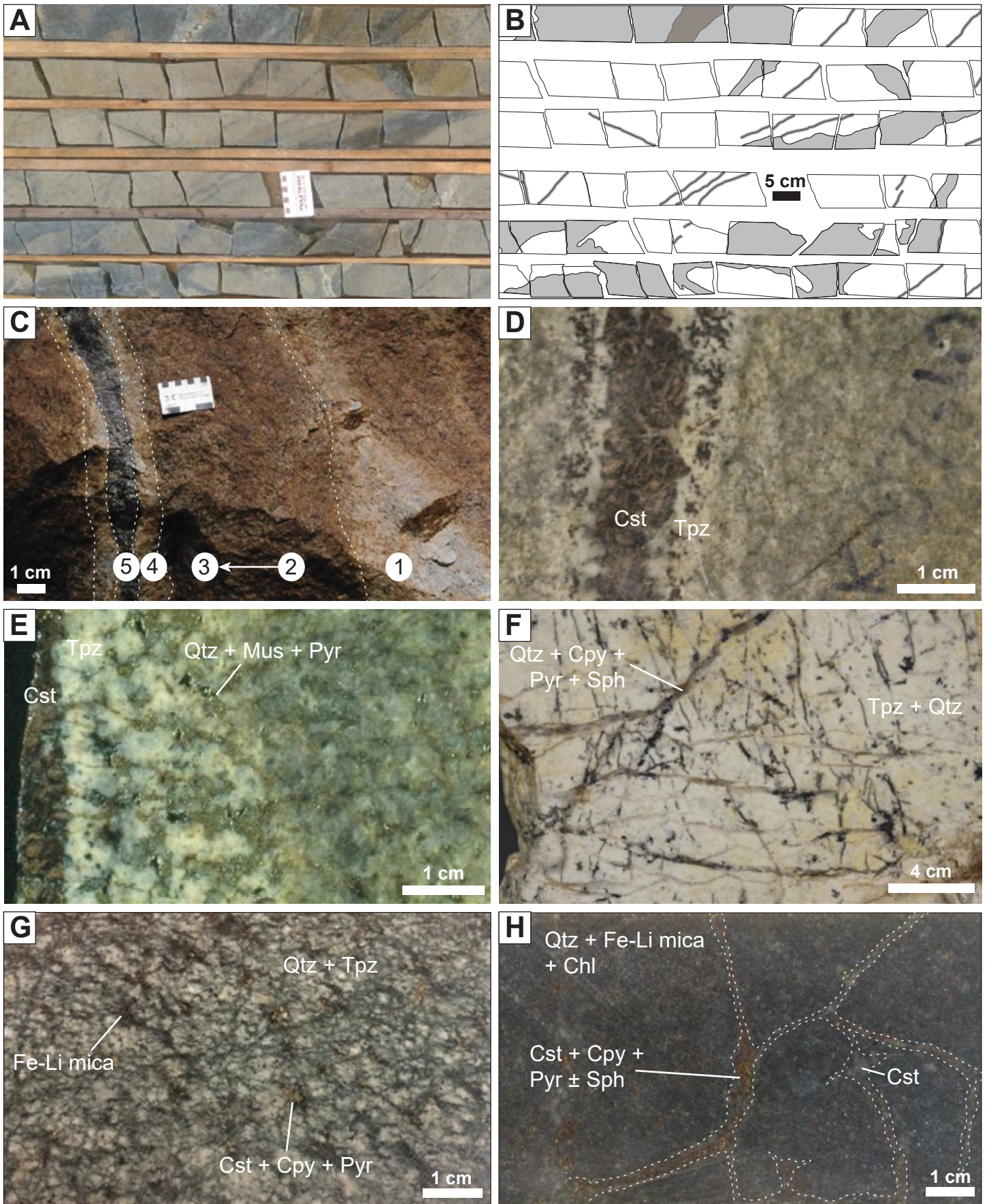


Figure 3–9

Figure 3–9. (A) Overview of drill core from the East Kemptville deposit (Main Zone) showing cm to m scale greisen zones (grey color) at consistent angles to the core axis. (B) Schematic of Fig. 3–9A with greisen zones shaded in grey and coarse topaz-cassiterite shaded in brown. (C) Outcrop photo of a zoned greisen with alteration domains identifiable by different colors: (1) least altered quartz-K-feldspar-albite-muscovite leucogranite; (2–3) greisenized quartz-(Fe-Li)mica-sericite leucogranite with increasing topaz and interstitial sulfides from 2 to 3; (4) dominantly quartz-topaz greisen; (5) coarse cassiterite-quartz core. (D) Hand sample of zoned greisen with coarse cassiterite core (Cst) and selvage of quartz-topaz (Tpz)-cassiterite. (E) Zoned greisen with quartz (Qtz), muscovite (Mus), pyrite (Pyr), and base-metal sulfides that have infilled porosity along fractures that extend into the East Kemptville leucogranite (EKL). (F) Rare thick quartz-topaz (Qtz-Tpz) greisen in EKL cross-cutting quartz-chalcopyrite-pyrite-sphalerite veins. (G) Hand sample of a light- to dark-grey quartz-albite-topaz variety of massive greisen from the BZ; homogeneous quartz, topaz, lesser albite and abundant diffuse-boundary microveinlets of dark grey Fe-Li-mica and disseminated to patchy ore mineralization. (H) Hand sample of dark grey quartz-mica variety of massive greisen from the BZ; dominantly quartz (Qtz), Fe-Li-mica, trace topaz and is cross-cut by network of microveinlets (outlined) containing quartz, cassiterite (Cst), chalcopyrite (Cpy), pyrite (Pyr), and sphalerite (Sph). Note coarser mineralization occurs at fracture junctions.

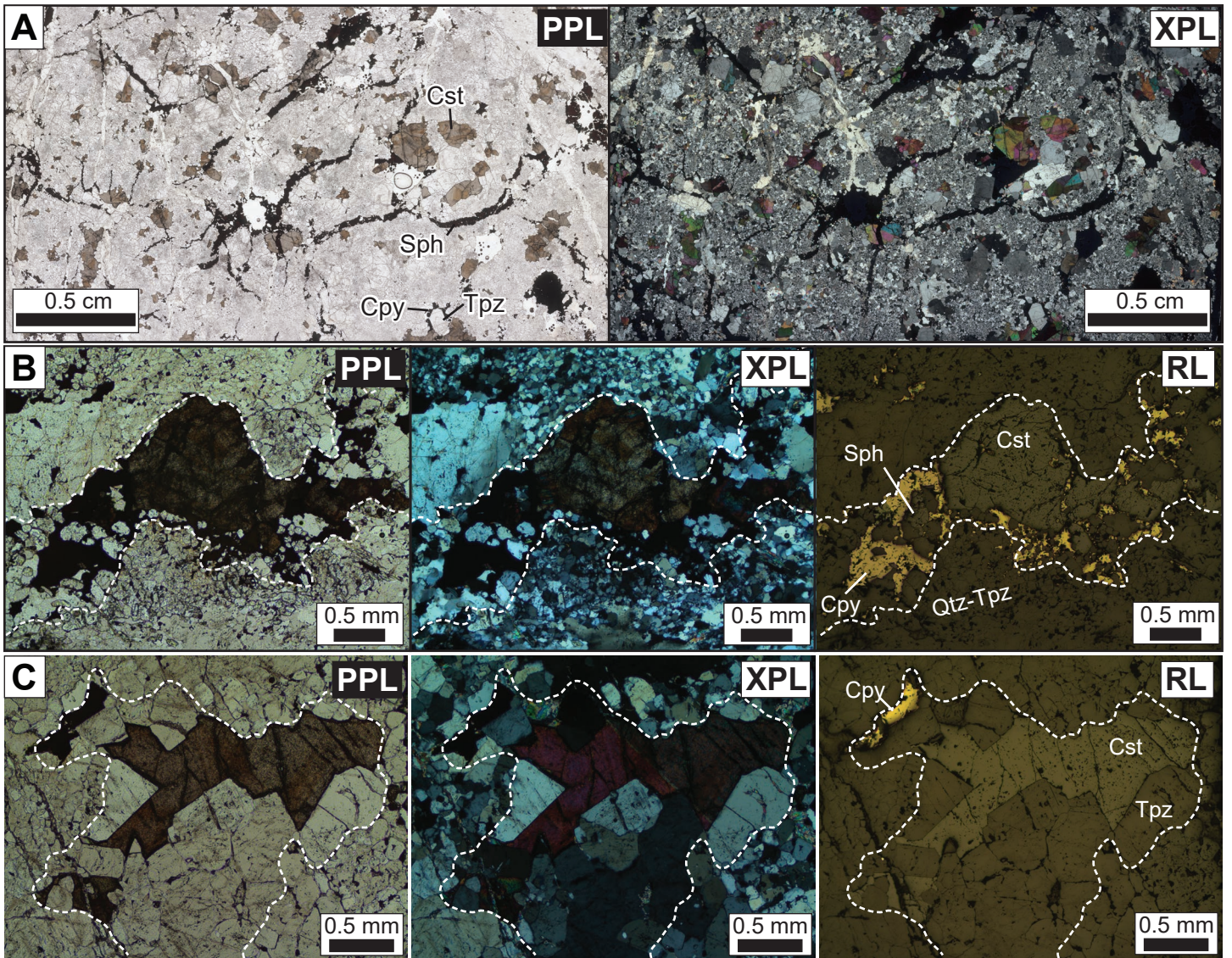


Figure 3-10

Figure 3–10. Petrography plate of samples from the East Kemptville deposit with photomicrographs. Modes of light include transmitted plane-polarized light (PPL), transmitted cross-polarized light (XPL) and reflected light (RL). **(A)** Example photomicrograph of massive greisen in BZ containing disseminated pockets of euhedral topaz (Tpz) with zoned cassiterite (Cst) and an overprinting network of brittle fractures infilled with base-metal sulfides, fluorite, and quartz (Qtz). **(B)** Coarse cassiterite infill of void (outlined) in the East Kemptville leucogranite after topaz alteration of muscovite-plagioclase and subsequently-emplaced sulfides (chalcopyrite, Cpy, followed by sphalerite, Sph). **(C)** Coarse euhedral topaz and coarse cassiterite infill in void (outlined) and subsequently emplaced sulfides (chalcopyrite).

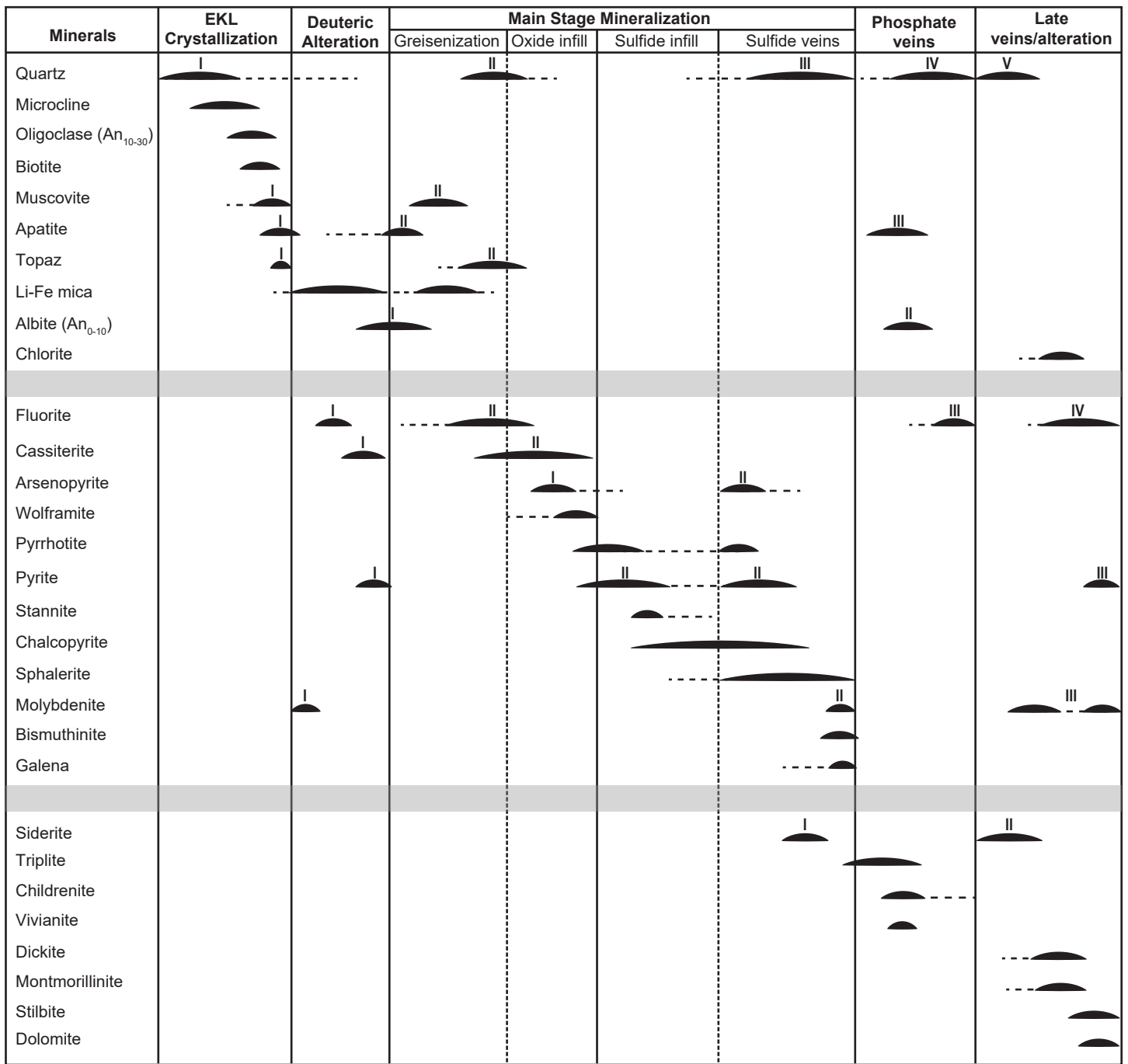


Figure 3 – 11

Figure 3–11. Detailed paragenesis of the East Kemptville leucogranite (EKL) and the mineralization of the East Kemptville Sn-Cu-Zn-Ag-In deposit; modified after Kontak, 1990. Main paragenetic stages are divided into cross-cutting relationships and textures observed in petrographic analyses throughout the deposit. The main-stage mineralization is subdivided into four stages but this can be observed as two temporally equivalent stages that follow the incipient greisen alteration (greisen infill and base-metal sulfide veins) that result in different grades. Multiple generations of one mineral type across the paragenesis are denoted with roman numerals.

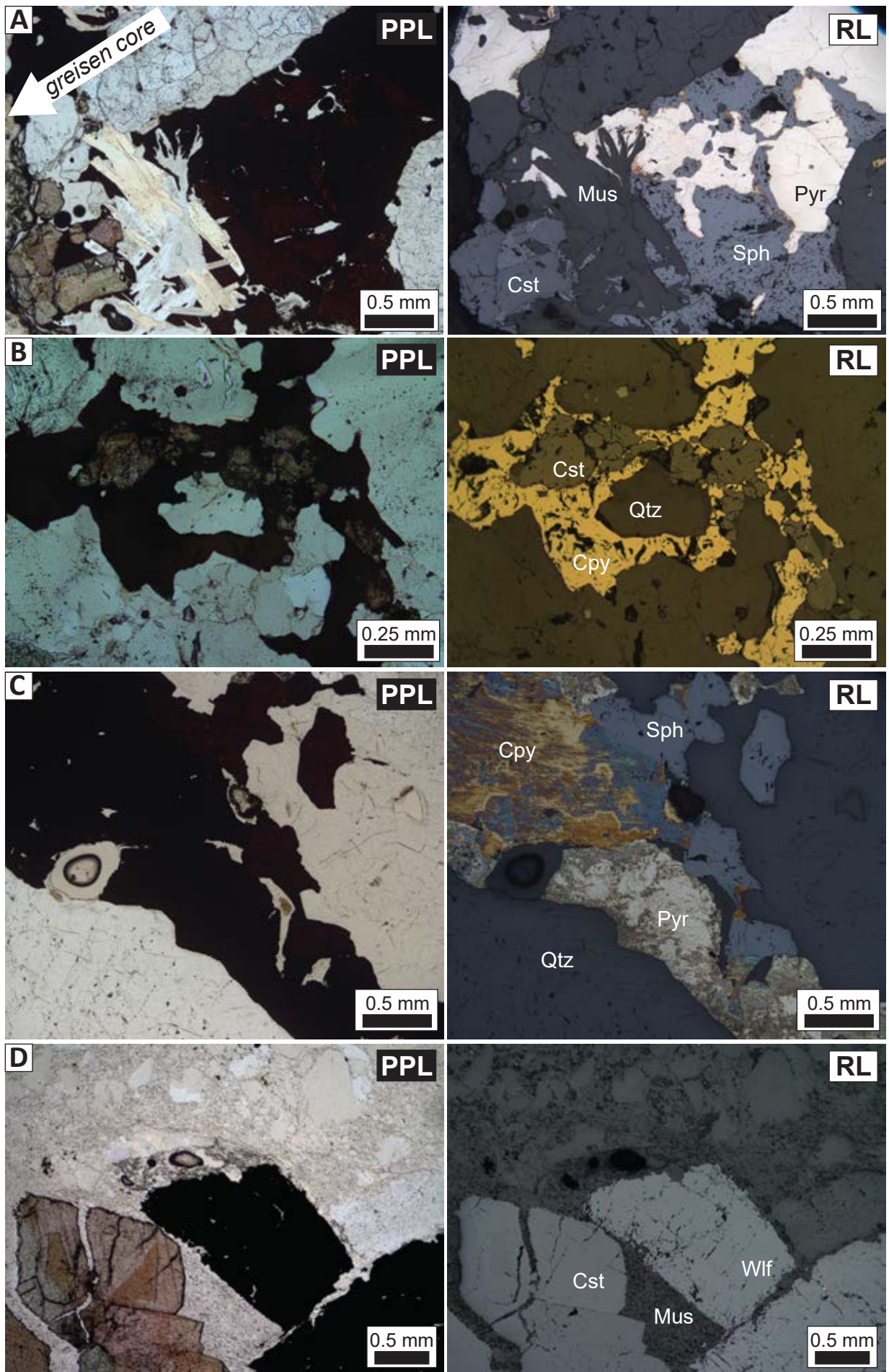


Figure 3-12

Figure 3–12. Photomicrographs of mineralized samples from the East Kemptville deposit. Modes of light include transmitted plane-polarized light (PPL, left) and reflected light (RL, right). **(A)** Thick vein with infill of quartz, pyrite (Pyr), sphalerite (Sph), and chalcopyrite, with rafts of muscovite (Mus) and cassiterite (Cst). **(B)** Irregular porosity infill by chalcopyrite (Cpy) with rafts of embayed quartz (Qtz) and partially digested cassiterite. **(C)** Coarse cassiterite (bottom left) and muscovite (Mus) crosscut by vein with sphalerite (Sph)-pyrite (Pyr) infill. **(D)** Coarse cassiterite and wolframite (Wlf) mineralization precipitated alongside quartz-sericite greisen proximal to contact with metasedimentary host rock.

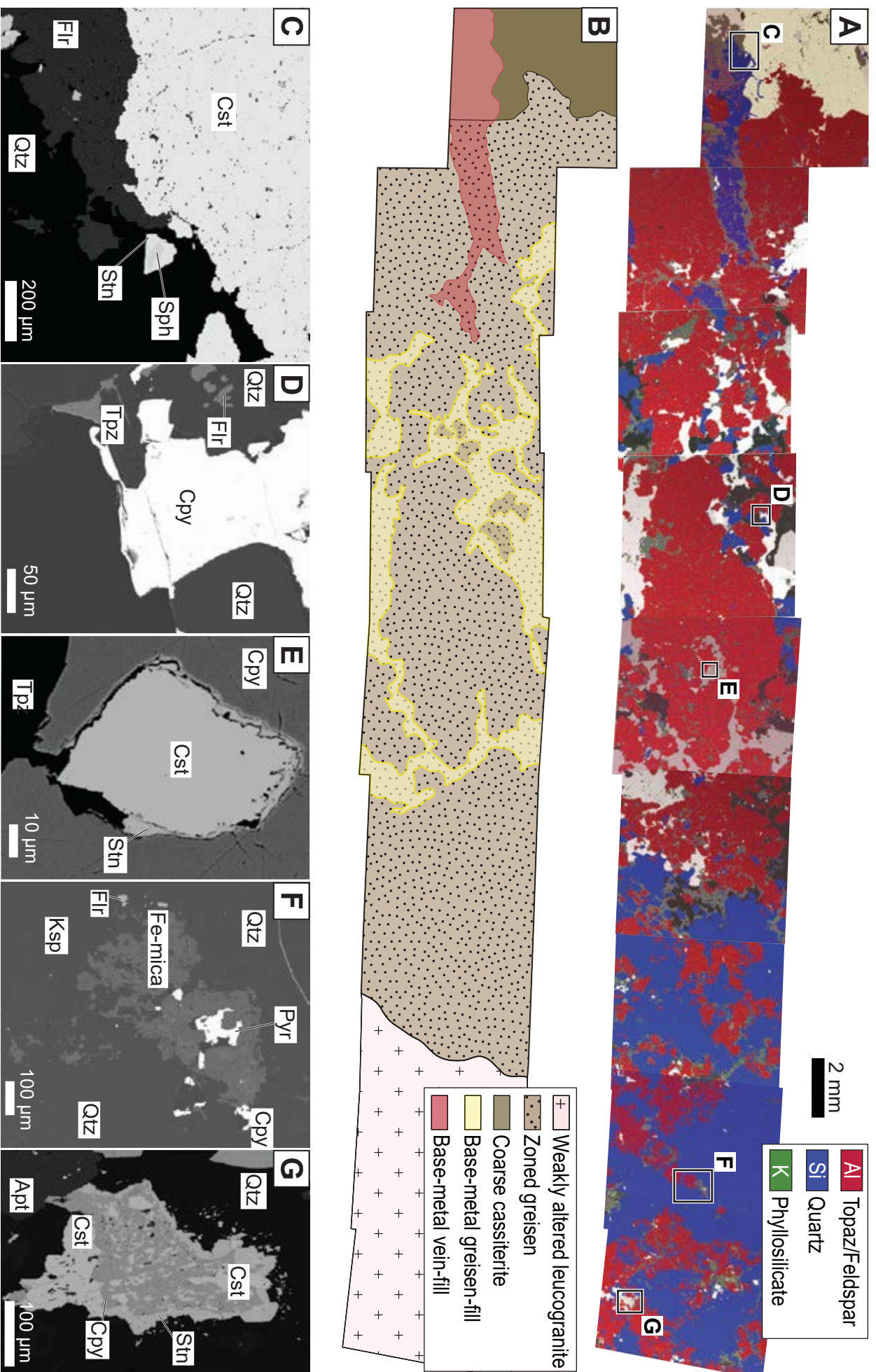


Figure 3-13

Figure 3–13. (A) Stitched SEM-EDS image of a zoned greisen in the East Kemptville deposit, colour-mapped by element to represent mineralogical changes across the greisen from relatively ungreisenized leucogranite (right) to coarse-cassiterite filled core (pale grey, left). Aluminum (red) is strongest in topaz and less so in feldspar, Silicon (blue) is strongest in quartz, and Potassium (green) is strongest in phyllosilicates. Sulfides and oxides are white to pale grey. (B) Sketch of the stitched image from Fig. 3–13A showing parts of image that are ungreisenized leucogranite, greisen, coarse cassiterite and gangue + base-metal vein/greisen infill. (C–G) close-up SEM-EDS images of mineralogical and textural relationships in the greisen and altered EKL. Cst – cassiterite, Flr – fluorite, Qtz – quartz, Stn – stannite, Tpz – topaz, Pyr – pyrite, Cpy – chalcopyrite, Ksp – feldspar, Apt – apatite.

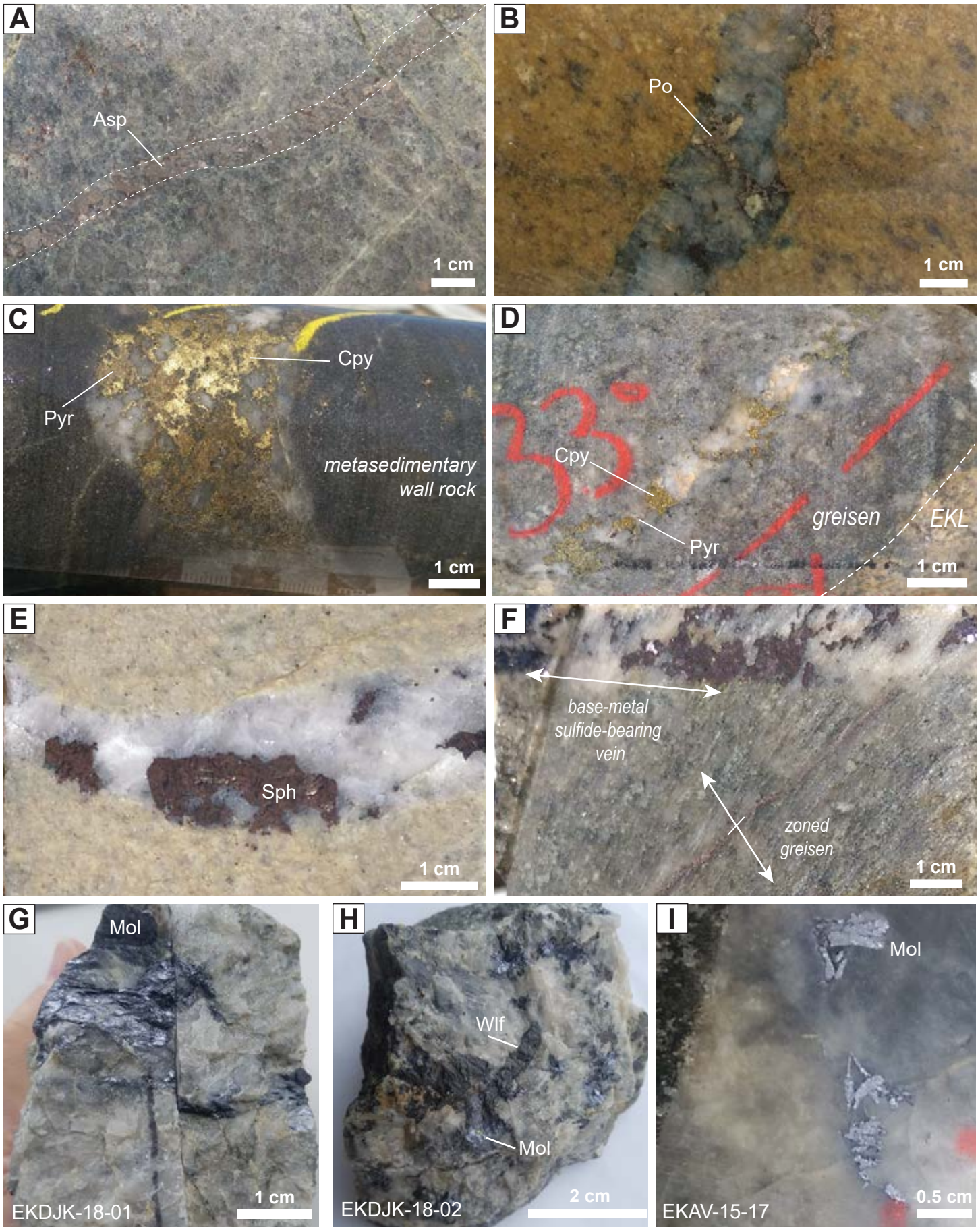


Figure 3-14

Figure 3–14. (A) Undulose vein of arsenopyrite (Asp) with diffuse vein boundaries cross-cutting dominantly quartz-sericite greisenized East Kemptville leucogranite (EKL). (B) Quartz-pyrrhotite (Po)-pyrite vein with discrete vein boundaries cross-cutting weakly altered EKL. (C) Vein of quartz and coarse chalcopyrite (Cpy)-pyrite (Pyr) cross-cutting metasedimentary host rock. (D) Thin vein of milky quartz and discontinuous chalcopyrite-pyrite cross-cutting quartz-sericite greisenized EKL. (E) Thick undulose vein of milk-white quartz and coarse discontinuous sphalerite (Sph) cross-cutting weakly altered EKL. (F) Quartz-sphalerite-chalcopyrite vein obliquely cross-cutting a zoned greisen. (G) Example of coarse molybdenite (Mol) in a granular quartz vein (EKDJK-18-01) from the Main Zone. (H) Example of coarse molybdenite hosted in a granular quartz vein intergrown with coarse euhedral wolframite (EKDJK-18-02) from the MZ. (I) Hydrothermal bladed molybdenite in a mineralized quartz-vein that crosscuts the EKL in the Main Zone, sample EKAV-15-17.

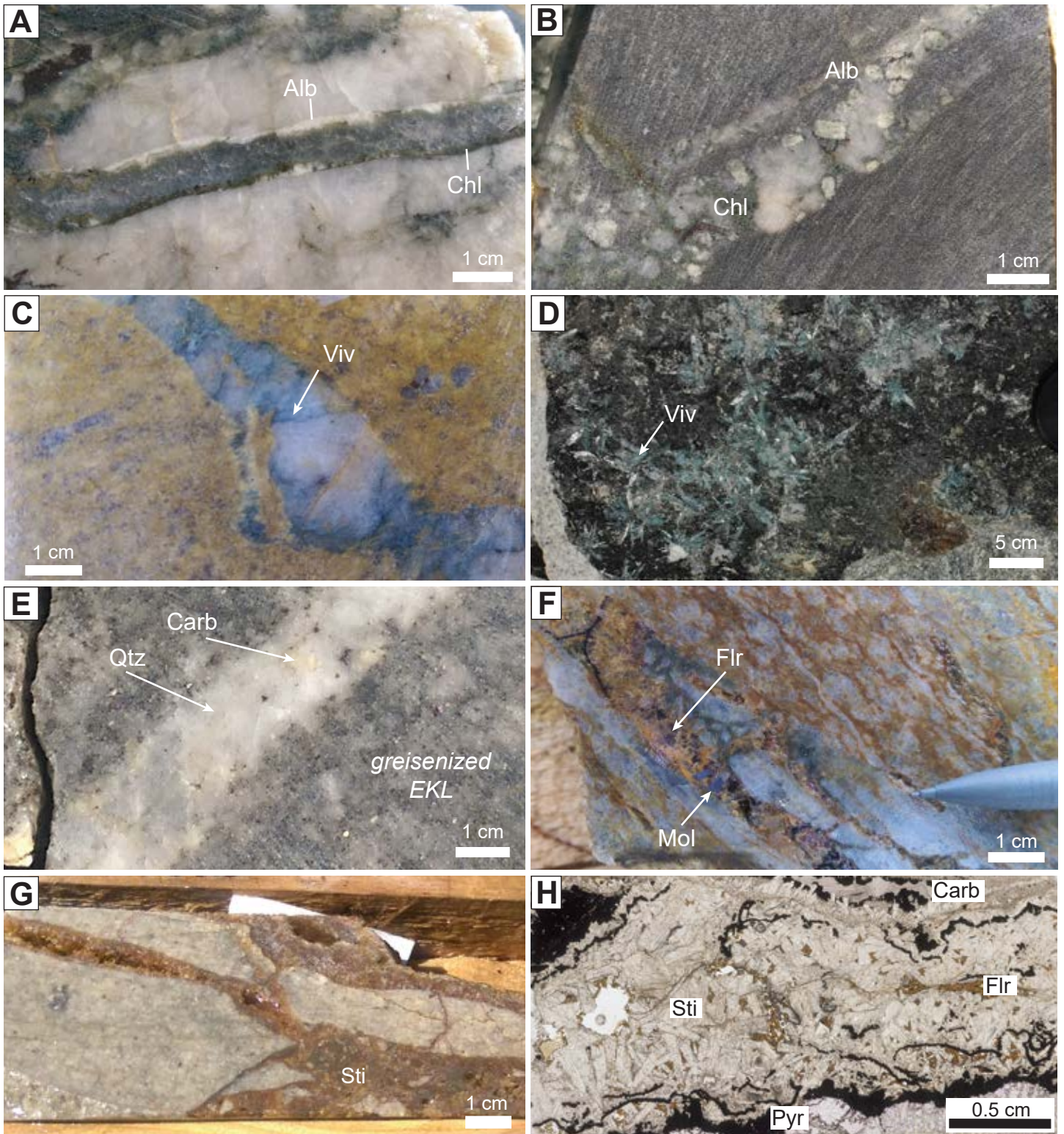


Figure 3-15

Figure 3–15. (A) Example of an extensional syntaxial clear quartz-albite (Alb)-chlorite (Chl) vein cross-cutting a thick milky quartz-sphalerite vein. (B) Ladder-extensional vein of quartz and euhedral albite with chlorite cross-cutting metasedimentary country rock. (C) Late quartz vein containing thin fibers of vivianite (blue phosphate, Viv). (D) Exposed surface of quartz-phosphate (vivianite, Viv) vein crosscutting EKL. (E) Unmineralized planar quartz (Qtz) vein with lesser carbonate (Carb) crosscutting greisenized EKL. (F) Extensional vein parallel to foliation of sheared East Kemptville leucogranite, exposing open space between quartz porphyroclasts; vein contains fluorite (Flr), stilbite, trace carbonate, and locally molybdenite (Mol). (G) Hand sample with thick breccia and extensional veins with dominant zeolite (stilbite, Sti) infill. (H) Photomicrograph example of Figure 3–15G in plane polarized transmitted light; Sti – stilbite, Carb – carbonate (dolomite), Flr – fluorite, Pyr - pyrite.

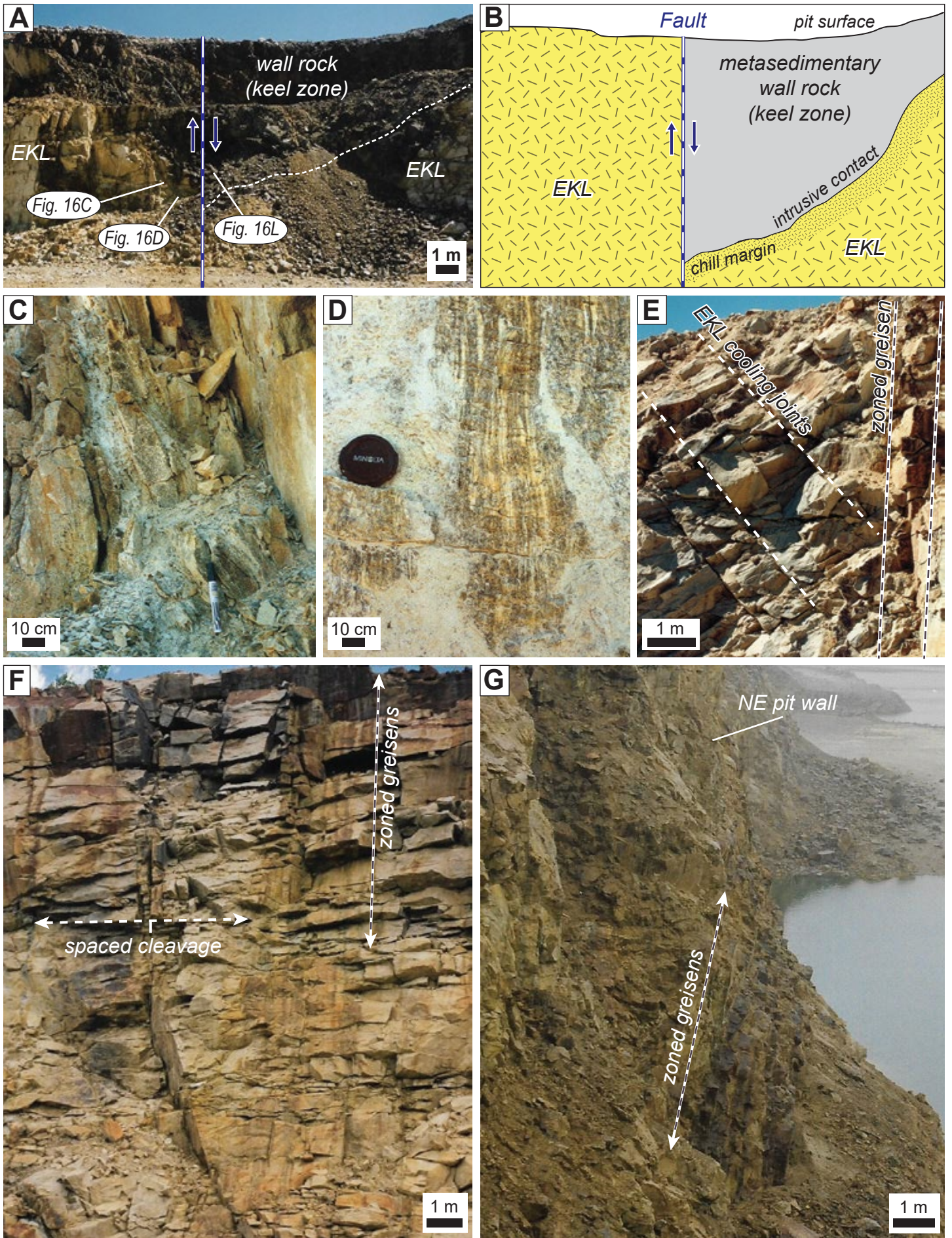


Figure 3-16

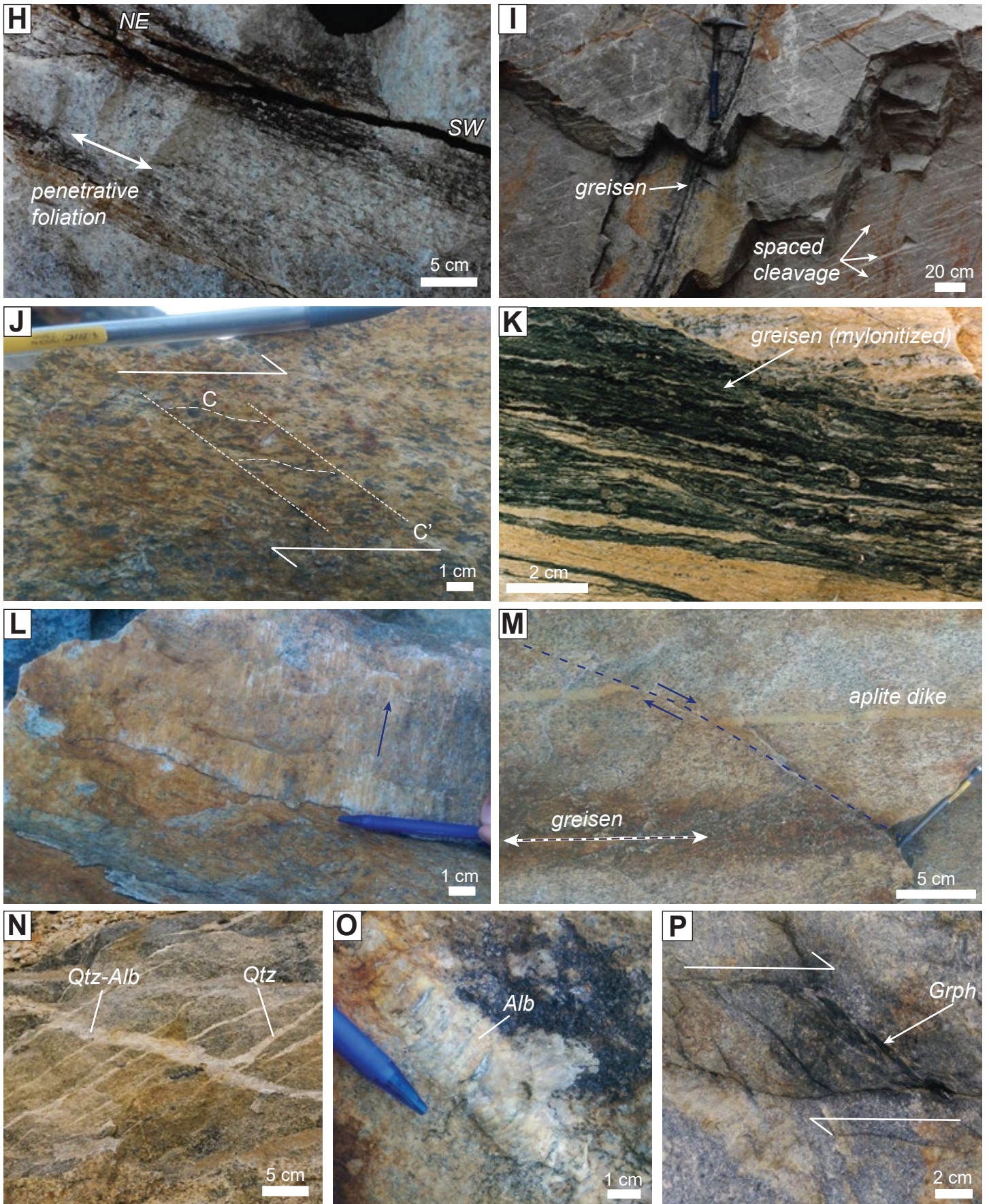


Figure 3–16, contd

Figure 3–16. Plate of outcrop photographs with structural features of the East Kemptville deposit. **(A)** Cross-sectional view of NE edge of Main Zone pit wall (Fig. 3–3B) with East Kemptville leucogranite (EKL)-metasedimentary rock contact normally offset by a fault (demarcated in blue **(B)** Schematic representation of Fig. 3–16A showing EKL chill margin (represented by fine grained EKL proximal the intrusive contact) and the structural boundary with a dominantly normal offset, with upward movement of the NW wall relative to SE footwall. Note approximate locations of fault plane close-up photographs C, D and J. **(C)** Fault zone (~15-cm) that is part mylonite and part gouge; zone oriented at 046°/84°W in the Main Zone. **(D)** Quartz-albite-topaz greisenization of mylonitized EKL, located on the main fault through the Main Zone (from Benn et al., 1997). **(E)** Conjugate cooling joints in relatively undeformed EKL (left) cut by vertical greisens along fault planes (right). **(F)** Open pit wall showing shallowly-dipping spaced cleavage (Fig. 3–3) and cross-cutting vertically-oriented zoned greisens. **(G)** View of NE pit wall (looking SW) showing vertical development of thick zoned greisens (darker color). **(H)** Outcrop example of NE striking near-vertical penetrative fabric in the EKL. **(I)** Outcrop example of spaced (2–5 cm) cleavage overprinting altered EKL. **(J)** Hand sample with C-C' fabric of sheared muscovite and feldspar ductily wrapping around deformed quartz grains, indicative of dextral shearing. **(K)** Ductile overprint on greisenized EKL with segmented porphyroclasts (pre-kinematic) of cassiterite and deformed quartz-sulfide veins. **(L)** Surface of a syn-kinematic quartz vein from the footwall to the main fault zone through the Main Zone; note slickenfiber growth with steps that indicative vertical upward movement of NW hanging wall relative to the sample location (A). **(M)** EKL hosted greisen and parallel aplite dike, both offset by late shear plane with dextral sense of movement. **(N)** En-echelon shear veins (barren quartz) with continuous feather vein parallel to the EKSZ cross-cutting thick quartz-albite (Qtz-Alb) vein. **(O)** Extensional syntaxial fibrous quartz-albite (Alb) vein with synthetic to antithetic mineral growth indicating syn-kinematic vein development. **(P)** Outcrop photo of shear plane cross-cutting greisenized EKL and cemented by chlorite and graphite (Grph, arrow). Note the dextral shear sense is the same as observed in early ductile foliation.

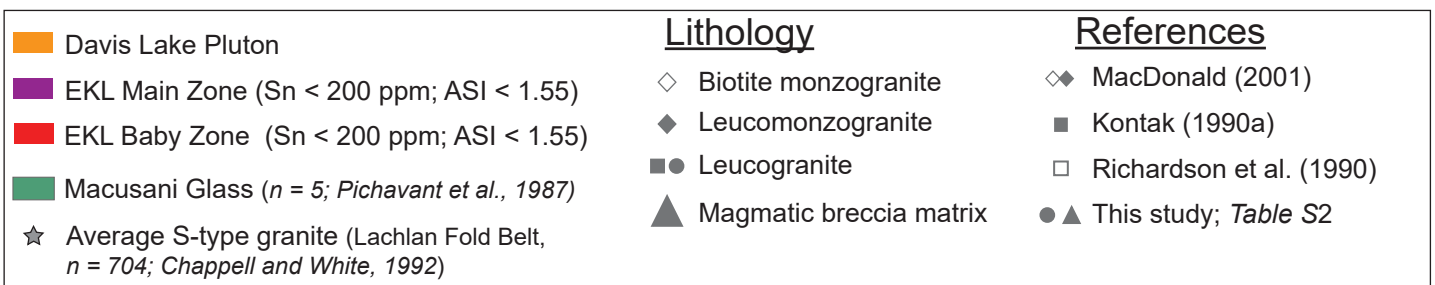
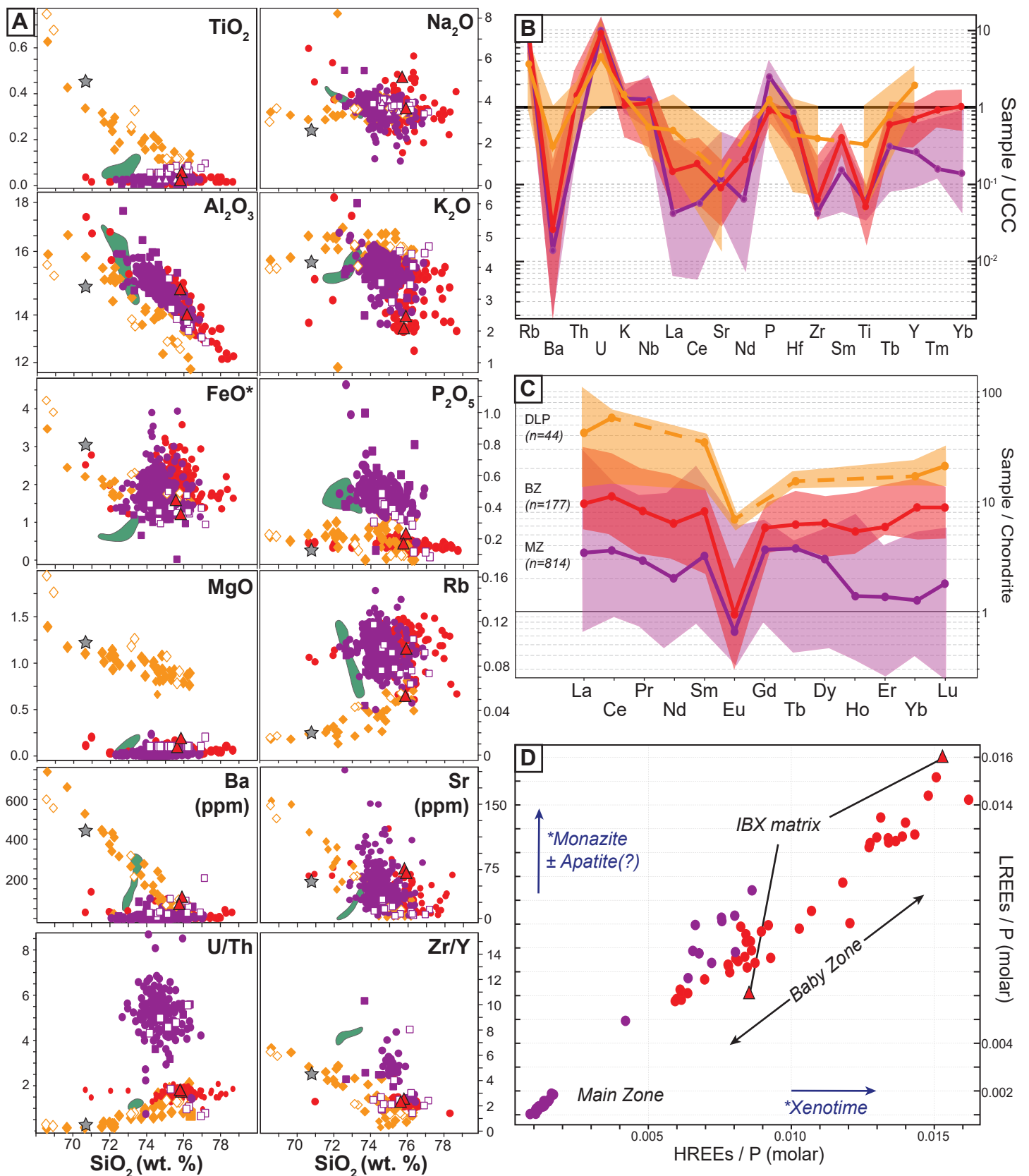


Figure 3-17

Figure 3–17. (A) Scatter plots of major and trace element concentrations as well as ratios in the less altered granitic rocks from various parts of the Davis Lake Pluton (DLP) and from the East Kemptville leucogranite (EKL) at the deposit (i.e., Baby and Main zones). The grey star depicts average values for S-Type granites (from Chappell and White, 1992) and the field of samples from the F-rich Macusani glass of Peru is shown in green (Pichavant et al., 1987). Note, number of samples shown in Fig. 3–17C. (B) Multi-element plot normalized to average upper continental crust (Taylor and McLennan, 1995) with least altered samples from both ore zones and the DLP plotted; fields for each suite are shown as different colors and averages (means) are shown as lines for each field. (C) Spider-diagram with average rare-earth element (REE) concentrations normalized to chondrite (McDonough and Sun, 1995) for each of the aforementioned suites of least altered granitic rocks; note the sample bias as the number of samples and suite of elements analyzed is greater and broader for rocks of the Baby and Main zones relative to historic analyses of the DLP. (D) Plot of molar light (L) REEs versus heavy (H) REEs, each normalized to P, showing the discrimination between ore zones in the least altered EKL samples; included is the felsic matrix to the magmatic breccias of the Baby Zone (IBX). Note that increases to molar HREEs versus LREEs (with P normalized) suggests an increase in xenotime versus monazite and apatite content.

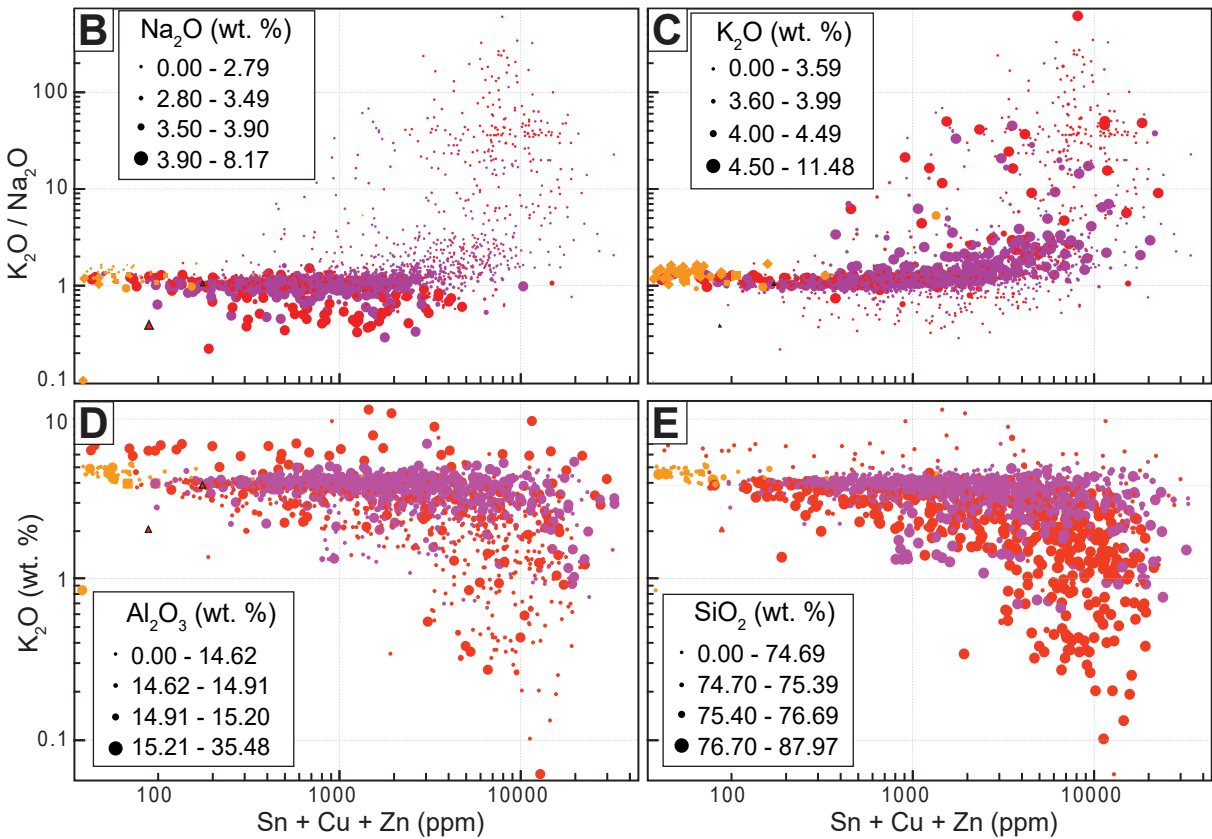
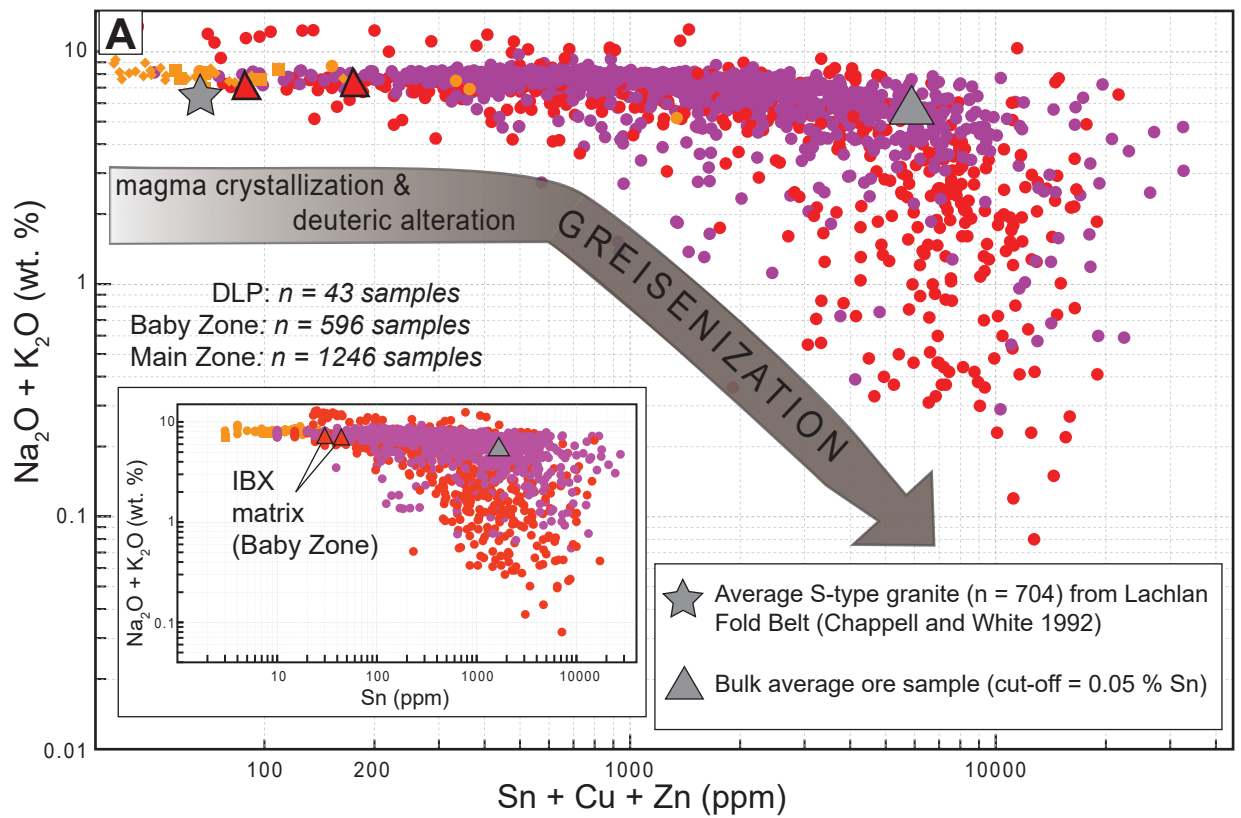


Figure 3–18

Figure 3–18. (A) Scatter plot showing $\text{Na}_2\text{O} + \text{K}_2\text{O}$ content versus ore-element content ($\text{Sn} + \text{Cu} + \text{Zn}$; Sn-only in inset) in DLP and East Kemptville leucogranite (EKL; entire sample suite, legend same as Fig. 3–17); logarithmic scale. Note that the concentration of $\text{Na}_2\text{O} + \text{K}_2\text{O}$ of the bulk average ore sample in the deposit is near equal to that of the less altered (moderate $\text{Na}_2\text{O} + \text{K}_2\text{O}$ concentration) granitic rocks, and the reduction of $\text{Na}_2\text{O} + \text{K}_2\text{O}$ content (suggestive of greisen development) is related to an inflection near the bulk average. (B–E) Log-log plots showing the ratio of $\text{K}_2\text{O} / \text{Na}_2\text{O}$ (B, C) or K_2O (D, E) versus ore-element content ($\text{Sn} + \text{Cu} + \text{Zn}$) in the EKL and Davis Lake Pluton samples (entire sample suite, legend same as Fig. 3–17), multiple major element changes are shown by point sizes in each plot and the inferred alteration represented is shown in parentheses: (B) Na_2O enrichment (albitization); (C) K_2O enrichment (sericitization); (D) Al_2O_3 enrichment (topaz-greisenization); (E) SiO_2 enrichment (greisenization and hydrothermal veining).

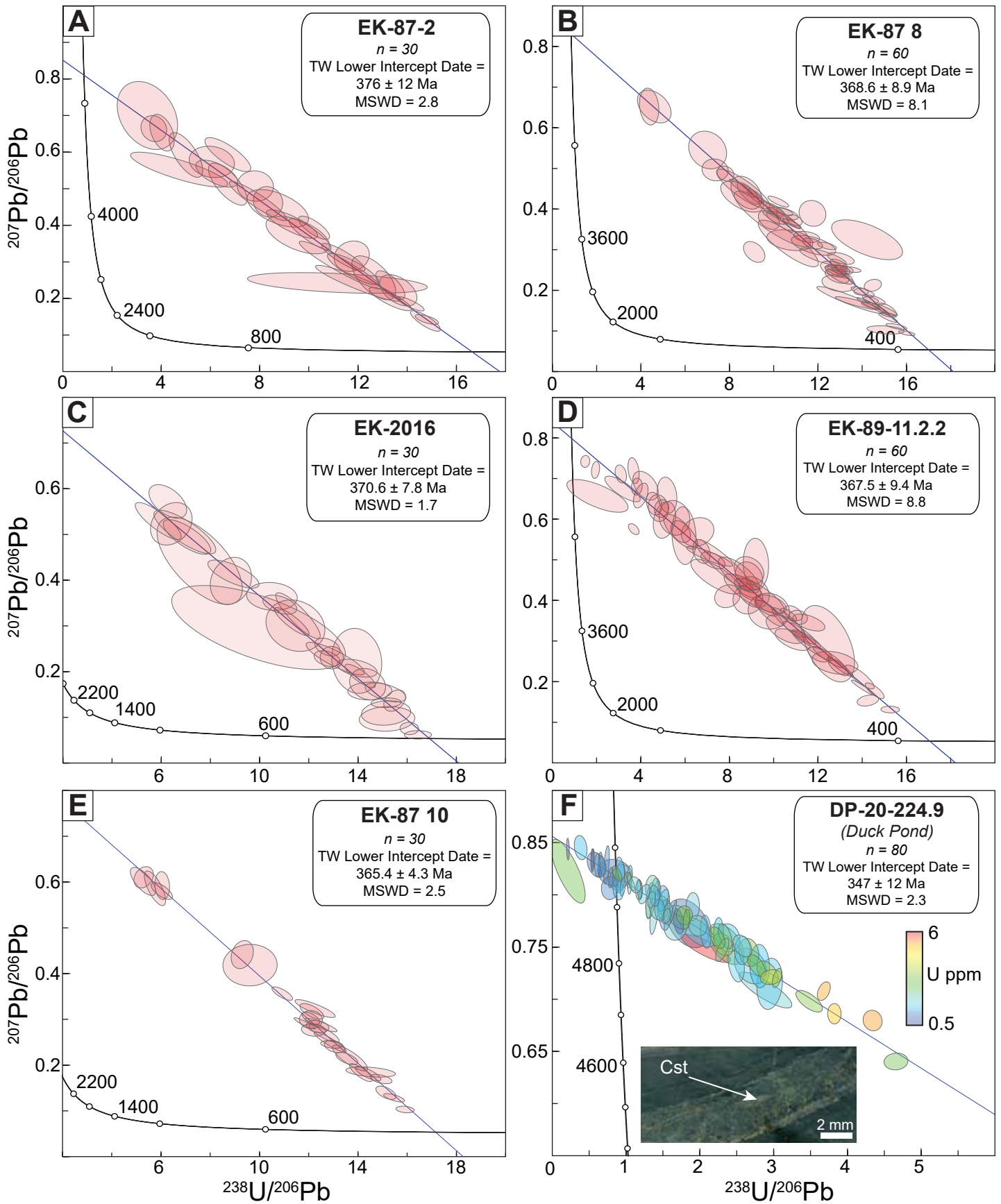


Figure 3–19

Figure 3–19. Tera-Wasserburg concordia diagrams for cassiterite samples from the East Kemptville deposit (**A-E**) and Duck Pond deposit (**F**) with an inset of dated material (cassiterite-bearing lens of greisen in metapelite). Data point error ellipses are 2σ .

Main Zone (MZ)

Baby Zone (BZ)

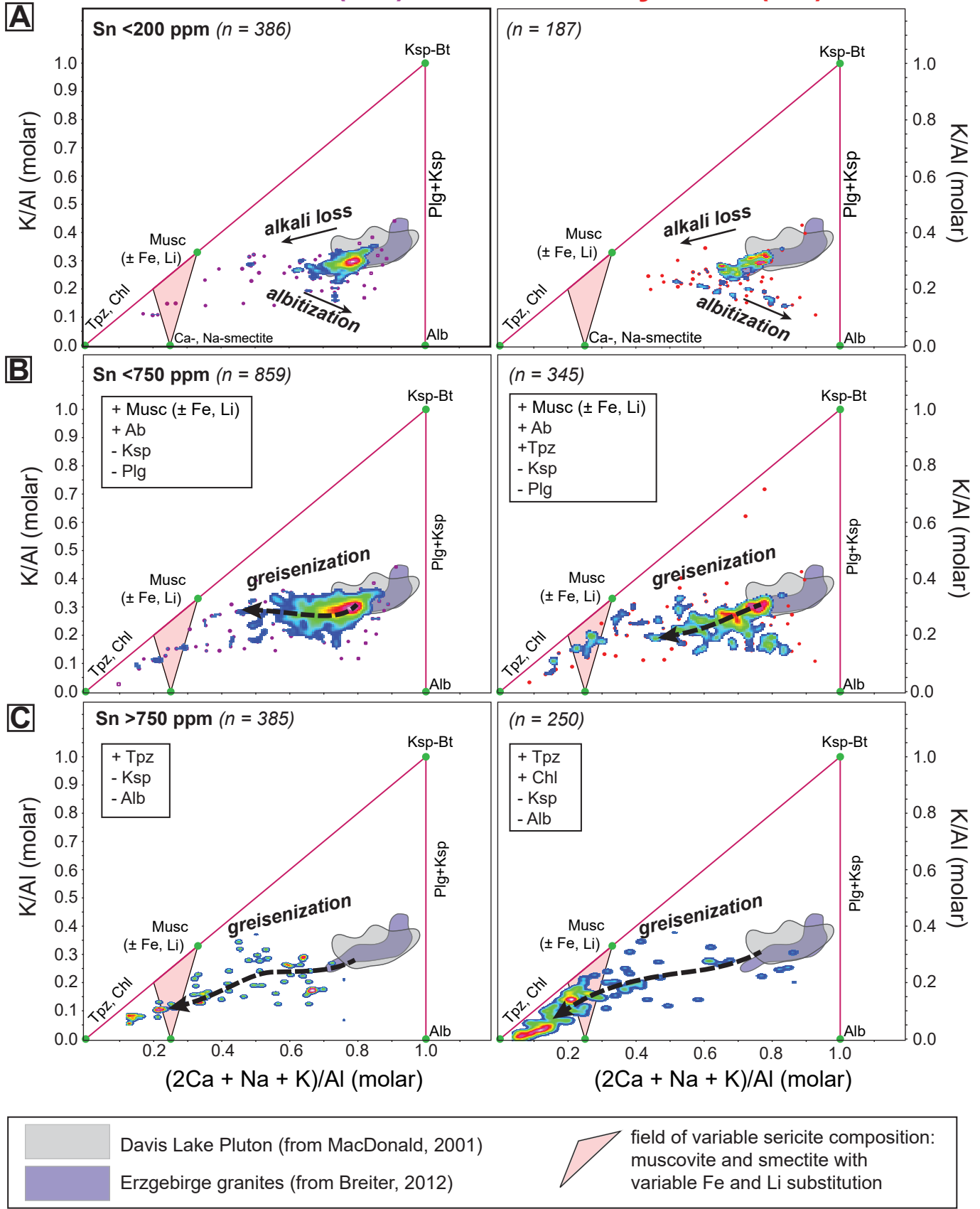


Figure 3–20

Figure 3–20. Modified Pearce-element ratio diagram depicting aluminosilicate mineral content (after Stanley and Madeisky, 1994) with population density clouds (red = dense sample data, blue = sparse sample data) of granitic rocks from the two ore zones in the deposit (Main Zone on left and Baby Zone on right) based on Sn-content tertials: (A) 0–205 ppm, (B) 0–739 ppm, (C) all assays. The grey field in each plot represents the population of the less-evolved Davis Lake Pluton (DLP) samples. Note the dashed black line in the plots of mineralized samples showing the evolution in net change of alkalis and mineral assemblages for higher grade rocks; elements added and removed from the deposit along these paths are shown in the inset to each plot. Ksp–K-feldspar, Bt–biotite, Tpz–topaz, Chl–chlorite, Mus– muscovite, Alb–albite, Plg–plagioclase. The shaded red triangle represents a field of variable mica content in sericite; between muscovite and smectite and including varying degrees of Fe and Li substitution into the K⁺ site for muscovite (represented along the [Tpz,Chl]–Mus tie-line).

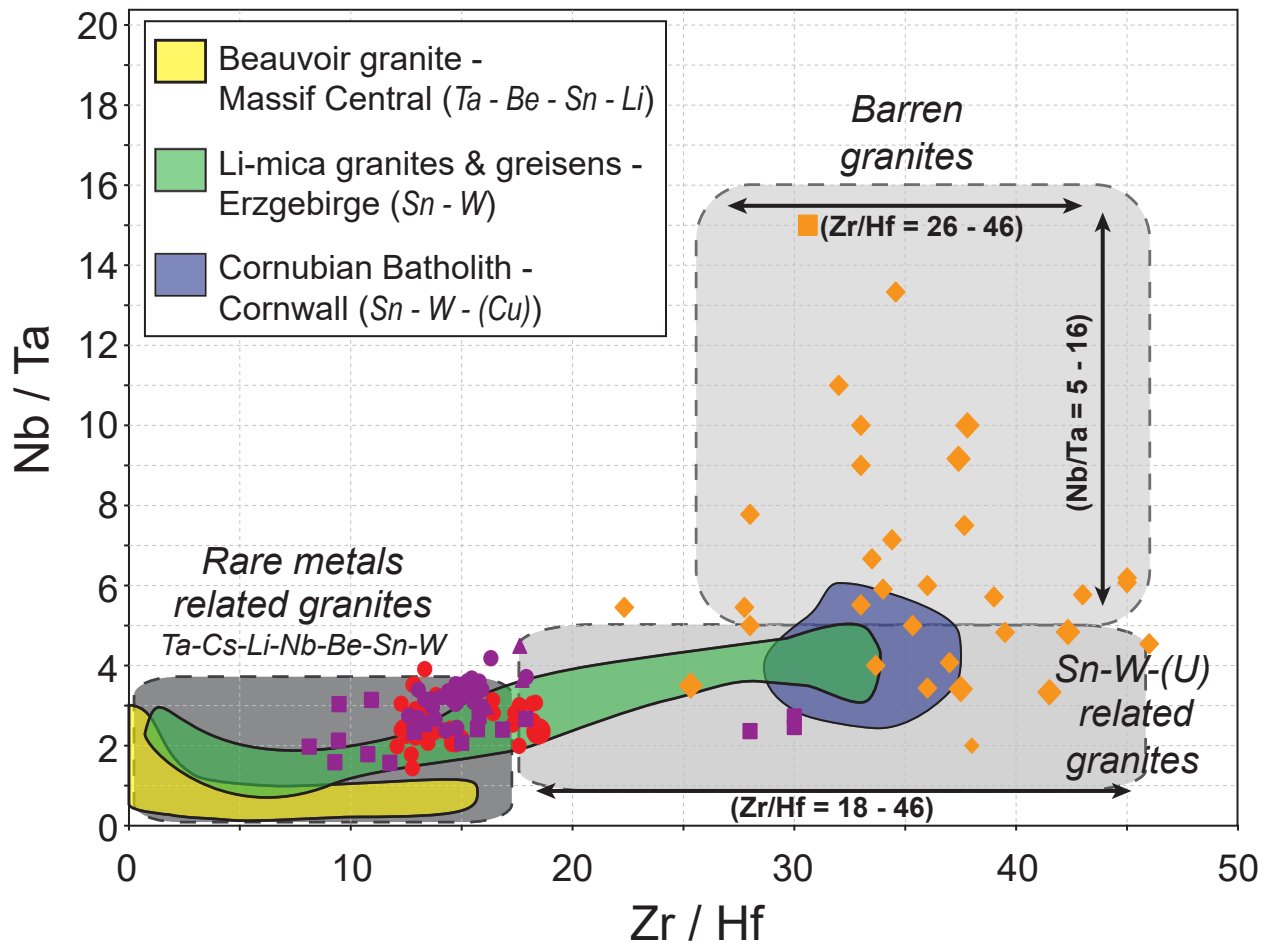


Figure 3-21

Figure 3–21. Plot of whole rock Nb/Ta versus Zr/Hf showing least altered East Kemptville leucogranite (EKL) sample data (legend same as previous geochemical figures) with fields of granite fertility for lithophile element mineralization between i) rare metal-related mineralization (Ta-Cs-Li-Nb-Be-Sn-W), ii) Sn-W-U related mineralization, and iii) barren granites; fields for leucogranite data from other global Sn-bearing deposits are also shown, the legend for which is depicted in the plot inset (modified from Ballouard et al., 2016). Note, a majority of Davis Lake Pluton samples plot within the ‘barren granite’ field, whereas a majority of the EKL samples (from both ore zones) plot within the ‘rare metal-related granite’ field and most closely related to the Li-mica granites and greisens of the Erzgebirge region.

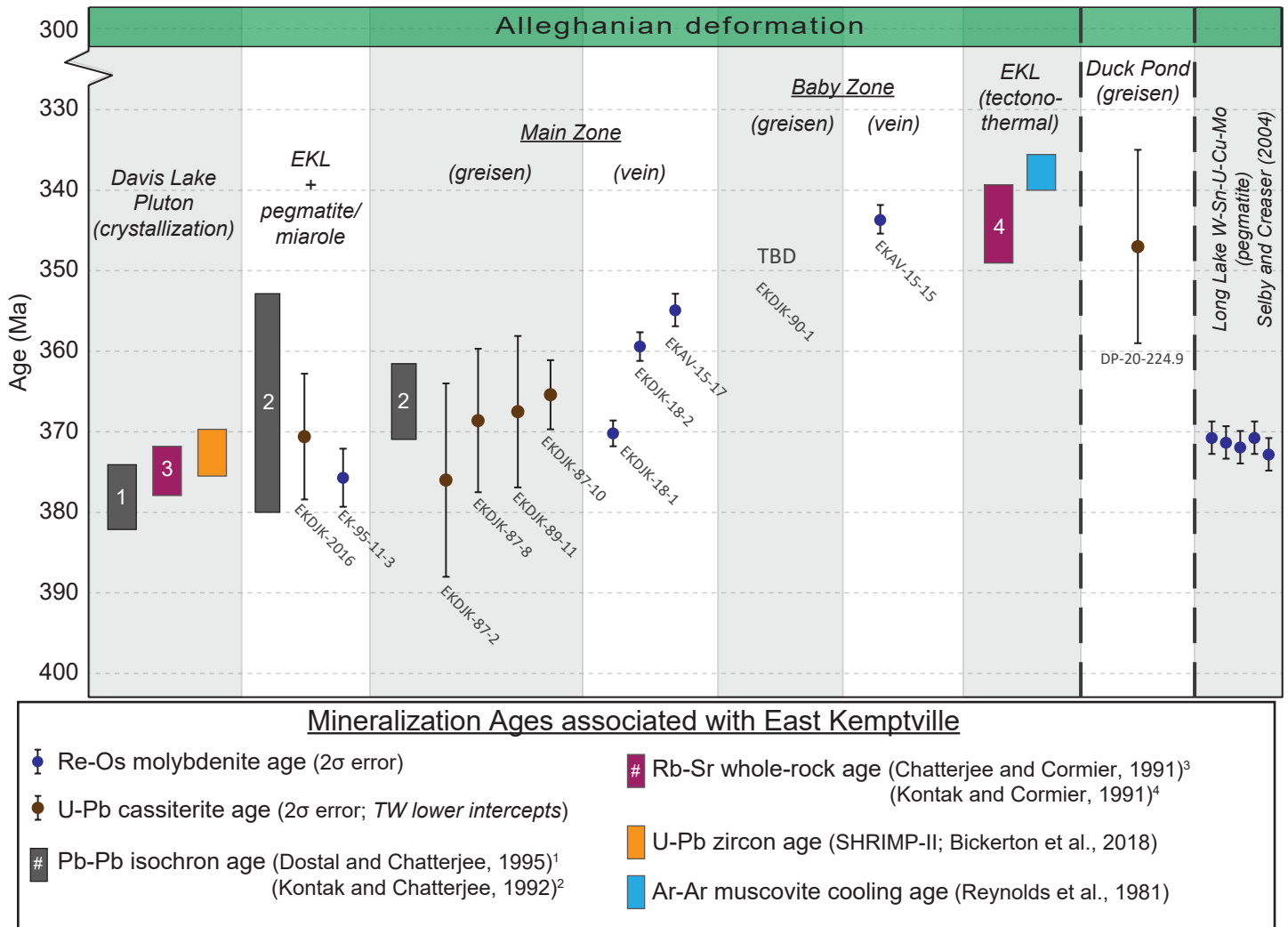


Figure 3–22

Figure 3–22. Comparison plot showing compiled Re-Os molybdenite and U-Pb cassiterite mineralization ages from this study. Also shown are previous geochronology (Rb-Sr whole rock, Ar-Ar muscovite, U-Pb zircon) of the East Kemptville deposit and Duck Pond prospect as well as associated intrusions. Also shown is the Re-Os molybdenite ages from the Long Lake deposit in the New Ross Pluton, within the South Mountain Batholith (Selby and Creaser, 2004).

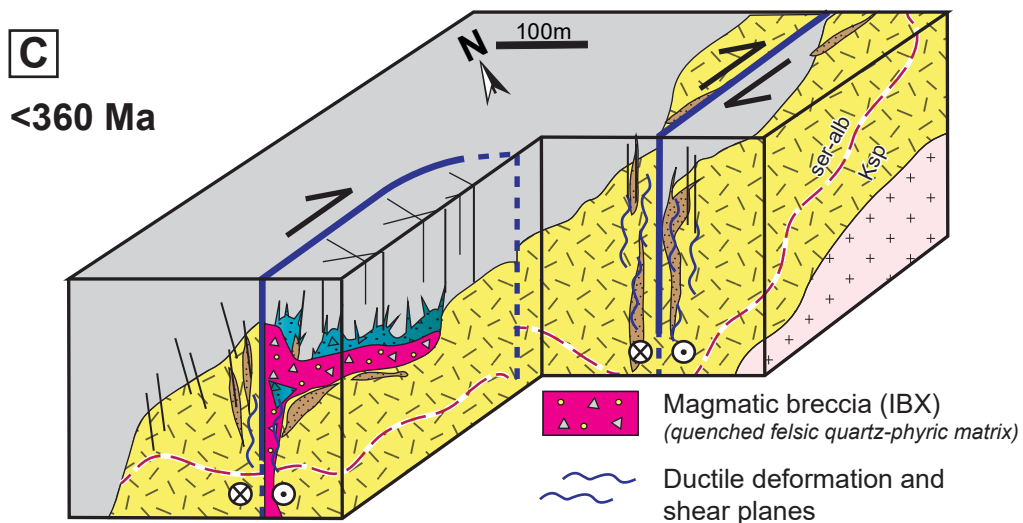
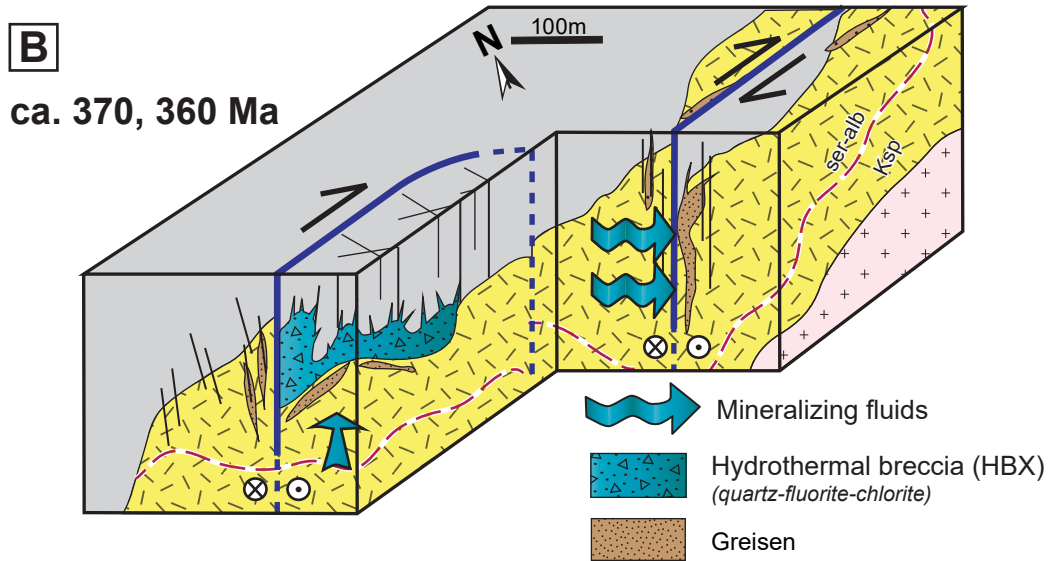
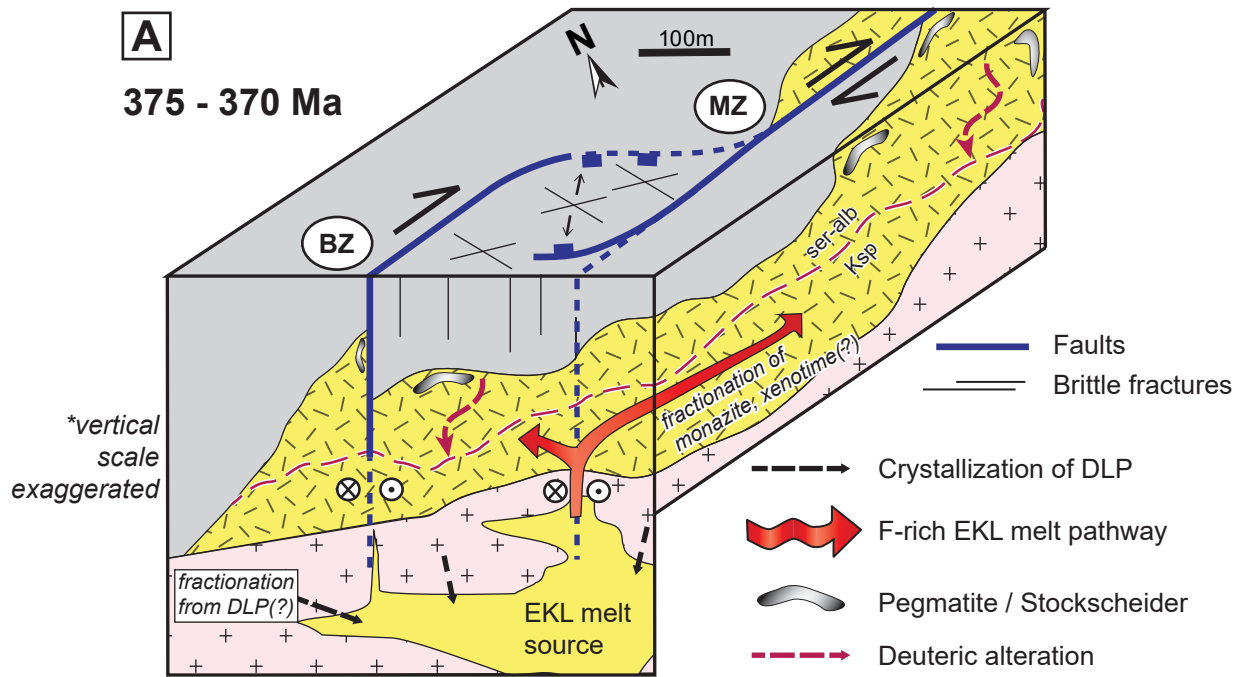


Figure 3-23

Figure 3–23. Schematic formation model for the East Kemptville Sn-Cu-Zn-Ag-In deposit. Note the structural control that preconditions each ore zone (Baby and Main; BZ and MZ) for their respective dominant greisen types. **(A)** Initial East Kemptville leucogranite (EKL) emplacement at ca. 375 Ma fractionates accessory phases between ore zones as F-rich porphyritic melt exposes a brittle accommodation zone within a stepover between shear planes of the East Kemptville-East Dalhousie Shear Zone; note subsequent deuteritic alteration (sericite and albite replacing K-feldspar; ser-alb/Ksp) and formation of pegmatites, stockscheiders, miaroles in a late stage fluid event between ca. 375 and 370 Ma. **(B)** mineralizing fluids, sourced from depth, overprint the deuteritic alteration along brittle fractures through the deposit by ca. 370 Ma; such fluids also form hydrothermal breccia (HBX) in the Baby Zone where transtensional stresses allow, and massive greisens occur in this zone. Continued fluid incursion along structures occurs intermittently to ca. 360 Ma, recorded by U-Pb cassiterite in greisens and Re-Os molybdenite in veins (Fig. 3–22). **(C)** After formation of deposit and prior to extensive ductile deformation, a magmatic breccia (IBX) exploits the Baby Zone fault plane and overprints mineralization.

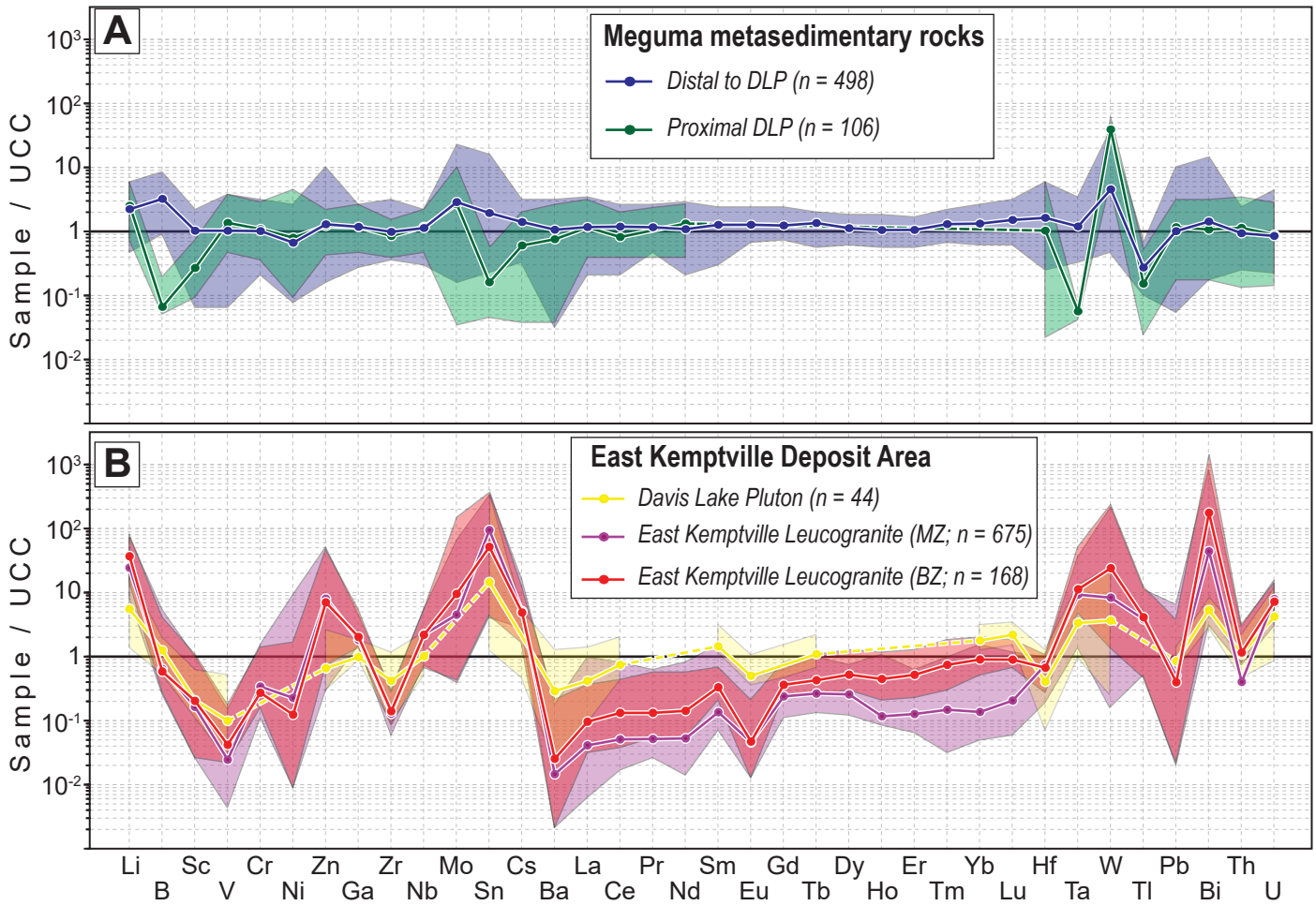


Figure 3–24

Figure 3–24. Multi-element plots normalized to upper continental crust (UCC; Rudnick and Gao, 2003) of (A) metasedimentary rocks of the Meguma terrane from southwest Nova Scotia, divided into western and southern portions of the region (White, 2010b) and (B) least-altered leucogranites of the Davis Lake Pluton and mineralization-associated East Kemptville Leucogranite, divided into the two ore zones of Baby (BZ) and Main (MZ). Note the fields represent all data and the lines represent average composition (mean). SW NS = southwest Nova Scotia (Fig. 3–2).

Table 3–1. Whole-rock major, minor, and rare-earth element abundances for granitic rocks in study area

Sample	16-EKLB-001	16-EKLB-003	16-EKLB-004	16-EKLB-005	16-EKLB-011	BIC068	BIC069
Unit	EKLG	EKLG	EKLG	EKLG	EKLG	IBXM	IBXM
Zone	MZ	MZ	MZ	MZ	MZ	BZ	BZ
SiO ₂ (%)	74.65	75.03	75.55	75.02	77.18	76.41	75.78
Al ₂ O ₃	15.2	14.97	14.56	15.04	13.44	13.81	14.8
Fe ₂ O ₃ (t)	1.2	1.37	1.65	1.49	2.73	1.52	1.21
MnO	0.04	0.06	0.06	0.07	0.07	0.1	0.04
MgO	0.04	0.06	0.05	0.07	0.3	0.06	0.18
CaO	0.45	0.49	0.56	0.48	0.66	0.43	0.53
Na ₂ O	3.96	4.09	3.54	3.47	0.11	3.65	5.22
K ₂ O	3.98	3.45	3.48	3.9	4.92	3.84	2.05
TiO ₂	0.03	0.03	0.03	0.03	0.04	0.04	0.02
P ₂ O ₅	0.45	0.44	0.53	0.42	0.53	0.15	0.17
Total	100	99.99	100.01	99.99	99.98	100.01	100
C	0.01	0.01	0.01	0.01	0.01	0.01	0.02
S	0.005	0.005	0.01	0.005	0.19	0.07	0.01
Li (ppm)	440	440	540	410	340	880	210
Cs	23.9	24.3	30.4	28.3	52.8	38.3	21.3
Rb	818	773	925	900	1240	957	530
Sr	43.3	54.8	87.5	19.9	26.2	29.9	102
Ba	11.2	8	10.4	6.4	73.7	20.3	70.5
Sc	2	2	2	2	2	3	2
Cr	<10	<10	<10	<10	10	<10	<10
Ni	2	1	1	<1	<1	<1	3
Co	<1	<1	<1	<1	2	<1	1
V	<5	<5	<5	<5	<5	<5	<5
Pb	14	4	5	3	4	5	3
Cu	21	27	104	36	459	24	17
Zn	29	36	56	70	2450	122	28
Mo	<1	4	1	<1	<1	<1	1
W	8	9	17	8	14	16	8
Sn	138	83	303	173	568	30	44
Ag	<0.5	<0.5	1.1	<0.5	1	<0.5	<0.5
In	0.562	0.555	1.475	2.26	7.63	0.202	0.072
As	2.2	3.3	10	5.2	5.3	9.4	2.6
Tl	0.63	0.67	0.75	0.74	1.33	1.09	0.59
Bi	1.12	5.5	17.25	2.59	5.33	7.81	1.14
Hf	2.1	1.8	1.9	2.2	1.1	2.6	1.9
Ta	6.5	10.4	11.7	8.4	3.1	11.5	16.4
Nb	29.2	30.9	36	30.6	13.7	27.1	35.4
Zr	37	29	30	39	19	48	28

Table 3–1, cont'd.

Sample	16-EKLB-001	16-EKLB-003	16-EKLB-004	16-EKLB-005	16-EKLB-011	BIC068	BIC069
Unit	EKLG	EKLG	EKLG	EKLG	EKLG	IBXM	IBXM
Zone	MZ	MZ	MZ	MZ	MZ	BZ	BZ
Y (ppm)	5.8	6.6	7.6	6.7	9.5	21.5	13.4
Th	5.09	6.63	4.9	5.92	8.11	17.95	13.35
U	26	24.7	19.85	18.25	47.5	28	19.95
Ga	32.8	35.6	38.2	35.6	47.3	36.9	35.8
Ge	<5	<5	<5	<5	<5	<5	<5
Hg	<0.005	0.009	0.007	0.019	0.009	<0.005	<0.005
Re	<0.001	<0.001	<0.001	<0.001	<0.001	<0.001	<0.001
Sb	0.07	0.06	0.08	0.05	0.05	0.09	0.07
Se	<0.2	0.2	0.2	0.3	0.5	<0.2	0.2
Te	<0.01	<0.01	<0.01	<0.01	<0.01	<0.01	<0.01
Cd	<0.5	<0.5	<0.5	<0.5	35.2	0.9	<0.5
La (ppm)	1.4	1.8	2.1	1.6	1.8	7	2.4
Ce	3.6	4.7	3.7	4.3	4.6	18.5	6.4
Pr	0.48	0.64	0.63	0.55	0.62	2.32	0.83
Nd	1.5	2.1	2.3	1.9	2.6	8.2	3.3
Sm	0.75	1.04	0.84	0.83	1.42	2.55	1.5
Eu	<0.03	<0.03	0.05	<0.03	0.09	<0.03	0.17
Gd	0.83	1.03	1	0.95	1.6	2.6	1.55
Tb	0.21	0.26	0.24	0.25	0.38	0.61	0.37
Dy	1.19	1.33	1.43	1.19	2.09	3.41	2.43
Ho	0.14	0.17	0.2	0.18	0.34	0.69	0.41
Er	0.33	0.37	0.46	0.43	0.66	2.2	1.25
Tm	0.05	0.05	0.05	0.05	0.1	0.34	0.23
Yb	0.27	0.3	0.37	0.26	0.55	2.93	2.07
Lu	0.03	0.02	0.04	0.03	0.06	0.4	0.26
A/CNK	1.81	1.86	1.92	1.92	2.36	1.74	1.90

Results are presented for whole rock geochemical analysis of 7 granitic rock samples from the East Kemptville deposit. Major and trace elements were analyzed at ALS Canada Ltd., in North Vancouver, British Columbia, combining whole rock analysis, trace elements by fusion, aqua regia digestion for the volatile trace elements, carbon and sulfur by combustion analysis, and several detection limit options for the base metals (detailed methods available at www.alsglobal.com). Although the least altered samples were collected for analysis, the abundance of some major and trace elements may not be representative of the original whole rock chemistry. Accordingly, major element weight per cents were recalculated to a volatile-free (anhydrous) basis. EKLG - East Kemptville Leucogranite, IBXM - igneous breccia matrix, MZ - Main Zone, BZ - Baby Zone.

Table 3–2. Re-Os Isotope Data for the East Kemptville molybdenite samples

Sample no.	Mineralization type	Zone	Total Re (ppm)	¹⁸⁷Re (ppb)	¹⁸⁷Os (ppb)	Re-Os Age (Ma)¹
EK-95-11-3	pegmatite	Baby	0.2375	0.1493	0.9385	376.2 ± 3.3
EKAV-15-15	border of IBX	Baby	0.1193	74.97	0.4310	343.7 ± 1.7
EKAV-15-17	vein	Main	0.03860	24.29	0.1440	354.9 ± 2.0
EKDJK-18-01	vein	Main	1.741	1095	6.800	370.2 ± 1.6
EKDJK-18-02	vein	Main	0.06500	41.00	0.1000	359.4 ± 1.8

Ages calculated using the decay constant $\lambda^{187}\text{Re} = 1.666 \times 10^{-11} \text{y}^{-1}$ (Smoliar et al. 1996); ¹2 σ

Table 3–3. U-Pb Cassiterite Summary of East Kemptville and Duck Pond samples

Sample no.	Mineralization type	Zone	Age (Ma)	error (2σ)	<i>n</i>	MSWD
EKDJK-87-2	zoned greisen	Main zone	376	± 12	30	2.8
EKDJK-2016	miarole	Main zone	370.6	± 7.8	30	1.7
EKDJK-87-8	zoned greisen	Main zone	368.6	± 8.9	60	8.1
EKDJK-89-11	zoned greisen	Main zone	367.5	± 9.4	60	8.8
EKDJK-87-10	zoned greisen	Main zone	365.4	± 4.3	30	2.5
DP-20-224.9	greisen	Duck Pond	347	± 12	80	2.3

Table 3–4. Historic geochronology of the Davis Lake Pluton and East Kemptville leucogranite.

Pluton	Rock Type	Mineral	Age (Ma)	Chronometer	Method	Age Interpretation	Reference
DLP	biotite-monzogranite	biotite	374*	$^{40}\text{Ar}/^{39}\text{Ar}$	step-heating	cooling	Reynolds et al. (1981)
DLP	leucomonzogranite	biotite	376*	$^{40}\text{Ar}/^{39}\text{Ar}$	step-heating	cooling	Reynolds et al. (1981)
DLP	leucomonzogranite	whole-rock	375 ± 3	Rb–Sr	isochron	crystallization	Chatterjee and Cormier (1991)
DLP	leucomonzogranite	K-Feldspar	378 ± 3.6	Pb–Pb	isochron	crystallization	Dostal and Chatterjee (1995)
DLP	leucogranite	zircon	372.8 ± 3.0	U–Pb	SHRIMP	crystallization	Bickerton et al. (2018)
EKLG	vein	muscovite	295 ± 3	$^{40}\text{Ar}/^{39}\text{Ar}$	step-heating	mineralization	Zentilli and Reynolds (1985)
EKLG	monzogranite**	muscovite	295 ± 3	$^{40}\text{Ar}/^{39}\text{Ar}$	step-heating	greisenization	Zentilli and Reynolds (1985)
EKLG	leucogranite***	muscovite	300	$^{40}\text{Ar}/^{39}\text{Ar}$	step-heating	tectonothermal event	Zentilli and Reynolds (1985)
EKLG	leucogranite	muscovite	ca. 350	$^{40}\text{Ar}/^{39}\text{Ar}$	step-heating	disturbed age spectrum	Zentilli and Reynolds (1985)
EKLG	leucogranite	whole-rock	337 ± 5	Rb–Sr	isochron	tectonothermal event	Richardson et al. (1989)
EKLG	leucogranite	muscovite	337	$^{40}\text{Ar}/^{39}\text{Ar}$	step-heating	disturbed age spectrum	Reynolds et al. (1981)
EKLG	leucogranite	whole-rock	344 ± 5	Rb–Sr	isochron	tectonothermal event	Kontak and Cormier (1991)
EKLG	leucogranite	whole-rock	354	Rb–Sr	isochron	errorchron	Kontak and Cormier (1991)
EKLG	leucogranite	whole-rock	254 ± 23	Rb–Sr	isochron	low-temp resetting	Kontak and Cormier (1991)
EKLG	leucogranite***	whole-rock	366 ± 4.5	Pb–Pb	isochron	greisenization	Kontak and Chatterjee (1992)
EKLG	leucogranite	whole-rock	367 ± 13	Pb–Pb	isochron	crystallization	Kontak and Chatterjee (1992)

Note the age interpretation provided here is based on review of literature in the context of ages obtained in this study , and is not representative of the original interpretations provided in each reference. * - adjusted for updated K-Ar decay constant; ** - sheared and greisenized; *** - greisenized; DLP - Davis Lake Pluton; EKLG - East Kemptville leucogranite; SHRIMP - Sensitive high-resolution ion-microprobe.

Chapter 4

Geochemical constraints of ore-forming fluids in a mesothermal Sn-Zn-Cu-Ag-In deposit, East Kemptville, Nova Scotia (Canada)

4.1 Abstract

The ca. 375 Ma Davis Lake Pluton in southwest Nova Scotia, Canada, hosts the greisen- and vein-type Sn-Cu-Zn-Ag-In East Kemptville deposit in a topaz-muscovite leucogranite. The pre- to syn-mineral pressure-temperature-compositional evolution of fluid is assessed by analysis of fluid inclusion assemblages (FIAs), their key characteristics include: 1) no petrographic evidence for fluid unmixing; 2) pervasive decrepitate textures result in primary FIAs being less common than those of indeterminate origin; 3) ore fluid types comprise, in order of appearance through the paragenesis, early liquid-vapor-halite (L-V-H \pm solids; 29-38 wt% NaCl equiv.), a L-V type (24-29 wt% NaCl equiv.), and a L-V \pm CO₂ type (10-23 wt% NaCl equiv.); 4) greisen and vein-hosted FIAs yield homogenization temperatures indicating a wide range of trapping pressures (i.e., 0.5-3.5 kbar) over a temperature range of 450–300°C; 5) evaporate mound analysis notes Na-K-Fe-Mn \pm Ca salts from early fluids and Na-K salt dominant mounds late in the paragenesis; 6) LA-ICP-MS analysis of early fluid types are weakly enriched in Sn (13-196 ppm), Cu (7-147 ppm), Fe (0.9-1.7 wt. %), In (0.5-2 ppm), and S (0.3-1.2 wt. %); and 7) $\delta^{18}\text{O}_{\text{quartz}}$ signatures through the paragenesis are similar, and indicate variable mixing between fluids, with initial $\delta^{18}\text{O}_{\text{H}_2\text{O}}$ values of 9.3–7.1‰ and values as low as ~2.8‰ by the late vein

stages. The results indicate two main mineralization stages; the first under mesothermal pressures between 450 and 400°C by magmatic fluids, and the second between 400 and 300°C under a range of pressures while the system was diluted by external fluids. A magmatic fluid source and fluid-rock exchange is suggested for the enrichment and precipitation in of early greisen-style ore, whereas fluid-fluid mixing is the precipitation mechanism of late coarse cassiterite and mineralized veins.

4.2 Introduction

Magmatic-hydrothermal tin mineralization is recognized globally to have dominantly formed in settings within and proximal to highly differentiated felsic granites; involving the saturation and exsolution of aqueous fluids from residual granitic melts, and partitioning Sn into the mobile fluid phase (e.g., Kelly and Turneure, 1970; Taylor, 1979; Charoy, 1986; Heinrich, 1990; Černý et al., 2005; Lehmann, 2020). These deposits typically form in high-level settings (i.e., <2 km depth) with a variety of styles, including: vein-type (stockwork, sheeted, massive lode); breccia; disseminated; skarn; pegmatite; and greisen (e.g., Sillitoe et al., 1975; Taylor, 1979; Černý et al., 2005; Kesler and Wilkinson, 2013). Less common are deposits localized to deeper settings (i.e., ~2 kbar; Table 4–1) that are associated with rare-metal pegmatites, such as Greenbushes, Australia (Partington et al., 1995) and Kamativi, Zimbabwe (Rijks and van der Veen, 1972), where mineralization is associated with late-stage metasomatic events of controversial origin (i.e., magmatic versus hydrothermal). The formation of these deposits requires: 1) Sn enrichment

in a magmatic reservoir, typically by extensive fractional crystallization and differentiation; 2) ore-bearing fluid transport, typically by focusing magmatic fluids into structural traps; and 3) precipitation of dissolved Sn by fluid-rock interaction, cooling, boiling or dilution by fluid mixing (e.g., Heinrich, 1990; Audétat et al., 2000; Korges et al., 2018; Schmidt, 2018).

Stanniferous greisen-style deposits are the product of acid feldspar-destructive hydrothermal alteration resulting in coarse-grained quartz-muscovite \pm tourmaline \pm fluorite/topaz \pm cassiterite rock (Lehmann, 2020), whereas vein-style Sn mineralization typically has variable size, morphology, and mineralogy, with the following major features (cf. Pollard and Taylor, 1986): i) a spatial relationship with the apices of host granites or overlying wall-rocks; (ii) formation of subparallel, sheeted vein systems; (iii) a diversity of mineral phases with zonal characteristics; and (iv) a general tendency for fluid evolution to progress from high-temperature, high-salinity fluids to later, lower temperature and lower salinity fluids (e.g., Kelly and Turneure, 1970; Eadington, 1983; Kontak and Clark, 2002).

Cassiterite (SnO_2) is the most economically important mineral in tin deposits. Cassiterite formation in granite-related hydrothermal veins is evidence for exsolution of magmatic aqueous fluids and thus highlights the role aqueous fluids play in the formation of these deposits. Fluid inclusion studies on cassiterite and paragenetically related quartz indicate typical formational conditions to be high-level (i.e., <1 kbar) with temperatures of 300–500°C and bimodal fluid salinity due to fluid unmixing, thus similar to what is found for porphyry Cu-Mo systems (from

~1 to >50 wt% NaCl equiv.; cf. Bodnar et al., 2014). In addition to the pressure-temperature (PT) setting during ore deposition, fluid inclusions are also used to quantify fluid chemistry and isotopic signature to understand fluid evolution and metal transport in many ore deposits: e.g., Cu-Mo (e.g., Heinrich et al., 1999; Ulrich et al., 2002; Williams-Jones and Heinrich, 2005); orogenic gold (e.g., Garofalo et al., 2014; Morales et al., 2016; Fusswinkel et al., 2017; Kerr et al., 2018; Tuba et al. 2019); and Sn-W (e.g., Audétat et al., 2000; Müller et al., 2001; Graupner et al., 2005; Harlaux et al., 2017).

The mechanism of cassiterite precipitation and the conditions required to yield economic concentrations may be better understood through fluid inclusion analysis. The various mineralization styles for these deposits require favorable conditions that include, but are likely not limited to, the oxidation and/or neutralization of an acidic ore-bearing fluid (Heinrich, 1990). To obtain equilibrium, these reactions are typically balanced with the reduction and/or hydrolysis of an externally-sourced fluid or host-rock/wall-rock components. Changes to the chemistry of the mineralizing fluid thus reflects chemical changes to the host rock and may be quantified by direct trace-element microanalysis of fluid inclusions hosted through a deposit paragenesis (e.g., Audétat et al., 1998; Heinrich et al., 1993). A similar approach that is relatively simple and efficient is the semi-quantitative analysis of evaporate mounds from induced decrepitation of fluid inclusions (e.g., Eadington, 1974; Haynes et al., 1988; Halter et al., 1998; Kontak, 2004). Integration of the latter data with standard thermometric measurements to determine relative

proportions of cation and anion of fluid inclusions may be used to quickly ascertain the major element composition of fluids and thus the stage of fluid evolution.

The East Kemptville Sn-Zn-Cu-Ag-In deposit (EKD) in southern Nova Scotia, Canada, is a low-grade, moderate-tonnage deposit with initial reserves of ca. 58 Mt at 0.17 % Sn (Richardson et al., 1982). This has since been updated by Avalon Advanced Materials Inc. following the historical (1985-1992) production to a remaining in-ground measured and indicated resource of 22.97 Mt at 0.15% Sn (for a 0.1% Sn cut-off grade; Gowans et al., 2018); this resource still remains the largest primary Sn deposit in North America. It is hosted by a topaz muscovite leucogranite with mineralization in massive and zoned topaz-muscovite greisens. Previous studies on the host leucogranite, mineral paragenesis and fluid-chemical attributes (e.g., Richardson et al., 1982, 1988, 1989; Kontak, 1990a, b, 1993, 1994; Halter et al., 1996, 1998; Kontak et al., 2001) have established the EKD as a magmatic-hydrothermal system, much like other Sn settings globally. However, in notable contrast to global analogues of this deposit type, the EKD has features more typical of a mesothermal setting, such as emplacement depth of the host leucogranite, the strong structural control of the greisens, and the PT conditions inferred from fluid inclusion assemblages (FIAs) throughout the ore stages. Previous work has also highlighted the unusually saline nature of mineralizing fluids (i.e., 25–40 wt% NaCl equiv.) that shows no evidence for fluid unmixing; hence another atypical feature compared to other Sn settings (e.g., Bodnar et al., 2014).

The greisen-related ore mineralization at the EKD is interpreted to result from oxidation and/or acid neutralization and increasing pH associated with the fluid-rock interaction that accompanied alteration along greisen fronts (Halter et al., 1996, 1998). The coarse-cassiterite coring to zoned greisens (e.g., Kontak, 1994), however, suggests localized differences in ore depositional style later in the deposit evolution. As ore deposition in many Sn systems involves fluids sourced from both a hydrous magma source and external to the generative magma (e.g., Heinrich, 1995), this study aims to identify and differentiate such influences and to quantify fluid-rock and fluid-fluid interaction in the context of hydrothermal processes that initiate ore deposition. To evaluate such conditions in any deposit setting, essential features need to be constrained, which in this study are: 1) the paragenetic stages in which metal concentration occur (i.e., greisen formation in the EKD; Chapter 3); 2) the PT characteristics of ore fluids relative to the host leucogranite; 3) the chemical characteristics of fluid types and notable changes through the deposit evolution (i.e., gains and losses of elements due to alteration and mineralization); and 4) the O isotopic signature of mineralizing fluids to determine whether mineralization was produced by fluids sourced from exsolution in the host leucogranite, or a deeper reservoir, or surrounding meteoric hydrothermal convection cells.

To assess the above constraints, the PT and chemistry (PTX) of fluids hosted by mineralized rocks in well-defined paragenetic stages were determined by integrating fluid inclusion and stable isotope studies. The fluids were characterized via fluid inclusion microthermometry, evaporate mound analysis, laser Raman microspectroscopy (LRM), in situ laser ablation

inductively coupled mass spectrometry (LA ICP-MS) of FIAs, as well as $\delta^{18}\text{O}$ using isotope-ratio mass spectrometry (IRMS) and in situ secondary ion mass spectrometry (SIMS) on quartz from throughout the paragenesis.

4.3 Geological Setting

4.3.1 Regional and Local Geological Setting

The EKD is hosted by the ca. 375 Ma South Mountain Batholith (SMB) located in the Meguma terrane (Nova Scotia, Canada), which is the most outboard lithotectonic terrane in the Appalachian orogen (Fig. 4–1) and comprises a Lower Paleozoic stratigraphy dominated by the metasedimentary rocks of the Meguma Supergroup. These rocks include Cambrian-Ordovician metasediments of the Goldenville Group and overlying slates and metasilts of the Halifax Group. The Meguma terrane also comprises less extensive late Ordovician–Devonian metasedimentary and rift-related metavolcanic rocks of the White Rock Formation, that lie unconformably on the Meguma Supergroup (Fig. 4–1). The SMB is but one of several Late Devonian felsic- to mafic intrusions that intrude these metasedimentary rocks. In the southwest part of the terrane, these include hybridized granitoids of similar age to the SMB (e.g., Shelburne, Port Mouton, Barrington Passage plutons) or up to ca. 10 Ma younger (e.g., Seal Island, Wedgeport, Clayton Hill plutons; Chapter 3, and references therein).

Neocadian deformation of the Paleozoic stratigraphy is seen as northeast-trending, shallowly-plunging open- to closed folds and related faults (Fig. 4–1A; Keppie and Dallmeyer, 1987; Culshaw and Lee, 2006; van Staal, 2007). Timing of the regional deformation is constrained from $^{40}\text{Ar}/^{39}\text{Ar}$ ages for whole-rock and neomorphic muscovite at 410 to 380 Ma (Reynolds et al., 1987; Hicks et al., 1999; Kontak et al., 1998). More localized deformation of Alleghanian age (ca. 300 Ma) is localized to the southwestern part of the Meguma terrane (Muecke et al., 1988; Culshaw and Liesa, 1997) and overprints the EKD (Kontak et al., 1995).

The meta- to peraluminous SMB, which is the largest intrusion in the Appalachian orogen (ca. 7300 km²), hosts a variety of lithophile-element mineralization occurrences (e.g., Sn, W, U, Ta, Nb; MacDonald, 2001). It is a composite granitoid intrusive complex with two plutonic stages distinguished based on textural and mineralogical characteristics: an early stage I dominated by biotite granodiorite to monzogranite, and a more evolved stage II of biotite-muscovite monzogranite to leucogranite (Fig. 4–1; MacDonald 2001). The SMB and other Late Devonian intrusions were emplaced syn- to post-tectonically (e.g., Horne et al., 1992; Benn et al., 1997, 1999) during the waning stages of the Neocadian orogeny. The thermal aureole around the SMB constrains its emplacement to ca. 3.5 kbar (~12 km depth in a normal geostatic gradient; e.g., Raeside and Mahoney, 1996; Hilchie and Jamieson, 2008, 2014), which is supported by several fluid inclusion studies on magmatic-hydrothermal settings (Kontak et al., 2001; Carruzzo et al., 2000; Kontak and Kyser, 2011 and references therein).

Following regional deformation and emplacement of the SMB and associated intrusions, the Meguma terrane experienced rapid uplift and erosion by ca. 360 Ma, as recorded by the clast content and presence of Tournaisian fossils in the overlying Horton Group (Martel et al., 1993; Murphy, 2000). Archibald et al. (2018) suggest uplift rates in the eastern Meguma terrane of 0.06 to 0.08 cm yr⁻¹ and an associated regional geothermal gradient in the northern Meguma terrane of between 39.5 °C km⁻¹ and 67.8 °C km⁻¹.

4.3.2 Davis Lake Pluton and East Kemptville Deposit

The Davis Lake Pluton, located in the southwestern part of the SMB, is a later stage II pluton in the batholith and the only one to host significant mineralization in the EKD. It is zoned from an early coarse-grained biotite to biotite-muscovite monzogranite to more evolved leucomonzogranite (Dostal and Chatterjee, 1995, 2000). In addition to the EKD, several Sn-Cu-Zn-Ag occurrences occur along the southwestern edge of the Davis Lake Pluton and further westwards; hosted both within the pluton and the adjacent metasedimentary rocks (Fig. 4–1A). The greisen mineralization of the EKD is hosted in the <1 km² East Kemptville muscovite-topaz leucogranite which is the most evolved part of the Davis Lake Pluton.

The southwestern termination of the Davis Lake Pluton is bound by two regional shear zones; the NE-trending East Kemptville shear zone at its furthest west extent (EKSZ; Horne et al., 1992; Kontak and Chatterjee, 1992; Figs. 4–1A to D, 4–2A, B), and the Tobeatic Shear Zone at its eastern edge (Giles, 1985). Both these shear zones contain extensive hydrothermal

mineralization that is deformed in a brittle-ductile strain regime: the Flintstone Rock silica-clay deposit formed dominantly by meteoric-dominant fluids in the latter (Kontak and Kyser, 2000); and the greisen-hosted EKD, formed dominantly by magmatic fluids in the former.

The EKD shows evidence of greisens that form pre- to syn-kinematically, with preferred alignment along the penetrative fabric through the deposit area (e.g., Fig. 4–2C). Deformation of the EKD continued episodically after ore deposition, as evidenced by post-greisenization structural features which include deformed greisen mineralization (e.g., Fig. 4–2D, E), post-mineralization shear planes that are locally cemented by assemblages of chlorite and graphite (e.g., Fig. 4–2F), en echelon shear veins of late, barren quartz (e.g., Fig. 4–2G), and extensional second-generation veins (e.g., quartz-phosphate-albite-fluorite, Fig. 4–2H; Chapter 3). The deposit area also records deformation and thermal overprinting related to the ca. 300 Ma Alleghanian deformation (Kontak and Cormier, 1991; Kontak et al., 1995).

The deposit has two ore zones, the Baby (Fig. 4–1C) and Main (Fig. 4–1D). Although both zones are enriched in similar elements (Sn, Zn, Cu, Ag, In) and centered on the EKSZ, their lithological characteristics and contact-relationships differ. In the Main zone, mineralization is wholly within the host East Kemptville leucogranite (EKL) with greisens most intensely developed at shallowly-dipping intrusive contacts or along shear planes in the 25–30 m wide EKSZ. In contrast, the Baby Zone is hosted by a pervasively greisenized leucogranite seated beneath a pipe-shaped magmatic-hydrothermal breccia body. Most of the Baby Zone breccia

comprises a collapse breccia, characterized by angular fragments of hornfelsed country-rock greywacke and argillite with thin reaction rims.

4.3.3 East Kemptville Mineralization and Paragenesis

The simplified paragenesis for the EKD (Fig. 4–3) is subdivided into several stages recognized at the macro- and microscopic scale (Richardson et al., 1990; Kontak, 1990b): 1) emplacement of the EKL, which includes crystallization of cassiterite-bearing pegmatites and miaroles (Fig. 4–4A) in the Main Zone, and deuteric alteration; 2) quartz-topaz (\pm cassiterite) greisens, the first of the two main ore stages, which involved partial replacement of the host leucogranite (i.e., K-feldspar \rightarrow albite \rightarrow muscovite \rightarrow topaz) and precipitation of early cassiterite (Fig. 4–4B to F); 3) a second hydrothermal ore stage with quartz-sulfide veins and late-stage sulfides, restricted to within the EKL and related breccias, occluding porosity in earlier greisens. These veins evolved from quartz + Cu-sulfide (chalcopyrite dominant) with lesser Sn (\pm W) oxide (Fig. 4–4D, E) to quartz + Zn-sulfide (sphalerite dominant; Fig. 4–4F) with lesser accessory sulfides, phosphates (e.g., apatite, triplite), and fluorite (Fig. 4–4G); 4) barren veins of quartz + carbonate \pm albite, fluorite, chlorite, and phosphates (Fig. 4–4H); and 5) veins with complex assemblages of carbonate, phosphate, and zeolites that are typically found coating shear planes, pockets, or joint surfaces. A minor but notable presence of graphite is in syn-kinematic veins throughout the EKSZ and within greisens parallel to the shear zone (e.g., Kontak, 1990b; Chapter 3); graphite occurs intergrown with sulfides or as fine-grained, disseminated masses (noted to result in the

dark grey greisen colour) and assays have indicated maximum amounts of 0.15 wt. % organic carbon (Kontak, 1994).

4.4 Methods

4.4.1 Petrography

Petrographic analysis of fluid inclusions was completed at the Fluid Inclusion Laboratory, Harquail School of Earth Sciences, Laurentian University (Sudbury, Ontario) using samples collected from drill-core and during the active mining phase. Twenty-six quartz- and topaz-bearing samples (Fig. 4–5) that collectively span the paragenesis were cut into polished thick sections (100-150 μm) and observed using an Olympus BX-51 research microscope equipped with a Qimaging MicroPublisher 5.0 RTV camera.

4.4.2 Microthermometry

Microthermometric measurements were performed in the aforementioned laboratory on a Linkam TMS600 heating-freezing stage coupled to an Olympus BX-51 research microscope. Calibration of the stage was done using synthetic fluid inclusions with measurements of the triple points for pure CO_2 ($T_m[\text{CO}_2]$ at -56.6°C) and pure water ($T_m[\text{Ice}]$ at 0°C), in addition to the critical point of pure water at 374°C . Total uncertainties for the microthermometric

measurements at a heating rate of 1°C/min, based on reproducibility of standards, range from $\pm 0.2^\circ\text{C}$ for $T_m[\text{CO}_2]$ and $T_m[\text{Ice}]$ and $\pm 2\text{--}3^\circ\text{C}$ for high temperature runs.

Measurements of changes in the fluid inclusions were made for a total of 56 FIAs and included: dissolution of halite ($T_m[\text{Halite}]$), total homogenization temperature ($T_h[\text{LV}\rightarrow\text{L}]$), freezing temperature (T_f), first ice-melting temperature (T_e), final ice-melting temperature ($T_m(\text{ice})$), and melting of hydrohalite ($T_m(\text{HH})$) for aqueous inclusions, and for aqueous-carbonic inclusions CO_2 melting ($T_m(\text{CO}_2)$) and homogenization ($T_h(\text{CO}_2; \text{LV}\rightarrow\text{V})$), clathrate melting ($T_m(\text{Clath})$, and the total homogenization ($T_h(\text{total})$). Salinities were calculated depending on the nature of the chemistry of the inclusions: 1) for complex multi-component systems (i.e., $\text{H}_2\text{O}\text{-NaCl} \pm \text{KCl} \pm \text{FeCl}_2 \pm \text{MnCl}_2 \pm \text{CaCl}_2$) microthermometric data were plotted on a ternary eutectic diagram (e.g., Lecumberri-Sanchez et al., 2015; Fig. 4–6); 2) for halite-bearing type 1 and 4b inclusions, microthermometric data were plotted on a binary $\text{H}_2\text{O}\text{-NaCl}$ eutectic diagram (e.g., Bodnar, 2003); 3) for simple two-phase type 2 inclusions, refined salinities were calculated from microthermometric data (i.e., $T_m(\text{ice})$ or $T_m(\text{HH})$) based on the equations of Bodnar (2003), Steele-MacInnis et al. (2012), and Lecumberri-Sanchez et al. (2015); and 4) for aqueous-carbonic inclusions in which CO_2 clathrates were noted, in all cases as $T_h(\text{CO}_2) > T_m(\text{Clath})$, the measured volumetric proportion of the carbonic phase at $T_h(\text{CO}_2)$ was input into the algorithms of Steele-MacInnis (2018) to calculate salinity (wt. % NaCl equiv.), molar volumes (cc/mol), and iosochores.

4.4.3 Evaporate mound analysis

Evaporate salt mounds were analyzed following the method of Kontak (2004) with results complementing earlier studies (Kontak, 2004; Kontak et al., 2001). Fluid inclusion-rich quartz chips from 26 previously studied fluid inclusion sections spanning the paragenetic stages were used. These quartz chips were heated in a Linkham stage at 50°C/min to induce decrepitation, which typically occurred between 350 and 500°C. Quartz chips were subsequently removed, placed on double-sided carbon tape adhered to a glass slide, and carbon coated. The salt mounds (Fig. 4–7) were imaged using a JEOL 6400 scanning electron microscope (SEM) coupled to an INCA Energy Dispersive Spectrometer (EDS) in the MicroAnalytical Centre (MAC) at Laurentian University. Operating conditions were: 20 kV accelerating voltage, 1.00 nA beam current, spot (<5 µm) or rastering mode depending mound size, and 5-40 s counting time. The use of rastering mode on larger mounds was to address the issue of elemental fractionation during mound formation (Kontak, 2004). The results were normalized to 100% after excluding Si and O which relates to interference from the quartz substrate, in particular for the smaller mounds.

4.4.4 Confocal Laser Raman Microspectroscopy

LRM was performed on aqueous-carbonic fluid inclusions in five polished wafer samples at Saint Mary's University (Halifax, Nova Scotia, Canada). Analysis was done using a Horiba

Jobin-Yvon LabRam HR confocal Raman microscope equipped with a 100 mW 532-nm (green) Nd-YAG diode laser that was used for excitation, an 800-mm spectrograph, and a Synapse 1024 \times 256-pixel charged-coupled device (CCD) detector. Measurements were made in confocal mode by focusing the laser beam through the optical path of an Olympus microscope using a 100x short path length objective. Instrumental conditions used for identification of fluid inclusion-hosted volatile phases, determination of the fermi diad spacing (between the SS-FD and 2 v_2 -FD Raman shift values of CO₂), and spectrum collection were the same as those detailed in Kerr et al. (2018). Determination of the presence and relative abundances (mol %) of volatile species (e.g., H₂O, CO₂, CH₄, N₂) was done using the empirical quantification parameters and methodologies summarized by Wopenka and Pasteris (1986, 1987), Dubessy et al. (1989), Burke (2001), Beeskow et al. (2005), and Frezzotti et al. (2012). Wavelength-dependent relative Raman scattering cross sections for each gas species were determined from Table 2 of Burke (2001, and references therein). Instrumental efficiency factors for CO₂ and CH₄ were calculated from 7 reference material samples to be 0.83 ± 0.14 and 0.96 ± 0.19 , respectively. Due to a lack of N₂ and H₂S standards, instrumental efficiency factors for these species are assumed to be unity; thus, quantification of these species yields maximum possible mol % concentrations.

4.4.5 LA-ICP-MS analysis

Major- and trace-element compositions of fluid inclusions were determined using LA ICP-MS at the Department of Earth Sciences, University of Toronto (Ontario, Canada) following the

protocols detailed in Heinrich et al. (2003) and Pettke (2006). The instrument used was an NWR 193 UC laser ablation system coupled to an Agilent 7900 inductively-coupled plasma quadrupole mass spectrometer. Flow rates used for a He carrier gas and an Ar plasma gas were 1.0 and 0.87 L/min, respectively, and tuning of the ICP-MS was done by monitoring mass-21/mass-42, ThO/Th, and U/Th ratios in order to maintain a ThO production rate of <0.3 % and U/Th ~ 1. Dwell times were set to 10 ms for all masses measured, except for Sn (40 ms) and In (20 ms). Entire fluid inclusions, hosted by quartz or topaz, from a total of 16 samples (and over 32 FIAs) across the mineral paragenesis, were pre-targeted and drilled out using a beam width set such that ablation pit diameters were ~5–10 mm larger than the inclusion ablated (Fig. 4–8A, B) and the resultant signals gave counts per second of combined background, host mineral, and inclusion (Fig. 4–8C). Data are reduced to mass concentrations (in ppm) using an internal standard based on wt% NaCl equiv., as determined from microthermometry. The elements used to calibrate the host mineral signature throughout each analysis were Si and Al in quartz and topaz, respectively. Trace-element quantification of fluid inclusions was performed using the SILLS software (Guillong et al., 2008). Analyte sensitivities were calibrated for drift correction by using the reference standard NIST610 that was ablated 2 times at the beginning and 2 times at the end of each block of inclusions (50 analyses).

Quartz and/or topaz crystallized throughout the paragenesis at East Kemptville and previous studies noted similar microthermometric properties of primary- to indeterminate-type fluid inclusions in each of these phases, as well as spatially-associated cassiterite (e.g., Kontak,

1994; Halter et al., 1998; Kontak et al., 2001). For this reason, inclusions hosted by quartz and topaz were subjected to LA-ICP-MS (and LRM) to fully characterize the chemistry of fluids responsible for precipitation of all spatially-associated phases.

4.4.6 O isotopes

Various generations of quartz from across the deposit paragenesis (host leucogranite, greisens, veins, breccia) were selected for oxygen isotopic analysis to characterize the $\delta^{18}\text{O}_{\text{H}_2\text{O}}$ of pre- syn- and post-mineralizing fluids. Complementary determination of $\delta^{18}\text{O}$ was done on high-quality quartz separates using conventional IRMS whereas in situ $\delta^{18}\text{O}$ was done by measuring mounted grains (25 per puck) using SIMS.

The SIMS analysis was done using a CAMECA 7f ion microprobe with a 3 nA cesium (Cs^+) primary beam accelerated (to 10 kV) onto the sample surface with a sputtering diameter of approximately 20 μm . The instrument operated with a 300 V offset, -9 kV secondary accelerating voltage, and a mass resolving power of 347 $\text{m}/\Delta\text{m}$. Grains of University of Wisconsin rose quartz (UWQ-1) with a $\delta^{18}\text{O}$ value of $12.3 \pm 0.1\text{‰}$ (Kelly et al., 2007) were used as the quartz standard for oxygen-isotope analysis. The SIMS results from the standard were compared to accepted isotopic compositions to calculate correction factors applied to the unknowns measured during the same analytical session (e.g., Holliger and Cathelineau, 1988). A detailed description on sample preparation, operating conditions, and method of correction for instrumental mass fractionation and matrix effects is found in Fayek et al. (2002). Values are

reported using the δ notation relative to V-SMOW (Vienna standard mean ocean water); replicate analyses were reproducible to $\leq 1.2\%$.

For quartz separates, oxygen isotopic analysis was done at the Department of Geological Sciences, University Saskatchewan, Saskatoon (Canada). Quartz was dissolved using the BrF₅ technique (Clayton and Mayeda, 1963) and stable isotope measurements measured using VG model 602C stable isotope mass spectrometer. As above, values are reported using the δ notation relative to V-SMOW and replicate $\delta^{18}\text{O}$ analyses were reproducible to $\pm 0.2\%$ based on replicate analyses of laboratory standards. Further details are provided in Kontak and Kerrich (1995).

4.5 Results

4.5.1 Fluid inclusion petrography and types

Quartz in the host EKL and various phases of the greisens and veins, such as quartz, topaz, cassiterite, sphalerite, apatite, carbonate, and fluorite, are typically inundated with fluid inclusions (Figs. 4–5 and 4–9A). Although each mineral contains abundant fluid inclusions, those in relatively undeformed quartz and topaz are typically most suited for microthermometric analysis due to their size ($>5\ \mu\text{m}$; Fig. 4–9) and that either one or both of these mineral phases occur in each stage of the paragenesis (Fig. 4–3); thus, FIAs in quartz and topaz formed the focus of this study. The fluid inclusion types, as seen at room temperature (i.e., $\sim 20\text{--}25^\circ\text{C}$), are described below and the features of the inclusions are summarized in Table 4–2, with

representative examples in Figure 4–9. The FIAs were characterized using: 1) types and proportion of phases; 2) shapes and size of inclusions; and 3) compositional data determined from microthermometry, mound analysis, and LRM. Classification of inclusions in terms of their time of entrapment (i.e., primary, secondary, pseudosecondary, indeterminate) follow the protocols of Goldstein and Reynolds (1994) and Bodnar (2003).

Five inclusion types are recognized: (i) type 1: three- or four-phase, hypersaline aqueous inclusions with halite(H) \pm another solid (S) with 15–25% vapor phase (at 20 °C); (ii) type 2: two- or three-phase aqueous and moderately saline inclusions (L-V \pm H) with 20–40% vapor phase; (iii) type 3: two- or three-phase aqueous-carbonic inclusions (i.e., L_{H2O}-V_{CO2} or L_{H2O}-L_{CO2}-V_{CO2}) of lower salinity with 30–50% vapor phase; (iv) type 4a: two-phase aqueous inclusions of lower salinity with 15–30% vapor phase; and (v) type 4b: three-phase moderately saline aqueous inclusions with 15–30% vapor phase. The 4a and 4b FIA types are dominantly recognized and distinguished from type 2 through their morphology and secondary origin; they occur exclusively along trails parallel to deformation planes in pre- and syn-mineralization quartz and topaz (Figs. 4–5A, D, 9F).

Of the five fluid inclusion types identified, types 1 to 3 are either of primary or of indeterminate origin, whereas types 4a and 4b are exclusively of secondary origin. The primary types define growth zones (Figs. 4–5C and 4–8B), whereas the indeterminate occur as generally large inclusions (>10% of crystal diameter) forming isolated groups in three-dimensional (3D), non-

planar arrays (Fig. 4–9B-E; cf. Roedder, 1984; Bodnar, 2003). Secondary inclusions occur as planar arrays defining healed fracture surfaces (Figs. 4–5A, D, 4–9F).

4.5.2 Features of inclusions and microthermometric data

The microthermometric data are presented in Table EA 4-1 (Electronic Appendix) and summarized for the different FIAs observed in Table 4–2 and Figure 4–10. The following points are noted: 1) the subscript notation CO₂ for carbonic phases does not infer the absence of trace CH₄, N₂, or H₂S; and 2) the data for types 4a and 4b include results of this study and is supplemented by the earlier work of Halter (1996).

Type 1: These L-V-H ± S aqueous inclusions are typically rounded to irregular in shape, from 5 to 10 μm, have a V phase volumetric proportion (i.e., φ) between 0.15 and 0.25, and typically occur as 3D non-planar arrays within relatively inclusion-poor magmatic quartz and topaz crystals in the host leucogranite (Fig. 4–9B). Microthermometry indicates T_e from -29 to -23°C and T_h(LV→L) ranges from 232 to 395°C (avg. = 288 ± 50°C; Fig. 4–10A, Table 4–2). These inclusions are hypersaline (29 ≤ wt% NaCl equiv. ≤ 38) and are hosted by EKL and pegmatites (Figs. 4–6, 4–10B). The solids in these inclusions, apart from halite, when present are typically small, rounded to sub-rounded, and highly birefringent.

Type 2: These L-V ± H aqueous inclusions are typically stubby with negative-shapes, are 5 to 30 μm, have a φ between 0.2 and 0.4, and are of varied abundances within quartz and topaz

(e.g., Fig. 4–9C, D) across much of the paragenesis. The T_e is lower, on average, than the other inclusion types with values from -50 to -24°C (Table 4–2). The $T_{m(\text{ice})}$ is also depressed, ranging from -32 to -19°C (avg. = $-24.6 \pm 2.3^\circ\text{C}$; Table 4–2) and, as a result, hydrohalite is typically the last phase to melt (e.g., greisen and vein hosted FIAs in Fig. 4–6) and defines moderate salinities ($24 \leq \text{wt\% NaCl equiv.} \leq 29$; Fig. 4–10B). This inclusion type changes color upon freezing to a dark- to reddish-brown, which indicates a Fe-Mn content and thus a more complex multi-component system required for microthermometry (i.e., $\text{H}_2\text{O-NaCl} \pm \text{KCl} \pm \text{FeCl}_2 \pm \text{MnCl}_2 \pm \text{CaCl}_2$; Fig. 4–6). These inclusions are rarely observed as primary types along growth zones in quartz and topaz from the greisens (Figs. 4–5C and 4–8B), are dominantly found as indeterminate FIAs with decreasing abundance from syn- to late-mineralization paragenetic stages (greisen through to phosphate-bearing veins), and are also seen in magmatic phases (i.e., quartz and topaz) as secondary FIAs.

Type 3: These three- ($\text{LH}_2\text{O-LCO}_2\text{-VCO}_2$) or two- ($\text{LH}_2\text{O-VCO}_2$) phase aqueous-carbonic inclusions can be difficult to distinguish optically at room temperature due to their low carbonic contents ($X_{\text{CO}_2} = <0.05$; see LRM data below for quantification), as inferred based on phase transition after cooling to low temperatures (i.e., freezing and CO_2 melting) and volume fractions (Bakker and Diamond, 2000; Bakker, 2003). Importantly, this inclusion type was not recognized in earlier studies of the EKD due to the features just noted (e.g., Kontak, 1990b; Halter, 1996). They are irregular in shape, due to re-equilibration from stretching, necking down and partial decrepitation (cf. Bodnar et al., 2003), are 5 to 50 μm (Fig. 4–9E) and have a ϕ between 0.3 and

0.5. The carbonic phase has a $T_m(\text{CO}_2)$ between -63.0 and -57.0°C (-59.8 ± 1.6), a $T_m(\text{Clath})$ between -8.7 and 4.2°C (-4.1 ± 3.4), and a $L \rightarrow V$ $T_h(\text{CO}_2)$, between -3.0 and 21.6°C (14.8 ± 6.0 ; Table 4–2). The aqueous-dominant phase has T_e values from -37 to -25°C and $T_m(\text{HH})$ from -14 to $+5^\circ\text{C}$ (avg. = $-4.7 \pm 4.3^\circ\text{C}$) which defines moderate- to high salinities ($10 \leq \text{wt\% NaCl equiv.} \leq 23$; Fig. 4–10B, Table 4–2). The $T_h(\text{total})$ values for type 3 FIAs range from 162 to 300°C (267 ± 33 ; Table 4–2).

This inclusion type is less common compared to other types and is notably absent in the greisen stage of the paragenesis. Most FIAs are indeterminate- to secondary types in the base-metal sulfide to quartz-phosphate veins and as indeterminate type in later-stage quartz-carbonate veins. The inclusions have similar phase relationships, salinity, and host minerals as type-2 FIAs, but typically contain a minor volatile component (i.e., $\text{CO}_2 + \text{CH}_4 + \text{N}_2 \pm \text{H}_2\text{S}$) that is absent in inclusion types 1 and 2, as determined using Raman spectroscopy.

Type 4a: These L-V aqueous inclusions are typically flat, elongate and negative-shaped, and 5 to $25 \mu\text{m}$ in size. They are typically found along secondary planes in quartz from all vein generations (Fig. 4–9F). The ϕ is between 0.15 and 0.3 and have lower salinities ($17 \leq \text{wt\% NaCl equiv.} \leq 24$; Fig. 4–10B) based on ice or hydrohalite melting. The $T_h(\text{total})$ values for type 4a FIAs range from 195 to 230°C (210 ± 14 ; Table 4–2).

Type 4b: These L-V-H aqueous inclusions are flat, elongate with negative shapes that range from 5 to $25 \mu\text{m}$. They have ϕ values between 0.15 and 0.3 and occur along secondary

planes, typically in late-stage, unmineralized quartz-carbonate veins. The $T_h(LV \rightarrow L)$ values for this fluid type was determined by previous workers to range between 125 and 250°C with a maxima at ~150°C, inferring a moderate salinity ($28 \leq \text{wt\% NaCl equiv.} \leq 30$; Halter et al., 1998). The salinities of these inclusions are similar to type 1 inclusions, but this subset is described separately based on their size, mode of occurrence, morphology, and phases present, which are all different from the indeterminate type 1 FIAs.

4.5.3 Evaporate mound analysis

The analysis of fluid inclusion decrepitate evaporate mounds was conducted on the same quartz chips from across the mineral paragenesis that were used for microthermometry; results are summarized in Table EA 4-2 (Electronic Appendix). The areas prepared for decrepitation were preselected based on petrographic study and microthermometric analysis, which identified areas containing type 2 and less abundant types 1 and 3 inclusions; thus, the mound analyses are assessed in this context. Mound compositions are normalized uniformly to the dominant fluid type identified in each area. Areas for specific inclusion types include: 1) type 1 inclusions in magmatic quartz from the leucogranite; 2) type 2 inclusions in quartz from greisens and base-metal and phosphate-bearing veins; 3) type 3 inclusions in quartz from phosphate-bearing and barren veins; and 4) type 4a inclusions in quartz from barren veins. A total of 205 mounds were analyzed and results are summarized in a variety of ternary diagrams in Figure 4–11.

Mounds are in general abundant and large, indicative of their high salinities (Fig. 4–10B). Their morphology varies across inclusion types due to variable fluid chemistry (Kontak, 2004); the Na-K dominant mounds are typically crystalline, but range in shape from discrete (Fig. 4–7A, C) to irregular and fibrous in shape (e.g., Fig. 4–7D). In contrast, Na-K ± Fe ± Mn mounds are typically massive and range in shape from irregular fibrous (Fig. 4–7B, see inset for detail) to regular compact (Fig. 4–7E). The chemical inhomogeneity typically seen in mounds due to elemental fractionation is seen via EDS X-ray mapping (Fig. 4–7E) which is why for mounds raster-type versus point analysis was done.

In general, all mounds are dominated by NaCl and KCl, with lesser FeCl₂ and MnCl₂, as well as trace amounts of CaCl₂ (Fig. 4–7E). These main components are plotted relative to one another in various ternaries in Figure 4–11, including a combined (MnCl₂ + FeCl₂) since these divalent cations typically substitute for one another. The mound analyses indicates fluids in the different stages have the following chemical features: 1) the weakly altered leucogranite (target area for type 1 is dominated by NaCl and KCl (Figs. 4–7E, 4–11); 2) the greisens (quartz-muscovite-topaz; target area for type 2 have higher concentrations of combined KCl and (Fe, Mn)Cl₂ relative to those from the weakly altered leucogranite; 3) the pervasive- to intense greisen (quartz-muscovite-topaz) has the highest concentration of (Fe, Mn)Cl₂ (Fig. 4–11); and 4) the later-stage veins (target area for type 3 are NaCl- and KCl-rich. Although Ca is generally not detected, it is present in some mounds at negligible concentrations, with calculated concentrations of <0.44 wt. % Ca (Fig. 4–11). Chlorine is the dominant anion, with lesser S

(≤ 2.5 wt. %; Figs. 4–7E and 4–11), and there is a notable absence of F apart from trace amounts in the mounds that contain Ca. The latter is significant given the abundance of F in mounds elsewhere in the SMB, but only where there is substantive Ca is present (Kontak and Kyser, 2011; Tweedale, 2019).

4.5.4 LA-ICP-MS analysis

The LA-ICP-MS analysis of each fluid inclusion type is summarized as ranges, means and medians in Table 4–3 and selected elements are shown in Figure 4–12A; detailed results are found in Table EA 4-3 (Electronic Appendix). A total of 129 fluid inclusions from 29 FIAs were analyzed. A representative ablation profile for a topaz-hosted fluid inclusion in Figure 4–8C shows how the host is used to track and correct for its elemental contribution to the chemistry of inclusions.

The data show a wide range of element concentrations for each inclusion type, the values of which vary slightly between each paragenetic stage. Thus, fluid types are depicted in Figure 4–12 based on their paragenetic stage, but the data are compiled by fluid type for the entire deposit in Table 4–3. Overall, the elemental concentrations fall in the range (in ppm) of 10s to 100s of thousands for Na and K, 1000s for Ca, S, Fe, Mn, Zn, Cs, and Rb, 10s to 100s for Li, Sn, Cu and As, <10s for W and <10 for Ga and In.

The range of element concentrations for each inclusion type is consistent in each paragenetic stage, with the exception of some major (i.e., Fe and Mn) and ore (i.e., Sn, Cu., Zn) elements. The concentrations of some elements with overall higher concentration in the fluid (i.e., Mn, Fe, and Zn) show a U-shaped pattern across the paragenesis, thus from higher concentration in type-1 FIAs in quartz of the weakly altered host leucogranite, decreasing in type-2 FIAs in quartz from greisenized leucogranite and quartz-sulfide bearing veins, and returning to higher concentrations in type-4 FIAs (although lower than the values in type 1 fluids) from quartz in barren veins (top plot in Fig. 4–12A). A similar pattern is recognized for many of the ore-related trace elements (i.e., Sn, Cu, As, W, In), apart from the concentrations measured in quartz-hosted type-3 FIAs from sulfide-bearing veins, which have higher concentrations than in type 2 inclusions from the same veins or in type 3 inclusions from phosphate-bearing veins (Fig. 4–12A, bottom plot). Type-2 FIAs from the greisen-infill stage of the paragenesis have anomalous concentrations of some elements relative to the patterns described above; these anomalies include lower S and Ga, as well as higher Li concentrations (Fig. 4–12A).

4.5.5 Confocal Laser Raman Microspectroscopy

The carbonic phase in quartz-hosted type 3 FIAs, first identified using microthermometry, was further evaluated and quantified using LRM. The results are summarized in Table 4–4 and representative spectra are shown in Figure 4–13. The analysis verified two of the main characteristics identified in fluid types from petrography and microthermometry: 1) fluid types 1

and 2 have no identifiable carbonic component; and 2) the CO₂-bearing phase in type 3 inclusions has variable trace amounts of N₂, H₂S, and CH₄. The average CO₂ density of type 3 inclusions in the greisen fill and quartz-sulfide veins is significantly higher (0.42 ± 0.26 g/cc) than similar inclusions in the quartz-carbonate veins (0.02 ± 0.13 g/cc). The concentration of CH₄ is relatively consistent through the paragenesis (<0.1 mol. %), but increases significantly in the later barren quartz-carbonate veins (<0.75 mol. % CH₄). Furthermore, both N₂ and H₂S increase in relative concentration from the early greisen-fill and quartz-sulfide vein stage (<0.05 mol. % N₂ and no detected mol. % H₂S) to the later stage barren quartz ± carbonate veins (<0.14 mol. % N₂ and <0.01 mol. % H₂S; Table 4–4, Fig. 4–13B, D). The increase in S is consistent with the results from LA-ICP-MS analysis.

4.5.6 O isotopes

The results for in situ SIMS $\delta^{18}\text{O}_{\text{quartz}}$ analysis are presented in Table 4–5 and Figure 4–14, where data are arranged in the context of paragenesis, with the TIMS $\delta^{18}\text{O}$ analysis on bulk mineral separates (i.e., quartz, cassiterite, albite) presented in Table 4–6. In situ quartz analysis provides insight to potential variation that may be averaged due to bulk sampling, and this method was used in part to assess the intermittent excursions in $\delta^{18}\text{O}_{\text{H}_2\text{O}}$ during the mineral paragenesis; as has been documented in other magmatic hydrothermal settings such as porphyry Cu (e.g., Allan and Yardley, 2007; Fekete et al., 2016) and orogenic gold (e.g., Kerr et al., 2018; McDivitt et al., 2021).

The in situ SIMS $\delta^{18}\text{O}_{\text{quartz}}$ data are mostly for Main Zone samples, the exceptions being two massive greisens and samples of igneous and hydrothermal breccia from the Baby Zone (Table 4–5). There is a wide overall range of $\delta^{18}\text{O}$ values, but little variation for individual quartz grains such that results fall within the error for an analytical session (i.e., 1.2‰).

For the Main Zone, magmatic quartz in the weak- to moderately altered leucogranite has average values of +9.5 and +10.3‰, respectively (Fig. 4–14), and a combined mean of +9.8‰. In contrast, hydrothermal quartz from the massive greisens shows a change to lower $\delta^{18}\text{O}$ values that range from +7.4 to 8.4‰, with a mean of +8.0‰. Quartz from greisen infill and base-metal bearing veins are similar in their population percentiles with 50% of the data ranging between +8.9 and +9.9‰ and +8.2 and +10.0‰, respectively (Fig. 4–14). Quartz from late-stage phosphate-bearing veins also fall within the latter range, as two samples yielded values of +8.5 and +8.8‰ (Table 4–5).

For the Baby Zone samples, the $\delta^{18}\text{O}$ values of quartz phenocrysts in the matrix of the igneous breccia range from +7.5 to +9.1‰ (mean of +8.5‰; Fig. 4–14). Quartz from the cement of the hydrothermal breccia yielded a wider range of $\delta^{18}\text{O}$ values from +7.5 to +11.7‰ (mean of +9.5‰; Fig. 4–14). The late-stage barren veins that crosscut the EKL and associated breccias have the highest average $\delta^{18}\text{O}$ values measured, with a range of +11.6 to +12.1‰ (Table 4–5) and a mean of +11.8‰ (Fig. 4–14).

The results from bulk $\delta^{18}\text{O}$ analysis are for samples from the Main Zone only and include material from the early greisen Sn, quartz-sulfide, and the late barren quartz-sulfate paragenetic stages (Table 4–6). Two quartz samples in the early greisen Sn stage had similar $\delta^{18}\text{O}$ values of 11.5 and 11.2‰, whereas two cassiterite samples from this stage have $\delta^{18}\text{O}$ values of 5.2 and 4.2‰. For the quartz-sulfide stage, $\delta^{18}\text{O}$ values for nine quartz samples range from 13 to 10.2‰ with an average of 10.8‰, but if the one anomalous sample at 13‰ is removed, the average is 10.6 ± 0.4 ‰. For the late barren quartz-sulfate stage veins, the four quartz samples have $\delta^{18}\text{O}$ values of 10.9 to 9.9‰ and two albites from this stage have $\delta^{18}\text{O}$ values of 8.8 and 8.1‰.

4.6 Discussion

The anomalous mesothermal-type character of the EKD, as evaluated based on its geological setting and nature of the greisen and veins (see Chapter 3 and references therein), has been further investigated here via the PTX of the hydrothermal fluids. The latter was done by characterizing the chemistry of fluid inclusions preserved through the mineral paragenesis from late in the evolution of the host leucogranite through to greisen formation, later greisen-fill and subsequent formation of various vein generations. The PTX controls on the hydrothermal evolution are therefore discussed in the following context: 1) the PT characteristics of the fluids over a range of emplacement conditions consistent with both the host leucogranite and shallower settings that typify Sn deposits; and 2) the fluid chemistry through the paragenesis as it relates to changes in element concentrations due to alteration (i.e., fluid:rock interaction) and

mineralization. These results provide the evidence to address the source of the mineralizing fluid, primary metal concentrations, and depositional processes relevant to formation of the EKD.

4.6.1 PT conditions during paragenetic evolution

Abundant previous work constrained the confining pressure of the SMB and the PT evolution of the EKD mineralized system. For the former, a variety of petrological, isotopic, and fluid inclusion studies at various settings proximal to the SMB intrusive contact constrain its emplacement at 3 to 4 kbar (i.e., the mesozonal regime at 10 ± 5 km depth; Raeside and Mahoney, 1996; Halter and Williams-Jones, 1999; Carruzzo et al., 2000; Hilchie and Jamieson, 2008, 2014; Kontak and Kyser, 2011); this is also supported by work at the age-equivalent Musquodoboit Batholith (Kontak et al., 1999, 2004). These data are used to constrain the purple box across Figure 4–15. For the EKD, previous workers provide important PT constraints: 1) pegmatite-hosted fluid inclusions constrain PT to 2.5–3.5 kbar and 550–600°C (Kontak et al., 2001; pink field in Fig. 4–15); 2) $\delta^{18}\text{O}_{\text{quartz-cassiterite}}$ geothermometry constrains greisen formation to 450–480°C (Halter et al., 1998; Kontak et al., 2001); 3) F-OH exchange between topaz and muscovite constrains greisen formation to 400–450°C (Halter and Williams-Jones, 1999; brown field in Fig. 4–15); and 4) fluid inclusions and $\delta^{34}\text{S}_{\text{sulfide}}$ geothermometry constrain veins to 250–325°C and 300–400°C (Kontak, 1990a; Willson, 2019; red field in Fig. 4–15). Additionally, the upper limit constraining temperature of mineralization is assumed to be the solidus for late-stage F-rich melts (Fig. 4–15), such as the EKL.

Previous work on the saline (ca. 40 wt% NaCl equiv.) quartz-hosted fluid inclusions in the EKL, as well as pegmatites and miarolitic cavities, are noted to have homogenization by halite dissolution ($T_m[\text{Halite}]$) that is $\leq 100^\circ\text{C}$ above the $T_h(\text{LV}\rightarrow\text{L})$ values (shaded fields of Fig. 4-16A). This suggests, if using a 20-25 bar/ $^\circ\text{C}$ slope for the isochores (cf. Bodnar, 1994), a minimum pressure estimate of 2.5 kbar during entrapment for these fluids (Kontak et al., 2001). Additionally, entrapment pressures determined in this study for each fluid type, with respect to the mineralization temperature constraints, range from 3.5 to as low as 0.25–1 kbar (i.e., from lithostatic to hydrostatic conditions at 5-10 km depth). Thus, hypersaline fluids presumed to have originated due to exsolution from a magma were trapped at pressures less than those interpreted to be recorded by the SMB contact aureole (i.e., 3.2 to 3.8 kbar; Raeside and Mahoney, 1996), and subsequent fluid incursion record highly variable PT conditions through the paragenesis.

The previously determined constraints are further refined in this study based on the new microthermometric data ($T_h(\text{total})$, uncorrected for pressure Table EA 4-1; Electronic Appendix), and the resultant isochores for the each fluid type categorized by their host mineralization stage in the deposit paragenesis (Fig. 4-15). The $T_m[\text{Halite}]$ values for type 1 fluids typically occur at temperatures similar to those of the $T_h(\text{LV}\rightarrow\text{L})$ values, with the exception of a number of FIAs with $T_h(\text{LV}\rightarrow\text{L})$ values that are ca. 100–150 $^\circ\text{C}$ higher than the $T_m[\text{Halite}]$ (Fig. 4-16A). In contrast to the typical $T_m[\text{Halite}]$ and $T_h(\text{LV}\rightarrow\text{L})$ value relationship, the FIAs we note with $T_h(\text{LV}\rightarrow\text{L})$ values higher than $T_m[\text{Halite}]$ are more similar to quartz-hosted fluids in the granite from the same study (Fig. 4-16). Thus, the higher $T_h(\text{LV}\rightarrow\text{L})$ values suggests type 1 fluids may

represent different PT conditions based on whether trapped in pegmatitic or altered EKL. Furthermore, the different PT conditions is recognized in isochores for the majority of type-1 FIAs, which intersect the emplacement pressure for the SMB (i.e., ca. 3.5 kbar; e.g., Hilchie and Jamieson, 2014) at two separate temperature windows that correspond to constraints listed above: greater than 550°C, intersecting the solidus for F-rich melts and similar to the calculated equilibration temperatures between magmatic fluids and pegmatites (Fig. 4–15); and between 450 and 480°C, overlapping the interpreted greisen mineralization temperature.

The $T_h(\text{total})$ values for type 2 inclusions show a bimodal distribution that is dependent on the host mineralization stage (Fig. 4–15, center); somewhat lower values where hosted by quartz-muscovite-topaz greisens (250–313°C) relative to a higher range of values in quartz-sulfide and quartz-phosphate veins (280–359°C; Fig 4–16B; Table EA 4-1, Electronic Appendix). The resultant isochores from type 2 fluids overlap with topaz greisen fluid-inclusion data from previous workers (i.e., yellow field of Fig. 4–15; Kontak et al., 2001). The isochores of greisen-hosted type 2 fluids (green in Fig. 4–15, center) roughly intersect the overlapping SMB emplacement pressures and constraints on EKD cassiterite formation (i.e., 400–480°C; Halter et al., 1996; Halter and Williams Jones, 1999; Kontak et al., 2001). The higher homogenization temperatures in type 2 inclusions from quartz-sulfide to quartz-phosphate veins, however, reflect entrapment at PT conditions different from those recorded in greisens. This suggests either an increase in temperature (at consistent pressure) or a decrease in pressure (with or without a decrease in temperature; green to red isochores, Fig. 4–15). The latter is more likely given the

localization of the EKD along a shear zone that was active during mineralization (cf. Chapter 3). The higher homogenization temperatures in vein-hosted type 2 inclusions is also consistent with lower temperature estimates from sulfur geothermometry in Kontak (1990a; i.e., 300–400°C) and the higher temperature estimates from sulfur geothermometry in Willson (2019; i.e., 250–325°C). To overlap each of these ranges, the temperature of formation for the main vein mineralization stage is herein interpreted to be between 300 and 400°C (red fields in Fig. 4–15).

The homogenization temperatures for types 1 and 2 inclusions are typically higher than those of aqueous-carbonic type 3 inclusions which display a wide range of $T_h(\text{total})$ (i.e., 162–300°C; Table 4–2). The respective fluid isochores, however, are calculated using measured volumetric proportion of the carbonic phase, $T_m[\text{Clath}]$ where present, and $T_h[\text{CO}_2]$ (Fig. 4–15, right). The latter two measurements are generally consistent in type 3 fluids, whether hosted by quartz sulfide/phosphate veins or in late-stage unmineralized veins. The slopes of isochores from type 3 inclusions suggest entrapment pressures lower than those interpreted from SMB emplacement (≤ 2.5 kbar) and, as such, these fluids record either an increase in temperature from <400 to 400–600°C (at low pressures), or a decrease in pressure at the same temperature range (i.e., 300 to 400°C; red field in Fig. 4–15). Entrapment of type 2 fluids was therefore likely repeated in the later mineralization stages of the paragenesis, and the variable fluid pressure along the EKSZ suggests pressure fluctuation was responsible for the range of PT signatures in these fluids.

All of the mineralization-associated fluids (types 1, 2 and 3) described above have higher homogenization temperatures and salinities than those recorded in the type-4 FIAs (125 to 285°C), hosted by the overprinting quartz-carbonate vein assemblage. Although this study did not conduct extensive microthermometry on this fluid type, the PT conditions are interpreted to be low temperature and low pressure with respect to the rest of the EKD inclusions.

The pressure variation during entrapment of types 2 and 3 fluids is best explained by hydrofracturing and mechanical slip due to sub-vertical movement on the EKSZ during mineralization. The EKSZ is a major structure that controlled the emplacement of parts of the SMB and the activity of which is also considered to have been synchronous to formation of the associated ore systems (Horne et al., 1992; MacDonald, 2001); in particular the EKD (Halter et al., 1996). We suggest, therefore, that the EKSZ experienced sudden pressure changes from lithostatic to near-hydrostatic (i.e., $\Delta P \leq 3$ kbar; Fig. 4–15) during the emplacement of the SMB. Porosity that is generated from greisenization as well as mechanical slip would infill with mineralization through the paragenesis, thus building the effective pressure in the deposit back to lithostatic conditions, until the cycle repeats with recurring slip along the EKSZ (see Fig. 4–17). The coupling of fluid infiltration and mineral precipitation with movement along the EKSZ is evidenced by: 1) the presence of quartz-albite-pyrite-sphalerite fiber veins on the EDSZ (Fig. 4–2H); and 2) late-stage echelon shear veins and extensional quartz-phosphate-albite-fluorite veins (Fig. 4–2G). This repetition is similar to that of the cyclical fault valve model (Sibson, 1990, 1992), and has been recorded in other types of hydrothermal ore settings: e.g., orogenic Au (e.g.,

Sibson et al., 1988; Taylor et al., 2021) and porphyry Cu (e.g., Redmond et al., 2004; Monecke et al., 2018). Importantly, the cyclical fault valve process that has been attributed with unmixing in CO₂-bearing fluids in greenstone-hosted mesothermal quartz-vein Au deposits (e.g., Sibson et al., 1988; Boullier and Robert, 1992; Micklethwaite et al., 2010). The pressure change recorded by inclusions for each seismic event may also depend on distance from the major fault zone (e.g., Sibson, 1994). For example, in the centers of high-pressure systems, the trapping pressures for fluid inclusions in single vein samples have ranged from 1 to 3.5 kbar (shear zone-related veins of the central Pyrenees; Henderson and McCaig, 1996). This may explain the range of pressures, between lithostatic and near-hydrostatic conditions, that are recorded by inclusions of the EKD.

Cyclical fluid pressure changes are also well documented in porphyry Cu deposits and these settings can provide insight to processes that formed the EKD. In such settings, the exsolved magmatic fluids maintain or exceed lithostatic fluid pressure values near the apex of a mineralizing intrusion (Fournier, 1999; Cox, 2005); thereby producing early, high-temperature steeply-dipping veins or, in some cases, magmatic-hydrothermal breccias (Sillitoe, 1985). The associated hydrofracturing in these settings allow for rapid drops in pressure, toward hydrostatic levels (Seedorf et al., 2008, and references therein). Notably, the fluctuating fluid pressure and hydrothermal activity in porphyry Cu systems has been attributed to seismic release (e.g., Richards, 2018) as well as to 1st and 2nd boiling of magmatic fluids (Burnham, 1979); the latter of which is identified in fluid inclusion types and is recognized as the primary cause for ore precipitation (e.g., Redmond et al., 2004). Pressure fluctuations in porphyry settings have also

been attributed to repeated boiling of new mineralizing fluids, resulting in inclusions with variable phase proportions and homogenization behaviors through a relatively static temperature window (e.g., El Teniente, Chile; Klemm et al., 2007).

Further evidence for fluctuating pressure during the paragenesis is observed at a microscopic scale by the presence of decrepitated and re-equilibrated fluid inclusions (e.g., Fig. 4–5). That inclusions can change shape owing to ΔP_{fluid} has been demonstrated for some time based on both natural (e.g., Pécher, 1989; Boullier, 1999; Vityk et al., 1994) and experimental (e.g., Pécher, 1981; Sterner and Bodnar, 1988; Vityk and Bodnar, 1995; Diamond et al., 2010). Such textures are common in samples from the EKD and this strongly supports the re-equilibration of inclusions during transient changes in ΔP_{fluid} . These textures are mostly restricted to larger inclusions and, combined with their shapes, this suggests formation when $P_{\text{internal}} > P_{\text{confining}}$ (cf. Sterner and Bodnar, 1989); therefore, decrepitation was likely initiated when $P_{\text{lithostatic}}$ changed to $P_{\text{hydrostatic}}$. Although such textures have rarely been integrated into fluid inclusion studies they are in fact widespread in a variety of ore deposit settings (Kontak and Tuba, 2017), as recent studies have shown (e.g., Zoheir et al., 2019; Sun et al., 2020; Tsuruoka et al., 2021). In the EKD, the fluid inclusion textures are commensurate with the structural setting and suggest an important role for ΔP_{fluid} in the deposit evolution.

4.6.2 Fluid chemistry

The geochemical changes through various stages of the paragenesis have previously been characterized through whole-rock litho-geochemistry and chemistry of the hydrothermal minerals (Halter et al., 1996; Kontak et al., 2001). In addition, inferences of fluid chemistry were made from evaporate mound and leachate analyses (Halter et al., 1995; Kontak et al. 2001) which showed the earliest fluids, as represented in the EKL and pegmatites, and those involved in greisen formation were saline and dominated by NaCl with lower abundances (i.e., < 6.5 wt. %) of Fe, Mn, and K. In this study, a more comprehensive characterization of fluid chemistry through the entire paragenesis was done via microthermometry, evaporate mound, and in situ LA-ICP-MS analysis, and LRM of inclusions. As a caveat to this discussion, we note that the spatial association of ore minerals with quartz and/or topaz hosting the fluid inclusions does not unequivocally indicate growth of these phases from the same mineralizing fluid, as generally inferred in most studies; the work of Campbell and Panter (1990) and Wilkinson (2001), among others, illustrate this point. Furthermore, we again note that the measured FIAs were dominantly of indeterminate origin, but where present primary FIAs were also measured.

4.6.2.1 Implications of Evaporate Mound Analysis

The majority of inclusions through the mineralized stages of the paragenesis have low eutectic (T_e) and $T_m[\text{ice}]$ values (i.e., -23 to -50°C and -19 to -32°C, respectively; Table 4–2) that indicate

the presence of divalent cations, in addition to Na and K (Steele-MacInnis et al., 2016). The dark brown to reddish-brown color of inclusions induced during freezing, as well as the presence of hydrohalite as the last phase to melt, confirm the presence of these cations, in particular Fe and Mn (Fig. 4–6), with subordinate Ca. These observations are complemented by similar findings using evaporate mounds and, with more select samples, LA-ICP-MS analyses (Figs. 4–11 and 4–12, respectively). Although these datasets are dominantly in agreement with each other, the latter data do suggest more Fe and Mn in hypersaline type 1 fluids than do the mound analysis. This observation may relate in part to precipitation efficiency of Fe and Mn salts relative to Na and K salts in mounds, as such details relating to mounds have yet to be studied in detail. The majority of data for the hypersaline type 1 inclusions, however, suggest that any non-halite solid phase is likely a Fe-K-Mn chloride and/or hydrate; similar, for example, to those identified in fluid inclusions from the Mount Pleasant Sn (-W-Mo-In) deposit (New Brunswick, Canada; Elmi Assadzadeh et al., 2016). The elevated Fe and Mn contents from both mound and LA-ICP-MS analysis (Figs. 4–11 and 4–12, respectively) support the presence of such phases.

The EKD contains abundant topaz indicating significant addition of F to the system, however the chemistry of evaporate mounds indicate fluid inclusion chemistry through the paragenesis contains no detectable F content (Table EA 4-2; Electronic Appendix). The LA-ICP-MS analysis did not measure F in the samples; whereby the high ionization potential of F precludes its detection, and electron microprobe measurements of F are limited to solid substrates with relatively high abundances (detection limits of 100 s ppm for F; see discussion in Hanley and

Koga, 2018). The absence of detectable F in the evaporate mound data, however, is an important observation as F has been documented in similar studies elsewhere in the SMB to be an important anion in the magmatic fluids (e.g., Kontak and Kyser, 2011; Tweedale et al., 2014, Tweedale, 2019). This may be related to the absence of Ca measured in fluid inclusions of the EKD, as Ca is needed to couple with F during mound formation, otherwise it is likely volatilized prior to analysis. The comparative SMB settings noted above, where F is found to be enriched in mound analysis, show a strong association of F with Ca (Kontak and Kyser, 2011; Tweedale, 2019). The abundance of secondary apatite in the EKD (see Chapter 3) may account for Ca depletion in fluid inclusions; apatite is the likely sink for any Ca liberated from primary plagioclase by albitization. Therefore, Ca is not present in the fluid inclusions whereas F is likely present, but as HF and thus lost during evaporate mound formation.

4.6.2.2 Implications of Confocal Laser Raman Microanalysis

The LRM analysis verified the carbonic phase as dominantly CO₂-bearing with variable amounts of N₂, H₂S, and CH₄. Through the paragenesis, carbonic phases have a higher CO₂ density where hosted by greisen infill and quartz-sulfide veins relative to those in later quartz-carbonate veins (Table 4–4). Although these fluids have similar salinity, this density change indicates variable pressure recorded during trapping of these inclusions. The relative difference of CO₂ density suggests the aqueous-carbonic inclusions in the greisen fill and quartz-sulfide veins were trapped at significantly higher pressures than those trapped in late stage quartz-carbonate veins.

The significant increase in CH₄ concentration is coupled with decreased density in carbonic phases of type 3 fluids, as noted between ore mineralization and late unmineralized veins; this change is similar for both N₂ and H₂S (Table 4–4). The heterogeneity of carbonic phases in type 3 fluid inclusions suggests their formation may be related to effervescence (phase separation); a process attributed to decreasing pressures during hydraulic fracturing. The intermittent changes to pressure in the EKD, as discussed above, explain repeated effervescence and the separation of N₂–CH₄ from CO₂ in varying proportions through the paragenesis (Table 4–4). The absence of H₂S in ore mineralization stages, however, is likely due to its uptake in precipitated sulfides.

The changes in CH₄ concentration are likely due to variable pressure; a process that has been recorded by previous studies which note relatively high CH₄ concentrations subsequent to a transition from lithostatic to hydrostatic conditions (e.g., Caumon et al., 2014). However, CH₄ concentrations may also increase as a result of cassiterite precipitation from CO₂-bearing fluids, where the oxidation of Sn(II)_{aq} to Sn(IV) is coupled with a simultaneous reduction of CO₂ to CH₄ (e.g., Schmidt, 2018). For the latter process to be prevalent, we would expect high CH₄ concentrations in aqueous-carbonic fluid types through the cassiterite mineralization stages; although evidence for this process is not pervasive in the EKD, it is present in a single example from type 3 inclusions from the greisen infill of EK-86-122A (Table 4–4).

4.6.2.3 Implications of LA-ICP-MS analysis

There are several aspects of the ore fluid chemistry that need to be accounted for, such as the decrease in concentration of many elements part-way through the paragenesis and the subsequent enrichment to levels similar to the initial stages (i.e., U-shaped pattern observed in Fig. 4–12A). The depletion of Mn, Fe, Zn, and S in mineralization stages may reflect co-precipitation of the relevant mineral phases that contain or substitute these elements (e.g., pyrite, chalcopyrite, sphalerite). The enrichment in relative concentrations of Mn, Fe, Zn, and S part-way through the paragenesis (Fig. 4–12A) suggests a replenishment of the initial ore-forming fluids prior to continued mineralization.

The relatively flat patterns of other elements (i.e., K, Cs, Rb, Li) through the paragenesis is due to the mobilization of these elements from the host rocks, coupled with accommodation into alteration products at each stage in the paragenesis, for example: K^+ released from hydrolysis of K-feldspar in the EKL is readily incorporated into muscovite alteration and subsequent greisen mica mineralogy; whereas Cs maintains high concentrations (~2000 ppm; Fig. 4–14A), which reflect a highly-fractionated magmatic exsolution source (cf. Audétat et al., 2008), due to it being largely a nonprecipitating element through the paragenesis. Subtle variation from the flat pattern of Rb and Li concentrations include two notable changes at different stages: 1) a decrease from type 1 to type 2 fluids, perhaps the result of dilution by an external fluid, and 2) a minor increase recorded by inclusions from the late greisen infill stages (Fig. 4–14A). The latter change in these

concentrations reflects the breakdown of muscovite in greisen cores (and the co-precipitation of cassiterite, chalcopyrite, and quartz) by type 2 fluids, resulting in the release of trace elements such as Rb and Li that readily substitute into the muscovite structure. The breakdown of greisen-hosted muscovite suggests an acidic nature to the mineralizing fluids; as supported by mass-balance observations at this stage of the paragenesis by Halter and Williams-Jones (1996), noting 3–5 vol % alteration-induced porosity in the EKD greisens.

The sinuous pattern in many ore-related metals (i.e., Sn, Cu, W, As, and In; Fig. 4–18A) through the paragenesis provides insight to the fluid evolution with respect to ore mineralization. The decreased Sn concentration in type 2 fluids indicate this fluid was entrapped during cassiterite precipitation, however the decrease of Cu, As, and W in this fluid type is not recognized until the greisen infill to sulfide-bearing vein stages (Fig. 4–18B). The latter decrease is consistent with precipitation of the associated ores (e.g., chalcopyrite, arsenopyrite, wolframite) as the type 2 fluid cooled. The sinuous pattern, noted above, is characterized by a replenishment in each of the aforementioned elements between types 2 and 3 fluid types. This suggests the type 3 inclusions represent a fluid source somewhat enriched in these elements, similar to that of the early ore-mineralizing (type 1) fluid source. Late stage mineralization (i.e., sulfide- and phosphate-bearing veins) again depletes the EKD fluids in these elements. In contrast, the type 4 fluids that are introduced with the last vein stages do not show a replenishment in any of the above metals and thus likely represent a different source relative to the other fluid types. The inferred replenishment represents addition of fluid that diluted the early hypersaline type 1 fluids.

The source of replenishment may be either: 1) a new magma pulse at depth, synchronous with fault reactivation that focused fluid flow, a process that is typical in porphyry Cu settings (cf. repeated degassing from magmas beneath a given system, Chelle-Michou et al., 2017); or 2) introduction of meteoric waters through hydrothermal convection cells, typical of late stages in Sn-W deposit formation (e.g., Sheppard, 1994; Thomas et al., 2003).

The chemistry of these fluid types provide a signature that can be compared to other deposits, globally, that are of variable style and character. Type 1 fluids contain a significant amount of S, Fe, Mn, K, Zn, Cs and Rb (Fig. 4–12A) with a low K/Rb ratio; typical of derivation from highly differentiated melts (e.g., Heinrich et al., 1999; Irber, 1999; Audétat et al., 2000). The low K/Rb ratio is maintained in types 2 and 3 fluids through the paragenesis, suggesting these fluid were influenced by sources similar to the type 1 inclusions. The signature of EKD fluids contrasts with those hosted by both less evolved, barren granites as well as porphyry magmatic-hydrothermal deposits alike. These deposit settings can thus be discriminated upon based on the K/Rb content of fluids. Fluids in the EKD have similar K/Rb ratios to felsic magmatic settings as well as other Sn-W deposits (e.g., Mole Granite, Ehrenfriedersdorf, Zinnwald; Fig. 4–19). Additionally, with respect to porphyry Cu deposits, the EKD fluids are enriched in most metals through the paragenesis; including Zn and Cu, both of which are typically enriched in fractionated melts relative to those that host porphyry-Cu deposits (the latter due to partitioning into the unmeasured vapor phase). Ore-element concentrations in type 1 fluids partially overlap with those recorded in high-grade Sn-deposits, most notably for Sn (Fig. 4–19). Thus, although the

EKD setting is suitable for low-grade, high-tonnage mineralization, the mineralizing fluid is depleted in Sn relative to other major deposits of this style; this perhaps is an important limiting factor to the overall deposit size.

4.6.3 Implications of $\delta^{18}\text{O}$ data

The O isotopic signature of mineralizing fluids through the EKD paragenesis is an indicator of fluid origin; e.g., F-rich EKL, a magmatic reservoir foreign to the EKL, or an external fluid source (e.g., wall-rock or surficial). The $\delta^{18}\text{O}$ data on quartz and more limited data on cassiterite and albite is compiled with previously published data on whole-rock samples from the deposit (Tables 4–5, 4–6 and Fig. 4–14) to fingerprint the mineralizing fluids. Assuming the type 1 fluids represent an original fluid composition, these signatures characterize the extent of fluid-rock interaction as well as dilution by external fluids, the latter of which temporally corresponds to cassiterite precipitation. To address the latter, a micro-scale SIMS analytical approach was used to provide higher resolution to $\delta^{18}\text{O}_{\text{H}_2\text{O}}$ changes relative to bulk analysis; this approach has demonstrated large variations due to the involvement of different fluid reservoirs for both magmatic-hydrothermal (e.g., Allan and Yardley, 2007; Fekete et al., 2016) and orogenic gold settings (Kerr et al., 2018; McDivitt et al., 2021).

The bulk mineral IRMS and in situ SIMS analyses in each mineralization stage yielded similar average $\delta^{18}\text{O}_{\text{quartz}}$ results, and appropriate mineral- H_2O fractionation (Fig. 4–20A) calculations collectively suggest multiple source and buffering influences on fluids in the EKD system

(summarized in Fig. 4–20B). To evaluate these influences, the $\delta^{18}\text{O}_{\text{quartz}}$ data is compared with relevant published $\delta^{18}\text{O}$ whole-rock data, shown in Figure 4–20B, for: 1) Meguma metapelitic country rocks (Longstaffe et al., 1980); 2) leucogranites of the SMB (Longstaffe et al., 1980; Poulson et al., 1991; Clarke et al., 1993); 3) the host EKL (Kontak, 1990b); and 4) intermediate plutons peripheral to the DLP (Longstaffe et al., 1980). These ranges were also compared with $\delta^{18}\text{O}_{\text{quartz}}$ values from pegmatites equivalent to the SMB leucogranites (Kontak et al., 2002; Fig. 4–20B).

The early stages of alteration in the EKD involved interaction between the host rock and a fluid of magmatic origin (pink box in Fig. 4–20A), the isotopic evolution of which is shown by the red trajectory in Figure 4–20B (cf. Sheppard, 1986). The data show that $\delta^{18}\text{O}_{\text{H}_2\text{O}}$ values in equilibrium with EKL quartz (i.e., the earliest mineralizing fluid; 5– 8.9‰, Table 4–5) are consistent with those from EKL whole rock samples ($\sim+8.6\%$; Kontak, 1990b) and data from pegmatite K-feldspars (8.6–11.2‰; Kontak et al., 2001). Importantly, the higher values from the above range are consistent with: 1) calculated $\delta^{18}\text{O}_{\text{H}_2\text{O}}$ values of 8.9‰ for magmatic water based on the $\delta^{18}\text{O}_{\text{zircon}}$ for the Davis Lake Pluton (see Chapter 3), using the $\Delta_{\text{zircon-H}_2\text{O}}$ fractionation of Krylov et al. (2002); 2) the range of previously published $\delta^{18}\text{O}$ values (excluding outliers $> 4\%$) from the SMB, both in whole-rock (9.5–13‰; Longstaffe et al., 1980; Kontak et al., 1988; 1991; 2002) and quartz (8.9–13.9‰; Kontak et al., 1991; Poulson et al., 1991); 3) the range of $\delta^{18}\text{O}_{\text{H}_2\text{O}}$ values determined in host rocks to mineralized greisens elsewhere in the SMB, i.e., the New Ross area (7.6–10.6‰; Carruzzo et al., 2004); and 4) the range of $\delta^{18}\text{O}$ whole rock values

obtained from the Shelburne, Barrington, and Wedgeport intermediate- to felsic plutons (7.8–10.1‰; Longstaffe et al., 1980), which are located ~30 km SW of the host Davis Lake Pluton and ca. 10 Ma younger (Fig. 4–1).

Quartz that forms from a cooling fluid should become progressively enriched in $\delta^{18}\text{O}$ (Fig. 4–20B). For example, relative to the EKL and based on a $\Delta_{\text{quartz-H}_2\text{O}}$ fractionation of 3.3 to 4.1‰ (at 450–400°C; Matsuhisa et al., 1979), quartz in greisens and early sulfide-bearing veins would be expected to be ~11–12‰ based on a typical magmatic trajectory. However, this study documents greisen stage $\delta^{18}\text{O}_{\text{H}_2\text{O}}$ values from 4.2–6.9‰ (at 450–400°C; Table 4–5 and Fig. 4–20). This indicates that greisen-hosted quartz precipitated in fluids with a lower $\delta^{18}\text{O}_{\text{H}_2\text{O}}$ signature than those that equilibrated with the host EKL and pegmatites (i.e., change from pink to brown fields in Fig. 4–20A). Such excursions in the evolution of $\delta^{18}\text{O}_{\text{H}_2\text{O}}$ signature are well known to occur in Sn-W systems due to fluid-fluid mixing (e.g., Ohmoto and Rye, 1979; Sun and Eadington, 1987; Wagner et al., 2009).

Although the anomalously low $\delta^{18}\text{O}_{\text{H}_2\text{O}}$ values in the EKD suggests incursion of externally-sourced ^{18}O -depleted fluids into the late-stage crystallization of the EKL, this process has rarely been documented through the rest of the SMB. Where such a process has been documented, the incursion is by ^{18}O -enriched fluids (e.g., Kontak et al., 1991; Carruzzo et al., 2004).

Additionally, sulfides in the EKD record a relatively restricted range of $\delta^{34}\text{S}$ values in IRMS analysis of mineral separates (3.6–7.0‰; Kontak, 1990a; Willson, 2019) and a wider range of in

situ analysis (i.e., SIMS), ranging from 0.7–6.7‰ in greisen-hosted sulfides and 2.9–9.8‰ in sulfide-bearing veins (Willson, 2019). The lower $\delta^{34}\text{S}$ values are consistent with H_2S -dominated ore fluids and reflecting a homogeneous magmatic source for sulfur (i.e., no significant change in the $\text{H}_2\text{S}/\text{SO}_4$ ratio of the fluid). Thus, the above $\delta^{18}\text{O}_{\text{H}_2\text{O}}$ signature evolution in the EKD indicates the main mineralizing stages (i.e., after incipient greisenization) involved mixing an initially primitive magmatic fluid with another $\delta^{18}\text{O}$ -depleted fluid that shows little equilibration with the surrounding wall-rocks (e.g., Fig. 4–20B).

Infill mineralization to greisens have a range of $\delta^{18}\text{O}_{\text{quartz}}$ values that is similar to those recorded in sulfide-bearing veins and the interpreted formational temperatures of subsequent mineralization stages (300–350°C; red field in Fig. 4–15) and yield equilibrium $\delta^{18}\text{O}_{\text{H}_2\text{O}}$ values between 0.6 and 6.7‰ (red field in Fig. 4–20A). These values suggest quartz in these stages precipitated from a fluid with a depleted $\delta^{18}\text{O}_{\text{H}_2\text{O}}$ signature relative to the earlier mineralization stages, and likely represent either less mixing with the original magmatic fluid or a cooler, more evolved equivalent to the externally-sourced fluid (noted above) with less rock buffering (e.g., green trajectory in Fig. 4–20B). This pattern continues into The late mineralized veins (i.e., quartz-albite-apatite) have $\delta^{18}\text{O}_{\text{quartz}}$ signatures (8.5–8.8‰; Table 4–5 and Fig. 4–14) consistent with an evolution from a fluid with a depleted $\delta^{18}\text{O}_{\text{H}_2\text{O}}$ signature. The data from the late mineralized vein stage yields $\delta^{18}\text{O}_{\text{H}_2\text{O}}$ values between +2 and 5‰ (assuming similar temperatures to the sulfide-bearing vein stage, red field in Fig. 4–20A). Lastly, overprinting quartz-carbonate vein have $\delta^{18}\text{O}_{\text{quartz}}$ signatures from 11.6 to 12.1‰, suggesting enrichment in ^{18}O and

equilibration with metasedimentary rocks of the Meguma terrane (Fig. 4–20B); based on corresponding whole rock $\delta^{18}\text{O}$ data (i.e., 8.6‰, Table 4–5; Kontak, 1990b) the calculated equilibration temperatures yield a range of $\delta^{18}\text{O}_{\text{H}_2\text{O}}$ values between 0 and +2‰ (hatched field in Fig. 4–20A), indicative of a meteoric origin.

The implications from limited $\delta^{18}\text{O}$ data on cassiterite and albite are consistent with those from the associated quartz discussed above. For cassiterite, the two samples have $\delta^{18}\text{O}_{\text{H}_2\text{O}}$ values (i.e., 8.0 and 9.3‰ at 400–450°C; Table 4–6) that overlap with associated quartz $\delta^{18}\text{O}$ values. Similar cassiterite data are reported by Halter et al. (1996), with enriched $\delta^{18}\text{O}$ relative to cassiterite in the EKL pegmatites (i.e., 2.8‰; Kontak et al., 2001). The two albite $\delta^{18}\text{O}$ data and their corresponding $\delta^{18}\text{O}_{\text{quartz}}$ values (from a phosphate bearing- and a late barren vein) provide $\delta^{18}\text{O}_{\text{H}_2\text{O}}$ and formational temperature information for the representative paragenetic stages. In regards to the latter, the $\Delta_{\text{quartz-albite}}$ fractionation indicates formation temperature of 382 and 258°C for the phosphate-bearing and barren veins, respectively, using appropriate equations (Matsuhisa et al., 1979; O’Neil and Taylor, 1967). Incorporating these calculated temperatures results in low $\delta^{18}\text{O}_{\text{H}_2\text{O}}$ values of 5.4 and 1.7‰ for the quartz-albite pairs in phosphate-bearing and unmineralized veins, respectively; these values are in agreement with the ranges derived from ^{18}O in quartz (above) for their respective paragenetic stage.

The $\delta^{18}\text{O}$ signatures at each stage of the paragenesis, as described above, indicate variable amounts of mixing of at least three discrete fluids (Fig. 4–20B). This first is a magmatic fluid

that initially interacted with the host EKL, causing early alteration and greisen formation. The second fluid mixed with the rock-buffered system and had a depleted $\delta^{18}\text{O}_{\text{H}_2\text{O}}$ signature; the amount of rock buffering and influence from the first fluid likely decreased through the paragenesis (i.e., from early and late greisenization to sulfide-bearing veins). The $\delta^{18}\text{O}_{\text{quartz}}$ values of Meguma metasedimentary rocks are high (10.1–12.9‰, grey field in Fig. 4–20B; Longstaffe et al., 1980), and thus we would expect quartz precipitated from wall-rock equilibrated fluids to have a heavier ^{18}O signature than indicated by the fluid-mixing model (Fig. 4–20B). The heavy signature, however, has not been observed in other SMB ore systems where such interaction has occurred; the depression of $\delta^{18}\text{O}$ values is rather recorded in muscovite and K-feldspar (see discussion in Carruzzo et al., 2004, and Kontak and Kyser, 2011). The Carruzzo et al. (2004) study estimated meteoric water equilibrated with Meguma metasedimentary rocks at ca. 380 Ma to have a $\delta^{18}\text{O}_{\text{H}_2\text{O}}$ of $-6 \pm 2\text{‰}$ and a $\delta\text{D}_{\text{H}_2\text{O}}$ of $-38 \pm 16\text{‰}$. Thus, although the origin of the fluid is somewhat enigmatic, partial equilibration with Meguma metasedimentary rocks would explain the ^{18}O depletion; further research on the $\delta\text{D}_{\text{H}_2\text{O}}$ values of the EKD fluids is required to quantify the influence of meteoric waters. Importantly, such a fluid has been noted as critical in the formation of the SMB-hosted Flintstone Rock silica-clay deposit, located ~20 km south of the EKD (Fig. 4–1A) along the western end of the Tobeatic Shear Zone (Kontak and Kyser, 2001); thus, a similar structural setting to that of the EKD. The third discrete fluid is attributed with forming the latest stage quartz-carbonate veins and presents a dramatic excursion in the $\delta^{18}\text{O}_{\text{quartz}}$ signature to higher values, suggesting this stage of the paragenesis involved

incursion of a fluid that, if formed at low temperatures, was more equilibrated with Meguma metasedimentary rock (i.e., low $\delta^{18}\text{O}_{\text{H}_2\text{O}}$).

4.6.4 Implications of anomalous salinity in East Kemptville Fluid Types

The development of highly evolved, fractionated systems typically results in enrichment of B and/or F, in addition to many other incompatible elements (e.g., the BeBLiP group of Strong, 1981; Černý et al., 2005 and references therein). The incompatible element content may stay enriched in a melt to temperatures as low as 500°C under upper crustal pressures (e.g., Manning and Pichavant, 1983; London et al., 1989, 1993; 1999; Morgan and London, 1999; Thomas et al., 2000; Sirbescu and Nabelek, 2003). At low pressure, fluids that exsolve from such magmas typically have low salinities, between 5 and 15 wt% NaCl equiv., based on many studies of natural samples (e.g., Cline and Bodnar, 1991; Williams-Jones and Heinrich, 2005; Audétat et al., 2008; Bodnar et al., 2014) as well as experiments (Iveson et al., 2019; Webster et al., 2020). The microthermometric properties (i.e., Th and salinities) of these exsolved fluids are consistent through different magmatic-hydrothermal settings, both for Sn ± W style and porphyry Cu and/or Mo style deposits (Bodnar et al., 2014). In these settings, the primary fluid type with low salinity has been credited with transporting significant metal content prior to separating into a brine and vapor (unmixing) at shallow depths and precipitating ore mineralization (e.g., Redmond et al., 2004). For the resultant brines, a decrease in salinity and Th from early to late in the deposit

paragenesis relates to cooling of the magmatic-derived fluids as well as the likely dilution from external fluid sources, such as meteoric waters (e.g., Audéat et al., 2000).

In contrast to the low salinity primary fluids that are recognized as early paragenetic fluids in Sn, W, Cu, and Mo deposits noted above, the type 1 inclusions found in the weakly altered EKL, inferred to be orthomagmatic in origin (see above), are hypersaline (29 to 38 wt% NaCl equiv.; Table 4–2, Fig. 4–16B). These inclusions, however, do not coexist with V-rich fluid inclusion types. The absence of V-rich fluid inclusions for the extensive suite of samples through the complete paragenesis in the Main Zone (i.e., granite, pegmatites, greisens and different vein types) is notable as a lack of evidence for phase separation; an important process for many magmatic-hydrothermal systems (Williams-Jones and Heinrich, 2005; Richards, 2011; Bodnar et al., 2014). This absence therefore highlights an unusual aspect of the EKD ore fluid relative to other magmatic-hydrothermal systems: the high to moderate-salinity character of fluids that has not been produced through fluid unmixing.

Subsequent to trapping of hypersaline type 1 inclusions, the fluid characteristics through the EKD ore mineralization stages (i.e., types 2 and 3 fluids) decrease in salinity and average Th values; a similar trend to what is described in magmatic-hydrothermal settings elsewhere, as noted above. The end of ore mineralization at the EKD, trapped fluids that record a decrease in salinity, from 29–38 to 10–23 wt% NaCl equiv., indicating a 2–3-fold dilution of the magmatic saline type 1 fluids that results in the type 3 fluid. This change is consistent with the difference

between calculated $\delta^{18}\text{O}_{\text{H}_2\text{O}}$ values for fluids that are interpreted to mineralized early greisens and late barren veins at 6.3–7.6 and 2.2–4.0‰, respectively (Table 4–5, Fig. 4–20). The shift in salinity and fluid isotope composition towards values of meteoric water indicates the diluting fluid is of meteoric origin; although the somewhat elevated ^{18}O values for these fluids, relative to a meteoric fluid, suggests a modest modification by isotope exchange with silicate rocks at high temperatures (i.e., > 300 °C, as indicated by fluid inclusions at the terminal mineralization stages). Alternatively, the diluting fluid may represent a mixture of meteoric water with low-salinity magmatic vapor that had previously condensed into this low salinity liquid (e.g., Audétat et al., 2008). This process may explain the chemical composition of low-salinity end-stage fluids that are typified in the EKD by enrichment of select ore elements (see discussion on sinuous pattern above, Fig. 4–12A) that are preferentially transported by magmatic vapor (e.g., S, Cu, As; cf. Fekete et al., 2016)

The derived isochores presented above suggest the hypersaline type 1 EKD fluids originated due to exsolution via combined 1st and 2nd boiling processes (e.g., Burnham, 1979), from a highly-evolved F-rich melt under relatively high pressures (Fig. 4–15); i.e., PT conditions similar to those recorded by the SMB and the associated EKL. Thermodynamic modelling on such melts by Webster and Holloway (1988) suggest an decreased capacity of Cl dissolution with higher pressures (i.e. up to ~2–2.2 kbar); however, without degassing at depth, crystallization of silicate minerals results in residual melts with excess Cl (up to 0.5 wt. % Cl after ~ 80 wt. % crystallization of the melt). Additionally, decreasing temperature and fractionation at depth of

magmas with high halogen/H₂O ratios, such as the EKL, exsolve a hydrosaline liquid (i.e., brine) with progressively decreasing salinity (Dolejš and Zajacz, 2018). As Cl partitions strongly into a fluid phase, any aqueous fluids derived from a magma under these conditions will thus be Cl-rich (i.e., from 0.3 to 11 wt. %) and highly saline (Webster and Halloway, 1990; Iveson et al., 2019; Webster et al., 2020). Although the SMB emplacement conditions indicate higher pressures (ca. 3.5 kbar) than these experiments, the high salinities and Cl concentrations measured in early type 1 fluids (i.e., 1.8 to 10.6 wt. % Cl; Table EA 4-3, Electronic Appendix) are similar to those predicted by the Webster et al. (2020) models.

The enrichment of Cl in peraluminous granitic melts has important consequences for partitioning of some ore metals, trace elements and the major elements (i.e., Na, K and Fe) into the fluid (e.g., Webster, 2004); this enrichment also, therefore, influences the subsequent efficiency of ore metal dissolution, transport, and deposition. The solubility of many ore metals is strongly enhanced by the presence of Cl in hydrothermal fluids (e.g., Heinrich et al., 1992; Hedenquist and Lowenstern, 1994; Candela and Piccoli, 1995; Seward and Barnes, 1997). Furthermore, if first boiling is the more dominant mechanism of fluid exsolution, a Cl-enriched melt will do so at greater relative pressures (i.e., at greater depths) than a felsic magma that exsolves an H₂O-rich fluid (Webster and Rebert, 1998). Consequently, Cl-enriched magmas need not ascend to near-surface depths to form magmatic-hydrothermal deposits.

The early exsolution of brines may sequester metals and trace elements prior to enrichment in residual melts; as such, resultant granites likely become barren to poorly-mineralized. As noted above, primary mineralizing fluids with salinities such as the EKD type 1 fluids are not common in Sn settings unless fluid unmixing has occurred, but rare cases are known such as in the Mount Bischoff Sn-greisen deposit, Tasmania (Halley and Walshe, 1995). The inferred formation conditions of Mount Bischoff, however, differ greatly from the EKD, with estimated pressures of ~0.2 kbar and temperatures of 360–320°C (Table 4–1). The work of Audetat and Pettke (2003), however, has shown several barren granites of northern New Mexico represent magmas which exsolved a Cl-rich fluid relatively early in their crystallization history (i.e., with < 30 % crystallization); this study, however, concluded these magmas did not generate significant mineralization due to low salinity of exsolved fluids

Volatile exsolution in magmas ascending in the crust may be driven dominantly by 2nd boiling due to cooling and crystallization; whereas a rapid rise of magmas (e.g., along dykes) undergo first boiling processes. For large, complex magma reservoirs that evolve over long timescales (e.g., Cooper and Kent, 2014), an exsolved volatile phase may occur sporadically with magma recharge events that are superimposed onto slower exsolved volatile production driven by cooling and crystallization (see discussion in Webster et al., 2020).

Studies from other magmatic systems using other mineral proxies have suggested the presence of pre-eruptive magmatic fluids, e.g.: hydrogen in orthopyroxenes of the Soufrière Hills Volcano

suggest volatile-saturated magma storage at depths of up to ~12 km (Edmonds et al., 2016); An-rich plagioclase xenocrysts in Al-rich melts and experimental phase-equilibria infer water-rich parental andesites beneath St. Kitts that crystallise over a pressure range from 1.5 to 6.0 kbar (Melekhova et al., 2017); Webster (2004) draws similarities between the volatile contents of melt inclusions from the potassic, alkaline magmas of Mt. Somma-Vesuvius (with high Cl/H₂O ratios) to those of the F-rich alkaline magmas associated with orthomagmatic gold–tellurium deposits of Cripple Creek, Colorado, where the veined ores are associated with fluid inclusions of CO₂-bearing brines containing up to 40 wt% NaCl equiv. (Thompson et al., 1985); Kamenetsky et al. 1999 document the occurrence of coexisting silicate melt, salt melt, and hypersaline fluids trapped as inclusions in clinopyroxene from the ore-bearing Balut dike at the Dinkidi Cu-Au porphyry deposit, Philippines. These naturally occurring examples provide evidence for chlorine-rich brines to exsolve under higher pressures, and highlight the significant potential for magmatic-hydrothermal ore deposition in such settings.

4.6.5 Cassiterite precipitation at the EKD

The EKD is defined by greisen-hosted cassiterite mineralization localized along the EKSZ, which extends regionally to define a trend of Sn-occurrences. This pattern indicates Sn-bearing ore fluids used the EKSZ as a conduit and the deposit formed as an open-system. The interpreted replenishment of fluid through the paragenesis (Fig. 4–18A) is consistent with open-system behavior and is also reflected by the fluctuating PT conditions recorded by the inclusions;

whereby seismically induced porosity allows for re-introduction of externally-sourced fluids. Pressure estimates of fluid inclusions suggest a repeated transition from lithostatic to near-hydrostatic fluid pressures during the temporal evolution of the system; in comparison, this process has been ascribed to the incursion of meteoric water into other mineralized hydrothermal systems (e.g., Mole granite, Australia, Audétat et al., 1998; Bingham Canyon, USA, Landtwing et al., 2010; Elatsite porphyry, Bulgaria, Stefanova et al., 2014). Whereas magmatic fluids sourced from 1st or 2nd boiling can displace meteoric water convection, hydrostatic pressures result in density-driven thermal convection through permeable rocks (e.g., Fournier, 1999; Weis et al., 2012). Simulated fluid flow models have also predicted this deposition control on the formation of porphyry copper ore shells; predicting a division between hot magmatic fluid upflow zones with near lithostatic fluid pressures and ostensibly ductile conditions, and cooler surrounding rock that hosts meteoric convection under near hydrostatic fluid-pressures and brittle conditions (cf. Weis, 2015). This divide provides both cooling and dilution to saline magmatic fluids expelled from a crystallizing upper magma chamber, and is a potential mechanism for cassiterite precipitation in the EKD.

The sources of ore fluids for tin deposits is typically one of a strictly magmatic origin (i.e., the host granite), an origin external to the host rock, or involves various fluid types from these sources (cf. Heinrich, 1995). The latter scenario is particularly relevant in the EKD as three distinct fluid sources have been suggested in this study, based on the fluid chemistry and $\delta^{18}\text{O}$ signatures discussed above. The three fluid sources include: 1) magmatic origin from a

mineralizing intrusion enriched in incompatible elements; 2) moderately saline magmatic fluid partially equilibrated with host-rock; and 3) low-salinity meteoric derived fluid. Ore precipitation that results from mixing saline magmatic and low-salinity meteoric fluids would result in a drop of multiple orders of magnitude for the solubility of many of the signature elements (e.g., K, Mn, Zn, Cs, Rb, Sn at Mole Granite; Audétat et al., 1998), whereas a mixture of two fluids with variable salinity may result in the more gradual decrease in ore element fluid concentrations observed in the EKD while nonprecipitating elements remain relatively constant through the paragenesis (i.e., Na, K, Cs, Rb; Table EA 4-3, Electronic Appendix). Type 3 fluids are recognized to be prevalent in the latest stages of mineralization and characterized by a carbonic component and low to moderate salinity, but with metal-to-trace element ratios that are similar to the type 1 fluids (Fig. 4–18B). The latter evidence suggests type 3 fluids have a similar source to the initial ore-bearing fluid, although the carbonic component suggest a partial influence from surrounding wall-rocks. The mixing of these fluids produced a diluted product through the mineralized stages, a dilution that favors the externally-sourced fluids in areas where fluid-fluid interaction is high (i.e., the later greisen infill and vein stages). The increased influence of the latter fluids is further evidenced by depleted $\delta^{18}\text{O}_{\text{H}_2\text{O}}$ signatures, as calculated for quartz in these veins, as well as the visible presence of minor CO_2 and CH_4 . The type 2 inclusions, which record relatively abrupt compositional enrichment and depletion of metals (Figs. 4–12A, 4–18A), thus represent a diluted product of the two magmatic fluid types discussed above and precipitate a majority of the mineralization in the EKD.

Cassiterite precipitation in areas of high fluid-fluid interaction may occur through the oxidation of $\text{Sn(II)}_{\text{aq}}$ in the original magmatic fluid by partially-equilibrated, CO_2 -bearing externally sourced magmatic fluids. Oxidation of $\text{Sn(II)}_{\text{aq}}$ is marked by the increase of CH_4 concentration in carbonic phases from type 3 fluids through the paragenesis. This process is evidenced by the presence of CH_4 in one sample from greisen infill and suggests this process may be responsible for cassiterite precipitation in the oxide-ore mineralization stages. The variation of CH_4 and CO_2 concentrations in type 3 fluids may also reflect buffering by graphite (e.g., Burnham and Ohmoto, 1980; Kreulen, 1987), a mineral present in syn-kinematic veins throughout the EKSZ and within greisens parallel to the shear zone (e.g., Kontak, 1990b; Chapter 3). The presence of graphite and variation in carbonic species complement the interpretation of incipient greisens and early cassiterite precipitation due to fluid-rock interaction (i.e., pH change; Halter et al., 1996, 1998), and later coarse cassiterite precipitating due to episodic dilution by a CO_2 -bearing foreign fluid.

Previous workers have established that cassiterite precipitation in the EKD that was required to form economic Sn grades (i.e., up to 2 wt. %) in part resulted from a pH increase in ore fluids, brought on by fluid-rock interaction (i.e., hydrolysis; Halter et al., 1996, 1998); however, the coarse-grained character to late greisen infill (i.e., zoned greisen cores) suggest late greisen-infill mineralization is responsible for the highest Sn grades (> 2 wt. % Sn; e.g., Chapter 3) with a fluid-dominant precipitation mechanism. The Halter et al. (1996, 1998) studies note changes in mineral (e.g., replacement of muscovite by topaz) and fluid compositions across zoned greisens

and proposed cassiterite deposition along an alteration front which is characterized by dissolution-reprecipitation related to greisen formation (cf. Heinrich, 1990); thus a rock-buffered precipitation mechanism. This style of cassiterite is present at the EKD, in addition to coarse-grained cassiterite that cores zoned greisens and is present as late greisen infill throughout massive greisens (i.e., areas that experienced extensive fluid-flow and minimal fluid-rock buffering). Therefore, the oxidation of $\text{Sn(II)}_{\text{aq}}$ in diluted magmatic fluids (type 2 from 1) by CO_2 -bearing foreign fluids (type-3) is a fluid-dominant precipitation mechanism that is required for the higher grade zones in the EKD.

The above structural setting for the EKD and cassiterite precipitation mechanisms built the deep-seated magmatic-hydrothermal deposit. Ore-fluids at the EKD have a similar trace element chemical signature to those recorded in other Sn-W-(Cu-Ag-Pb-Zn) deposits (Fig. 4–19); however, in contrast to these high-grade deposits, the type 1 fluids from this study are, overall, relatively depleted in Sn; fluid types that appear later in the paragenesis also show this relative depletion. Thus, the replenishment events of fluids along the EKSZ contributed to extensive greisen formation and resulted in the high-tonnage of the EKD. The relative Sn depletion in mineralizing fluid, however, may reflect deposition of higher-grade Sn elsewhere in the system (i.e., lower) in addition to being the most limiting factor in the average grade of the deposit.

4.7 Conclusions

The PTX characteristics of mineralizing fluids in the EKD were determined through fluid inclusion and stable isotope analysis to assess fluid sources, controls on mineralization, and deposit evolution in a regional context. The absence of evidence for fluid immiscibility and anomalously saline magmatic fluids are the result of deep emplacement for the highly fractionated and F-rich host EKL, or similar intrusion at depth; whereby crystallization forced exsolution of a Cl-enriched aqueous fluid with a trace element chemistry that is roughly similar to fluids from higher-grade Sn deposits globally.

The Cl-rich type 1 fluids in the EKD formed through combined 1st and 2nd boiling from a highly-evolved F-rich melt under relatively high pressures; fluid-rock interaction resulted in precipitation of cassiterite as early greisen-style ore. Abundant decrepitate textures and large ranges in PT isochores for quartz-hosted fluid inclusions through the rest of the mineral paragenesis indicates pressure cycling subsequently controlled fluid flow in the ore system through hydro-fracturing. The interpreted depth of formation for the SMB and localization of the EKD along the long-lived EKSZ support the conditions interpreted from the fluid inclusion evidence. Strike-slip and dip-slip movement along the EKSZ focused externally-sourced fluids and provided a corridor of fluid incursion into the EKD setting and propagated greisen formation in the host rock. The greisen formation involved high fluid-rock interaction and cassiterite precipitation that resulted from an increasing pH in mineralizing fluids. The permeability

generated in these greisens were subsequently infilled with late coarse cassiterite mineralization and quartz-sulfide assemblages that fill veins throughout the deposit. This latter ore is deposited with a low fluid-rock interaction and increasing influence of externally-sourced metal-enriched fluids that have partially equilibrated with surrounding wall-rocks.

The relatively sinuous pattern of ore metals and U-shaped pattern of select trace elements through the paragenesis suggest that, despite the distinct sources of types 1 and 3 fluids, both are somewhat enriched in trace lithophile elements and thus likely magmatic in origin. That they represent two distinct fluid reservoirs suggests that fluid exsolution from a new magma replenished the ore system, a typical process in most porphyry Cu deposits but rarely recorded in Sn-W deposits.

The type 2 fluids are a product of mixing between ore element-enriched types 1 and 3 fluids. The resultant fluid is lower in salinity and depleted in elements that precipitated minerals during the dilution event. The permeability generated through alteration of the host rock allowed for extensive and efficient mixing by foreign fluids which utilized the EKSZ during seismic events; temporarily shifting the lithostatic fluid pressures to near hydrostatic conditions and causing incursion of the externally sourced fluids. The minor CO₂ component in type 3 fluids that is not recognized in any of the earlier fluid types and depleted $\delta^{18}\text{O}$ signature of quartz in the late mineralization stages suggests the late fluid had a partial equilibration with the surrounding carbonaceous Meguma metasedimentary rock.

4.8 Acknowledgements

Thanks to Avalon Advanced Materials Inc. and Bill Mercer for their support and contribution to this research. Special thanks to Dr. Jacob Hanley and the Saint Mary's University Earth Sciences Department, Halifax, NS, for their support on this project.

4.9 References

- Allan, M.M., and Yardley, B.W., 2007, Tracking meteoric infiltration into a magmatic-hydrothermal system: A cathodoluminescence, oxygen isotope and trace element study of quartz from Mt. Leyshon, Australia: *Chemical Geology*, v. 240, p. 343–360.
- Audétat, A., and Pettke, T., 2003, The magmatic-hydrothermal evolution of two barren granites: A melt and fluid inclusion study of the Rito del Medio and Canada Pinabete plutons in northern New Mexico (USA): *Geochimica et Cosmochimica Acta*, v. 67, p. 97–121.
- Audétat, A., Günther, D., and Heinrich, C.A., 1998, Formation of a magmatic-hydrothermal ore deposit: Insights with LA-ICP-MS analysis of fluid inclusions: *Science*, v. 279, p. 2091–2094.
- Audétat, A. Günther, D., and Heinrich, C.A., 2000, Causes for large scale metal zonation around mineralized plutons: fluid inclusion LA-ICP-MS evidence from the Mole Granite, Australia: *Economic Geology*, v. 95, p. 1563–1581.

- Audétat, A., Pettke, T., Heinrich, C. A., and Bodnar, R.J., 2008, The composition of magmatic-hydrothermal fluids in barren and mineralized intrusions: *Economic Geology*, v. 103, p. 877–908.
- Archibald, D.B., Murphy, J.B., Reddy, S.M., Jourdan, F., Gillespie, J., and Glorie, S., 2018, Post-accretionary exhumation of the Meguma terrane relative to the Avalon terrane in the Canadian Appalachians: *Tectonophysics*, v. 747, p. 343–356.
- Artiaga, D., Torres, B., Torró, L., Tauler, E., Melgarejo, J.C., and Arce, O.R., 2013, The Viloco Sn-W-Mo-As deposits, Bolivia: geology and mineralogy [ext. abs.]: 12th SGA Biennial Meeting “Mineral deposit research for a high-tech world”, Uppsala, Sweden, Extended Abstracts, p. 1327–1330.
- Bakker, R.J., 1999, Adaption of Bowers and Helgeson (1983) equation of state to isochore and fugacity coefficient calculation in the H₂O-CO₂-CH₄-N₂-NaCl fluid system: *Chemical Geology*, v. 154, p. 225–236.
- Bakker, R.J., 2003, Package FLUIDS 1. Computer programs for analysis of fluid inclusion data and for modelling bulk fluid properties: *Chemical Geology*, v. 194, p. 3–23.
- Bakker, R.J., and Diamond, L.W., 2000, Determination of the composition and molar volume of H₂O-CO₂ fluid inclusions by microthermometry: *Geochimica et Cosmochimica Acta*, v. 64, p. 1753–1764.

- Beaudoin, G., and Therrien, P., 2004, The web stable isotope fractionation calculator, in De Groot, P.A., ed., *Handbook of stable isotope analytical techniques, Volume-I*: Elsevier, p. 1045–1047.
- Beeskow, B., Rankin, A.H., Murphy, P.J., and Treloar, P.J., 2005, Mixed CH₄–CO₂ fluid inclusions in quartz from the South Wales Coalfield as suitable natural calibration standards for microthermometry and Raman spectroscopy: *Chemical Geology*, v. 223, p. 3–15.
- Benn, K., Horne, R.J., Kontak, D.J., Pignotta, G.S., and Evans, N.G., 1997, Syn-Acadian emplacement model for the South Mountain Batholith, Meguma Terrane, Nova Scotia: Magnetic fabric and structural analyses: *Geological Society of America Bulletin*, v. 109, p. 1279–1293.
- Benn, K., Roest, W.R., Rochette, P., Evans, N.G., and Pignotta, G.S., 1999, Geophysical and structural signatures of syntectonic batholith construction: the South Mountain Batholith, Meguma Terrane, Nova Scotia: *Geophysical Journal International*, v. 136, p.144-158.
- Bettencourt, J.S., Leite Jr, W.B., Goraieb, C.L., Sparrenberger, I., Bello, R.M., and Payolla, B.L., 2005, Sn-polymetallic greisen-type deposits associated with late-stage rapakivi granites, Brazil: fluid inclusion and stable isotope characteristics: *Lithos*, v. 80, 363–386.
- Bickerton, L., Kontak, D.J., Samson, I.M., Murphy, J.B., and Kellett, D.A., 2018, U–Pb geochronology of the South Mountain Batholith, Nova Scotia, in Rogers, N., ed.,

- Targeted Geoscience Initiative: 2017 report of activities, volume 1, Geological Survey of Canada, Open File 8358, 2018, p. 51–55.
- Bodnar, R.J., 1994, Synthetic fluid inclusions: XII. The system H₂O–NaCl. Experimental determination of the halite liquidus and isochores for a 40 wt% NaCl solution: *Geochimica et Cosmochimica Acta*, v. 58, p. 1053–1063.
- Bodnar, R.J., 2003, Introduction to aqueous-electrolyte fluid inclusions, in I.M. Samson, A. Anderson, and D. Marshall, eds., *Fluid Inclusions: Analysis and Interpretation: Mineralogical Association of Canada Short Course*, v. 32, p. 81–99.
- Bodnar, R.J., Lecumberri-Sanchez, P., Moncada, D., and Steele-MacInnis, M., 2014, Fluid Inclusions in Hydrothermal Ore Deposits, in H.D. Holland and K.K. Turekian, eds., *Treatise on Geochemistry, Second Edition*, v. 13, p. 119–142.
- Boullier, A.-M., 1999, Fluid inclusions: tectonic indicators: *Journal of Structural Geology*, v. 21, p. 1229–1235.
- Boullier, A.-M., and Robert, F., 1992, Palaeoseismic events recorded in Archaean gold-quartz vein networks, Val d'Or, Abitibi, Quebec, Canada: *Journal of Structural Geology*, v. 14, p. 161–179.
- Boullier, A.-M., Charoy, B., and Pollard, P.J., 1994, Fluctuation in porosity and fluid pressure during hydrothermal events: textural evidence in the Emuford District, Australia: *Journal of Structural Geology*, v. 16, p. 1417–1429.

- Burnham, C.W., 1979, Magmas and hydrothermal fluids, in Barnes, H.L., ed., *Geochemistry of hydrothermal ore deposits*: John Wiley and Sons, New York, p. 71–136.
- Burnham, C.W., and Ohmoto, H., 1980, Late-stage processes of felsic magmatism: *Min. Geol. Spec. Issue* 8, p. 1–11.
- Burke, E.A., 2001, Raman microspectrometry of fluid inclusions: *Lithos*, v. 55, p. 139–158.
- Campbell, A.R., and Panter, K.S., 1990, Comparison of fluid inclusions in coexisting (cogenetic?) wolframite, cassiterite, and quartz from St. Michael's Mount and Cligga Head, Cornwall, England: *Geochimica et Cosmochimica Acta*, v. 54, p. 673–681.
- Candela, P.A., Piccoli, P.M., 1995, Model ore–metal partitioning from melts into vapor and vapor/brine mixtures, in Thompson, J.F.H., ed., *Magmas, Fluids, and Ore Deposits*, vol. 23: Mineralogical Society of Canada, Nepean, Ontario, Canada, p. 101–127
- Candela, P.A., 1995, Model ore-metal partitioning from melts into vapor and vapor/brine mixtures: *Mineralogical Association of Canada Short Course*, p. 101–122.
- Carruzzo, S., Kontak, D.J., and Clarke, D.B., 2000, Granite-hosted mineral deposits of the New Ross area, South Mountain Batholith, Nova Scotia, Canada: P, T and X constraints of fluids using fluid inclusion thermometry and decrepitate analysis: *Transactions of the Royal Society of Edinburgh: Earth Sciences*, v. 91, p. 303–319.
- Carruzzo, S., Kontak, D.J., Clarke, D.B., and Kyser, T.K., 2004, An integrated fluid–mineral stable-isotope study of the granite-hosted mineral deposits of the New Ross area, south

- mountain batholith, Nova Scotia, Canada: evidence for multiple reservoirs: *The Canadian Mineralogist*, v. 42, p. 1425–1441.
- Caumon, M.C., Robert, P., Laverret, E., Tarantola, A., Randi, A., Pironon, J., Dubessy, J., and Girard, J.P., 2014, Determination of methane content in NaCl–H₂O fluid inclusions by Raman spectroscopy. Calibration and application to the external part of the Central Alps (Switzerland): *Chemical Geology*, v. 378, p. 52–61.
- Černý, P., Blevin, P.L., Cuney, M., and London, D., 2005, Granite related ore deposits: *Economic Geology 100th Anniversary Volume*, p. 337–370.
- Chelle-Michou, C., Rottier, B., Caricchi, L., and Simpson, G., 2017, Tempo of magma degassing and the genesis of porphyry copper deposits: *Scientific reports*, v. 7, p. 1–12.
- Clarke, D.B., Chatterjee, A.K., and Giles, P.S., 1993, Petrochemistry, tectonic history, and Sr-Nd systematics of the Liscomb Complex, Meguma Lithotectonic Zone, Nova Scotia: *Canadian Journal of Earth Sciences*, v. 30, p. 449–464.
- Clayton, R.N., and Mayeda, T.K., 1963, The use of bromine pentafluoride in the extraction of oxygen from oxides and silicates for isotopic analysis: *Geochimica et cosmochimica acta*, v. 27, p. 43–52.
- Cline, J.S., and Bodnar, R.J., 1991, Can economic porphyry copper mineralization be generated by a typical calc-alkaline melt?: *Journal of Geophysical Research*, v. 96, p. 8113–8126.

- Collins, P.L.F., 1981, The geology and genesis of the Cleveland tin deposit, western Tasmania; fluid inclusion and stable isotope studies: *Economic Geology*, v. 76, p. 365–392.
- Cooper, K.M., and Kent, A.J., 2014, Rapid remobilization of magmatic crystals kept in cold storage: *Nature*, v. 506, p. 480–483.
- Cox, S.F., 2005, Coupling between deformation, fluid pressures, and fluid flow in ore-producing hydrothermal systems at depth in the crust: *Economic Geology 100th Anniversary Volume*, p. 39–75.
- Culshaw, N., and Lee, S.K., 2006, The Acadian fold belt in the Meguma Terrane, Nova Scotia: Cross sections, fold mechanisms, and tectonic implications: *Tectonics*, v. 25.
- Culshaw, N., and Liesa, M., 1997, Alleghanian reactivation of the Acadian fold belt, Meguma Zone, southwest Nova Scotia: *Canadian Journal of Earth Sciences*, v. 34, p. 833–847.
- Cuney, M., Maignac, C., and Weisbrod, A., 1992, The Beauvoir Topaz-Lepidolite Albite Granite (Massif Central, France): The Disseminated Magmatic Sn-Li-Ta-Nb-Be Mineralization: *Economic Geology*, v. 87, p. 1766–1794.
- Darling, R.S., 1991, An extended equation to calculate NaCl contents from final clathrate melting temperatures in H₂O-CO₂-NaCl fluid inclusions: Implications for PT isochore location: *Geochimica et Cosmochimica Acta*, v. 55, p. 3869–3871.

- Desanois, L., Lüders, V., Niedermann, S., and Trumbull, R.B., 2019, Formation of epithermal Sn-Ag-(Zn) vein-type mineralization at the Pirquitas deposit, NW Argentina: fluid inclusion and noble gas isotopic constraints: *Chemical Geology*, v. 508, p. 78–91.
- Diamond, L.W., Tarantola, A., Stünitz, H., 2010, Modification of fluid inclusions in quartz by deviatoric stress. II: experimentally induced changes in inclusion volume and composition: *Contributions to Mineralogy and Petrology*, v. 160, p. 845–864.
- Dolejš, D., and Zajacz, Z., 2018, Halogens in silicic magmas and their hydrothermal systems, in Harlov, D.E., and Aranovich, L., eds., *The Role of Halogens in Terrestrial and Extraterrestrial Geochemical Processes*: Springer, p. 431–543.
- Dostal, J., and Chatterjee, A.K., 1995, Origin of topaz-bearing and related peraluminous granites of late Devonian Davis Lake pluton, Nova Scotia, Canada: *Chemical Geology*, v. 123, p. 67–88.
- Dostal, J., and Chatterjee, A. K., 2000, Contrasting behaviour of Nb/Ta and Zr/Hf ratios in a peraluminous granitic pluton (Nova Scotia, Canada): *Chemical Geology*, v. 163, p. 207–218.
- Dubessy, J., Poty, B., and Ramboz, C., 1989, Advances in COHNS fluid geochemistry based on micro-Raman spectrometric analysis of fluid inclusions: *European journal of Mineralogy*, v. 1, p. 517–534.

Eadington, P.J., 1974, Microprobe analysis of the non-volatile constituents of fluid inclusions:

Neues Jahrb Mineral., Monatsh, p. 518–525.

Eadington, P.J., 1983, A fluid inclusion investigation of ore formation in a tin-mineralized

granite, New England, New South Wales: *Economic Geology*, v. 78, p. 1204–1221.

Elmi Assadzadeh, G., Samson, I.M., and Gagnon, J.E., 2016, Identification of Fluid Inclusion

Solid Phases Using A Focused Ion Beam Scanning Electron Microscope With Energy

Dispersive Spectroscopy: Implications For Interpreting Microthermometric Data and

Composition of Fluids In SN (-W-Mo) Deposits: *The Canadian Mineralogist*, v. 54, 737–

754.

Fall, A., Tattitch, B., and Bodnar, R.J., 2011, Combined microthermometric and Raman

spectroscopic technique to determine the salinity of H₂O–CO₂–NaCl fluid inclusions

based on clathrate melting: *Geochimica et Cosmochimica Acta*, v. 75, p. 951–964.

Fayek, M., Harrison, T. M., Ewing, R. C., Grove, M., and Coath, C. D., 2002, O and Pb isotopic

analyses of uranium minerals by ion microprobe and U-Pb ages from the Cigar Lake

deposit: *Chemical Geology*, v. 185, p. 205–225.

Fekete, S., Weis, P., Driesner, T., Bouvier, A.-S., Baumgartner, L., and Heinrich, C.A., 2016,

Contrasting hydrological processes of meteoric water incursion during magmatic–

hydrothermal ore deposition: An oxygen isotope study by ion microprobe: *Earth and*

Planetary Science Letters, v. 451, p. 263–271.

- Fournier, R.O., 1999, Hydrothermal processes related to movement of fluid from plastic into brittle rock in the magmatic-epithermal environment: *Economic Geology*, v. 94, p. 1193–1211.
- Frezzotti, M.L., Tecce, F. and Casagli, A., 2012, Raman spectroscopy for fluid inclusion analysis: *Journal of Geochemical Exploration*, v. 112, p. 1–20.
- Fusswinkel, T., Wagner, T. and Sakellaris, G., 2017, Fluid evolution of the Neoproterozoic Pampalo orogenic gold deposit (E Finland): Constraints from LA-ICPMS fluid inclusion microanalysis: *Chemical Geology*, v. 450, p. 96–121.
- Garofalo, P.S., Fricker, M.B., Günther, D., Bersani, D., and Lottici, P.P., 2014, Physical-chemical properties and metal budget of Au-transporting hydrothermal fluids in orogenic deposits: *Geological Society, London, Special Publications*, v. 402, p. 71–102.
- Giles, P.S., 1985, A major post-Visean sinistral shear zone – new perspectives on Devonian and Carboniferous rocks of southern Nova Scotia, in A.K. Chatterjee and D.B. Clarke, eds., *Guide to the granites and mineral deposits of southwestern Nova Scotia*: Nova Scotia Department of Mines and Energy, Paper 85-3, p. 233–248.
- Goldstein, R.H., and Reynolds, T.J., 1994, Systematics of fluid inclusions in diagenetic minerals. Short Course 31, Society of Economic Paleontologists and Mineralogists, Tulsa, 199 p.

- Gowans, R., Jacobs, C., Anderson, D., Spooner, J., Mercer, W., Hains, D.H., Smith, R., 2018, The East Kemptville Tin Production and Site Remediation Project Preliminary Economic Assessment Nova Scotia, Canada: NI-43-101 Technical Report, 296 pp.
- Graupner, T., Brätz, H., and Klemd, R., 2005, LA-ICP-MS micro-analysis of fluid inclusions in quartz using a commercial Merchantek 266 nm Nd: YAG laser: a pilot study: *European Journal of Mineralogy*, v. 17, p. 93–102.
- Guillong M., Meier D. L., Allan M. M., Heinrich C. A., and Yardley, B.W.D., 2008, Appendix A6: SILLS: a Matlab-based program for the reduction of Laser Ablation ICP–MS data of homogeneous materials and inclusions: *Short Course, Mineral. Association of Canada*, v. 40, p. 328–333.
- Halley, S.W., and Walshe, J.L., 1995, A re-examination of the Mount Bischoff cassiterite sulfide skarn, western Tasmania: *Economic Geology*, v. 90, p. 1676–1693.
- Halter, W.E., 1996, *Physiochemical controls of greisen formation and cassiterite deposition at the East Kemptville Tin deposit, Nova Scotia: PhD Thesis, McGill University*, 317pp.
- Halter, W.E., and Williams-Jones, A.E., 1999, Application of topaz muscovite F-OH exchange as a geothermometer: *Economic Geology*, v. 94, p. 1249–1258.
- Halter, W.E., Williams-Jones, A.E., and Kontak, D.J., 1996, The role of greisenization in cassiterite precipitation at the East Kemptville tin deposit, Nova Scotia: *Economic Geology*, v. 91, p. 368–385.

- Halter, W.E., Williams-Jones, A.E. and Kontak, D.J., 1998, Modeling fluid–rock interaction during greisenization at the East Kemptville tin deposit: implications for mineralization: *Chemical Geology*, v. 150, p. 1–17.
- Hanley, J.J., and Koga, K.T., 2018, Halogens in terrestrial and cosmic geochemical systems: abundances, geochemical behaviors, and analytical methods, in *The role of halogens in terrestrial and extraterrestrial geochemical processes*: Springer, Cham, p. 21–121.
- Hanus, D., 1982, The Colquiri tin deposit: a contribution to its genesis, in *Ore Genesis*: Springer, Berlin, Heidelberg, p. 308–318.
- Harlaux, M., Mercadier, J., Bonzi, W.M.E., Kremer, V., Marignac, C., and Cuney, M., 2017, Geochemical signature of magmatic-hydrothermal fluids exsolved from the Beauvoir rare-metal granite (Massif Central, France): Insights from LA-ICPMS analysis of primary fluid inclusions: *Geofluids*, 2017.
- Haynes, F.M., Sterner, S.M., and Bodnar, R.J., 1988, Synthetic fluid inclusions in natural quartz. IV. Chemical analyses of fluid inclusions by SEM/EDA: evaluation and method: *Geochimica et Cosmochimica Acta*, v. 52, p. 969–977.
- Hedenquist, J.W., and Lowenstern, J.B., 1994, The role of magmas in the formation of hydrothermal ore deposits: *Nature*, v. 370, p. 519–527.
- Heinrich, C.A., 1990, The chemistry of hydrothermal tin (-tungsten) ore deposition: *Economic Geology*, v. 85, p. 457–481.

- Heinrich, C.A., 1995, Geochemical evolution and hydrothermal mineral deposition in Sn (-W-base-metal) and other granite-related ore systems: Some conclusions from Australian examples: Short Course Handbook, Mineralogical Association of Canada, v. 23, p. 203–220.
- Heinrich, C.A., Ryan, C.G., Mernagh, T.P., and Eadington, P.J., 1992, Segregation of ore metals between magmatic brine and vapor; a fluid inclusion study using PIXE microanalysis: *Economic Geology*, v. 87, p. 1566–1583.
- Heinrich, C.A., Gunther, D., Audétat, A., Ulrich, T., and Frischknecht, R., 1999, Metal fractionation between magmatic brine and vapor, determined by microanalysis of fluid inclusions: *Geology*, v. 27, p. 755–758.
- Heinrich, C.A., Pettke, T., Halter, W.E., Aigner-Torres, M., Audétat, A., Günther, D., Hattendorf, B., Bleiner, D., Guillong, M. and Horn, I., 2003, Quantitative multi-element analysis of minerals, fluid and melt inclusions by laser-ablation inductively-coupled-plasma mass-spectrometry: *Geochimica et Cosmochimica Acta*, v. 67, p. 3473–3497.
- Henderson, I.H.C., and McCaig, A.M., 1996, Fluid pressure and salinity variations in shear zone-related veins, central Pyrenees, France: Implications for the fault-valve model. *Tectonophysics*, v. 262, p. 321–348.

- Hicks, R.J., Jamieson, R.A., and Reynolds, P.H., 1999, Detrital and metamorphic $^{40}\text{Ar}/^{39}\text{Ar}$ ages from muscovite and whole-rock samples, Meguma Supergroup, southern Nova Scotia: Canadian Journal of Earth Sciences, v. 36, p. 23–32.
- Hilchie, L., and Jamieson, R.A., 2008, Graphite thermometry in the Halifax contact aureole: Atlantic Geology, v. 44, p. 16–17.
- Hilchie, L.J., and Jamieson, R.A., 2014, Graphite thermometry in a low-pressure contact aureole, Halifax, Nova Scotia: Lithos, v. 208, p. 21–33.
- Holliger, P., and Cathelineau, M., 1988, In situ U-Pb age determination by secondary ion mass spectrometry: Chemical Geology, v. 70, 173pp.
- Horne, R.J., MacDonald, M.A., Corey, M.C., and Ham, L.J., 1992, Structure and emplacement of the South Mountain Batholith, southwestern Nova Scotia: Atlantic Geology, v. 28, p. 29–50.
- Horne, R.J., King, M.S., Kontak, D.J., O'Reilly, G.A., and Black, D., 2006, The Kemptville shear zone: Regional shear related to emplacement and mineralization, in MacDonald, D.R., ed., Mines and Minerals Branch Report of Activities 2005: Nova Scotia Department of Natural Resources, Report 2006-1, p. 19–37.
- Irber, W., 1999. The lanthanide tetrad effect and its correlation with K/Rb, Eu/Eu*, Sr/Eu, Y/Ho, and Zr/Hf of evolving peraluminous granite suites: Geochimica et Cosmochimica Acta, v. 63, p. 489–508.

- Iveson, A.A., Webster, J.D., Rowe, M.C., and Neill, O.K., 2019, Fluid-melt trace-element partitioning behaviour between evolved melts and aqueous fluids: Experimental constraints on the magmatic-hydrothermal transport of metals: *Chemical Geology*, v. 516, p. 18–41.
- Jackson, N.J., Willis-Richards, J., Manning, M., and Satns, M., 1989, Evolution of the Cornubian ore field: Part II. Ore deposits and mineralizing processes: *Economic Geology*, v. 84, p. 1101–1133.
- Kelly, J.L., Fu, B., Kita, N.T., and Valley, J.W., 2007, Optically continuous silcrete quartz cements of the St. Peter Sandstone: High precision oxygen isotope analysis by ion microprobe: *Geochimica et Cosmochimica Acta*, v. 71, p. 3812–3832.
- Kelly, W.C., and Rye, R.O., 1979, Geologic, fluid inclusion and stable isotope studies of the tin–tungsten deposits of Panasqueira, Portugal: *Economic Geology*, 74, p. 1721–1822.
- Kelly, W.C., and Turneure, F.S., 1970, Mineralogy, paragenesis and geothermometry of the tin and tungsten deposits of the Eastern Andes, Bolivia: *Economic Geology*, v. 65, p. 609–680.
- Keppie, J.D., and Dallmeyer, R.D., 1987, Dating transcurrent terrane accretion: an example from the Meguma and Avalon composite terranes in the northern Appalachians: *Tectonics*, v. 6, p. 831–847.

- Kerr, M.J., Hanley, J.J., Kontak, D.J., Morrison, G.G., Petrus, J., and Fayek, M., 2018, Evidence of upgrading of gold tenor in an orogenic quartz-carbonate vein system by late magmatic-hydrothermal fluids at the Madrid Deposit, Hope Bay Greenstone Belt, Nunavut, Canada: *Geochimica et Cosmochimica Acta*, v. 241, p. 180–218.
- Kesler, S.E., and Wilkinson, B.H., 2015, Tectonic-diffusion estimates of global mineral resources: extending the method: granitic tin deposits: Geological Society, London, Special Publications, v. 393, p. 277–290.
- Klemm, L.M., Pettke, T., Heinrich, C.A. and Campos, E., 2007, Hydrothermal evolution of the El Teniente deposit, Chile: Porphyry Cu-Mo ore deposition from low-salinity magmatic fluids: *Economic Geology*, v. 102, p. 1021–1045.
- Kobayashi, S., Kado, S., Oishi, T., Ohshima, S., Kagawa, T., Nagae, Y., Yamamoto, S., Mizuuchi, T., Nagasaki, K., Okada, H. and Minami, T., 2012, Density fluctuation measurements using beam emission spectroscopy on Heliotron J: *Review of Scientific Instruments*, v. 83, p.10D535.
- Kontak, D.J., 1990a, A sulfur isotopic study of main-stage tin and base-metal mineralization at the East Kemptville tin deposit, Yarmouth County, Nova Scotia, Canada: evidence for magmatic origin of metals and sulfur: *Economic Geology*, v. 85, p. 399–407.

Kontak, D.J., 1990b, The East Kemptville topaz-muscovite leucogranite, Nova Scotia. I.

Geological setting and whole rock geochemistry: *Canadian Mineralogist*, v. 28, p. 787–825.

Kontak, D.J., 1993, Geological, geochemical and isotopic studies of the East Kemptville Sn-(Zn-

Cu-Ag) deposit, Yarmouth County, Nova Scotia, Canada: Proceedings of the Eighth Quadrennial IAGOD Symposium E. Schweizerbart'sche Verlagsbuchhandlung, Stuttgart, Germany, p. 383–409.

Kontak, D.J., 1994, Geological and geochemical studies of alteration processes in a fluorine-rich

environment: The East Kemptville Sn-(Zn-Cu-Ag) deposit, Yarmouth County, Nova Scotia, Canada, in Lentz, D.R., ed., *Alteration and Alteration Processes associated with Ore-forming Systems: Geological Association of Canada, Short Course Notes*, v. 11, p. 261–314.

Kontak, D.J., 2004, Analysis of evaporate mounds as a complement to fluid-inclusion

thermometric data: Case studies from granitic environments in Nova Scotia and Peru: *The Canadian Mineralogist*, v. 42, p. 1315–1329.

Kontak, D.J., and Cormier, R.F., 1991, Geochronological evidence for multiple tectono-thermal

overprinting events in the East Kemptville muscovite-topaz leucogranite, Yarmouth County, Nova Scotia, Canada: *Canadian Journal of Earth Science*, v. 28, p. 209–224.

- Kontak, D.J., and Chatterjee, A.K., 1992, The East Kemptville tin deposit, Yarmouth County, Nova Scotia. A Pb isotope study of the leucogranite and mineralized greisens: Evidence for a 366 Ma metallogenic event: *Canadian Journal of Earth Sciences*, v. 29, p. 1180–1196.
- Kontak, D.J., and Clark, A.H., 2002, Genesis of the giant, bonanza San Rafael lode tin deposit, Peru: origin and significance of pervasive alteration: *Economic Geology*, v. 97, p. 1741–1777.
- Kontak, D.J., and Kerrich, R., 1995, Geological and geochemical studies of a metaturbidite hosted lode gold deposit: The Beaver Dam deposit, Nova Scotia: II: Isotopic Studies: *Economic Geology*, v. 90, p. 885–901.
- Kontak, D.J., and Kyser, T.K., 2001, Preliminary fluid inclusion and oxygen isotope studies of the Flintstone Rock (NTS 21N04) silica-clay deposit, Yarmouth County, Nova Scotia, in MacDonald, D.R., ed., *Minerals and Energy Branch, Report of Activities: Nova Scotia Department of Natural Resources 2000, Report ME 2001-1*, p. 37-48.
- Kontak, D.J., and Kyser, T.K., 2011, Fingerprinting multiple fluid reservoirs in a 380 Ma Intrusion-Related Gold (IRG) setting, Nova Scotia, Canada: Implications for the nature and origin of IRG deposits, *Mineralium Deposita*, v. 46, p. 337–363.
- Kontak, D.J., Strong, D.F., and Kerrich, R., 1988, Crystal-melt±fluid phase equilibria versus late-stage fluid-rock interaction in granitoid rocks of the South Mountain Batholith, Nova

- Scotia: whole rock geochemistry and oxygen isotope evidence: *Atlantic Geology*, v. 24, p. 97–110.
- Kontak, D.J., Kerrich, R., and Strong, D.F., 1991, The role of fluids in the late-stage evolution of the South Mountain Batholith, Nova Scotia: further geochemical and oxygen isotopic studies: *Atlantic Geology*, v. 27, p. 29–47.
- Kontak, D.J., Farrar, E., McBride, S.M., and Martin, R.F., 1995, Mineral chemistry and $^{40}\text{Ar}/^{39}\text{Ar}$ dating of muscovite from the East Kemptville leucogranite, southern Nova Scotia: evidence for localised resetting of $^{40}\text{Ar}/^{39}\text{Ar}$ systematics in a shear zone: *Canadian Mineralogist*, v. 33, p. 1237–1253.
- Kontak, D.J., Home, R.J., Sandeman, H., Archibald, D., and Lee, K.W., 1998, $^{40}\text{Ar}/^{39}\text{Ar}$ dating of ribbon-textured veins and wall-rock material from Meguma lode gold deposits, Nova Scotia: implications for timing and duration of vein formation in slate-belt hosted vein gold deposits: *Canadian Journal of Earth Sciences*, v. 35, p. 746-761.
- Kontak, D.J., Ansdell, K., and Archibald, D.A., 1999, New constraints on the age and origin of the Dunbrack Pb-Cu-Zn-Ag deposit, Musquodoboit Batholith, southern Nova Scotia: *Atlantic Geology*, v. 35, p. 19-42.
- Kontak, D.J., Dostal, J., Ansdell, K., Halter, W., Martin, R.F., and Williams-Jones, A.E., 2001, The nature and origin of pegmatite in a fluorine-rich leucogranite, East Kemptville, Nova

- Scotia: Transactions of the Royal Society of Edinburgh: Earth Sciences, v. 92, p. 173–200.
- Kontak, D.J., Ham. L.J., and Dunning, G., 2004, U/Pb dating of the Musquodoboit Batholith, southern Nova Scotia: evidence for a protracted magmatic-hydrothermal event in a Devonian intrusion: *Atlantic Geology*, v. 40, p. 207–216.
- Kontak, D.J. and Tuba, G., 2017, How can fluid inclusion studies better constrain orogenic gold deposit models: case studies from the Superior Province and Meguma terrane, Canada [ext. abs.]: Society for Geology Applied to Mineral Deposits (SGA) Biennial Meeting, 14th, Quebec City, Canada, Extended Abstracts, p. 55–58.
- Korges, M., Weis, P., Lüders, V., and Laurent, O., 2018, Depressurization and boiling of a single magmatic fluid as a mechanism for tin-tungsten deposit formation: *Geology*, v. 46, p.75–78.
- Kreulen, R., 1987, Thermodynamic calculations of the C–O–H system applied to fluid inclusions: Are fluid inclusions unbiased samples of ancient fluids?: *Chemical Geology*, v. 61, p. 59–64.
- Krylov, D.P., Zagnitko, V.N., Hoernes, S., Lugovaja, I.P., and Hoffbauer, R., 2002, Oxygen isotope fractionation between zircon and water: experimental determination and comparison with quartz-zircon calibrations: *European Journal of Mineralogy*, v. 14, p. 849–853.

- Landtwing, M.R., Pettke, T., Halter, W.E., Heinrich, C.A., Redmond, P.B., Einaudi, M.T., and Kunze, K., 2005, Copper deposition during quartz dissolution by cooling magmatic–hydrothermal fluids: the Bingham porphyry: *Earth and Planetary Science Letters*, v. 235, p. 229–243.
- Lecumberri-Sanchez, P., Steele-MacInnis, M., and Bodnar, R.J. 2015. Synthetic fluid inclusions XIX. Experimental determination of the vapor-saturated liquidus of the system H₂O–NaCl–FeCl₂: *Geochimica et Cosmochimica Acta*, v. 148, p. 34–49.
- Lehmann, B., 2020, Formation of tin ore deposits: A reassessment: *Lithos*, 105756.
- London D., Morgan G.B.VI, and Hervig, R.L., 1989, Vapor-undersaturated experiments in the system macusanite-H₂O at 200 MPa, and the internal differentiation of granitic pegmatites: *Contributions to Mineralogy and Petrology*, v. 102, p. 1–17.
- London, D., Morgan, G.B., VI, Babb, H.A., and Loomis, J.L., 1993, Behavior and effects of phosphorus in the system Na₂O–K₂O–Al₂O₃–SiO₂–P₂O₅–H₂O at 200 MPa (H₂O): *Contrib. Mineral. Petrol.*, v. 113, p. 450–465.
- London, D., Wolf, M.B., Morgan, G.B., and Garrido, M.G., 1999, Experimental silicate–phosphate equilibria in peraluminous granitic magmas, with a case study of the Albuquerque batholith at Tres Arroyos, Badajoz, Spain: *Journal of Petrology*, v. 40, p. 215–240.

- Longstaffe, F.J., Smith, T.E., and Muehlenbachs, K., 1980, Oxygen isotope evidence for the genesis of Upper Paleozoic granitoids from southwestern Nova Scotia: *Canadian Journal of Earth Sciences*, v. 17, p. 132–141.
- MacDonald, M.A., Horne, R.J., Corey, M.C., and Ham, L.J., 1992, An overview of recent bedrock mapping and follow-up petrological studies of the South Mountain batholith, southwestern Nova Scotia, Canada: *Atlantic Geology*, v. 28, p. 7–28.
- MacDonald, M.A., 2001, *Geology of the South Mountain Batholith, southwestern Nova Scotia*. Nova Scotia Department of Natural Resources, Open File Report ME2001-2.
- MacLean, N. J., Barr, S. M., White, C. E., and Ketchum, J. W. F., 2004. New U-Pb (zircon) age and geochemistry of the Wedgeport pluton, Meguma terrane, Nova Scotia: *Atlantic Geology*, v. 39, p. 239–253.
- Manning, D.A.C., and Pichavant, M., 1983, The role of fluorine and boron in the generation of granitic melts [ext. abs.]: High grade metamorphism, migmatites and melting: Meeting of the Geochemical Group of the Mineralogical Society, Extended Abstracts, p. 94–109.
- Martel, A.T., McGregor, D.C., and Utting, J., 1993, Stratigraphic significance of Upper Devonian and Lower Carboniferous miospores from the type area of the Horton Group, Nova Scotia: *Canadian Journal of Earth Sciences*, v. 30, p. 1091–1098.

- Matsuhisa, Y., Goldsmith, J. R., and Clayton, R.N., 1979, Oxygen isotopic fractionation in the system quartz-albite-anorthite-water: *Geochimica et Cosmochimica Acta*, v. 43, p. 1131–1140.
- McDivitt, J.A., Kontak, D.J., Lafrance, B., Petrus, J.A., and Fayek, M., 2021, A trace metal, stable isotope (H, O, S), and geochronological (U-Pb titanite) characterization of hybridized gold orebodies in the Missanabie-Renabie district, Wawa subprovince (Canada): *Mineralium Deposita*, v. 56, p. 1-22.
- Micklethwaite, S., Sheldon, H. A., and Baker, T., 2010, Active fault and shear processes and their implications for mineral deposit formation and discovery: *Journal of Structural Geology*, v. 32, p. 151–165.
- Monecke, T., Monecke, J., Reynolds, T.J., Tsuruoka, S., Bennett, M.M., Skewes, W.B. and Palin, R.M., 2018, Quartz solubility in the H₂O-NaCl system: A framework for understanding vein formation in porphyry copper deposits: *Economic Geology*, v. 113, p. 1007–1046.
- Morales, M.J., e Silva, R.C.F., Lobato, L.M., Gomes, S.D., Gomes, C.C. and Banks, D.A., 2016, Metal source and fluid–rock interaction in the Archean BIF-hosted Lamego gold mineralization: Microthermometric and LA-ICP-MS analyses of fluid inclusions in quartz veins, Rio das Velhas greenstone belt, Brazil: *Ore Geology Reviews*, v. 72, p. 510–531.

- Morgan, G.B., VI, and London, D., 1999, Crystallization of the Little Three layered pegmatite-aplite dike, Ramona district, California: *Contributions to Mineralogy and Petrology* , v. 136, p. 310–330.
- Muecke, G.K., Elias, P., and Reynolds, P. H., 1988, Hercynian/Alleghanian overprinting of an Acadian terrane: $^{40}\text{Ar}/^{39}\text{Ar}$ studies in the Meguma zone, Nova Scotia, Canada: *Chemical Geology (Isotope Geoscience Section)*, v. 73, p. 153–167.
- Müller, B., Frischknecht, R., Seward, T. M., Heinrich, C. A., and Camargo Gallegos, W., 2001, A fluid inclusion reconnaissance study of the Huanuni tin deposit (Bolivia), using LA-ICP-MS micro-analysis: *Mineralium Deposita*, v. 36, p. 680–688.
- Murphy, J.B., 2000, Tectonic influence on sedimentation along the southern flank of the late Paleozoic Magdalen basin in the Canadian Appalachians: Geochemical and isotopic constraints on the Horton Group in the St. Marys basin, Nova Scotia: *Geological Society of America Bulletin*, v. 112, p. 997–1011.
- O'Neil, J.R., and Taylor, H.P.Jr., 1967. The oxygen isotope and cation exchange chemistry of feldspars: *American Mineralogist*, v. 52, p. 1414–1437.
- Ohmoto, H., Rye, R.O., 1979, Isotopes of sulfur and carbon, in, Barnes, H.L., ed., *Geochemistry of Hydrothermal Ore Deposits*: Wiley, New York, p. 509–567.

- Partington, G.A., McNaughton, N.J., and Williams, I.S., 1995, A review of the geology, mineralization, and geochronology of the Greenbushes pegmatite, Western Australia: *Economic Geology*, v. 90, p. 616-635.
- Pécher, A., 1981, Experimental decrepitation and reequilibration of fluid inclusions in synthetic quartz: *Tectonophysics*, v. 78, p. 567–584.
- Pécher, A., 1989, The metamorphism in the central Himalaya: *Journal of Metamorphic Geology*, v. 7, p. 31–41.
- Pettke, T., 2006, In-situ Laser-Ablation-ICP-MS chemical analysis of melt inclusion and prospects for constraining subduction zone magmas, in Webster, J.D., ed., *Melt inclusions in plutonic rocks: Mineralogical Association of Canada, Montreal, Short Course Series*, v. 36, p. 51–80.
- Pollard, P.J., and Taylor, R.G., 1986, Progressive evolution of alteration and tin mineralization; controls by interstitial permeability and fracture-related tapping of magmatic fluid reservoirs in tin granites: *Economic Geology*, v. 81, p. 1795–1800.
- Poulson, S.R., Kubilius, W.P., and Ohmoto, H., 1991, Geochemical behavior of sulfur in granitoids during intrusion of the South Mountain Batholith, Nova Scotia, Canada: *Geochimica et Cosmochimica Acta*, v. 55, p. 3809–3830.

- Raeside, R.P. and Mahoney, K.M., 1996, The contact metamorphic aureole of the South Mountain Batholith, southern Nova Scotia [ext. abs.]: Geological Association of Canada – Mineralogical Association of Canada, Program Abstracts, 21.
- Redmond, P.B., Einaudi, M.T., Inan, E.E., Landtwing, M.R. and Heinrich, C.A., 2004, Copper deposition by fluid cooling in intrusion-centered systems: New insights from the Bingham porphyry ore deposit, Utah: *Geology*, v. 32, p. 217–220.
- Reynolds, P.H., Elias, P., Muecke, G.K., and Grist, A.M., 1987, Thermal history of the southwestern Meguma Zone, Nova Scotia, from an $^{40}\text{Ar}/^{39}\text{Ar}$ and fission track dating study of intrusive rocks: *Canadian Journal of Earth Sciences*, v. 24, p. 1952–1965.
- Richards, J.P., 2011, High Sr/Y arc magmas and porphyry Cu±Mo±Au deposits: just add water: *Economic Geology*, v. 106, p. 1075–1081.
- Richards, J.P., 2018, A shake-up in the porphyry world?: *Economic Geology*, v. 113, p. 1225–1233.
- Richardson, J.M., Spooner, E.T.C., and McAuslan, D.A., 1982, the East Kemptville tin deposit. Nova Scotia; An example of large tonnage, low grade greisen-hosted tin mineralization: *Canada Geological Survey Paper 82-IB*, p. 27–32.
- Richardson, J.M., Blenkinsop, J., and Bell, K., 1988. Extreme variations (0.729-0.828) in initial $^{87}\text{Sr}/^{86}\text{Sr}$ ratios in magmato-hydrothermal fluids derived from the East Kemptville greisen tin deposit, Nova Scotia, Canada: *Chemical Geology*, v. 70, p. 136.

- Richardson, J. M Bell, K., Blenkinsop, J., and Watkinson, D.H., 1989, Geochemical distinctions between the Carboniferous tin-bearing Davis Lake complex and the Devonian South Mountain batholith, Meguma Terrane, N.S., Canada: *Canadian Journal of Earth Sciences*, v. 26, p. 2044–2061.
- Richardson, J. M., Bell, K., Watkinson, D. H., and Blenkinsop, J., 1990, Genesis and fluid evolution of the East Kemptville greisen hosted tin mine, southwestern Nova Scotia, Canada, in Stein, H.J., and Hannah, J.L., eds., *Ore-bearing Granite Systems; Petrogenesis and Mineralizing Processes: Geological Society of American Special Paper 246*, p. 181–203.
- Rickers, K., Thomas, R. and Heinrich, W., 2006, The behavior of trace elements during the chemical evolution of the H₂O-, B-, and F-rich granite–pegmatite–hydrothermal system at Ehrenfriedersdorf, Germany: a SXRF study of melt and fluid inclusions: *Mineralium Deposita*, v. 41, p. 229–245.
- Rijks, H.R.P., and Van Der Veen, A.H., 1972, The geology of the tin-bearing pegmatites in the eastern part of the Kamativi district, Rhodesia: *Mineralium Deposita*, v. 7, p. 383–395.
- Roedder, E., 1984. Fluid inclusions: *Mineralogical Society of America. Reviews in Mineralogy*, v. 12, 644p.

- Rosso, K.M., and Bodnar, R.J., 1995, Microthermometric and Raman spectroscopic detection limits of CO₂ in fluid inclusions and the Raman spectroscopic characterization of CO₂: *Geochimica et Cosmochimica Acta*, v. 59, p. 3961–3975.
- Rusk, B.G., Reed, M.H., Dilles, J.H., Klemm, L.M. and Heinrich, C.A., 2004, Compositions of magmatic hydrothermal fluids determined by LA-ICP-MS of fluid inclusions from the porphyry copper–molybdenum deposit at Butte, MT: *Chemical Geology*, v. 210, p. 173–199.
- Samson, I.M., 1990, Fluid evolution and mineralization in a subvolcanic granite stock; the Mount Pleasant W-Mo-Sn deposits, New Brunswick, Canada: *Economic Geology*, v. 85, p. 145–163.
- Schmidt, C., 2018, Formation of hydrothermal tin deposits: Raman spectroscopic evidence for an important role of aqueous Sn (IV) species: *Geochimica et Cosmochimica Acta*, v. 220, p. 499–511.
- Schwartz, M.O., and Surjono, 1990, Greisenization and albitization at the Tikus tin-tungsten deposit, Belitung, Indonesia: *Economic Geology*, v. 85, p. 691–713.
- Seedorff, E., Barton, M.D., Stavast, W.J., and Maher, D.J., 2008, Root zones of porphyry systems: Extending the porphyry model to depth: *Economic Geology*, v. 103, p. 939–956.

- Seward, T.M., and Barnes, H.L., 1997, Metal transport by hydrothermal ore fluids, in Barnes, H.L., ed., *Geochemistry of hydrothermal ore deposits*, 3rd ed.: New York, Wiley, p. 435–486.
- Sillitoe, R.H., 1985, Ore breccias in volcanoplutonic arcs: *Economic Geology*, v. 80, p. 1467–1514.
- Sheppard, S.M., 1986, Characterization and isotopic variations in natural waters, in Valley, J.W., Taylor, H.P., and O’Neil, eds., *Stable isotopes in high temperature geological processes: Reviews in Mineralogy*, v. 16, p. 165–184.
- Sheppard, S.M.F., 1994, Stable Isotope and Fluid Inclusion Evidence for the Origin and Evolution of Hercynian Mineralizing Fluids, in Seltmann, R., Kampf, H., and Moller, P., eds., *Metallogeny of Collisional Orogens: Proc. IAGOD Erzgebirge Meeting*, Geyer, June 4–6, 1993, Czech Geological Survey, Prague, p. 49–60.
- Sibson, R. H., 1990, Conditions for fault-valve behaviour, in Knipe, R.J., and Rutter, E.H., eds., *Deformation Mechanisms, Rheology and Tectonics: Geological Society, London, Special Publications*, v. 54, p. 15–28.
- Sibson, R.H., 1992, Implications of fault-valve behaviour for rupture nucleation and recurrence: *Tectonophysics*, v. 211, p. 283–293.

- Sibson, R. H., 1994, Crustal stress, faulting and fluid flow, in Parnell, J., ed., *Geofluids: Origin, Migration and Evolution of Fluids in Sedimentary Basins: Geological Society Special Publication*, v. 78, p. 69–84.
- Sibson, R.H., Robert, F., and Poulsen, K.H., 1988, High-angle reverse faults, fluid pressure cycling and mesothermal gold-quartz deposits: *Geology*, v. 16, p. 551–555.
- Sirbescu, M.L.C., and Nabelek, P.I., 2003, Crustal melts below 400 C: *Geology*, v. 31, p. 685–688.
- Soloviev, S.G., Kryazhev, S.G., and Dvurechenskaya, S.S., 2017, *Geology, mineralization, stable isotope, and fluid inclusion characteristics of the Vostok-2 reduced W-Cu skarn and Au-W-Bi-As stockwork deposit, Sikhote-Alin, Russia: Ore Geology Reviews*, v. 86, p. 338–365.
- Steele-MacInnis, M., 2018, Fluid inclusions in the system H₂O-NaCl-CO₂: An algorithm to determine composition, density and isochore: *Chemical Geology*, v. 498, p. 31–44.
- Steele-MacInnis, M., Lecumberri-Sanchez, P., and Bodnar, R. J., 2012, HOKIEFLINCS-H₂O-NACL: A Microsoft Excel spreadsheet for interpreting microthermometric data from fluid inclusions based on the PVTX properties of H₂O-NaCl: *Comput. Geosci.*, v. 49, p. 334–337.

- Steele-MacInnis, M., Ridley, J., Lecumberri-Sanchez, P., Schlegel, T.U. and Heinrich, C.A., 2016, Application of low-temperature microthermometric data for interpreting multicomponent fluid inclusion compositions: *Earth-Science Reviews*, v. 159, p. 14–35.
- Sterner, S.M., Bodnar, R.J., 1989, Synthetic fluid inclusions—VII. Re-equilibration of fluid inclusions in quartz during laboratory-simulated metamorphic burial and uplift: *Journal of Metamorphic Geology*, v. 7, p. 243–260.
- Strong, D. F., 1981, Ore deposit models — 5. A model for granophile mineral deposits. - *Geoscience Canada*, 8, 155–161.
- Sugaki, A., 1985, Geological study on the ore deposits in the La Paz district, Bolivia. *Sci. Rept. Tohoku Univ., Ser. III*, v. 16, p. 131–198.
- Sun, S., and Eadington, P.J., 1987, Oxygen isotope evidence for the mixing of magmatic and meteoric waters during tin mineralization in the Mole Granite, New South Wales, Australia: *Economic Geology*, v. 82, p. 43–52
- Sun, M., Monecke, T., Reynolds, T.J., and Yang, Z., 2020, Understanding the evolution of magmatic-hydrothermal systems based on microtextural relationships, fluid inclusion petrography, and quartz solubility constraints: insights into the formation of the Yulong Cu-Mo porphyry deposit, eastern Tibetan Plateau, China: *Mineralium Deposita*, p. 1–20.
- Taylor Jr, H.P., 1978, Oxygen and hydrogen isotope studies of plutonic granitic rocks. *Earth and Planetary Science Letters*, v. 38, p. 177–210.

- Taylor, R.D., Monecke, T., Reynolds, T.J. and Monecke, J., 2021, Paragenesis of an Orogenic Gold Deposit: New Insights on Mineralizing Processes at the Grass Valley District, California: *Economic Geology*, v. 116, p. 323–356.
- Taylor, R.G., 1979, *Geology of Tin Deposits*: Elsevier, Amsterdam, 543pp.
- Thomas, R., Webster, J.D. and Heinrich, W., 2000, Melt inclusions in pegmatite quartz: complete miscibility between silicate melts and hydrous fluids at low pressure: *Contributions to Mineralogy and Petrology*, v. 139, p. 394–401.
- Thomas, R., Förster, H. J., and Heinrich, W., 2003, The behaviour of boron in a peraluminous granite-pegmatite system and associated hydrothermal solutions: a melt and fluid-inclusion study: *Contributions to Mineralogy and Petrology*, v. 144, p. 457–472.
- Tsuruoka, S., Monecke, T. and Reynolds, T.J., 2021. Evolution of the Magmatic-Hydrothermal System at the Santa Rita Porphyry Cu Deposit, New Mexico, USA: Importance of Intermediate-Density Fluids in Ore Formation. *Economic Geology*, in press.
- Tuba, G., Kontak, D.J., Zajacz, Z. and Petrus, J.A., 2019, Bulk microanalysis of assemblages of small fluid inclusions by LA-ICP-MS: Methodology and application to orogenic gold systems: *Chemical Geology*, v. 529, p.119-326.
- Tuttle, O.F., and Bowen, N.L., 1958, *Origin of Granite in the Light of Experimental Studies in the System: NaAlSi₃O₈ (No. 74)*: Geological Society of America.

- Tweedale, F.M., 2019, Bulk Compositional Analysis of Quartz-hosted Fluid Inclusions from the South Mountain Batholith, Nova Scotia. MSc Thesis, Saint Mary's University, 279pp.
- Tweedale, F., Hanley, J., Kontak, D.J., Rogers, N., 2014, Using evaporate mound chemistry of fluid inclusions to assess the metal fertility and fluid:rock interaction in a large peraluminous batholith: A case study of the mineralized (Sn-W-U-Cu-Zn-Ag) South Mountain Batholith, Nova Scotia [ext. abs.]: 12th Pan-American Current Research on Fluid Inclusions Conference, Denver. CO, Canada Program with Abstracts, p. 54–55.
- Ulrich, T., Günther, D. and Heinrich, C.A., 1999, Gold concentrations of magmatic brines and the metal budget of porphyry copper deposits: *Nature*, v. 399, p. 676–679.
- Ulrich, T., Günther, D., and Heinrich, C.A., 2002, The evolution of a porphyry Cu-Au deposit, based on LA-ICP-MS analysis of fluid inclusions: Bajo de la Alumbrera, Argentina: *Economic Geology*, v. 97, p. 1889–1920.
- van Staal, C.R., 2007, Pre-Carboniferous tectonic evolution and metallogeny of the Canadian Appalachians, in Goodfellow, W.D., ed., *Mineral Deposits of Canada: Geological Association of Canada Special Publication*, v. 5, p. 793–818.
- Vityk, M.O., Bodnar, R.J., 1995, Textural evolution of synthetic fluid inclusions in quartz during reequilibration, with applications to tectonic reconstruction: *Contributions to Mineralogy and Petrology*, v. 121, p. 309–323.

- Vityk, M.O., Bodnar, R.J., Schmidt, C.S., 1994, Fluid inclusions as tectonothermobarometers: relation between pressure-temperature history and reequilibration morphology during crustal thickening: *Geology*, v. 22, pp. 731–734.
- Wagner, T., Mlynarczyk, M.S., Williams-Jones, A.E. and Boyce, A.J., 2009, Stable isotope constraints on ore formation at the San Rafael tin-copper deposit, Southeast Peru: *Economic Geology*, v. 104, p. 223–248.
- Wang X., Chou I. M., Hu W., Burruss R. C., Sun Q., and Song Y., 2011, Raman spectroscopic measurements of CO₂ density: Experimental calibration with high-pressure optical cell (HPOC) and fused silica capillary capsule (FSCC) with application to fluid inclusion observations: *Geochimica et Cosmochimica Acta*, v. 75, p. 4080–4093.
- Webster, J.D., 1997, Chloride Solubility in Felsic Melts and the Role of Chloride in Magmatic Degassing: *Journal of Petrology*, v. 38, p. 1793–1807.
- Webster, J.D., 2004, The exsolution of magmatic hydrosaline chloride liquids: *Chemical Geology*, v. 210, p. 33–48.
- Webster, J.D., and Holloway, J.R., 1990, Partitioning of F and Cl between magmatic—hydrothermal fluids and highly evolved granitic magmas. *Ore-Bearing Granite Systems: Petrogenesis and Mineralizing Processes: Geological Society of America Special Paper* 246, 21p.

- Webster, J.D. and Rebbert, C.R., 1998, Experimental investigation of H₂O and Cl⁻ solubilities in F-enriched silicate liquids; implications for volatile saturation of topaz rhyolite magmas: *Contributions to Mineralogy and Petrology*, v. 132, p. 198–207.
- Webster, J.D., Iveson, A.A., Rowe, M.C., and Webster, P.M., 2020, Chlorine and felsic magma evolution: Modeling the behavior of an under-appreciated volatile component: *Geochimica et Cosmochimica Acta*, v. 271, p. 248–288.
- Weis, P., 2015, The dynamic interplay between saline fluid flow and rock permeability in magmatic-hydrothermal systems: *Geofluids*, v. 15, p. 350–371.
- White, C.E., 2010, Stratigraphy of the Lower Paleozoic Goldenville and Halifax groups in southwestern Nova Scotia: *Atlantic Geology*, v. 46, p. 136–154.
- White, C. E., and Barr, S. M., 2010, Lithochemistry of the Lower Paleozoic Goldenville and Halifax groups, southwestern Nova Scotia, Canada: Implications for stratigraphy, provenance, and tectonic setting of the Meguma terrane, in Tollo, R.P., Bartholomew, M.J., Hibbard, J.P., and Karabinos, P.M., eds., *From Rodinia to Pangea: The Lithotectonic Record of the Appalachian Region: Geological Society of America Memoir* 206, p. 347–366.
- Wilkinson, J.J., 2001, Fluid inclusions in hydrothermal ore deposits, *Lithos*, v. 55, p. 229–272.

- Williams-Jones, A.E. and Heinrich, C.A., 2005, 100th Anniversary special paper: vapor transport of metals and the formation of magmatic-hydrothermal ore deposits: *Economic Geology*, v. 100, p. 1287–1312.
- Willson, J., 2019, Character and genesis of Indium mineralization, East Kemptville, Nova Scotia. MSc Thesis, University of Windsor, 111pp.
- Wopenka, B. and Pasteris, J., 1986, Limitations to Quantitative Analysis of Fluid Inclusions in Geological Samples by Laser Raman Microprobe Spectroscopy: *Applied Spectroscopy*, v. 40, p. 144–151.
- Wopenka, B., and J. Pasteris, J., 1987, Raman intensities and detection limits of geochemically relevant gas mixtures for a laser Raman microprobe: *Analytical Chemistry*, v. 59, p. 2165–2170.
- Wright, J. H. and Kwak, T.A.P., 1989, Tin-bearing greisens of mount Bischoff, northwestern Tasmania, Australia. *Economic Geology*, v. 84, p. 551–574.
- Yamamoto, J., and Kagi, H., 2006, Extended micro-Raman densimeter for CO₂ applicable to mantle-originated fluid inclusions: *Chemistry Letters*, v. 35, p. 610–611.
- Yamamoto, J., Kagi, H., Kaneoka, I., Lai, Y., Prikhod'ko, V. S., and Arai, S., 2002, Fossil pressures of fluid inclusions in mantle xenoliths exhibiting rheology of mantle minerals: implications for the geobarometry of mantle minerals using micro-Raman spectroscopy: *Earth and Planetary Science Letters*, v. 198, p. 511–519.

- Zajacz, Z., Hanley, J.J., Heinrich, C.A., Halter, W.E., and Guillong, M., 2009, Diffusive reequilibration of quartz-hosted silicate melt and fluid inclusions: Are all metal concentrations unmodified?: *Geochimica et Cosmochimica Acta*, v. 73, p. 3013–3027.
- Zoheir, B., Steele-MacInnis, M. and Garbe-Schönberg, D., 2019, Orogenic gold formation in an evolving, decompressing hydrothermal system: Genesis of the Samut gold deposit, Eastern Desert, Egypt: *Ore Geology Reviews*, v. 105, p. 236–257.
- Zhao, Z.F., and Zheng, Y.F., 2003, Calculation of oxygen isotope fractionation in magmatic rocks, *Chemical Geology*, v. 193, p. 59–80.
- Zheng, Y.F., 1993, Calculation of oxygen isotope fractionation in hydroxyl-bearing silicates. *Earth and Planetary Science Letters*, v. 120, p. 247–263.

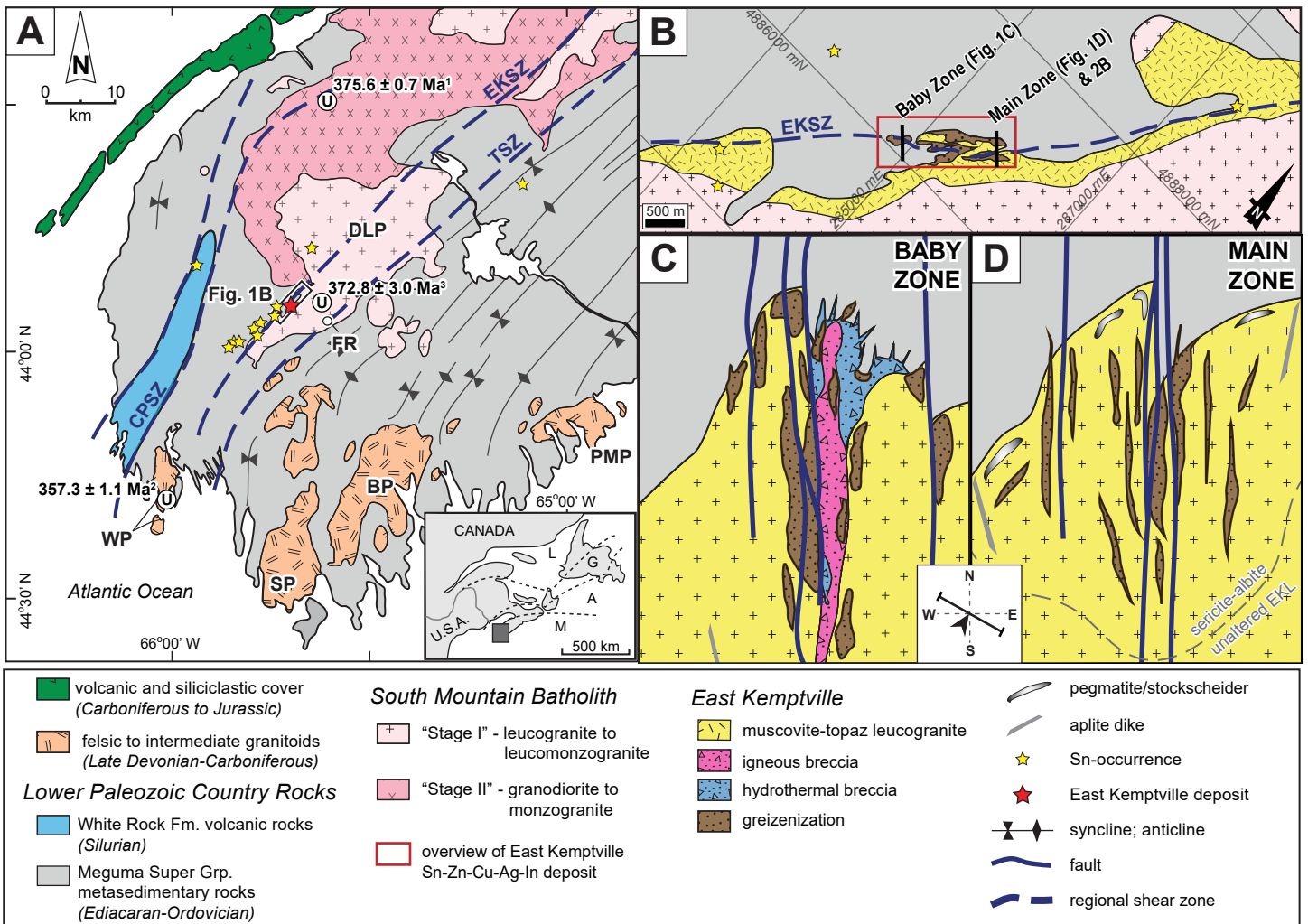


Figure 4-1

Figure 4–1. (A) Regional geology of SW Nova Scotia, Canada (modified after MacDonald et al., 1992; White, 2010) showing the location of the East Kemptville deposit, hosted a muscovite-topaz leucogranite (Fig. 4–1B) in the western part of the Davis Lake pluton (DLP), which is dominantly a biotite monzogranite and part of the composite South Mountain Batholith. U-Pb (zircon) ages displayed (1 – Bickerton et al., submitted; 2 – MacLean et al., 2004; 3 – Bickerton et al., 2018) and regional shear zones are outlined (CPSZ – Chebogue Point shear zone, White and Barr 2010; EKSZ – East Kemptville shear zone, Horne et al. 2006; TSZ – Tobeatic shear zone, Giles 1985). WP – Wedgeport Pluton; SP – Shelburne Pluton; BP – Barrington Passage Pluton; PMP – Port Mouton Pluton; FR – Flintstone Rock Silica-Clay deposit. Note the Sn mineralization occurrences in this part of the SMB. (B) Plan view of the East Kemptville deposit area showing the extent of the F-rich EKL and EKSZ-hosted deposit. (C & D) Schematic cross-sections of the two main ore zones in the East Kemptville deposit which show markedly different lithological characteristics, the southwestern Baby zone and the northeastern Main zone. Note the presence of the magmatic and hydrothermal breccia bodies that are restricted to the Baby zone.

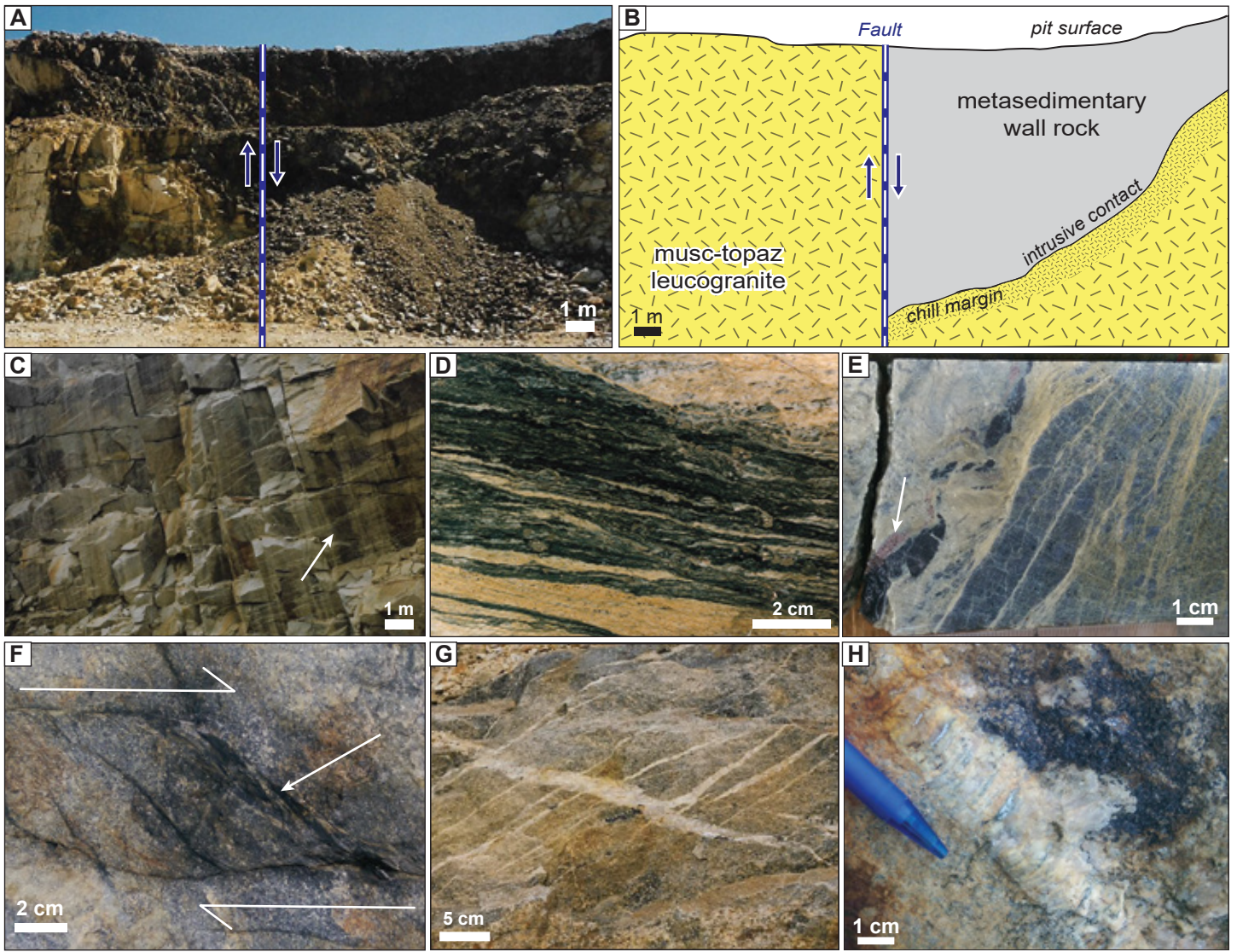


Figure 4 – 2

Figure 4–2. Outcrop photographs with structural features of the EKD. (A) View of NE edge of Main Zone pit wall (Fig. 4–1B) with EKL-metasedimentary rock contact offset by a fault that is part of the East Kemptville shear zone. (B) Schematic representation of Figure 4–2A showing lithological contacts and structural boundary. Note the chill margin observed in the leucogranite proximal to the intrusive contact (right), whereas the leucogranite is coarser grained throughout the adjacent fault block (left) suggesting significant offset. (C) View of East Kemptville pit wall with sub-vertical cleavage and fabric-parallel zoned greisens (arrow). (D) Shear deformation overprint on greisenized leucogranite with segmented porphyroclasts (pre-kinematic) of cassiterite and quartz-sulfide veins. (E) Sheared vein of quartz-cassiterite (arrow)-wolframite in quartz-topaz-muscovite greisen. (F) Outcrop photo of shear plane cross-cutting greisenized leucogranite and cemented by chlorite and graphite (arrow). Note the dextral shear sense is the same as observed in early ductile foliation. (G) Late-stage echelon shear veins (barren quartz) with continuous feather veins parallel to the EKSZ indicative of shear movement and brittle deformation post-dates the main mineralization stage. (H) Extensional syntaxial fibrous quartz-albite vein with synthetic to antithetic mineral growth indicating syn-kinematic vein development.

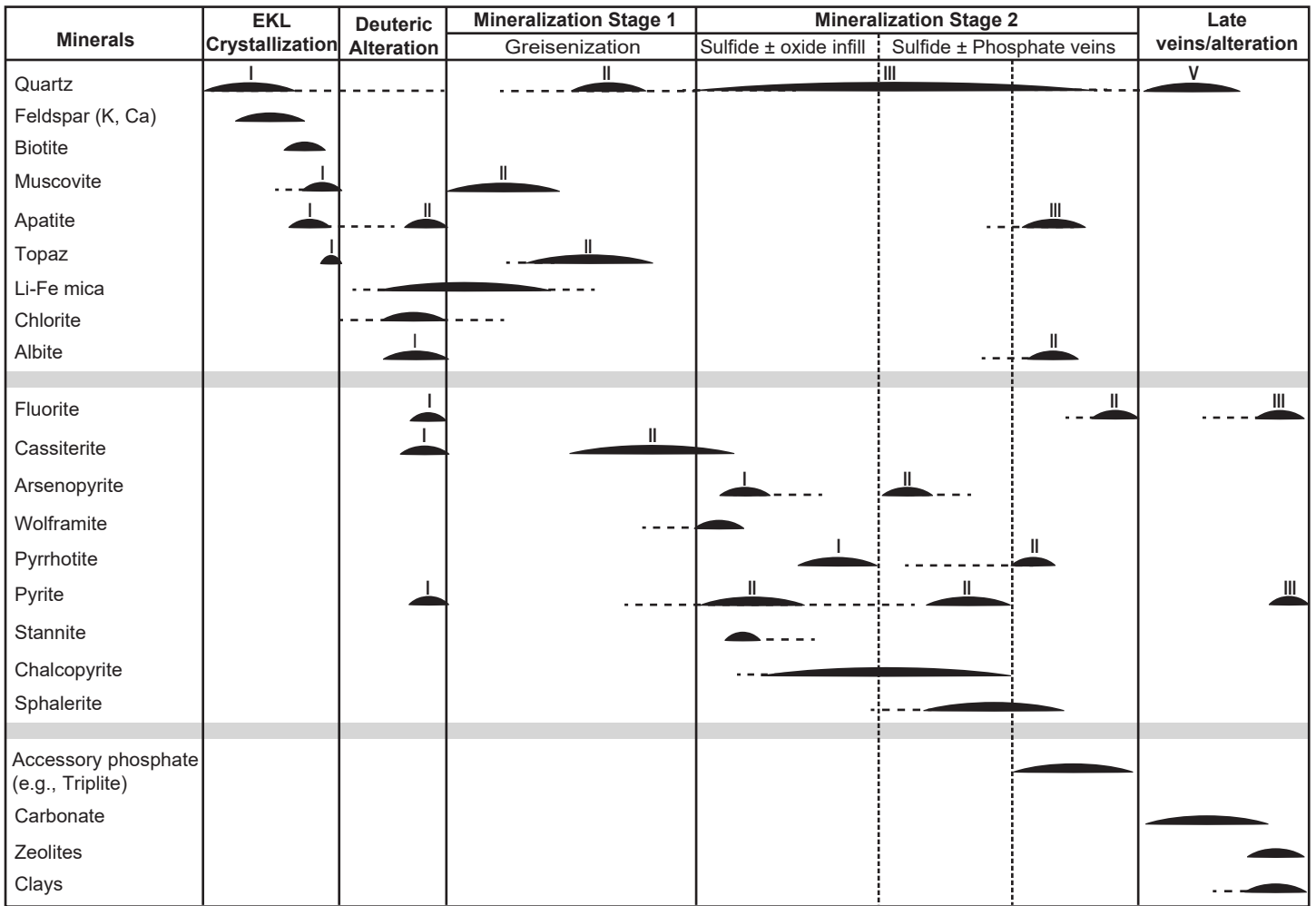


Figure 4-3

Figure 4–3. Summary paragenesis of the East Kemptville leucogranite (EKL) and the associated alteration as well as mineralization of the East Kemptville Sn-Cu-Zn-Ag-In deposit. Main paragenetic stages are divided into cross-cutting relationships and textures observed in petrographic analyses throughout the deposit. Note the main stage hydrothermal ore precipitation mineralization is divided into two stages and the latter stage is subdivided into three temporally equivalent to continuous mineralization events that follow greisen alteration (greisen infill to base-metal sulfide and quartz-sulfide-phosphate veins). Multiple generations of one mineral type across the paragenesis are denoted with roman numerals.

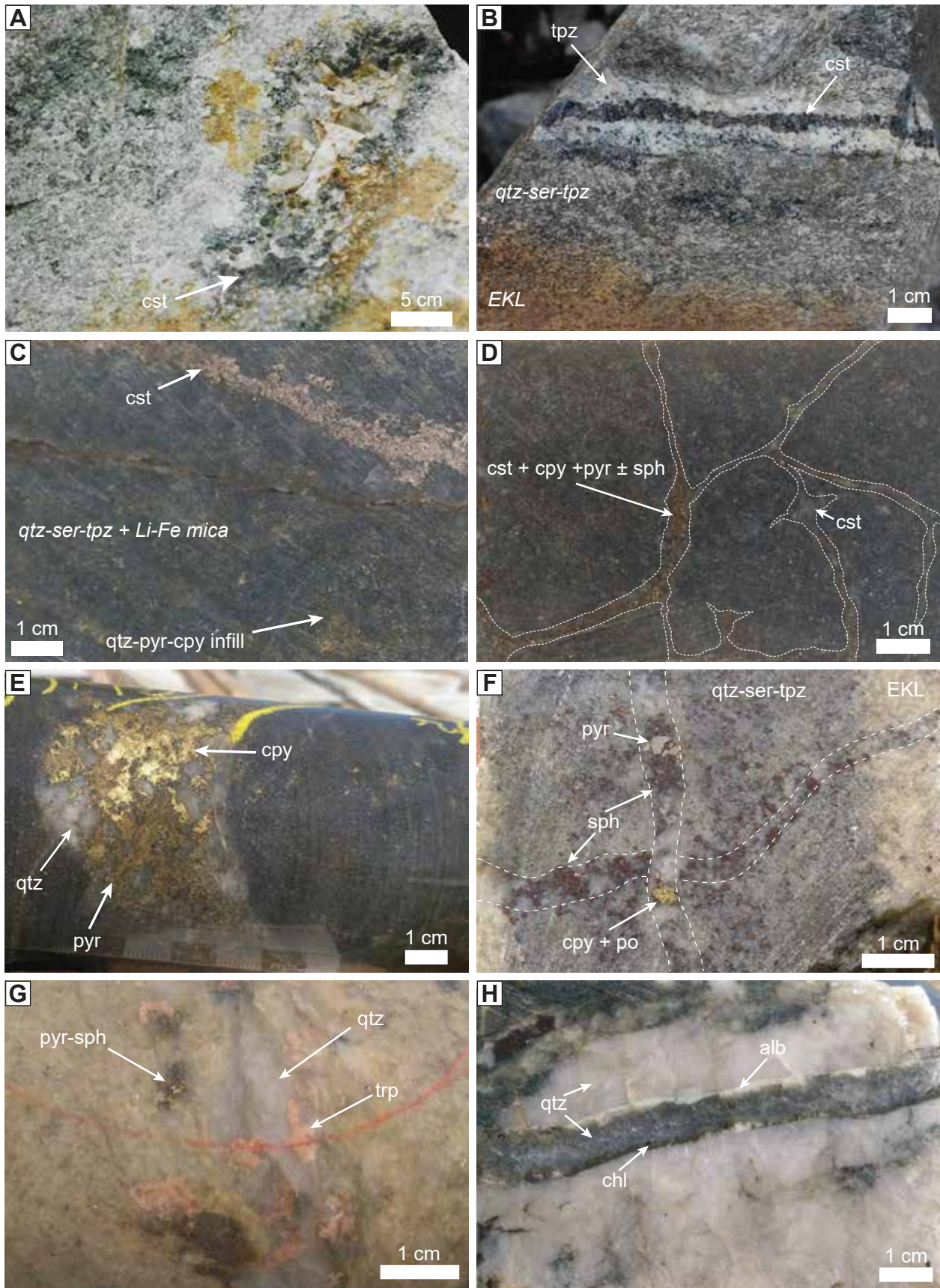


Figure 4-4

Figure 4–4. (A) Hand sample with miarole rimmed by coarse albite and containing primary cassiterite (cst; arrow). (B) Outcrop photo of a zoned greisen with coarse cassiterite core and selvage of milky white topaz and quartz that transitions into a dark grey quartz-muscovite-topaz (\pm Li-Fe mica and chlorite) greisen. (C) Zoned greisen with a core of coarse cassiterite that transitions to a quartz-sericite-topaz (\pm Li-Fe mica and chlorite) greisen with interconnected later infill of base-metal sulfide mineralization. (D) Hand sample of dark grey quartz-mica variety of massive greisen from the BZ. Rock in photograph is dominantly quartz, Fe-Li-mica, trace topaz and is cross-cut by network of microveinlets (outlined) containing quartz, cassiterite, chalcopyrite, pyrite, and sphalerite. Note coarser mineralization occurs in fracture junctions. (E) Thick vein of quartz-chalcopyrite-pyrite cross-cutting grey-green micaceous greisenized EKL. (F) Example of multiple vein sets of the quartz-sulfide vein generation cross-cutting a zoned greisen at different angles; thin undulose milky quartz and discontinuous sphalerite \pm chalcopyrite and pyrite crosscut the greisen obliquely and subsequently cross-cut both the greisen and previous vein along the greisen core. (G) Late milky quartz vein containing clotty pyrite, sphalerite \pm chalcopyrite and pink phosphate (triplite). (H) Example of an extensional syntaxial clear quartz and albite with chlorite vein cross-cutting a thick milky quartz-sphalerite vein.

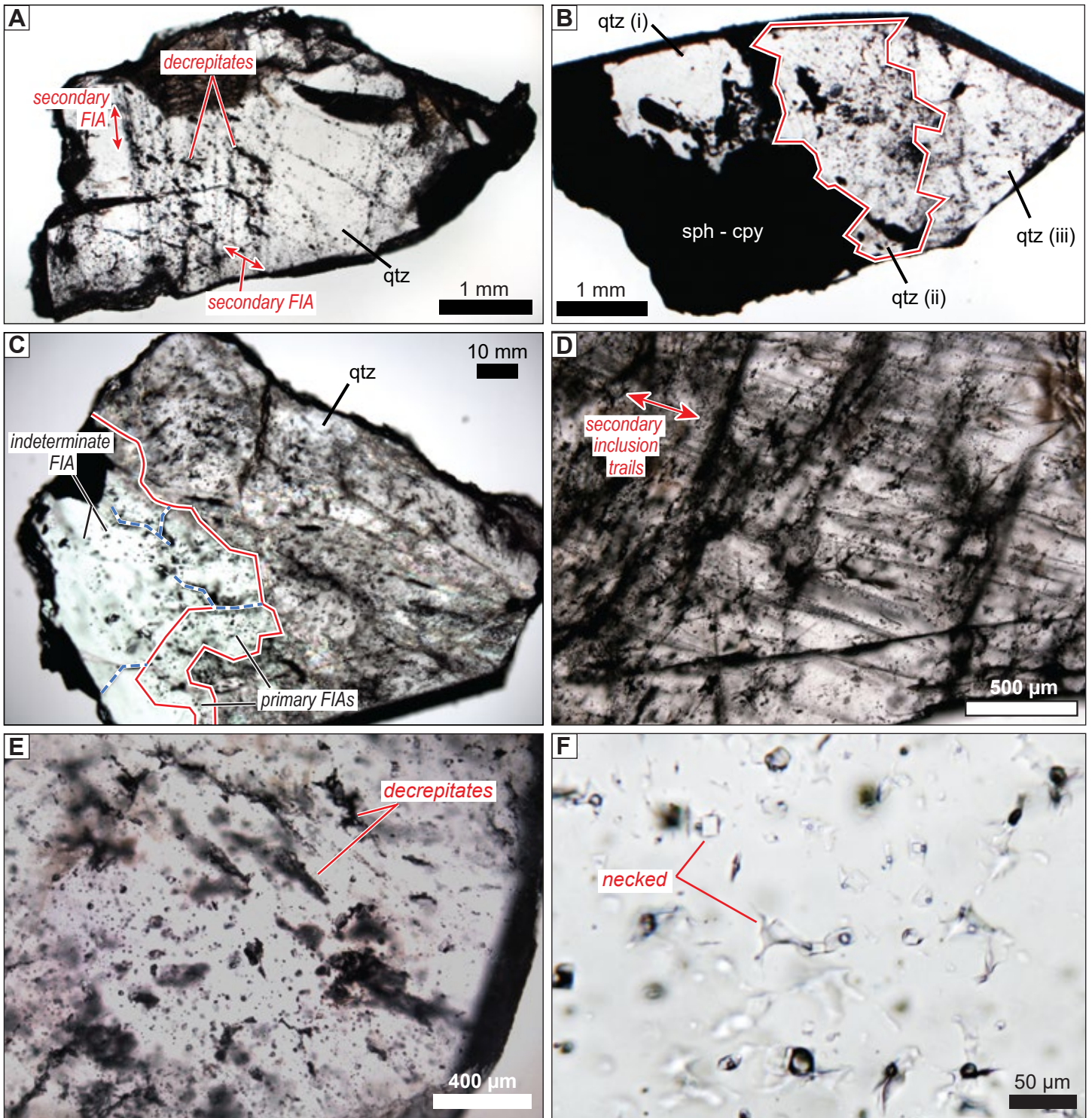


Figure 4-5

Figure 4–5. Macroscopic images of quartz thick-sections with a range of fluid inclusion content, both indeterminate and secondary. (A) Example of euhedral quartz that contains secondary inclusion trails with two dominant orientations, one of which (NW-SE) has abundant decrepitated inclusions. Indeterminate inclusions are sparsely populated between the secondary trails. (B) Example of re-crystallized euhedral quartz, initially grown synchronously with base-metal sulfides, that contains decrepitated and indeterminate inclusions of variable density (i - sparse density and indeterminate, ii - dense and small decrepitated, indeterminate, iii - somewhat dense indeterminate and along sub-grain boundaries). (C) Example of euhedral quartz grown with base-metal sulfides (left side) and grown over quartz with abundant decrepitated inclusions (right side). Indeterminate inclusions populate the interior of euhedral quartz and within growth zones in part of the sample (bottom, outlined in red). Healed fracture surfaces cross-cut growth zones and contain decrepitated inclusions (outlined in blue). (D) Example of quartz with abundant secondary trails of fluid inclusions. (E) Close-up of decrepitate inclusions in quartz. (F) Close-up example of abundant necked inclusions in quartz. Note: each inclusion has variable ratios of Laq : V : H. Abbreviations: qtz – quartz; sph – sphalerite; cpy – chalcopyrite.

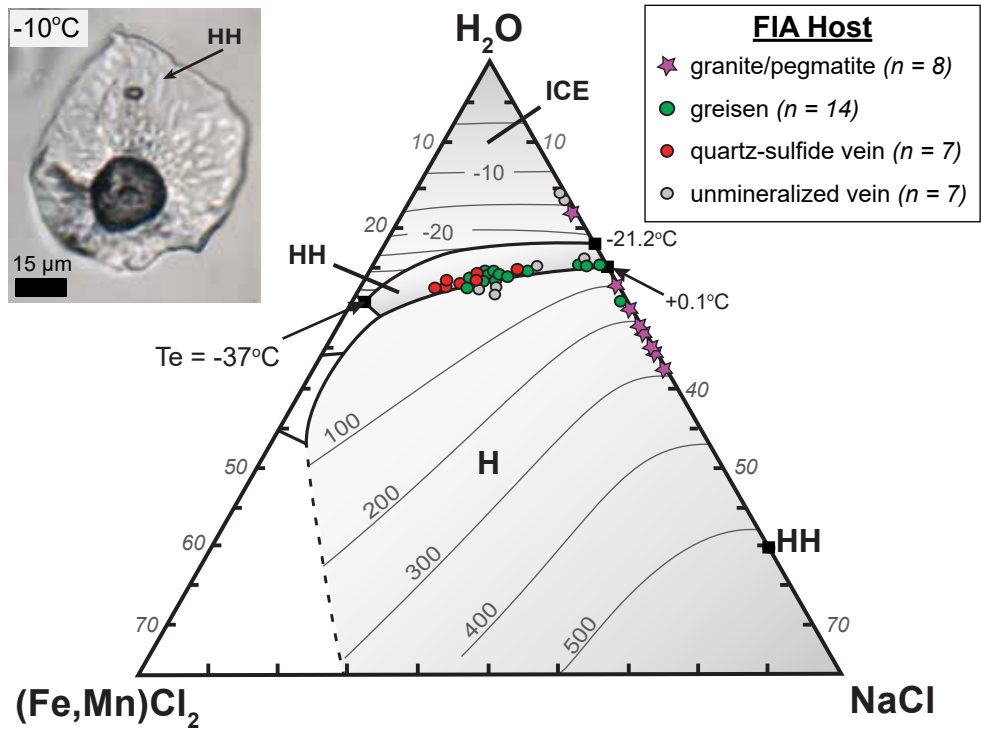


Figure 4-6

Figure 4–6. Ternary phase diagram (H_2O -[Fe,Mn] Cl_2 -NaCl; modified after Lecumberri-Sanchez et al., 2015) with temperature-solubility contours and microthermometric data points of East Kemptville FIAs. Each data point represents a quartz-hosted FIA and the legend divides the FIAs into which paragenetic phase the quartz was associated with (n infers number of FIAs plotted for each host). Inset shows an example of hydrohalite phase in a fluid inclusion at -10°C during heating-freezing microthermometric analysis. HH – hydrohalite, H – halite. Note: The salinity of halite-bearing L-V-H \pm Solid(s) FIAs, typically hosted by quartz in the granite/pegmatite paragenetic stage, was determined through temperature of homogenization through halite dissolution; thus, the data plot along the H_2O -NaCl binary and not influenced by divalent cation-content (Fe^{2+} , Mn^{2+}) in the fluid.

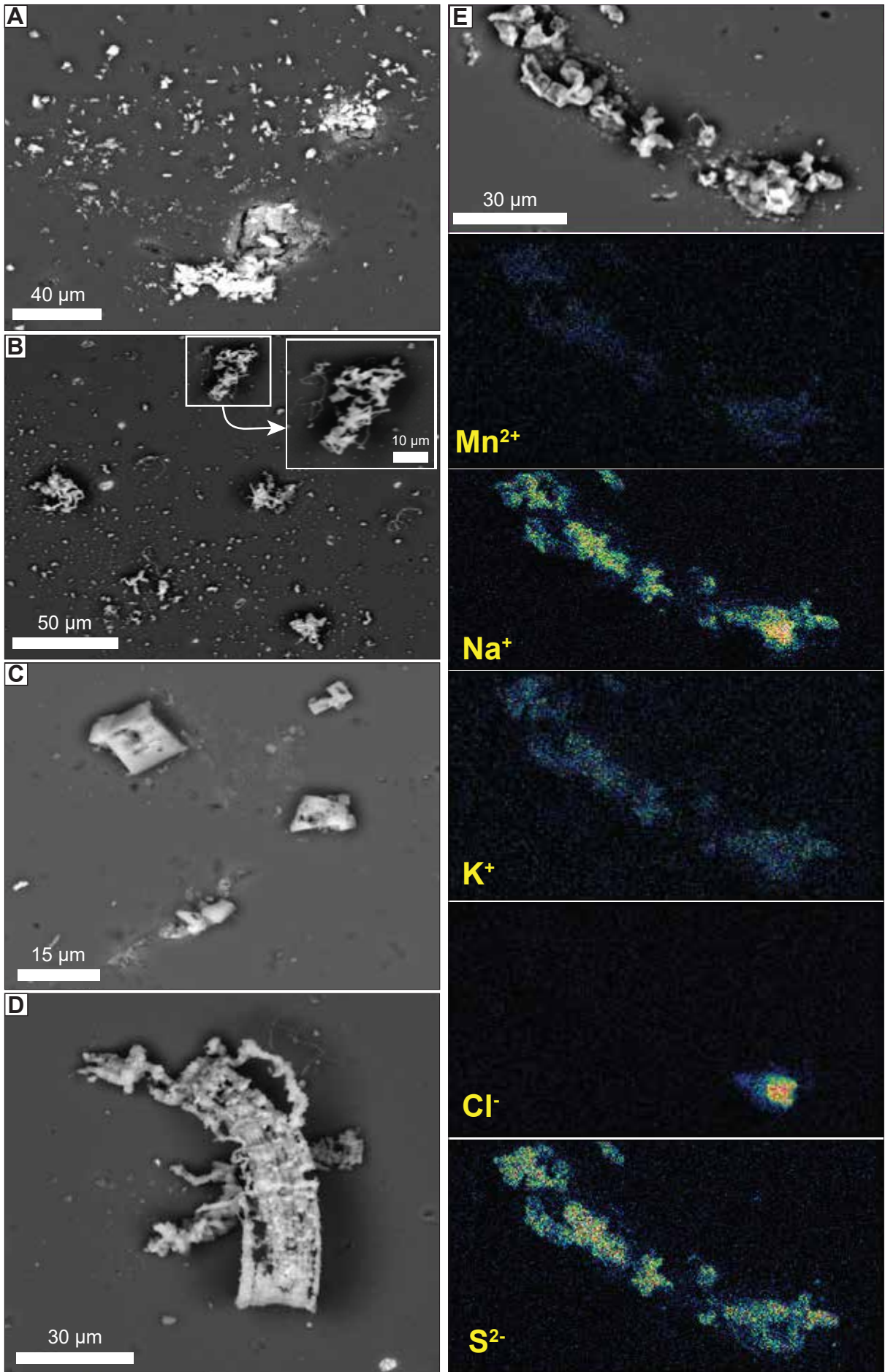


Figure 4-7

Figure 4–7. (A-D) Scanning Electron Microscopy (SEM) images of induced decrepitate salt mounds with variable morphology on the surface of quartz wafers: **(A)** Fine clustered Na-K bearing mounds from FIA in unmineralized vein. **(B)** Fibrous Na-K \pm Fe, Mn bearing massive mounds from FIA in quartz-sulfide vein. **(C)** Euhedral Na-K salt mounds on quartz of base-metal-mineralized vein. **(D)** Mound of homogeneous fibrous NaCl spotted with fine KCl salts from quartz in a weakly greisenized EKL. **(E)** Example of fluid inclusion evaporate mound mapped by energy-dispersive X-ray spectroscopy (EDS). Salt mounds containing $S^{(x-)}$ as the dominant anion, with homogeneous weak Mn^+ , K^+ , and Na^+ content and a single locality of NaCl, from quartz in a mineralized greisen sample; note the top frame is an SEM image of the mound which was mapped by the element in each image beneath.

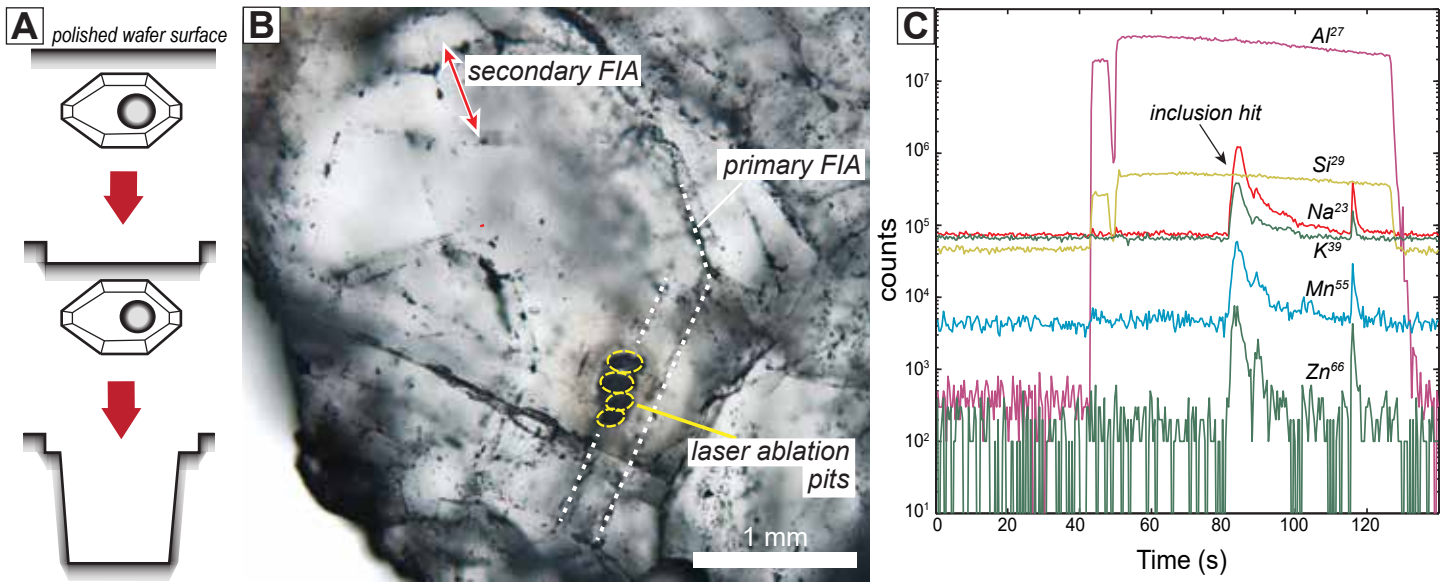


Figure 4–8

Figure 4–8. Example methodology for LA-ICP-MS analysis of fluid inclusions hosted by quartz and/or topaz at East Kemptville. (A) Schematic example of laser ablation approach to reaching a fluid inclusion beneath the sample surface. Note: ablation pit diameter is typically larger than inclusion size. (B) Example of topaz in mineralized greisen from East Kemptville with ablation pits along primary FIA trail after LA-ICP-MS analysis. (C) Example of LA-ICP-MS readout from topaz-hosted fluid inclusion with selected elemental isotope signals. Note: host mineral ablation begins at approximately 40s and inclusion intercepted at approximately 80s.

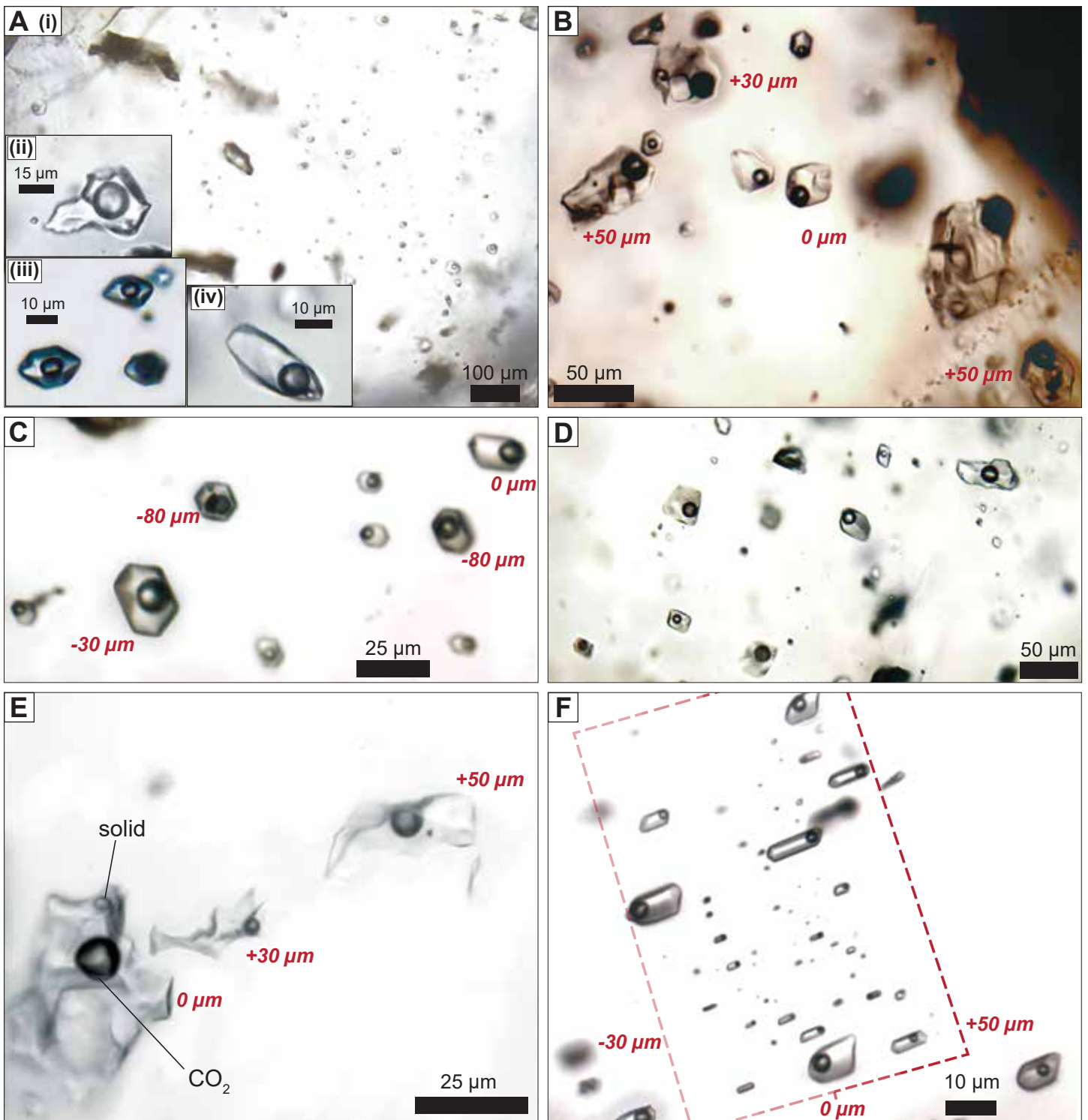


Figure 4-9

Figure 4–9. Photomicrographs of various fluid inclusion types hosted by quartz and topaz in the East Kemptville deposit. Inclusions not in plane of focus have been included, with relative position to the photomicrographic plane captioned. **(A)** [i] $L_{aq-V} +/-$ solid indeterminate and secondary FIAs in quartz at 22°C. [ii - iv] close-ups of $L_{aq-V} +/-$ s inclusions from slightly immature (ii) to mature negative crystal shape (iii). **(B)** Indeterminant 3 to 4-phase (L_{aq-V} -H-solid(s)) FIA with somewhat immature shape and variable sizes that range from 5 to 50 μ m in core of a quartz crystal within weakly altered EKL at 22°C. **(C)** Indeterminant L_{aq-V} negative-crystal shaped inclusions in mineralized greisen quartz fill at 22°C. **(D)** Indeterminant L_{aq-V} moderately mature inclusions in quartz of base-metal-sulfide vein at 22°C. **(E)** Close up of indeterminant and immature $L_{Carb-V_{Carb}}-L_{aq}$ -solid FIA hosted by topaz of mineralized greisen at 20°C. **(F)** Secondary plane of mature L_{aq-V} FIA hosted by quartz in a base-metal-sulfide vein at 22°C.

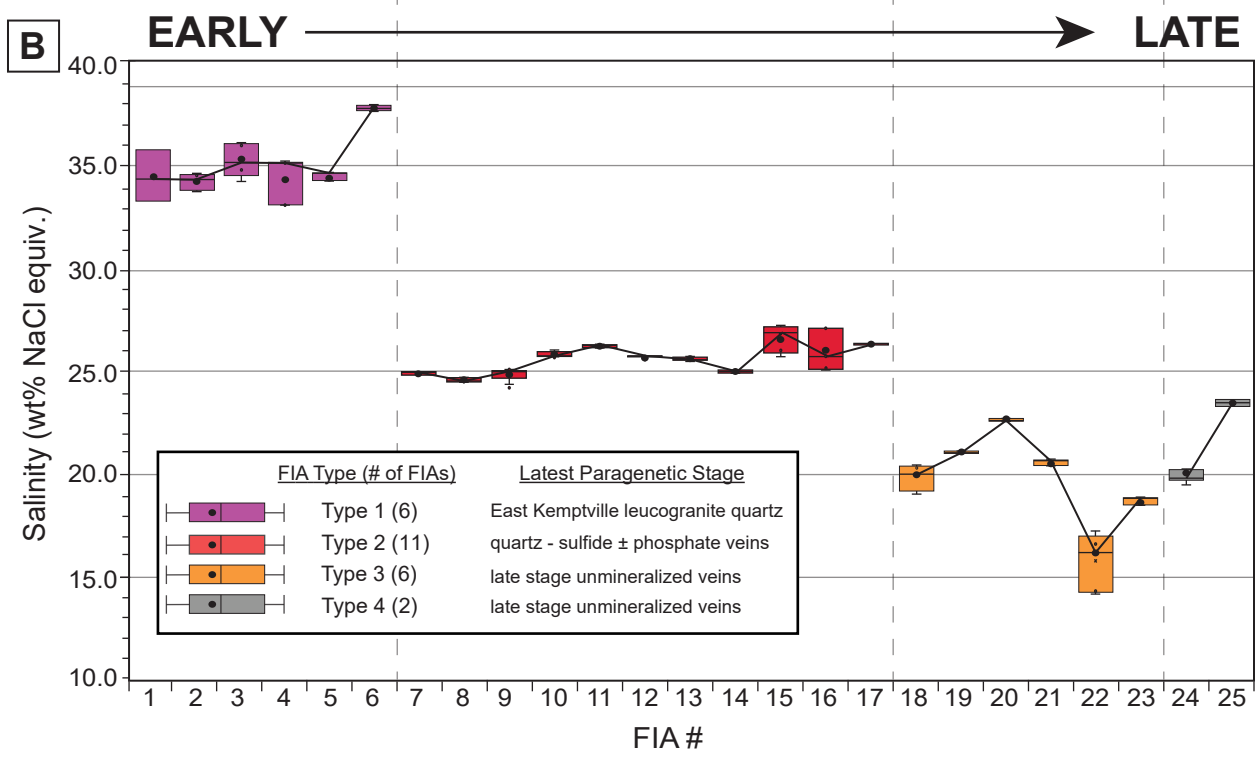
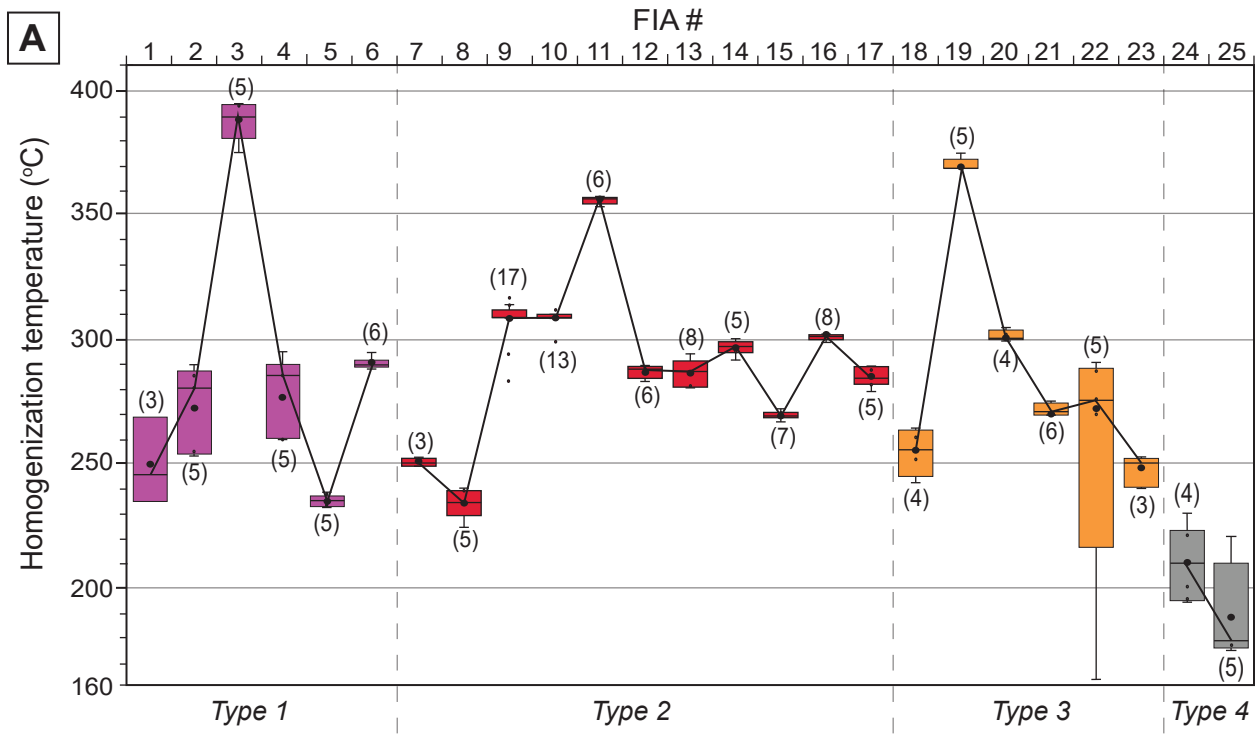


Figure 4–10

Figure 4–10. (A) Homogenization temperatures of fluid inclusion types 1 through 4, represented by FIAs hosted in quartz from each stage of the paragenesis at the East Kemptville deposit, plotted as a function of relative age. (b) Salinities of fluid inclusions inclusion types 1 through 4, hosted in quartz from each stage of the paragenesis, shown in Figure 4–10A, plotted as a function of relative age. Each box represent an individual FIA analyzed and the number of inclusions is denoted above the boxes in Figure 4–10A; the box ends constrain the middle 50 % of data for the groups of analyses, whiskers represent maximum and minimum values in each dataset, solid line in box represents the data median and solid circle box represents data mean for each dataset (summarized in Table EA 4-1, Electronic Appendix).

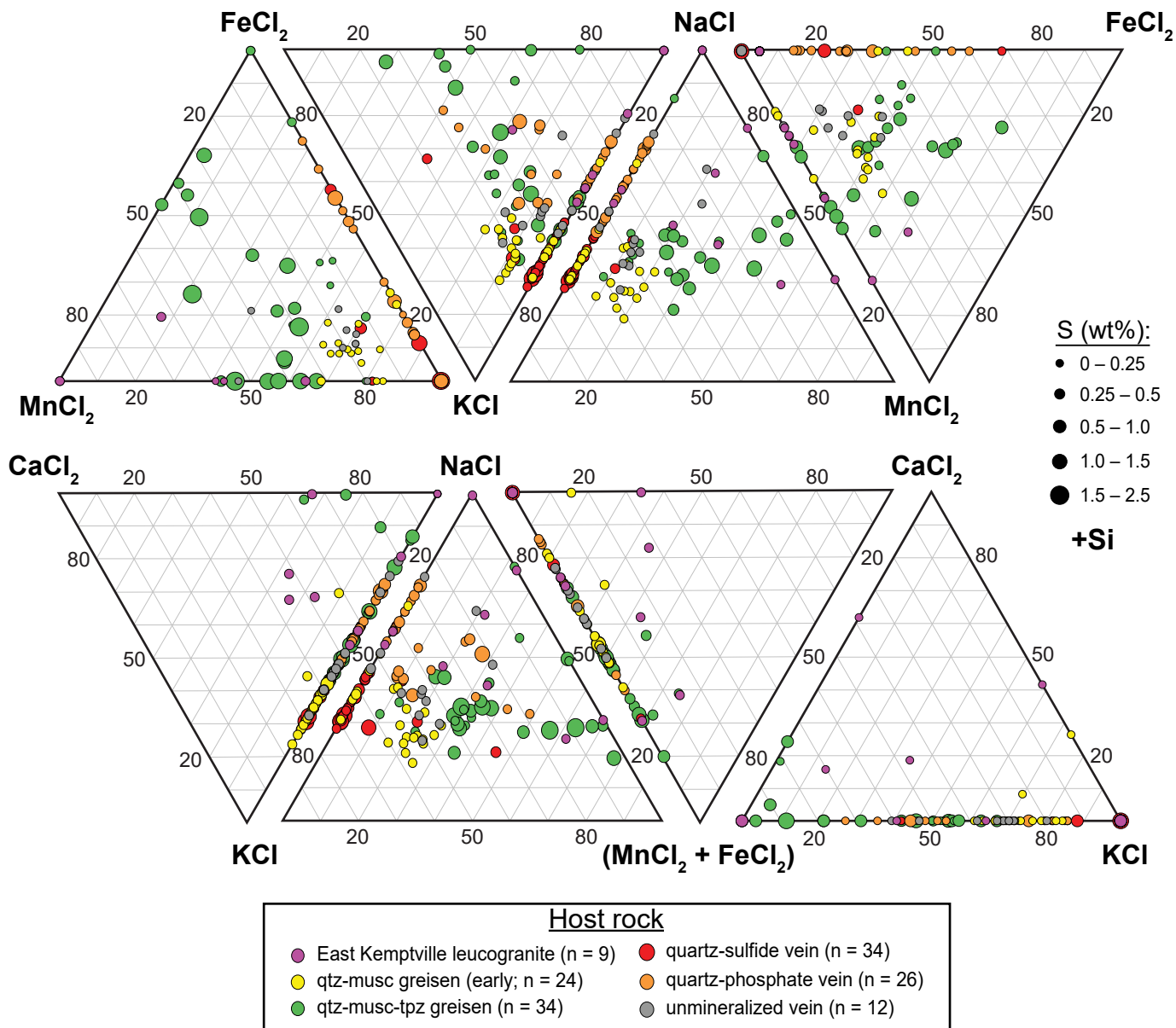


Figure 4–11

Figure 4–11. Evaporate mounds produced by thermally decrepitating FIAs with subsequent imaging and analysis with a coupled SEM-EDS system. Both relative and absolute element concentrations (wt. %) were determined from rasters of the evaporate mounds (e.g., yellow outlines in inset SEM-EDS image) by using known inclusion salinities as an internal standard. The ternary plots summarize the evaporate mound major element concentration data for East Kemptville, averaged for each FIA analyzed, across the deposit mineral paragenesis. Note bubble size in each plot gives a fourth measurement that corresponds to average S content (wt. %) in each FIA analyzed. Note the presence of FeCl_2 and MnCl_2 in evaporate mounds measured from the greisen stages and less so in the later vein stages, but relative absence of CaCl_2 in all samples.

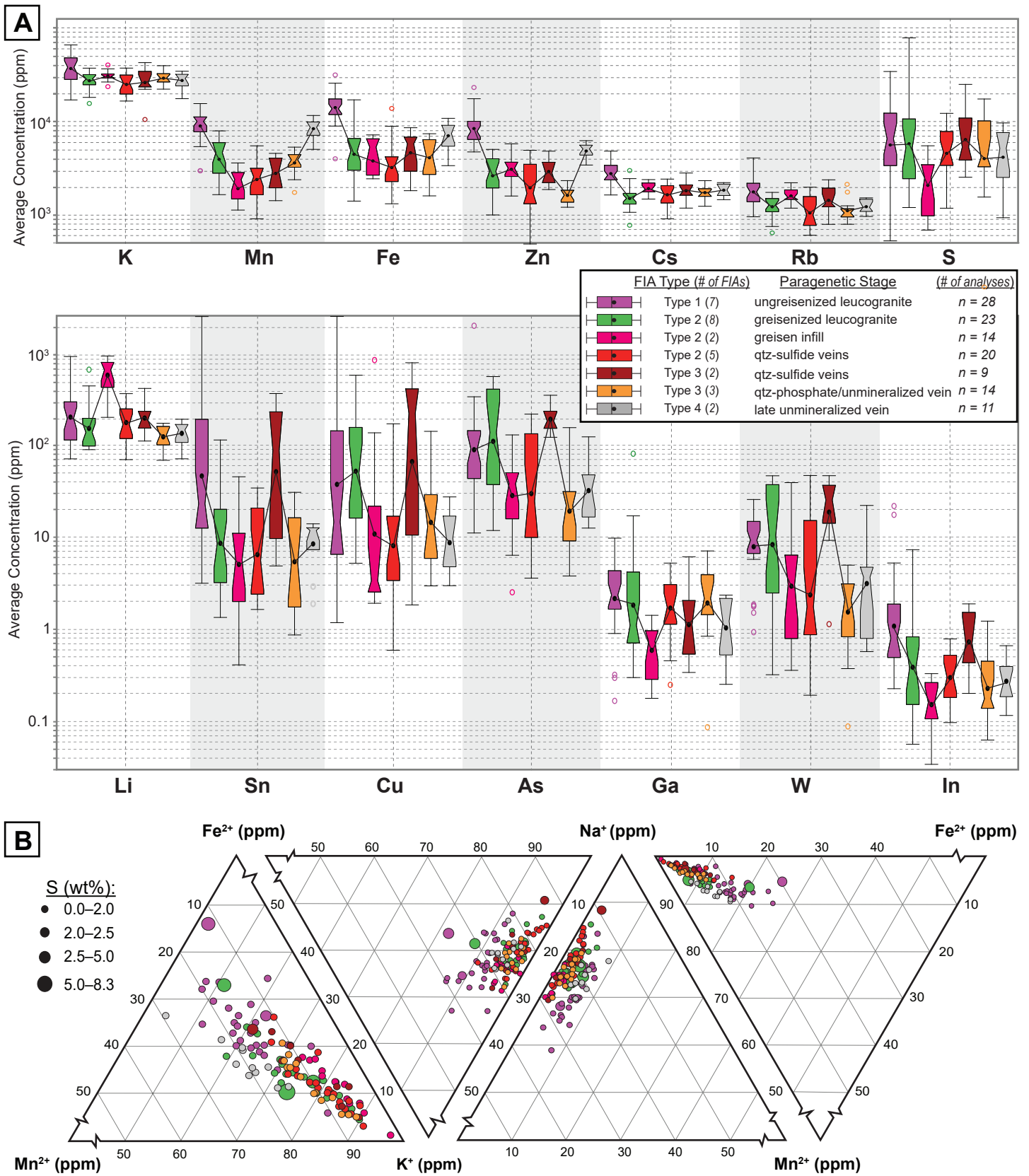


Figure 4–12

Figure 4–12. (A) Average trace element concentration (ppm, logarithmic scale) of quartz- and topaz-hosted fluid inclusion assemblages; determined by LA-ICP-MS analysis and presented as box plots for the selected elements with highest recognizable concentration (excluding Na and Cl). Boxes represent the FIA types analyzed from quartz and/or topaz in each paragenetic stage (see legend inset). Each upper box end (Q3) and lower box end (Q1) constrain the middle 50 % of data for the groups of analyses, whiskers represent maximum and minimum values in each dataset, indent in box represents the data median and solid circle represents data mean for each dataset (summarized in Table 4–3). Outliers represent data points that are further than $1.5 \times (Q3 - Q1)$ away from the box for each dataset. The detailed results are found in Table EA 4-3 (Electronic Appendix). (B) Ternary plots summarizing relative elemental concentrations from LA-ICP-MS analyses of various fluid types, legend in Figure 4–12A applies to this data. Note bubble size in each plot gives a fourth measurement that corresponds to average S content (wt. %) in each FIA analyzed.

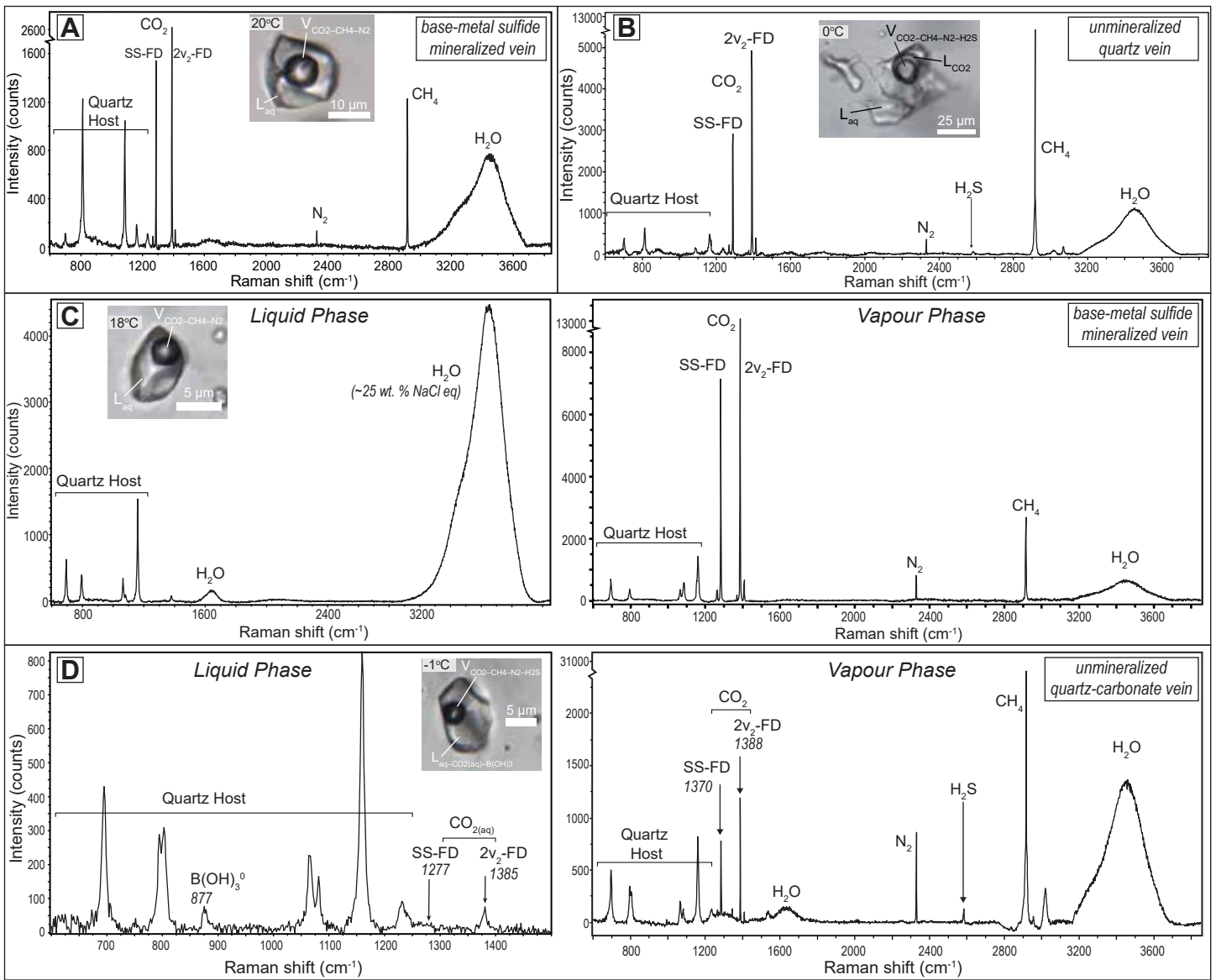


Figure 4-13

Figure 4–13. Raman spectra (at 22°C) for Type-3 aqueous carbonic fluid inclusions from East Kemptville. **(A)** Quartz-hosted $L_{aq}-V_{CO_2-CH_4-N_2}$ -Solid from a base-metal-sulfide mineralized vein. **(B)** Quartz-hosted $L_{aq}-L_{CO_2}-V_{CO_2-CH_4-N_2-H_2S}$ from a unmineralized quartz vein. Note occurrence of H_2S in the vapour bubble. **(C)** Quartz-hosted $L_{aq}-V_{CO_2-CH_4-N_2}$ from a base-metal-sulfide mineralized vein. Raman spectra of the liquid phase on left and spectra of the vapour phase on the right. **(D)** Quartz-hosted $L_{aq}-V_{CO_2-CH_4-N_2-H_2S}$ from a unmineralized quartz-carbonate vein. Raman spectra of the liquid phase on left and spectra of the vapour phase on the right. Note the aqueous liquid has dissolved aqueous CO_2 and $B(OH)_3^0$ phases. Phases identified: CO_2 doublet occurs at 1,285 and 1,388 cm^{-1} ; N_2 peak at 2,331 cm^{-1} ; CH_4 peak at 2,917 cm^{-1} ; H_2S peak from 2570 to 2590 cm^{-1} . A broad H_2O peak from 3,050 to 3,700 cm^{-1} , and a weak bending mode at ~ 1630 cm^{-1} , reflects the L_{aq} phase adjacent to the carbonic liquid.

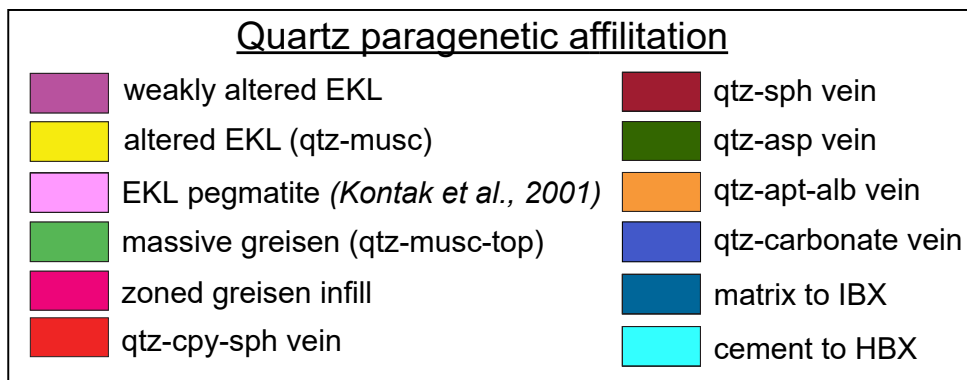
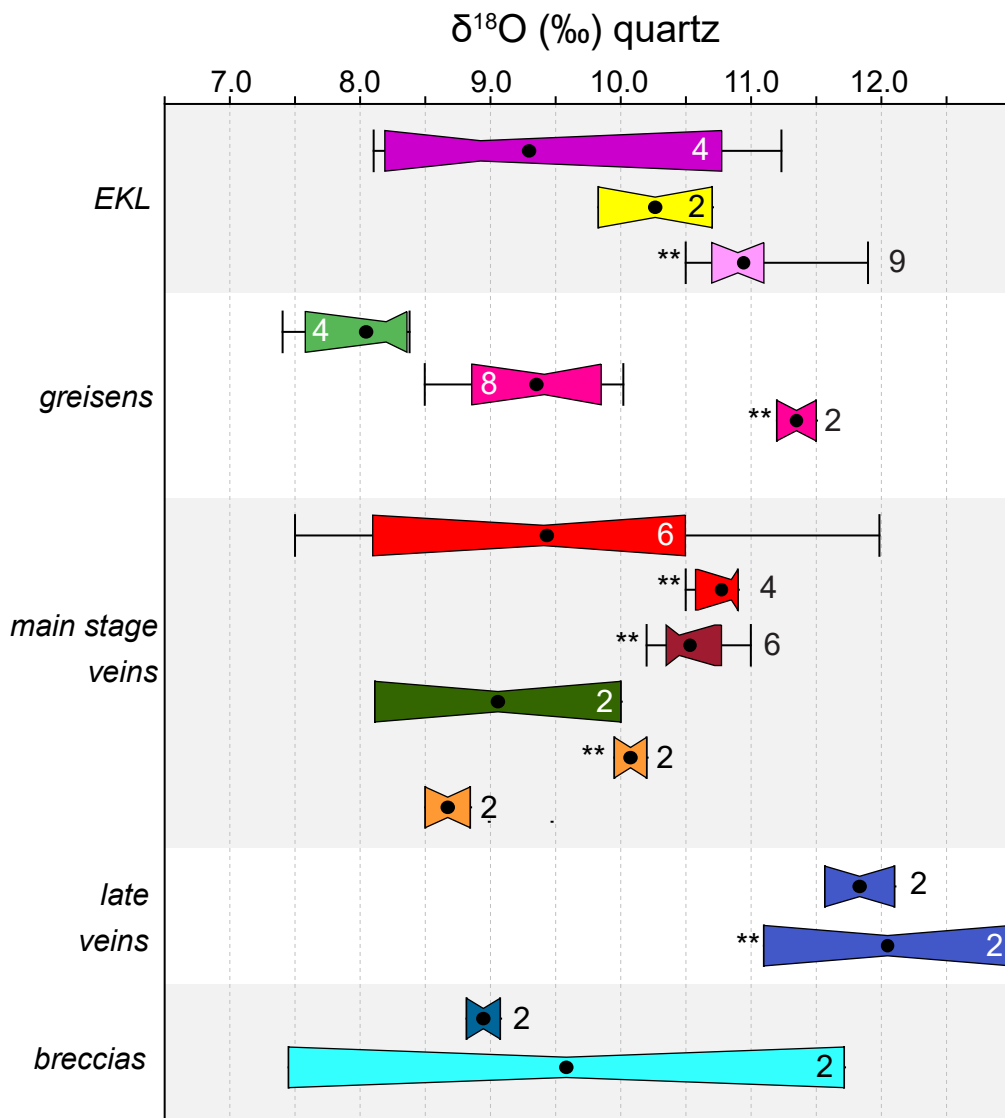


Figure 4-14

Figure 4–14. Comparative box and whisker plots of the oxygen isotope signature ($\delta^{18}\text{O}$) in ‰ for quartz from samples representative of lithologies and mineralization through the deposit paragenesis (backgrounded with different shades in plot): from EKL with various alteration and associated pegmatites (from Kontak et al., 2001); mineralized greisens and zoned greisen cores/infill; mineralized quartz-sulfide main stage veins; and unmineralized late stage veins (noted in legend). **i indicates data derived from bulk mineral separates using TIMS analysis; remaining data from in situ SIMS analysis.. Boxes contain middle 50% of data collected, whiskers represent spread of upper and lower 25%, number of samples denoted on or adjacent to each box, box indentation represents the sample population median and black dots represent the means. Note that each sample, with the exception of the magmatic-hydrothermal breccia quartz and one massive greisen, was sampled from the Main Zone at the East Kemptville deposit. Legend abbreviations: EKL – East Kemptville Leucogranite, alb – albite, apt – apatite, asp – arsenopyrite, carb – carbonate cpy – chalcopyrite, musc – muscovite, qtz – quartz, sph – sphalerite, top – topaz.

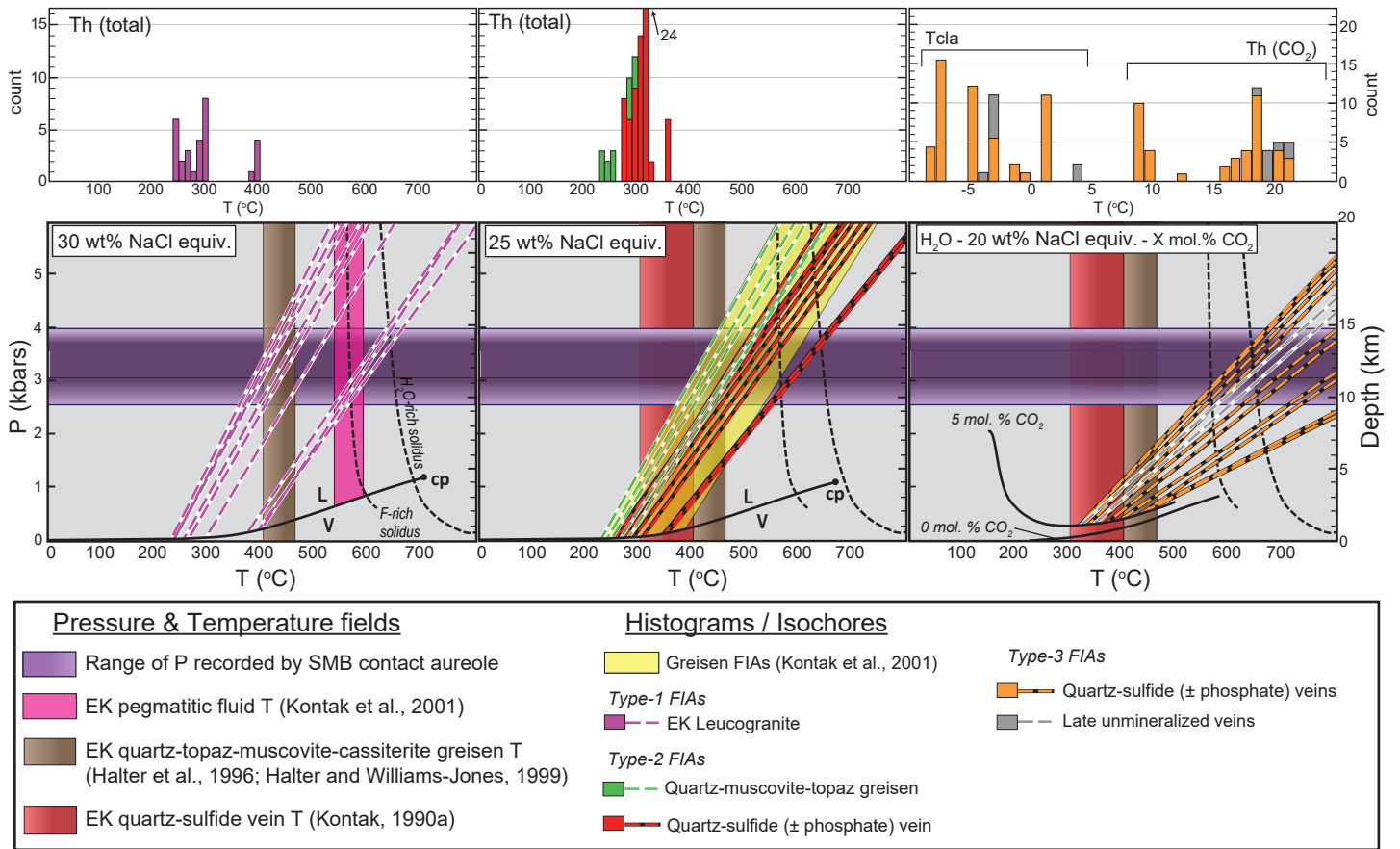


Figure 4-15

Figure 4–15. Histograms (above) with counts of Th(total) values, for aqueous fluid inclusions, and $T_{cl} + Th(CO_2)$ values, for aqueous carbonic inclusions, from individual fluid inclusions of respective P–T plots (below). Isochores on the P–T plots calculated from Th(total) values (points on LV-curve) for type-1 FIAs in quartz of weakly altered EKL (left), from hydrothermal quartz-hosted type-2 FIAs in greisens and base-metal-sulfide veins (center), as well as type-3 FIAs hosted in base-metal-sulfide bearing veins and unmineralized late carbonate-bearing veins (right). Isochores for aqueous FIAs calculated using ISOC (Bakker, 2003) and aqueous-carbonic FIAs calculated using algorithm from Steele-MacInnis (2018). A field of calculated isochores from a previous study of FIAs in topaz-greisens is shaded in grey (Kontak et al. 2001) and the estimated mineralization temperature range (ca. 300–400°C) is shaded in red. Calculated cassiterite-quartz thermometry from East Kemptville pegmatites is shown (Kontak et al. 2001) in addition to the estimated emplacement P from the SMB (after Kontak and Kyser 2011). Note: the solvi are plotted for H₂O-saturated (Tuttle and Bowen 1958) and F-rich haplogranites (Cuney et al. 1992). The H₂O-NaCl-CO₂ solvi are calculated using algorithm from Steele-MacInnis (2018).

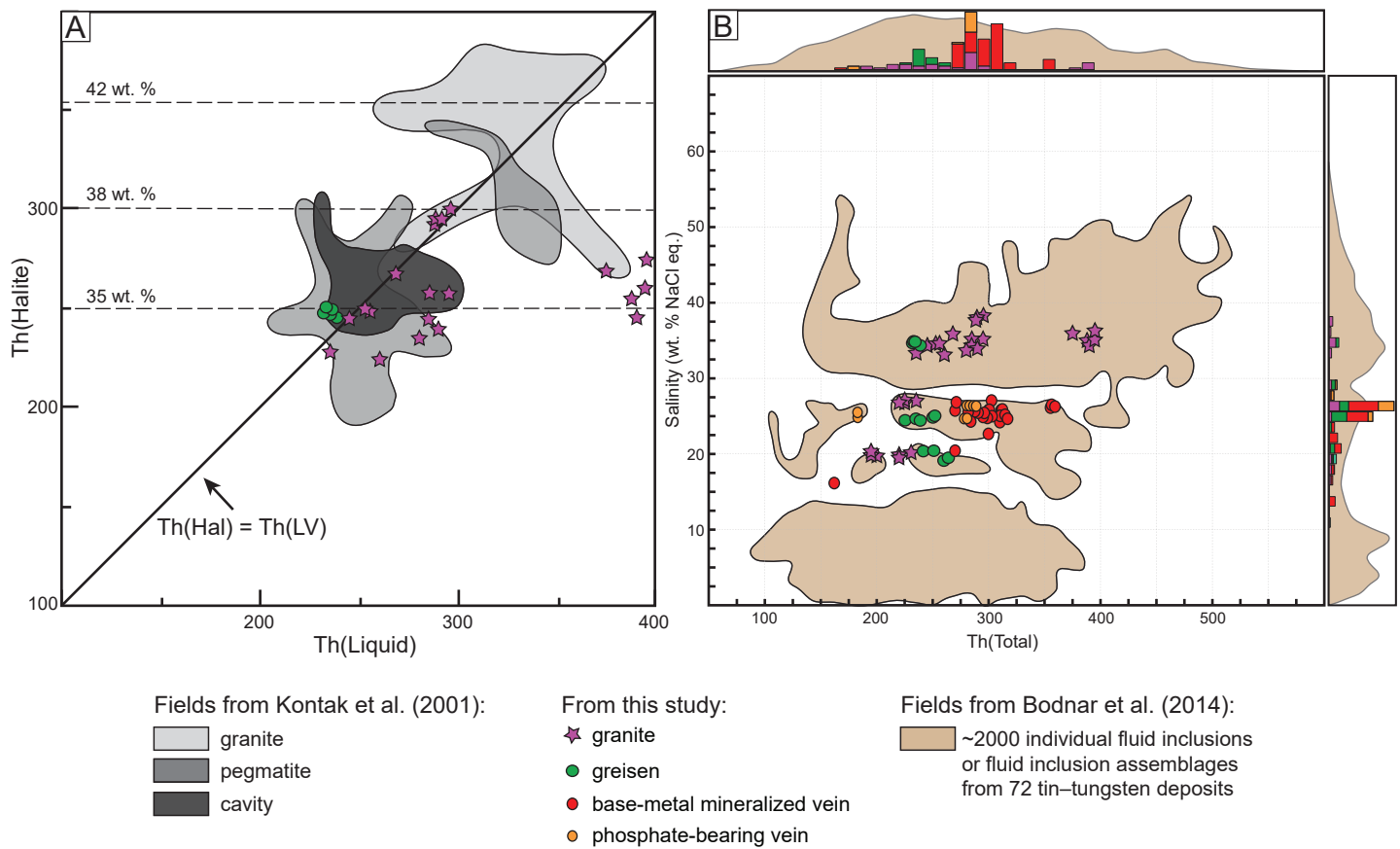


Figure 4-16

Figure 4–16. (A) Thermometric data of halite dissolution versus total homogenization temperatures for quartz-hosted fluid inclusions from this study and Kontak et al. (2001). Fluid inclusions hosted by quartz in leucogranite, greisenized leucogranite, pegmatites, and miaroles of the East Kemptville deposit. (B) Thermometric data of total homogenization temperatures and salinity for quartz-hosted fluid inclusions from various paragenetic stages in this study over top of fields representing fluid inclusions from 72 Sn-W deposits, compiled by Bodnar et al. (2014).

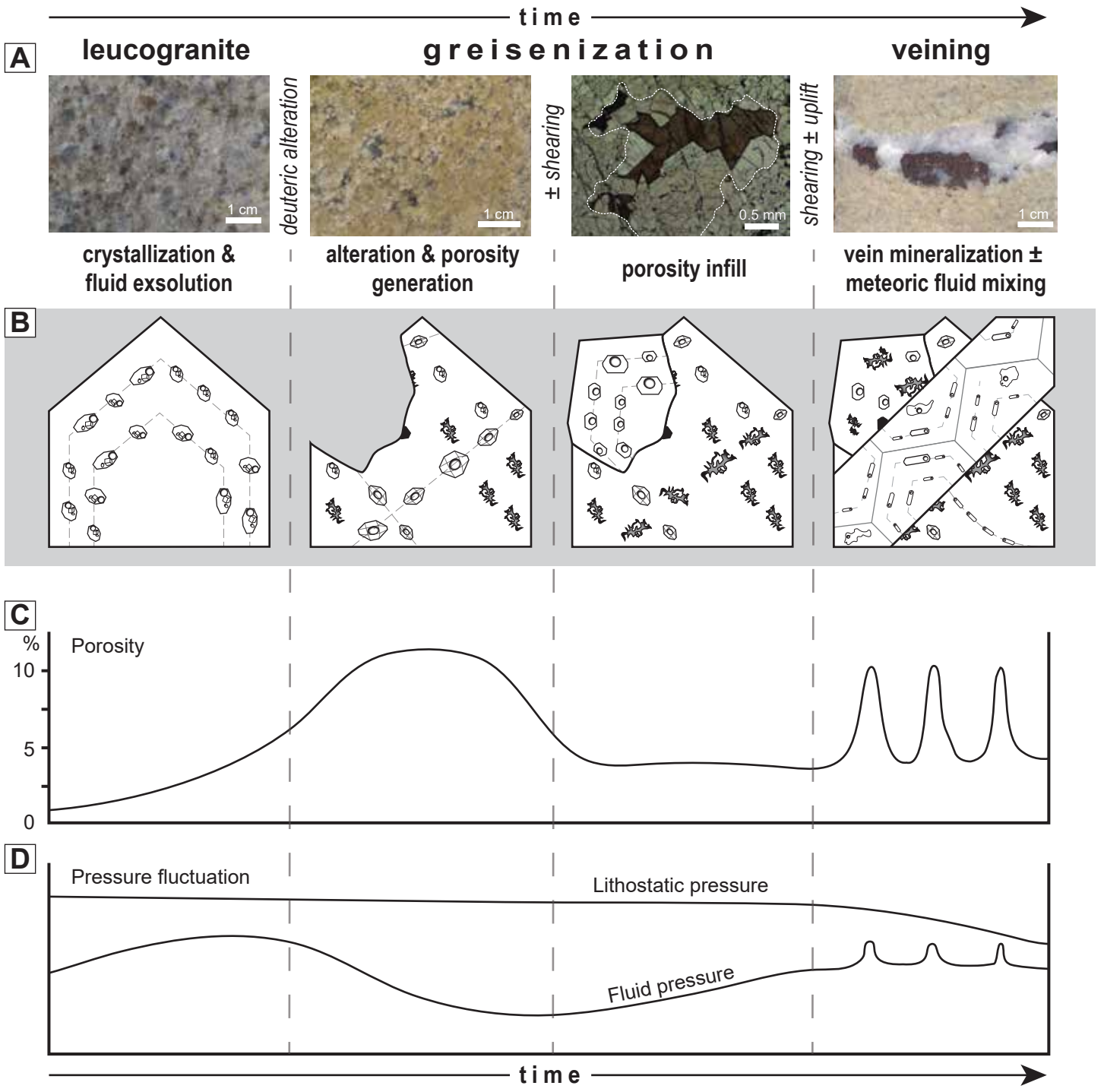


Figure 4-17

Figure 4–17. (A) Example hand samples and photomicrograph of resultant alteration and mineralization brought about by hydrothermal processes during the paragenetic stages of the East Kemptville deposit formation. (B) Schematic crystal growth and fluid inclusion entrapment, from types 1 to 4, through the paragenesis. Note the formation of decrepitates and secondary inclusion trails with each stage of deformation as well as mineral dissolution and subsequent formation. (C) Schematic plot of interpreted porosity in the EKL during deposit formation as a result of alteration and deformation (modified after Boullier et al., 1994). Note the gradual increase and decrease in porosity during the main mineralization stage that resulted from greisenization (mineral dissolution) and greisen infill. Porosity scale determined by percent of rock now filled by veining and greisen mineralization (sulfides, fluorides and oxides; cf. Halter et al., 1996). The late stage veining infilled voids formed during brittle deformation (relatively instantaneous increases in porosity). (D) Schematic plot of the interpreted relative pressure fluctuation (both fluid and lithostatic pressure) felt at East Kemptville through the paragenesis (modified after Boullier et al., 1994). Although mineral dissolution during greisenization reduces fluid pressure, the later vein stages indicate fluctuation of fluid pressure in the deposit, suggesting a decrease in lithostatic pressure by this point in the hydrothermal evolution.

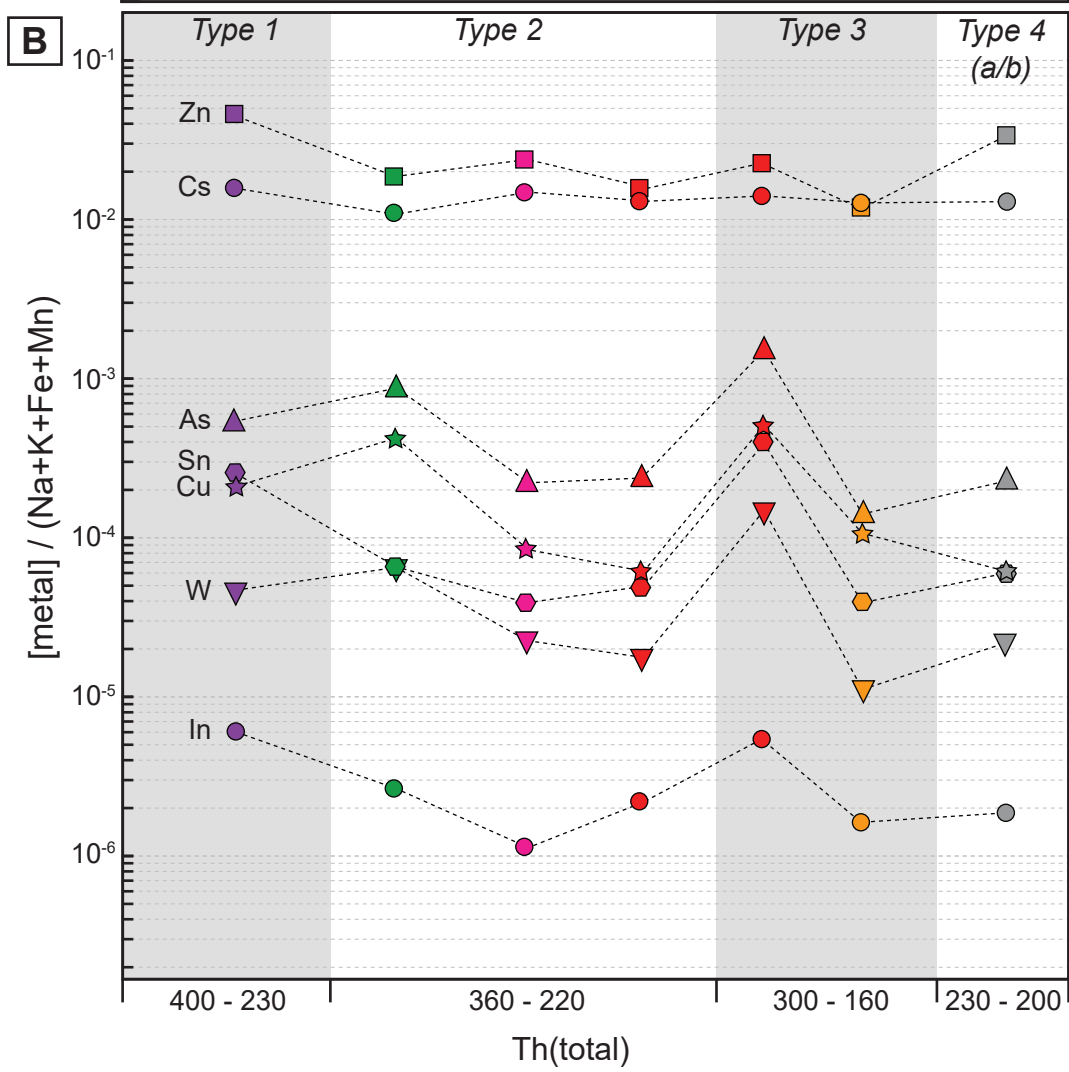
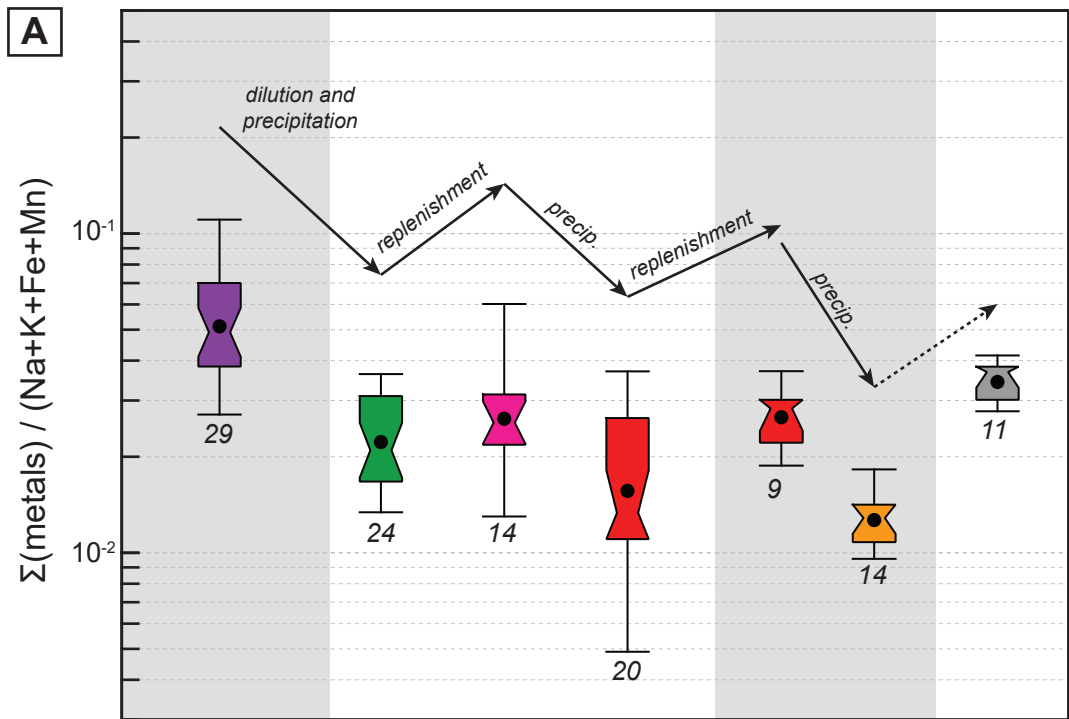


Figure 4-18

Figure 4–18. The evolution of individual (**A**; mean values) and sum of (**B**) ore metals relative to the sum of primary elements in the fluids (Na + K + Mn + Fe) through the paragenesis, with the range of homogenisation temperatures recorded from each fluid type. Number of inclusions analyzed noted beneath boxes, each upper box end and lower box end constrain the middle 50 % of data for the groups of analyses, whiskers represent maximum and minimum values in each dataset, indent in box represents the data median and solid circle represents data mean for each dataset. Paragenetic stage legend is the same as in Figure 4–14. In (**B**), Cs is plotted as an elements not involved in precipitation processes, as such it shows a constant ratio through the fluid evolution. Ore metals, however, show a sinuous trend through the paragenesis that suggest dilution and/or mixing between trapping of new fluid types, and a notable replenishment of metal-bearing type 2 fluid between the greisen formation and greisen infill stages.

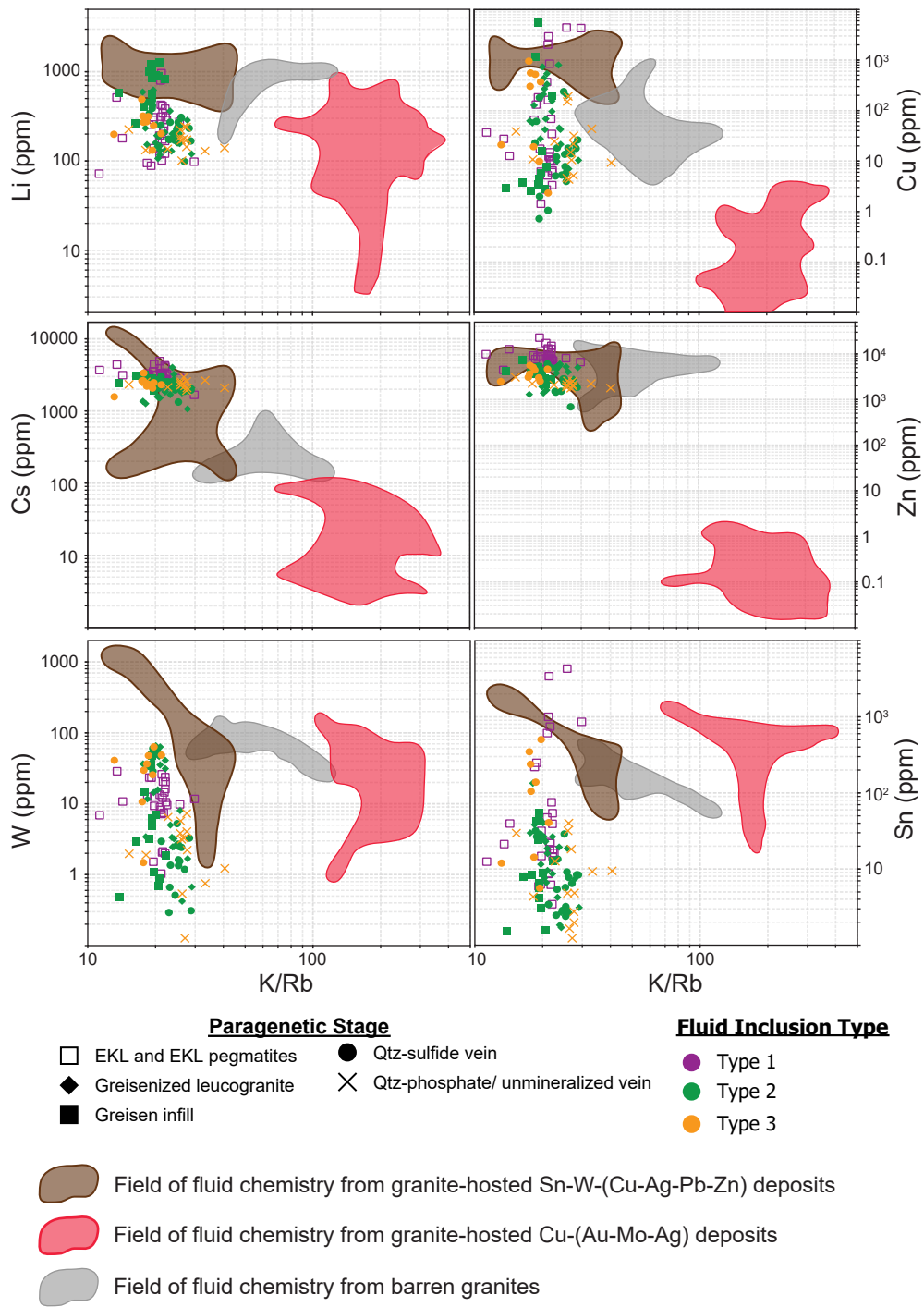


Figure 4–19

Figure 4–19. Discriminatory fluid chemistry plots of K/Rb versus various metals for fluid types from the East Kemptville deposit, through the paragenesis. Fields of fluid chemistry (brines) from other styles of mineral deposit are shown, compiled from previous studies: Sn-W-(Cu-Ag-Pb-Zn) field includes fluids from Mole Granite (Audétat et al. 2000), Ehrenfriedersdorf (Rickers et al. 2006; Zajacz et al., 2008), Zinnwald (Heinrich et al. 1999); Cu-(Au-Mo-Ag) field includes fluids from Bajo de la Alumbrera (Ulrich et al. 2002), Grasberg (Ulrich et al. 1999), Bingham (Landtwing et al. 2005; Heinrich et al., 1999), Butte (Rusk et al. 2004); and the barren granite field includes fluids from Baveno, Mt. Malosa, Cuasso al Monte (Zajacz et al., 2008), and Rito del Medio (Audétat and Pettke, 2003).

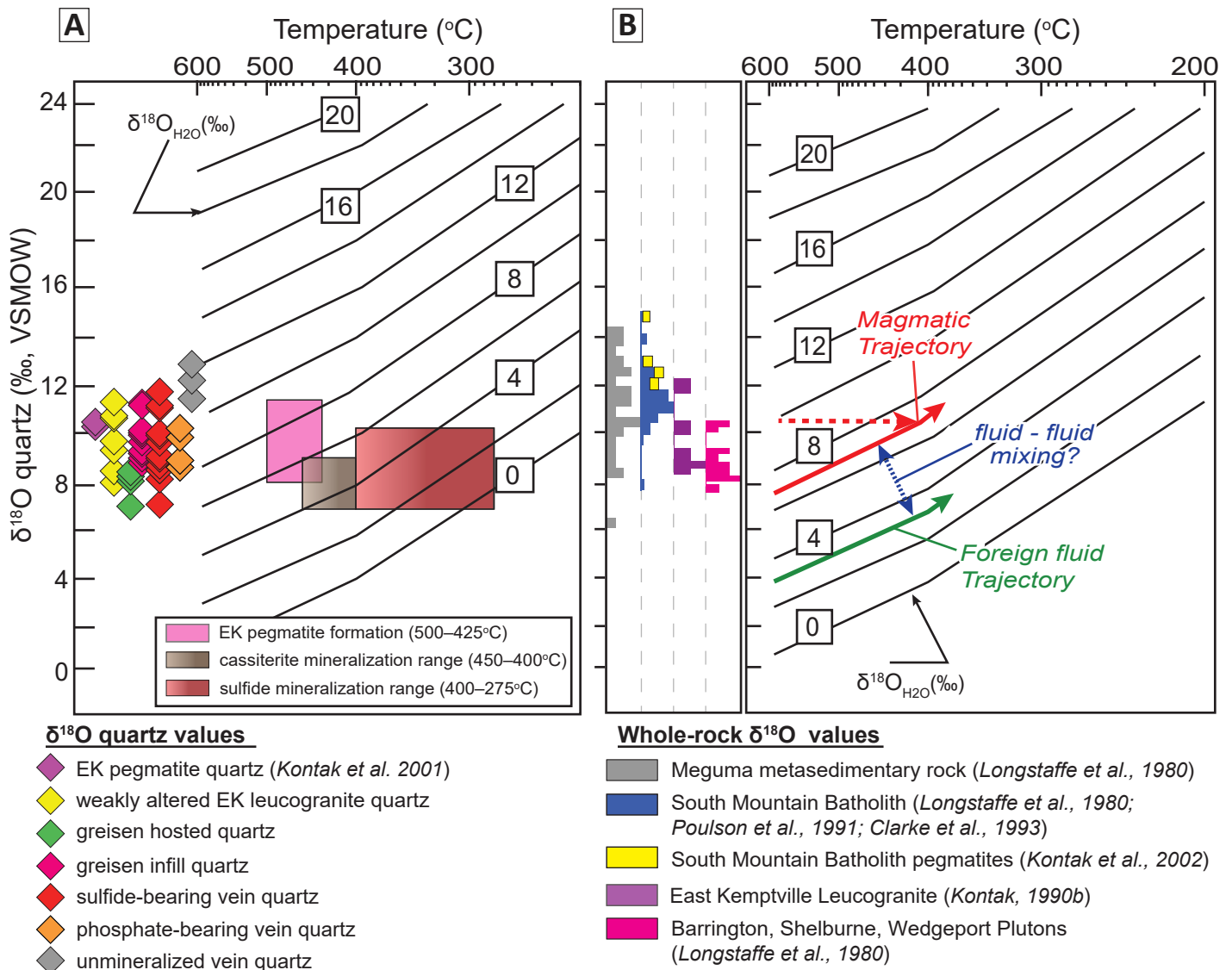


Figure 4–20

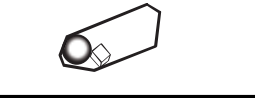
Figure 4–20. Plots of Temperature ($^{\circ}\text{C}$) versus $\delta^{18}\text{O}(\text{quartz})$ contoured for isopleths of $\delta^{18}\text{O}_{\text{H}_2\text{O}}$. The fractionation equation of Matsuhisa et al. (1979) used to construct the diagrams. **(A)** $\delta^{18}\text{O}(\text{quartz})$ values through the East Kemptville deposit paragenesis are plotted along the left axis, whereas the fields represent ranges of $\delta^{18}\text{O}(\text{quartz})$ correlated with temperature of formation for i) pegmatites at East Kemptville (pink), ii) greisens (brown), and iii) sulfide- to phosphate-bearing veins (red); see text for detail. **(B)** Fractionation trends for magmatic water (red) and a foreign (blue) water, based on an initial $\delta^{18}\text{O}(\text{quartz})$ value of +7‰ and +3‰, respectively. The expected trend of contamination between these fluids is displayed in blue. Note that the $\delta^{18}\text{O}(\text{quartz})$ values from mineralized rocks at East Kemptville are lower than is capable of the fractionation trend that the magmatic water follows; thus mixing with a foreign fluid is likely to have occurred. Left of the plot is relative probability histograms of $\delta^{18}\text{O}(\text{whole rock})$ values for various intrusive units associated with the EKD as well as $\delta^{18}\text{O}(\text{quartz})$ values from pegmatites elsewhere in the SMB.

Table 4–1. Sn-W Global deposit analogues for mineralizing fluids

Ore Deposit	Region/ Metalotect	Age (Ma)	Primary Mineralization	Style	Associated Lithology	Formation Conditions		Sn-Mineralizing Fluid		Reference
						P (kbars)	T (°C)	Th _{TOT} (°C)	Salinity (wt% NaCl equiv.)	
Colquiri	Bolivian Tin Belt	early Mesozoic	Sn-Pb-Zn	Veins	metasedimentary rock	0.66	300 - 400	191 – 383	1.2 – 6.4	Hanus, 1982; Sugaki, 1985
Panasqueira	Portugal	340 – 260	W-Sn-Cu	Veins	monzogranite / metasedimentary rock	0.15 – 0.03	230 – 360	255 – 320	6 – 9	Kelly and Rye, 1979
Mount Pleasant	New Brunswick, Canada	Late Devonian	W-Mo-Sn	Veins	granite porphyry	0.75 – 0.25	450 – 600	92 – 353	< 10	Samson, 1990
Pirquitas	Bolivian Tin Belt	15 – 9	Sn-Ag-Zn	Veins	metasedimentary rock	> 0.15	< 400	217 – 370	0 – 10.6	Desanois et al., 2019
Huanuni	Bolivian Tin Belt	Miocene	Sn	Veins	metasedimentary rock	–	–	364 – 385	3 – 11.1	Müller et al., 2001
Cleveland	W Tasmania	Late Devonian	Sn - Cu	Veins	granite / graywacke-argillite	1.4 – 0.3	480 – 500	300 – 380	7 – 14	Collins, 1981
San Rafael	Bolivian Tin Belt	22.7 – 21.9 ± 0.5	Sn-Cu	Veins	monzogranite / metasedimentary rock	0.62 – 0.15	< 500	215 – 420	0 – 20	Kontak and Clark, 2002
Viloco	Bolivian Tin Belt	26.2 ± 0.2	Sn-W-Mo-As	Veins	cordierite-granodiorite / metapelite	–	–	256 – 494	16.9 – 26	Artiaga et al., 2013; Sugaki, 1985
Yankee Lode	Mole Granite, E Australia	Permian-Triassic	Sn - W	Veins	leucogranite / siltstone & mudstones	0.25	422 – 528	350 – 420	20 – 40	Eadington, 1983
Tikus	Belitung, Indonesia	195 ± 12	Sn-W	Greisen	granite / metasedimentary rock	2.0 – 0.7	–	200 – 340	0.8 – 7	Schwartz and Surjono, 1990
Oriente Novo	Itu, Brazil	–	Sn-W-Ta-Nb	Greisen	zinnwaldite-granite	2.4 – 1.0	250 – 370	250 – 370	0.4 – 13.8	Bettencourt et al., 2005
Correas	Rondonia, Brazil	619 ± 11	Sn-W-Zn-Cu	Greisen	topaz-muscovite-granite	2.0 – 1.3	300 – 440	300 – 360	0 – 19	Bettencourt et al., 2005
South Crofty	Cornwall, UK	300 – 270	Sn-W-Cu-Zn	Greisen	peraluminous granite / metasedimentary rock	1.5 – 1.0	200 – 500	300 – 450	10 – 30	Jackson et al., 1989
Mount Bischoff	W Tasmania	Late Devonian	Sn	Greisen	Adamellite / shale-sandstone	0.2	320 – 360	280 – 365	30 - 36 / c. 12	Wright and Kwak, 1989; Halley and Walshe, 1995
Chorukh-Dairon	Tien Shan, Central Asia	319 – 315	W-Cu-Mo	Skarn	monzogranite / metasedimentary rock	1.1 – 0.7	400 – 500	320 – 400	30-38 / 15-22	Soloviev and Kryazhev, 2017

Note: Deposits sorted by a) mineralization style and b) salinity of main Sn-mineralizing fluids. Formation conditions are those described for the primary Sn-mineralizing event in each deposit. Abbreviations: P = Pressure; T = Temperature; Th_{TOT} = Total homogenization temperature.

Table 4–2. Summary of fluid inclusion types and properties that were identified in quartz and topaz across each paragenetic stage at the East Kemptville Deposit.

Properties	FI types				
	Type 1:	Type 2:	Type 3:	Type 4a:	Type 4b:
Representative inclusion appearance					
Phases present (20°C)	$(\text{H}_2\text{O}-[\text{K},\text{Na}]\text{Cl}-[\text{Fe},\text{Mn}]\text{Cl}_2)_\text{L} + (\text{NaCl})_\text{S} + (\text{H}_2\text{O})_\text{V} \pm ([\text{Fe},\text{Mn}]\text{Cl}_2)_\text{S} \pm (\text{KCl})_\text{S}$	$(\text{H}_2\text{O}-[\text{K},\text{Na}]\text{Cl}-[\text{Fe},\text{Mn}]\text{Cl}_2)_\text{L} + (\text{H}_2\text{O})_\text{V} \pm ([\text{Fe},\text{Mn}]\text{Cl}_2)_\text{S}$	$(\text{H}_2\text{O}-\text{NaCl})_\text{L} + (\text{CO}_2 \pm \text{CH}_4 \pm \text{N}_2)_\text{V} \pm (\text{CO}_2 \pm \text{H}_2\text{S})_\text{V}$	$(\text{H}_2\text{O}-\text{NaCl})_\text{L} + (\text{H}_2\text{O})_\text{V}$	$(\text{H}_2\text{O}-\text{NaCl})_\text{L} + (\text{NaCl})_\text{S} + (\text{H}_2\text{O})_\text{V}$
Paragenetic stage association	quartz in East Kemptville leucogranite and in mineralized greisens at the EKD.	quartz in the East Kemptville leucogranite; quartz and topaz in mineralized greisens of the EKD; quartz of base-metal mineralized veins; quartz of phosphate-bearing veins.	quartz of unmineralized late-stage veins; quartz of base-metal mineralized veins; quartz and topaz in mineralized greisens of the EKD; quartz of phosphate-bearing veins.	quartz of unmineralized late-stage veins; quartz of base-metal mineralized veins; quartz of phosphate-bearing veins; quartz and topaz in mineralized greisens of the EKD; quartz in East Kemptville leucogranite.	quartz of unmineralized late-stage veins; quartz of base-metal mineralized veins; quartz of phosphate-bearing veins; quartz and topaz in mineralized greisens of the EKD; quartz in East Kemptville leucogranite.
Occurrence and origin	Rare; indeterminate origin clustered in cores of primary quartz. Typically necked or decrepitated.	Common; indeterminate origin, along grain boundaries, clustered and decrepitated, along S planes.	Uncommon; indeterminate origin clustered in cores of hydrothermal quartz. Typically decrepitated or in decrepitate haloes.	Uncommon; along S planes cross-cutting grain boundaries and early S planes.	Uncommon; along S planes cross-cutting grain boundaries and early S planes.
# of inclusions measured	37 (8 FIA)	182 (33 FIA)	64 (14 FIA)	25 (5 FIA)	–
Size (µm)	5 – 10	5 – 35	5 – 50	5 – 30	5 – 25*
% vapor phase at 20 °C	15 – 25	20 – 40	30 – 50	15 – 30	15 – 30*
T_e	–29 to –23 (–27.0 ± 2.4); $n = 13$	–50 to –24 (–32.7 ± 5.6); $n = 183$	–37 to –25 (–28.9 ± 3.3); $n = 60$	–34 to –21 (–25.7 ± 4.9); $n = 25$	–
$T_m(\text{Ice})$	–29 to –23 (–26.7 ± 2.3); $n = 13$	–32 to –19 (–24.6 ± 2.5); $n = 176$	–25 to –22 (–23.9 ± 0.9); $n = 58$	–18.3 to –12.9 (–16.1 ± 2.0); $n = 21$	–
$T_m(\text{HH})$	ND	–14 to 18 (–3.3 ± 6.3); $n = 170$	–14 to 5 (–4.7 ± 4.3); $n = 64$	–22.5 to –18.5 (–21.1 ± 1.3); $n = 15$	–
$T_m(\text{Halite})$	217 – 300 (255.4 ± 23.4); $n = 37$	9 – 22 (14.8 ± 4.1); $n = 18$	ND	ND	150 – 300*
$T_m(\text{Clath})$	ND	ND	–8.7 to 4.2 (–4.1 ± 3.4); $n = 64$	ND	–
Salinity (wt% NaCl equiv.)	29 – 38 (34.0 ± 2.9); $n = 37$	24 – 29 (25.9 ± 0.9); $n = 183$	10 – 23 (19.3 ± 3.3); $n = 64$	17 – 24 (20.1 ± 2.1); $n = 25$	28 – 30*
$T_m(\text{CO}_2)$	ND	ND	–63 to –57 (–59.78 ± 1.61); $n = 58$	ND	ND
$T_h(\text{CO}_2)$	ND	ND	–3.0 to 21.6 (14.78 ± 5.97); $n = 59$	ND	ND
$T_h(\text{total})$	232 – 395 (288.1 ± 50.6); $n = 29$	220 – 359 (291.9 ± 29.3); $n = 94$	162 – 300 (266.6 ± 33.0); $n = 15$	195 – 230 (210.0 ± 13.8); $n = 6$	–
ρ_{total} (g/cm ³)	0.960 – 1.129 (1.076 ± 0.051); $n = 29$	0.914 – 1.060 (0.979 ± 0.030); $n = 94$	0.623 – 0.864 (0.781 ± 0.067); $n = 59$	0.995 – 1.028 (1.011 ± 0.014); $n = 6$	–
X_{CO_2}	0	0	0.03 – 0.07 (0.05 ± 0.01); $n = 59$	0	0

Note: All temperature data reported in °C. The % Vapor phase value considers the volume % of vapor, or all carbonic phases present (e.g., type 3 inclusions containing $L_{\text{CO}_2} + V_{\text{CO}_2}$); the remaining volume % is aqueous liquid. Salinity of the aqueous phase was determined via final ice/hydrohalite melting or halite dissolution temperatures using HOKIEFLINCS_H2O-NaCl (Steele-MacInnis et al. 2012) or final clathrate melting temperatures using the equation of Darling (1991). X_{CO_2} is bulk fluid inclusion values. Bulk density values were calculated by applying the equations of state outlined by Bakker (1999). The X_{CO_2} of inclusions were calculated using the program BULK (Bakker, 2003). Data in brackets represent averages ± 1σ standard deviation. The presence of CO₂ in type 3 inclusions was confirmed via Raman spectroscopy. Dashes represent the absence of data. Type 4b inclusions were not measured as part of this study. Abbreviations: FIA - fluid inclusion assemblage; S - secondary; T_e - eutectic (first ice melting) temperature; T_m(Ice) - final ice melting; T_m(HH) - final hydrohalite melting; T_m(Halite) - halite dissolution; T_m(Clath) - final clathrate dissociation; T_m(CO₂) – final melting of CO₂; T_h(CO₂) – CO₂ homogenization; T_h(total) – total homogenization. *values from Halter (1996)

Table 4–3. Summary of results from LA-ICP-MS analyses of FIAs in the East Kemptville deposit.

Salinity ² (wt% NaCl equiv.) Th(total) ³	Type-1 FIAs (<i>n</i> ¹ = 28)				Type-2 FIAs (<i>n</i> ¹ = 60)				Type-3 FIAs (<i>n</i> ¹ = 23)				Type-4 FIAs (<i>n</i> ¹ = 6)			
	30.42 ± 2.59				25.13 ± 1.04				19.69 ± 1.77				21.08 ± 1.58			
	288.07 ± 50.62				291.85 ± 29.32				266.60 ± 33.04				210.00 ± 13.84			
<i>Element</i>	<i>min</i>	<i>max</i>	<i>mean</i>	<i>median</i>	<i>min</i>	<i>max</i>	<i>mean</i>	<i>median</i>	<i>min</i>	<i>max</i>	<i>mean</i>	<i>median</i>	<i>min</i>	<i>max</i>	<i>mean</i>	<i>median</i>
Si	271	22482	4770	2985	444	34450	4117	2418	105	12617	3019	2158	403	4013	2054	2056
Al	29	4095	823	244	4	3839	384	213	28	1376	554	540	106	813	265	176
K	21523	65096	41614	44336	22617	48479	35905	37269	13585	50521	36901	37346	17675	32691	28076	28861
Ca	467	37915	4521	1753	88	14636	3094	1686	248	16210	4020	2590	412	10244	3378	2448
Fe	4408	31203	16492	15586	479	17836	5937	5199	2134	10991	6272	6797	4454	10593	7420	7120
Mn	3672	15468	10310	10966	498	9783	4168	3611	1634	6883	4531	4781	6102	11704	8633	8490
Mg	2	6023	574	44	5	1530	120	30	9	408	88	39	7	589	78	28
B	62	1543	559	468	133	3726	1230	1004	942	2274	1489	1535	498	996	718	676
S	552	106074	10827	7189	957	66412	8410	5156	250	32101	8650	5793	1012	10088	5097	5052
Li	72	954	299	254	99	1256	383	244	101	487	211	199	72	188	146	166
Sn	3	4289	410	23	1	135	16	8	1	504	69	13	2	14	10	12
W	1	29	12	11	0	66	17	4	0	64	15	4	1	23	6	4
Cu	1	4299	530	17	1	5375	200	18	2	932	141	21	3	29	11	10
Zn	4479	22957	9753	8664	689	7353	3537	3594	1769	5632	2835	2485	3863	5963	4967	5066
Mo	0	15	3	2	0	28	3	1	0	12	3	2	0	2	1	1
Ni	6	471	92	52	7	866	87	37	2	266	77	43	6	54	34	37
As	14	2072	198	103	3	781	159	55	4	467	128	45	14	124	40	36
Co	0	10	2	1	0	23	2	1	0	9	2	1	0	3	1	1
Ga	0	10	3	3	0	71	4	2	0	9	3	2	0	2	1	1
In	0	23	3	1	0	8	1	0	0	3	1	0	0	1	0	0
Ba	5	88	47	43	1	128	37	34	9	332	71	53	27	48	38	37
Rb	965	4081	2068	2071	853	2833	1698	1594	1040	2855	1669	1540	1040	1468	1266	1282
Sr	5	239	139	142	52	310	146	129	44	356	195	216	54	93	72	73
Cs	1647	4821	3208	3137	1049	3942	2220	2255	1548	3295	2336	2302	1487	2228	1901	1995
Nb	0	3	0	0	0	8	1	0	0	1	0	0	0	0	0	0
Ta	0	1	0	0	0	2	0	0	0	1	0	0	0	0	0	0
Pb	244	3050	1308	1377	184	2346	1004	830	427	1215	777	780	1287	2395	1799	1849
Th	0	375	15	0	0	1018	34	0	0	2877	165	0	0	308	30	0
U	0	18	1	0	0	2	0	0	0	3	0	0	0	0	0	0

Note: Elemental concentrations of quartz- and topaz-hosted fluid inclusions based on fluid type. Further subdivided and presented as box plots based on paragenetic stage in Figure 11A. ¹Total number of fluid inclusions measured, ²Salinities calculated for aqueous inclusions based on the equations of Bodnar (2003) and Steele-MacInnis et al. (2012), and from aqueous-carbonic inclusions based on equations of Steele-MacInnis (2018). ³Homogenization temperatures taken from microthermometric summaries (Table 4–2).

Table 4–4. Examples of Raman Spectra for vapour phases of type-3 aqueous-carbonic inclusions at East Kempville

Sample ID	Paragenetic stage	Peak Areas					Fermi diad spacing (cm ⁻¹)	CO ₂ Density (g/cm ³)*	All gas phases (ζ=1)			
		CO _{2v1}	CO _{2v2}	CH ₄	N ₂	H ₂ S			X _{CO2}	X _{CH4}	X _{N2}	X _{H2S}
EK-86-101_FIA1_Fi1	greisen-fill	14646	23848	4364	791	–	103.96	0.57	0.95	0.02	0.03	0.00
EK-86-101_FIA1_Fi2	greisen-fill	11825	19824	3475	541	–	103.45	0.34	0.95	0.02	0.03	0.00
EK-86-101_FIA2_Fi1	greisen-fill	7934	12312	6662	497	–	105.05	1.00	0.90	0.06	0.04	0.00
EK-86-101_FIA2_Fi2	greisen-fill	19045	32065	20494	1124	–	103.52	0.38	0.90	0.07	0.03	0.00
EK-86-101_FIA2_Fi3	greisen-fill	8510	14543	2935	359	–	105.05	1.00	0.95	0.02	0.02	0.00
EK-86-122A_FIA1_Fi1	greisen-fill	10763	16965	62989	869	–	103.51	0.37	0.66	0.30	0.03	0.00
EK-86-122A_FIA1_Fi2	greisen-fill	9696	15187	28244	–	–	103.43	0.33	0.81	0.19	0.00	0.00
EK-86-122A_FIA1_Fi3	greisen-fill	3096	5095	18836	202	–	103.45	0.34	0.67	0.31	0.03	0.00
EK-86-055_FIA1_Fi1	qtz-sulfide vein	23189	38330	13525	1758	–	103.47	0.35	0.92	0.04	0.04	0.00
EK-86-055_FIA1_Fi2	qtz-sulfide vein	11521	18702	8232	1054	–	103.52	0.38	0.90	0.05	0.05	0.00
EK-86-111-1_FIA2_Fi1	qtz-sulfide vein	1047	1511	942	63	–	102.61	0.01	0.90	0.07	0.04	0.00
EK-86-111-1_FIA2_Fi2	qtz-sulfide vein	1957	3181	1547	135	–	103.05	0.17	0.91	0.05	0.04	0.00
EK-86-111-1_FIA3_Fi1	qtz-sulfide vein	4246	7402	4614	368	–	103.43	0.33	0.88	0.07	0.05	0.00
EK-86-111-1_FIA3_Fi2	qtz-sulfide vein	1809	3354	1843	127	–	103.43	0.33	0.90	0.06	0.04	0.00
EK-90-17-2_FIA1_Fi1	qtz-carb vein	876	1412	39843	876	301	102.62	0.02	0.19	0.68	0.12	0.01
EK-90-17-2_FIA1_Fi2	qtz-carb vein	740	1127	89029	1891	749	102.62	0.02	0.08	0.77	0.14	0.01
EK-90-17-2_FIA2_Fi3	qtz-carb vein	1737	2565	111550	2266	1073	102.62	0.02	0.14	0.73	0.12	0.01
EK-90-17-2_FIA2_Fi4	qtz-carb vein	252	166	19140	275	–	102.04	-0.29	0.09	0.81	0.10	0.00

Note: Each analysis is of the vapour phase in quartz-hosted type 3 inclusions. Each sample hosted by quartz. *Density calculation the average of multiple studies: Wang et al. (2011), Kobayashi et al. (2012) after Yamamoto and Kagi (2006), Fall et al. (2011), Rosso and Bodnar (1995), Yamamoto et al. (2002). The error on averaging these calculations increases with lowest density, negative values reflect this. Measurement of X_{CO2} and X_{CH4} represent minimum values and measurements of X_{N2} and X_{H2S} represent maximum values. Abbreviations: Fi - fluid inclusion, qtz - quartz, carb - carbonate.

Table 4-5. $\delta^{18}\text{O}_{\text{V-SMOW}}$ Results from SIMS analyses on quartz in the East Kemptville Deposit.

Sample	Spot	Host Lithology	Comments	$\delta^{18}\text{O}$ (‰) quartz	$\delta^{18}\text{O}$ (‰) WR*	T (°C)	$\delta^{18}\text{O}$ (‰) H ₂ O
<i>Main Zone</i>							
BIC070	EK-1-1	Weakly altered EKL	in situ qtz w/ ksp	9.4		450-500	6.3 - 7.1
	EK-1-2			8.4			5.3 - 6.1
EK-86-071	EK-3-1	Weakly altered EKL	in situ qtz w/ alb	11.2		450-500	8.1 - 8.9
	EK-3-2			8.1			5.0 - 5.8
EK-86-023B	EK-4-1	Altered EKL	in situ qtz w/ alb-ser	10.7	8.6	385**	6.3
	EK-4-2			9.8		511**	7.6
EK-86-1084	EK-12-1	Massive greisen	in situ qtz w/ ser-sulfides	8.3		400-450	4.2 - 5.2
	EK-12-2			7.4			3.3 - 4.3
BIC038	EK-7-1	Zoned greisen	qtz; qtz-top-cst greisen fill	9.9		400-450	5.8 - 6.8
	EK-7-2			9.4			5.3 - 6.3
EK-86-159	EK-9-1	Zoned greisen	qtz; qtz-top-cst greisen fill	9.4		400-450	5.3 - 6.3
	EK-9-2			10.0			5.9 - 6.9
EK-86-170	EK-10-1	Zoned greisen	qtz; qtz-top-cst greisen fill	9.7		400-450	5.6 - 6.6
	EK-10-2			9.1			5.0 - 6.0
EK-86-110	EK-15-1	Zoned greisen	qtz; coarse qtz-cst-wlf infill	8.8		400-450	4.7 - 5.7
	EK-15-2			8.5			4.4 - 5.4
EK-86-112	EK-13-1	Qtz-cpy-sph vein	qtz; cross-cuts greisenized EKL	9.7		300-350	2.8 - 4.4
	EK-13-2			7.5			0.6 - 2.2
EK-86-155	EK-14-1	Qtz-cpy-sph vein	qtz; cross-cuts greisenized EKL	10.0		300-350	3.1 - 4.7
	EK-14-2			9.1			2.2 - 3.8
EK-86-106	EK-16-1	Qtz-cpy-sph vein	qtz; cross-cuts greisenized EKL	8.3		300-350	1.4 - 3.0
	EK-16-2			12.0			5.1 - 6.7
EK-93-22	EK-18-1	Qtz-asy vein	qtz; cross-cuts wall rock	10.0		300-350	3.1 - 4.7
	EK-18-2			8.1			1.2 - 2.8
EK-87-4	EK-20-1	Qtz-apt-alb vein	qtz; cross-cuts EKL	8.5		300-350	1.6 - 3.2
	EK-20-2			8.8			1.9 - 3.5
EK-86-23C	EK-2-1	Qtz vein	late; cross-cuts EKL	12.1	8.6	229**	2.2
	EK-2-2			11.6		281**	4.0
<i>Baby Zone</i>							
BIC032	EK-11-1	Massive greisen	in situ qtz w/ ser-sulfides	8.1		400-450	4.0 - 5.0
	EK-11-2			8.4			4.3 - 5.3
BIC003	EK-5-1	Matrix to IBX	euhedral qtz phenocryst	9.1		400-450	5.0 - 6.0
	EK-5-2			8.8			4.7 - 5.7
BIC026	EK-6-1	Cement to HBX	qtz; fragment-supported HBX	7.5		400-450	3.4 - 4.4
	EK-6-2			11.7			7.6 - 8.6

Note: Spot-to-spot reproducibility on the quartz standard = 0.6–0.9 ‰. Each analyses has a 1 σ error of 1.2 ‰. Multiple analyses for each sample represent spots across the respective quartz grain. *Whole-rock values of same EKL sample from Kontak et al. (1990b). **Calculated temperature of formation from Matsuhisa et al. (1979; quartz \rightleftharpoons H₂O) and Zhao and Zheng (2003; granite \rightleftharpoons H₂O) using Alpha-Delta software (Beaudoin and Therrien 2004). All other temperatures are assumed based on constraints by previous workers (described in text). $\delta^{18}\text{O}$ (‰)H₂O values derived from Matsuhisa et al. (1979; quartz \rightleftharpoons H₂O) using Alpha-Delta software (Beaudoin and Therrien 2004). Abbreviations: SIMS - secondary ion mass spectrometry; WR - Whole Rock; EKL - East Kemptville Leucogranite; IBX - igneous breccia of the East Kemptville Baby Zone (Chapter 3); HBX - hydrothermal breccia of the East Kemptville Baby Zone; qtz - quartz; ksp - potassium feldspar; alb - albite; ser - sericite; cpy - chalcopyrite; sph - sphalerite; cst - cassiterite; wlf - wolframite; aspy - arsenopyrite; apt - apatite.

Table 4–6. $\delta^{18}\text{O}_{\text{V-SMOW}}$ Results from TIMS analyses on minerals in the East Kemptville Deposit.

Sample	Host Lithology	Interpreted Temperature(°C)	Comments	$\delta^{18}\text{O}$ (‰)	$\delta^{18}\text{O}$ (‰)	$\delta^{18}\text{O}$ (‰)	Calculated	$\delta^{18}\text{O}$ (‰) H ₂ O
				quartz	cassiterite	albite	$\delta^{18}\text{O}$ (‰) H ₂ O	Calculation reference
86-005	Zoned greisen	400-450	qtz-top-cst	11.5			7.4	Matsuhisa et al. (1979)
86-076A	Zoned greisen	400-450	qtz-top-cst	11.2			7.1	Matsuhisa et al. (1979)
86-074	Zoned greisen	400-450	qtz-top-cst		4.2		8.0 - 9.3	Zhang et al. (1994)
86-154	Zoned greisen	400-450	qtz-top-cst-pyr		5.2		9.0 - 9.3	Zhang et al. (1994)
86-155	Qtz-sulfide vein	300-400	qtz-cpy-sph-py-po	10.5			3.6 - 6.4	Matsuhisa et al. (1979)
86-066	Qtz-cpy-sph vein	300-400	cross-cuts massive greisen	10.8			3.9 - 6.7	Matsuhisa et al. (1979)
86-122A	Qtz-sph vein	300-350	cross-cuts greisen	10.2			3.3 - 4.9	Matsuhisa et al. (1979)
86-019	Qtz-sph vein	300-350	cross-cuts EKL	10.5			3.6 - 5.2	Matsuhisa et al. (1979)
86-055	Qtz-sph vein	300-350	cross-cuts altered EKL	11.0			4.1 - 5.7	Matsuhisa et al. (1979)
86-102	Qtz-sph-cpy-trip vein	300-350	cross-cuts greisen	10.9			4.0 - 5.6	Matsuhisa et al. (1979)
86-178	Qtz-py-sph-cst-wlf vein	300-350		10.4			3.5 - 5.1	Matsuhisa et al. (1979)
87-1	Qtz-sph vein	300-350		10.4			3.5 - 5.1	Matsuhisa et al. (1979)
86-152	Qtz-sph-flr vein	300-350	cross-cuts greisen	10.7			2.8 - 5.4	Matsuhisa et al. (1979)
86-113	Qtz-alb-apt vein	382*	cross-cuts EKL	9.9		8.8	5.4	Matsuhisa et al. (1979)
86-101	Qtz-alb vein	258*	cross-cuts greisen	10.2		8.1	1.7	Matsuhisa et al. (1979)
86-110	Qtz-sph-cpy-trip vein	300-350	cross-cuts EKL	10.9			4.0 - 5.6	Matsuhisa et al. (1979)
86-112	Qtz-pyr-clay vein	300-350	late; cross-cuts EKL	11.1			4.2 - 5.8	Matsuhisa et al. (1979)
86-111	Qtz-sph-py-clay vein	300-350	late; cross-cuts EKL	13.0			6.1 - 7.7	Matsuhisa et al. (1979)

Note: All samples collected from the Main Zone. Temperature estimates are discussed in the text and constrained for the quartz in zoned greisens (Halter and Williams-Jones, 1999; this study), sulfide-bearing veins (Kontak, 1990a; Kontak, 1994; Willson, 2019; this study). The remaining stages of the paragenesis are assumed to have similar range in temperatures to the sulfide-bearing veins. *Equilibration temperatures were calculated from quartz-albite pairs using Matsuhisa et al. (1979; $\text{quartz} \rightleftharpoons \text{H}_2\text{O}$) and O'Neil and Taylor (1967; $\text{H}_2\text{O} \rightleftharpoons \text{albite-K-Feldspar}$) using Alpha-Delta software (Beaudoin and Therrien 2004). Abbreviations: TIMS - thermal ionization mass spectrometry; alb - albite; apt - apatite; cpy - chalcopyrite; cst - cassiterite; flr - fluorite; pyr - pyrite; qtz - quartz; sph - sphalerite; top - topaz; wlf - wolframite.

Chapter 5

5.1 Conclusions

This thesis documents and characterizes tin mineralization in a mesothermal intrusive setting, providing an interpretation on the conditions needed to form such deposits. The thesis also characterizes a magmatic evolution and emplacement history of the host batholith and, based on this, the implications for tin fertility in this part of the Canadian Appalachian Sn-W metallotect. In summary, the thesis provides the following:

- Chapter 2 presents a new understanding of the emplacement history for the large peraluminous South Mountain Batholith and its genetic link to tin mineralized centres in the Canadian Appalachians. Evidence from comprehensive U-Pb zircon dating across the batholith indicates it was constructed from a long-lived magmatic system (~8 Myr of overlapping magmatic activity), but crystallized in two main intrusive events: 1) a bulk of the less evolved granodiorite phases between 378.7 ± 0.6 and 375.6 ± 0.5 Ma, and 2) the more highly fractionated phases between 375.4 ± 0.8 and 371.8 ± 0.8 Ma. The zircon in the batholith record multiple crystallization events that preceded final emplacement by a margin of error that often overlaps with the crystallization age interpretation; these ages (dominantly between ~380 and 390 Ma) represent crystallization of early partial melts. These early crystallization ages indicate a prolonged history of heating and melt underplating in this region. A majority of the SMB evolved from a melt derived from a metasomatized mantle that underwent significant

contamination by Meguma terrane metasedimentary rocks and partially by an early arc crust similar in age to the Avalon terrane. The Davis Lake Pluton (DLP) underwent similar contamination, although it and subsequent intermediate to mafic intrusions in southwest Nova Scotia likely evolved from a lower crustal source, thus different than the source for the rest of the batholith and a source enriched in Sn to allow for multiple mineralization occurrences localized to the SW part of the terrane.

Chapter 3 presents a detailed interpretation for distinct alteration stages at East Kemptville that is identified petrographically and geochemically. These stages include: 1) deuteric alteration through the deposit area represented by weak pervasive partial replacement of Ca-rich plagioclase and K-feldspar by albite and sericite with consequential apatite precipitation; 2) strong to intense sericitization and muscovite \pm Fe-Li mica formation (early greisens) along brittle fractures through the deposit; and 3) complete replacement of the host EKL by quartz and topaz with lesser muscovite and ore mineralization, localized to well developed greisens. Greisens occur as two different styles that are more prominent in their respective ore zones at East Kemptville, with the Baby Zone containing massive greisens and the Main Zone zoned greisens. The character of each greisen style is largely controlled by the main structure through the deposit and the availability of fractures for increased fluid-rock interaction. Whereas massive greisens form among dense brittle fractures in the EKL, zoned greisens follow vertical brittle fracture planes that are oriented sub-parallel to the dominant fault zone crosscutting the deposit.

The contrast between these mineralization styles may be the result of a step-over along the above fault zone that localized extensive brittle features to accommodate strain in the Baby Zone area and thus acted as a preferred conduit for higher fluid flux in this area. Given the mesothermal conditions at the time of formation, however, the ore fluids were still constrained by overlying lithostatic pressures, and thus either escaped laterally, without reacting to wall-rocks, or accumulated in the EKL ore zones. New interpreted mineralization ages at East Kemptville define three general ages, the earliest of which includes: previously interpreted crystallization of the host EKL, determined from pegmatite molybdenite at ca. 376 Ma; U-Pb cassiterite at 370 ± 4 Ma and Re-Os molybdenite at 371 ± 2.0 Ma from greisens and veins, respectively, in the Main Zone; and ≥ 10 Ma younger mineralization that is associated with crosscutting veins introduced along the deposit-hosting fault zone; i.e., Re-Os molybdenite in veinlets at 354.9 ± 2.0 Ma and 343.7 ± 1.7 Ma. The latter of these ages is similar to the 347 ± 12 Ma obtained for cassiterite from the nearby metasedimentary rock-hosted Duck Pond skarn-style deposit. Although a reliable U-Pb cassiterite age has yet to be obtained from the Baby Zone, the spectrum of younger ages associated with veins suggest many features of the Baby Zone were not temporally equivalent to the Main Zone, and thus the contrast in character between the ore zones may be the result of continued magmatic-hydrothermal activity along the host fault zone and mineralization synchronous with fault propagation between the main over-stepping fault zones through the deposit.

- Chapter 4 presents abundant fluid inclusion evidence of repetitive changes to pressure during the formation of the East Kemptville deposit through its paragenesis; indicative of continued mechanical fracturing as the hydrothermal system cooled. The early, anomalously saline orthomagmatic fluids present at East Kemptville are interpreted to be the result of exsolution of Cl-enriched aqueous fluids at depth for the highly fractionated and F-rich host leucogranite. The in situ $\delta^{18}\text{O}_{\text{quartz}}$ values from mineralized greisens in this study and the interpreted range of precipitation temperatures suggest mixing and equilibration between fluids exsolved from the host rock leucogranite and externally derived magmatic fluids, both enriched in ore elements. Fluid-rock interaction at East Kemptville is interpreted to transition from rock-dominant in the early mineralization stages to fluid-dominant in the main mineralization stage (i.e., during coarse cassiterite and base-metal sulfide precipitation). Paragenetically late fluids in the mineralizing system show evidence of a minor CO_2 component that is not recognized in any fluid type associated to paragenetic stages prior to veining; these reduced fluids were derived from an external magmatic source, likely at depth, and were partially equilibrated to surrounding wall-rocks. The resultant precipitation of late coarse cassiterite and base-metal sulfide mineralization occurred in greisen cores, vugs, and tensional veins at East Kemptville.

5.2 Future Work

In Chapter 2, evidence for structural controls on the two ore zones in the East Kemptville deposit suggest the East Kemptville–East Dalhousie Shear Zone (EKEDSZ) was the primary corridor for

mineralizing fluids and that releasing bends along this shear zone host the highest grade mineralization. Therefore, future work should be aimed at the trace of this fault zone and the identification of similar step-over features that host abundant fracturing necessary for hosting greisen formation. This identification is crucial for further Sn-Zn-Cu-Ag-In exploration.

Additionally, the geochemistry of the least altered East Kemptville leucogranite (EKL) samples in the deposit suggest a fractionation vector between the DLP and the host rocks to the deposit is missing; this interpretation contrasts with previous interpretations on the geochemistry of the DLP, which used Nb/Ta as a fractionation vector. A review of the DLP would benefit from additional sampling with a spatial respect to the EKEDSZ to evaluate the relative influence of alteration and fractional crystallization of the DLP trace element chemistry along this structural corridor. Lastly, this study is awaiting results from U-Pb cassiterite age-dating in the Baby Zone greisens as evidence for the potential temporal contrast between the two ore zones.

Chapter 3 presented evidence for physiochemical changes in mineralizing fluids through the East Kemptville deposit paragenesis. This study, however, was unable to identify measurable fluid inclusion assemblages in the Baby Zone of the deposit, and thus the work was constrained to greisens and veins from the Main Zone. Future work should therefore be aimed at identifying and characterizing fluid inclusion assemblages from the Baby Zone, where possible; given the brecciation present in the ore zone, the presence of phase separation (boiling) in fluid inclusions should be tested. The presence of graphite in the EKEDSZ as well as a CO₂ volatile presence in

later stage fluids warrants a genetic investigation of the carbonic component in mineralizing fluids through C isotope analysis.

Chapter 4 presented evidence for a younger, more juvenile signature for zircon from the DLP that hosts the East Kemptville mineralization, deposited along a regional shear zone that is interpreted to control the emplacement of the SMB. A follow up study on the SMB should focus on the leucogranite phases that intrude along the regional shear zones to further constrain the timing of the most evolved plutonic phases that are associated with mineralization. To further investigate the juvenile signature to these later magmas that has been indicated by this study, and evaluate contamination relative to the rest of the SMB, an investigation into melt inclusions within zircon of the SMB would be beneficial to the understanding of the early magmatic evolution.